Strukturuntersuchungen an der Wechselwirkung zwischen humanem Prionprotein und Amyloid-β-Oligomeren mittels Festkörper-NMR-Spektroskopie

Inaugural-Dissertation

zur Erlangung des Doktorgrades
der Mathematisch-Naturwissenschaftlichen Fakultät
der Heinrich-Heine-Universität Düsseldorf

vorgelegt von

Anna Stephanie König geb. Schulze
aus Zittau

Jülich, Januar 2021

aus dem Institut für Physikalische Biologie
der Heinrich-Heine-Universität Düsseldorf

Gedruckt mit der Genehmigung der
Mathematisch-Naturwissenschaftlichen Fakultät der
Heinrich-Heine-Universität Düsseldorf

Berichterstatter:

1. Prof. Dr. Henrike Heise

2. Prof. Dr. Birgit Strodel

Tag der mündlichen Prüfung: 24. 02. 2021

„Ich fühle mich nicht zu dem Glauben verpflichtet, dass derselbe Gott, der uns mit Sinnen, Vernunft und Verstand ausgestattet hat, von uns verlangt, dieselben nicht zu benutzen."

Galileo Galilei

Inhalt

Abbildungsverzeichnis

Abkürzungsverzeichnis

AD	*Alzheimer's disease*	Alzheimersche Demenz
ADDLs	*Aβ-derived diffusible ligands*	
AFM	*Atomic force microscopy*	Rasterkraftmikroskopie
AICD	*Amyloid Precursor Protein Intracellular Domain*	Intrazelluläre Domäne des APP
APP	*Amyloid Precursor Protein*	Amyloid-Vorläuferprotein
Aβ		Amyloid-β
BSE		Bovine spongiforme Enzephalopathie
BVPrP	*Bank-vole Prion Protein*	Rötelmaus-Prionprotein
C83		C-terminales APP-Fragment mit 83 Aminosäureresten
C99		C-terminales APP-Fragment mit 99 Aminosäureresten
CP	*Cross polarization*	Kreuzpolarisation
C-Terminus		Carboxy-Terminus
DARR	*Dipolar Assisted Rotational Resonance*	
DE	*Direct excitation*	Direktanregung
DGZ		Dichtegradientenzentrifugation
DMSO		Dimethylsulfoxid
DNS		Desoxyribonukleinsäure
EM	*Electron microscopy*	Elektronenmikroskopie
FAD	*Familial Alzheimer's disease*	Familiäre Alzheimersche Erkrankung
FID	*Free induction decay*	Freier Induktionsabfall
FUS	*Fused in Sarcoma*	
GPI		Glycosylphosphatidylinositol
HET-s	*Heterokaryon incompatibility protein s*	

huPrP		humanes Prionprotein
INEPT	*Insensitive nuclei enhanced by polarization transfer*	
K		Kelvin
kDa		Kilodalton
kHz		Kilohertz
LC	*low-complexity*	
MAS	*Magic Angle Spinning*	Rotation im magischen Winkel
MDa		Megadalton
mGluR5	*Metabotropic glutamate receptor 5*	metabotroper Glutamatrezeptor 5
NMDA		N-Methyl-D-Aspartat
NMR	*Nuclear Magnetic Resonance*	Kernmagnetische Resonanz
N-Terminus		Amino-Terminus
PDSD	*proton driven spin diffusion*	
pH	lat. *potentia hydrogenii*	
PMCA	*protein misfolding cyclic amplification*	
PMEL	*pre-melanosomal protein*	premelanosomales Protein
PMSA	*protein misfolding shaking amplification*	
PrP		Prionprotein
RNA	*ribonucleic acid*	Ribonukleinsäure
RP-HPLC	*reversed phases high performance liquid chromatography*	Umkehrphasen-Hochleistungsflüssigkeits-chromatographie
SAD	*Sporadic Alzheimer's disease*	Sporadische Alzheimersche Erkrankung
sAPP	*soluble APP*	lösliches APP-Fragment
SDS	*sodium dodecyl sulfate*	Natriumdodecylsulfat
SPC-5	*supercycled permutationally offset stabilized C5*	
TgVole		transgenes, Rötelmaus-PrP exprimierendes Mausmodell

Zusammenfassung

Sowohl das Prionprotein (PrP) als auch Amyloid-β (Aβ) kann fehlfalten und neurotoxische Aggregate bilden, die eine wichtige Rolle in der Pathogenese neurodegenerativer Erkrankungen spielen. Aβ-Oligomere wurden als neurotoxische Substanzen in der Pathogenese der Alzheimerschen Demenz (AD) identifiziert, während fehlgefaltetes PrP als infektiöses Protein (Prion) transmissible spongiforme Enzephalopathien in verschiedenen Spezies auslösen kann. Humanes PrP (huPrP) ist außerdem ein Rezeptor für Aβ-Oligomere in AD. In einer vorangegangenen, in dieser Dissertation aufgeführten Studie konnten wir diese Interaktion biochemisch nachweisen und die Entstehung großer Heteroaggregate zeigen.

In dieser Dissertation wird die Interaktion zwischen dem huPrP und Aβ(1-42)-Oligomeren mittels Festkörper-MAS-NMR-Spektroskopie untersucht. Dabei werden verschiedene rekombinant hergestellte Proben des huPrP-Aβ(1-42)-Oligomeren-Komplexes eingesetzt, bei welchem jeweils entweder huPrP oder die Aβ-Oligomere uniform ^{13}C,^{15}N-markiert sind. Obwohl eine ortsspezifische Resonanzzuordnung für huPrP wegen des hohen Grades an Resonanzüberlappung und der geringen Signaldispersion nicht möglich war, konnten wir folgende Schlüsse ziehen: Der N-terminale Teil von huPrP ist immobilisiert und deswegen in dipolaren Spektren sichtbar. Die chemischen Verschiebungen der meisten N-terminalen Reste sind charakteristisch für das Fehlen einer Sekundärstruktur (*Random Coil*). Allerdings gehen einige Ala- und Val-Reste um Position 115 während der Komplexbildung zu α-helikalen Konformationen über. Der gut definierte C-terminale Teil des huPrP ist größtenteils ebenfalls starr, aber verliert seine Sekundärstruktur in den letzten beiden α-Helices. Die sekundären chemischen Verschiebungen der Aβ(1-42)-Oligomere im Komplex mit huPrP zeigen beträchtlichen β-Faltblatt-Anteil. Außerdem besitzen die einzelnen Aβ(1-42)-Moleküle im Komplex unterschiedliche Konformationen. Unser ^{13}C-^{13}C-Korrelationsspektrum (*Proton Driven Spin Diffusion*, PDSD) der Aβ(1-42)-Oligomere im Komplex mit huPrP überlappt stark mit den Resonanzen verschiedener publizierter Aβ(1-42)-(Proto)Fibrillenstrukturen. Außerdem wird vermutet, dass Oligomere bereits die Sekundärstruktur von ausgewachsenen Fibrillen besitzen. Somit könnte der Grund für diese nicht-äquivalenten Konformere der Aβ(1-42)-Oligomere sein, dass verschiedene (Proto)Fibrillentypen (konformationeller Polymorphismus) bereits in der Struktur der Oligomere angelegt sind.

Im zweiten Teil dieser Dissertation wurde eine Rötelmaus-PrP-Fibrille mittels Festkörper-MAS-NMR-Spektroskopie untersucht. Dabei konnten keine hoch-flexiblen Bereiche, aber viele Resonanzen im zweidimensionalen PDSD-Spektrum beobachtet werden, u. A. unterscheidbare Signale von Ala, Thr, Ile und Val. Außerdem zeigte der überwiegende Teil der Resonanzen β-Strang-ähnliche chemische Verschiebungen, was zur erwarteten Struktur einer Fibrille passt. Dadurch konnte gezeigt werden, dass die neuentwickelte PMSA-Methode zur Proteinherstellung größerer Mengen mehrfach-markierter Probe, wie sie für die Festkörper-MAS-NMR-Spektroskopie (und potentiell andere Strukturuntersuchungsmethoden) nötig sind, geeignet ist. Die PMSA-Methode nutzt dabei Schüttler anstelle Ultraschalls zur Vervielfältigung eines Prionen-Stammes.

Abstract

Both prion protein (PrP) and amyloid beta (Aβ) can misfold and form neurotoxic assemblies that play important roles in the pathogenesis of neurodegenerative disorders. Aβ oligomers have been identified as neurotoxic agents relevant for the pathogenesis of Alzheimer's disease (AD), whereas misfolded PrP can cause transmissible spongiform encephalopathies as a proteinaceous infectious particle (prion) in various species. Additionally, human PrP (huPrP) is a receptor for oligomeric Aβ in AD. In a previous study, listed in this dissertation, we were able to confirm this interaction biochemically and to demonstrate the formation of large heteroassemblies.

In this dissertation, we investigated the interaction between huPrP and Aβ(1-42) oligomers by solid-state MAS NMR spectroscopy using different samples of Aβ(1-42) oligomers complexed by recombinant huPrP, in which either huPrP or Aβ(1-42) was uniformly ^{13}C, ^{15}N isotope labeled. Although a site-specific resonance assignment for huPrP was not possible due to the high degree of resonance overlap and low signal dispersion, we could conclude: The N-terminal part of huPrP in the complex is immobilized and therefore visible in dipolar spectra. The chemical shifts for most N-terminal residues are characteristic for absence of a regular secondary structure (random coil). However, some Ala and Val residues around position 115 undergo transition to an α-helical conformation upon complex formation. Most of the well-defined C-terminal part of huPrP is part of the rigid complex, but shows a loss in regular secondary structure in the last two α-helices. For Aβ(1-42) oligomers in complex with huPrP, secondary chemical shifts point towards substantial β-sheet content. Additionally, Aβ(1-42) molecules within the complex do not have identical conformations. Our ^{13}C-^{13}C correlation spectrum (proton driven spin diffusion, PDSD) of Aβ(1-42) oligomers in complex with huPrP highly overlaps with different published Aβ(1-42) protofibril and fibril structures. Additionally, it is expected that oligomers already show the secondary structure of major fibrils. Therefore these inequivalent conformers of the Aβ(1-42) oligomers might be due to different protofibril and fibril types (polymorphism) inherent in the structure of the oligomers.

In a second project of this dissertation, a bank vole PrP fibril (BVPrP) was investigated using solid-state NMR MAS spectroscopy. Thereby, we did not observe highly flexible parts in the BVPrP fibril, rather a lot of resonances in a 2D PDSD spectrum, whereof

some could be distinguished to be Ala, Thr, Ile and Val. Most of these resonances showed β-strand-like chemical shifts, underlining the existence of a fibril. These results indicate that a newly developed method using shaking instead of sonication for amplification of one prion strain (PMSA) is useful for the production of large amounts of labeled material, as it is necessary for solid-state MAS NMR spectroscopy and other structure determination methods.

1 Einleitung

Der technische und medizinische Fortschritt des letztens Jahrhunderts bewirkte, zusammen mit einer Politik des Friedens der letzten drei Jahrzehnte in West- und Mitteleuropa, einen zunehmenden Wohlstand. Daraus folgte eine verbesserte medizinische Versorgung in Europa und allen anderen Teilen der ersten Welt. Dies führt wiederum zu einer deutlich erhöhten Lebenserwartung gegenüber früherer Generation, z. B. der unserer Urgroßeltern. Gleichzeitig treten nun gehäuft Erkrankungen auf, die man früher einfach als einen Teil des Alterungsprozesses angesehen hat. Die wissenschaftlichen Entdeckungen der letzten Jahrzehnte legen allerdings nahe, dass dies keineswegs rein natürliche Vorgänge sind, sondern dass es sich um Erkrankungen im Gehirn, sogenannte neurodegenerative Erkrankungen (z. B. die Alzheimersche Demenz oder Parkinson'sche Erkrankung), handelt. Ein Grund für diese Erkenntnis ist der Umstand, dass man auch ohne solcherlei Symptome zu zeigen, sehr alt werden kann. Hat man noch in den 70er und 80er Jahren vermehrt auftretende Depressionen im mittleren Alter lieber verschwiegen und nicht behandelt, werden sie heute als erstes Symptom der Parkinson'schen Erkrankung genannt.

Das gehäufte Auftreten von Erkrankungen wie der Parkinson'schen Erkrankung und Demenzen, hauptsächlich der Alzheimerschen Demenz, führt neben der hohen Belastung für unser Sozialsystem und der hohen Auslastung der Pflegeheime und Krankenhäuser, auch zu weitreichender psychischer und seelischer Belastung des Patienten und seiner Angehörigen. Es lässt sich kaum nachvollziehen, wie traumatisch das Wissen um die eigene Vergesslichkeit, das Gefühl der Nutzlosigkeit, des ständigen Scheiterns und Zur-Last-fallens für den Patienten sein muss, und auf der anderen Seite wie belastend es ist, den Persönlichkeitsverlust eines nahen Angehörigen mitansehen zu müssen, ganz zu schweigen von der Belastung, diesen Menschen zu versorgen und zu pflegen.

Doch trotz all unseres technischen und medizinischen Fortschritts sind Erkrankungen, die das Gehirn betreffen, noch kaum behandelbar, geschweige denn heilbar. Allenfalls ist es möglich, den Verlauf hinauszuzögern. Die Unheilbarkeit dieser Erkrankungen ist auch dem Umstand geschuldet, dass wir das Gehirn in seiner Komplexität und seinem genauen Zusammenspiel mit anderen Organen (z. B. dem Darm) bisher nur wenig verstehen. Forschung auf dem Gebiet der neurodegenerativen Erkrankungen und die

Erforschung des Gehirns sind also Forschungen direkt für den Menschen und diese Fragestellungen bedürfen deshalb einer dringenden Lösung. Diese Doktorarbeit möchte einen kleinen Teil dazu beitragen.

Wenn man sich eingehender mit neurodegenerativen Erkrankungen und ihren zugrundeliegenden Mechanismen beschäftigt, stößt man zuerst auf Proteine, ihre Funktion im Gehirn (soweit bekannt) und ihre Fehlfaltung und Aggregation.

1.1 Fehlfaltung und Aggregation von Proteinen

Proteine sind einer der wichtigsten Bestandteile höherer Organismen, da sie an allen lebenswichtigen Prozessen, wie Stoff- und Energiewechsel, Fortpflanzung und Vererbung sowie Enzymkatalyse beteiligt sind. Sie bestehen aus den zwanzig natürlich vorkommenden proteinogenen Aminosäuren in unterschiedlichen Anteilen und können beim Menschen eine molekulare Masse von bis zu 3,6 MDa (Titin, größtes bekanntes menschliches Protein) aufweisen. Diese durch die sogenannte Peptidbindung, ähnlich der Perlen einer Perlenkette, verbundenen Aminosäuren können anschließend eine bestimmte Sekundärstruktur ausbilden. Zu den Sekundärstrukturen gehören hauptsächlich α-Helices und β-Faltblätter (neben 3_{10}- und π-Helices, Kollagentrippelhelices, β-Schleifen und β-Helices[1,2]). Indes besitzt nicht jedes Protein eine festgelegte Sekundärstruktur, sondern kann auch ungefaltet vorliegen. Diese Proteine oder Proteinabschnitte nennt man intrinsisch ungeordnet (sogenannte *intrinsically disordered proteins,* IDPs) und ihre Struktur wird als *Random Coil* bezeichnet, was bedeutet, dass im zeitlichen Mittel sowohl α-helix- als auch β-faltblatt-artige Strukturen auftreten. Im NMR-Spektrum zeigen sich in einem solchen Fall gemittelte chemische Verschiebungen[3-7], die bei niedrigen Temperaturen (100 K) in α-helix- und β-faltblatt-artige chemische Verschiebungen ausgefroren werden können[8,9]. Im nativen Zustand besitzt ein Protein eine bestimmte dreidimensionale Faltung, die Tertiärstruktur, bei Assoziation mehrerer Proteine auch eine Quartärstruktur, die der Sekundärstruktur übergeordnet und für die sehr spezifische Funktion des Proteins erforderlich sind.

Durch bestimmte Einflüsse kann ein Protein seine Quartär-, Tertiär- und Sekundärstruktur verlieren und eine fehlgefaltete Struktur einnehmen. Dies führt einerseits zum Verlust seiner spezifischen Funktion, kann aber andererseits zur

Aggregation führen, die dem Organismus zusätzlich schadet und mit verschiedensten Erkrankungen in Verbindung steht[10-12].

1.1.1 Allgemeiner Mechanismus

Unter Aggregation versteht man eine Kaskade von Mechanismen, die zum Fibrillieren eines Proteins führen. Dabei lagern sich mehrere Monomere eines Proteins, das seine Sekundärstruktur verloren hat, zu sogenannten Oligomeren zusammen, wobei ein Oligomer in seiner Größe (Dimere bis 50-mere[13]) und Struktur stark variieren kann. Diesen Prozess bezeichnet man als primäre Nukleation (siehe **Abbildung 1A**). Er ist durch ein Gleichgewicht zwischen Monomer und Oligomer gekennzeichnet und findet bei einigen Erkrankungen jahrelang unbemerkt statt, ohne dass der Patient krankheitsspezifische Symptome zeigt. Wird eine bestimmte Oligomergröße überschritten, entstehen durch Anlagerung weiterer Monomere, der Elongation (siehe **Abbildung 1A** und **B**), sogenannte Amyloid-Fibrillen (bestehend aus Tausenden bis Millionen von Monomeren[13]), die wiederum fragmentieren können. Es gibt allerdings auch sogenannte *off-pathway* (englisch für „vom Pfad abweichend") Oligomere, die nicht in der Lage sind, sich in Fibrillen umzuwandeln. Aβ(1-42)-*off-pathway*-Oligomer-Präparate werden häufig genutzt, wenn Signalwege im Gehirn, Toxizität oder Struktur von Aβ(1-42)-Oligomeren untersucht werden sollen. Zur Aggregationsförderung werden entweder DMSO oder SDS, letzteres mit einer Konzentration kurz unter der kritischen Mizellbildungskonzentration, genutzt. Bei ersterem entstehen sogenannte *Aβ-derived diffusible ligands* (ADDLs), bei letzterem sogenannte Globulomäre und 150-kDa-Oligomere[13]. Eine Vorstufe der Amyloid-Fibrillen hingegen sind die sogenannten Protofibrillen (bestehend aus hunderten von Monomeren[13-15]). Ein weiterer Prozess zur Entstehung von Amyloid-Fibrillen ist die sekundäre Nukleation, bei welcher sich Monomere an der Oberfläche bestehender Fibrillen zusammenlagern und Oligomere bilden, die dann als Keim für reife Amyloid-Fibrillen dienen (siehe **Abbildung 1C**). An dieser Stelle sollte allerdings auch erwähnt werden, dass in den letzten Jahren berechtigte Zweifel darüber erwuchsen, ob Oligomere und Protofibrillen tatsächlich eine Vorstufe von Amyloid-Fibrillen sind. Hasecke et al. ermittelten, dass Oligomere, die sie als „globuläre Oligomere" und „curvilineare Fibrillen" bezeichnen, oberhalb einer kritischen Monomerkonzentration entstehen, allerdings *off-pathway* sind, da sie sich nicht in Fibrillen umwandeln können. Im Gegenteil behindern sie eher

die Fibrillenentstehung, da sie die Monomerbindestellen der Amyloid-Fibrillen, an welchen sekundäre Nukleation stattfinden kann, blockieren[16-18].

A
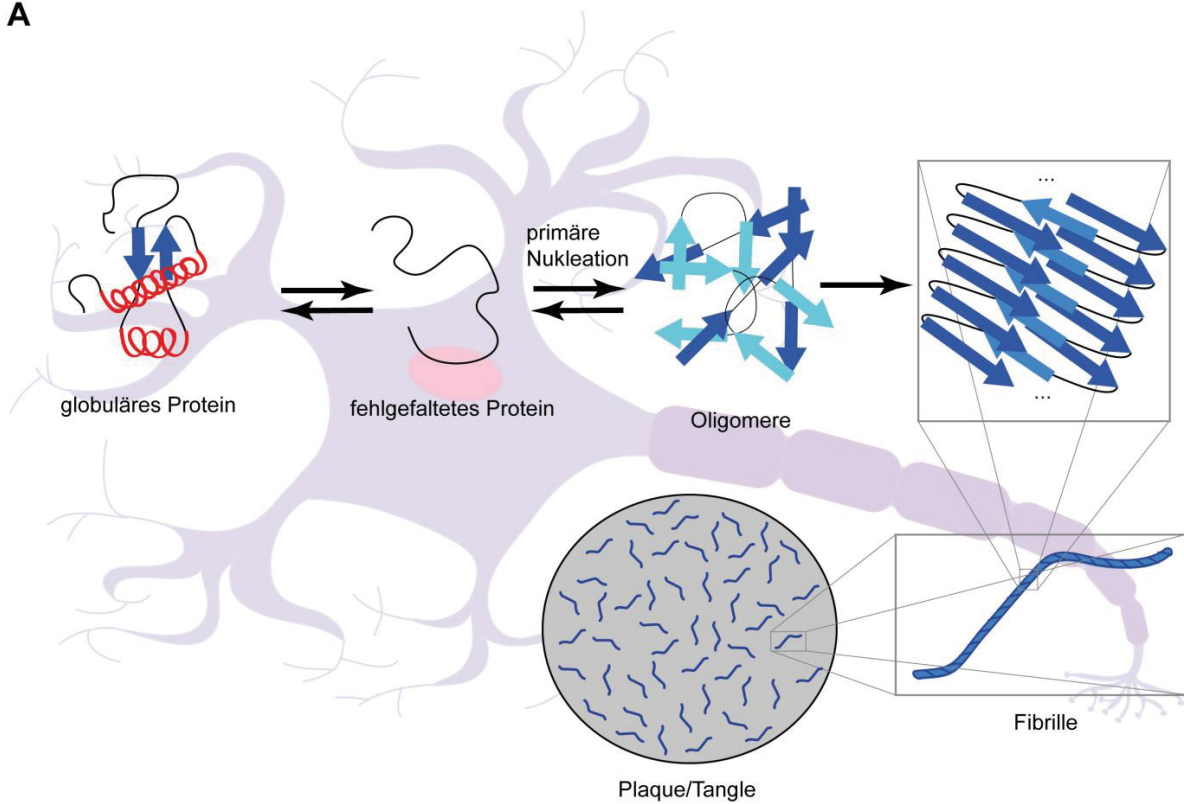
B
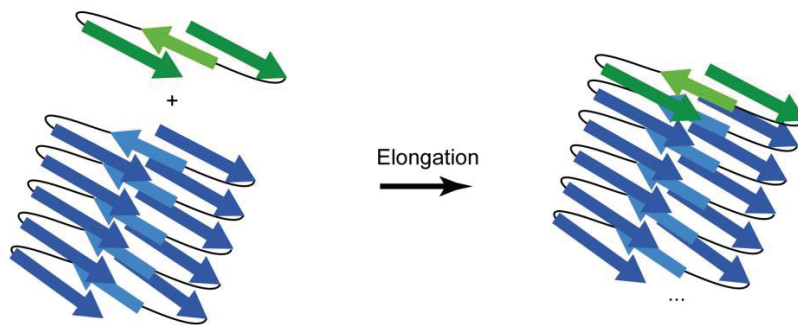
C
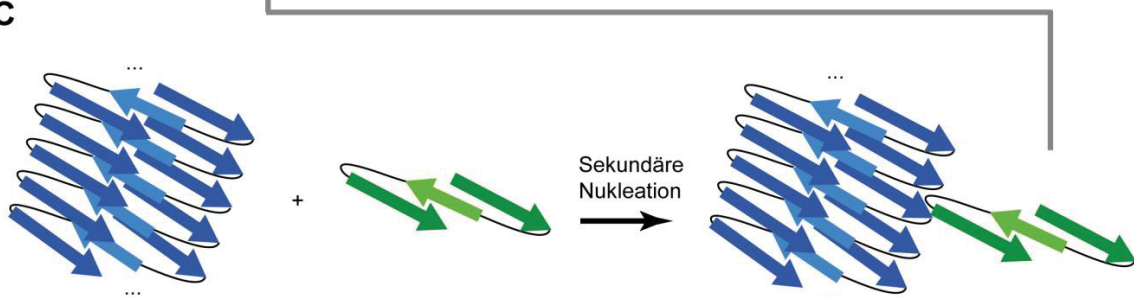
Abbildung 1: **A** *Schematische Darstellung der einzelnen Aggregationsschritte* **B** *Schematische Darstellung der Elongation* **C** *Schematische Darstellung der sekundären Nukleation. α-Helices sind als rote Spiralen dargestellt, β-Faltblätter jeweils als blaue oder*

grüne Pfeile. Anzahl und genaue Anordnung der α-Helices und β-Faltblätter sind beispielhaft zu verstehen.

Amyloid-Fibrillen sind gekennzeichnet durch eine hochgeordnete, im Rasterkraftmikroskop auflösbare faserartige Struktur mit hohem β-Faltblatt-Anteil in der Sekundärstruktur. Ihre Größe beträgt mehrere Nanometer im Durchmesser und einige Mikrometer in der Länge[19].

Eisenberg et al. unterscheiden vier verschiedene Möglichkeiten der β-Faltblatt-Anordnung, die sich jeweils in zwei Möglichkeiten aufteilen: erstens *in-register* oder *out-of-register*, zweitens *parallel* oder *antiparallel*, drittens *face-to-face* oder *face-to-back* und viertens *up-up* oder *up-down* (siehe **Abbildung 2**)[20]. Da *out-of-register*-Anordnungen eher selten sind, lassen sich Fibrillen in acht Klassen (zwei Eigenschaften in drei Klassen: $2^3=8$) einordnen, von denen sieben (mit Ausnahme der *parallel-, face-to-face-, up-down*-Anordnung) in Proteinfragmenten aus sechs bis acht Aminosäuren experimentell nachgewiesen werden konnten[20]. Da es sich allerdings um Peptidkristalle handelt, ist eine Übertragung auf reife Fibrillen nicht eins zu eins möglich. Dessen ungeachtet lassen sich diese acht Klassen zum Vergleich verschiedener Fibrillen heranziehen.
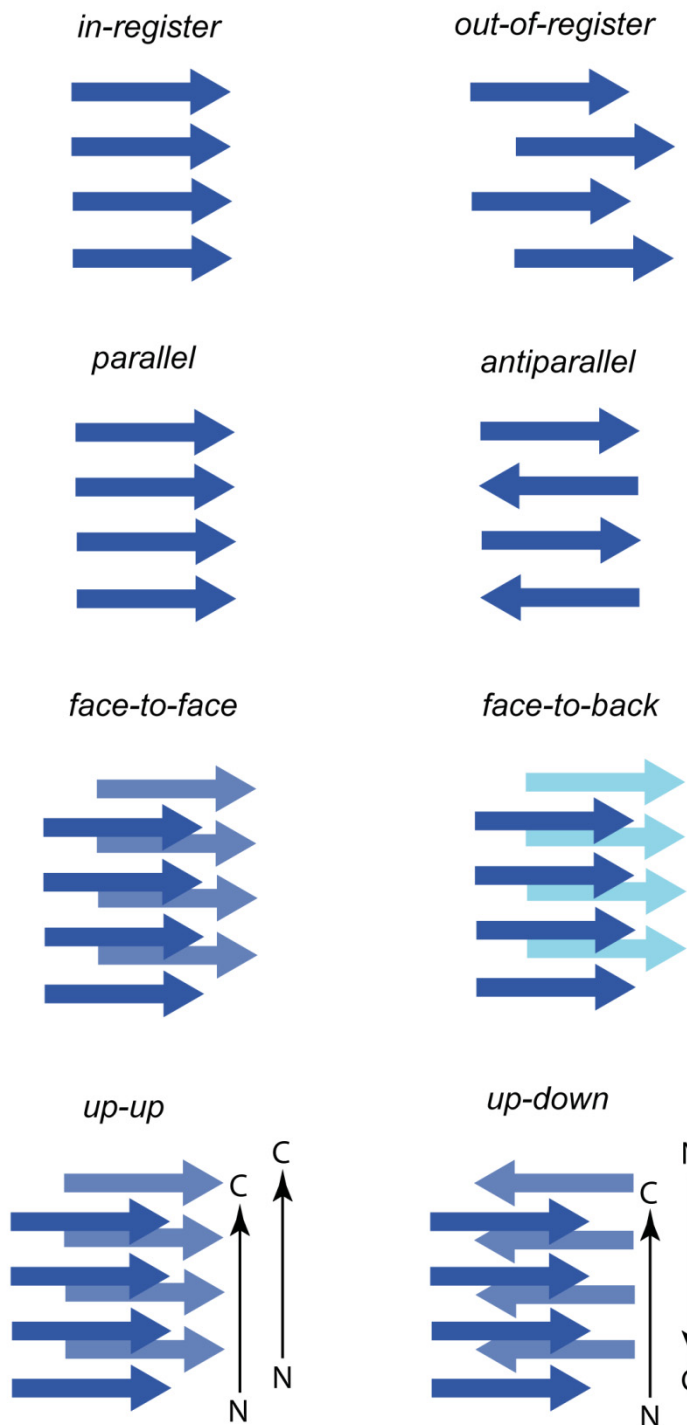
Abbildung 2: *Die vier Möglichkeiten der β-Faltblatt-Anordnung nach Eisenberg et al.[20], die sich in jeweils zwei Möglichkeiten aufteilen. β-Faltblätter sind als blaue Pfeile dargestellt, die Vorderseite dunkelblau, die Rückseite hellblau.*

Während fast alle Proteine unter bestimmten Bedingungen fibrillieren können[12,21], bilden etwa 50 Proteine unter physiologischen Bedingungen Amyloid-Fibrillen[22], darunter Aβ(1-40)[23-31], Aβ(1-42)[32-36], Tau[37-39], PrP[40-44], α-Synuclein[45-47], *Islet amyloid polypeptide* (IAPP)[48-51], Transthyretin[52-54], β2-Mikroglobulin[55,56], HET-s-Prionen[57,58],

Prionen aus verschiedenen Hefen[59-63], Curli[64,65] und die LC-Domäne des RNA-Bindungsproteins FUS[66]. Nach heutigem Wissensstand besitzen die meisten pathogenen Amyloid-Fibrillen eine in-register parallele Anordnung der β-Faltblätter[19,36,67,68] mit Ausnahme der Glucagon-Fibrille, der eine antiparallele Anordnung mit zwei unterschiedlichen β-Strang-Konformationen[69], und der PrP^{Sc}-Fibrille, der eine β-Solenoid-Struktur zugeschrieben wird[70,71]. Letztere Zuordnung beruht auf Ergebnissen der Röntgen-Faserbeugung (*X-ray fiber diffraction*) (Überblick in Quelle [71]), einem cryo-elektronen-mikroskopischen (Cryo-EM) Modell geringer Auflösung (β-Solenoid aus vier Windungen pro Monomer)[72] und einem Moleküldynamik-Simulationsmodell, das alle neueren strukturellen Erkenntnisse aufgreift[73]. Ein β-Solenoid ist gekennzeichnet durch aneinandergelagerte Monomere die ein oder mehrere intramolekulare β-Faltblätter bilden, indem sie eine helix-artige Struktur mit mehreren Windungen ausbilden[72]. Die erste β-Solenoid-Struktur wurde in einer Fibrille des HET-s(218-289)-Prions identifiziert[57]. Rekombinant hergestellte Prion-Fibrillen (rPrP) hingegen zeigen ebenfalls eine in-register parallele Anordnung[44,74], auf welche in Abschnitt 1.3.2 näher eingegangen wird. Da β-Faltblätter in einer Fibrille senkrecht zur Fibrillenachse verlaufen, bezeichnet man die Struktur als *Cross-β*-Struktur, mit einem Abstand von 4,8 Å zwischen zwei β-Strängen im selben β-Faltblatt und 6 bis 12 Å zwischen zwei β-Faltblättern[20]. Außerdem sind Amyloid-Fibrillen partiell resistent gegen Proteasen, zeigen Doppelbrechung unter Kongorotfärbung[75] und verstärkte Fluoreszenz-Emission durch Bindung an Thioflavin-T[76]. Zur Struktur der Oligomere lässt sich sagen, dass es Hinweise darauf gibt, dass Oligomere bereits die Sekundärstruktur (mit hohem β-Faltblatt-Anteil[77]) der Amyloid-Fibrillen besitzen, aber sich in der Tertiärstruktur von diesen unterscheiden[78-81].

Auch bei gleicher Aminosäuresequenz kann sich die Morphologie, also die äußere Gestalt der Fibrillen unterscheiden. Dabei wurde der Begriff Polymorphismus geprägt, der, im Gegensatz zur Bedeutung in der Genetik, an dieser Stelle die Möglichkeit der Ausbildung unterschiedlicher Konformationen (Fibrillentypen) beschreibt (konformationeller Polymorphismus). Es gibt häufig verschiedene Fibrillentypen in einem Organismus (z. B. in derselben Person)[54,82,83], aber auch unterschiedliche Fibrillentypen z. B. zwischen zwei Alzheimer-Patienten[31]. Auch unterschiedliche Herstellungsbedingungen in vitro können zu abweichenden Fibrillentypen führen. Der genaue Mechanismus, der die Entstehung eines speziellen Fibrillentyps begünstigt, ist

meist bisher nicht bekannt. Allerdings kann sogenanntes *seeding*, also die Keimung mit reifen Fibrillen eines Fibrillentyps, die Anzahl der Fibrillentypen reduzieren[80].

Nicht unerwähnt bleiben sollte, dass solche Amyloidbildungen in verschiedenen Organismen auftreten, aber häufig nicht pathogenen, sondern funktionellen Ursprunges sind. So gibt es zum Beispiel in Hefen Fibrillen, die eine spezielle Funktion besitzen und deshalb zu den funktionellen Amyloiden gezählt werden[84]. Als Beispiel ist hier die oben erwähnte HET-s(218-289)-Fibrille zu nennen: Sie ist ein Protein des Fadenpilzes *Podospora anserina* und zählt (als Prion) zu den funktionellen Amyloiden, da sie eine Rolle in Schutzmechanismen des Pilzes gegen verschiedene Parasiten spielt[57]. Als weiteres Beispiel seien hier Peptidhormone, wie das menschliche Parathormon, genannt, die in ihrer Amyloidform in membranumhüllten Granula gespeichert werden[85]. Ein drittes Beispiel ist das premelanosomale Protein (PMEL), das in den (menschlichen) Melanozyten zeitlich vor der dort verorteten Melaninsynthese (Melanine sind Haut- und Haarpigmente) amyloide Fibrillen bildet. Diesen PMEL-Fibrillen werden dabei zwei mögliche Funktionen zugeschrieben: erstens die Bildung eines Gerüstes, das die Melanozyten vor der Toxizität der Melanin-Intermediate schützt und zweitens die Erleichterung des Melanintransfers zu den Keratinozyten in der Haut[86]. Allgemein wird angenommen, dass funktionelle Amyloide häufig eine β-Solenoid-Struktur aufweisen, wie die bereits erwähnte HET-s(218-289)- und die Curli-Fibrille[68], mit Ausnahme der Peptidhormone, deren Aminosäuresequenz zu kurz für die Ausbildung einer β-Solenoid-Struktur ist.

1.1.2 Neurodegenerative Erkrankungen

Eine Erkrankung, die durch die Ablagerung von Amyloid-Fibrillen gekennzeichnet ist, wird als Amyloidose bezeichnet. Je nach Ort der Ablagerung und Art des Proteins sind verschiedene Erkrankungen bekannt, die man unter diesen Oberbegriff eingruppieren kann. Im Folgenden werden Erkrankungen im Gehirn, sogenannte neurodegenerative Erkrankungen, näher beleuchtet. Wie der Begriff bereits verdeutlicht, geht mit der Aggregation und Ablagerung von Fibrillen im Gehirn häufig die Zerstörung von Nervenzellen einher. Fibrillen sind also neurotoxisch, wobei z. B. bei der Alzheimerschen Demenz allerdings die Vorstufe der Fibrillen, die Oligomere, als stärker neurotoxisch eingeordnet werden[87].

Zu den neurodegenerativen Erkrankungen zählt man unter anderem die Alzheimersche Demenz (AD), die Parkinson'sche Erkrankung und die Prionenkrankheiten, wie zum Beispiel die Bovine spongiforme Enzephalopathie (BSE) bei Rindern, Scrapie bei Schafen und die Creutzfeldt-Jakob-Krankheit beim Menschen. Im Folgenden wird genauer auf die Alzheimersche Demenz und die Prionenkrankheiten eingegangen, weil die im Zuge dieser Doktorarbeit untersuchten Proteine bei diesen Erkrankungen eine wichtige Rolle spielen.

Laut *Alzheimer's Disease International* waren im Jahr 2019 weltweit mehr als 50 Millionen Menschen an Demenz erkrankt[88], wobei 60 bis 80 % aller Fälle auf die Alzheimersche Demenz zurückzuführen sind[89]. Die Alzheimersche Demenz ist mikroskopisch durch die Ablagerung von Plaques im Gehirn nachweisbar, welche hauptsächlich aus fibrillären Aggregaten des Proteins Amyloid β (Aβ) bestehen[90]. Symptomatisch ist diese Erkrankung geprägt durch fortschreitende Demenz bis hin zum Persönlichkeitsverlust. Man unterscheidet dabei zwei Varianten: Die familiäre AD (FAD) wird durch die Mutation in drei Genen hervorgerufen, der Präsenilin-1- und -2-Gene (PSEN1 und PSEN2) und des *Amyloid-Precursor-Proteins* (*APP*). Weiterhin gibt es auch Gene, zum Beispiel das des Apolipoprotein Es (ApoE), die als Risikogene eingeordnet werden, weil man mit einer Mutation in diesen Genen ein erhöhtes Risiko hat an AD zu erkranken, aber nicht in jedem Fall erkrankt. Zusätzlich ist zu erwähnen, dass Menschen mit Down-Syndrom, die eine Verdreifachung des Chromosoms 21 besitzen, ein erhöhtes Alzheimer-Risiko haben, da das oben erwähnte *APP*-Gen auf diesem Chromosom liegt[91]. Alle FAD-Varianten haben gemeinsam, dass sie deutlich früher auftreten als die sogenannte sporadische AD (SAD). Diese wird häufig erst im fortgeschrittenen Alter (ab etwa 65 Jahren) diagnostiziert und deren Auftreten steigt ab diesem Zeitpunkt drastisch an. So beträgt die Wahrscheinlichkeit ab dem Alter von 65 Jahren an AD zu erkranken bei Frauen ≈ 21,1 % und bei Männern ≈ 11,6 %[92,93].

Alle Prionenerkrankungen haben gemeinsam, dass die Fehlfaltung eines Proteins, des Prions, unter bestimmten Bedingungen von einem Organismus zum anderen, ähnlich der Infektion eines Virus, übertragen werden kann. Dies erfolgt ohne Beteiligung von Viren (*Protein-Only*-Hypothese)[94], indem ein Prion dem nativ gefalteten Protein seine fehlgefaltete Struktur aufzwingt. Die Übertragbarkeit zwischen verschiedenen Spezies hängt von der Sequenz-Ähnlichkeit und der Prionen-Polymorphe beider Prionproteine ab. So ist eine Übertragung vom Schaf zum Rind und vom Rind zum Menschen

möglich, aber eine Übertragung vom Schaf zum Menschen nicht, was man als Artenbarriere (*species barrier*) bezeichnet. Den konformationellen Unterschied zwischen zwei Prionen-Polymorphen oder -Stämmen (*strains*) nennt man hingegen *strain barrier*, beides zusammengenommen wird als Übertragungsbarriere (*transmission barrier*) bezeichnet[95]. Verschiedene Prionenstämme werden dabei anhand ihrer Bevorzugung bestimmter Hirnregionen, der Bildung morphologisch unterschiedlicher Aggregate, unterschiedlicher physikochemischer Eigenschaften und unterschiedlicher Kapazitäten zum Selbsttemplating (*self-templating*) und zur Kreuzkeimung (*cross seeding*) unterschieden[96]. Symptomatisch sind die Prionenerkrankungen beim Menschen durch psychische Auffälligkeiten, motorische Störungen und Verlust der motorischen Kontrolle (Ataxie), sowie hauptsächlich durch schnell fortschreitende Demenz gekennzeichnet[94,97].

1.2 Festkörper-MAS-NMR-Spektroskopie

Bei Struktur-Untersuchungen an Proteinen kommen häufig Lösungs-NMR- und Röntgen-Kristallografie-Verfahren zum Einsatz, weil sie detaillierte Einblicke in die Struktur auf atomarer Ebene liefern. Diese Verfahren gelangen jedoch an ihre Grenzen, sobald ein Protein nicht löslich oder kristallisierbar ist. Trotz der hohen Ordnung sind Fibrillen, wie auch die BVPrP-Fibrille, amorphe, unlösliche Strukturen. Das Gleiche gilt für den Aβ-huPrP-Komplex. Deswegen kommt in dieser Doktorarbeit die Festkörper-MAS-NMR-Spektroskopie zum Einsatz, die sowohl für unlösliche, als auch für amorphe (aber auch teilkristalline und kristalline) Proteine geeignet ist. In der Festkörper-NMR-Spektroskopie tragen wegen der fehlenden Molekularbewegung die anisotropen Anteile der verschiedenen Kopplungen zur Linienverbreiterung in den Spektren bei. Diese können effizient durch die Rotation der Probe um den sogenannten Magischen Winkel (≈ 54,74°, *magic angle spinning*, MAS) ausgemittelt werden[98-100]. Dadurch wird die Linienbreite reduziert und die Zuordnung einzelner Korrelationen möglich.
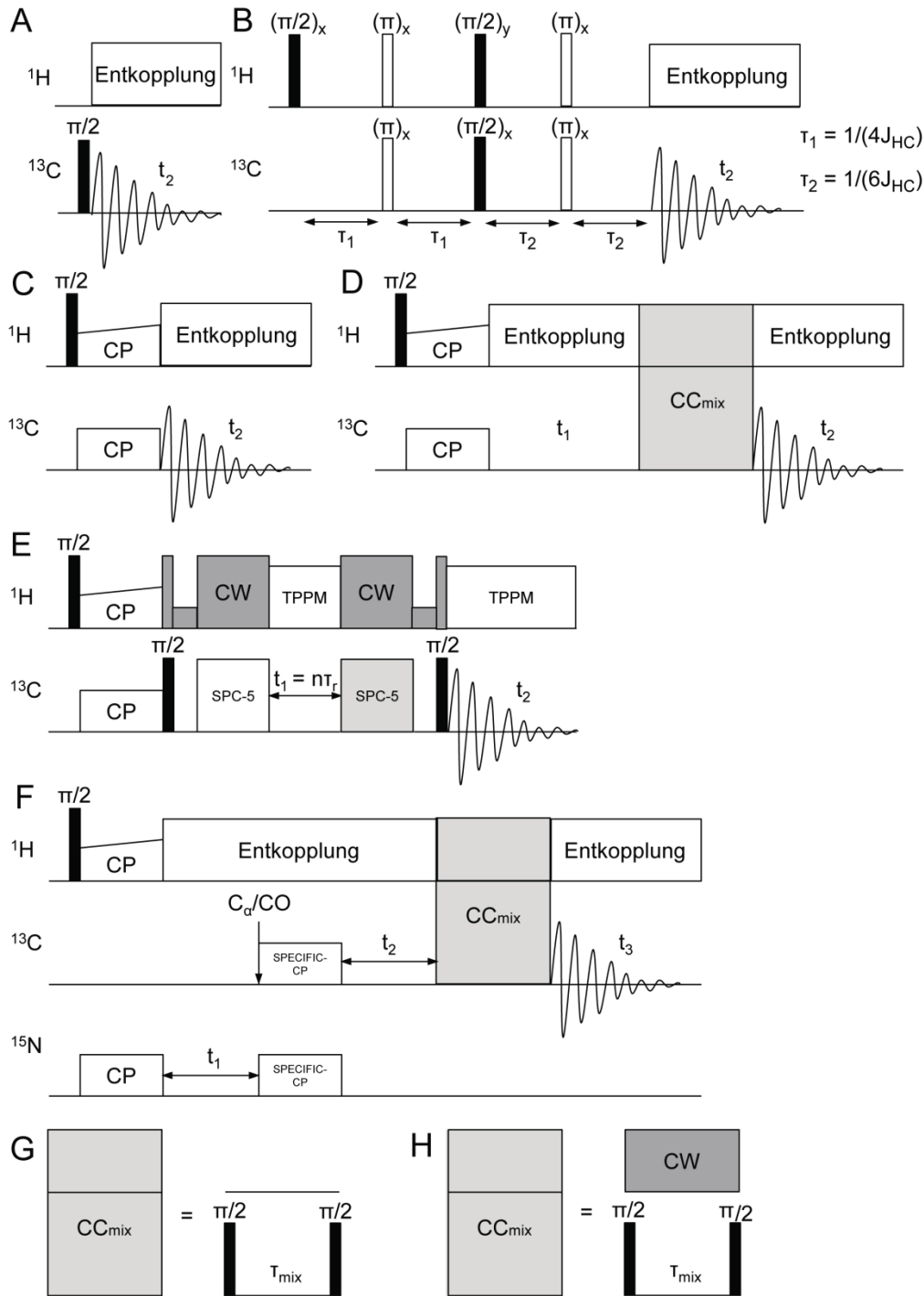
Abbildung 3: *Pulssequenzen der in dieser Arbeit verwendeten Festkörper-MAS-NMR-Experimente. **A** ^{13}C-Direktanregung, **B** refokussiertes ^1H-^{13}C-INEPT, **C** ^1H-^{13}C-CP, **D** generelle ^{13}C-^{13}C-Spindiffusion, **E** DQ-SPC5, **F** NCACX oder NCOCX mit SPECIFIC-CP, **G** PDSD-Mischsequenz (ohne Entkopplung auf ^1H), **H** DARR-Mischsequenz (mit CW-Entkopplung auf ^1H). CW bedeutet continuous wave Entkopplung, TPPM two-pulse phase-modulated Entkopplung. 90°-Pulse sind schwarz dargestellt (π/2), 180°-Pulse weiß (π). Mischsequenzen sind jeweils hellgrau hinterlegt, τ_{mix} ist die Mischzeit. τ und t sind jeweils Zeitintervalle, die Aufnahme (acquisition) ist in Form eines FIDs dargestellt. Adaptiert aus [101].*

Im nächsten Abschnitt wird auf die verwendeten Festkörper-MAS-NMR-Experimente und deren Nutzen eingegangen, die zugehörigen Pulssequenzen sind in **Abbildung 3** dargestellt. Bei der Untersuchung eines Proteins sollte im ersten Schritt untersucht werden, welche Sequenzabschnitte mobil und welche starr sind. Während erstere in Festkörper-NMR-Spektren, die auf dipolaren Kopplungen beruhen, nicht sichtbar sind, tragen letztere zu solchen Spektren bei. Mobile Bereiche können in sogenannten *„Insensitive nuclei enhanced by polarization transfer"* (INEPT)[102]-Spektren identifiziert werden, die auf J-Kopplungen beruhen, also den Kopplungen über Bindungen zwischen gebundenen Protonen und ^{13}C-Kernen. Starre Bereiche können wiederum in ^{1}H-^{13}C-Kreuzpolarisationsspektren (engl. *Cross polarization,* CP) identifiziert werden. Dabei werden die Protonen durch einen 90°-Puls angeregt und deren Magnetisierung anschließend durch einen *Spin-Lock* an die ^{13}C-Kerne weitergegeben. Dies funktioniert nur, wenn die Hartmann-Hahn-Bedingung erfüllt ist ($\gamma^{H}B_1^{H}=\gamma^{X}B_1^{X}$; X = z. B. ^{13}C oder ^{15}N)[103,104]. Schaefer und Stejskal entwickelten diese Methode für die Rotation im magischen Winkel weiter[105]. Dies ist eines der Grundexperimente der Festkörper-MAS-NMR-Spektroskopie: Die durch Direktanregung (engl. *direct excitation,* DE) der Protonen erhaltenen Spektren zeigen eine zu geringe Auflösung, weil die dipolaren Kopplungen zwischen den Protonen durch moderates Rotieren um den magischen Winkel (11 bis 20 kHz) nicht ausgemittelt werden. Die direkte Anregung der ^{13}C-Kerne hingegen führt aufgrund deren geringeren gyromagnetischen Verhältnisses und häufig langen Spin-Gitter-Relaxationszeiten (longitudinale Relaxationszeiten, T_1) zu langen Messzeiten. Durch die Übertragung der Magnetisierung von Protonen auf die ^{13}C-Kerne, wird das etwa vierfach höhere gyromagnetische Verhältnis der Protonen ausgenutzt. Gleichzeitig hängt das Wiederholungsintervall (*recycle delay*) nun von den kürzeren T_1-Relaxationszeiten der Protonen ab, was eine häufigere Wiederholung des Experiments in derselben Messzeit erlaubt[100]. Die optimale Länge des *Spin-Locks* (Kontaktzeit) ist dabei abhängig von der Anzahl und der Nähe der Protonen, also abhängig von der Stärke der Dipolkopplung zwischen diesen und den ^{13}C-Kernen. So wird die maximale Signalintensität der aliphatischen Region bereits bei kürzeren Kontaktzeiten als die der CO-Region erreicht. An dieser Stelle muss allerdings auch erwähnt werden, dass es einen intermediären dynamischen Bereich zwischen INEPT und CP gibt, der durch beide Experimente nicht abgedeckt wird. Zusätzlich kann man oben erwähnte Direktanregungsexperimente (*direct excitation*, DE-Experimente), bestehend aus

einem 90°-Puls auf die ^{13}C-Kerne, durchführen, um zusätzliche Bereiche ohne gebundene Protonen zu identifizieren, die in CP-Spektren unterrepräsentiert sind (CO-Region), oder solche die mobiler sind[100].

All die vorgenannten Experimente werden meist als eindimensionale Experimente durchgeführt und geben im Falle eines Proteins einen groben Überblick über die enthaltenen (erwarteten) ^{13}C-Resonanzen. Vor allem bei sehr starren Fibrillen, sind häufig keine mobilen Anteile vorhanden, sodass die INEPT-Spektren keine Signale zeigen. Die ^{13}C-Resonanzen im eindimensionalen Spektrum überlagern sich aber aufgrund der hohen Anzahl der ^{13}C-Atome eines Proteins stark, sodass eine genaue Zuordnung nicht möglich ist. Allenfalls lassen sich einzelne Bereiche (CO-, Aromatische und Aliphatische Region) unterscheiden. Zur Zuordnung müssen deshalb zwei- und dreidimensionale Spektren herangezogen werden.

In sogenannten *„Proton driven spin diffusion"* (PDSD)[106]-Experimenten erfolgt nach dem *CP-Spin-Lock* eine Mischsequenz (zwei 90°-Pulse auf ^{13}C im Abstand einer festgelegten Mischzeit), in welcher die Magnetisierung auf alle ^{13}C-Kerne innerhalb eines bestimmten Abstandes übertragen wird. Bei kurzer Mischzeit (bis ca. 50 ms) können dabei hauptsächlich intraresiduale Korrelationen auftreten, bei längerer Mischzeit (ca. 100 bis 500 ms) auch länger reichende Korrelationen (z. B. Lys C_α-C_ϵ) und interresiduale Korrelationen zwischen sequenziell benachbarten Aminosäure-resten. Das *„Dipolar Assisted Rotational Resonance"* (DARR)-Experiment stellt eine Variante des PDSD-Experimentes dar, bei welchem zusätzlich während der Mischzeit ein konstantes Radiofrequenzfeld auf die Protonen eingestrahlt wird, dessen Amplitude gleich der oder doppelt so hoch wie die Rotationsfrequenz ist. Dadurch werden ^{1}H-^{13}C-dipolare Kopplungen wieder eingekoppelt, was ermöglicht, höhere Rotationsfrequenzen als für das PDSD-Experiment (Effizienzverlust ab 20 kHz) zu nutzen und länger reichende Korrelationen auch bei kürzerer Mischzeit zu erhalten. Beide Experimente nutzt man zur Identifikation des Aminosäuretyps einer Kreuzkorrelation und zur Zuordnung dieser zu einem (oder zwei) Spinsystemen. Ein Spinsystem ist die Gesamtheit aller ^{13}C-Atome eines speziellen Aminosäurerests in der Sequenz.

Diese Informationen zum Aminosäuretyp und Spinsystem lassen sich auch aus sogenannten Doppelquanten-Experimenten (DQ-Experimenten) erhalten, in welchen Doppelquanten-Kohärenzen wieder eingekoppelt werden. Dafür nutzt man symmetrie-

basierte C-Sequenzen[107-111], bei welchen Radiofrequenzfeldamplitude und Rotationsfrequenz ein Vielfaches zueinander sein müssen. In diesem Fall wurde eine SPC-5-Anregung (*supercycled permutationally offset stabilized C5*)[112] genutzt, bei welcher die Radiofrequenzfeldamplitude des SPC-5-Blocks das fünffache der Rotationsfrequenz betragen muss. Führt man die DQ-Kohärenz in der indirekten Dimension ein, evolviert sie mit der Summe der chemischen Verschiebungen der koppelnden Spins[101,113-115]. Man erhält ein DQ/SQ-Spektrum, bei welchem jeweils zwei Kreuzkorrelationen auf einer horizontalen Linie korrelieren und dabei in der direkten Dimension jeweils dieselben ^{13}C-chemischen Verschiebungen zeigen, wie im PDSD, in der indirekten Dimension allerdings die Summe ihrer ^{13}C-chemischen Verschiebungen. Im Gegensatz zu PDSD Spektren, zeigen DQ/SQ-Spektren nur Korrelationen von direkt-gebundenen ^{13}C-Kernen und keine Diagonalsignale oder interresidualen Kreuzkorrelationen.

Des Weiteren liefern PDSD-, DARR- und DQ-Spektren Hinweise zur Homogenität der Probe. Resonanzen mit inhomogener Linienverbreiterung und damit verbundener geringer Auflösung weisen auf eine gewisse konformationelle Heterogenität hin. Auf der anderen Seite kann bei Auftreten gut aufgelöster/getrennter Resonanzen, deren Anzahl die laut Aminosäuresequenz erwartbare Anzahl übersteigt, auf mehrere Konformationen in einzelnen Teilen der Sequenz oder dem gesamten Protein geschlossen werden.

Neben der direkten Umgebung um den jeweiligen Kern liefert die chemische Verschiebung auch Hinweise auf die Sekundärstruktur, in welcher deren Aminosäurerest vorliegt – ganz besonders die C_α- und C_β-Atome sind dafür ausschlaggebend[116]. Während C_α-Atome bei α-helikaler Sekundärstruktur eher höhere chemische Verschiebungen im Vergleich zur Random-Coil-Struktur annehmen, zeigen C_β-Atome eher niedrigere chemische Verschiebungen. Bei β-Strang-ähnlicher Sekundärstruktur ist die Tendenz umgekehrt: C_α-chemische Verschiebungen sind niedriger, C_β-chemische Verschiebungen höher als in der ungeordneten Struktur[3-7].

Um eine sequenzielle Zuordnung der Kreuzkorrelationen zu erreichen, müssen im nächsten Schritt die ^{15}N-chemischen Verschiebungen zu den ^{13}C-chemischen Verschiebungen desselben Aminosäurerestes zugeordnet werden. Dazu werden NCA-Experimente genutzt, bei welchen die Magnetisierung nach einem CP-Spin-Lock auf ^{15}N von diesen in einem weiteren CP-Schritt (SPECIFIC-CP[117]) selektiv auf direkt

gebundene $^{13}C_\alpha$-Kerne innerhalb desselben Aminosäurerestes übertragen wird. Anschließend kann die Magnetisierung durch eine PDSD- oder DARR-Mischsequenz auf alle ^{13}C-Kerne in der Seitenkette des Aminosäurerestes übertragen werden (NCACX).

Die eigentliche sequenzielle Zuordnung erfolgt dann mit Hilfe von NCO- und NCOCX-Experimenten, bei welchen die Magnetisierung nach einem CP-Spin-Lock auf ^{15}N in einem weiteren CP-Schritt (SPECIFIC-CP[117]) von diesen selektiv auf direkt gebundene ^{13}CO-Kerne übertragen wird (NCO), die aus dem in der Aminosäuresequenz davor befindlichen Aminosäurerest herstammen ($^{15}N_i$ zu $^{13}CO_{i-1}$). Anschließend kann wie auch im NCACX in einer PDSD- oder DARR-Mischsequenz die Magnetisierung auf alle ^{13}C-Kerne in der Seitenkette dieses Aminosäurerestes übertragen werden (NCOCX).

Eine sequenzielle Zuordnung ist immer der erste Schritt, um Sekundär-strukturelemente sequenziell zu bestimmen oder eine dreidimensionale Struktur zu modellieren. Letzteres konnte an den hier untersuchten Proben nicht durchgeführt werden, da aufgrund der Heterogenität oder Überlappung gering aufgelöster Signale, z. B. gleicher Aminosäuretypen, keine (vollständige) sequenzielle Zuordnung möglich war.

Ein Nachteil der Festkörper-MAS-NMR-Spektroskopie ist die inhärent niedrige Empfindlichkeit, weswegen Spurenanalytik mit dieser Methode nicht möglich ist. Um diesen Nachteil zu umgehen, nutzt man die sogenannte *Dynamic Nuclear Polarization* (DNP)[118-123], die das um das 660-fache höhere gyromagnetische Verhältnis der Elektronen gegenüber den Protonen ausnutzt (theoretischer Verstärkungsfaktor). Mit Hilfe von in die Lösung eingeführten Radikalen und Mikrowellenstrahlung werden die Protonen in einen angeregten Zustand versetzt, der anschließend auf die Heterokerne des Proteins übertragen wird. Auf die genaue Methodik soll hier nicht eingegangen werden, der interessierte Leser wird auf den im Abschnitt „3 Publikationen" genannten Review: „3.4 Hyperpolarized MAS NMR of unfolded and misfolded proteins"[123] und das Buchkapitel: „3.5 Chapter 10 Isotopically Enriched Systems"[101] verwiesen. Da DNP noch eine sehr junge spektroskopische Methode ist und somit noch Routine-Experimente und -Methoden entwickelt werden, ist sie nicht für jede Fragestellung geeignet. Die bisweilen schlechte Auflösung macht sie für die Untersuchung uniform-^{13}C,^{15}N-markierter Proteine mit z. T. langer Aminosäuresequenz, wie sie im Zuge

dieser Arbeit verwendet wurden, ungeeignet. Die DNP-Festkörper-MAS-NMR-Spektroskopie zeigt ihre Stärke in der Untersuchung besonders geordneter (gut aufgelöster) Strukturen und selektiv-[13]C- und/oder -^{15}N-markierter Proben[123], aber auch bei geringer effektiver Konzentration des Analyten, z. B. bei der selektiven Untersuchung von Oberflächen oder kleiner Moleküle in einer Matrix[122].

1.3 Zu Fehlfaltungen neigende Proteine

Im Folgenden werden die bei der Alzheimerschen Demenz und den Prionenerkrankungen an der Fehlfaltung und Aggregation beteiligten Proteine näher beschrieben, deren Funktion im nativen Zustand beleuchtet und auch auf den wissenschaftlichen Stand der Struktur dieser Proteine im nativen und fehlgefalteten Zustand eingegangen. Zuerst wird Amyloid-β (Aβ), das bei Alzheimerscher Demenz eine Rolle spielt, näher betrachtet, anschließend das humane Prionprotein (huPrP), das bei Prionenerkrankungen im Menschen fehlgefaltet wird. Beide bilden einen Komplex, der im Zuge dieser Doktorarbeit mittels Festkörper-NMR-Spektroskopie untersucht wurde (im Folgenden als Projekt 1 bezeichnet) und am Ende des Kapitels ebenfalls näher erläutert wird. An dritter Stelle folgt das Rötelmaus-Prionprotein (BVPrP), das in der Rötelmaus (engl. *bank vole*; *myodes glareolus*) auftritt und dessen Fibrille in einem weiteren Projekt mittels Festkörper-NMR-Spektroskopie untersucht wurde (nachfolgend Projekt 2 genannt).

1.3.1 Amyloid-β

Das Peptid Amyloid-β (Aβ), das bei der Alzheimerschen Demenz eine wesentliche Rolle spielt, entsteht bei der Spaltung des zellmembran-gebundenen Amyloidvorläuferproteins (*amyloid precursor protein*, APP) durch β- und γ-Sekretasen. Dabei schneidet erst die β-Sekretase extrazellulär und trennt dabei ein lösliches Fragment ab. Anschließend schneidet die γ-Sekretase innerhalb der Transmembrandomäne, wobei das Aβ von der Transmembrandomäne abgetrennt wird (siehe **Abbildung 4A**). Die Schnittpositionen sind nicht immer exakt identisch, weswegen Aβ zwischen 39 und 43 Aminosäuren besitzen kann[124]. Bei der Alzheimerschen Demenz spielen die beiden Varianten Aβ(1-40) und Aβ(1-42), die neben Aβ(4-42) die dominierenden Aβ-Varianten im Gehirn (Kleinhirn, Hippocampus und Cortex) darstellen[125], eine Rolle. Aβ(1-42) neigt dabei stärker zur Aggregation[126] und ist weitaus neurotoxischer als Aβ(1-40)[127]. Dies könnte, nahegelegt durch

Molekulardynamik-Simulationen, bereits in unterschiedlichen Dimerkonformationen zu Beginn des Aggregationsprozesses begründet sein[128]. Erwähnt werden sollte an dieser Stelle, dass beide Varianten auch in gesunden Menschen auftreten, ihr Vorkommen allein also noch nicht auf die Alzheimersche Demenz hindeutet, zumal Aβ-Peptide unter normaler physiologischer Funktion durch verschiedene Peptidasen abgebaut werden[129]. Es wird diskutiert, ob das Auftreten der Alzheimerschen Demenz eine Folge des Ungleichgewichts zwischen der Entstehung und dem Abbau von Aβ ist[129]. Allerdings wird nicht die Konzentration des Aβ(1-40) oder Aβ(1-42), sondern das Verhältnis von Aβ(1-42) zu Aβ(1-40) in der Gehirn-Rückenmarksflüssigkeit (*Liquor cerebrospinalis*, engl. *Cerebrospinal fluid*, CSF) als Marker für das Fortschreiten der Alzheimerschen Demenz genutzt, da diese stärker korrelieren[130]. Bisher konnte keine Funktion für Aβ aufgeklärt werden. Es wird allerdings diskutiert, dass es eine Rolle bei der Bekämpfung schädlicher Mikroben im Gehirn spielen könnte. So konnten Soscia et al. eine antimikrobielle Aktivität von sowohl Aβ(1-40) als auch Aβ(1-42) gegen mehrere grampositive und negative Bakterien und einen Hefepilz nachweisen[131]. Aβ-Oligomere hingegen haben einige toxische Eigenschaften: sie können Membranen zerstören, Zelloberflächen-rezeptoren binden und inaktivieren und mit der intrazellulären Maschinerie wechselwirken[129,132]. Bisher gibt es keine detaillierten Informationen zu Aβ-Oligomer-Strukturen *in vivo*, weil sie eine sich rapide verändernde Übergangsform darstellen und somit in ihrer Größe und Struktur stark variieren können. Dies schlägt sich auch im Vorhandensein mehrerer *in vitro* Oligomer-Präparate verschiedener Zusammensetzung aus unterschiedlicher Anzahl an Monomeren, Größe, Toxizität und *on-* oder *off-pathway* Einordnung nieder[133]. Die Strukturuntersuchungen vieler isolierter Oligomere scheitern daran, dass diese Oligomeraufbereitungen nicht-native Mutationen oder Vernetzungen enthalten, *off-pathway*, also nicht in der Lage sind, sich zu Fibrillen umzuformen oder nicht lange genug existieren, um ihre Struktur hochaufgelöst zu untersuchen[132]. Trotzdem gibt es einige Strukturuntersuchungen an selektiv-^{13}C-und/oder-^{15}N-markierten Aβ-Oligomeren und durch Bindeproteine stabilisierten Monomeren, sowie mehrere Untersuchungen an Protofibrillen von Aβ(1-40)[78-81,134-138], Aβ(1-42)[13,138-143] und pyroGlu-Aβ(3/11-40)[144]. Alle diese Untersuchungen stimmen darin überein, dass die Sekundärstrukturen der Oligomere und Protofibrillen bereits einen hohen Anteil an β-Faltblättern aufweisen, wie dies auch in ausgewachsenen Fibrillen der Fall ist[32-35,145,146]. Da sich die im Zuge dieser Doktorarbeit durchgeführten Untersuchungen

speziell auf Aβ(1-42) beschränken, ist in **Abbildung 4B** dessen Aminosäure-Sequenz dargestellt.
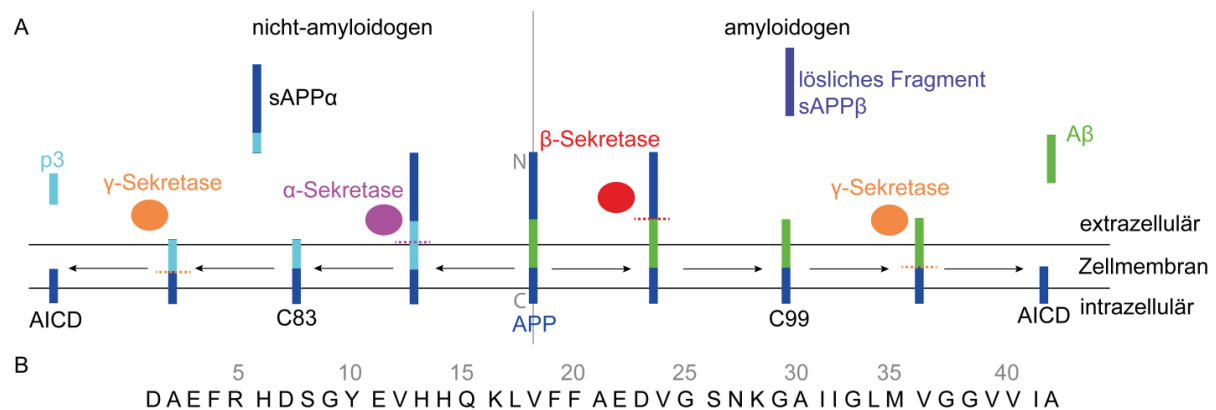
Abbildung 4: A *APP-Metabolismus unter Sekretasen-Beteiligung.* ***B*** *Aminosäuresequenz von Aβ(1-42).* ***A*** *Im nicht-amyloidogenen Pfad schneiden α- und γ-Sekretase, dabei entsteht ein Fragment namens p3. Die α-Sekretase schneidet dabei innerhalb des Aβ-Sequenzabschnittes von APP. Im amyloidogenen Pfad schneiden erst die β-Sekretase und anschließend die γ-Sekretase innerhalb der Transmembrandomäne. Dabei entsteht das Peptid Aβ, das bei Alzheimerscher Demenz aggregiert und akkumuliert. C83 und C99 sind zwei C-terminale Fragmente, mit jeweils 83 oder 99 Aminosäureresten. Die Abkürzung sAPP bedeutet solubile APP, stellt also jeweils ein lösliches APP-Fragment dar. AICD steht für Amyloid Precursor Protein Intracellular Domain – die intrazelluläre Domäne des APP.* ***B*** *Aminosäuresequenz von Aβ(1-42), das im Zuge dieser Doktorarbeit verwendet wurde.*

1.3.2 Humanes Prionprotein

Das humane Prionprotein (huPrP^C) besteht aus 208 Aminosäuren und hat eine absolute Molekülmasse von 23 kDa. Es wird meist ab Aminosäurerest K23 beschrieben, weil die ersten 22 Aminosäuren das Signalprotein darstellen, das durch Signalpeptidasen im Endoplasmatischen Retikulum abgespalten wird[147]. Außerdem ist huPrP^C über einen Glycosylphosphatidylinositol-Anker (GPI-Anker) an der Zellmembran befestigt. **Abbildung 5** zeigt die Aminosäuresequenz und die Faltung im nativen Zustand. Der ungefaltete N-Terminus enthält fünf Oktarepeats (PHGGGWGQ) und das sogenannte Palindrom AGAAAAGA. Der gefaltete C-Terminus besteht aus zwei β-Strängen (Aminosäuren Y128 bis G131 und V161 bis R164) und drei α-Helices (Aminosäuren D144 bis M154, N173 bis K194 und E200 bis R228). Außerdem befindet sich zwischen C179 und C214 eine Disulfidbrücke[97].

Aβ-Binderegion   Octa-Repeat-Region

CH₃ — K K R P K P G G W N T G G S R Y P G Q G S P G G N R Y P P Q G G G G W G Q P H G G G W G Q P H G G G W G Q P H G G G

Aβ-Binderegion

W G Q P H G G G W G Q G G G T H S Q W N K P S K P K T N M K H M A G A A A A G A V V G G L G G Y M L G S A M S R P I I H

F G S D Y E D R Y Y R E N M H R Y P N Q V Y Y R P M D E Y S N Q N N F V H D C V N I T I K Q H T V T T T K G E N F T E

S — S

T D V K M M E R V V E Q M C I T Q Y E R E S Q A Y Y Q R G S — GPI-Anker

➡ β-Strang   ∿ α-Helix   —S–S— Disulfidbrücke

Signalsequenz: [1]M A N L G C W M L V L F V A T W S D L G L C[22]
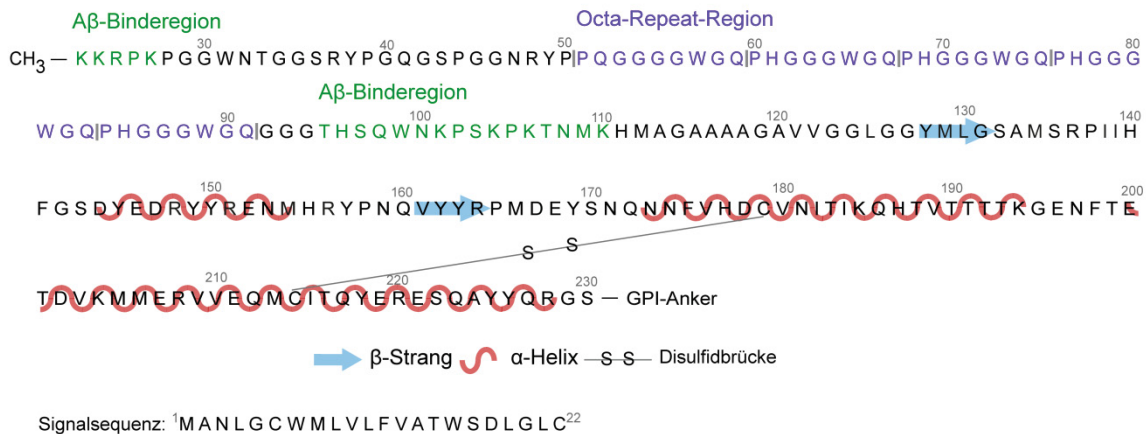
Abbildung 5: *Aminosäuresequenz des nativ-gefalteten humanen Prionproteins. α-Helices sind als rote Wellenlinien, β-Stränge als blaue Pfeile eingezeichnet. Die Octa-Repeat-Region ist violett und die Aβ-Binderegionen grün gekennzeichnet.*

Es wurden unterschiedliche Funktionen für das Zell-verankerte huPrP^C vorgeschlagen, wovon bisher nur die Aufrechterhaltung der Myelinscheide um die Axone der Neuronen bestätigt werden konnte[148]. Es scheint aber auch eine Rolle bei anderen neurodegenerativen Erkrankungen wie der Parkinson'schen Erkrankung, im Immunsystem und das Immunsystem betreffenden Erkrankungen und bei Krebs zu spielen[149]. Wird huPrP^C fehlgefaltet, entsteht das sogenannte Prion (PrP^{Sc}), das, wie bereits erwähnt, infektiös ist und eine Amyloid-Fibrillen-Struktur besitzt. *In vitro* rekombinant hergestellte PrP-Fibrillen (rPrP) zeigen jeweils unterschiedliche Fibrillentypen (Polymorphismus). So besteht ein huPrP(23-144)-Fibrillentyp aus drei parallel in-register angeordneten β-Strängen (M112 bis A115, A118 bis V122 und L130 bis I139) in zwei Protofilamenten mit C$_2$-Symmetrie[40,150]. Ein mittels Cryo-EM aufgeklärtes Strukturmodell eines huPrP(94-178)-Fibrillentyps besteht hingegen aus vier parallel in-register angeordneten β-Strängen (K106 bis M109, A115 bis L125, A133 bis S135 und I138 bis H140) in zwei Protofilamenten mit einer 2$_1$-Schraubenachse, wobei das Palindrom AGAAAAGA hierbei das Interface zwischen den beiden Protofilamenten darstellt[44]. Erst kürzlich wurde ein weiteres rekombinant-hergestelltes huPrP-Fibrillen-Strukturmodell mittels Cryo-EM aufgeklärt, diesmal allerdings in voller Länge (Aminosäuren 23-231). Es umfasst zwei helikal umeinander gewundene Protofilamente aus sechs parallel in-register angeordneten β-Strängen im C-Terminus (Q172 bis D178, V180 bis Q186, T188 bis T192, N197 bis T199, Q212 bis T216 und S222 bis Q227). Interessanterweise konnten dabei sechs Elektronendichten wahrgenommen werden, die nicht dem huPrP zugeordnet werden können. Drei davon

sind Lösungsmittelmoleküle, weitere drei hingegen konnten nicht näher identifiziert werden und könnten Kontaminationen sein. Es zeigt sich in diesem Modell, dass bei der Aggregation vom nativen Zustand zur Fibrille eine Umwandlung der zweiten α-Helix zu β_1 bis β_3, der Verbindung zwischen α_2 und α_3 zu β_4 und der dritten α-Helix zu β_5 und β_6 erfolgen muss[74]. Im Zuge dieser Doktorarbeit wurde sowohl das Volllängen-huPrP(23-230), als auch ein verkürztes N-terminales Konstrukt, huPrP(23-144), im nativen Zustand, allerdings ohne GPI-Anker, im Komplex mit Aβ-Oligomeren strukturell untersucht. Auf den Komplex dieser beiden Proteine wird in Abschnitt 1.4 näher eingegangen.

1.3.3 Rötelmaus-Prionprotein (Projekt 2)

Das Prionprotein der Rötelmaus (*myodes glareolus*, engl. *bank vole*, BVPrP), dessen Fibrillen in Projekt 2 untersucht wurden, kann somit ebenfalls aggregieren und Prionenerkrankungen in der Rötelmaus auslösen. Allerdings sind diese Prionenerkrankungen von außen induziert und spontane Fälle nicht bekannt[151]. Warum untersucht man also gerade BVPrP? BVPrP wird neben dem Maus- (*mus musculus*) und dem Hamster-Prionprotein (*mesocricetus auratus*) als Model für die Prionenerkrankungen genutzt, weil es einige besondere Eigenschaften aufweist: Erstens kann es *in vitro* spontan aggregieren[96] und seine Überexprimierung in transgenen Mäusen führt zur Entstehung einer rasch übertragbaren Prionenerkrankung[151]. Zweitens gilt die Rötelmaus als universeller Prionenakzeptor, weil sie mit einer Vielfalt an Prionenstämmen verschiedener Ausgangsorganismen infiziert werden kann, genauer gesagt, mit den Prionen der Wiesenwühlmaus, der Maus, des Hamsters, Meerschweinchens, Schafs, Wapitis, Rinds und des Menschen[95]. Wenn die Rötelmaus zum Beispiel mit Prionen des Hirschs [Prionenerkrankung *Chronic Wasting Disease* (CWD)] infiziert wird, zeigt sie die kürzeste Inkubationszeit aller bekannter Prionenerkrankungen[152], denn Veränderungen im Verhalten traten schon nach 25 bis 28 Tagen nach der Infektion auf[152].

BVPrP hat eine absolute Molekülmasse von 23 kDa, seine Sequenz besteht aus 210 Aminosäuren, ist polymorph an Position 109 (Met oder Ile) (**Abbildung 6**, hier in der Variante I109) und unterscheidet sich zu huPrP in ≈ 15 Aminosäuren (Gemeinsamkeit 93 %). Die native Struktur von BVPrP bei 20 °C und einem pH-Wert von 4,5 ist ähnlich der von huPrP, mit einem flexiblen N-Terminus und zwei β-Strängen (Y128 bis G131

und V161 bis R164), die ein β-Faltblatt bilden, drei α-Helices (D144 bis R156, Q172 bis K194 und E200 bis Y225), von denen α-Helix 1 und 2 am Ende jeweils eine 3_{10}-Helix ausbilden, und zusätzlich einer 3_{10}-Helix (P165 bis Y169) in der strukturierten C-terminalen Domäne. Die Verbindung zwischen β-Strang 2 und α-Helix 2 ist exakt definiert und wird durch nahen Kontakt des C-terminalen Endes von α-Helix 3 stabilisiert[153]. Zu den Strukturen des BVPrP^{Sc} ist allerdings noch nicht viel bekannt. Gallager-Jones et al. konnten mittels Cryo-EM die dreidimensionale Struktur eines rekombinant hergestellten Peptides von BVPrP, genauer gesagt der Aminosäuren Q168 bis V176 (Verbindung zwischen β-Strang 2 und α-Helix 2 in nativ gefaltetem BVPrP), aufklären: Sie identifizierten eine parallele in-register *face-to-back* Anordnung der β-Faltblätter und bezeichnen die entstehenden Motive als „polare Spangen" („*polar clasps*")[154]. Allerdings handelt es sich dabei nicht um eine Fibrille im eigentlichen Sinne, sondern um einen Protein-Nanokristall, dessen strukturelle Vergleichbarkeit zu rekombinant-hergestellten und aus Hirnhomogenat erhaltenen Fibrillen in Frage zu stellen ist. Somit stellen jegliche neue Erkenntnisse zu BVPrP-Fibrillen-Strukturen grundlegende Ergebnisse dar, die zum allgemeinen Verständnis der Übertragbarkeit von Prionenerkrankungen beitragen können – so zum Beispiel zur Frage, warum BVPrP ein universeller Prionenakzeptor ist.

Strukturuntersuchungen an Proteinen mittels hochauflösender Spektroskopie, wie der Festkörper-MAS-NMR-Spektroskopie, benötigen relativ homogene Proben ohne konformationellen Polymorphismus. Dieser Polymorphismus ist im Falle der Festkörper-MAS-NMR-Spektroskopie zwar durch eine hohe Linienbreite oder das Auftreten mehrerer Signale für einen Aminosäurerest als solcher im Spektrum sichtbar. Allerdings wird die Zuordnung der Signale dadurch erschwert, womit wiederum eine dreidimensionale Strukturbestimmung unmöglich wird. Zu konformationellem Polymorphismus kann auch das Auftreten verschiedener Prionenstämme innerhalb einer Probe führen. Es ist aber auch möglich, dass sich diese in unterschiedlichen Tertiär- und Quartärstrukturen widerspiegeln, die man im Festkörper-NMR-Spektrum nicht unterscheiden kann. Somit ist es in jedem Fall sinnvoll das Auftreten mehrerer Prionenstämme zu unterdrücken und einen Prionenstamm zu bevorzugen. Dies ist z. T. möglich durch die bereits erwähnte, sogenannte Keimung (*seeding*) des nicht-aggregierten PrPs mit reifen rekombinant-hergestellten Fibrillen (oder Hirnhomogenaten). Dabei übernimmt das nicht-aggregierte PrP die Fibrillen-Strukturen der Keime. Durch Fragmentierung (z. B. durch Ultraschall) der

entstehenden Fibrillen, Einsetzen dieser Fragmente in einer erneuten Keimung und mehrfacher Wiederholung dieses Vorganges können dabei ein oder einige wenige Fibrillentypen (Reduzierung des Polymorphismus) bevorzugt werden, wie an Aβ(1-40)-Fibrillen der Iowa-Mutante (D23N) gezeigt werden konnte[80]. Außerdem konnten Fernández-Borges et al. demonstrieren, dass auch polyanionische Cofaktoren, wie Dextransulfat, RNA oder DNA-Plasmide, *in vitro* einen oder mehrere rekombinant hergestellte, infektiöse BVPrP-Stämme bevorzugen können und zwar unabhängig davon, ob der Ausgangspunkt eine Keimung oder eine spontane Aggregation war. Auf der anderen Seite sind Cofaktoren aber nicht unerlässlich für die Aggregation rPrPs. So konnten Fernández-Borges et al. außerdem zeigen, dass rPrP auch spontan, also ohne Keimung, aggregieren kann, die resultierenden Prionenstämme aber nicht in jedem Fall infektiös sind[96]. Ein bestehendes Problem bleibt, dass es bisher nicht möglich ist, einen spezifischen Prionenstamm zu erhalten oder vorherzusagen, welcher Prionenstamm bevorzugt wird.

Der wichtigste Aspekt von PrP^Sc ist seine Infektiosität. Allerdings stellte die Herstellung ausreichender Mengen infektiösen, aggregierten, rekombinant hergestellten PrPs lange Zeit eine Herausforderung dar. Soto et al. entwickelten eine neue Methode, die sogenannte *protein misfolding cyclic amplification* (PMCA), die die wichtigsten Schritte der *in vivo* PrP^Sc-Vervielfältigung aufgreift und beschleunigt: Es wird eine geringe Menge aggregiertes, infektiöses PrP mit nicht-aggregiertem PrP im Überschuss inkubiert, was zur Aggregation und Umwandlung des nicht-aggregierten PrPs in infektiöse PrP-Fibrillen führt. Anschließend werden diese Fibrillen durch Ultraschall in kleinere Fragmente gebrochen, die wiederum als Keim zur weiteren Aggregation dienen können. Der Ultraschallvorgang kann beliebig oft wiederholt werden, bis eine ausreichende Menge an Prionen-Material erhalten wird[155]. Dabei kann das aggregierte infektiöse PrP spontan entstanden (*Unseeded PMCA*), rekombinant hergestellt (*Seeded RecPMCA*) oder aus Hirnhomogenat erhalten worden sein (*Seeded Brain-PMCA*)[96]. Saá et al. konnten außerdem zeigen, dass diese Methode automatisierbar ist und dabei eine hohe Reproduzierbarkeit und Spezifität aufweist. Darüber hinaus zeigten sie, dass im Fall von mit Scrapie infiziertem Hirnhomogenat bereits 26 PrP-Monomere detektiert werden konnten, was einer drei-Milliarden-fachen Sensitivitätssteigerung (nach sieben PMCA-Durchgängen) gegenüber herkömmlicher Western Blot-Analyse entspricht, und einer etwa 20-Millionen-fachen Steigerung der Infektiosität[155]. Im Jahr 2004 wurden erstmals Prionen *in vitro* hergestellt, genauer

gesagt Prionen einer verkürzten Maus-Variante (recMoPrP(89-230))[156]. Castilla et al. stellten mit Hilfe der PMCA infektiöses PrP aus rekombinant-hergestelltem PrP her, das strukturelle und biochemische Eigenschaften mit PrP^{Sc} teilt. Dabei wurde Hamster-Hirnhomogenat als Keim verwendet. Castilla et al. argumentieren jedoch, dass durch die bis zu 1000-fache Verdünnung eine Infektiosität allein aufgrund des Keims ausgeschlossen und somit die Prionhypothese untermauert werden kann[157]. Außerdem ist die PMCA auch geeignet, Mutationen, die zu erblichen Prionenerkrankungen, wie dem Gerstmann-Sträussler-Scheinker-Syndrom (GSSS), führen können, zu untersuchen. Dabei wurde in diesem Fall rekombinant-hergestelltes huPrP, das die jeweilige Mutation trägt, mit Hirnhomogenat von Mäusen, deren PrP-Gen ausgeschlossen wurde (*PRNP-Knockout*), zur spontanen Aggregation angeregt. Es wurden 16 Mutation-Polymorphismus-Kombinationen getestet, von denen acht spontan aggregierten[158].

Ein Nachteil ist allerdings, dass die mittels der PMCA herstellbare Menge an aggregiertem, rekombinant-hergestelltem, infektiösem PrP (rPrP) nicht für Strukturuntersuchungen, wie der mittels Festkörper-MAS-NMR-Spektroskopie, ausreicht. Deshalb wird in Publikation 3.3 dieser Doktorarbeit eine neue Methode namens *protein misfolding shaking amplification* (PMSA) eingeführt, die durch die Verwendung eines Schüttlers anstelle Ultraschalls ein mehr als 1000-faches *Scaling-up* an aggregiertem infektiösem Material im Vergleich zur PMCA ermöglicht[159].

In der vorliegenden Doktorarbeit wird eine uniform-^{13}C,^{15}N-markierte rekombinant hergestellte BVPrP-Fibrille (Aminosäuren 23 bis 231) mit Ile an Position 109 mittels Festkörper-MAS-NMR-Spektroskopie untersucht, um die Verwendbarkeit der neu-eingeführten PMSA-Methode zur Herstellung ausreichender Mengen aggregierten Proteins eines Prionenstammes für Strukturuntersuchungen mittels hochaufgelöster spektroskopischer Verfahren zu zeigen.
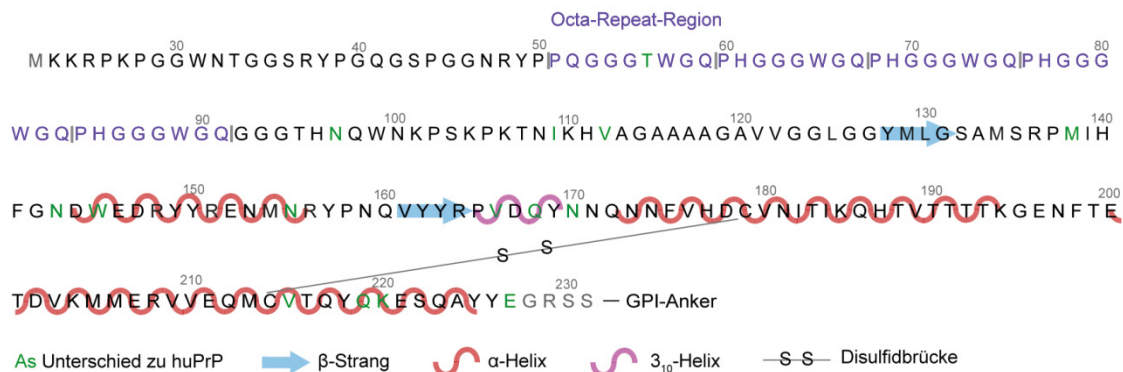
Abbildung 6: *Aminosäuresequenz des nativ-gefalteten Rötelmaus-Prionproteins. α-Helices sind als rote, 3₁₀-Helices als pinke Wellenlinien und β-Stränge als blaue Pfeile eingezeichnet. Die Octa-Repeat-Region ist violett und Aminosäurereste, die sich zu huPrP unterscheiden, grün (oder am Anfang und am Ende grau) gekennzeichnet.*

1.4 Komplex aus humanem Prionprotein und Amyloid-β (Projekt 1)

Der Hauptteil dieser Doktorarbeit beschäftigt sich mit der Festkörper-MAS-NMR-spektroskopischen Untersuchung des Komplexes aus humanem Prionprotein und Amyloid-β Oligomeren.

Es konnte gezeigt werden, dass die native Form des huPrP Aβ-Oligomere mit hoher Affinität bindet, im Gegensatz dazu aber Fibrillen und Monomere mit weit geringerer Affinität[160,161]. In einem Drosophila-Modell konnte herausgestellt werden, dass PrP die Aβ-Oligomere stabilisiert und die Toxizität von Aβ erhöht, wahrscheinlich indem erste Fibrillen fragmentiert werden. Denn die Fruchtfliegen zeigten nur bei Co-Expression beider Proteine eine verkürzte Lebenszeit und einen veränderten Schlaf-Wach-Rhythmus[162]. Die Interaktion zwischen huPrP und Aβ scheint eine Rolle in der Alzheimerschen Demenz zu spielen, die anfänglich stark hinterfragt wurde[163-166], aber mittlerweile als bewiesen gilt[167-169]. Dieser anfängliche Disput deutet darauf hin, dass die verwendete Aβ-Spezies und -Zusammensetzung (in Größe und Art der verwendeten Oligomere) ausschlaggebend für das Auftreten einer Interaktion zwischen huPrP und Aβ ist[170]. So scheinen OC-Antikörper-bindende Aβ(1-42)-Oligomere (OC-Antikörper detektieren eine in-register parallele Anordnung der β-Faltblätter) stärker an huPrP zu binden und dadurch neurotoxisch zu sein, während A11-Antikörper-bindende Aβ(1-42)-Oligomere (A11-Antikörper detektieren eine out-of-register anti-parallele Anordnung der β-Faltblätter) auch ohne die Anwesenheit von huPrP neurotoxisch sind[171]. Das humane PrP ist also ein Rezeptor

für Aβ-Oligomere, es gibt allerdings noch einige andere, denen eine Rolle bei der Alzheimerschen Demenz zugeschrieben wird[172]. Im Detail konnten dieser Interaktion sowohl toxische als auch protektive Einflüsse nachgewiesen werden: Zu den toxischen Einflüssen zählt die Eigenschaft membrangebundenen huPrP^{C}s die Transzytose des Aβ durch die Blut-Hirn-Schranke zu unterstützen[173] und damit die Internalisierung und daraus folgende Akkumulation der Aβ-Oligomere zu ermöglichen[174]. Zusätzlich trägt es mit Hilfe des Aβ zur Zerstörung von Synapsen bei[175] und aktiviert Fyn-Kinase-Signalwege[176,177], die zur Blockade der Langzeit-Potenzierung, der langandauernden Verstärkung der synaptischen Übertragung, führen[160,178]. Dies hat wiederum das Verlernen erlernter Tätigkeiten und Sachverhalte zur Folge. Die Signalübertragung in die Zelle erfolgt dabei durch eine durch die Aβ-Oligomere verstärkte Bindung des huPrP^C an das Transmembranprotein metabotroper Glutamatrezeptor 5 (mGluR5)[179-182]. Die Fyn-Kinase selbst kann dann eine Hyperphosphorylierung von Tau auslösen[183], welche die in der Alzheimerschen Demenz zusätzlich auftretenden neurofibrillären Bündel (*neurofibrillary tangles*) verursacht. Ein zweiter Signalweg nutzt die N-Methyl-D-Aspartat-Rezeptoren (NMDA-Rezeptoren): Im physiologischen Zustand bindet huPrP^C Kupfer-Ionen und kann dadurch an die NMDA-Rezeptoren binden, wodurch deren Affinität zu Glycin reduziert wird. Bilden die Kupfer-Ionen aber mit Aβ-Monomeren und -Oligomeren einen Chelatkomplex oder können durch die Bindung des Aβ an huPrP^C nicht mehr selbst an das huPrP^C binden, wird die Affinität der NMDA-Rezeptoren zu Glycin und damit der Calciumeinstrom in die Nervenzelle erhöht und diese dadurch zerstört[184]. Zu den protektiven Einflüssen zählen die Eigenschaften von gelöstem PrP, die Toxizität von Aβ zu reduzieren, indem erstens die Aβ-Fibrillierung gehemmt und die Bildung von Aβ-Oligomeren verhindert[185], zweitens die Aβ-Fibrillen-Elongation gehemmt wird[186] (wahrscheinlich durch bevorzugte Bindung an das schneller wachsende Ende der Fibrille[187]), drittens die toxischen Aβ-Oligomere eingefangen werden[174,185] und viertens in Exosom-Vesikeln gebundenes huPrP die Aβ-Aggregation vorantreibt und damit die Aβ-Oligomer-induzierte Neurotoxizität reduziert[188]. Die toxischen und protektiven Eigenschaften des huPrP^C sind dabei kein Widerspruch in sich, denn erstere werden, wie erwähnt, durch membrangebundenes huPrP^C vermittelt, letztere durch gelöstes (oder in Exosom-Vesikeln gebundenes) huPrP.

Die oben genannten Signalwege könnten für neue therapeutische Ansätze in der Alzheimerschen Demenz genutzt werden[189]. So konnten bereits mehrere Substanzen

identifiziert werden, die die Aβ-PrP-Interaktion hemmen oder blockieren[190-193]. Interessanterweise gibt es immer mehr Hinweise darauf, dass huPrP^C auch mit Tau[194,195] und α-Synuclein[194,196], das bei der Parkinson'schen Erkrankung aggregiert, interagiert und huPrP^C somit an verschiedenen neurodegenerativen Erkrankungen beteiligt sein könnte.

Über die Bindung zwischen huPrP und Aβ im Detail ist noch nicht sehr viel bekannt. Zwar wurden zwei lysinreiche Bereiche (Sequenzposition 23 bis 27 und etwa 95 bis 110, siehe **Abbildung 5**) als Bindestellen am huPrP identifiziert[193,197-201]. Außerdem konnten Nicoll et al. demonstrieren, dass huPrP Aβ-Nanoröhrchen mit tripelhelikaler Struktur bindet[202]. Hinweise darauf, welche Bereiche beim Aβ an das huPrP binden, gibt es bisher jedoch keine. Eine Festkörper-NMR-Studie von Kostylev et al. aus jüngster Zeit zeigt, dass Aβ im Komplex starr, PrP hingegen eher beweglich ist. Sie beschreiben dabei allerdings einen Prozess der Flüssig-Flüssig-Phasentrennung und bezeichnen den Komplex als Hydrogel. Außerdem schlagen sie eine Konformationsänderung im N-Terminus von huPrP^C durch Bindung an Aβ-Oligomere vor[203]. Im Zuge dieser Doktorarbeit wurde sowohl ein Komplex aus Volllängen-huPrP (Reste 23 bis 230) und Aβ-Oligomeren, als auch ein Komplex aus einem N-terminalen Konstrukt [huPrP(23-144)] mit Aβ-Oligomeren untersucht. Denn es konnte demonstriert werden, dass auch kürzere Konstrukte, die beide Bindestellen besitzen, effizient an Aβ-Oligomere binden, so z. B. das natürlich entstehende N-terminale huPrP-Fragment N1 [huPrP(23-111)][198,204]. Außerdem hemmen kleinere huPrP-Fragmente mit nur einer der beiden Bindestellen bereits die Neurotoxizität[205]. Während unsere Aβ-Oligomere sphärische Gebilde mit einer Höhe bis zu etwa 10 nm bilden, was mit Hilfe von Rasterkraftmikroskopie (AFM) nachgewiesen werden konnte, zeigt unser Komplex aus huPrP(23-144/230) und Aβ-Oligomeren unter dem AFM eine wolkenartige Morphologie[193,206]. Weiterhin konnten wir demonstrieren, dass der Komplex mit huPrP im Überschuss, also unter Abdeckung aller Bindestellen, eine Monomerzusammensetzung Aβ zu huPrP von 4 : 1 aufweist[193]. Da ein Aβ-Oligomer im Mittel aus 23 Monomeren[77] besteht, kann somit ein Aβ-Oligomer im Mittel sechs huPrP binden. Es entsteht also ein dreidimensionales Netzwerk, was auch die wolkenartige Morphologie nahelegt. Insgesamt wurden im Zuge dieser Doktorarbeit vier Proben mittels Festkörper-MAS-NMR-Spektroskopie untersucht: Zuerst wurde eine Probe mit uniform-^{13}C,^{15}N-markiertem huPrP(23-144) und unmarkierten Aβ-Oligomeren untersucht, bei welchem ausschließlich strukturelle Informationen des

N-Terminus von huPrP erhalten werden können. Dabei wurden PDSD-Spektren auch mit ^{13}C-^{13}C-TOCSY-Spektren von huPrP(23-144) in Lösung verglichen, das über seine gesamte Sequenz hinweg ungeordnet (*Random-Coil*-Struktur) vorliegt. Des Weiteren wurde eine Probe mit uniform-^{13}C,^{15}N-markiertem Volllängen-huPrP(23-230) im Komplex mit unmarkierten Aβ-Oligomeren untersucht, um strukturelle Informationen zum C-Terminus zu erhalten. Dabei wurden PDSD-Spektren mit simulierten Spektren aus chemischen Verschiebungen von nativ-gefaltetem huPrP(23-230) ohne Aβ verglichen, welches, wie zuvor bereits beschrieben, aus zwei β-Faltblättern und drei α-Helices besteht[97]. Außerdem wurde eine Probe mit uniform-^{13}C,^{15}N-markierten Aβ-Oligomeren mit unmarkiertem huPrP(23-144) untersucht. Dabei konnten strukturelle Informationen zu den Aβ-Oligomeren erhalten werden, so zum Beispiel durch einen Vergleich von PDSD-Spektren mit ^{13}C-^{13}C-TOCSY-Spektren von monomerem Aβ in Lösung, aber auch durch den Vergleich mit aus der Literatur bekannten Fibrillen- und Protofibrillen-Strukturen (Vergleich eines PDSD-Spektrums mit simulierten Spektren aus chemischen Verschiebungen dieser Strukturen). Bei diesen aus der Literatur bekannten Fibrillen- und Protofibrillen-Strukturen handelte es sich genauer gesagt um die Gremer-Fibrille bei pH 2[35], die Meier-[33] und Griffin-Fibrillen[34] bei pH 7,4 und eine artifizielle Protofibrille mit zwei Alanin-zu-Cystein-Mutationen (A21C, A30C)[140]. Außerdem konnte eine teilweise sequenzielle Zuordnung erfolgen, die allerdings durch die Heterogenität der Probe erschwert wurde. Die vierte Probe unterschied sich zur dritten Probe nicht in der Markierung, aber im Aβ-huPrP-Verhältnis. Während dieses bei der dritten Probe 8,6 : 1 betrug, wurde in der vierten Probe huPrP(23-144) im Überschuss zugesetzt, das Aβ-huPrP-Verhältnis betrug somit 3,7 ± 0,12 : 1. Dadurch sollte ausgeschlossen werden, dass sich die Heterogenität der Probe mit unbesetzten Aβ-Bindestellen erklären lässt. **Abbildung 7** zeigt eine schematische Darstellung des huPrP-Aβ-Oligomer-Komplexes mit den wichtigsten strukturellen Erkenntnissen[206].
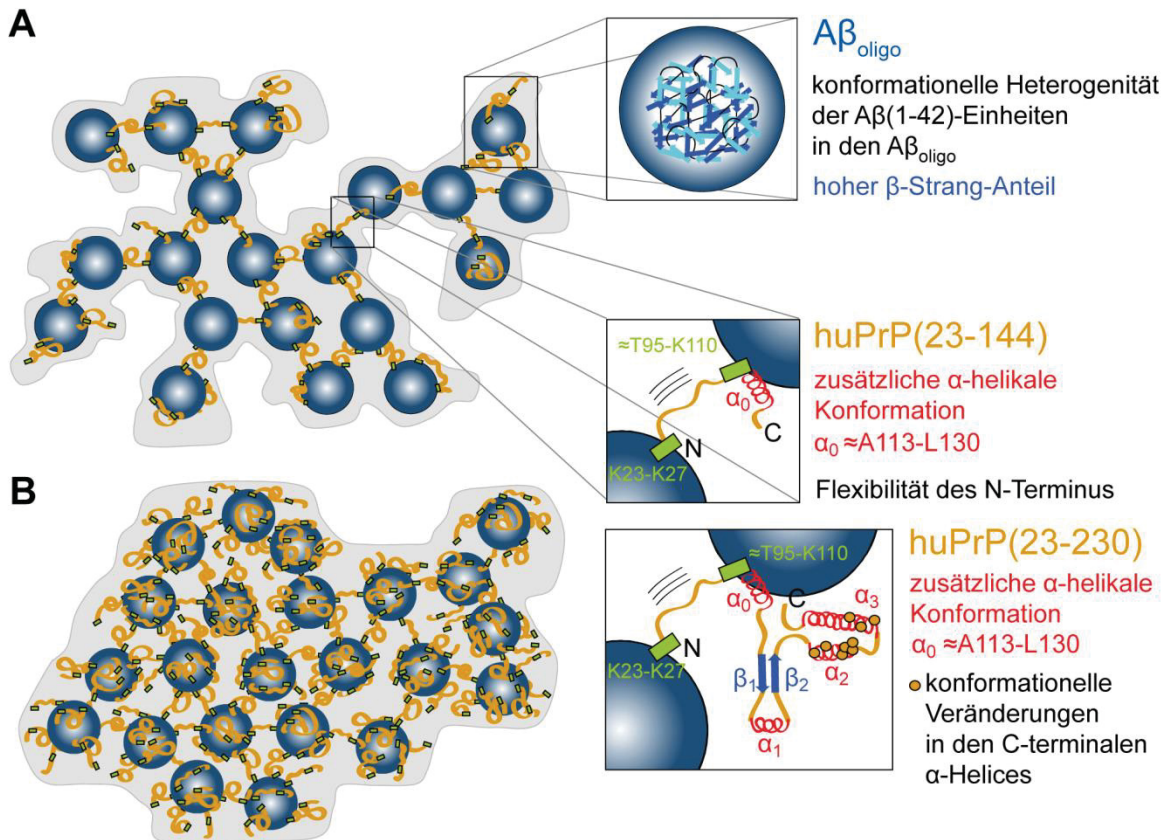
Abbildung 7: *Schema des huPrP-Aβ-Oligomer-Komplexes mit den wichtigsten strukturellen Erkenntnissen[206]. **A** Bei hohem Aβ-huPrP-Verhältnis, wie in der Probe mit uniform-^{13}C,^{15}N-markierten Aβ-Oligomeren mit unmarkiertem huPrP(23-144). **B** Bei einem Aβ-huPrP-Verhältnis von ≈ 4 : 1, wie in der Probe mit uniform-^{13}C,^{15}N-markierten Aβ-Oligomeren mit unmarkiertem huPrP(23-144) im Überschuss. Die Aβ-Oligomere sind als blaue Kugeln, das huPrP als orange Linien, α-Helices als rote Windungen, β-Stränge als blaue Pfeile, die Aβ-Bindestellen am huPrP (K23 bis K27 und ≈ T95 bis K110) als grüne Kästchen und konformationelle Veränderungen in den C-terminalen α-helices von huPrP(23-230) als orange Punkte dargestellt. Adaptiert aus [193,206].*

2 Ziel der Arbeit

In der vorliegenden Arbeit wurden Proteine, die bei Alzheimerscher Demenz (Projekt 1), aber auch bei den Prionenerkrankungen (Projekt 2) eine Rolle spielen, strukturell untersucht.

Dabei wurden in Projekt 1 (Publikation „Structural details of amyloid β oligomers in complex with human prion protein as revealed by solid-state MAS NMR spectroscopy"[206]) strukturelle Eigenschaften des Komplexes aus humanem Prionprotein in Volllängen- (Aminosäurereste 23 bis 230) und N-terminalem Konstrukt (Aminosäurereste 23 bis 144) mit Aβ(1-42)-Oligomeren mit uniformer ^{13}C,^{15}N-Markierung, entweder des huPrPs oder Aβ(1-42)s, ermittelt[206]. Die biochemische Charakterisierung des Komplexes mittels Rasterkraftmikroskopie (AFM), Dichtegradienten-Zentrifugation (DGZ) und Umkehrphasen-Hochleistungsflüssigkeitschromatographie (*reversed phases high performance liquid chromatography*, *RP-HPLC*) erfolgte in der Veröffentlichung „A d-enantiomeric peptide interferes with heteroassociation of amyloid-beta oligomers and prion protein"[193].

In Projekt 2 (Publikation „Development of a new largely scalable in vitro prion propagation method for the production of infectious recombinant prions for high resolution structural studies"[159]) geht es um erste strukturelle Untersuchungen von BVPrP-Fibrillen, die mittels der bereits erwähnten PMSA-Methode erhalten wurden. PMSA stellt, wie bereits erwähnt, ein neues Verfahren dar, bei welchem durch die Verwendung eines Schüttlers anstelle Ultraschalls größere Mengen (mehr als 1000-faches *Scaling-up* im Vergleich zur PMCA) aggregierten, rekombinant hergestellten, infektiösen Prionproteins (rPrP) hergestellt werden können, wie sie für Strukturuntersuchungen, wie der mittels Festkörper-MAS-NMR-Spektroskopie, nötig sind. Die PMSA-Methode wird in dieser Publikation u. A. mit Hilfe von Proteinase K-Verdau und einem transgenen Maus- (TgVole) und Rötelmaus-Modell validiert[159].

Zur Strukturuntersuchung in beiden Projekten wird die Festkörper-MAS-NMR-Spektroskopie genutzt, die gerade bei Untersuchungen unlöslicher, amorpher Proteine im atomaren Bereich die Methode der Wahl darstellt. Die Veröffentlichung „Chapter 10 Isotopically Enriched Systems" aus dem Buch

„Modern Methods in Solid-state NMR: A Practitioner's Guide"[101] gibt einen Überblick über die für Strukturuntersuchungen mittels Festkörper-MAS-NMR-Spektroskopie an Proteinen und anderen isotopenmarkierten biologischen Proben einsetzbaren Markierungstechniken und Festkörper-MAS-NMR-Experimente zusammen mit deren Zweck, Vorteilen und Nachteilen[101].

Außerdem wird in der Veröffentlichung „Hyperpolarized MAS NMR of unfolded and misfolded proteins"[123] näher auf die neu-entwickelte Methode der *Dynamik Nuclear Polarization* und deren Anwendungen auf und Nutzen für intrinsisch ungeordnete und aggregierte Proteine eingegangen[123].

All diese Verfahren zusammengenommen liefern Informationen, die zum Verständnis der dreidimensionalen Struktur dieser Proteine beitragen. Ein solches Verständnis, wenn es auch nur einen punktuellen Beitrag zur Erklärung der jeweiligen Neurodegenerativen Erkrankung liefert, kann zum einen die Suche nach Therapien und Heilmitteln für diese Erkrankungen erleichtern, zum anderen aber auch zum allgemeinen Verständnis von, sowohl nativen als auch pathogenen, Mechanismen im Gehirn beitragen.

3 Publikationen

3.1 Structural details of amyloid β oligomers in complex with human prion protein as revealed by solid-state MAS NMR spectroscopy

König, A. S., Rösener, N. S., Gremer, L., Tusche, M., Flender, D., Reinartz, E., Hoyer, W., Neudecker, P., Willbold, D. and Heise, H.

Zeitschrift: *Journal of Biological Chemistry* (2021) **296**, 100499

Impact-Faktor: 4,238 (2019)

DOI: 10.1016/j.jbc.2021.100499

Corresponding Author: Henrike Heise, h.heise@fz-juelich.de; Dieter Willbold, d.willbold@fz-juelich.de

Mitwirkung: 70 %

Involviert in die Konzeption. Durchführung aller Festkörper-NMR-Experimente und Zuordnung und Auswertung aller Festkörper-NMR-Spektren. Durchführung zusätzlicher Datenanalysen. Involviert in das Verfassen des Manuskriptes.

Nachdruck: Im Anhang befindet sich ein vollständiger Nachdruck der Publikation König, A. S., Rösener, N. S., Gremer, L., Tusche, M., Flender, D., Reinartz, E., Hoyer, W., Neudecker, P., Willbold, D. and Heise, H., Structural details of amyloid β oligomers in complex with human prion protein as revealed by solid-state MAS NMR spectroscopy, *The Journal of Biological Chemistry* (2021) **296**, 100499, DOI: 10.1016/j.jbc.2021.100499. This is an open access article distributed under the terms of the Creative Commons CC-BY license, which permits unrestricted use, distribution, and reproduction in any medium, provided the original work is properly cited.

3.2 A d-enantiomeric peptide interferes with heteroassociation of amyloid-beta oligomers and prion protein

Rösener, N. S., Gremer, L., Reinartz, E., <u>König, A.</u>, Brener, O., Heise, H., Hoyer, W., Neudecker, P., and Willbold, D.

Zeitschrift: *Journal of Biological Chemistry* (2018) **293**, 15748-15764

Impact-Faktor: 4,238 (2019)

DOI: <u>10.1074/jbc.RA118.003116</u>

Corresponding Author: Dieter Willbold, <u>dieter.willbold@hhu.de</u>

Mitwirkung: 5 %

Involviert in die Diskussion der Daten und das Erstellen eines Modells. Korrekturlesen des Manuskriptes.

Nachdruck: Im Anhang befindet sich ein vollständiger Nachdruck der Publikation Rösener, N. S., Gremer, L., Reinartz, E., <u>König, A.</u>, Brener, O., Heise, H., Hoyer, W., Neudecker, P., and Willbold, D. A d-enantiomeric peptide interferes with heteroassociation of amyloid-beta oligomers and prion protein. J Biol Chem 2018; 293: 15748-15764, DOI: <u>10.1074/jbc.RA118.003116</u>. This is an open access article distributed under the terms of the <u>Creative Commons CC-BY</u> license, which permits unrestricted use, distribution, and reproduction in any medium, provided the original work is properly cited.

3.3 Development of a new largely scalable in vitro prion propagation method for the production of infectious recombinant prions for high resolution structural studies

Eraña, H., Charco, J. M., Di Bari, M. A., Díaz-Domínguez, C. M., López-Moreno, R., Vidal, E., González-Miranda, E., Pérez-Castro, M. A., García-Martínez, S., Bravo, S., Fernández-Borges, N., Geijo, M., D'Agostino, C., Garrido, J., Bian, J., König, A., Uluca-Yazgi, B., Sabate, R., Khaychuk, V., Vanni, I., Telling, G. C., Heise, H., Nonno, R., Requena, J. R., and Castilla, J.

Zeitschrift: *PLoS Pathogens* (2019) **15**, e1008117

Impact-Faktor: 6,218 (2020)

DOI: 10.1371/journal.ppat.1008117

Corresponding Author: Joaquín Castilla, castilla@joaquincastilla.com

Mitwirkung: 2 %

Involviert in Durchführung und Auswertung der Festkörper-NMR-Experimente. Korrekturlesen des Festkörper-NMR-Teiles des Manuskriptes.

Nachdruck: Im Anhang befindet sich ein vollständiger Nachdruck der Publikation Eraña, H., Charco, J. M., Di Bari, M. A., Díaz-Domínguez, C. M., López-Moreno, R., Vidal, E., González-Miranda, E., Pérez-Castro, M. A., García-Martínez, S., Bravo, S., Fernández-Borges, N., Geijo, M., D'Agostino, C., Garrido, J., Bian, J., König, A., Uluca-Yazgi, B., Sabate, R., Khaychuk, V., Vanni, I., Telling, G. C., Heise, H., Nonno, R., Requena, J. R., and Castilla, J., Development of a new largely scalable in vitro prion propagation method for the production of infectious recombinant prions for high resolution structural studies, *PLoS Pathogens* (2019) **15**, e1008117, Doi: 10.1371/journal.ppat.1008117. © 2019 Eraña et al. This is an open access article distributed under the terms of the Creative Commons Attribution License, which permits unrestricted use, distribution, and reproduction in any medium, provided the original author and source are credited.

3.4 Hyperpolarized MAS NMR of unfolded and misfolded proteins

König, A., Schölzel, D., Uluca, B., Viennet, T., Akbey, Ü., and Heise, H.

Corresponding Author: Henrike Heise, h.heise@fz-juelich.de

Mitwirkung: 17 %

Verfassen einiger Teile des Abschnittes „DNP-enhanced MAS NMR of disordered proteins".

3.5 Chapter 10 Isotopically Enriched Systems

Beumer, C., <u>König, A.</u>, Schölzel, D., Uluca, B., Weirich, F., and Heise, H.

Publisher: The Royal Society of Chemistry

Buchtitel: *Modern Methods in Solid-state NMR: A Practitioner's Guide*

Editor: Paul Hodgkinson, paul.hodgkinson@durham.ac.uk

Typ: Buchkapitel, Seiten 289-321, 2018

DOI: 10.1039/9781788010467-00289

eISBN: 978-1-78801-046-7

Mitwirkung: 17 %

Verfassen des Abschnittes „Second-order Homonuclear Dipolar Recoupling".

Dieses Buchkapitel ist zu finden unter:

http://pubs.rsc.org/en/content/chapterhtml/2018/bk9781782628545-00289?isbn=978-1-78262-854-5&sercode=bk

4 Fazit

Auf dem Weg zu einem Heilmittel, ist ein umfassendes Verständnis der pathologischen Prozesse neurodegenerativer Erkrankungen im Gehirn nötig. Da es sich um biologisch-chemische Prozesse auf Basis verschiedener zur Aggregation neigender und aggregierter Proteine handelt, ist eine strukturelle Untersuchung dieser Proteinaggregate und -komplexe unumgänglich. In dieser Doktorarbeit wurde zur Strukturuntersuchung die Festkörper-MAS-NMR-Spektroskopie herangezogen, weil sie im Vergleich zur Röntgenkristallografie, Cryo-EM und Lösungs-NMR-Spektroskopie wichtige strukturelle Informationen von festen, amorphen nicht-kristallisierbaren Proteinen auf atomarer Ebene liefert. Dabei wurde auch auf die Anwendung der Festkörper-MAS-NMR-Spektroskopie auf isotopenmarkierte biologische Proben allgemein[101] und die Anwendung der DNP-MAS-NMR-Spektroskopie speziell auf dem Gebiet der aggregierten Proteine eingegangen[123]. Zwei solcher aggregierter Proteinstrukturen wurden im Zuge dieser Doktorarbeit näher untersucht: zum einen ein Komplex aus humanem Prionprotein und Amyloid-β-Oligomeren[206], der bei der Alzheimerschen Erkrankung eine Rolle spielt, und zum anderen ein Fibrillentyp des Rötelmaus-Prionproteins[159], das bei den Prionenerkrankungen aggregiert.

Bei der Untersuchung des Komplexes aus humanem Prionprotein und Amyloid-β-Oligomeren in Projekt 1 konnten mehrere wichtige Aspekte gezeigt werden: (1) Der N-Terminus des Prionproteins ist sowohl in einem Volllängen-, als auch in einem verkürzten Konstrukt (huPrP(23-144)) ungefaltet (Random Coil), aber starr genug, um im Kreuzpolarisationspektrum der Festkörper-MAS-NMR-Spektroskopie Signale zu zeigen. Nur ein kurzer Abschnitt ab dem Palindrom-Segment (Aminosäuren A113 bis L130) besitzt α-helikale Anteile. (2) Der nativ-strukturierte C-Terminus des Prionproteins (zwei β-Stränge, drei α-Helices) weist eine zumindest teilweise Auffaltung in den letzten beiden α-Helices auf, da sich die chemischen Verschiebungen von Thr und Val zu Random-Coil-Werten verschieben. (3) Amyloid-β-Oligomere zeigen einen hohen Anteil an β-Faltblatt-Strukturen, sind aber heterogen, was auf das Vorhandensein mehrerer Fibrillentypen hindeutet. Dabei kann es sich zum einen um Polymorphismus innerhalb eines Oligomers bedingt durch die Nähe oder Entfernung zu huPrP handeln. Ein Vergleich mit den chemischen Verschiebungen dreier in der Literatur beschriebener Fibrillen-Strukturen und einer artifiziellen

Protofibrille lässt zum anderen Spekulationen über das Vorhandensein aller dieser Strukturen zu. Bisherige Untersuchungen mehrerer Forschungsgruppen an Amyloid-β-Oligomeren legen nahe, dass die Sekundärstruktur des Oligomers bereits dem der Fibrille entspricht, während sich die Tertiärstruktur unterscheidet[81,134]. So könnte der Polymorphismus der Amyloid-β-Oligomere auch mit dem Auftreten der Sekundärstrukturen mehrerer (Proto)Fibrillentypen erklärt werden[206].

Bei der Untersuchung der Rötelmaus-Prionprotein-Fibrille im Projekt 2 konnten keine hoch-flexiblen Bereiche, aber viele Resonanzen im zweidimensionalen PDSD-Spektrum beobachtet werden, darunter waren u. A. unterscheidbare Signale von Ala, Thr, Ile und Val. Außerdem zeigte der überwiegende Teil der Resonanzen β-Strang-ähnliche chemische Verschiebungen, was zur erwarteten Struktur einer Fibrille passt. Dadurch konnte nachgewiesen werden, dass die bereits erwähnte neuentwickelte PMSA-Methode zur Proteinherstellung für mehrfach-markierte Festkörper-NMR-Proben (und potentiell andere Strukturuntersuchungsmethoden) geeignet ist[159].

Diese Erkenntnisse auf den Gebieten der Alzheimerschen Erkrankung und der Prionenerkrankungen können zum Verständnis dieser Krankheiten und somit zur Entwicklung neuer Therapiestrategien auf dem Weg zum Heilmittel beitragen. Außerdem wird sich zeigen, ob einige dieser Erkenntnisse auf andere Proteinfehlfaltungserkrankungen übertragen werden können, um den allgemeinen Mechanismus solcher Erkrankungen und auch die Funktion des Gehirns auf chemischer Ebene besser zu verstehen.

Quellenverzeichnis

1   Creighton, T. E. *Proteins: Structures and Molecular Properties*. 182-188 (W. H. Freeman, 1993).

2   Stryer, L. *Biochemie*. 4. edn 28-31, 289 (Spektrum, 1995).

3   Wishart, D. S., Sykes, B. D. & Richards, F. M. Relationship between nuclear magnetic resonance chemical shift and protein secondary structure. *J. Mol. Biol.* **222**, 311-333, (1991).

4   Spera, S. & Bax, A. Empirical correlation between protein backbone conformation and C.alpha. and C.beta. 13C nuclear magnetic resonance chemical shifts. *J. Am. Chem. Soc.* **113**, 5490-5492, (1991).

5   Wishart, D. S., Sykes, B. D. & Richards, F. M. The chemical shift index: a fast and simple method for the assignment of protein secondary structure through NMR spectroscopy. *Biochemistry* **31**, 1647-1651, (1992).

6   Wishart, D. S. & Sykes, B. D. The [13]C Chemical-Shift Index: A simple method for the identification of protein secondary structure using ^{13}C chemical-shift data. *J. Biomol. NMR* **4**, 171-180, (1994).

7   Wishart, D. S. & Case, D. A. in *Methods Enzymol.* Vol. 338 (eds T. L. James, V. Dötsch, & U. Schmitz) Ch. [1] Use of Chemical Shifts in Macromolecular Structure Determination, 3-34 (Academic Press, 2002).

8   Uluca, B. *et al.* DNP-Enhanced MAS NMR: A Tool to Snapshot Conformational Ensembles of α-Synuclein in Different States. *Biophys. J.* **114**, 1614-1623, (2018).

9   Siemer, A. B. Advances in studying protein disorder with solid-state NMR. *Solid State Nucl. Magn. Reson.* **106**, 101643, (2020).

10   Dobson, C. M. Protein misfolding, evolution and disease. *Trends Biochem. Sci.* **24**, 329-332, (1999).

11   Dobson, C. M. & Karplus, M. The fundamentals of protein folding: bringing together theory and experiment. *Curr. Opin. Struct. Biol.* **9**, 92-101, (1999).

12   Chiti, F. *et al.* Designing conditions for in vitro formation of amyloid protofilaments and fibrils. *Proc. Natl. Acad. Sci.* **96**, 3590-3594, (1999).

13   Gao, Y. *et al.* Out-of-Register Parallel β-Sheets and Antiparallel β-Sheets Coexist in 150-kDa Oligomers Formed by Amyloid-β(1–42). *J. Mol. Biol.* **432**, 4388-4407, (2020).

14   Upadhaya, A. R., Lungrin, I., Yamaguchi, H., Fändrich, M. & Thal, D. R. High-molecular weight Aβ oligomers and protofibrils are the predominant Aβ species in the native soluble protein fraction of the AD brain. *J. Cell. Mol. Med.* **16**, 287-295, (2012).

15   Grüning, C. S. R. *et al.* The off-rate of monomers dissociating from amyloid-β protofibrils. *J. Biol. Chem.* **288**, 37104-37111, (2013).

16   Hasecke, F. *et al.* Origin of metastable oligomers and their effects on amyloid fibril self-assembly. *Chem. Sci.* **9**, 5937-5948, (2018).

17   Perez, C. *et al.* Mechanism of Fibril and Soluble Oligomer Formation in Amyloid Beta and Hen Egg White Lysozyme Proteins. *J. Phys. Chem. B* **123**, 5678-5689, (2019).

18   Hasecke, F. *et al.* Protofibril–Fibril Interactions Inhibit Amyloid Fibril Assembly by Obstructing Secondary Nucleation. *Angew. Chem. Int. Ed.* **60**, 3016-3021, (2021).

19   Jaroniec, C. P. Two decades of progress in structural and dynamic studies of amyloids by solid-state NMR. *J. Magn. Reson.* **306**, 42-47, (2019).

20   Riek, R. & Eisenberg, D. S. The activities of amyloids from a structural perspective. *Nature* **539**, 227-235, (2016).

21   Goldschmidt, L., Teng, P. K., Riek, R. & Eisenberg, D. Identifying the amylome, proteins capable of forming amyloid-like fibrils. *Proc. Natl. Acad. Sci.* **107**, 3487-3492, (2010).

22   Knowles, T. P. J., Vendruscolo, M. & Dobson, C. M. The amyloid state and its association with protein misfolding diseases. *Nat. Rev. Mol. Cell Biol.* **15**, 384-396, (2014).

23   Antzutkin, O. N. *et al.* Multiple quantum solid-state NMR indicates a parallel, not antiparallel, organization of β-sheets in Alzheimer's β-amyloid fibrils. *Proc. Natl. Acad. Sci. U. S. A.* **97**, 13045-13050, (2000).

24   Antzutkin, O. N., Leapman, R. D., Balbach, J. J. & Tycko, R. Supramolecular structural constraints on Alzheimer's β-amyloid fibrils from electron microscopy and solid-state nuclear magnetic resonance. *Biochemistry* **41**, 15436-15450, (2002).

25   Balbach, J. J. *et al.* Supramolecular Structure in Full-Length Alzheimer's β-Amyloid Fibrils: Evidence for a Parallel β-Sheet Organization from Solid-State Nuclear Magnetic Resonance. *Biophys. J.* **83**, 1205-1216, (2002).

26   Petkova, A. T. *et al.* A structural model for Alzheimer's β-amyloid fibrils based on experimental constraints from solid state NMR. *Proc. Natl. Acad. Sci. U. S. A.* **99**, 16742-16747, (2002).

27   Petkova, A. T. *et al.* Self-Propagating, Molecular-Level Polymorphism in Alzheimer's ß-Amyloid Fibrils. *Science* **307**, 262-265, (2005).

28   Petkova, A. T., Yau, W.-M. & Tycko, R. Experimental Constraints on Quaternary Structure in Alzheimer's β-Amyloid Fibrils. *Biochemistry* **45**, 498-512, (2006).

29   Paravastu, A. K., Leapman, R. D., Yau, W.-M. & Tycko, R. Molecular structural basis for polymorphism in Alzheimer's β-amyloid fibrils. *Proc. Natl. Acad. Sci.* **105**, 18349-18354, (2008).

30   Bertini, I., Gonnelli, L., Luchinat, C., Mao, J. & Nesi, A. A New Structural Model of Aβ40 Fibrils. *J. Am. Chem. Soc.* **133**, 16013-16022, (2011).

31   Lu, J.-X. *et al.* Molecular Structure of β-Amyloid Fibrils in Alzheimer's Disease Brain Tissue. *Cell* **154**, 1257-1268, (2013).

32   Xiao, Y. *et al.* Aβ(1-42) fibril structure illuminates self-recognition and replication of amyloid in Alzheimer's disease. *Nat. Struct. Mol. Biol.* **22**, 499-505, (2015).

33   Wälti, M. A. *et al.* Atomic-resolution structure of a disease-relevant Aβ(1–42) amyloid fibril. *Proc. Natl. Acad. Sci.* **113**, E4976-E4984, (2016).

34   Colvin, M. T. *et al.* Atomic Resolution Structure of Monomorphic Aβ42 Amyloid Fibrils. *J. Am. Chem. Soc.* **138**, 9663-9674, (2016).

35   Gremer, L. *et al.* Fibril structure of amyloid-beta(1-42) by cryo-electron microscopy. *Science* **358**, 116-119, (2017).

36   Meier, B. H., Riek, R. & Böckmann, A. Emerging Structural Understanding of Amyloid Fibrils by Solid-State NMR. *Trends Biochem. Sci.* **42**, 777-787, (2017).

37   Andronesi, O. C. *et al.* Characterization of Alzheimer's-like Paired Helical Filaments from the Core Domain of Tau Protein Using Solid-State NMR Spectroscopy. *J. Am. Chem. Soc.* **130**, 5922-5928, (2008).

38   Fitzpatrick, A. W. P. *et al.* Cryo-EM structures of tau filaments from Alzheimer's disease. *Nature* **547**, 185-190, (2017).

39   Dregni, A. J. *et al.* In vitro 0N4R tau fibrils contain a monomorphic β-sheet core enclosed by dynamically heterogeneous fuzzy coat segments. *Proc. Natl. Acad. Sci.* **116**, 16357-16366, (2019).

40   Helmus, J. J., Surewicz, K., Nadaud, P. S., Surewicz, W. K. & Jaroniec, C. P. Molecular conformation and dynamics of the Y145Stop variant of human prion protein in amyloid fibrils. *Proc. Natl. Acad. Sci.* **105**, 6284-6289, (2008).

41   Helmus, J. J., Surewicz, K., Surewicz, W. K. & Jaroniec, C. P. Conformational flexibility of Y145stop human prion protein amyloid fibrils probed by solid-state nuclear magnetic resonance spectroscopy. *J. Am. Chem. Soc.* **132**, 2393-2403, (2010).

42   Helmus, J. J., Surewicz, K., Apostol, M. I., Surewicz, W. K. & Jaroniec, C. P. Intermolecular alignment in Y145Stop human prion protein amyloid fibrils probed by solid-state NMR spectroscopy. *J. Am. Chem. Soc.* **133**, 13934-13937, (2011).

43   Theint, T., Nadaud, P. S., Surewicz, K., Surewicz, W. K. & Jaroniec, C. P. 13C and 15N chemical shift assignments of mammalian Y145Stop prion protein amyloid fibrils. *Biomol. NMR Assign.* **11**, 75-80, (2017).

44   Glynn, C. *et al.* Cryo-EM structure of a human prion fibril with a hydrophobic, protease-resistant core. *Nat. Struct. Mol. Biol.* **27**, 417-423, (2020).

45   Heise, H. *et al.* Molecular-level secondary structure, polymorphism, and dynamics of full-length α-synuclein fibrils studied by solid-state NMR. *Proc. Natl. Acad. Sci. U. S. A.* **102**, 15871-15876, (2005).

46   Tuttle, M. D. *et al.* Solid-state NMR structure of a pathogenic fibril of full-length human α-synuclein. *Nat. Struct. Mol. Biol.* **23**, 409-415, (2016).

47   Guerrero-Ferreira, R. *et al.* Two new polymorphic structures of human full-length alpha-synuclein fibrils solved by cryo-electron microscopy. *Elife* **8**, e48907, (2019).

48   Luca, S., Yau, W.-M., Leapman, R. & Tycko, R. Peptide conformation and supramolecular organization in amylin fibrils: constraints from solid-state NMR. *Biochemistry* **46**, 13505-13522, (2007).

49   Madine, J. *et al.* Structural Insights into the Polymorphism of Amyloid-Like Fibrils Formed by Region 20−29 of Amylin Revealed by Solid-State NMR and X-ray Fiber Diffraction. *J. Am. Chem. Soc.* **130**, 14990-15001, (2008).

50   Nielsen, J. T. *et al.* Unique Identification of Supramolecular Structures in Amyloid Fibrils by Solid-State NMR Spectroscopy. *Angew. Chem. Int. Ed.* **48**, 2118-2121, (2009).

51   Weirich, F. *et al.* Structural Characterization of Fibrils from Recombinant Human Islet Amyloid Polypeptide by Solid-State NMR: The Central FGAILS Segment Is Part of the β-Sheet Core. *PLoS One* **11**, e0161243, (2016).

52   Jaroniec, C. P. *et al.* High-resolution molecular structure of a peptide in an amyloid fibril determined by magic angle spinning NMR spectroscopy. *Proc. Natl. Acad. Sci. U. S. A.* **101**, 711-716, (2004).

53   Debelouchina, G. T. *et al.* Higher order amyloid fibril structure by MAS NMR and DNP spectroscopy. *J. Am. Chem. Soc.* **135**, 19237-19247, (2013).

54   Fitzpatrick, A. W. P. *et al.* Atomic structure and hierarchical assembly of a cross-β amyloid fibril. *Proc. Natl. Acad. Sci.* **110**, 5468-5473, (2013).

55   Iwata, K. *et al.* 3D structure of amyloid protofilaments of beta2-microglobulin fragment probed by solid-state NMR. *Proc. Natl. Acad. Sci. U. S. A.* **103**, 18119-18124, (2006).

56   Barbet-Massin, E. *et al.* Fibrillar vs Crystalline Full-Length β-2-Microglobulin Studied by High-Resolution Solid-State NMR Spectroscopy. *J. Am. Chem. Soc.* **132**, 5556-5557, (2010).

57   Wasmer, C. *et al.* Amyloid Fibrils of the HET-s(218–289) Prion Form a β Solenoid with a Triangular Hydrophobic Core. *Science* **319**, 1523-1526, (2008).

58   Van Melckebeke, H. *et al.* Atomic-Resolution Three-Dimensional Structure of HET-s(218−289) Amyloid Fibrils by Solid-State NMR Spectroscopy. *J. Am. Chem. Soc.* **132**, 13765-13775, (2010).

59   Shewmaker, F., Kryndushkin, D., Chen, B., Tycko, R. & Wickner, R. B. Two Prion Variants of Sup35p Have In-Register Parallel β-Sheet Structures, Independent of Hydration. *Biochemistry* **48**, 5074-5082, (2009).

60   Shewmaker, F., Wickner, R. B. & Tycko, R. Amyloid of the prion domain of Sup35p has an in-register parallel β-sheet structure. *Proc. Natl. Acad. Sci.* **103**, 19754-19759, (2006).

61   Baxa, U. *et al.* Characterization of β-Sheet Structure in Ure2p1-89 Yeast Prion Fibrils by Solid-State Nuclear Magnetic Resonance. *Biochemistry* **46**, 13149-13162, (2007).

62   Shewmaker, F., Ross, E. D., Tycko, R. & Wickner, R. B. Amyloids of Shuffled Prion Domains That Form Prions Have a Parallel In-Register β-Sheet Structure. *Biochemistry* **47**, 4000-4007, (2008).

63   Wickner, R. B., Dyda, F. & Tycko, R. Amyloid of Rnq1p, the basis of the [*PIN*⁺] prion, has a parallel in-register β-sheet structure. *Proc. Natl. Acad. Sci.* **105**, 2403-2408, (2008).

64   Shewmaker, F. *et al.* The Functional Curli Amyloid Is Not Based on In-register Parallel β-Sheet Structure. *J. Biol. Chem.* **284**, 25065-25076, (2009).

65   Wang, X. & Chapman, M. R. Curli provide the template for understanding controlled amyloid propagation. *Prion* **2**, 57-60, (2008).

66   Murray, D. T. *et al.* Structure of FUS Protein Fibrils and Its Relevance to Self-Assembly and Phase Separation of Low-Complexity Domains. *Cell* **171**, 615-627.e16, (2017).

67   Tycko, R. Solid-State NMR Studies of Amyloid Fibril Structure. *Annu. Rev. Phys. Chem.* **62**, 279-299, (2011).

68   van der Wel, P. C. A. Insights into protein misfolding and aggregation enabled by solid-state NMR spectroscopy. *Solid State Nucl. Magn. Reson.* **88**, 1-14, (2017).

69   Gelenter, M. D. *et al.* The peptide hormone glucagon forms amyloid fibrils with two coexisting β-strand conformations. *Nat. Struct. Mol. Biol.* **26**, 592-598, (2019).

70   Flores-Fernández, J., Rathod, V. & Wille, H. Comparing the Folds of Prions and Other Pathogenic Amyloids. *Pathogens* **7**, 50, (2018).

71   Requena, J. R. & Wille, H. The structure of the infectious prion protein: experimental data and molecular models. *Prion* **8**, 60-66, (2014).

72   Vázquez-Fernández, E. *et al.* The Structural Architecture of an Infectious Mammalian Prion Using Electron Cryomicroscopy. *PLoS Pathog.* **12**, e1005835, (2016).

73   Spagnolli, G. *et al.* Full atomistic model of prion structure and conversion. *PLoS Pathog.* **15**, e1007864, (2019).

74   Wang, L.-Q. *et al.* Cryo-EM structure of an amyloid fibril formed by full-length human prion protein. *Nat. Struct. Mol. Biol.* **27**, 598-602, (2020).

75   Sipe, J. D. AMYLOIDOSIS. *Annu. Rev. Biochem.* **61**, 947-975, (1992).

76   Biancalana, M. & Koide, S. Molecular mechanism of Thioflavin-T binding to amyloid fibrils. *Biochim. Biophys. Acta* **1804**, 1405-1412, (2010).

77   Brener, O. *et al.* QIAD assay for quantitating a compound's efficacy in elimination of toxic Aβ oligomers. *Sci. Rep.* **5**, 13222-13234, (2015).

78   Scheidt, H. A., Morgado, I., Rothemund, S., Huster, D. & Fändrich, M. Solid-State NMR Spectroscopic Investigation of Aβ Protofibrils: Implication of a β-Sheet Remodeling upon Maturation into Terminal Amyloid Fibrils. *Angew. Chem. Int. Ed.* **50**, 2837-2840, (2011).

79   Scheidt, H. A., Morgado, I. & Huster, D. Solid-state NMR reveals a close structural relationship between amyloid-β protofibrils and oligomers. *J. Biol. Chem.* **287**, 22822-22826, (2012).

80   Qiang, W., Yau, W.-M. & Tycko, R. Structural evolution of Iowa mutant β-amyloid fibrils from polymorphic to homogeneous states under repeated seeded growth. *J. Am. Chem. Soc.* **133**, 4018-4029, (2011).

81   Potapov, A., Yau, W. M., Ghirlando, R., Thurber, K. R. & Tycko, R. Successive Stages of Amyloid-beta Self-Assembly Characterized by Solid-State Nuclear Magnetic Resonance with Dynamic Nuclear Polarization. *J. Am. Chem. Soc.* **137**, 8294-8307, (2015).

82   Kollmer, M. *et al.* Cryo-EM structure and polymorphism of Aβ amyloid fibrils purified from Alzheimer's brain tissue. *Nat. Commun.* **10**, 4760, (2019).

83   Paravastu, A. K., Qahwash, I., Leapman, R. D., Meredith, S. C. & Tycko, R. Seeded growth of β-amyloid fibrils from Alzheimer's brain–derived fibrils produces a distinct fibril structure. *Proc. Natl. Acad. Sci.*, pnas.0812033106, (2009).

84   Maury, C. P. J. The emerging concept of functional amyloid. *J. Intern. Med.* **265**, 329-334, (2009).

85   Gopalswamy, M. *et al.* Structural characterization of amyloid fibrils from the human parathyroid hormone. *Biochim. Biophys. Acta* **1854**, 249-257, (2015).

86   Bissig, C., Rochin, L. & van Niel, G. PMEL Amyloid Fibril Formation: The Bright Steps of Pigmentation. *Int. J. Mol. Sci.* **17**, 1438, (2016).

87   Dahlgren, K. N. *et al.* Oligomeric and Fibrillar Species of Amyloid-β Peptides Differentially Affect Neuronal Viability. *J. Biol. Chem.* **277**, 32046-32053, (2002).

88   World Alzheimer Report 2019: Attitudes to dementia. (Alzheimer's Disease International, London, 2019).

89   2018 Alzheimer's disease facts and figures. *Alzheimers Dement.* **14**, 367-429, (2018).

90   Selkoe, D. J. Soluble oligomers of the amyloid β-protein impair synaptic plasticity and behavior. *Behav. Brain Res.* **192**, 106-113, (2008).

91   Hattori, M. *et al.* The DNA sequence of human chromosome 21. *Nature* **405**, 311-319, (2000).

92   2020 Alzheimer's disease facts and figures. *Alzheimers Dement.* **16**, 391-460, (2020).

93   Chêne, G. *et al.* Gender and incidence of dementia in the Framingham Heart Study from mid-adult life. *Alzheimers Dement.* **11**, 310-320, (2015).

94   Prusiner, S. B. Prions. *Proc. Natl. Acad. Sci.* **95**, 13363-13383, (1998).

95   Watts, J. C. *et al.* Evidence That Bank Vole PrP Is a Universal Acceptor for Prions. *PLoS Pathog.* **10**, e1003990, (2014).

96   Fernández-Borges, N. *et al.* Cofactors influence the biological properties of infectious recombinant prions. *Acta Neuropathol.* **135**, 179-199, (2018).

97   Zahn, R. *et al.* NMR solution structure of the human prion protein. *Proc. Natl. Acad. Sci.* **97**, 145-150, (2000).

98   Andrew, E. R., Bradbury, A. & Eades, R. G. Nuclear Magnetic Resonance Spectra from a Crystal rotated at High Speed. *Nature* **182**, 1659-1659, (1958).

99   Lowe, I. J. Free Induction Decays of Rotating Solids. *Phys. Rev. Lett.* **2**, 285-287, (1959).

100   Apperley, D. C., Harris, R. K. & Hodgkinson, P. *Solid-state NMR : basic principles & practice*. (Momentum Press, 2012).

101   Beumer, C. *et al.* in *Modern Methods in Solid-state NMR: A Practitioner's Guide* Ch. 10 Isotopically Enriched Systems, 289-321 (The Royal Society of Chemistry, 2018).

102   Morris, G. A. & Freeman, R. Enhancement of nuclear magnetic resonance signals by polarization transfer. *J. Am. Chem. Soc.* **101**, 760-762, (1979).

103   Hartmann, S. R. & Hahn, E. L. Nuclear Double Resonance in the Rotating Frame. *Phys. Rev.* **128**, 2042-2053, (1962).

104   Pines, A., Gibby, M. G. & Waugh, J. S. Proton-Enhanced Nuclear Induction Spectroscopy. A Method for High Resolution NMR of Dilute Spins in Solids. *J. Chem. Phys.* **56**, 1776-1777, (1972).

105   Schaefer, J. & Stejskal, E. O. Carbon-13 nuclear magnetic resonance of polymers spinning at the magic angle. *J. Am. Chem. Soc.* **98**, 1031-1032, (1976).

106   Szeverenyi, N. M., Sullivan, M. J. & Maciel, G. E. Observation of spin exchange by two-dimensional fourier transform 13C cross polarization-magic-angle spinning. *J. Magn. Reson. (1969)* **47**, 462-475, (1982).

107   Nielsen, N. C., Bildso/e, H., Jakobsen, H. J. & Levitt, M. H. Double-quantum homonuclear rotary resonance: Efficient dipolar recovery in magic-angle spinning nuclear magnetic resonance. *J. Chem. Phys.* **101**, 1805-1812, (1994).

108   Lee, Y. K. *et al.* Efficient dipolar recoupling in the NMR of rotating solids. A sevenfold symmetric radiofrequency pulse sequence. *Chem. Phys. Lett.* **242**, 304-309, (1995).

109   Rienstra, C. M. *et al.* Efficient Multispin Homonuclear Double-Quantum Recoupling for Magic-Angle Spinning NMR: 13C−13C Correlation Spectroscopy of U-13C-Erythromycin A. *J. Am. Chem. Soc.* **120**, 10602-10612, (1998).

110   Hohwy, M., Jakobsen, H. J., Edén, M., Levitt, M. H. & Nielsen, N. C. Broadband dipolar recoupling in the nuclear magnetic resonance of rotating solids: A compensated C7 pulse sequence. *J. Chem. Phys.* **108**, 2686-2694, (1998).

111   Brinkmann, A., Edén, M. & Levitt, M. H. Synchronous helical pulse sequences in magic-angle spinning nuclear magnetic resonance: Double quantum recoupling of multiple-spin systems. *J. Chem. Phys.* **112**, 8539-8554, (2000).

112   Hohwy, M., Rienstra, C. M., Jaroniec, C. P. & Griffin, R. G. Fivefold symmetric homonuclear dipolar recoupling in rotating solids: Application to double quantum spectroscopy. *J. Chem. Phys.* **110**, 7983-7992, (1999).

113   Bax, A., Freeman, R. & Kempsell, S. P. Natural abundance carbon-13-carbon-13 coupling observed via double-quantum coherence. *J. Am. Chem. Soc.* **102**, 4849-4851, (1980).

114   Bax, A., Freeman, R. & Frenkiel, T. A. An NMR technique for tracing out the carbon skeleton of an organic molecule. *J. Am. Chem. Soc.* **103**, 2102-2104, (1981).

115 Freeman, R., Frenkiel, T. & Rubin, M. B. Structure of a photodimer determined by natural-abundance ^{13}C-^{13}C coupling. *J. Am. Chem. Soc.* **104**, 5545-5547, (1982).

116 Fritzsching, K. J., Yang, Y., Schmidt-Rohr, K. & Hong, M. Practical use of chemical shift databases for protein solid-state NMR: 2D chemical shift maps and amino-acid assignment with secondary-structure information. *J. Biomol. NMR* **56**, 155-167, (2013).

117 Baldus, M., Petkova, A. T., Herzfeld, J. & Griffin, R. G. Cross polarization in the tilted frame: assignment and spectral simplification in heteronuclear spin systems. *Mol. Phys.* **95**, 1197-1207, (1998).

118 Un, S. *et al.* Pulsed dynamic nuclear polarization at 5 T. *Chem. Phys. Lett.* **189**, 54-59, (1992).

119 Becerra, L. R. *et al.* A Spectrometer for Dynamic Nuclear Polarization and Electron Paramagnetic Resonance at High Frequencies. *J. Magn. Reson., Ser A* **117**, 28-40, (1995).

120 Hall, D. A. *et al.* Polarization-Enhanced NMR Spectroscopy of Biomolecules in Frozen Solution. *Science* **276**, 930-932, (1997).

121 Rosay, M., Weis, V., Kreischer, K. E., Temkin, R. J. & Griffin, R. G. Two-Dimensional 13C−13C Correlation Spectroscopy with Magic Angle Spinning and Dynamic Nuclear Polarization. *J. Am. Chem. Soc.* **124**, 3214-3215, (2002).

122 Lilly Thankamony, A. S., Wittmann, J. J., Kaushik, M. & Corzilius, B. Dynamic nuclear polarization for sensitivity enhancement in modern solid-state NMR. *Prog. Nucl. Magn. Reson. Spectrosc.* **102-103**, 120-195, (2017).

123 König, A. *et al.* Hyperpolarized MAS NMR of unfolded and misfolded proteins. *Solid State Nucl. Magn. Reson.* **98**, 1-11, (2019).

124 Selkoe, D. J. & Hardy, J. The amyloid hypothesis of Alzheimer's disease at 25 years. *EMBO Mol. Med.* **8**, 595-608, (2016).

125 Portelius, E. *et al.* Mass spectrometric characterization of brain amyloid beta isoform signatures in familial and sporadic Alzheimer's disease. *Acta Neuropathol.* **120**, 185-193, (2010).

126 Haass, C. & Selkoe, D. J. Soluble protein oligomers in neurodegeneration: lessons from the Alzheimer's amyloid β-peptide. *Nat. Rev. Mol. Cell Biol.* **8**, 101-112, (2007).

127 Ovchinnikova, O. Y., Finder, V. H., Vodopivec, I., Nitsch, R. M. & Glockshuber, R. The Osaka FAD Mutation E22Δ Leads to the Formation of a Previously Unknown Type of Amyloid β Fibrils and Modulates Aβ Neurotoxicity. *J. Mol. Biol.* **408**, 780-791, (2011).

128 Barz, B., Liao, Q. & Strodel, B. Pathways of Amyloid-β Aggregation Depend on Oligomer Shape. *J. Am. Chem. Soc.* **140**, 319-327, (2018).

129 Cavallucci, V., D'Amelio, M. & Cecconi, F. Aβ Toxicity in Alzheimer's Disease. *Mol. Neurobiol.* **45**, 366-378, (2012).

130 Janelidze, S. *et al.* CSF Aβ42/Aβ40 and Aβ42/Aβ38 ratios: better diagnostic markers of Alzheimer disease. *Ann. Clin. Transl. Neurol.* **3**, 154-165, (2016).

131 Soscia, S. J. *et al.* The Alzheimer's Disease-Associated Amyloid β-Protein Is an Antimicrobial Peptide. *PLoS One* **5**, e9505, (2010).

132 Sahoo, B. R., Cox, S. J. & Ramamoorthy, A. High-resolution probing of early events in amyloid-β aggregation related to Alzheimer's disease. *Chem. Commun.* **56**, 4627-4639, (2020).

133   Benilova, I., Karran, E. & De Strooper, B. The toxic Aβ oligomer and Alzheimer's disease: an emperor in need of clothes. *Nat. Neurosci.* **15**, 349-357, (2012).

134   Chimon, S. *et al.* Evidence of fibril-like β-sheet structures in a neurotoxic amyloid intermediate of Alzheimer's β-amyloid. *Nat. Struct. Mol. Biol.* **14**, 1157-1164, (2007).

135   Hoyer, W., Grönwall, C., Jonsson, A., Ståhl, S. & Härd, T. Stabilization of a β-hairpin in monomeric Alzheimer's amyloid-β peptide inhibits amyloid formation. *Proc. Natl. Acad. Sci.* **105**, 5099-5104, (2008).

136   Lopez del Amo, J. M. *et al.* Structural Properties of EGCG-Induced, Nontoxic Alzheimer's Disease Aβ Oligomers. *J. Mol. Biol.* **421**, 517-524, (2012).

137   Qiang, W., Yau, W.-M., Luo, Y., Mattson, M. P. & Tycko, R. Antiparallel β-sheet architecture in Iowa-mutant β-amyloid fibrils. *Proc. Natl. Acad. Sci. U. S. A.* **109**, 4443-4448, (2012).

138   Sandberg, A. *et al.* Stabilization of neurotoxic Alzheimer amyloid-β oligomers by protein engineering. *Proc. Natl. Acad. Sci.* **107**, 15595-15600, (2010).

139   Ahmed, M. *et al.* Structural conversion of neurotoxic amyloid-β_{1-42} oligomers to fibrils. *Nat. Struct. Mol. Biol.* **17**, 561-567, (2010).

140   Lendel, C. *et al.* A Hexameric Peptide Barrel as Building Block of Amyloid-β Protofibrils. *Angew. Chem. Int. Ed. Engl.* **126**, 12970-12974, (2014).

141   Huang, D. *et al.* Antiparallel β-Sheet Structure within the C-Terminal Region of 42-Residue Alzheimer's Amyloid-β Peptides When They Form 150-kDa Oligomers. *J. Mol. Biol.* **427**, 2319-2328, (2015).

142   Tay, W. M., Huang, D., Rosenberry, T. L. & Paravastu, A. K. The Alzheimer's Amyloid-β(1–42) Peptide Forms Off-Pathway Oligomers and Fibrils That Are Distinguished Structurally by Intermolecular Organization. *J. Mol. Biol.* **425**, 2494-2508, (2013).

143   Xiao, Y. *et al.* NMR-based site-resolved profiling of β-amyloid misfolding reveals structural transitions from pathologically relevant spherical oligomer to fibril. *J. Biol. Chem.* **295**, 458-467, (2020).

144   Scheidt, H. A. *et al.* Structural characteristics of oligomers formed by pyroglutamate-modified amyloid β peptides studied by solid-state NMR. *Phys. Chem. Chem. Phys.* **22**, 16887-16895, (2020).

145   Parthasarathy, S. *et al.* Structural Insight into an Alzheimer's Brain-Derived Spherical Assembly of Amyloid β by Solid-State NMR. *J. Am. Chem. Soc.* **137**, 6480-6483, (2015).

146   Qiang, W., Yau, W. M., Lu, J. X., Collinge, J. & Tycko, R. Structural variation in amyloid-beta fibrils from Alzheimer's disease clinical subtypes. *Nature* **541**, 217-221, (2017).

147   Altmeppen, H. C. *et al.* Proteolytic processing of the prion protein in health and disease. *Am. J. Neurodegener. Dis.* **1**, 15-31, (2012).

148   Bremer, J. *et al.* Axonal prion protein is required for peripheral myelin maintenance. *Nat. Neurosci.* **13**, 310-318, (2010).

149   Manni, G. *et al.* The cellular prion protein beyond prion diseases. *Swiss Med. Wkly.* **150**, w20222, (2020).

150   Theint, T. *et al.* Species-dependent structural polymorphism of Y145Stop prion protein amyloid revealed by solid-state NMR spectroscopy. *Nat. Commun.* **8**, 753, (2017).

151   Watts, J. C. *et al.* Spontaneous generation of rapidly transmissible prions in transgenic mice expressing wild-type bank vole prion protein. *Proc. Natl. Acad. Sci.* **109**, 3498-3503, (2012).

152   Di Bari, M. A. *et al.* Chronic Wasting Disease in Bank Voles: Characterisation of the Shortest Incubation Time Model for Prion Diseases. *PLoS Pathog.* **9**, e1003219, (2013).

153   Christen, B., Pérez, D. R., Hornemann, S. & Wüthrich, K. NMR Structure of the Bank Vole Prion Protein at 20 °C Contains a Structured Loop of Residues 165–171. *J. Mol. Biol.* **383**, 306-312, (2008).

154   Gallagher-Jones, M. *et al.* Sub-ångström cryo-EM structure of a prion protofibril reveals a polar clasp. *Nat. Struct. Mol. Biol.* **25**, 131-134, (2018).

155   Saá, P., Castilla, J. & Soto, C. Ultra-efficient Replication of Infectious Prions by Automated Protein Misfolding Cyclic Amplification. *J. Biol. Chem.* **281**, 35245-35252, (2006).

156   Legname, G. *et al.* Synthetic Mammalian Prions. *Science* **305**, 673-676, (2004).

157   Castilla, J., Saá, P., Hetz, C. & Soto, C. In Vitro Generation of Infectious Scrapie Prions. *Cell* **121**, 195-206, (2005).

158   Elezgarai, S. R. *et al.* Generation of a new infectious recombinant prion: a model to understand Gerstmann–Sträussler–Scheinker syndrome. *Sci. Rep.* **7**, 9584, (2017).

159   Eraña, H. *et al.* Development of a new largely scalable in vitro prion propagation method for the production of infectious recombinant prions for high resolution structural studies. *PLoS Pathog.* **15**, e1008117, (2019).

160   Lauren, J., Gimbel, D. A., Nygaard, H. B., Gilbert, J. W. & Strittmatter, S. M. Cellular prion protein mediates impairment of synaptic plasticity by amyloid-β oligomers. *Nature* **457**, 1128-1132, (2009).

161   Zou, W.-Q. *et al.* Amyloid-β42 Interacts Mainly with Insoluble Prion Protein in the Alzheimer Brain. *J. Biol. Chem.* **286**, 15095-15105, (2011).

162   Younan, N. D., Chen, K.-F., Rose, R.-S., Crowther, D. C. & Viles, J. H. Prion protein stabilizes amyloid-β (Aβ) oligomers and enhances Aβ neurotoxicity in a Drosophila model of Alzheimer's disease. *J. Biol. Chem.* **293**, 13090-13099, (2018).

163   Balducci, C. *et al.* Synthetic amyloid-β oligomers impair long-term memory independently of cellular prion protein. *Proc. Natl. Acad. Sci.* **107**, 2295-2300, (2010).

164   Calella, A. M. *et al.* Prion protein and Aβ-related synaptic toxicity impairment. *EMBO Mol. Med.* **2**, 306-314, (2010).

165   Kessels, H. W., Nguyen, L. N., Nabavi, S. & Malinow, R. The prion protein as a receptor for amyloid-β. *Nature* **466**, E3-E4, (2010).

166   Cissé, M. *et al.* Ablation of Cellular Prion Protein Does Not Ameliorate Abnormal Neural Network Activity or Cognitive Dysfunction in the J20 Line of Human Amyloid Precursor Protein Transgenic Mice. *J. Neurosci.* **31**, 10427-10431, (2011).

167   Gimbel, D. A. *et al.* Memory Impairment in Transgenic Alzheimer Mice Requires Cellular Prion Protein. *J. Neurosci.* **30**, 6367-6374, (2010).

168   Freir, D. B. *et al.* Interaction between prion protein and toxic amyloid β assemblies can be therapeutically targeted at multiple sites. *Nat. Commun.* **2**, 336-344, (2011).

169   Chung, E. *et al.* Anti-PrPC monoclonal antibody infusion as a novel treatment for cognitive deficits in an Alzheimer's disease model mouse. *BMC Neurosci.* **11**, 130-140, (2010).

170   Kostylev, M. A. *et al.* Prion-Protein-interacting Amyloid-β Oligomers of High Molecular Weight Are Tightly Correlated with Memory Impairment in Multiple Alzheimer Mouse Models. *J. Biol. Chem.* **290**, 17415-17438, (2015).

171   Madhu, P. & Mukhopadhyay, S. Preferential Recruitment of Conformationally Distinct Amyloid-β Oligomers by the Intrinsically Disordered Region of the Human Prion Protein. *ACS Chem. Neurosci.* **11**, 86-98, (2020).

172   Mroczko, B., Groblewska, M., Litman-Zawadzka, A., Kornhuber, J. & Lewczuk, P. Cellular Receptors of Amyloid β Oligomers (AβOs) in Alzheimer's Disease. *Int. J. Mol. Sci.* **19**, 1884, (2018).

173   Pflanzner, T. *et al.* Cellular Prion Protein Participates in Amyloid-β Transcytosis across the Blood—Brain Barrier. *J. Cereb. Blood Flow Metab.* **32**, 628-632, (2012).

174   Pagano, K. *et al.* Effects of Prion Protein on Aβ42 and Pyroglutamate-Modified AβpE3-42 Oligomerization and Toxicity. *Mol. Neurobiol.* **56**, 1957-1971, (2019).

175   Bate, C. & Williams, A. Amyloid-β-induced Synapse Damage Is Mediated via Cross-linkage of Cellular Prion Proteins. *J. Biol. Chem.* **286**, 37955-37963, (2011).

176   Um, J. W. *et al.* Alzheimer amyloid-β oligomer bound to postsynaptic prion protein activates Fyn to impair neurons. *Nat. Neurosci.* **15**, 1227-1235, (2012).

177   Um, J. W. & Strittmatter, S. M. Amyloid-β induced signaling by cellular prion protein and Fyn kinase in Alzheimer disease. *Prion* **7**, 37-41, (2013).

178   Barry, A. E. *et al.* Alzheimer's disease brain-derived amyloid-β-mediated inhibition of LTP in vivo is prevented by immunotargeting cellular prion protein. *J. Neurosci.* **31**, 7259-7263, (2011).

179   Um, J. W. *et al.* Metabotropic glutamate receptor 5 is a coreceptor for Alzheimer aβ oligomer bound to cellular prion protein. *Neuron* **79**, 887-902, (2013).

180   Hu, N.-W. *et al.* mGlu5 receptors and cellular prion protein mediate amyloid-β-facilitated synaptic long-term depression in vivo. *Nat. Commun.* **5**, 3374, (2014).

181   Haas, L. T. *et al.* Metabotropic glutamate receptor 5 couples cellular prion protein to intracellular signalling in Alzheimer's disease. *Brain* **139**, 526-546, (2016).

182   Brody, A. H. & Strittmatter, S. M. Synaptotoxic Signaling by Amyloid Beta Oligomers in Alzheimer's Disease Through Prion Protein and mGluR5. *Adv. Pharmacol.* **82**, 293-323, (2018).

183   Larson, M. *et al.* The Complex PrP[C]-Fyn Couples Human Oligomeric Aβ with Pathological Tau Changes in Alzheimer's Disease. *J. Neurosci.* **32**, 16857-16871, (2012).

184   You, H. *et al.* Aβ neurotoxicity depends on interactions between copper ions, prion protein, and N-methyl-D-aspartate receptors. *Proc. Natl. Acad. Sci.* **109**, 1737-1742, (2012).

185   Nieznanski, K., Choi, J.-K., Chen, S., Surewicz, K. & Surewicz, W. K. Soluble prion protein inhibits Amyloid-β (Aβ) Fibrillization and Toxicity. *J. Biol. Chem.* **287**, 33104-33108, (2012).

186   Bove-Fenderson, E., Urano, R., Straub, J. E. & Harris, D. A. Cellular prion protein targets amyloid-beta fibril ends via its C-terminal domain to prevent elongation. *J. Biol. Chem.* **292**, 16858-16871, (2017).

187   Amin, L. & Harris, D. A. Aβ receptors specifically recognize molecular features displayed by fibril ends and neurotoxic oligomers. *bioRxiv*, 822361, (2019).

188   Falker, C. *et al.* Exosomal cellular prion protein drives fibrillization of amyloid beta and counteracts amyloid beta-mediated neurotoxicity. *J. Neurochem.* **137**, 88-100, (2016).

189   Elezgarai Saioa, R. & Biasini, E. Common therapeutic strategies for prion and Alzheimer's diseases. *Biol. Chem.* **397**, 1115-1124, (2016).

190   Kudo, W. *et al.* Cellular prion protein is essential for oligomeric amyloid-β-induced neuronal cell death. *Hum. Mol. Genet.* **21**, 1138-1144, (2012).

191   Aimi, T., Suzuki, K., Hoshino, T. & Mizushima, T. Dextran sulfate sodium inhibits amyloid-β oligomer binding to cellular prion protein. *J. Neurochem.* **134**, 611-617, (2015).

192   Risse, E. *et al.* Identification of a Compound That Disrupts Binding of Amyloid-β to the Prion Protein Using a Novel Fluorescence-based Assay. *J. Biol. Chem.* **290**, 17020-17028, (2015).

193   Rösener, N. S. *et al.* A d-enantiomeric peptide interferes with heteroassociation of amyloid-beta oligomers and prion protein. *J. Biol. Chem.* **293**, 15748-15764, (2018).

194   Corbett, G. T. *et al.* PrP is a central player in toxicity mediated by soluble aggregates of neurodegeneration-causing proteins. *Acta Neuropathol.* **139**, 503-526, (2020).

195   Gomes, L. A. *et al.* Aβ-induced acceleration of Alzheimer-related τ-pathology spreading and its association with prion protein. *Acta Neuropathol.* **138**, 913-941, (2019).

196   Rösener, N. S. *et al.* Clustering of human prion protein and α-synuclein oligomers requires the prion protein N-terminus. *Communications Biology* **3**, 365, (2020).

197   Chen, S., Yadav, S. P. & Surewicz, W. K. Interaction between human prion protein and amyloid-β (Aβ) oligomers: Role of N-terminal residues. *J. Biol. Chem.* **285**, 26377-26383, (2010).

198   Fluharty, B. R. *et al.* An N-terminal Fragment of the Prion Protein Binds to Amyloid-beta Oligomers and Inhibits Their Neurotoxicity in Vivo. *J. Biol. Chem.* **288**, 7857-7866, (2013).

199   Kang, M., Kim, S. Y., An, S. S. & Ju, Y. R. Characterizing affinity epitopes between prion protein and beta-amyloid using an epitope mapping immunoassay. *Exp. Mol. Med.* **45**, e34, (2013).

200   Dohler, F. *et al.* High molecular mass assemblies of amyloid-β oligomers bind prion protein in patients with Alzheimer's disease. *Brain* **137**, 873-886, (2014).

201   Younan, N. D., Sarell, C. J., Davies, P., Brown, D. R. & Viles, J. H. The cellular prion protein traps Alzheimer's Aβ in an oligomeric form and disassembles amyloid fibers. *FASEB J.* **27**, 1847-1858, (2013).

202   Nicoll, A. J. *et al.* Amyloid-beta nanotubes are associated with prion protein-dependent synaptotoxicity. *Nat. Commun.* **4**, 2416-2424, (2013).

203   Kostylev, M. A. *et al.* Liquid and Hydrogel Phases of PrP(C) Linked to Conformation Shifts and Triggered by Alzheimer's Amyloid-beta Oligomers. *Mol. Cell* **72**, 426-443.e12, (2018).

204   Mohammadi, B. *et al.* Transgenic Overexpression of the Disordered Prion Protein N1 Fragment in Mice Does Not Protect Against Neurodegenerative Diseases Due to Impaired ER Translocation. *Mol. Neurobiol.* **57**, 2812–2829, (2020).

205   Nieznanska, H. *et al.* Identification of prion protein-derived peptides of potential use in Alzheimer's disease therapy. *Biochim. Biophys. Acta, Mol. Basis Dis.* **1864**, 2143-2153, (2018).

206   König, A. S. *et al.* Structural details of amyloid β oligomers in complex with human prion protein as revealed by solid-state MAS NMR spectroscopy. *J. Biol. Chem.* **296**, 100499, (2021).

207   Massiot, D. *et al.* Modelling one- and two-dimensional solid-state NMR spectra. *Magn. Reson. Chem.* **40**, 70-76, (2002).

208   Bak, M., Rasmussen, J. T. & Nielsen, N. C. SIMPSON: A General Simulation Program for Solid-State NMR Spectroscopy. *J. Magn. Reson.* **147**, 296-330, (2000).

209   Gu, Z., Zambrano, R. & McDermott, A. Hydrogen Bonding of Carboxyl Groups in Solid-State Amino Acids and Peptides: Comparison of Carbon Chemical Shielding, Infrared Frequencies, and Structures. *J. Am. Chem. Soc.* **116**, 6368-6372, (1994).

210   Bhate, M. P. & McDermott, A. E. Protonation state of E71 in KcsA and its role for channel collapse and inactivation. *Proc. Natl. Acad. Sci.* **109**, 15265-15270, (2012).

211   Rovnyak, D., Hoch, J. C., Stern, A. S. & Wagner, G. Resolution and sensitivity of high field nuclear magnetic resonance spectroscopy. *J. Biomol. NMR* **30**, 1-10, (2004).

212   De Paëpe, G., Lewandowski, J. R., Loquet, A., Böckmann, A. & Griffin, R. G. Proton assisted recoupling and protein structure determination. *J. Chem. Phys.* **129**, 245101-245101, (2008).

213   De Paëpe, G. *et al.* Heteronuclear proton assisted recoupling. *J. Chem. Phys.* **134**, 095101, (2011).

214   Tycko, R. Symmetry-based constant-time homonuclear dipolar recoupling in solid state NMR. *J. Chem. Phys.* **126**, 064506, (2007).

Danksagung

Eidesstattliche Erklärung

Ich versichere an Eides Statt, dass die Dissertation von mir selbständig und ohne unzulässige fremde Hilfe unter Beachtung der „Grundsätze zur Sicherung guter wissenschaftlicher Praxis an der Heinrich-Heine-Universität Düsseldorf" erstellt worden ist.

Ferner erkläre ich, dass ich in keinem anderen Dissertationsverfahren mit oder ohne Erfolg versucht habe, diese Dissertation einzureichen.

Jülich, den   _____

                                                        Anna König

Anhang

NMR-Experimente, die nicht publiziert wurden:

Carboxyl-Protonierungsgrad von Glu C_δ und Ala42 CO von huPrP(23-144)-$A\beta_{oligo}$*

Es wurde ein PDSD-Spektrum der Probe aus N-terminalem huPrP (23-144) mit uniform $^{13}C,^{15}N$-markierten Aβ-Oligomeren bei einer Rotationsfrequenz von 5 kHz gemessen (^1H-Frequenz = 800 MHz; Mischzeit = 30 ms; Temperatur ≈ 0 °C; Einstrahlpunkt = 90,170 ppm; Kontaktzeit = 600/800 µs; t_1-Inkremente = 1429; Spektrale Weite (t_1) = 119,048 kHz; t_2-Inkremente = 120; Spektrale Weite (t_2) = 40 kHz; Anzahl der Scans = 576; Basisfrequenz (^{13}C) = 201,141 MHz). Bei dieser vergleichsweise langsamen Rotation um den magischen Winkel wird die chemische Verschiebungsanisotropie der Carboxyl-Kohlenstoffatome nicht vollständig ausgemittelt und ist in Form von Seitenbanden zu erkennen. Diese können nur bei ausreichender Intensität und Trennung von anderen Signalen, z. B. dem CO-Signal aller anderen Aminosäurereste (bei ca. 175 ppm), ausgewertet werden. Dies war für Ala42 (δ_{iso}(CO) = 182 ppm) und ein Glu (δ_{iso}(C_δ) = 184 ppm) der Fall. Nach der Prozessierung des Spektrums mit um 0,35 π verschobener Sinus-Quadrat-Funktion und Basislinienkorrektur (MED900) wurden die 1D-Schnitte von Interesse extrahiert (Ala42 Cα = 54,12 ppm; Glu Cγ = 35,93 ppm), als Text-Datei gespeichert und mittels Matlab eine x-Achse generiert. Diese Text-Datei wurde anschließend in das Programm DMFit[207] eingeladen, mittels welchem durch Fitten die Tensorparameter Asymmetrie (η) und Anisotropie ($\Delta\delta$) und die isotrope chemische Verschiebung (δ_{iso}) bestimmt wurden. Dabei wurde auch der Tensor der CO-Region bei 175 ppm gefittet. DMFit nutzt dabei dieselbe CSA-Tensor-Konvention wie das Simulationsprogramm SIMPSON[208] (Haeberlen-Mehring-Konvention). Aus den Tensorparametern lassen sich mittels folgender Gleichungen die Haupttensorwerte des anisotropen chemischen Verschiebungstensors errechnen:

$$\Delta\delta = \delta_{33} - \delta_{iso} \tag{1}$$

$$\eta = \frac{\delta_{22} - \delta_{11}}{\Delta\delta} \tag{2}$$

$$\delta_{iso} = \frac{\delta_{33} + \delta_{22} + \delta_{11}}{3} \tag{3}$$

Nach Umstellen und ineinander Einsetzen ergibt sich:

$$\delta_{33} = \Delta\delta + \delta_{iso} \tag{4}$$

$$\delta_{22} = \frac{\eta \cdot \Delta\delta + 3 \cdot \delta_{iso} - \delta_{33}}{2} \tag{5}$$

$$\delta_{11} = 3 \cdot \delta_{iso} - \delta_{33} - \delta_{22} \tag{6}$$

Nach Gu et al.[209] und Bhate et al.[210] kann man anhand des ersten Tensorhauptwertes (δ_{11}) den Protonierungszustand des Carboxyl-Substituenten bestimmen. Ist der erste Tensorhauptwert kleiner als 250 ppm, liegt dieser Carboxyl-Substituent deprotoniert vor.

Für Ala42 (siehe **Abbildung 8**) ließen sich die Tensorhauptwerte sehr gut bestimmen: δ_{11} = 237 ppm; δ_{22} = 186 ppm; δ_{33} = 122 ppm (δ_{iso} = 182 ppm; $\Delta\delta$ = -60 ppm; η = 0,85). Es handelt sich dabei um das C-terminale Kohlenstoffatom, das im Komplex mit huPrP(23-144) also deprotoniert vorliegt, was bei einem pH-Wert von 7,4 auch zu erwarten ist.
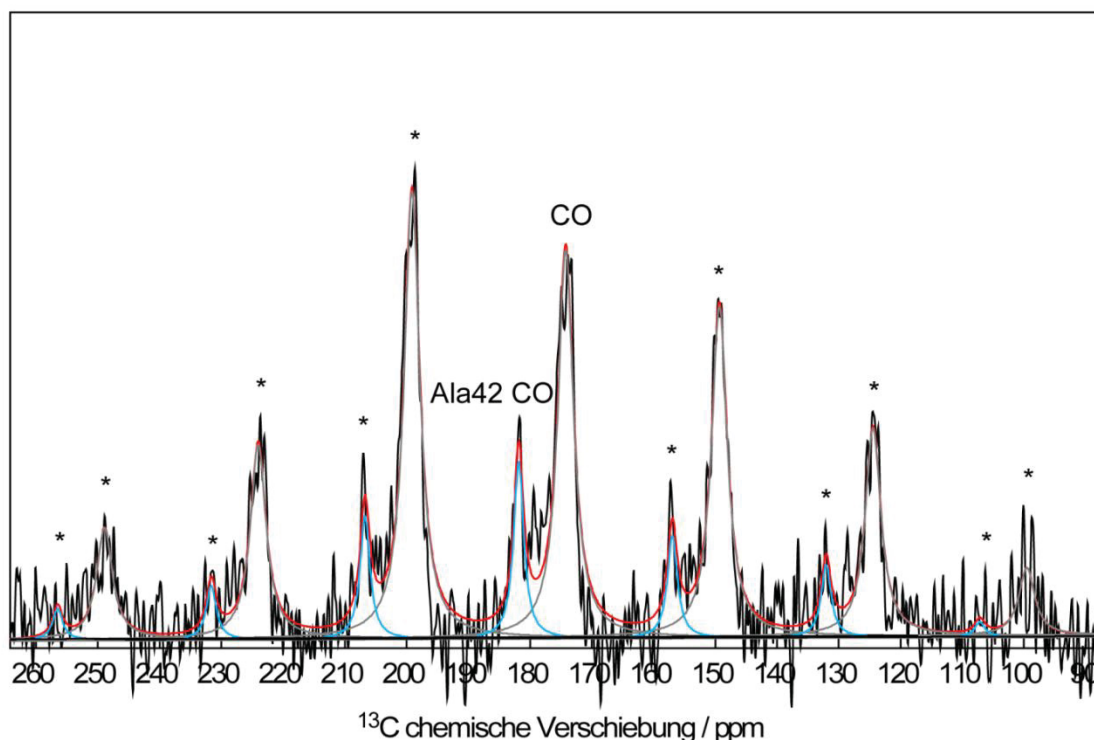
Abbildung 8: *Fit des 1D-Schnittes bei 54,12 ppm eines PDSD-Spektrums zur Ermittlung der CSA-Parameter und -Tensor-Hauptwerte. Messparameter: ^{1}H-Frequenz = 800 MHz; Mischzeit = 30 ms; Rotationsfrequenz = 5 kHz; Temperatur ≈ 0 °C; Anzahl der Scans = 576. Dargestellt*

ist der Fit (rot) für Ala42 CO (blau) und dem überlagerten CO-Signal der meisten Aminosäurereste (grau). Rotationsseitenbanden sind mit einem Stern (*) markiert.

Für Glu war die Intensität der Rotationsseitenbanden, die im Rauschen liegen, zu gering, um eine Aussage zu treffen.

T_1- und T_2-Relaxationszeiten der Probe huPrP(23-144)-Aβ_{oligo}*

<u>T_1-Relaxationszeiten von ^{1}H via ^{13}C</u>

Die Ermittlung der Protonen-T_1-Relaxationszeiten erfolgte mit Hilfe der Pulssequenz „t1hcpx" am 600MHz-Oxford-Spektrometer. Diese Pulssequenz entspricht einem *Inversion Recovery* auf ^{1}H mit anschließendem CP zur Detektion auf ^{13}C. Aus dem Nulldurchgang der Intensität des jeweiligen Signals lässt sich T_1 ermitteln. In erster Näherung ergab sich T_1 = Nulldurchgang/ln(2) = 310 ms/ln(2) = 447 ms. Eine genauere Bestimmung erfolgte über die Signalintensitäten, welche mittels CCPN ausgelesen und mittels Origin gefittet wurden.

Folgende Gleichung für den Fit wurde genutzt:

$$I = I_0 \cdot (2 \cdot e^{\left(-\frac{t}{T_1}\right)} - 1) \tag{7}$$

I ist dabei die Intensität des jeweiligen Signals, *I_0* die Ausgangsintensität und *t* die Zeit, die von 0 bis 350 ms in 10 ms-Schritten inkrementiert wurde.
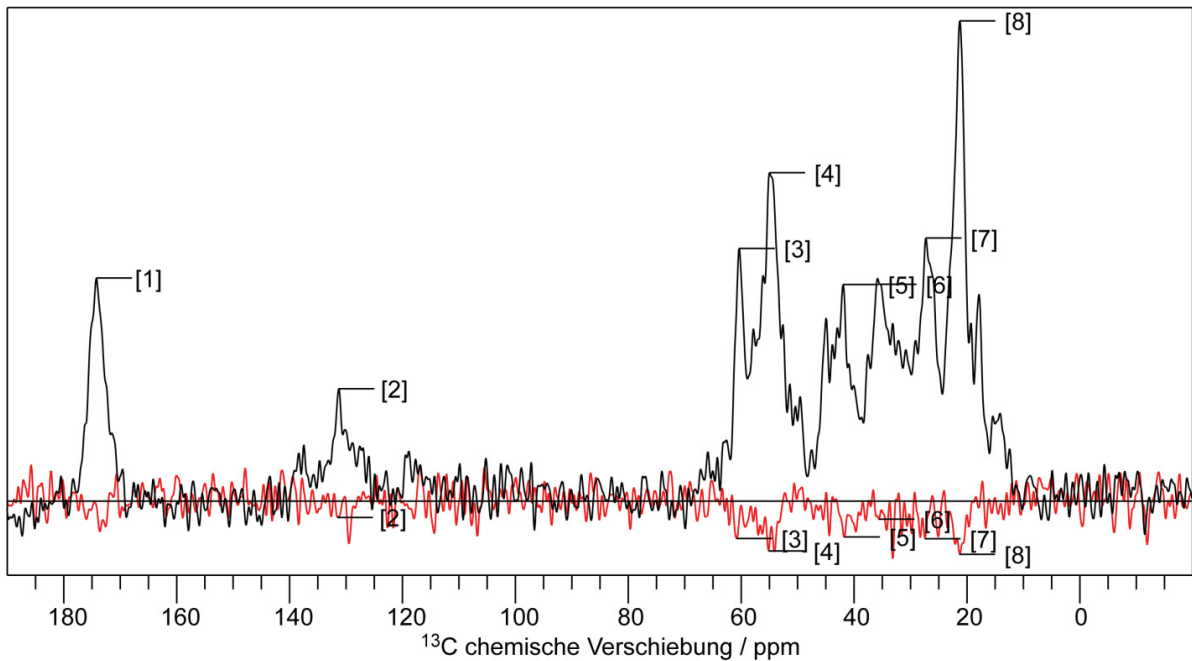
Abbildung 9*: 1D-^{13}C-t1hcpx-Spektrum der Probe huPrP(23-144)-Aβ$_{oligo}$* zum Zeitpunkt d_2 = 0 ms (schwarz) und d_2 = 350 ms (rot). Neben der Nummerierung der Signale ist zu erkennen, dass eine Invertierung der Signalintensität erfolgt ist. Die Messung erfolgte mit folgenden Parametern: Rotationsfrequenz = 11 kHz; Temperatur ≈ 0 °C; Einstrahlpunkt = 70,978 ppm; CP-Kontaktzeit = 400 µs; Spektrale Weite = 37,879 kHz; t_1-Inkremente = 454; Anzahl der Scans = 16; Glättungsfunktion: quadratische Sinusfunktion um 0,35 π verschoben.*

Für die in **Abbildung 9** gekennzeichneten Signale des Spektrums wurden die in **Abbildung 10** dargestellten Relaxationskurven erhalten. **Tabelle 1** zeigt die ermittelten T_1-Zeiten für verschiedene Signale des Spektrums (siehe **Abbildung 9**).
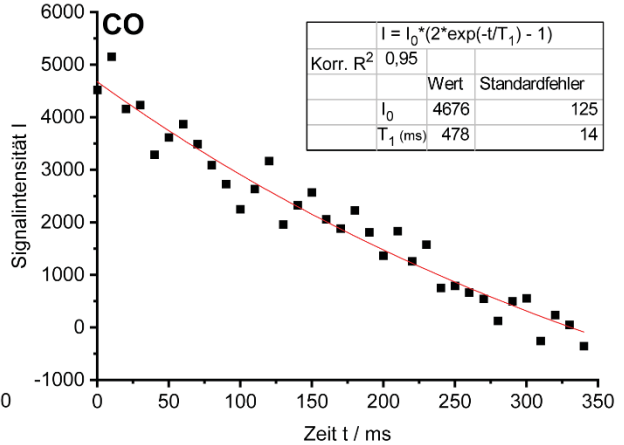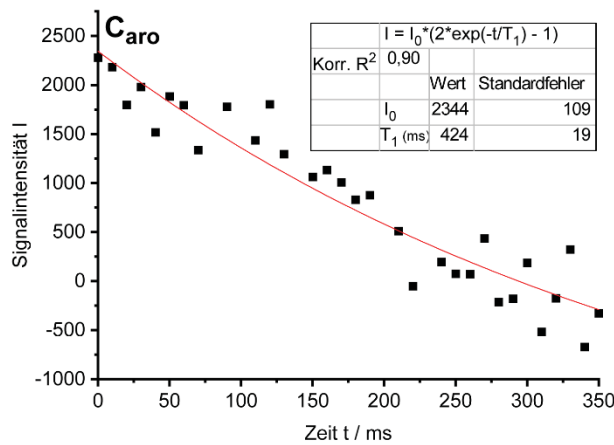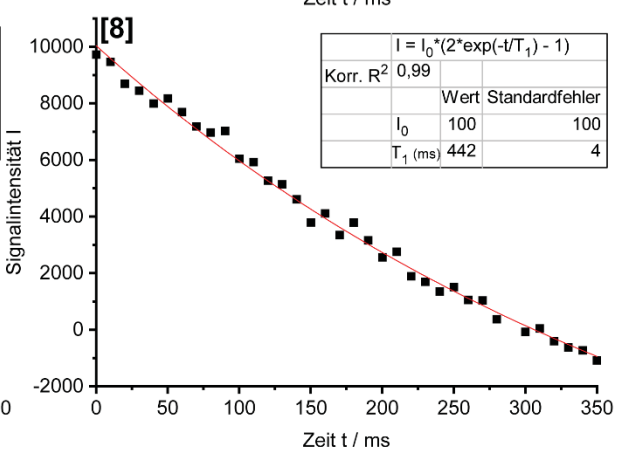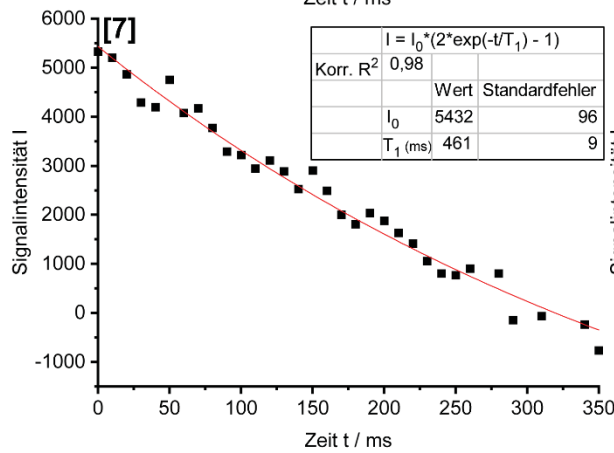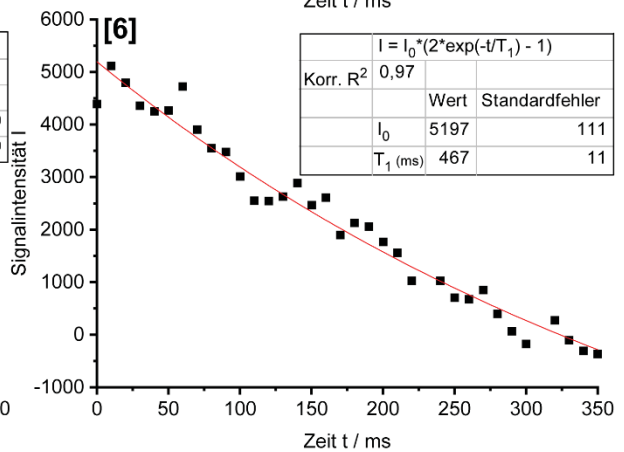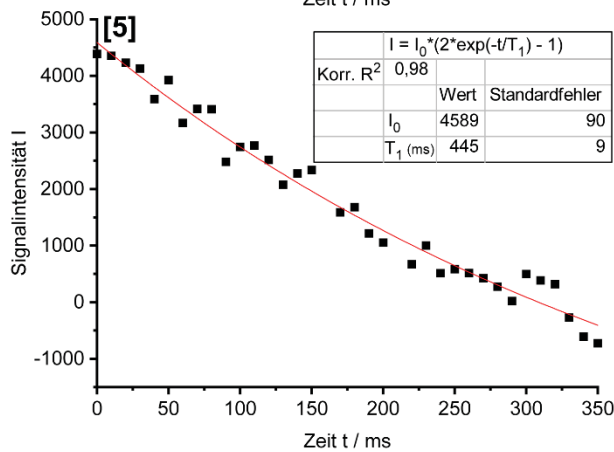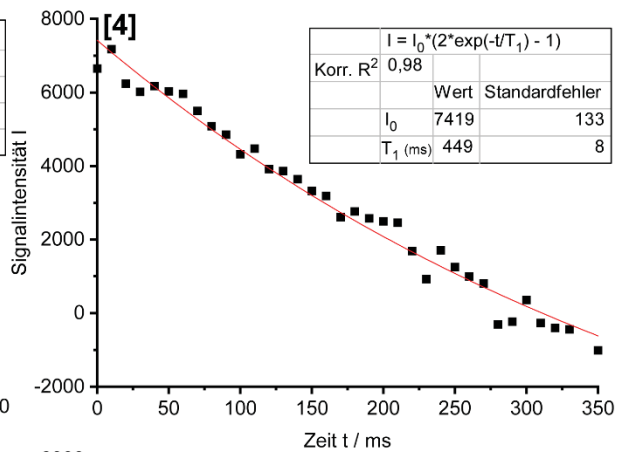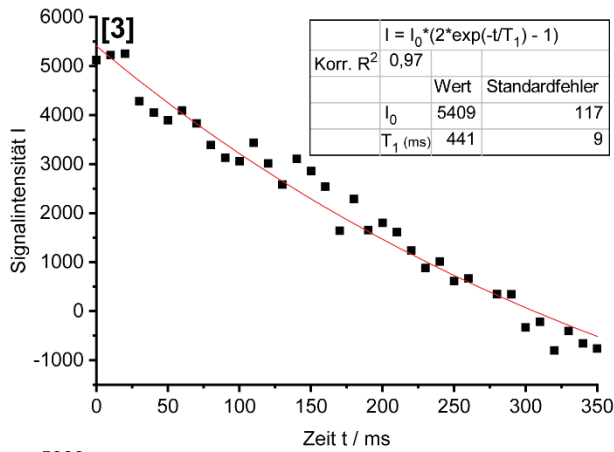
Abbildung 10: *Relaxationskurven der Probe huPrP(23-144)-Aβ$_{oligo}$* zur Ermittlung der T$_1$-Relaxationszeiten von ^{1}H. Die genutzten Fit-Gleichungen, sowie die Güte des Fits (Korrigiertes R^2) und die erhaltenen Werte für T$_1$ und I$_0$ gemeinsam mit deren Standardfehlern sind in der jeweils zugehörigen Tabelle angegeben.*

Tabelle 1: *T$_1$-Relaxationszeiten von ^{1}H ermittelt via ^{13}C*

Region	Signalnummern	T$_1$ (ms)	Standardfehler des Fits (ms)
C$_\alpha$	[3], [4], [5], [8]	441 - 449	4 - 9
C$_\alpha$	[6], [7]	461 - 467	9 - 11
C$_{aro}$	[2]	424	19
CO	[1]	478	14

Die Ermittlung der T$_1$-Relaxationszeiten der Protonen ist wichtig für die Ermittlung des optimalen *Recycle Delays* d$_1$. Er sollte 5*T$_1$ entsprechen, um eine Relaxation von 99 % der Magnetisierung zu gewährleisten. Aus 5*478 ms ergeben sich 2,39 s. Eine Länge von 3 s für den *Recycle Delay* wäre also optimal. Meist wurden 2 s genutzt, was einer Relaxation von etwa 95 % der Magnetisierung entspricht und ebenfalls ausreichend ist.

T$_1$-Relaxationszeiten von ^{13}C

Die Ermittlung der ^{13}C-T$_1$-Relaxationszeiten erfolgte mit Hilfe der Pulssequenz „t1xcp" am 600MHz-Oxford-Spektrometer. Diese Pulssequenz entspricht einem *Saturation Recovery* auf ^{13}C mit vorausgestelltem CP. Aus dem Intensitätsabfall auf null des jeweiligen Signals lässt sich T$_1$ ermitteln. Die Signalintensitäten wurden mittels CCPN ausgelesen, der Fit erfolgte mittels Origin.

Folgende Gleichung für den Fit von C$_\alpha$ und CO wurde genutzt:

$$I = A \cdot e^{\left(-\frac{t}{T_1}\right)} + I_0 \tag{8}$$

Für C$_{aro}$ wurde folgende Gleichung genutzt:

$$I = A \cdot e^{\left(-\frac{t}{T_1}\right)} \tag{9}$$

I ist dabei die Intensität des jeweiligen Signals, I_0 die Ausgangsintensität, *A* eine Proportionalitätskonstante und *t* die Zeit, die von 0 bis 9 s in 0,5 s-Schritten inkrementiert wurde.
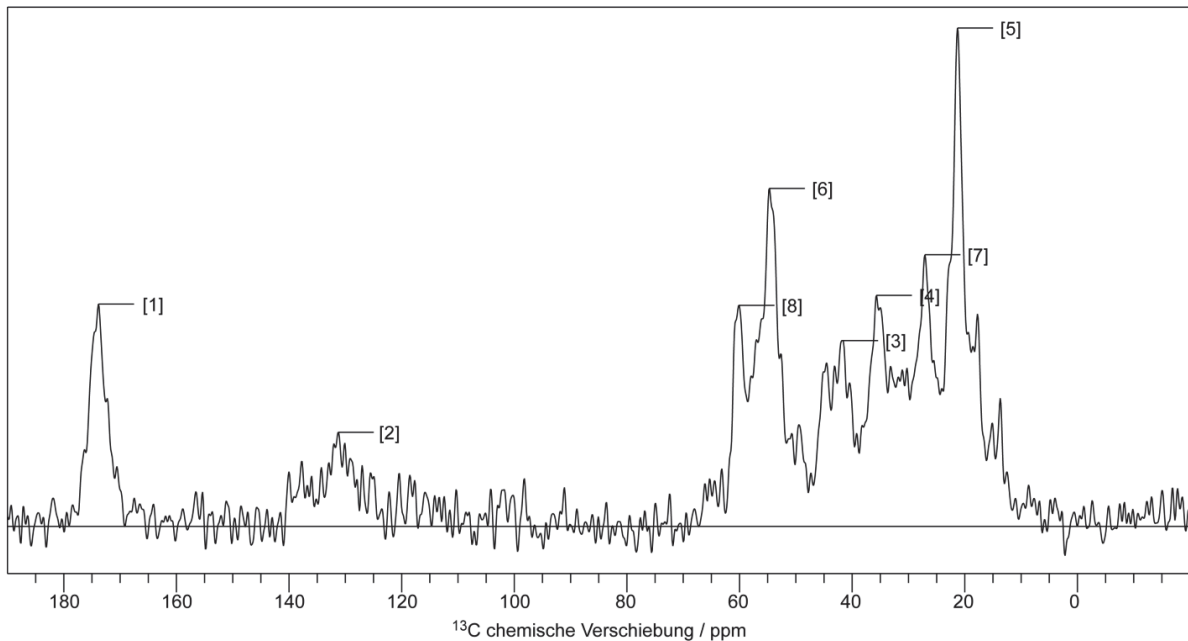
Abbildung 11: *1D-^{13}C-t1xcp-Spektrum der Probe huPrP(23-144)-Aβ$_{oligo}$* zum Zeitpunkt d_2 = 0 s. Die Nummerierung der Signale ist zu erkennen. Die Messung erfolgte mit folgenden Parametern: Rotationsfrequenz = 11 kHz; Temperatur ≈ 0 °C; Einstrahlpunkt = 70,978 ppm; CP-Kontaktzeit = 400 µs; Spektrale Weite = 37,879 kHz; t_1-Inkremente = 454; Anzahl der Scans = 16; Glättungsfunktion: quadratische Sinusfunktion um 0,35 π verschoben.*

Für die in **Abbildung 11** gekennzeichneten Signale des Spektrums wurden die in **Abbildung 12** dargestellten Relaxationskurven erhalten. **Tabelle 2** zeigt die ermittelten T_1-Zeiten für verschiedene Signale des Spektrums (siehe **Abbildung 11**).

[3]

I = A*exp(-t/T$_1$) + I$_0$		
Korr. R^2	0,99	
	Wert	Standardfehler
I$_0$	816,2	85,7
A	3125,9	144,3
T$_1$ (s)	0,9	0,1

[4]

I = A*exp(-t/T$_1$) + I$_0$		
Korr. R^2	0,95	
	Wert	Standardfehler
I$_0$	847,2	220,6
A	3925,9	350,1
T$_1$ (s)	0,8	0,2

[5]

I = A*exp(-t/T$_1$) + I$_0$		
Korr. R^2	0,98	
	Wert	Standardfehler
I$_0$	1109,6	197,3
A	9283,3	476,6
T$_1$ (s)	0,6	0,1

[6]

I = A*exp(-t/T$_1$) + I$_0$		
Korr. R^2	0,99	
	Wert	Standardfehler
I$_0$	872,1	147,6
A	6277,9	211,9
T$_1$ (s)	1,2	0,1

[7]

I = A*exp(-t/T$_1$) + I$_0$		
Korr. R^2	0,96	
	Wert	Standardfehler
I$_0$	866,0	144,8
A	4734,2	301,4
T$_1$ (s)	0,7	0,1

[8]

I = A*exp(-t/T$_1$) + I$_0$		
Korr. R^2	0,95	
	Wert	Standardfehler
I$_0$	615,5	223,2
A	4144,2	350,7
T$_1$ (s)	1,0	0,2

C$_{aro}$

I = A*exp(-t/T$_1$)		
Korr. R^2	0,89	
	Wert	Standardfehler
T$_1$ (s)	2,5	0,4
A	2112,4	171,9

CO

| I = A*exp(-t/T$_1$) + I$_0$		
Korr. R^2	0,98	
	Wert	Standardfehler
I$_0$	430,6	241,4
A	7282,7	563,6
T$_1$ (s)	1,8	0,3

Abbildung 12: Relaxationskurven der Probe huPrP(23-144)-Aβ$_{oligo}$* zur Ermittlung der T$_1$-Relaxationszeiten von ^{13}C. Die genutzten Fit-Gleichungen, sowie die Güte des Fits (Korrigiertes R^2) und die erhaltenen Werte für T$_1$, A und I$_0$ gemeinsam mit deren Standardfehlern sind in der jeweils zugehörigen Tabelle angegeben.

Tabelle 2: T$_1$-Relaxationszeiten von ^{13}C

Region	Signalnummern	T$_1$ (s)	Standardfehler des Fits (s)
C$_\alpha$	[3], [4], [6], [7], [8]	0,8 – 1,2	0,1 – 0,2
C$_\alpha$	[5]	0,6	0,1
C$_{aro}$	[2]	2,5	0,4
CO	[1]	1,8	0,3

Der Ermittlung der T$_1$-Relaxationszeiten ist wichtig für die Ermittlung der optimalen Aufnahmezeit. Es ergab sich, dass die genutzten 2 bis 3 s für diese Probe ausreichend sind.

T$_1$-Relaxationszeiten von ^{15}N

Die Ermittlung der ^{15}N-T$_1$-Relaxationszeiten erfolgte ebenfalls mit Hilfe der Pulssequenz „tancpxt1" am 600MHz-Varian-Spektrometer. Diese Pulssequenz entspricht einem *Saturation Recovery* auf ^{15}N mit vorausgestelltem CP (Messparameter: Rotationsfrequenz = 11 kHz; Temperatur ≈ 0 °C; Einstrahlpunkt = 119,979 ppm; CP-Kontaktzeit = 700 µs; Spektrale Weite = 13,587 kHz; t$_1$-Inkremente = 136; Anzahl der Scans = 64; Glättungsfunktion: quadratische Sinusfunktion um 0,35 π verschoben). Aus dem Intensitätsabfall auf null des jeweiligen Signals lässt sich T$_1$ ermitteln. Die Signalintensitäten wurden mittels CCPN ausgelesen, der Fit erfolgte mittels Origin.

Folgende Gleichung für den Fit wurde genutzt:

$$I = A \cdot e^{\left(-\frac{t}{T_1}\right)} + I_0 \tag{10}$$

I ist dabei die Intensität des jeweiligen Signals, *I$_0$* die Ausgangsintensität, *A* eine Proportionalitätskonstante und *t* die Zeit, die von 0 bis 260 s in 20 s-Schritten inkrementiert wurde. **Abbildung 13** zeigt die erhaltene Relaxationskurve und **Tabelle 3** die ermittelte T$_1$-Zeit für das ^{15}N-Hauptsignal des Spektrums, denn im

1D-Spektrum lassen sich verschiedene ^{15}N-chemische Verschiebungen des Proteinrückrades nicht unterscheiden und Seitenketten-^{15}N-Signale zeigten eine zu geringe Intensität.

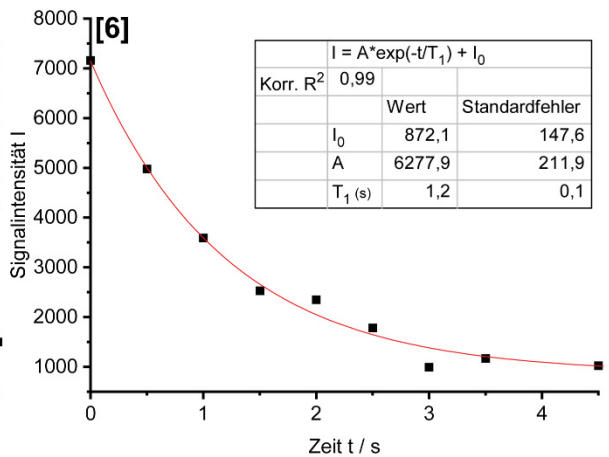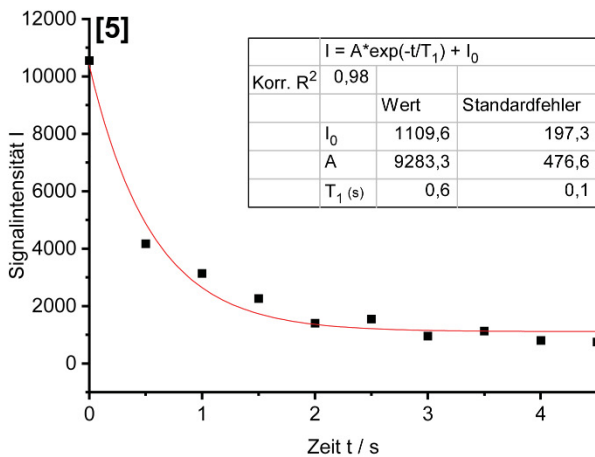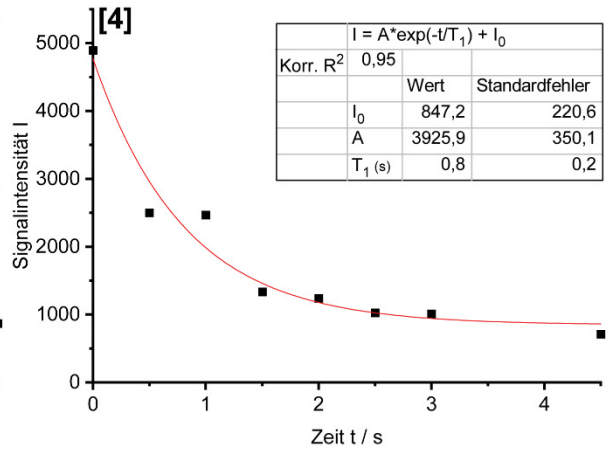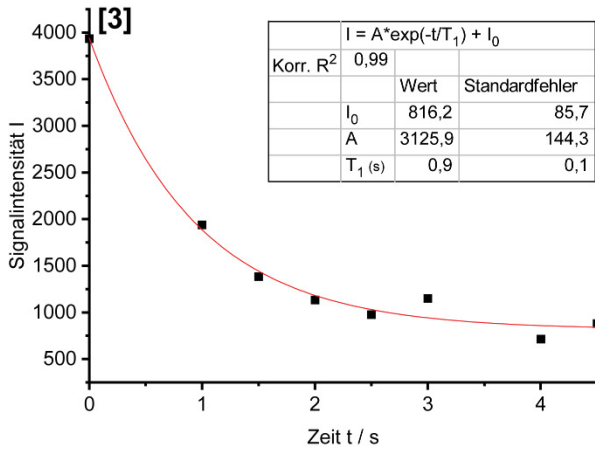|	I = A*exp(-t/T_1) + I_0		
Korr. R^2	0,96		
		Wert	Standardfehler
I_0		174	71
A		2424	131
T_1 (s)		53	7

Abbildung 13: *Relaxationskurve der Probe huPrP(23-144)-Aβ$_{oligo}$* zur Ermittlung der T_1-Relaxationszeit von ^{15}N. Die genutzte Fit-Gleichung, sowie die Güte des Fits (Korrigiertes R^2) und die erhaltenen Werte für T_1, A und I_0 gemeinsam mit deren Standardfehlern sind in der jeweils zugehörigen Tabelle angegeben.*

Tabelle 3: *T_1-Relaxationszeiten von ^{15}N*

Region	Signalnummern	T_1 (s)	Standardfehler des Fits (s)
N$_{haupt}$	[1]	53	7

Der Ermittlung der T_1-Relaxationszeiten ist wichtig für die Ermittlung der optimalen Aufnahmezeit. Es ergaben sich ≈ 60 s für die optimale Aufnahmezeit, allerdings war nicht erkennbar, ob die Signalintensität nach 260 s tatsächlich auf null abgefallen ist.

T$_2$-Relaxationszeiten von ^{13}C

Die Ermittlung der ^{13}C-T_2-Relaxationszeiten erfolgte mit Hilfe der Pulssequenz „tancpxecho" am 600MHz-Varian-Spektrometer. Diese Pulssequenz entspricht einem Hahn-Echo auf ^{13}C mit CP anstelle des ersten 90°-Pulses. Aus dem Intensitätsabfall

auf null des jeweiligen Signals lässt sich T_2 ermitteln. Die Signalintensitäten wurden mittels CCPN ausgelesen, der Fit erfolgte mittels Origin.

Folgende Gleichung für den Fit wurde genutzt:

$$I = A \cdot e^{\left(-\frac{t}{T_2}\right)}$$

(11)

I ist dabei die Intensität des jeweiligen Signals, A eine Proportionalitätskonstante und t die Zeit, die von 0 bis 8 ms in 0,5 ms-Schritten inkrementiert wurde. Dabei wurden die beiden Echo-Intervalle vor und nach dem 180°-Puls gleichzeitig und mit den gleichen Zeiten inkrementiert. Es wurden zwei Experimente, eines mit dem Einstrahlpunkt in der aliphatischen Region (55 ppm) und eines mit dem Einstrahlpunkt in der CO-Region (175 ppm), durchgeführt.
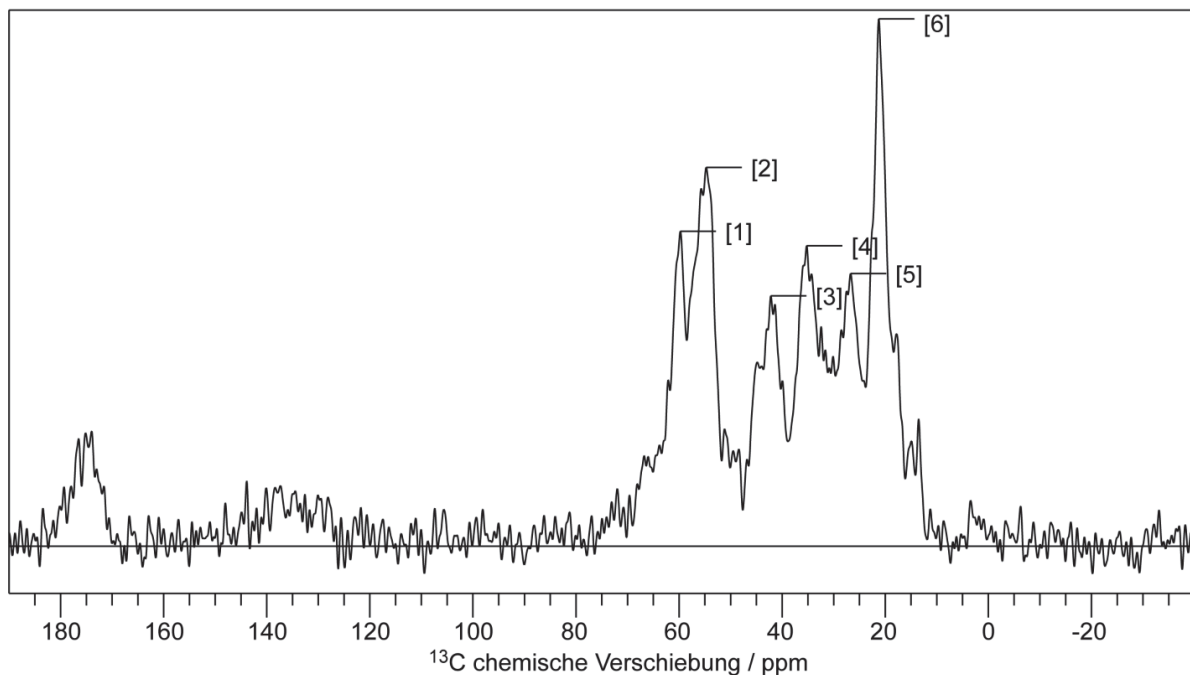
Abbildung 14: *1D-^{13}C-tancpxecho-Spektrum der Probe huPrP(23-144)-Aβ$_{oligo}$* für die aliphatische Region zum Zeitpunkt t1xecho = t2xecho = 0 ms. Die Nummerierung der Signale ist zu erkennen. Die Messung erfolgte mit folgenden Parametern: Rotationsfrequenz = 10 kHz; Temperatur ≈ 0 °C; Einstrahlpunkt = 55,062 ppm; CP-Kontaktzeit = 300 μs; Spektrale Weite = 44,643 kHz; t$_1$-Inkremente = 536; Anzahl der Scans = 128; Glättungsfunktion: quadratische Sinusfunktion um 0,35 π verschoben. Die Messung für die CO-Region erfolgte mit folgenden Messparametern: Rotationsfrequenz = 10 kHz; Temperatur ≈ 0 °C; Einstrahlpunkt = 174,975 ppm; CP-Kontaktzeit = 900 μs; Spektrale Weite = 73,729 kHz; t$_1$-Inkremente = 883; Anzahl der Scans = 128; Glättungsfunktion: quadratische Sinusfunktion um 0,35 π verschoben.*

Für die in **Abbildung 14** gekennzeichneten Signale des Spektrums wurden die in **Abbildung 15** dargestellten Relaxationskurven erhalten. **Tabelle 4** zeigt die ermittelten T_2-Zeiten für verschiedene Signale des Spektrums (siehe **Abbildung 14** für die Signalzuordnung der aliphatischen Region).
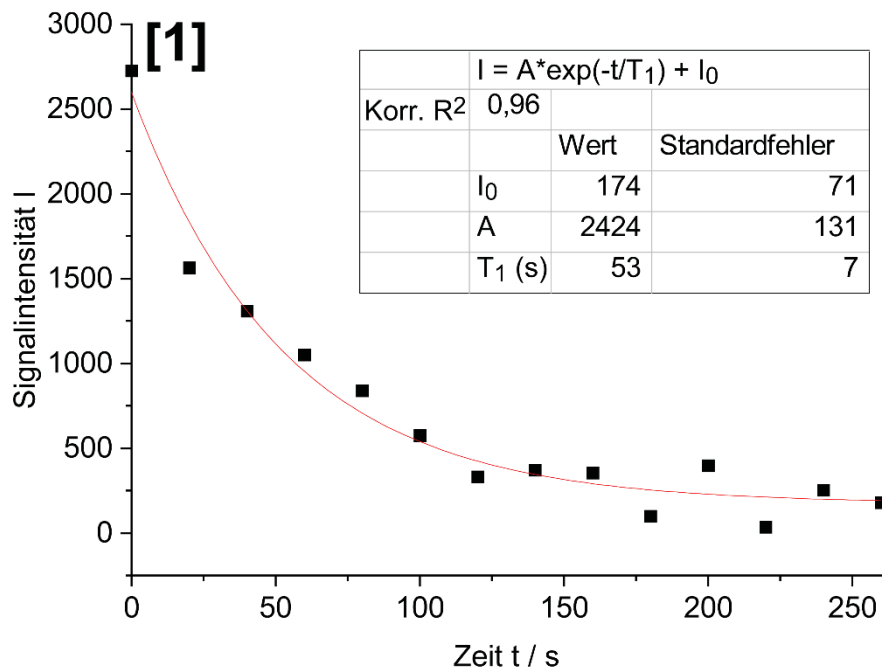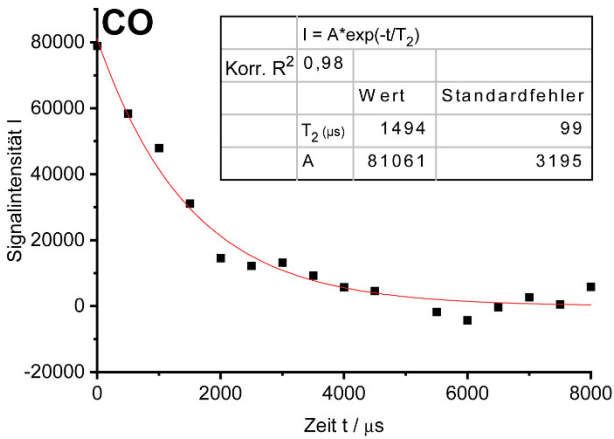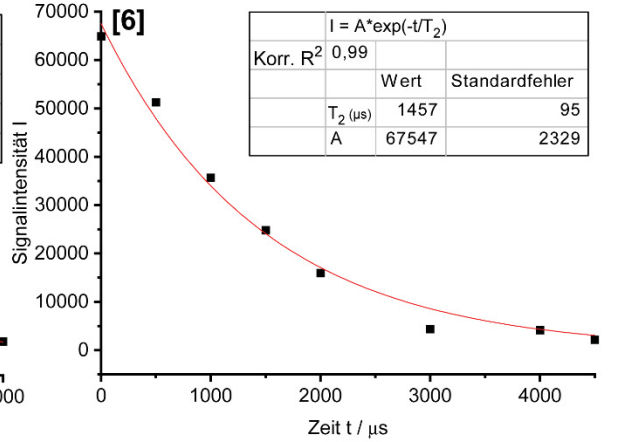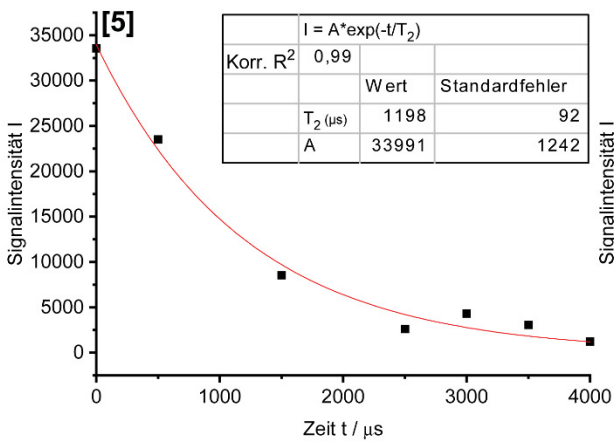
__Abbildung 15:__ Relaxationskurven der Probe huPrP(23-144)-Aβ_{oligo}* zur Ermittlung der T_2-Relaxationszeiten von ^{13}C. Die genutzten Fit-Gleichungen, sowie die Güte des Fits (Korrigiertes R^2) und die erhaltenen Werte für T_2 und A gemeinsam mit deren Standardfehlern sind in der jeweils zugehörigen Tabelle angegeben.

__Tabelle 4__: T_2-Relaxationszeiten von ^{13}C

Region	Signalnummern	T_2 (ms)	Standardfehler des Fits (ms)
C_α	[1], [2], [3], [4], [5]	0,82 – 1,20	0,05 – 0,13
C_α	[6]	1,46	0,09
CO	[1]	1,49	0,10

Für die aromatischen Kohlenstoffatome (C_{aro}) konnte auf Grund des niedrigen Signal-zu-Rausch-Verhältnisses kein belastbarer Wert für T_2 bestimmt werden.

Der Ermittlung der T_2-Relaxationszeiten ist wichtig für die Ermittlung der optimalen Aufnahmezeit in der indirekten Dimension, diese sollte $1,26*T_2$ entsprechen (Rovnyak-Limit[211]; maximales Signal-zu-Rausch-Verhältnis). Es ergaben sich $1,26*1,46$ ms $= 1,84$ ms für C_α und $1,26*1,49$ ms $= 1,88$ ms für CO. Genutzt wurden allerdings meist 6 ms als Kompromiss zwischen einem verschlechterten Signal-zu-Rausch-Verhältnis und einer verbesserten Auflösung.

<u>T_2-Relaxationszeiten von ^{15}N</u>

Die Ermittlung der ^{15}N-T_2-Relaxationszeiten erfolgte ebenfalls mit Hilfe der Pulssequenz „tancpxecho" am 600MHz-Varian-Spektrometer. Diese Pulssequenz entspricht einem Hahn-Echo auf ^{13}C mit CP statt des ersten 90°-Pulses (Messparameter: Rotationsfrequenz = 10 kHz; Temperatur ≈ 0 °C; Einstrahlpunkt = 119,979 ppm; CP-Kontaktzeit = 700 µs; Spektrale Weite = 13,587 kHz; t_1-Inkremente = 136; Anzahl der Scans = 256; Glättungsfunktion: quadratische Sinusfunktion um 0,35 π verschoben). Aus dem Intensitätsabfall auf null des jeweiligen Signals lässt sich T_2 ermitteln. Die Signalintensitäten wurden mittels CCPN ausgelesen, der Fit erfolgte mittels Origin.

Folgende Gleichung für den Fit wurde genutzt:

$$I = A \cdot e^{\left(-\frac{t}{T_2}\right)}$$

(12)

I ist dabei die Intensität des jeweiligen Signals, *A* eine Proportionalitätskonstante und *t* die Zeit, die von 0 bis 22 ms in 0,5 ms-Schritten inkrementiert wurde. Dabei wurden die beiden Echo-Intervalle vor und nach dem 180°-Puls gleichzeitig und mit den gleichen Zeiten inkrementiert.
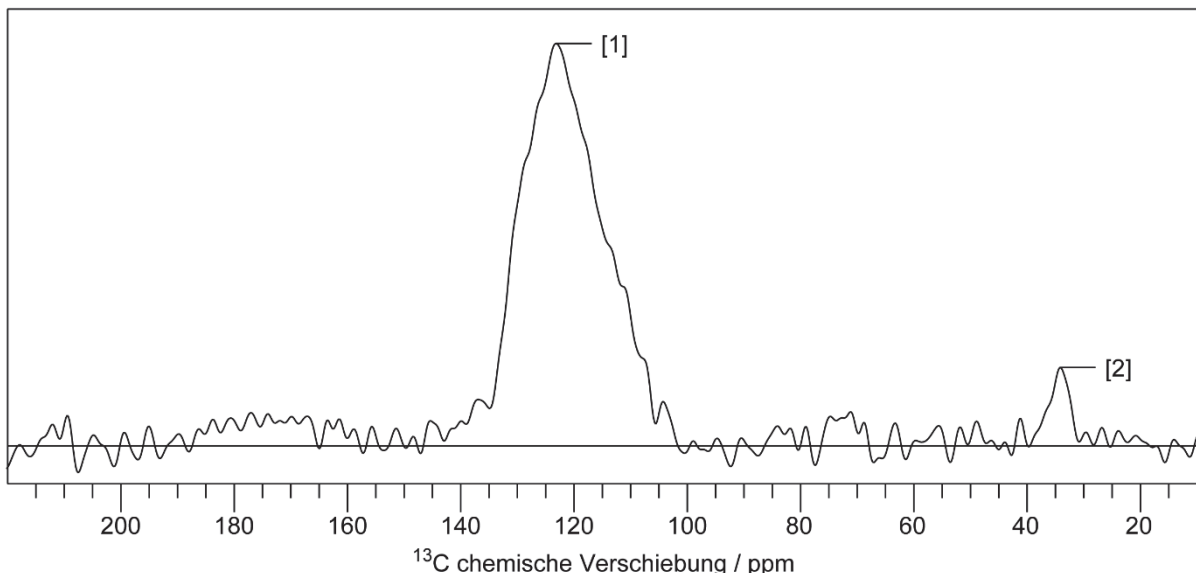
Abbildung 16: *1D-^{15}N-tancpxecho-Spektrum der Probe huPrP(23-144)-Aβ$_{oligo}$* zum Zeitpunkt t1xecho = t2xecho = 0 ms. Die Nummerierung der Signale ist zu erkennen. Die Messung erfolgte mit folgenden Parametern: Rotationsfrequenz = 10 kHz; Temperatur ≈ 0 °C; Einstrahlpunkt = 119,979 ppm; CP-Kontaktzeit = 700 µs; Spektrale Weite = 13,587 kHz;*

t_1-Inkremente = 136; Anzahl der Scans = 256; Glättungsfunktion: quadratische Sinusfunktion um 0,35 π verschoben.

Abbildung 16 zeigt ein exemplarisches 1D-Spektrum mit Zuordnung der ^{15}N-Signale, **Abbildung 17** die erhaltenen Relaxationskurven und **Tabelle 5** die ermittelten T_2-Zeiten für verschiedene Signale des Spektrums.

	I = A*exp(-t/T_2)		
Korr. R^2	0,9		
		Wert	Standardfehler
T_2 (µs)		3932	125
A		10136	213

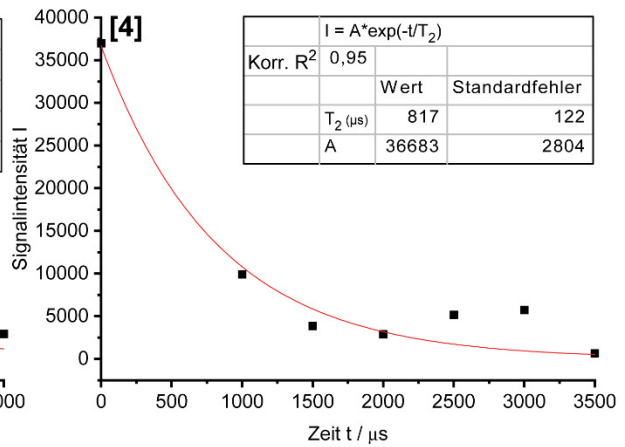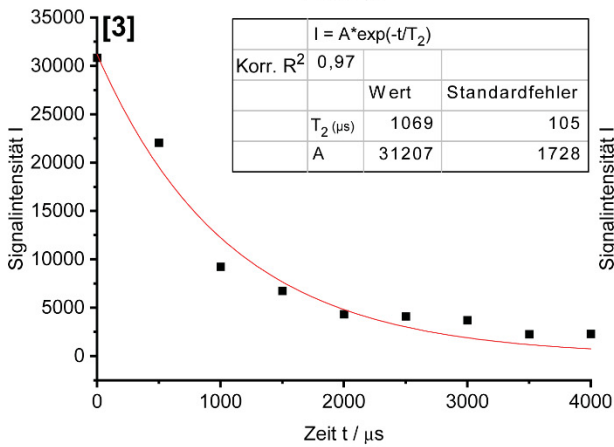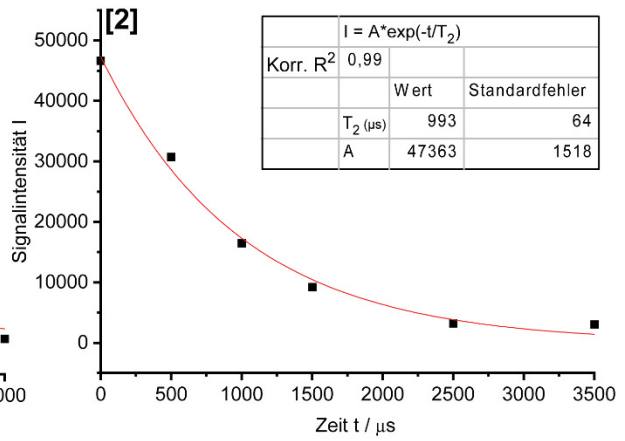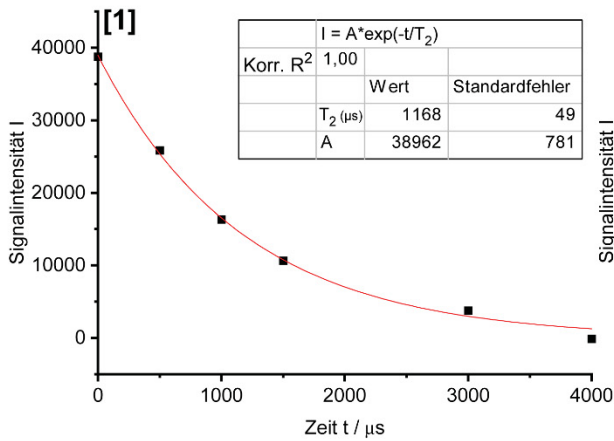|	I = A*exp(-t/T_2)		
Korr. R^2	0,82		
		Wert	Standardfehler
T_2 (µs)		9341	829
A		1984	111
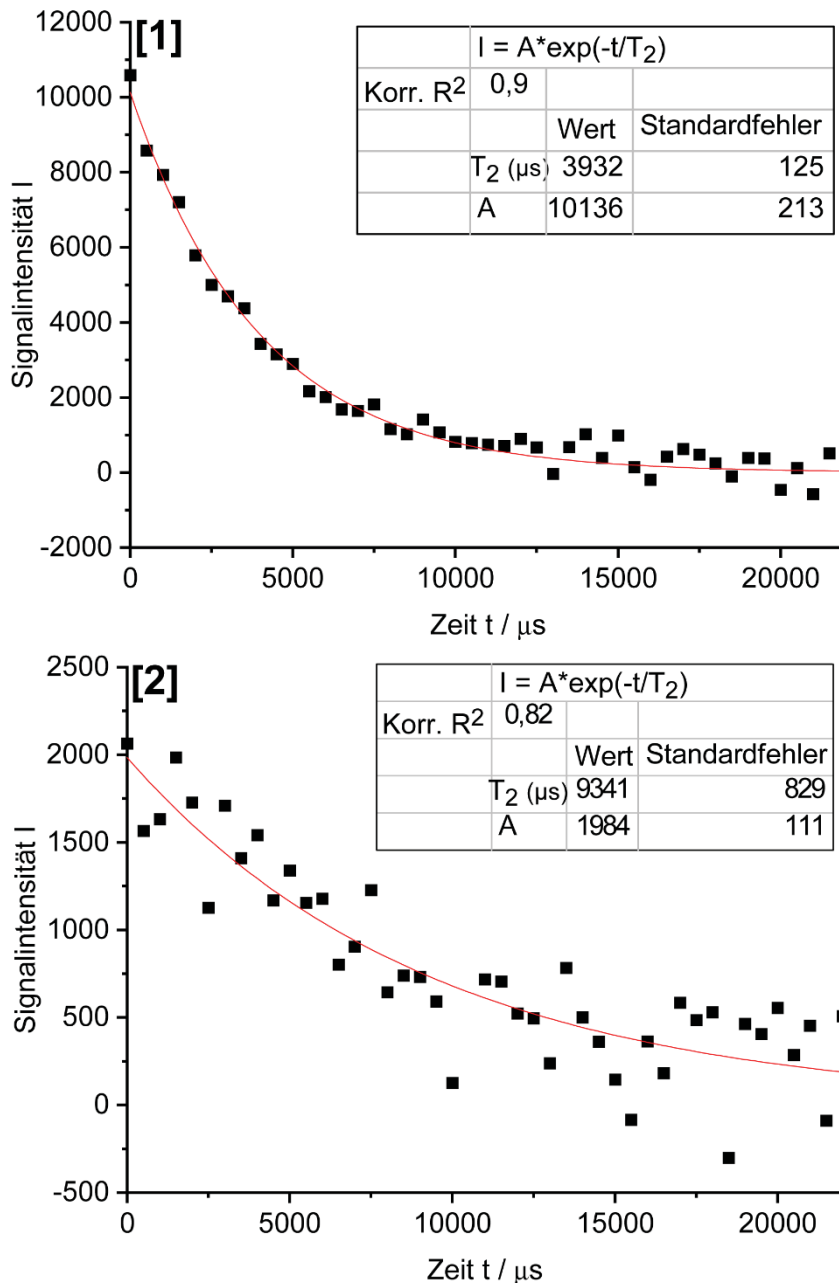
Abbildung 17: *Relaxationskurven der Probe huPrP(23-144)-Aβ$_{oligo}$* zur Ermittlung der T_2-Relaxationszeiten von [15]N. Die genutzten Fit-Gleichungen, sowie die Güte des Fits (Korrigiertes R^2) und die erhaltenen Werte für T_2 und A gemeinsam mit deren Standardfehlern sind in der jeweils zugehörigen Tabelle angegeben.*

Tabelle 5: T_2-Relaxationszeiten von ^{15}N

Region	Signalnummern	T_2 (ms)	Standardfehler des Fits (ms)
N_{haupt}	[1]	3,93	0,12
N_ζ Lys	[2]	9,34	0,83

Der Wert für N_ζ von Lys ist aufgrund des niedrigen Signal-zu-Rausch-Verhältnisses dieses Signals mit großen Unsicherheiten behaftet.

Der Ermittlung der T_2-Relaxationszeiten ist wichtig für die Ermittlung der optimalen Aufnahmezeit in der indirekten Dimension, diese sollte $1,26*T_2$ entsprechen (Rovnyak-Limit[211]), wie oben erwähnt. Es ergaben sich $1,26*3,93$ ms = 4,95 ms für N_{haupt}. Genutzt wurden meist 5 oder 6 ms, was somit ausreichend war.

Proton-assited-recoupling-Spektren (*PAR*) der Probe huPrP(23-144)-Aβ$_{oligo}$*
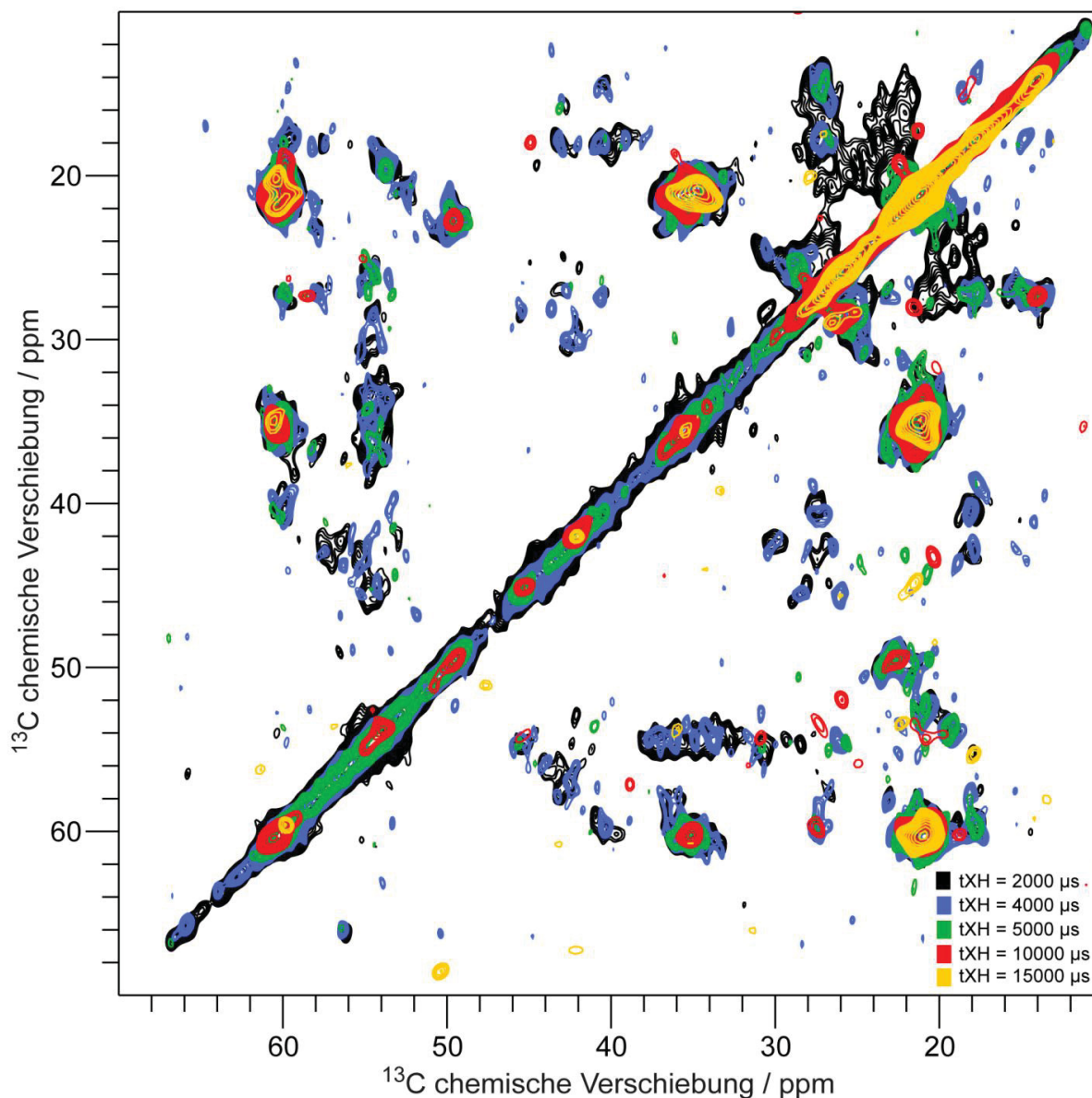
Abbildung 18: 2D-^{13}C-^{13}C-Proton-assited-recoupling-Spektren (PAR) der Probe huPrP(23-144)-Aβ$_{oligo}$* (Messparameter siehe **Tabelle 6**) bei verschiedenen PAR-Transfer-Kontaktzeiten (tXH): schwarz: tXH = 2000 µs; blau: tXH = 4000 µs; grün: tXH = 5000 µs; rot: tXH = 10000 µs; gelb: tXH = 15000 µs.

Laut De Paëpe et al.[212] sind die optimalen ^{13}C- und ^{1}H-RF-Feldstärken (jeweils ω_{1C} und ω_{1H}) während des PAR-Transfers annähernd gleich und es gilt $p_C = \omega_{1C}/\omega_{rot}$; $p_H = \omega_{1H}/\omega_{rot}$; $p_C \geq p_H$ und $p_C > 2,25$ (um Hartmann-Hahn- und *Rotary-Resonance*-Bedingungen auszuschließen), wobei ω_{rot} die Rotationsfrequenz ist. Nach Optimierung mittels „parcc1d" ergab sich die beste Transfer-Effizienz für $p_C \approx 2,67$ und für $p_H \approx 2,42$.

Es ist festzustellen, dass der Magnetisierungstransfer und damit die Anzahl der Signale abnehmen, je länger die PAR-Transfer-Kontaktzeit ist. Es treten hauptsächlich Signale resultierend aus intraresidualen Korrelationen auf, welche bereits aus den PDSD-Spektren bekannt waren. Zusätzliche interresiduale Signale konnten aufgrund der Überlappung nicht eindeutig zugeordnet werden. Außerdem konnte zum Zeitpunkt der Messung eine Alterung der Probe (Probe war mehr als 15 Monate alt) nicht zweifelsfrei ausgeschlossen werden.

Tabelle 6: Messparameter für die 2D-^{13}C-^{13}C-PAR-Spektren der Probe huPrP(23-144)-Aβ$_{oligo}$* (siehe **Abbildung 18**). Die Spektren wurden am 600MHz-Oxford-Spektrometer mit der Pulssequenz „parcc1d" optimiert und mittels „parcc2d" gemessen.

^{1}H-Frequenz (MHz)	600
Rotationsfrequenz (kHz)	15
VT-Gastemperatur (°C)	-8
Transfer 1	HC CP
^{13}C-Einstrahlpunkt (ppm)	50,050
CP-Kontaktzeit (µs)	500
Transfer 2	CH PAR
^{1}H-Einstrahlpunkt (ppm)	3,333
Kontaktzeit PAR-Transfer (µs)	(1) 2000 (2) 4000 (3) 5000 (4) 10000 (5) 15000
^{13}C-RF-Feldstärke (kHz)	40,515
^{1}H-RF-Feldstärke (kHz)	(1) 36,630-37,502 (2) 36,630 (3) & (4) & (5) 37,502
t_1-Inkremente	(1) & (2) & (3) 535 (4) 268 (5) 223
t_1-Spektrale Weite (kHz)	44,643
t_2-Inkremente	(1) & (2) & (3) 180 (4) & (5) 150
t_2-Spektrale Weite (kHz)	29,996
Anzahl der Scans	(1) 800 (2) 784 (3) 816 (4) 864 (5) 672
Glättungsfunktion	Quadratische Sinusfunktion um 0,35 π verschoben

Proton-Assisted-Insensitive-Nuclei-CP-Spektren (PAIN-CP) der Probe huPrP(23-144)-Aβ_{oligo}*
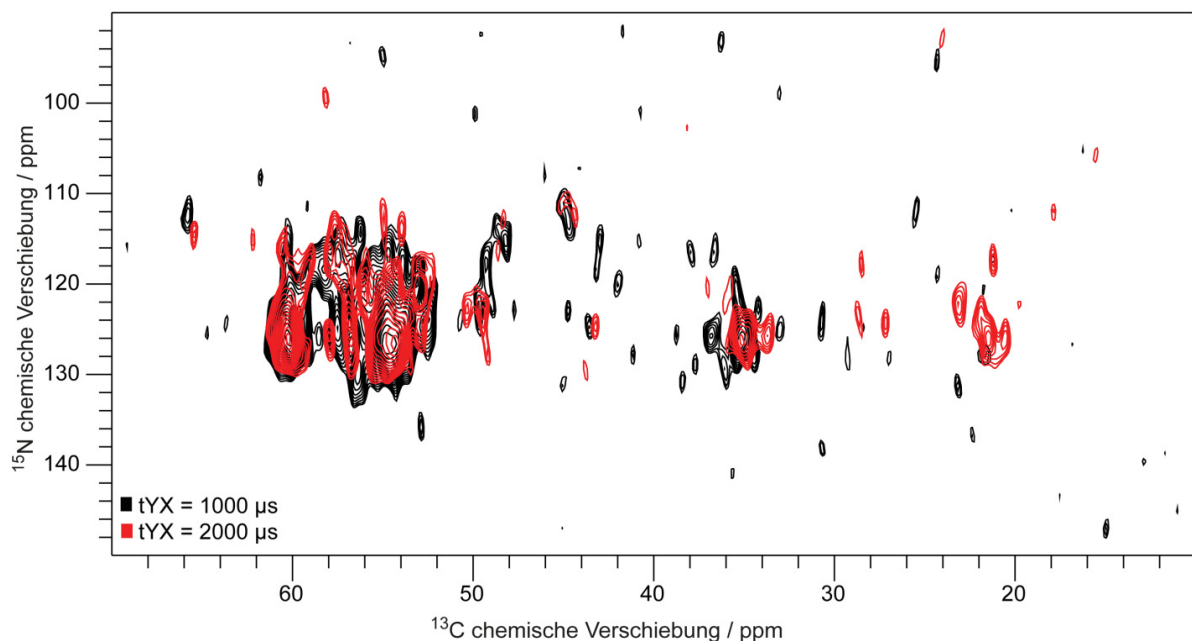
***Abbildung 19**: 2D-^{13}C-^{15}N-Proton-Assisted-Insensitive-Nuclei-CP-Spektren (PAIN-CP) der Probe huPrP(23-144)-Aβ_{oligo}* (Messparameter siehe **Tabelle 7**) bei verschiedenen PAIN-Transfer-Kontaktzeiten (tYX): tYX = 1000 µs (schwarz) und tYX = 2000 µs (rot).*

Es ist festzustellen, dass der Magnetisierungstransfer und damit die Anzahl der Signale abnehmen, je länger die PAIN-Transfer-Kontaktzeit ist. Es treten hauptsächlich Signale auf, welche bereits aus den NCACX-Spektren bekannt waren. Die genutzte PAIN-Bedingung zeigte nur ein geringes Signal-zu-Rauschverhältnis, woraus lange Messzeiten resultierten. Trotz langer Messzeit sind im Vergleich zum NCACX-Spektrum nur wenige Signale vorhanden, weswegen die PAIN-Spektren keinen Mehrwert an Informationen liefern konnten. Außerdem konnte zum Zeitpunkt der Messung eine Alterung der Probe nicht zweifelsfrei ausgeschlossen werden. Laut De Paëpe et al.[213] sind die optimalen ^{13}C- und ^{15}N-RF-Feldstärken (jeweils ω_{1C} und ω_{1N}) während des PAIN-Transfers annähernd gleich, was der Hartmann-Hahn-Bedingung bei n = 0 entspricht. Als gute Bedingung wird $\omega_{1C} = \omega_{1N} = 1{,}6{*}\omega_{rot}$ und $\omega_{1H} = 1{*}\omega_{rot}$ oder $3{*}\omega_{rot}$ angegeben, wobei ω_{1H} die ^{1}H-RF-Feldstärke und ω_{rot} die Rotationsfrequenz sind. Nach Optimierung ergab sich für $\omega_{1C} = 1{,}55{*}\omega_{rot}$, für $\omega_{1N} = 1{,}63{*}\omega_{rot}$ und für $\omega_{1H} = 3{,}1{*}\omega_{rot}$.

Tabelle 7: Messparameter für die 2D-^{13}C-^{15}N-PAIN-Spektren der Probe huPrP(23-144)-Aβ$_{oligo}$ (siehe **Abbildung 19**). Die Spektren wurden am 600MHz-Oxford-Spektrometer mit der Pulssequenz „dcptan2d" optimiert und gemessen.*

^{1}H-Frequenz (MHz)	600
Rotationsfrequenz (kHz)	15
VT-Gastemperatur (°C)	-10
Transfer 1	HN CP
^{15}N-Einstrahlpunkt (ppm)	120,159
CP-Kontaktzeit (μs)	500
Transfer 2	NC PAIN
^{13}C-Einstrahlpunkt (ppm)	50,991
Kontaktzeit PAR-Transfer (μs)	(1) 1000 (2) 2000
^{13}C-RF-Feldstärke (kHz)	23,310
^{15}N-RF-Feldstärke (kHz)	24,420
^{1}H-RF-Feldstärke (kHz)	(1) 46,224-47,096 (2) 47,096
t_1-Inkremente	365
t_1-Spektrale Weite (kHz)	30,488
t_2-Inkremente	15
t_2-Spektrale Weite (kHz)	3,600
Anzahl der Scans	(1) 7904 (2) 3840
Glättungsfunktion	Quadratische Sinusfunktion um 0,35 π verschoben

PITHIRDS-CT-Messungen der Probe Phe-BVPrP

Es erfolgten Pithirds-CT-Messungen[214] einer Probe aus BVPrP-Fibrillen, die spezifisch auf CO der Phe ^{13}C-markiert wurde, um die β-Faltblatt-Anordnung der Fibrillen zu ermitteln. Das Pithirds-CT-Experiment beruht auf der Wiedereinkopplung der dipolaren Kopplungen, deren Größe indirekt proportional zum Abstand zwischen zwei ^{13}C-Atomen ist, durch eine Sequenz von rotorsynchronisierten 180°-Pulsen. Die Pulssequenz der 180°-Pulse besteht dabei aus drei verschiedenen Blöcken: A (vier 180°-Pulse jeweils im ersten Drittel der Rotorperiode), B (vier 180°-Pulse jeweils im mittleren Drittel der Rotorperiode) und C (vier 180°-Pulse jeweils im letzten Drittel der Rotorperiode). Jeder Block besteht also aus viermal der Zeit für eine Rotorumdrehung τ_R. Diese Blöcke werden dann in einer bestimmten Anzahl und Reihenfolge hintereinander gesetzt, genauer gesagt $k_2*(k_1*A\ k_1*B\ k_1*C)\ k_3*(3k_1*B)$, sodass sich eine konstante Gesamtzeit von $12*k_1*(k_2+k_3)*\tau_R$ ergibt, wobei k_1, k_2 und k_3 die Anzahl der Wiederholungen sind. Bei einer Rotationsfrequenz von 20 kHz beträgt

die Länge eines 180°-Pulses also 16,6666 µs (ein Drittel der Rotorperiode), um eine Rotorsynchronisation zu gewährleisten. Tycko et al. nutzen ebenfalls eine Rotationsfrequenz von 20 kHz[214], bei kleineren Rotationsfrequenzen würde sich der 180°-Puls verlängern, was die Wahrscheinlichkeit für Rotordesynchronitäten erhöht.

Die Probe wurde im Zuge der Kollaboration mit den Arbeitsgruppen um Joaquín Castilla [*CIC bioGUNE, Derio (Bizkaia) und IKERBasque, Basque Foundation for Science, Bilbao (Bizkaia), Spain*] und Jesús R. Requena (*CIMUS Biomedical Research Institute, University of Santiago de Compostela-IDIS, Spain*) von diesen hergestellt. Allerdings musste die Phe-BVPrP-Probe, wegen einer möglichen Infektiosität der BVPrP-Fibrillen, in einem bruchsicheren Insert aus Delrin in den Rotor eingesetzt werden. Daraus resultierte ein sehr geringes Probenvolumen. Zudem gibt es in der aus 133 Aminosäureresten bestehenden Sequenz insgesamt nur drei Phe-Reste. Das geringe Probenvolumen und die geringe Anzahl an markierten Aminosäureresten hatte eine sehr geringe Signalintensität zur Folge (siehe **Abbildung 20 A** und **B**):
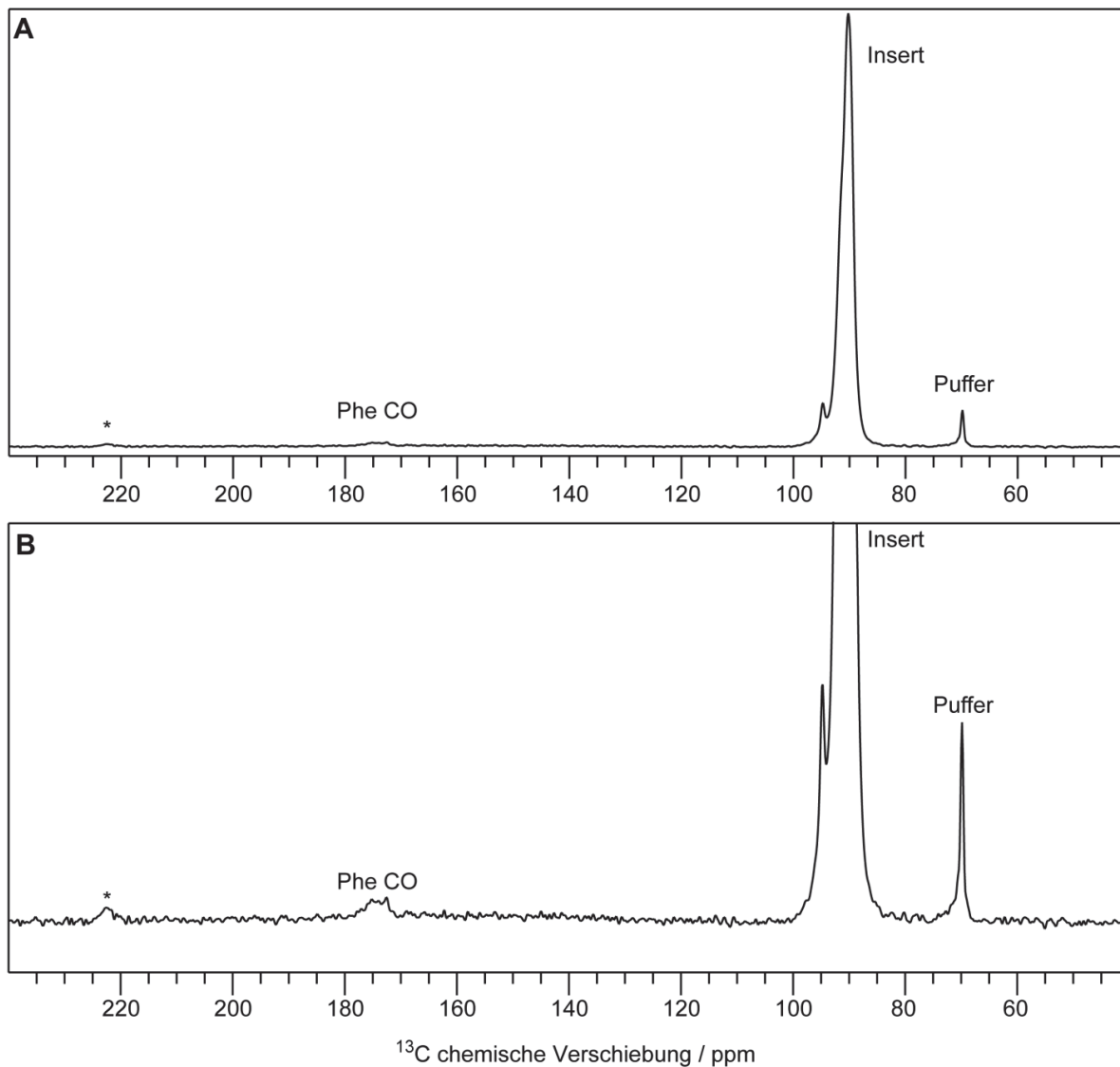
Abbildung 20: ^{13}C-CP-Spektrum der Probe Phe-BVPrP (Messparameter: Rotationsfrequenz = 20 kHz; Temperatur ≈ 28 °C; Einstrahlpunkt = 178,232 ppm; CP-Kontaktzeit = 900 µs; Spektrale Weite = 44,643 kHz; t_1-Inkremente = 536; Recycle Delay = 5 s; Anzahl der Scans = 13170; Glättungsfunktion: quadratische Sinusfunktion um 0,35 π verschoben). Eine Rotationsseitenbande des Inserts ist mit einem Stern (*) markiert. Das Phe-CO-Signal befindet sich bei ≈ 175 ppm. Die Signale des Inserts und des Puffers resultieren aus ^{13}C in natürlicher Häufigkeit. **A** Gesamtes ^{13}C-CP-Spektrum **B** Das Insert-Signal ist der Verdeutlichung halber abgeschnitten.

Es benötigte mindestens 6000 Scans (≈ 3,5 h) in einem normalen Kreuzpolarisationsexperiment (CP) um das Phe-CO-Signal zu erkennen (das Doppelte des Rauschens), deshalb wurde die Optimierung an 1-^{13}C-Gly vorgenommen. Eine beispielhafte Pithirds-CT-Messung von 1-^{13}C-Gly ist in **Abbildung 21** dargestellt.
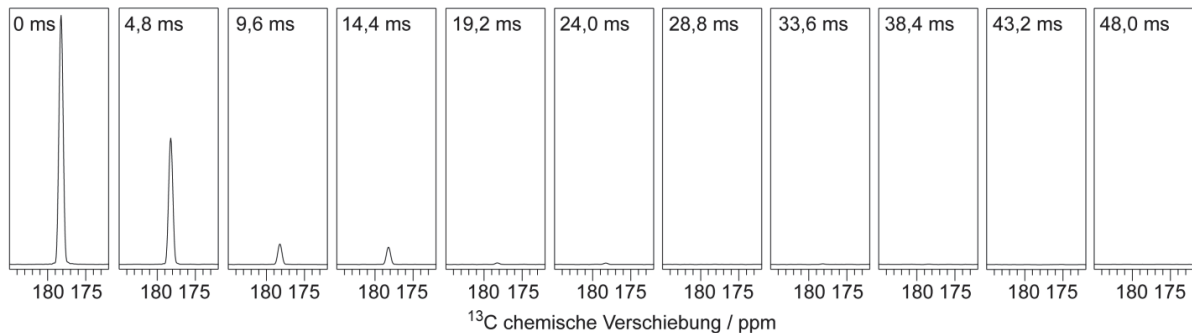
Abbildung 21: *Pithirds-CT-Spektren der CO-Region von 1-^{13}C-Gly bei einer effektiven Evolutionzeit τ_D' zwischen 0 und 48 ms. Messparameter: Rotationsfrequenz = 20 kHz; Temperatur ≈ 25 °C; Einstrahlpunkt = 178,232 ppm; CP-Kontaktzeit = 900 µs; k_1 = 4; k_2 = 20 – 0; k_2-Inkrement = -2; k_3 = 0 – 20; k_3-Inkrement = 2; k_2 und k_3 werden zeitgleich variiert; ^{13}C-RF-Feldstärke der Pithirds-Pulse = 21,235 kHz; ^{13}C-180°-Pulslänge = 16,675 µs; Spektrale Weite = 44,643 kHz; t_1-Inkremente = 536; Recycle Delay = 4 s; Anzahl der Scans = 16; Glättungsfunktion: quadratische Sinusfunktion um 0,5 π verschoben.*

Die einzelnen Spektren der ersten Pithirds-CT-Messung an der Probe Phe-BVPrP mit 62928 Scans (insgesamt 32,5 Tage Messzeit, aufaddiert) bei verschiedenen effektiven Evolutionszeiten sind in **Abbildung 22** und **23** dargestellt, jeweils ohne oder mit Magnitude-Mode prozessiert.
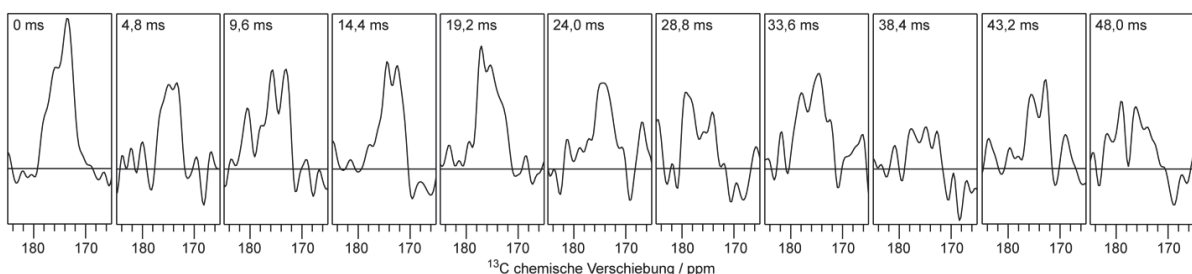
Abbildung 22: *Pithirds-CT-Spektren der Phe-CO-Region der Probe Phe-BVPrP bei einer effektiven Evolutionzeit τ_D' zwischen 0 und 48 ms. Messparameter: Rotationsfrequenz = 20 kHz; Temperatur ≈ 25 °C; Anzahl der Scans = 62928; siehe **Tabelle 8**.*
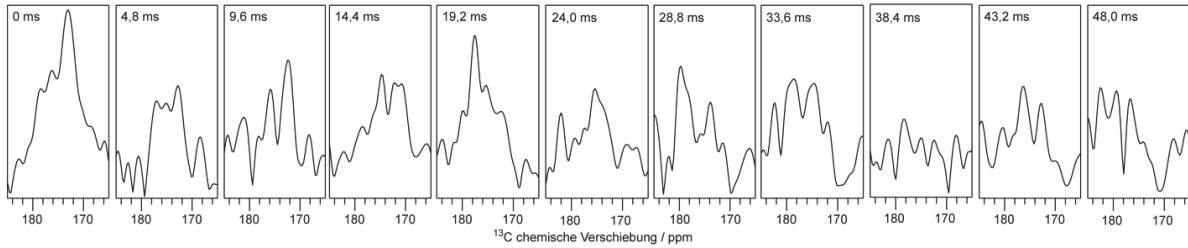
Abbildung 23: *Pithirds-CT-Spektren der Phe-CO-Region der Probe Phe-BVPrP bei einer effektiven Evolutionzeit τ$_D$' zwischen 0 und 48 ms. Messparameter: Rotationsfrequenz = 20 kHz; Temperatur ≈ 25 °C; Anzahl der Scans = 62928; prozessiert in Magnitude-Mode; siehe* **Tabelle 8***.*

Anschließend wurden aus den Signalintensitäten des CO-Signals bei verschiedenen effektiven Evolutionszeiten die Dephasierungskurven erstellt[214]:

Normierung

$$13C\ NMR\ Signal\ (origi)[\%] = \frac{\sum_n I_{Sig} \cdot 100}{I_{max}} \tag{13}$$

I_{Sig} = Intensität des Phe-CO-Signals bei jedem Datenpunkt

n = Anzahl der Datenpunkte des Phe-CO-Signals

I_{max} = maximale Intensität des Phe-CO-Signals (Datenpunkt 529)

Korrektur für natürliche Häufigkeit

$$13C\ NMR\ Signal\ (corr)[\%] = \frac{13C\ NMR\ Signal\ (origi) - f_{na} \cdot (100 - 0,39 \cdot \tau'_D)}{1 - f_{na}} \tag{14}$$

$$f_{na} = \frac{N_{na} \cdot 0,011}{N_{lab} + (N_{na} \cdot 0,011)} \tag{15}$$

f_{na} = Korrekturfaktor für natürliche Häufigkeit = 0,322799097

N_{na} = Anzahl der Aminosäurereste in natürlicher Häufigkeit = 130

N_{lab} = Anzahl der markierten Aminosäurereste = 3

τ_D' = Effektive Evolutionszeit (ms)

Der Term (100-0,39*τ$_D$') ist die Geradengleichung für den Abfall des Signals aller ^{13}C-Atome in natürlicher Häufigkeit, der Wert -0,39 ist also der negative Anstieg dieser Gleichung. Es ergibt sich, dass das Signal resultierend aus ^{13}C-Atomen in natürlicher Häufigkeit bei einer effektiven Evolutionszeit von 48 ms auf ≈ 81 % abfällt.

<u>Fehlerbalken</u>

$$Mittelwert\ Rauschen = \frac{Mittelwert(Abs(I_{linkes\ Rauschen})) + Mittelwert(Abs(I_{rechtes\ Rauschen}))}{2} \quad (16)$$

$I_{linkes\ Rauschen}$ = Intensitäten des Rauschens auf der linken Seite des Signals

$I_{rechtes\ Rauschen}$ = Intensitäten des Rauschens auf der rechten Seite des Signals

$$Fehler\ [\%] = \frac{Mittelwert\ Rauschen * \sqrt{n} * 100}{I_{max}} \quad (17)$$

n = Anzahl der Datenpunkte des Phe-CO-Signals

I_{max} = maximale Intensität des Phe-CO-Signals (Datenpunkt 529)

Es zeigte sich, dass das Ergebnis stark davon abhängt welche und wie viele Datenpunkte des Signals addiert wurden und wieviel Rauschen dazu beiträgt. Deshalb wurden nur fünf Datenpunkte vor und nach dem Signalmaximum (Signalmaximum bei Datenpunkt 529), also elf Datenpunkte (Datenpunkt 524 bis 534) addiert und somit der Einfluss des Rauschens auf ein Minimum reduziert.

<u>Simulationen der Dephasierungskurven bei verschiedenen ^{13}C-^{13}C-Abständen</u>

Die Simulationen der Dephasierungskurven bei verschiedenen ^{13}C-^{13}C-Abständen erfolgten mit Hilfe des Simulationsprogrammes SIMPSON[208], dabei entspricht ein Abstand von 4,8 Å einer parallelen in-register Anordnung der β-Faltblätter und ein Abstand > 8 Å einer Anordnung in einem β-Solenoid. Außerdem wurden gemischte Zustände aus zwei (der drei) Phe in einer Verbindung (*loop*) und einem in β-Strang-Konformation oder einem Phe in einer Verbindung und zwei in β-Strang-Konformation simuliert.

Abbildung 24 zeigt die simulierten Dephasierungskurven bei verschiedenen ^{13}C-^{13}C-Abständen zusammen mit den gemessenen Datenpunkten für Phe-BVPrP (orange Quadrate).
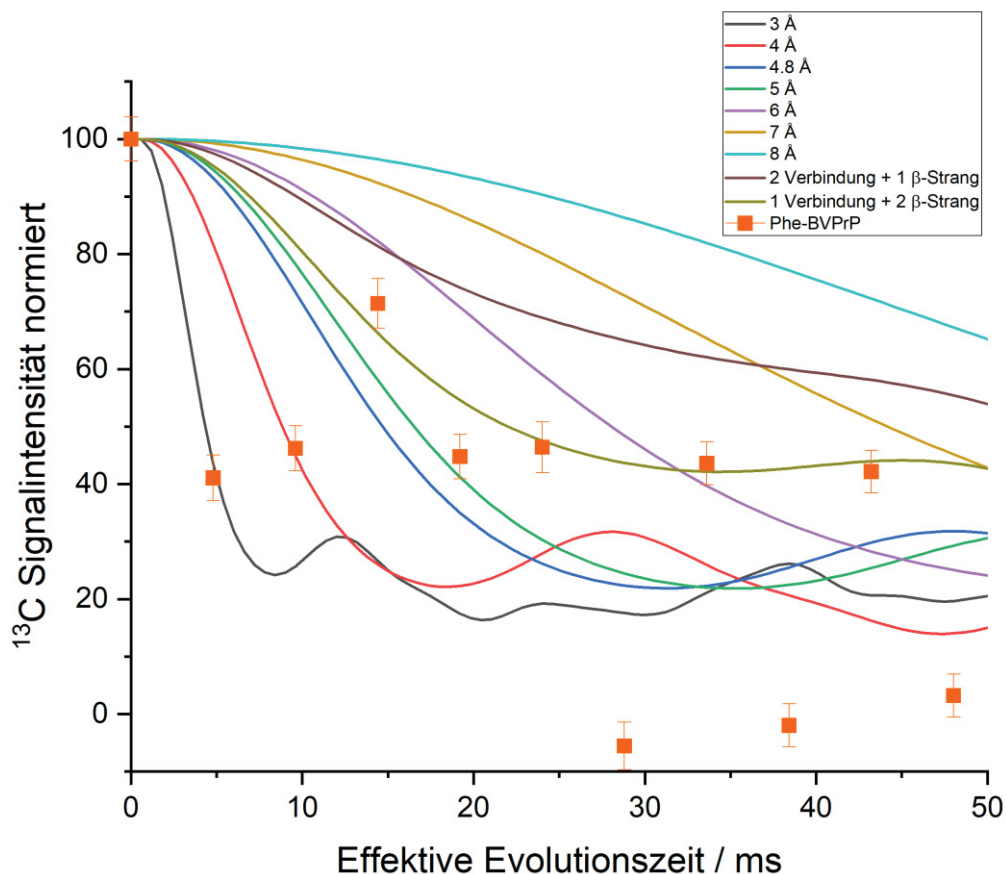
Abbildung 24*: Pithirds-CT-Dephasierungskurve der Probe Phe-BVPrP (Messparameter siehe **Tabelle 8**) der Datenpunkte 524 bis 534 (orange Quadrate) und simulierte Dephasierungskurven für verschiedene ^{13}C-^{13}C-Abstände (unterschiedliche Farben) erstellt mit SIMPSON[208], 4.8 Å entspricht parallel in-register.*

Die Messwerte deuten auf 4 Å hin, also eine parallele in-register Anordnung der β-Faltblätter. Da Phasieren aufgrund des schlechten Signal-zu-Rausch-Verhältnisses allerdings schwierig war, wurde die Prozessierung im Magnitude-Mode wiederholt (in NMRpipe), um Phasenfehler zu minimieren. **Abbildung 25** zeigt die Pithirds-CT-Dephasierungkurve prozessiert im Magnitude-Mode.
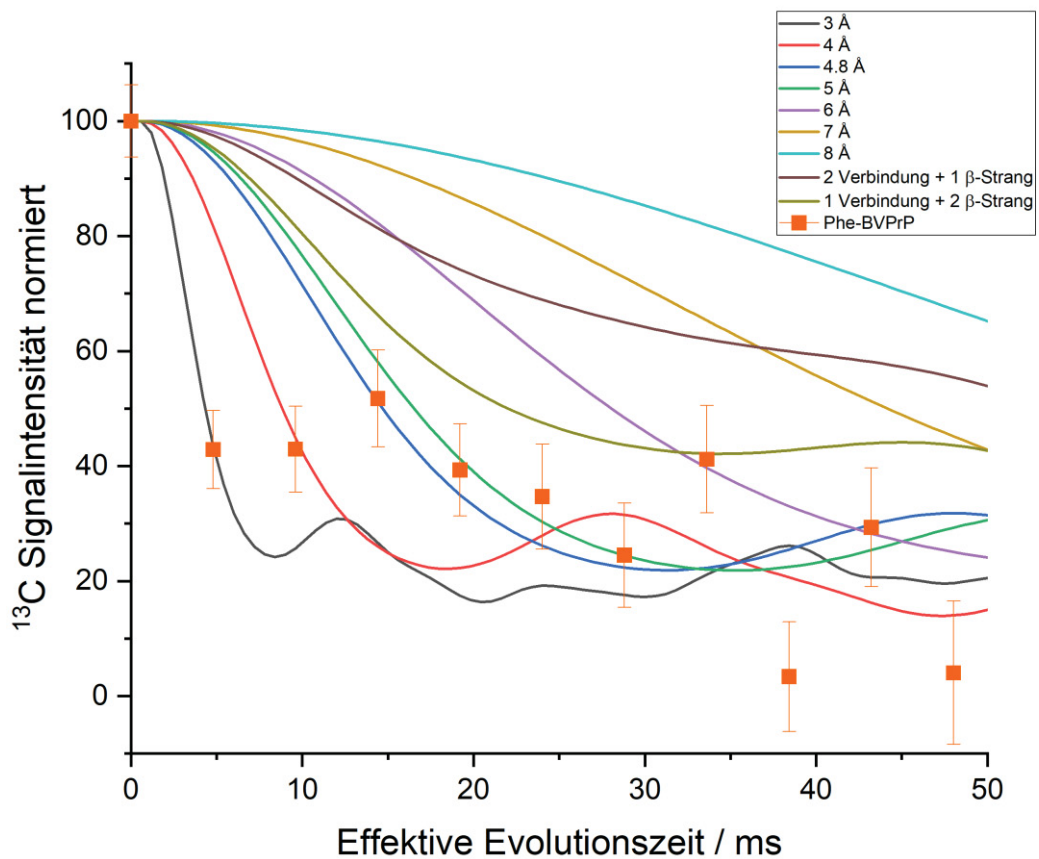
Abbildung 25: *Pithirds-CT-Dephasierungskurve der Probe Phe-BVPrP prozessiert im Magnitude-Mode (Messparameter siehe **Tabelle 8**) der Datenpunkte 524 bis 534 (orange Quadrate) und simulierte Dephasierungskurven für verschiedene ^{13}C-^{13}C-Abstände (unterschiedliche Farben) erstellt mit SIMPSON[208], 4.8 Å entspricht parallel in-register.*

Abbildung 25 zeigt ebenfalls eine Tendenz für eine parallele in-register Anordnung der β-Faltblätter und nicht die hypothetische Anordnung eines β-Solenoids (^{13}C-^{13}C-Abstand wäre > 8 Å).

Um dieses Ergebnis zu verifizieren, wurde die Messung anschließend mit 50000 Scans (≈ 26 Tage) wiederholt. Deren Pithirds-CT-Dephasierungskurve ist in **Abbildung 26** dargestellt.
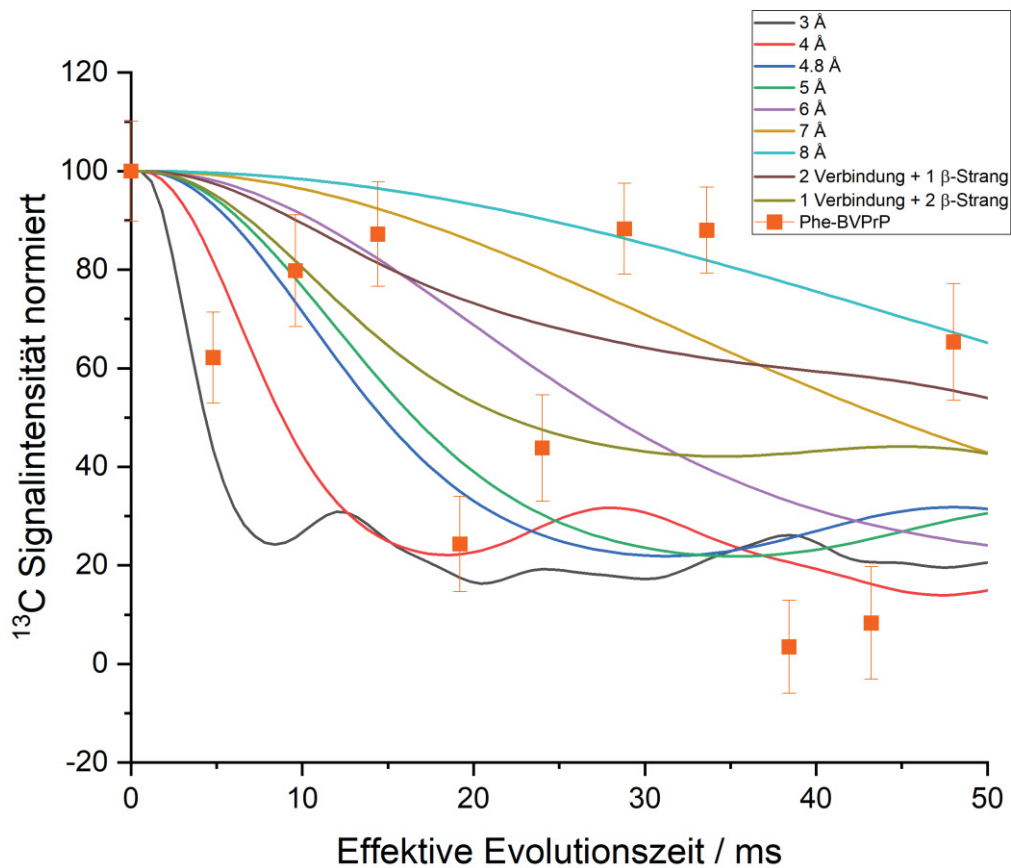
Abbildung 26: *Später gemessene Pithirds-CT-Dephasierungskurve der Probe Phe-BVPrP prozessiert im Magnitude-Mode (Messparameter siehe **Tabelle 8**) der Datenpunkte 524 bis 534 (orange Quadrate) und simulierte Dephasierungskurven für verschiedene ^{13}C-^{13}C-Abstände (unterschiedliche Farben) erstellt mit SIMPSON[208], 4.8 Å entspricht parallel in-register.*

Hier konnte die zuvor beobachtete Tendenz nicht bestätigt werden, überdies war überhaupt keine Aussage über eine Tendenz möglich. Dies könnte, neben dem geringen Signal-zu-Rausch-Verhältnis, auch durch Veränderungen zum Beispiel der RF-Feldstärke der 180°-Pulse während der sehr langen Messzeit erklärt werden. Es wäre also eine Optimierung dieses Parameters nach einiger Zeit nötig gewesen, die aber aufgrund des geringen Signal-zu-Rauschverhältnisses, wie oben erwähnt, nicht möglich war.

Zusammenfassend lässt sich also sagen, dass aufgrund des zu geringen Signal-zu-Rauschverhältnisses resultierend aus dem geringen Probenvolumen im Insert kein belastbares Ergebnis gewonnen werden konnte. Die Messung ohne Insert ist allerdings aufgrund der möglichen Infektiosität nicht zu empfehlen und auch eine Messung in einem größeren Rotor ist nicht möglich, da in solchen die für Pithirds-CT-Messungen nötige Rotationsfrequenz von 20 kHz nicht erreicht werden kann. Auch eine Messung mittels DNP gestaltete sich schwierig, da mit der vorhandenen Ausrüstung keine Probenrotation von 20 kHz möglich war.

Tabelle 8: *Messparameter für die ^{13}C-Pithirds-CT-Messungen[214] der Probe Phe-BVPrP (siehe Abbildungen 22 und 23). Die Spektren wurden am 600MHz-Varian-Spektrometer mit der Pulssequenz „pithirds_simonsharp" an Phe-BVPrP gemessen (und an 1-^{13}C-Gly optimiert).*

^{1}H-Frequenz (MHz)	600
Rotationsfrequenz (kHz)	20
VT-Gastemperatur (°C)	15
Transfer 1	HC CP
^{13}C-Einstrahlpunkt (ppm)	178,232
CP-Kontaktzeit (µs)	900
Transfer 2	Pithirds-CT
k_1	4
k_2; zeitgleich mit k_2 variiert	20 – 0
k_2-Inkrement	-2
k_3; zeitgleich mit k_3 variiert	0 – 20
k_3-Inkrement	2
^{13}C-RF-Feldstärke der Pithirds-Pulse (kHz)	21,235
^{13}C-180°-Pulslänge (µs); rotorsynchron	16,675
t_1-Inkremente	223
t_1-Spektrale Weite (kHz)	44,643
Recycle Delay (s)	4
Interleaved-Mode	Nein, liefert unsinnige Ergebnisse!
Anzahl der Scans	(1) 62928 (2) 50000
Glättungsfunktion	Quadratische Sinusfunktion um 0,5 π verschoben

Structural details of amyloid β oligomers in complex with human prion protein as revealed by solid-state MAS NMR spectroscopy

Anna S. König[1,2], Nadine S. Rösener[1,2], Lothar Gremer[1,2,3], Markus Tusche[1], Daniel Flender[2], Elke Reinartz[2], Wolfgang Hoyer[1,2], Philipp Neudecker[1,2], Dieter Willbold[1,2,3,*], and Henrike Heise[1,2,*]

From the [1]Institute of Biological Information Processing (IBI-7: Structural Biochemistry) and JuStruct: Jülich Center for Structural Biology, Forschungszentrum Jülich, Jülich, Germany; [2]Institut für Physikalische Biologie, Heinrich-Heine-Universität Düsseldorf, Düsseldorf, Germany; [3]Research Center for Molecular Mechanisms of Aging and Age-Related Diseases, Moscow Institute of Physics and Technology (State University), Dolgoprudny, Russia

Edited by Wolfgang Peti

Human PrP (huPrP) is a high-affinity receptor for oligomeric amyloid β (Aβ) protein aggregates. Binding of Aβ oligomers to membrane-anchored huPrP has been suggested to trigger neurotoxic cell signaling in Alzheimer's disease, while an N-terminal soluble fragment of huPrP can sequester Aβ oligomers and reduce their toxicity. Synthetic oligomeric Aβ species are known to be heterogeneous, dynamic, and transient, rendering their structural investigation particularly challenging. Here, using huPrP to preserve Aβ oligomers by coprecipitating them into large heteroassemblies, we investigated the conformations of Aβ(1–42) oligomers and huPrP in the complex by solid-state MAS NMR spectroscopy. The disordered N-terminal region of huPrP becomes immobilized in the complex and therefore visible in dipolar spectra without adopting chemical shifts characteristic of a regular secondary structure. Most of the well-defined C-terminal part of huPrP is part of the rigid complex, and solid-state NMR spectra suggest a loss in regular secondary structure in the two C-terminal α-helices. For Aβ(1–42) oligomers in complex with huPrP, secondary chemical shifts reveal substantial β-strand content. Importantly, not all Aβ(1–42) molecules within the complex have identical conformations. Comparison with the chemical shifts of synthetic Aβ fibrils suggests that the Aβ oligomer preparation represents a heterogeneous mixture of β-strand-rich assemblies, of which some have the potential to evolve and elongate into different fibril polymorphs, reflecting a general propensity of Aβ to adopt variable β-strand-rich conformers. Taken together, our results reveal structural changes in huPrP upon binding to Aβ oligomers that suggest a role of the C terminus of huPrP in cell signaling. Trapping Aβ(1–42) oligomers by binding to huPrP has proved to be a useful tool for studying the structure of these highly heterogeneous β-strand-rich assemblies.

* For correspondence: Dieter Willbold, d.willbold@fz-juelich.de; Henrike Heise, h.heise@fz-juelich.de.
Present address for Daniel Flender: Institut für Mikrobiologie, Universität Greifswald, Greifswald, Germany.

Alzheimer's disease (AD) accounts for an estimated 60 to 80% of all types of dementia (1). One of the hallmarks of AD is the formation of amyloid plaques, which consist mainly of amyloid β (Aβ) peptides comprising 39 to 43 residues (2). Aβ is produced by cleavage of the amyloid precursor protein (APP) by β- and γ-secretases (3). Of the two most abundant species Aβ(1–40) and Aβ(1–42), the latter is more prone to aggregation and its aggregates are more toxic (3). Small to moderately sized Aβ oligomers (Aβ$_{oligos}$) have been identified as the most neurotoxic factor in the pathogenesis of AD, whereas large fibrils are known to be the main component of insoluble plaques (4). Detailed structural information on Aβ(1–42)$_{oligo}$ is thus of paramount interest, and in recent years, structural studies on different oligomer preparations of Aβ(1–42)$_{oligo}$, Aβ(1–40)$_{oligo}$ (5, 6) (or pyro-Glu-Aβ(3/11–40) oligomers (7)) by solid-state NMR-spectroscopy have been conducted (8–15). Shape, morphology, and structural details of those oligomers were strongly dependent on preparation conditions, and while all of these oligomers had a high prevalence of β-strand secondary structure, tertiary fold and supramolecular arrangement of β-strands were found to differ strongly between different preparations. While in most mature fibrils β-strands are arranged in parallel in-register β-sheets (16, 17), quaternary structures in oligomers are much more variable, and, depending on the fibrillation pathway, parallel (12), antiparallel (18) β-sheets or even a mixture of both (11) have been found. A major challenge to structural studies of oligomers is their transient nature, and thus, most oligomer preparations exhibit substantial structural heterogeneity. Stabilization of oligomers is essential for long-term structural investigations. In most cases, further aggregation of oligomers was prevented by freeze-trapping with subsequent lyophilization (7–12, 14). In this study, we used the recombinant human prion protein in its native cellular prion protein (PrP^C) conformation to trap Aβ oligomers by coprecipitating them into large heteroassemblies, in which the growth of Aβ$_{oligo}$ is prevented, as demonstrated by long-term solid-state NMR measurements over 11 months.

The PrP^C is a high-affinity cell-surface receptor for Aβ$_{oligo}$ (19, 20), and PrP^C is also able to bind to fibrillar Aβ (21–23). It

Solid-state MAS NMR of the complex of huPrP and Aβ$_{oligo}$

has been suggested that binding of Aβ$_{oligo}$ to membrane-anchored PrP^C mediates Aβ toxicity during AD by mediating synapse damage (24) and the blockade of long-term potentiation by Aβ$_{oligo}$ (19, 25) *via* activation of Fyn-kinase pathways (26, 27) (Fig. S1), but this has also been questioned (28–31). It has also been described that soluble PrP (32) and its N-terminal fragment PrP(23–111) (33, 34) have a protective role by inhibiting Aβ fibrillation and sequestration of Aβ$_{oligo}$.

Several *in vitro* studies on the Aβ-PrP interaction suggest that Aβ$_{oligos}$ bind at two Lys-rich parts (residues 23–27 and ≈95–110) on PrP (35–40), but an additional involvement of the C terminus of PrP has also been suggested (21). Interestingly, the N terminus of human PrP is also able to bind oligomeric α-synuclein with high affinity (41–43). A structural study of insoluble PrP^C-Aβ$_{oligo}$ complexes described them as a "hydrogel," in which the Aβ(1–42)$_{oligos}$ were rigid, while PrP still has high molecular mobility (44). Additionally, this study reported a conformational change in the N terminus of PrP^C upon complexation with Aβ$_{oligo}$. We recently demonstrated that Aβ$_{oligo}$ forms large heteroassemblies with either full-length (huPrP(23–230)) or C-terminally truncated (huPrP(23–144)) membrane-anchorless monomeric PrP (40). These assemblies have a size of a few micrometers as determined by dynamic light scattering and show cloud-like morphologies as seen by atomic force microscopy (40). The Aβ:huPrP stoichiometry of the heteroassemblies depends on the amount of huPrP added to Aβ$_{oligo}$ and reaches a value of 4:1 (monomer ratio Aβ:huPrP) if either huPrP(23–144) or huPrP(23–230) is added to the oligomer solution in excess (40). In all these *in vitro* preparations, Aβ oligomers and early-stage protofibrils are stabilized and prevented from elongation by PrP, which has been shown to preferentially bind to fast-growing fibril and oligomer ends (22).

Here we exploit this stabilizing effect in an NMR study on different samples of Aβ$_{oligo}$ complexed by huPrP. Isotope labeling of either huPrP or Aβ allowed us to characterize both components of the complex separately. While the N-terminal region of huPrP in the complex remains largely devoid of secondary structure and still undergoes fast backbone conformational averaging on the microsecond to millisecond timescale, Aβ$_{oligos}$ exhibit a high degree of β-strand conformation. While these Aβ$_{oligos}$ are highly heterogeneous, solid-state NMR spectra reveal similarities with the corresponding spectra of all fibril polymorphs published so far (45–47).

Results

The N-terminal construct huPrP(23–144) is disordered in solution at mildly acidic and neutral pH

The solution structure of huPrP(23–230) had originally been determined in acetate buffer at an acidic pH of 4.5 and a temperature of 20 °C (48), whereas the huPrP-Aβ(1–42)$_{oligo}$ complex samples for solid-state NMR were prepared at a pH value close to neutral. As a basis for studying the interaction between huPrP and Aβ$_{oligo}$, we therefore first investigated free huPrP(23–144) by NMR spectroscopy in solution at different pH values ranging from 4.5 to 7.0 and at a temperature of

5.0 °C, which is closer to the temperature used for the solid-state NMR experiments. As reported previously, the chemical shifts of the N-terminal amino acid residues 23 to 124 in truncated huPrP(23–144) are almost identical to those of huPrP(23–230), whereas residues 125 to 144, which are part of the well-ordered globular domain of huPrP(23–230), are strongly affected by the truncation at position 144 (40).

We obtained almost complete sequence-specific ^{1}H, ^{13}C, and ^{15}N backbone resonance assignments for huPrP(23–144) at pH values of 4.5 and 7.0 and a temperature of 5.0 °C using a combination of HNCO, HNCACB, and BEST-TROSY-(H)N(COCA)NH triple-resonance experiments (Fig. S2). The assigned chemical shifts at pH 4.5 and pH 7.0 have been deposited with the Biological Magnetic Resonance Data Bank (BMRB) under accession codes 28115 and 28116, respectively.

As expected, side-chain titration in this pH range causes significant chemical shift changes for all seven histidine residues and for residues next to histidine. Other than that, the chemical shifts at pH 4.5 and pH 7.0 are very similar to each other and very close to random coil shifts (49). Quantitative analysis reveals that the Random Coil Index (RCI) order parameters (50) S_{RCI}^2, which are a measure of how different the backbone chemical shifts are from those of a disordered random coil on a scale of 0 (typical for a random coil) to 1 (typical for a well-ordered backbone conformation), are consistently below ≈0.6 (Fig. S3). This demonstrates conclusively that free huPrP(23–144) in solution at neutral and mildly acidic pH is highly disordered and devoid of any stable secondary structure.

The flexible N terminus of huPrP becomes immobilized but remains almost devoid of regular secondary structure upon binding to Aβ$_{oligo}$

High-molecular-weight heteroassemblies of oligomeric Aβ(1–42) and huPrP(23–144) or of oligomeric Aβ(1–42) and huPrP(23–230) were prepared by adding the respective huPrP construct to a preincubated solution of Aβ(1–42), as described previously (40). Immediately after addition of huPrP to the solution, precipitation of a solid fine white powder was observed.

These formed high-molecular-weight heteroassemblies were analyzed by an MTT cell viability test (Fig. 1A). Both huPrP(23–230) and huPrP(23–144) reduce Aβ(1–42)$_{oligo}$ toxicity in a concentration-dependent manner, thus these complexes are not toxic, and huPrP has a protective effect. As our complexes do not exhibit a GPI anchor, this fits to the observation of a protective role for non-membrane-bound huPrP fragments (32, 36) in contrast to membrane-anchored huPrP, which mediates neurotoxicity (19, 24, 25). The fragment huPrP(121–230), which was shown to not form any heteroassemblies (40), however, does not rescue Aβ(1–42)$_{oligo}$ toxicity and was used as a negative control. None of the huPrP fragments alone is toxic for the cells (Fig. 1A).

High-molecular-weight assemblies of Aβ(1–42)$_{oligo}$ and huPrP(23–144) were further analyzed by sucrose density gradient ultracentrifugation (DGC) and subsequent SDS-
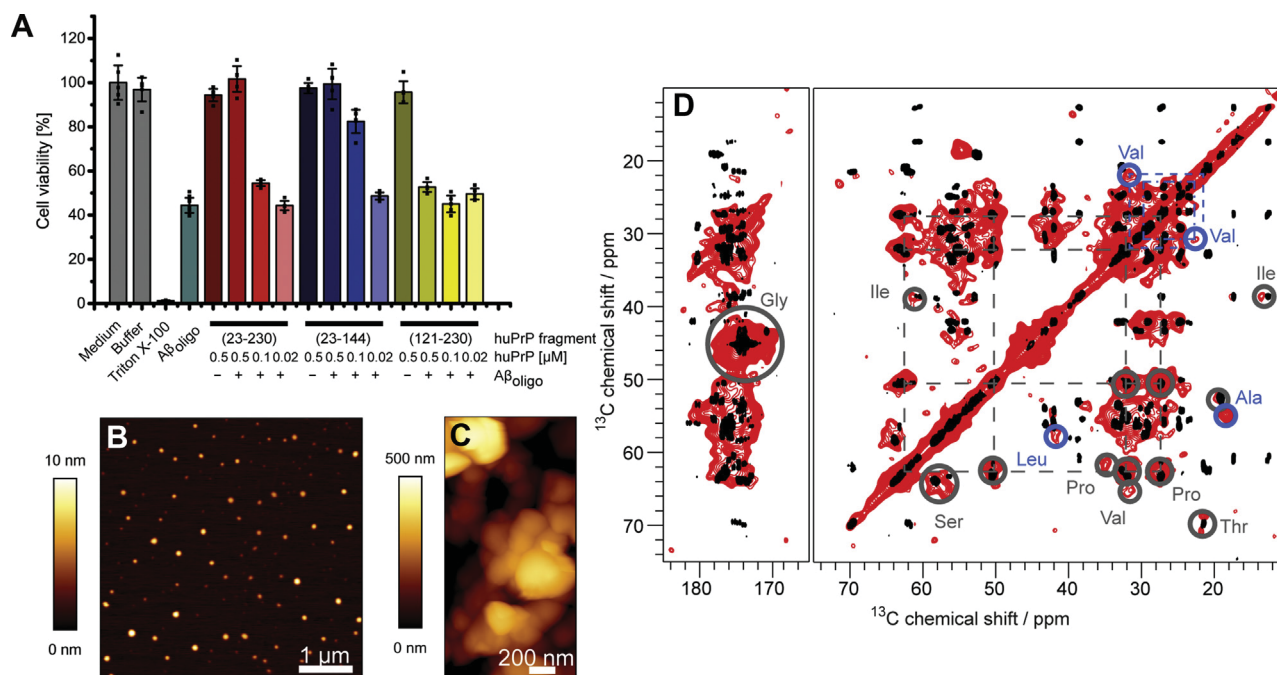
Figure 1. *A*, MTT assay of 1 μM Aβ_{oligo} and of 1 μM Aβ_{oligo} in complex with either 0.5 μM, 0.1 μM, or 0.02 μM of either huPrP(23–230), huPrP(23–144) or huPrP(121–230). Both huPrP(23–230) and huPrP(23–144) reduce Aβ_{oligo} toxicity in a concentration-dependent manner. In contrast, the C-terminal fragment huPrP(121–230) does not. None of the huPrP fragments alone reduces cell viability. This reduction of toxicity has been seen for non-membrane-bound huPrP fragments before (32, 36) and is in contrast to toxic effects of membrane-anchored huPrP (19, 24, 25). As our complexes do not exhibit a GPI-anchor, the reduction of toxicity reflects these observations. *B*, 5 μm × 5 μm AFM image of 440 nM Aβ_{oligo} and *C*, 2 μm × 1 μm AFM image of Aβ_{oligo}-huPrP(23–144) coprecipitates generated with 80 μM preincubated Aβ(1–42) and 40 μM huPrP(23–144). The aggregates have sizes up to 1 μm spanning clusters with a smooth surface appearance, whereas Aβ_{oligo} are small nm spheres. *D*, comparison of a PDSD spectrum of huPrP(23–144)*-Aβ (* species is ¹³C, ¹⁵N uniformly labeled) in *red* with a ¹³C-¹³C TOCSY spectrum of monomeric huPrP(23–144) in *black*. The PDSD spectrum was recorded at a temperature of ≈−6 °C, a spinning frequency of 11 kHz and a mixing time of 30 ms and the TOCSY spectrum at a temperature of 5.0 °C, at pH 6.7. *Gray circles* indicate some identified amino acid types, *dashed lines* Pro and Val connections in the PDSD spectrum. Due to broad line widths and a low signal dispersion in the PDSD spectrum several correlations overlap, especially for the residues in the octarepeat region. Nevertheless, spin systems for most of the amino acid types present in the sequence could be identified and an amino-acid-type specific resonance assignment was possible. Differences between the PDSD and TOCSY spectrum are highlighted with *blue circles*. For an additional PDSD spectrum see Fig. S6, the corresponding double quantum-single quantum correlation spectrum (DQ-SPC5) is shown in Fig. S7.

PAGE and RP-HPLC (40) (Fig. S4). As previously described (40), a molar ratio of Aβ:PrP of 4:1 is obtained in the assemblies if huPrP is added in excess; for higher Aβ:PrP ratios, not all potential PrP-binding sites on Aβ_{oligo} are saturated with huPrP(23–144) (as in sample huPrP(23–144)-Aβ*, * indicates that the Aβ moiety of the complex is ¹³C, ¹⁵N labeled).

In Figure 1 typical AFM images of Aβ_{oligo} alone (Fig. 1*B*) or in complex with N-terminal huPrP(23–144) (Fig. 1*C*) are shown. Spherical Aβ oligomers can clearly be identified (Fig. 1*B*), and no fibrils are observed in the huPrP(23–144)-Aβ condensates (Fig. 1*C*). Next, we focused on investigating structural features of the complex by NMR spectroscopy.

To probe the flexibility of the N-terminal construct huPrP(23–144) in the complex, we recorded a ¹H-¹³C insensitive nuclei enhanced by polarization transfer (INEPT)-NMR spectrum as well as dipolar-based ¹H-¹³C and ¹H-¹⁵N cross polarization (CP)-MAS spectra (51). The INEPT-NMR spectrum of this sample did not show any protein signals at a sample temperature of ≈27 °C (spectrum not shown), whereas in ¹H-¹³C (recorded at a sample temperature of ≈0 °C) and ¹H-¹⁵N CP spectra (recorded at a sample temperature of ≈−6 °C) strong signals typical for all amino acid types can be seen (Fig. S5). This indicates that huPrP(23–144) in complex with Aβ(1–42)_{oligo} is

immobilized and does not undergo rapid isotropic reorientation as in solution.

In Figure 1*D* a typical 2D ¹³C-¹³C-correlation spectrum obtained with proton-driven spin-diffusion (PDSD) of huPrP(23–144)*-Aβ (* indicates that the huPrP moiety of the complex is ¹³C, ¹⁵N labeled) is overlaid with a ¹³C-¹³C total correlation spectrum (TOCSY) of monomeric huPrP(23–144) in solution at pH 6.7. Except for some Val and Ala resonances, most of the peaks align well. This indicates that the natively unfolded N terminus of huPrP does not undergo a major conformational rearrangement upon complex formation with Aβ_{oligo}, but conformational averaging of backbone conformations is still possible on the microsecond to millisecond timescale. Due to the lack of secondary structure in the intrinsically unstructured N terminus as well as the repetiveness of the amino acid sequence in the octarepeats, the signal overlap is so severe that sequence-specific resonance assignment for the solid-state NMR spectra was not possible.

While most of the resonances of huPrP(23–144) in complex with Aβ_{oligo} have the same chemical shifts as huPrP(23–144) in solution, some differences can be clearly seen; in particular, some Ala, Val, and Leu resonances are shifted from random coil toward α-helical secondary chemical shifts. Six out of seven Ala residues

Solid-state MAS NMR of the complex of huPrP and Aβ_oligo

Figure 2. *A*, amino acid sequence of huPrP(23–230) (48) **used in this study.** The Aβ-binding regions K23–K27 and T95–K110 (35–40) and the five octarepeats are indicated above the sequence. *B*, 3D structure of the natively folded prion domain (residues 125–228) of full-length huPrP(23–230) in solution. β-strands are colored *blue*, α-helices *red*. Picture adapted from PDB-File 1QLZ (48). Residues whose entire spin system is missing or shifted in the PDSD spectra (Figs. S10–S12) are highlighted in *purple* in *A* and *B*.

as well as both Val and Leu residues present in the sequence are located within a short stretch from residue 113 to 130, a region that starts with the so-called palindrome segment (A^{113}GAAAAGA^{120}) (see Fig. 2*A*). Thus, structural changes upon complexation with Aβ_oligo in N-terminal huPrP(23–144) seem to be confined mainly to the region between A113 and L130.

These findings are also supported by analysis of secondary chemical shifts (Fig. S8). Most secondary chemical shifts of huPrP(23–144) in solution are random coil chemical shifts indicative of a lack of regular secondary structure. Likewise, most spin systems of huPrP(23–144) in complex with Aβ_oligo are typical random coil chemical shifts, with some α-helical shifts found for Ala, Leu, and Val, which are not found for monomeric huPrP(23–144). Notably, almost no β-strand-like secondary chemical shifts were identified for complexed huPrP(23–144). This finding is an indication that huPrP(23–144) did not aggregate into amyloid fibrils. We also compared the chemical shifts of huPrP(23–144) fibrils (52, 53) with our correlation spectrum of huPrP(23–144)*-Aβ (Fig. S9A). Most of the signals observed for fibrillar huPrP(23–144) do not overlap with the signals in our huPrP(23–144)*-Aβ spectra. We therefore conclude that the conformations of huPrP(23–144) in huPrP(23–144)*-Aβ and the huPrP(23–144) fibril are very different, and the interaction with Aβ_oligo did not induce huPrP(23–144) fibril formation.

The C terminus of huPrP shows changes in α-helices 2 and 3 upon Aβ_oligo binding

For full-length huPrP in complex with Aβ_oligo, huPrP(23–230)*-Aβ (see Table 1), no signals were detected at ≈30 °C in the INEPT spectrum (not shown), which indicates that not only the N terminus, but also the C terminus of huPrP is not highly dynamic. By contrast, excitation with ^{1}H-^{13}C CP results in a typical ^{13}C NMR spectrum expected for a protein. To test whether the full protein is visible in the spectrum or whether a substantial part of the protein is too mobile for dipolar transfer, we compared 1D spectra obtained with ^{13}C direct excitation (DE) and ^{1}H-^{13}C CP spectra recorded at sample temperatures of ≈30, 10, and –10 °C (Fig. 3). At all three temperatures, no substantial differences between the

Table 1

Details of the samples used for the solid-state NMR measurements (* species is ^{13}C, ^{15}N uniformly labeled)

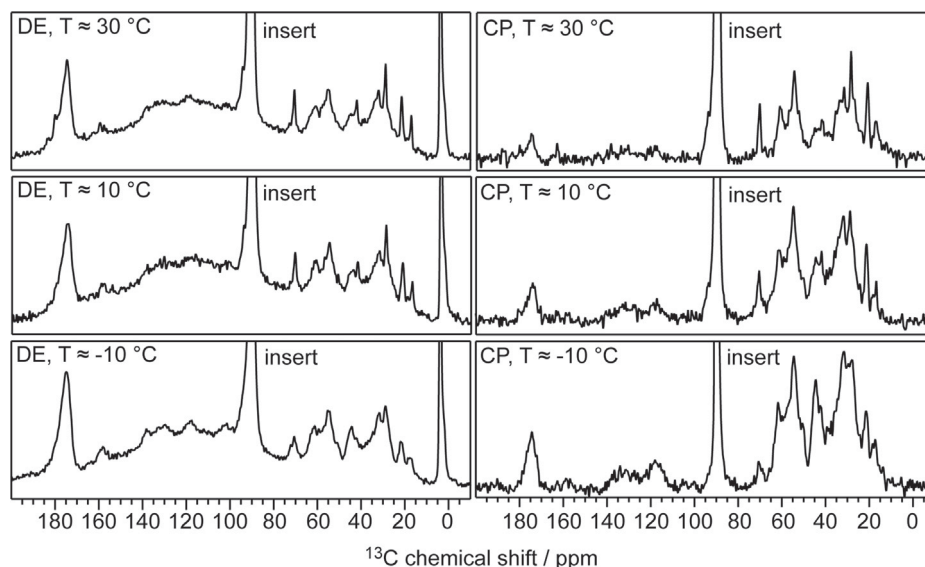| Sample	^{13}C, ^{15}N labeled species	Monomer stoichiometry Aβ:huPrP (initial mixture)	Monomer stoichiometry Aβ:huPrP (in complexes)
huPrP(23–144)*-Aβ	huPrP(23–144)	6:1	not estimated
huPrP(23–230)*-Aβ	huPrP(23–230)	4:1	not estimated
huPrP(23–144)-Aβ*	Aβ(1–42)	8:1	8.6:1
huPrP(23–144)_exc-Aβ*	Aβ(1–42)	2:1	(3.7 ± 0.12):1

Figure 3. ^{13}C Direct excitation (DE) and ^{1}H-^{13}C CP spectra of huPrP(23–230)*-Aβ (* species is ^{13}C, ^{15}N uniformly labeled) recorded at temperatures of ≈30, 10, and −10 °C and 11 kHz spinning frequency. Recycle delays of 20 s and 2 s were used for DE and ^{1}H-^{13}C CP experiments, respectively. The signal at 90 ppm is caused by the rotor insert (Delrin) and is cut off for clarity. The signal at around 0 ppm in the ^{13}C DE spectrum belongs to a silicone-based rotor inlet and is likewise cut off for clarity, the broad bump centred at 120 ppm however is the Teflon background of the probe. Both signals are not detected in the CP spectra. Signal intensities were scaled to the number of scans for each spectrum. Even at the lowest temperature the free water in the sample was not completely frozen, as verified by ^{1}H spectra (not shown).

spectra are visible. Signal intensities in both types of spectra are roughly proportional to 1/T following Curie's law, and at all temperatures signal intensities in CP spectra are up to two times higher than in the respective DE spectra. This is an indication that the complete huPrP molecule is fully immobilized over the whole temperature range and does not undergo major mobility changes (44). Some signals (*e.g.,* ≈70 ppm, C_β of Thr) show broader linewidths at lower temperatures, indicating reduced motional averaging of chemical shifts.

In Figure 4, a typical 2D PDSD spectrum of the huPrP(23–230)*-Aβ complex is displayed. A line width of ≈1 ppm is observed for the ^{13}C resonances, and due to the large number of resonances and the limited signal dispersion, the signal overlap is so substantial that a sequential resonance assignment or even a quantitative analysis of residue-specific correlations was not possible. Nevertheless, a comparison with the corresponding 2D ^{13}C-^{13}C correlation spectrum of the N-terminal construct huPrP(23–144) in complex with oligomeric Aβ (red outline in Fig. 4) allows some conclusions about the structure of full-length complexed huPrP: First, almost all resonances observed in the spectrum of C-terminally truncated huPrP(23–144) appear to be also visible in the spectrum of full-length huPrP(23–230)*-Aβ (Fig. 4). These findings suggest that the C terminus of full-length huPrP(23–230) does not have a major impact on the conformation of the N terminus and its interaction with Aβ$_{oligo}$, in line with previous results (35–37, 40). Second, the spectrum of full-length huPrP complexed by Aβ$_{oligo}$ displays additional resonances, which are absent in the spectrum of N-terminal huPrP(23–144) in complex with Aβ$_{oligo}$. Some of the amino acid residues occurring mainly in the C terminus (*e.g.,* Ile, Thr, and Val) give rise to cross peaks that can be unambiguously

identified in 2D ^{13}C-^{13}C correlation spectra. However, for most C-terminal amino acid residues (*e.g.,* Asp, Glu, Tyr, etc., Fig. 2*A*), the 2D correlations overlap with other resonances and can therefore not be unambiguously assigned.

We compared our 2D ^{13}C-^{13}C correlation spectrum with the expected correlations between the chemical shifts obtained experimentally for natively folded full-length huPrP in solution
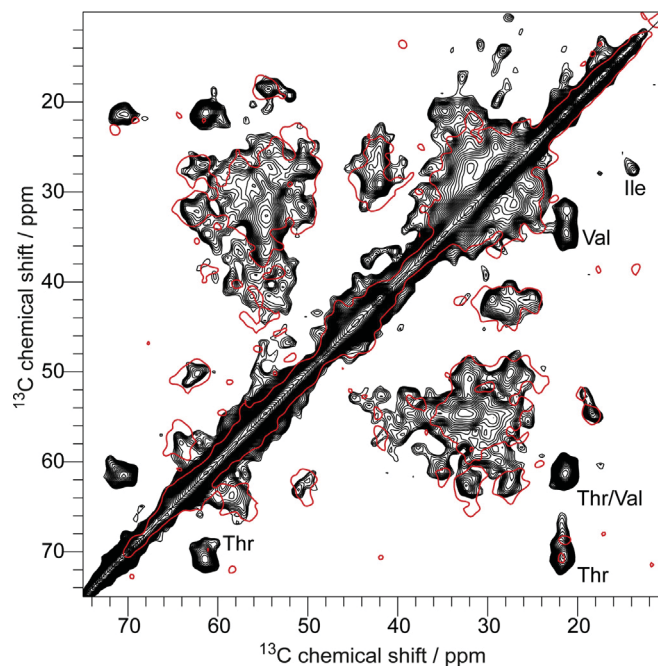

Figure 4. Comparison of two PDSD spectra of huPrP(23–230)*-Aβ (* species is ^{13}C, ^{15}N uniformly labeled), shown in *black*, and huPrP(23–144)*-Aβ, shown as *red contour*. Both spectra were recorded at a spinning frequency of 11 kHz and a mixing time of 30 ms, but the *black one* at a temperature of ≈0 °C and the *red one* at ≈−6 °C.

at pH 4.5 (48). While the predicted N-terminal cross peaks (residues 23–124) superimpose well with the spectrum of huPrP(23–230)*-Aβ, some discrepancies between the experimental and the predicted spectrum are observed for the C terminus (residues 125–230) (Fig. S10).

In particular, correlation signals for Ile, Thr, and Val in α-helical conformation from α-helices 2 and 3 in natively folded huPrP are completely missing in the experimental spectrum (Fig. S11). Instead, correlation signals for Thr and Val with secondary chemical shifts indicative of β-strands that are not observed in natively folded huPrP are clearly visible in the experimental spectrum (Figs. S10–S12). This suggests that at least for a substantial fraction of the huPrP molecules within the complex, some parts of a region between either V121 and I139 and/or V176 and I215 (located in α-helices 2 and 3) have undergone some structural rearrangements including β-strand formation (Fig. 2B). We could not see any fibril formation in huPrP(23–230) within the complexes; nevertheless, we overlaid our spectrum with predicted peaks for two recently published fibrils from huPrP and its fragment huPrP(94–178). The huPrP(94–178) fibril structure exhibits a β-strand in the palindrome region (54), which is likewise not supported by our α-helical-like Ala chemical shifts (Fig. S9B). However, a fibril structure recently published for full-length huPrP (55) (see Fig. S9C) shows a lot of similarities to our spectrum especially for Thr and Val residues, suggesting a rearrangement of the C terminus to more β-sheet-like chemical shifts.

High β-strand content of Aβ$_{oligo}$ in huPrP(23–144)-Aβ complexes

We also investigated the homogeneity and structural characteristics of Aβ$_{oligo}$ using two samples containing uniformly ^{13}C, ^{15}N labeled Aβ$_{oligo}$ in complex with nonlabeled huPrP(23–144) in two different molar ratios (Table 1). In the first sample (indicated as huPrP(23–144)-Aβ*), the molar ratio between Aβ monomers and huPrP was roughly 8:1, whereas in the second preparation (indicated as huPrP(23–144)$_{exc}$-Aβ*), addition of huPrP(23–144) in excess to the Aβ oligomers resulted in a molar ratio of ≈4:1.

INEPT spectra recorded at ≈20 °C of both samples are devoid of protein signals (not shown), whereas ^{1}H-^{13}C and ^{1}H-^{15}N CP spectra recorded at ≈0 °C display strong signals typical for all amino acid residue types (Fig. S13). These findings indicate that also the Aβ molecules are rigid in the complex. In all 2D and 3D homonuclear ^{13}C-^{13}C and heteronuclear ^{15}N-^{13}C correlation spectra (see Fig. 5 and Figs. S14–S18), linewidths are rather broad (0.9 ppm for ^{13}C and 3.3 ppm for ^{15}N), which is an indication for conformational heterogeneity of the Aβ molecules within the complex. In 2D ^{13}C-^{13}C correlation spectra (Fig. 5 and Fig. S14), ^{13}C side chain and backbone resonances can be identified for almost every amino acid residue type in the sequence. For several amino acid residue types, the number of distinct spin systems visible in the spectra is larger than the number of amino acid residues of this type in the amino acid sequence. For example, six Ala spin systems have been found although the sequence of Aβ(1–42)
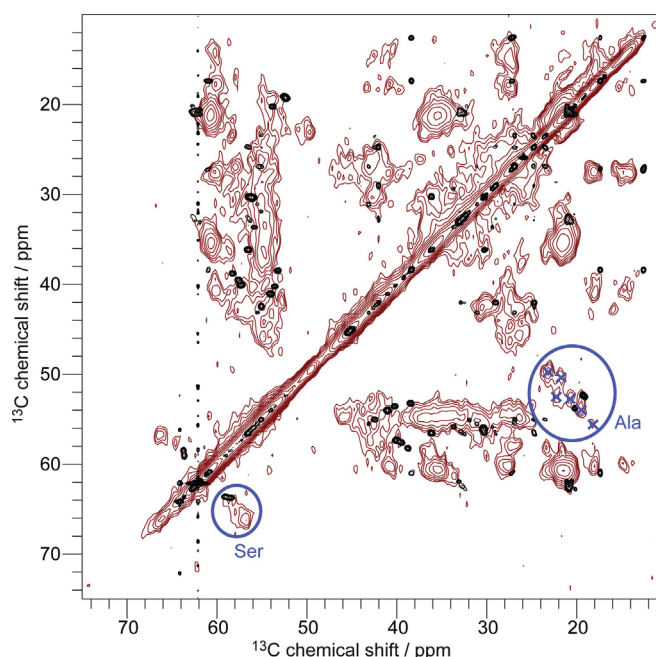

Figure 5. Overlay of a PDSD spectrum of huPrP(23–144)-Aβ* (* species is ^{13}C, ^{15}N uniformly labeled), measured at a temperature of ≈0 °C, a spinning frequency of 11 kHz and a mixing time of 50 ms, in *red* with a ^{13}C-^{13}C TOCSY spectrum of uniformly ^{13}C, ^{15}N isotope labeled Aβ monomers in solution (measured at a temperature of 5.0 °C and pH 7.2 in 30 mM Tris-HCl buffer) in *black* (the strong resonances at 62.1 ppm and 64.2 ppm with the t$_1$ noise are from the Tris buffer). Ala and Ser C$_α$-C$_β$ peaks are highlighted with *blue circles* and six identified Ala spin systems are shown with *blue crosses*. Chemical shift differences for both residue types between the Aβ monomers (typical random coil chemical shifts) and huPrP(23–144)-Aβ* (β-strand-like conformations) can be observed.

only contains four Ala residues (Fig. 5). This means that not all Aβ molecules within the complex experience identical environments.

A comparison between a solid-state NMR ^{13}C-^{13}C correlation spectrum of Aβ$_{oligo}$ in complex with huPrP(23–144) and a ^{13}C-^{13}C TOCSY correlation spectrum of Aβ monomers in solution (Fig. 5) reveals strong chemical shift differences and thus indicates that the Aβ monomer building blocks in oligomers have undergone significant structural changes upon oligomerization. While all signals of the solution spectrum have chemical shifts indicative of a random coil, a strong shift to chemical shifts indicative of β-strand-like secondary structure is observed for almost all spin systems of Aβ$_{oligo}$ in the spectrum of the complex. For Cα/Cβ cross peaks of Ala, Ile, Ser, and Val (Fig. 5) in α-helical, unstructured, and β-strand-like conformations, a quantification was possible by integration of the peak regions (see Fig. S19). Hence, these residues are predominantly in a β-strand conformation. For Gly, which is a β-strand breaker, CO/Cα cross peaks are mainly indicative of random coil conformation.

Due to conformational heterogeneity, inhomogeneous line broadening, and substantial resonance overlap in the ^{13}C-^{13}C and ^{15}N-^{13}C spectra, a full sequential resonance assignment for Aβ$_{oligo}$ in complex with huPrP was not possible. However, from a series of PDSD spectra with different mixing times as well as 2D and 3D NCACX and NCOCX spectra, it was

possible to identify some interresidual correlations and to obtain site-specific assignments for some parts of Aβ in one predominant conformation (Table S1). However, it is not clear whether all assigned resonances belong to one type of conformer or to different conformers.

To elucidate whether the stoichiometry of Aβ and huPrP in the heteroassemblies has an influence on the conformations of Aβ molecules, we prepared and investigated a second sample, in which huPrP(23–144) was added in excess to ^{13}C, ^{15}N labeled Aβ_oligo. In this sample, all potential huPrP-binding sites on Aβ_oligo should be occupied. Overall there is not much difference between sample huPrP(23–144)-Aβ* and huPrP(23–144)_exc-Aβ* in a PDSD spectrum with a mixing time of 50 ms, except for minor changes (Fig. S20). As there are no major structural changes upon altering the huPrP concentration, we conclude that the conformational heterogeneity is not due to unoccupied huPrP-binding sites in Aβ_oligo, but rather Aβ_oligos in complex with huPrP consist of inequivalent conformers and/or Aβ_oligo assemblies are different from each other.

Discussion

In this study we investigated the interaction of Aβ(1–42)_oligo and huPrP by solid-state NMR spectroscopy. As mentioned above, Aβ(1–42)_oligo play a crucial role in AD, as they are neurotoxic (4). Determining structural information of Aβ(1–42)_oligo is challenging because of their transient and fast-aggregating nature. Therefore, trapping Aβ(1–42)_oligo with huPrP and inhibiting their aggregation is a convenient way to study their structure. The interaction between Aβ(1–42)_oligo and huPrP has also a role in AD: Nieznanski *et al.* and others showed that soluble huPrP is able to inhibit Aβ fibril formation (32, 56), particularly the naturally secreted huPrP fragment N1 (huPrP(23–111)) (33, 34) and sequesters toxic Aβ(1–42)_oligo (32). Additionally, soluble huPrP reduces the toxic effects of Aβ(1–42)_oligo, as seen by us (see Fig. 1A and (40)) and others (32, 36).

Aside from the protective role of soluble huPrP in AD, membrane-anchored huPrP is mediating neurotoxicity of Aβ(1–42)_oligo (19, 24, 25) *via* Fyn-kinase (26, 27) or NMDA receptor pathways (57). Although Aβ(1–42)_oligo toxicity is not solely dependent on huPrP (28–31), it has been shown that especially small Aβ(1–42)_oligo (58) and high-molecular-weight Aβ(1–42)_oligo (59, 60) mediate toxicity by huPrP. To target this interaction efficient inhibitors might prevent Aβ(1–42)_oligos' detrimental effects. Indeed, Aβ(1–42)_oligo-binding D-enantiomeric peptides (40, 61) and antibodies (19, 62–64) have been shown to efficiently block the interaction between huPrP and Aβ(1–42)_oligo, but more efficient inhibitors are needed. The process of research for efficient inhibitors will be speeded up by detailed knowledge of the binding between Aβ(1–42)_oligo and huPrP in terms of structure, because targeted research and rational design of either huPrP- or Aβ(1–42)_oligo-binding agents will be possible.

In this study, high-molecular-weight aggregates were formed by addition of N-terminal or full-length human PrP to preformed Aβ(1–42)_oligos. These aggregates formed immediately

upon addition of huPrP, visible as the precipitation of a fine white solid powder. The rigidity of this complex was further confirmed by DE and CP NMR spectra recorded at different temperatures (see Fig. 3).

In a previous study, Kostylev *et al.* (44) investigated complexes formed between huPrP(23–111) or huPrP(23–230) and oligomeric Met-Aβ(1–42). In that study, the complexes were described as a hydrogel, and PrP molecules exhibited a higher degree of flexibility. The difference between their and our complexes may be explained by differences in the preparation of the complex (different buffer system), and in particular of the Aβ oligomers, which consisted of ≈12 molecules in the study of Kostylev *et al.* and of on average ≈23 monomers (61) in our study, which most certainly has an effect on their oligomer structure. Also, the Aβ(1–42) species used by Kostylev *et al.* contained an additional methionine residue at the N terminus, which could lead to different behavior of the Aβ(1–42) oligomers, although Silvers *et al.* (65) could show that Met-Aβ(1–42) and Aβ(1–42) fibrils exhibit the same aggregation kinetics and, except for a slight change in flexibility of the N terminus, are structurally comparable. Additionally, Kostylev *et al.* (44) used huPrP(23–111) for the majority of their investigations, whereas we used a slightly longer construct (huPrP(23–144)). This could also account for the different physical behavior in terms of flexibility.

As just mentioned, we did most of the investigations on an N-terminal construct of huPrP (huPrP(23–144)) for the following reasons: Firstly, the N terminus of huPrP is sufficient for binding Aβ(1–42)_oligo, as shown by us (40) and others (35–39). Further, using huPrP(23–144) instead of huPrP(23–230) drastically reduces signal overlap in the spectra making it more straightforward to draw conclusions for the N terminus. The naturally secreted soluble N1 fragment (although slightly shorter: 23–111) exhibits a protective role in AD by reducing the cytotoxicity of Aβ(1–42)_oligo (34). We could show by MTT toxicity tests that also our construct huPrP(23–144) as well as soluble full-length huPrP(23–230) significantly reduced Aβ(1–42)_oligo toxicity (Fig. 1A). From a comparison of 2D ^{13}C-^{13}C spectra, we could show that the C terminus of huPrP(23–230) has no impact on the binding of the N terminus (23–144) to Aβ(1–42)_oligo, suggesting that the protective effect of soluble huPrP is linked to the N terminus of huPrP. Therefore, the different roles of huPrP in the etiology of AD (*i.e.*, mediation of neurodegeneration *versus* neuroprotection) might be rather attributed to the place of action (membrane-anchored *versus* soluble) than to the length of the protein.

All the findings of this study are summarized in a schematic representation of the structural features of the huPrP-Aβ_oligo complex in Figure 6. The N-terminal region of huPrP is rigid but has no regular secondary structure in the complex with Aβ_oligo. This is the case for both analyzed huPrP constructs. Minor structural changes to more α-helical-like secondary structure are restricted to a region between A113 and L130, including the palindrome region AGAAAAGA. This palindrome, known as the "hydrophobic core," is highly conserved and highly amyloidogenic (66). The palindrome segment has
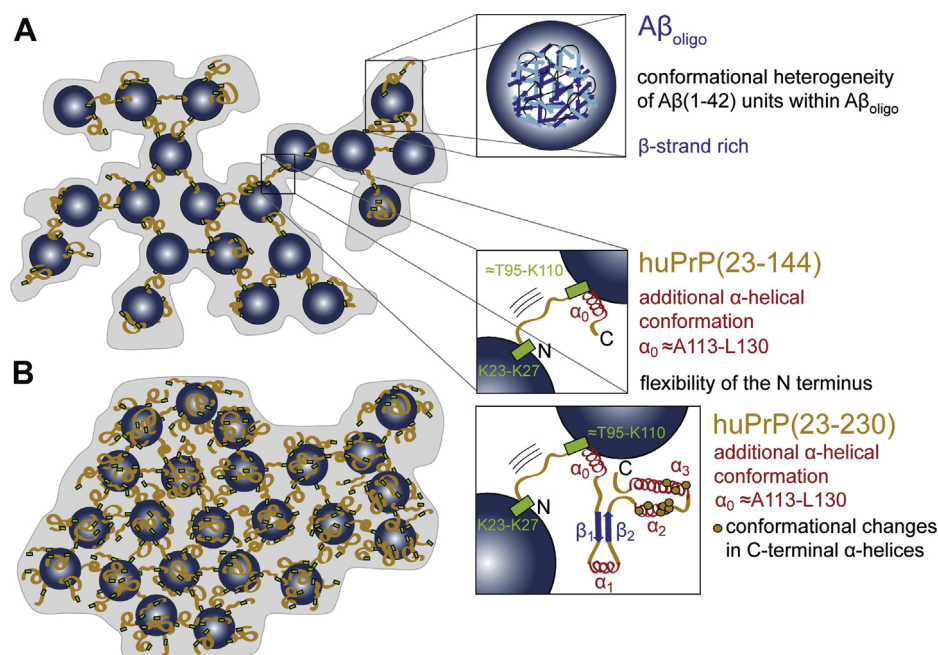
Figure 6. Schematic representation showing structural features of the huPrP-Aβ_{oligo} complex for *A*, low huPrP content as in the sample where huPrP(23–144) is not in excess (huPrP(23–144)-Aβ*) and *B*, with high huPrP content as in the sample where huPrP(23–144) was added in excess (huPrP(23–144)_{exc}-Aβ*). huPrP is shown as *orange lines*, Aβ_{oligo} as *blue spheres*, α-helices are *red*, and β-strands *blue*. Binding regions at huPrP are shown as *light green boxes*, conformational changes in the C terminus of huPrP as *orange dots*. Picture adapted from Rösener *et al.* (40).

previously been suggested to be required for the attainment of the PrP^{Sc} conformation and to facilitate the proper association of PrP^{Sc} with PrP^{C} to enable prion propagation (67). Trapping the "hydrophobic core" by binding to Aβ(1–42)$_{oligo}$ might explain the Aβ(1–42)-oligomer-induced inhibition of prion propagation proposed by Sarell *et al.* (68). In the already discussed above study of a hydrogel-termed complex of full-length huPrP and Aβ$_{oligo}$ (44), the formation of two additional α-helices, one in the octarepeat region (residues 51–91) and one in the palindrome segment (A^{113}GAAAAGA^{120}), was postulated from the observation that chemical shifts observed for Gly and Ala are predominantly α-helical in their spectra (44). Our results support the formation of the latter α-helix in the complex with full-length huPrP. Chemical shifts of Gly residues as well as all other N-terminal residues are predominantly random coil-like in the spectra (see Fig. 1*D*), suggesting that the octarepeat region does not undergo major structural rearrangements upon complex formation. These differences are explainable by the different preparation conditions and huPrP and Aβ(1–42)$_{oligo}$ constructs used as stated above.

For full-length huPrP in complex with Aβ$_{oligo}$ we observed some changes for Thr and Val residues from α-helical to random coil or even β-strand-like secondary chemical shifts compared with well-folded monomeric huPrP in solution (48). The residues affected by these chemical shift changes are mainly located in α-helices 2 and 3, thus suggesting that the helical structure of this region is at least partially lost in complex with Aβ$_{oligo}$. For huPrP in a hydrogel with Aβ$_{oligo}$ chemical shift changes from α-helical to random coil values were also described for Thr residues, which are mainly located in α-helices 2 and 3 (44). This observation was attributed to a loss of secondary structure during liquid–liquid phase

separation of PrP and in the complex with Aβ$_{oligo}$. The loss of secondary structure in the complex with Aβ$_{oligo}$ is confirmed by us. This observed change in secondary structure in the C-terminal domain of PrP^{C} upon binding to Aβ oligomers suggests that also the C-terminal domain of PrP^{C} interacts with Aβ$_{oligo}$. On the contrary, the C-terminal domain is not able to bind Aβ$_{oligo}$ on its own (40), so chemical shift changes in the C terminus might be some type of steric hindrance, a disfavor of α-helical conformations in close proximity to the β-strand-like Aβ$_{oligo}$ or simply a structural change induced by binding of Aβ$_{oligo}$ to the N terminus. As we could show that Aβ$_{oligo}$ and the C-terminal fragment huPrP(121–230) do not form high-molecular-weight aggregates (40) and that this huPrP fragment does not reduce Aβ$_{oligo}$ cytotoxicity (see Fig. 1*A*), a direct binding of Aβ$_{oligo}$ and the C terminus of huPrP is rather unlikely. Consequently the C terminus is free to interact with any secondary (transmembrane) receptors necessary for the signal transduction, because PrP^{C} itself is no transmembrane protein and therefore requires a secondary receptor, such as NMDAR (57) or the metabotropic glutamate receptor 5 (mGluR5) (69) to facilitate Aβ$_{oligo}$-induced neurotoxicity. Indeed the Aβ$_{oligo}$-PrP^{C}-mGluR5 complex has been shown to mediate neurotoxic Fyn-kinase pathways: Um *et al.* demonstrated that the interaction between membrane-anchored full-length PrP^{C} and mGluR5 is stabilized by Aβ$_{oligo}$. This interaction in turn enables binding to Fyn-kinase and leads to the subsequent Fyn-kinase cascade and independent of that to increased calcium influx into the cell (69). Additionally, the Aβ$_{oligo}$-PrP^{C}-mGluR5 complex enables NMDA and muscarinic-acetylcholine receptor-independent long-term depression (70) and modulates the binding to intracellular proteins (71). It might be attractive to speculate that these interactions are

mediated by a structural change in the C terminus of PrP^C. This has to be further investigated. In another study (21), PrP constructs encompassing the N-terminal but lacking the C-terminal domain were inactive in inhibiting Aβ polymerization, even though they still bound to fibrils, whereas full-length PrP^C completely inhibited fibril elongation. This implied that the C-terminal domain might play some role in inhibiting polymerization. It is thus tempting to speculate that the conformational transition of the C-terminal domain to more β-strand-like structures could also be due to the incorporation into a fibril equivalent surface on Aβ oligomers. This is also supported by the finding that the C-terminal chemical shifts of huPrP overlap well with a recently published full-length huPrP fibril structure (55) (see Fig. S9*C*). Nevertheless, we should keep in mind that other studies following the aggregation of Aβ in presence of different huPrP constructs suggested the N terminus necessary for inhibiting Aβ aggregation (32, 36, 39) and also our own data argue against a direct binding of Aβ$_{oligo}$ to the C terminus of huPrP (40), as stated above.

Aβ$_{oligo}$ in complex with huPrP consists of nonidentical Aβ conformers. This is not surprising given the fact that the complex of huPrP(23–144) and Aβ$_{oligo}$ contains four times more Aβ (monomer equivalent) than huPrP(23–144) molecules (40). Not every monomer within the oligomer (containing ≈23 monomer units on average (61)) might be able to bind to huPrP(23–144) in the same way and has therefore the same conformation (40), as described above. These nonidentical conformers can have different origins: (i) different types of monomers within the oligomer, because not every monomer can bind to huPrP (Aβ-huPrP *versus* Aβ-Aβ interactions); (ii) polymorphism within the oligomer independent of the binding to huPrP (iii) polymorphism between different oligomers; or (iv) a combination thereof.

The secondary structure of Aβ$_{oligo}$ in complex with huPrP shows a high degree of β-strand content. Because we took care not to obtain any fibrils in our samples during preparation (see exemplarily Fig. 1*C*) and because there were no major chemical shift changes in the CP and PDSD spectra in the following 11 months (during which the sample was kept at temperatures between 4 °C and 8 °C), it is very unlikely that any significant amount of fibrils might have formed over time. Instead, the high degree of β-strand content indicates that Aβ$_{oligos}$ already contain Aβ monomer units that have at least in part the same secondary structure as in fibrils or protofibrils, but probably differ in tertiary structure. This phenomenon has already been observed in early stage Aβ oligomers (8, 72) and is supported by the finding that huPrP-mediated toxicity depends partially on high-molecular-weight fibrillar-like Aβ$_{oligo}$ (59, 60). Assuming that the Aβ$_{oligo}$ preparation yielded a heterogeneous collection of fibril-like conformers in terms of secondary structure, of which most if not all were obviously elongation incompetent when trapped by adding huPrP, one would expect that the solid-state NMR resonances of Aβ$_{oligo}$ in complex with huPrP are the sum of the resonances of different fibril conformations together with resonances from Aβ units that experience different environments due to edge effects and/or huPrP interaction. To assess the structural similarity of Aβ$_{oligo}$ with fibrils and protofibrils, we superimposed all available

resonances from three different Aβ(1–42) fibril types (45–47) and one artificial protofibril (13) with the PDSD spectrum of Aβ$_{oligo}$ in complex with huPrP (Fig. 7 and Figs. S21–S24). A large fraction of the predicted correlations from these different protofibril and fibril types are represented by correlation peaks in our oligomer spectra, with some minor deviations found for Ala correlations. These findings suggest that the Aβ$_{oligo}$ preparation represents a heterogeneous mixture of β-strand-rich assemblies, of which some may have the potential to evolve into the different fibril types when not trapped by huPrP. The conformational heterogeneity of Aβ$_{oligo}$ is closely related to the polymorphism of Aβ fibrils and reflects the general propensity of Aβ to adopt variable β-structure conformers. Although we did not directly detect the binding site on Aβ$_{oligo}$, our data suggest that the high β-strand content might be necessary for the binding, as monomers, which do not show β-strand content, have no or only little affinity for huPrP (35, 73). Aβ fibrils do bind PrP (20), but with much lower affinity than Aβ$_{oligo}$. This might be due to the different tertiary structure compared with Aβ$_{oligo}$. This hypothesis is also supported by others, who assume that a 3D structure rather than a special part of the sequence is necessary for binding, as elucidated by epitope mapping (37).

The propensity of huPrP to efficiently bind to Aβ$_{oligo}$ and to "freeze" them in a nondynamic and nonelongating state allowed us to investigate the conformers of Aβ$_{oligo}$ and the huPrP moiety by NMR over several months without noticeable changes in the sample. It is tempting to speculate whether this property of huPrP is a coincidence, or whether it is part of the long-sought function of PrP. Regardless of whether PrP inhibits elongation of Aβ oligomers and fibrils or whether PrP is a mediator of cytotoxicity of Aβ$_{oligos}$, substances that compete with PrP for Aβ$_{oligo}$ binding and which thus can do the same
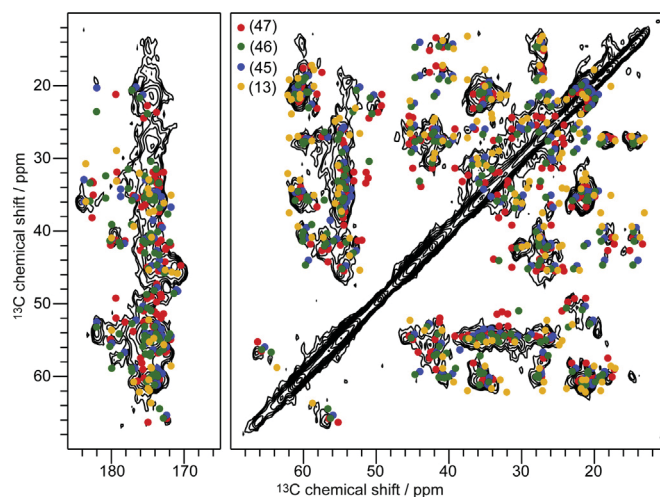

Figure 7. A PDSD spectrum (measured at a temperature of ≈0 °C, a spinning frequency of 11 kHz and a mixing time of 50 ms, same spectrum as in Fig. 5) of huPrP(23–144)-Aβ* (* species is ^{13}C, ^{15}N uniformly labeled) in comparison with predicted cross peaks (up to two bonds) for three different fibril types, which are obtained at pH values of 2 (*red*) (47) or 7.4 (*green* (46) and *blue* (45)) and an artificial protofibril (*yellow*) (13). Separate overlays of this PDSD spectrum with spectra of these fibrils are shown in Figs. S21–S24.

job without the potential of mediating cytotoxicity may be of high therapeutic potential.

Experimental procedures

Proteins

Aβ

For preparation of NMR samples with unlabeled Aβ, synthetic Aβ(1–42) obtained from Bachem AG was used. (For preparation of stocks see below.) Uniformly ^{13}C, ^{15}N labeled Aβ(1–42) was purchased from Isoloid GmbH.

huPrP

The purification of recombinant full-length huPrP(23–230) and C-terminally truncated huPrP(23–144) either unlabeled or uniformly ^{13}C, ^{15}N labeled, and of recombinant unlabeled huPrP(121–230) was performed as described previously (40).

Preparation of Aβ(1–42) stocks

Synthetic unlabeled Aβ(1–42) (Bachem AG, 1 mg aliquot) was incubated with 700 μl hexafluoro-2-propanol (HFIP) overnight and divided into 108 μg doses in LoBind reaction tubes (Eppendorf AG). Samples were lyophilized in a rotational vacuum concentrator system connected to a cold trap (both Martin Christ Gefriertrocknungsanlagen GmbH). The lyophilizates were stored at room temperature and protected from light.

Preparation of high-molecular-weight heteroassemblies from amyloid β oligomers and different human prion protein constructs in different molar ratios

For sample preparation, Aβ(1–42) lyophilizates (either uniformly ^{13}C, ^{15}N labeled or unlabeled) were dissolved in 30 mM Tris-HCl buffer, pH 7.4, yielding Aβ(1–42) concentrations of 160–300 μM. After 2 h of incubation at 22 °C and 600 rpm shaking to obtain Aβ_{oligo}, either huPrP(23–144) or huPrP(23–230) was added to yield concentrations of 40 to 80 μM within the initial mixture leading to the molar ratios mentioned in Table 1. The addition of huPrP resulted in immediate sedimentation of the complex as a powder-like precipitate (40).

After addition of 0.03% of sodium azide and incubation for 30 min, the samples were centrifuged for 2 to 5 min at 16,100*g*, and the supernatant was removed. The sediment was washed twice with up to 2 ml of 30 mM Tris-HCl buffer, 0.03% sodium azide, pH 7.4 to remove excess monomeric PrP. After removal of the supernatant, the samples were transferred into 3.2 mm MAS rotors with a Hamilton syringe and centrifuged. In total, four different samples were prepared in which either huPrP or Aβ(1–42) was uniformly ^{13}C, ^{15}N labeled, using different huPrP constructs and molar ratios between huPrP and Aβ(1–42) (Table 1).

Characterization by density gradient ultracentrifugation, SDS-PAGE, and RP-HPLC

For biophysical characterization of *e.g.*, sample huPrP(23–144)-Aβ*, sucrose density gradient

ultracentrifugation (DGC) was performed. To this end, 10 μl of the sedimented but unwashed sample was diluted with 90 μl of 30 mM Tris-HCl buffer, pH 7.4 and applied on a discontinuous sucrose gradient (see (40)) and centrifuged for 3 h at 259,000*g* and 4 °C. After fractionation, each of the 14 fractions was analyzed by Tris-Tricine SDS-PAGE and RP-HPLC as previously described (40) (Fig. S4).

RP-HPLC revealed the Aβ:huPrP(23–144) stoichiometry shown in Table 1 as determined in a single measurement. Sample huPrP(23–144)_{exc}-Aβ* was not separated by DGC but measured by RP-HPLC and revealed an Aβ:huPrP(23–144) stoichiometry of 3.7 ± 0.12 to 1 after fivefold measurement of the same sample. All stoichiometries represent monomer equivalents.

MTT cell viability tests

Potential cell viability rescue of rat pheochromocytoma PC-12 cells (Leibniz Institute DSMZ) from Aβ(1–42)_{oligo}-induced toxicity through addition of soluble huPrP(23–144), huPrP(23–230), or huPrP(121–230) in a concentration-dependent manner was measured in MTT (3-(4,5-dimethylthiazol-2-yl)-2,5-diphenyltetrazolium bromide) cell viability tests (40, 61).

PC-12 cells were cultivated in RPMI 1640 medium supplemented with 10% fetal calf serum and 5% horse serum, seeded (10,000 cells in 100 μl per well) on collagen-coated 96-well plates (Gibco, Life Technologies), and incubated in a 95% humidified atmosphere with 5% CO$_2$ at 37 °C for 24 h. Then final concentrations of 1 μM Aβ(1–42)_{oligo} either in the absence or after mixing and further incubation for 30 min at 22 °C with 0.02, 0.1, or 0.5 μM (final concentrations) of the respective huPrP protein were added. In addition, the toxicity of the respective huPrP proteins alone at 0.5 μM final concentrations was also determined.

After further incubation in a 95% humidified atmosphere with 5% CO$_2$ at 37 °C for 24 h, cell viability was measured using the Cell Proliferation Kit I (MTT) (Roche Applied Science) according to manufacturer's protocol. The MTT formazan product was determined by measuring the absorbance at 570 nm corrected by subtraction of the absorbance at 660 nm in a FluoroStar Optima plate reader (BMG Labtech). The arithmetic mean of five independent measurements per approach ±SD was calculated. All results were normalized to untreated cells grown in medium only.

AFM measurements

The samples used for AFM were either Aβ(1–42)_{oligo} or Aβ(1–42)_{oligo} complexed by huPrP(23–144).

For formation of Aβ(1–42)_{oligo}, monomeric Aβ(1–42) was incubated at a concentration of 80 μM in 30 mM Tris-HCl, pH 7.4 for 2.5 h at 22 °C and 600 rpm shaking. For AFM the sample was then diluted to 0.44 μM with buffer and 50 μl of the solution was transferred to freshly cleaved mica and incubated for 30 min at room temperature for mica adhesion.

Preparation of the Aβ(1–42)_{oligo}-huPrP(23–144) sample was done as follows: Monomeric Aβ(1–42) at a concentration of

120 μM in 30 mM Tris-HCl, pH 7.4 was incubated for 2 h, 22 °C and 600 rpm shaking. Then huPrP(23–144) was added leading to a final concentration of 80 μM Aβ(1–42) and 40 μM huPrP(23–144) in the sample. The sample was incubated further for 30 min. The generated precipitates are cleared from possibly unbound Aβ(1–42) or huPrP(23–144) by centrifugation at 16,100*g* and 4 °C for 30 min. The pellet containing the pure Aβ(1–42)$_{oligo}$-huPrP(23–144) precipitate was washed twice with 100 μl 30 mM Tris-HCl, pH 7.4 with centrifugation steps at 16,100*g* in between. After resuspension of the condensates in 100 μl of 30 mM Tris-HCl, pH 7.4, then 50 μl of the sample was incubated on freshly cleaved mica for 30 min.

All samples were washed three times with MilliQ water and dried in a gentle stream of N$_2$. Both samples were measured in a Nanowizard 3 system (JPK Instruments AG) using intermittent contact mode with a resolution of 1024 pixels and line rates of 0.5 to 1 Hz in ambient conditions with a silicon cantilever with nominal spring constant of 26 N/m and average tip radius of 7 nm (Olympus OMCL-AC160TS). Due to the curvature and adhesion of the Aβ(1–42)$_{oligo}$-huPrP(23–144) condensates, the imaging parameters (amplitude, setpoint, and gain) had to be adapted slightly and the cantilever had to be changed often. The height image of Aβ(1–42)$_{oligo}$ was flattened with the JPK Data Processing software 5.0.69.

Preparation of solution NMR samples

For the sequence-specific backbone resonance assignments, samples of 0.36 mM uniformly ^{13}C, ^{15}N labeled huPrP(23–144) with 50 mM sodium acetate buffer in 10% (v/v) D$_2$O (pH 4.5) and 0.30 mM uniformly ^{13}C, ^{15}N labeled huPrP(23–144) with 50 mM HEPES buffer in 10% (v/v) D$_2$O (pH 7.0) were prepared as reported previously (Rösener *et al.* (40)). ^{13}C-^{13}C "TOtal Correlated SpectroscopY" (TOCSY) NMR measurements in solution were performed on a sample containing 0.33 mM uniformly ^{13}C, ^{15}N labeled huPrP(23–144) monomers (Rösener *et al.* (40)) with 0.02% (w/v) NaN$_3$ in 30 mM HEPES buffer and 10% (v/v) D$_2$O (pH 6.7) and on a sample of 95 μM uniformly ^{13}C, ^{15}N labeled Aβ(1–42) (Isoloid GmbH) in 30 mM Tris-HCl buffer and 10% (v/v) D$_2$O (pH 7.2) at a temperature of 5.0 °C.

Solid-state NMR experiments

The solid-state NMR measurements were performed either on Varian INOVA NMR spectrometers operating at field strengths of 14.1 T (ω(^{1}H)/(2π) = 600 MHz) for samples huPrP(23–144)*-Aβ, huPrP(23–230)*-Aβ and huPrP(23–144)-Aβ* or a Bruker AEON 18.8 T (ω(^{1}H)/(2π) = 800 MHz) spectrometer for sample huPrP(23–144)$_{exc}$-Aβ*, equipped with 3.2 mm standard (Varian) or wide bore (Bruker) triple-resonance MAS probes. Therefore either 3.2 mm thick wall (25 μl, for samples huPrP(23–144)*-Aβ and huPrP(23–230)*-Aβ) or thin wall (36 μl, for sample huPrP(23–144)-Aβ*) rotors from Varian (Agilent) or 3.2 mm thick wall (46.7 μl, for sample huPrP(23–144)$_{exc}$-Aβ*) rotors from Bruker were used. For sample huPrP(23–230)*-Aβ an insert (signal at ≈90 ppm) was used as a precaution because at the beginning of the study

it was not known if PrP in huPrP(23–230)*-Aβ was present in its pathogenic PrP^{Sc} conformation.

Sample temperatures were indirectly determined with an accuracy of ±5 °C for each spinning speed using nickelocene as an external reference (74). Initial magnetization transfer from protons to ^{13}C or ^{15}N was either achieved by "insensitive nuclei enhanced by polarization transfer" (INEPT) (75) to selectively excite mobile regions *via* scalar coupling through bond magnetization transfer from ^{1}H to ^{13}C (at ≈20, 27, or 30 °C) or by CP (measured at ≈30, 10, 7, 0, –6, or –10 °C) *via* dipolar coupling through space transfer for rigid parts. DE experiments for sample huPrP(23–230)*-Aβ were conducted at ≈30, 10, and –10 °C. In this temperature range, the free water in the samples was not fully frozen, as could be observed from the water signal in ^{1}H spectra (not shown). Additionally, several multidimensional homo- and heteronuclear correlation experiments for the assignment were recorded. Experimental details of all spectra recorded are given in Tables S2–S6. For homonuclear ^{13}C-^{13}C spectra, proton-driven spin diffusion (PDSD) (76) with mixing times between 10 and 300 ms was employed. Homonuclear double quantum correlation spectra were recorded with SPC5 recoupling (77).

For site-specific assignment ^{15}N-^{13}C correlation spectra were recorded using SPECIFIC-CP (78) for frequency selective polarization transfer from ^{15}N to either ^{13}Cα or ^{13}CO and subsequent DARR-mixing. 2D NCA, NCACX and 3D NCACX and NCOCX spectra were used for the sequential walk through the backbone. During all acquisition and evolution times, high-power broadband proton decoupling with SPINAL phase modulation (79) (radio frequency intensity between 71 and 91 kHz) was used. All spectra were processed with NMRPipe (80) with either squared and shifted sine bell or Gaussian window functions. The line width (FWHM) was estimated in 1D-slices (spectra processed with squared sine bell shifted by 0.35π or 0.40π) of 2D PDSD or NCACX/NCOCX spectra. ^{13}C chemical shifts were externally referenced with adamantane by setting the low-frequency signal of adamantane to 31.4 ppm on the DSS reference scale. ^{15}N chemical shifts were indirectly referenced *via* the ^{13}C chemical shifts. All resonances were assigned in CCPN (81). Integration of Aβ peaks was done in Topspin *via* the box sum method in a PDSD spectrum of huPrP(23–144)-Aβ*, measured at a temperature of ≈0 °C, a spinning frequency of 11 kHz, and a mixing time of 50 ms.

Solution NMR experiments

For the sequence-specific backbone resonance assignments of uniformly ^{13}C, ^{15}N labeled huPrP(23–144) in solution at pH 4.5, the following experiments were recorded at 5.0 °C on a Bruker AVANCE III HD 600 MHz NMR spectrometer equipped with an inverse triple-resonance probe: 2D ^{1}H-^{15}N HSQC (82), 3D HNCO (83), and 3D HNCACB (84) (further experimental details are given in Table S7). Sequence-specific backbone resonance assignments at pH 7.0 were obtained from 2D ^{1}H-^{15}N HSQC (82), 3D HNCO (83), 3D HNCACB (84), and 3D BEST-TROSY-(H)N(COCA)NH (85)

experiments recorded at 5.0 °C on a Varian VNMRS 800 MHz NMR spectrometer equipped with an inverse triple-resonance probe. Two 2D ^{13}C-^{13}C TOCSY spectra covering either the aliphatic (bandwidth 70 ppm) or full (bandwidth 182 ppm) spectral region with a 13.6 ms 13.9 kHz (aliphatic) or 21.1 ms 15.6 kHz (full) FLOPSY-16 isotropic mixing scheme (86) of 0.33 mM uniformly ^{13}C, ^{15}N labeled huPrP(23–144) at 5.0 °C was recorded on a Bruker AVANCE III HD 700 MHz NMR spectrometer equipped with an inverse triple-resonance probe. Because of the comparatively low protein concentration, a 2D ^{13}C-^{13}C TOCSY spectrum covering the aliphatic region (bandwidth 70 ppm) with a 15.1 ms 15.6 kHz FLOPSY-16 isotropic mixing scheme (86) of 95 μM uniformly ^{13}C, ^{15}N labeled Aβ(1–42) at 5.0 °C was recorded on a Bruker AVANCE III HD 800 MHz NMR spectrometer equipped with a ^{13}C/^{15}N observe triple-resonance probe; a total of 1536 transients was collected over the course of 3 weeks and added up to further improve the signal-to-noise ratio. All triple-resonance probes were cryogenically cooled and equipped with z axis pulsed field gradient capabilities. The sample temperature was calibrated using methanol-d$_4$ (87). The ^{1}H$_2$O resonance was suppressed by gradient coherence selection with water flip-back (88), with quadrature detection in the indirect dimensions achieved by States-TPPI (89) and the echo–antiecho method (90, 91). All solution NMR spectra were processed with NMRPipe (80) software and analyzed with NMRViewJ (92) and CCPN (81). ^{1}H chemical shifts were referenced with respect to external DSS in D$_2$O, ^{13}C and ^{15}N chemical shifts were referenced indirectly (93). RCI (50) backbone order parameters, S_{RCI}^2, were calculated from the backbone chemical shifts using TALOS-N (94) with the default parameters.

To obtain sequence-specific backbone resonance assignments for huPrP(23–144) at different pH values ranging from 4.5 to 7.0 and at a temperature of 5.0 °C, we employed the following strategy: (i) In the first step, as many resonance assignments as possible (see above) were transferred from huPrP(23–230) to the ^{1}H-^{15}N HSQC spectrum of huPrP(23–144) at pH 4.5 and 20.0 °C. (ii) Next, these resonance assignments were propagated along a temperature series of ^{1}H-^{15}N HSQC spectra of huPrP(23–144) at pH 4.5 recorded at temperatures of 15.0 °C, 10.0 °C, and 5.0 °C. (iii) The resulting sequence-specific backbone resonance assignments at pH 4.5 and 5.0 °C were verified and completed using HNCO and HNCACB triple-resonance experiments. (iv) These resonance assignments were then propagated along a pH series of ^{1}H-^{15}N HSQC spectra of huPrP(23–144) recorded at pH values of 5.3, 6.0, and 7.0 at a temperature of 5.0 °C. (v) Finally, the resulting sequence-specific backbone resonance assignments at pH 7.0 and 5.0 °C were verified and completed using HNCO, HNCACB, and BEST-TROSY-(H)N(COCA)NH triple-resonance experiments (Fig. S2).

Data availability

The assigned chemical shifts of huPrP(23–144) at pH 4.5 and pH 7.0 have been deposited with the Biological Magnetic Resonance Data Bank (BMRB) under accession codes 28115 and 28116, respectively.

Abbreviations—The abbreviations used are: Aβ, amyloid β; AD, Alzheimer's disease; CP, cross polarization; DE, direct excitation; INEPT, insensitive nuclei enhancement by polarizaiton transfer; PDSD, proton-driven spin-diffusion; PrP^C, cellular prion protein; RCI, Random Coil Index.

References

1. 2018 Alzheimer's disease facts and figures. *Alzheimers Dement.* **14**, (2018), 367–429
2. Selkoe, D. J., and Hardy, J. (2016) The amyloid hypothesis of Alzheimer's disease at 25 years. *EMBO Mol. Med.* **8**, 595–608
3. Kellett, K. A. B., and Hooper, N. M. (2009) Prion protein and Alzheimer disease. *Prion* **3**, 190–194
4. Selkoe, D. J. (2008) Soluble oligomers of the amyloid β-protein impair synaptic plasticity and behavior. *Behav. Brain Res.* **192**, 106–113
5. Lopez del Amo, J. M., Fink, U., Dasari, M., Grelle, G., Wanker, E. E., Bieschke, J., and Reif, B. (2012) Structural properties of EGCG-induced, nontoxic Alzheimer's disease Aβ oligomers. *J. Mol. Biol.* **421**, 517–524
6. Scheidt, H. A., Morgado, I., Rothemund, S., Huster, D., and Fandrich, M. (2011) Solid-state NMR spectroscopic investigation of Abeta protofibrils: Implication of a beta-sheet remodeling upon maturation into terminal amyloid fibrils. *Angew. Chem. Int. Ed. Engl.* **50**, 2837–2840
7. Scheidt, H. A., Das, A., Korn, A., Krueger, M., Maiti, S., and Huster, D. (2020) Structural characteristics of oligomers formed by pyroglutamate-modified amyloid β peptides studied by solid-state NMR. *Phys. Chem. Chem. Phys.* **22**, 16887–16895
8. Chimon, S., Shaibat, M. A., Jones, C. R., Calero, D. C., Aizezi, B., and Ishii, Y. (2007) Evidence of fibril-like β-sheet structures in a neurotoxic

amyloid intermediate of Alzheimer's β-amyloid. *Nat. Struct. Mol. Biol.* **14**, 1157–1164

9. Parthasarathy, S., Inoue, M., Xiao, Y., Matsumura, Y., Nabeshima, Y.-i., Hoshi, M., and Ishii, Y. (2015) Structural insight into an Alzheimer's brain-derived spherical assembly of amyloid β by solid-state NMR. *J. Am. Chem. Soc.* **137**, 6480–6483

10. Xiao, Y., Matsuda, I., Inoue, M., Sasahara, T., Hoshi, M., and Ishii, Y. (2020) NMR-based site-resolved profiling of β-amyloid misfolding reveals structural transitions from pathologically relevant spherical oligomer to fibril. *J. Biol. Chem.* **295**, 458–467

11. Gao, Y., Guo, C., Watzlawik, J. O., Randolph, P. S., Lee, E. J., Huang, D., Stagg, S. M., Zhou, H.-X., Rosenberry, T. L., and Paravastu, A. K. (2020) Out-of-register parallel β-sheets and antiparallel β-sheets coexist in 150-kDa oligomers formed by amyloid-β(1–42). *J. Mol. Biol.* **432**, 4388–4407

12. Ahmed, M., Davis, J., Aucoin, D., Sato, T., Ahuja, S., Aimoto, S., Elliott, J. I., Van Nostrand, W. E., and Smith, S. O. (2010) Structural conversion of neurotoxic amyloid-beta(1-42) oligomers to fibrils. *Nat. Struct. Mol. Biol.* **17**, 561–567

13. Lendel, C., Bjerring, M., Dubnovitsky, A., Kelly, R. T., Filippov, A., Antzutkin, O. N., Nielsen, N. C., and Härd, T. (2014) A hexameric peptide barrel as building block of amyloid-β protofibrils. *Angew. Chem. Int. Ed. Engl.* **53**, 12756–12760

14. Tay, W. M., Huang, D., Rosenberry, T. L., and Paravastu, A. K. (2013) The Alzheimer's amyloid-β(1–42) peptide forms off-pathway oligomers and fibrils that are distinguished structurally by intermolecular organization. *J. Mol. Biol.* **425**, 2494–2508

15. Sahoo, B. R., Cox, S. J., and Ramamoorthy, A. (2020) High-resolution probing of early events in amyloid-β aggregation related to Alzheimer's disease. *Chem. Commun.* **56**, 4627–4639

16. Jaroniec, C. P. (2019) Two decades of progress in structural and dynamic studies of amyloids by solid-state NMR. *J. Magn. Reson.* **306**, 42–47

17. Li, D., and Liu, C. (2020) Structural diversity of amyloid fibrils and advances in their structure determination. *Biochemistry* **59**, 639–646

18. Ciudad, S., Puig, E., Botzanowski, T., Meigooni, M., Arango, A. S., Do, J., Mayzel, M., Bayoumi, M., Chaignepain, S., Maglia, G., Cianferani, S., Orekhov, V., Tajkhorshid, E., Bardiaux, B., and Carulla, N. (2020) Aβ(1-42) tetramer and octamer structures reveal edge conductivity pores as a mechanism for membrane damage. *Nat. Commun.* **11**, 3014

19. Lauren, J., Gimbel, D. A., Nygaard, H. B., Gilbert, J. W., and Strittmatter, S. M. (2009) Cellular prion protein mediates impairment of synaptic plasticity by amyloid-β oligomers. *Nature* **457**, 1128–1132

20. Zou, W.-Q., Xiao, X., Yuan, J., Puoti, G., Fujioka, H., Wang, X., Richardson, S., Zhou, X., Zou, R., Li, S., Zhu, X., McGeer, P. L., McGeehan, J., Kneale, G., Rincon-Limas, D. E., *et al.* (2011) Amyloid-β42 interacts mainly with insoluble prion protein in the Alzheimer brain. *J. Biol. Chem.* **286**, 15095–15105

21. Bove-Fenderson, E., Urano, R., Straub, J. E., and Harris, D. A. (2017) Cellular prion protein targets amyloid-beta fibril ends via its C-terminal domain to prevent elongation. *J. Biol. Chem.* **292**, 16858–16871

22. Amin, L., and Harris, D. A. (2019) Aβ receptors specifically recognize molecular features displayed by fibril ends and neurotoxic oligomers. *bioRxiv*. https://doi.org/10.1101/822361

23. Nicoll, A. J., Panico, S., Freir, D. B., Wright, D., Terry, C., Risse, E., Herron, C. E., O'Malley, T., Wadsworth, J. D., Farrow, M. A., Walsh, D. M., Saibil, H. R., and Collinge, J. (2013) Amyloid-beta nanotubes are associated with prion protein-dependent synaptotoxicity. *Nat. Commun.* **4**, 2416

24. Bate, C., and Williams, A. (2011) Amyloid-β-induced synapse damage is mediated via cross-linkage of cellular prion proteins. *J. Biol. Chem.* **286**, 37955–37963

25. Barry, A. E., Klyubin, I., McDonald, J. M., Mably, A. J., Farrell, M. A., Scott, M., Walsh, D. M., and Rowan, M. J. (2011) Alzheimer's disease brain-derived amyloid-β-mediated inhibition of LTP *in vivo* is prevented by immunotargeting cellular prion protein. *J. Neurosci.* **31**, 7259–7263

26. Um, J. W., Nygaard, H. B., Heiss, J. K., Kostylev, M. A., Stagi, M., Vortmeyer, A., Wisniewski, T., Gunther, E. C., and Strittmatter, S. M. (2012) Alzheimer amyloid-β oligomer bound to postsynaptic prion protein activates Fyn to impair neurons. *Nat. Neurosci.* **15**, 1227–1235

27. Um, J. W., and Strittmatter, S. M. (2013) Amyloid-β induced signaling by cellular prion protein and Fyn kinase in Alzheimer disease. *Prion* **7**, 37–41

28. Balducci, C., Beeg, M., Stravalaci, M., Bastone, A., Sclip, A., Biasini, E., Tapella, L., Colombo, L., Manzoni, C., Borsello, T., Chiesa, R., Gobbi, M., Salmona, M., and Forloni, G. (2010) Synthetic amyloid-β oligomers impair long-term memory independently of cellular prion protein. *Proc. Natl. Acad. Sci. U. S. A.* **107**, 2295–2300

29. Calella, A. M., Farinelli, M., Nuvolone, M., Mirante, O., Moos, R., Falsig, J., Mansuy, I. M., and Aguzzi, A. (2010) Prion protein and Aβ-related synaptic toxicity impairment. *EMBO Mol. Med.* **2**, 306–314

30. Kessels, H. W., Nguyen, L. N., Nabavi, S., and Malinow, R. (2010) The prion protein as a receptor for amyloid-β. *Nature* **466**, E3–E4

31. Cissé, M., Sanchez, P. E., Kim, D. H., Ho, K., Yu, G.-Q., and Mucke, L. (2011) Ablation of cellular prion protein does not ameliorate abnormal neural network activity or cognitive dysfunction in the J20 line of human amyloid precursor protein transgenic mice. *J. Neurosci.* **31**, 10427–10431

32. Nieznanski, K., Choi, J.-K., Chen, S., Surewicz, K., and Surewicz, W. K. (2012) Soluble prion protein inhibits amyloid-β (Aβ) fibrillization and toxicity. *J. Biol. Chem.* **287**, 33104–33108

33. Mohammadi, B., Linsenmeier, L., Shafiq, M., Puig, B., Galliciotti, G., Giudici, C., Willem, M., Eden, T., Koch-Nolte, F., Lin, Y.-H., Tatzelt, J., Glatzel, M., and Altmeppen, H. C. (2020) Transgenic overexpression of the disordered prion protein N1 fragment in mice does not protect against neurodegenerative diseases due to impaired ER translocation. *Mol. Neurobiol.* **57**, 2812–2829

34. Guillot-Sestier, M.-V., Sunyach, C., Ferreira, S. T., Marzolo, M.-P., Bauer, C., Thevenet, A., and Checler, F. (2012) α-Secretase-derived fragment of cellular prion, N1, protects against monomeric and oligomeric amyloid β (Aβ)-associated cell death. *J. Biol. Chem.* **287**, 5021–5032

35. Chen, S., Yadav, S. P., and Surewicz, W. K. (2010) Interaction between human prion protein and amyloid-β (Aβ) oligomers: Role of N-terminal residues. *J. Biol. Chem.* **285**, 26377–26383

36. Fluharty, B. R., Biasini, E., Stravalaci, M., Sclip, A., Diomede, L., Balducci, C., La Vitola, P., Messa, M., Colombo, L., Forloni, G., Borsello, T., Gobbi, M., and Harris, D. A. (2013) An N-terminal fragment of the prion protein binds to amyloid-beta oligomers and inhibits their neurotoxicity *in vivo*. *J. Biol. Chem.* **288**, 7857–7866

37. Kang, M., Kim, S. Y., An, S. S., and Ju, Y. R. (2013) Characterizing affinity epitopes between prion protein and beta-amyloid using an epitope mapping immunoassay. *Exp. Mol. Med.* **45**, e34

38. Dohler, F., Sepulveda-Falla, D., Krasemann, S., Altmeppen, H., Schlüter, H., Hildebrand, D., Zerr, I., Matschke, J., and Glatzel, M. (2014) High molecular mass assemblies of amyloid-β oligomers bind prion protein in patients with Alzheimer's disease. *Brain* **137**, 873–886

39. Younan, N. D., Sarell, C. J., Davies, P., Brown, D. R., and Viles, J. H. (2013) The cellular prion protein traps Alzheimer's Aβ in an oligomeric form and disassembles amyloid fibers. *FASEB J.* **27**, 1847–1858

40. Rösener, N. S., Gremer, L., Reinartz, E., König, A., Brener, O., Heise, H., Hoyer, W., Neudecker, P., and Willbold, D. (2018) A d-enantiomeric peptide interferes with heteroassociation of amyloid-β oligomers and prion protein. *J. Biol. Chem.* **293**, 15748–15764

41. Rösener, N. S., Gremer, L., Wördehoff, M. M., Kupreichyk, T., Etzkorn, M., Neudecker, P., and Hoyer, W. (2020) Clustering of human prion protein and α-synuclein oligomers requires the prion protein N-terminus. *Commun. Biol.* **3**, 365

42. Corbett, G. T., Wang, Z., Hong, W., Colom-Cadena, M., Rose, J., Liao, M., Asfaw, A., Hall, T. C., Ding, L., DeSousa, A., Frosch, M. P., Collinge, J., Harris, D. A., Perkinton, M. S., Spires-Jones, T. L., *et al.* (2020) PrP is a central player in toxicity mediated by soluble aggregates of neurodegeneration-causing proteins. *Acta Neuropathol.* **139**, 503–526

43. Ferreira, D. G., Temido-Ferreira, M., Miranda, H. V., Batalha, V. L., Coelho, J. E., Szegö, É. M., Marques-Morgado, I., Vaz, S. H., Rhee, J. S., and Schmitz, M. (2017) α-synuclein interacts with PrP C to induce cognitive impairment through mGluR5 and NMDAR2B. *Nat. Neurosci.* **20**, 1569

44. Kostylev, M. A., Tuttle, M. D., Lee, S., Klein, L. E., Takahashi, H., Cox, T. O., Gunther, E. C., Zilm, K. W., and Strittmatter, S. M. (2018) Liquid and hydrogel phases of PrP(C) linked to conformation shifts and triggered by Alzheimer's amyloid-beta oligomers. *Mol. Cell* **72**, 426–443.e012

45. Colvin, M. T., Silvers, R., Ni, Q. Z., Can, T. V., Sergeyev, I., Rosay, M., Donovan, K. J., Michael, B., Wall, J., Linse, S., and Griffin, R. G. (2016)

Solid-state MAS NMR of the complex of huPrP and Aβ_oligo

Atomic resolution structure of monomorphic Aβ42 amyloid fibrils. *J. Am. Chem. Soc.* **138**, 9663–9674

46. Wälti, M. A., Ravotti, F., Arai, H., Glabe, C. G., Wall, J. S., Böckmann, A., Güntert, P., Meier, B. H., and Riek, R. (2016) Atomic-resolution structure of a disease-relevant Aβ(1–42) amyloid fibril. *Proc. Natl. Acad. Sci. U. S. A.* **113**, E4976–E4984

47. Gremer, L., Schölzel, D., Schenk, C., Reinartz, E., Labahn, J., Ravelli, R. B. G., Tusche, M., Lopez-Iglesias, C., Hoyer, W., Heise, H., Willbold, D., and Schröder, G. F. (2017) Fibril structure of amyloid-β(1–42) by cryo–electron microscopy. *Science* **358**, 116–119

48. Zahn, R., Liu, A., Lührs, T., Riek, R., von Schroetter, C., López García, F., Billeter, M., Calzolai, L., Wider, G., and Wüthrich, K. (2000) NMR solution structure of the human prion protein. *Proc. Natl. Acad. Sci. U. S. A.* **97**, 145–150

49. Wishart, D. S., Bigam, C. G., Holm, A., Hodges, R. S., and Sykes, B. D. (1995) H-1, C-13 and N-15 random coil NMR chemical-shifts of the common amino-acids.1. Investigations of nearest-neighbor effects. *J. Biomol. NMR* **5**, 67–81

50. Berjanskii, M. V., and Wishart, D. S. (2005) A simple method to predict protein flexibility using secondary chemical shifts. *J. Am. Chem. Soc.* **127**, 14970–14971

51. Andronesi, O. C., Becker, S., Seidel, K., Heise, H., Young, H. S., and Baldus, M. (2005) Determination of membrane protein structure and dynamics by magic-angle-spinning solid-state NMR spectroscopy. *J. Am. Chem. Soc.* **127**, 12965–12974

52. Helmus, J. J., Surewicz, K., Nadaud, P. S., Surewicz, W. K., and Jaroniec, C. P. (2008) Molecular conformation and dynamics of the Y145Stop variant of human prion protein in amyloid fibrils. *Proc. Natl. Acad. Sci. U. S. A.* **105**, 6284–6289

53. Theint, T., Nadaud, P. S., Surewicz, K., Surewicz, W. K., and Jaroniec, C. P. (2017) 13C and 15N chemical shift assignments of mammalian Y145Stop prion protein amyloid fibrils. *Biomol. NMR Assign.* **11**, 75–80

54. Glynn, C., Sawaya, M. R., Ge, P., Gallagher-Jones, M., Short, C. W., Bowman, R., Apostol, M., Zhou, Z. H., Eisenberg, D. S., and Rodriguez, J. A. (2020) Cryo-EM structure of a human prion fibril with a hydrophobic, protease-resistant core. *Nat. Struct. Mol. Biol.* **27**, 417–423

55. Wang, L.-Q., Zhao, K., Yuan, H.-Y., Wang, Q., Guan, Z., Tao, J., Li, X.-N., Sun, Y., Yi, C.-W., Chen, J., Li, D., Zhang, D., Yin, P., Liu, C., and Liang, Y. (2020) Cryo-EM structure of an amyloid fibril formed by full-length human prion protein. *Nat. Struct. Mol. Biol.* **27**, 598–602

56. Pagano, K., Galante, D., D'Arrigo, C., Corsaro, A., Nizzari, M., Florio, T., Molinari, H., Tomaselli, S., and Ragona, L. (2019) Effects of prion protein on Aβ42 and pyroglutamate-modified AβpE3-42 oligomerization and toxicity. *Mol. Neurobiol.* **56**, 1957–1971

57. You, H., Tsutsui, S., Hameed, S., Kannanayakal, T. J., Chen, L., Xia, P., Engbers, J. D. T., Lipton, S. A., Stys, P. K., and Zamponi, G. W. (2012) Aβ neurotoxicity depends on interactions between copper ions, prion protein, and N-methyl-D-aspartate receptors. *Proc. Natl. Acad. Sci. U. S. A.* **109**, 1737–1742

58. Williams, T. L., Choi, J.-K., Surewicz, K., and Surewicz, W. K. (2015) Soluble prion protein binds isolated low molecular weight amyloid-β oligomers causing cytotoxicity inhibition. *ACS Chem. Neurosci.* **6**, 1972–1980

59. Kostylev, M. A., Kaufman, A. C., Nygaard, H. B., Patel, P., Haas, L. T., Gunther, E. C., Vortmeyer, A., and Strittmatter, S. M. (2015) Prion-protein-interacting amyloid-β oligomers of high molecular weight are tightly correlated with memory impairment in multiple Alzheimer mouse models. *J. Biol. Chem.* **290**, 17415–17438

60. Madhu, P., and Mukhopadhyay, S. (2020) Preferential recruitment of conformationally distinct amyloid-β oligomers by the intrinsically disordered region of the human prion protein. *ACS Chem. Neurosci.* **11**, 86–98

61. Brener, O., Dunkelmann, T., Gremer, L., van Groen, T., Mirecka, E. A., Kadish, I., Willuweit, A., Kutzsche, J., Jürgens, D., Rudolph, S., Tusche, M., Bongen, P., Pietruszka, J., Oesterhelt, F., Langen, K.-J., *et al.* (2015) QIAD assay for quantitating a compound's efficacy in elimination of toxic Aβ oligomers. *Sci. Rep.* **5**, 13222–13234

62. Freir, D. B., Nicoll, A. J., Klyubin, I., Panico, S., Mc Donald, J. M., Risse, E., Asante, E. A., Farrow, M. A., Sessions, R. B., Saibil, H. R., Clarke, A. R.,

Rowan, M. J., Walsh, D. M., and Collinge, J. (2011) Interaction between prion protein and toxic amyloid β assemblies can be therapeutically targeted at multiple sites. *Nat. Commun.* **2**, 336

63. Kudo, W., Lee, H.-P., Zou, W.-Q., Wang, X., Perry, G., Zhu, X., Smith, M. A., Petersen, R. B., and Lee, H.-g. (2012) Cellular prion protein is essential for oligomeric amyloid-β-induced neuronal cell death. *Hum. Mol. Genet.* **21**, 1138–1144

64. Peters, C., Espinoza, M. P., Gallegos, S., Opazo, C., and Aguayo, L. G. (2015) Alzheimer's Aβ interacts with cellular prion protein inducing neuronal membrane damage and synaptotoxicity. *Neurobiol. Aging* **36**, 1369–1377

65. Silvers, R., Colvin, M. T., Frederick, K. K., Jacavone, A. C., Lindquist, S., Linse, S., and Griffin, R. G. (2017) Aggregation and fibril structure of AβM01–42 and Aβ1–42. *Biochemistry* **56**, 4850–4859

66. Gasset, M., Baldwin, M. A., Lloyd, D. H., Gabriel, J. M., Holtzman, D. M., Cohen, F., Fletterick, R., and Prusiner, S. B. (1992) Predicted alpha-helical regions of the prion protein when synthesized as peptides form amyloid. *Proc. Natl. Acad. Sci. U. S. A.* **89**, 10940–10944

67. Norstrom, E. M., and Mastrianni, J. A. (2005) The AGAAAAGA palindrome in PrP is required to generate a productive PrPSc-PrPC complex that leads to prion propagation. *J. Biol. Chem.* **280**, 27236–27243

68. Sarell, C. J., Quarterman, E., Yip, D. C., Terry, C., Nicoll, A. J., Wadsworth, J. D. F., Farrow, M. A., Walsh, D. M., and Collinge, J. (2017) Soluble Abeta aggregates can inhibit prion propagation. *Open Biol.* **7**, 170158

69. Um, J. W., Kaufman, A. C., Kostylev, M., Heiss, J. K., Stagi, M., Takahashi, H., Kerrisk, M. E., Vortmeyer, A., Wisniewski, T., Koleske, A. J., Gunther, E. C., Nygaard, H. B., and Strittmatter, S. M. (2013) Metabotropic glutamate receptor 5 is a coreceptor for Alzheimer aβ oligomer bound to cellular prion protein. *Neuron* **79**, 887–902

70. Hu, N.-W., Nicoll, A. J., Zhang, D., Mably, A. J., O'Malley, T., Purro, S. A., Terry, C., Collinge, J., Walsh, D. M., and Rowan, M. J. (2014) mGlu5 receptors and cellular prion protein mediate amyloid-β-facilitated synaptic long-term depression *in vivo*. *Nat. Commun.* **5**, 3374

71. Haas, L. T., Salazar, S. V., Kostylev, M. A., Um, J. W., Kaufman, A. C., and Strittmatter, S. M. (2016) Metabotropic glutamate receptor 5 couples cellular prion protein to intracellular signalling in Alzheimer's disease. *Brain* **139**, 526–546

72. Potapov, A., Yau, W. M., Ghirlando, R., Thurber, K. R., and Tycko, R. (2015) Successive stages of amyloid-beta self-assembly characterized by solid-state nuclear magnetic resonance with dynamic nuclear polarization. *J. Am. Chem. Soc.* **137**, 8294–8307

73. Mengel, D., Hong, W., Corbett, G. T., Liu, W., DeSousa, A., Solforosi, L., Fang, C., Frosch, M. P., Collinge, J., Harris, D. A., and Walsh, D. M. (2019) PrP-grafted antibodies bind certain amyloid β-protein aggregates, but do not prevent toxicity. *Brain Res.* **1710**, 125–135

74. Heise, H., Köhler, F. H., and Xie, X. L. (2001) Solid-state NMR spectroscopy of paramagnetic metallocenes. *J. Magn. Reson.* **150**, 198–206

75. Morris, G. A., and Freeman, R. (1979) Enhancement of nuclear magnetic resonance signals by polarization transfer. *J. Am. Chem. Soc.* **101**, 760–762

76. Szeverenyi, N. M., Sullivan, M. J., and Maciel, G. E. (1982) Observation of spin exchange by two-dimensional Fourier transform 13C cross polarization-magic-angle spinning. *J. Magn. Reson. (1969)* **47**, 462–475

77. Hohwy, M., Rienstra, C. M., Jaroniec, C. P., and Griffin, R. G. (1999) Fivefold symmetric homonuclear dipolar recoupling in rotating solids: Application to double quantum spectroscopy. *J. Chem. Phys.* **110**, 7983–7992

78. Baldus, M., Petkova, A. T., Herzfeld, J., and Griffin, R. G. (1998) Cross polarization in the tilted frame: Assignment and spectral simplification in heteronuclear spin systems. *Mol. Phys.* **95**, 1197–1207

79. Fung, B. M., Khitrin, A. K., and Ermolaev, K. (2000) An improved broadband decoupling sequence for liquid crystals and solids. *J. Magn. Reson.* **142**, 97–101

80. Delaglio, F., Grzesiek, S., Vuister, G. W., Zhu, G., Pfeifer, J., and Bax, A. (1995) NMRPipe: A multidimensional spectral processing system based on UNIX pipes. *J. Biomol. NMR* **6**, 277–293

81. Skinner, S. P., Fogh, R. H., Boucher, W., Ragan, T. J., Mureddu, L. G., and Vuister, G. W. (2016) CcpNmr AnalysisAssign: A flexible platform for integrated NMR analysis. *J. Biomol. NMR* **66**, 111–124

ASBMB

82. Zhang, O., Kay, L. E., Olivier, J. P., and Forman-Kay, J. D. (1994) Backbone 1H and 15N resonance assignments of the N-terminal SH3 domain of drk in folded and unfolded states using enhanced-sensitivity pulsed field gradient NMR techniques. *J. Biomol. NMR* **4**, 845–858

83. Ikura, M., Kay, L. E., and Bax, A. (1990) A novel approach for sequential assignment of 1H, 13C, and 15N spectra of larger proteins: Heteronuclear triple-resonance three-dimensional NMR spectroscopy. Application to calmodulin. *Biochemistry* **29**, 4659–4667

84. Wittekind, M., and Mueller, L. (1993) HNCACB, a high-sensitivity 3D NMR experiment to correlate amide-proton and nitrogen resonances with the alpha- and beta-carbon resonances in proteins. *J. Magn. Reson. Ser. B* **101**, 201–205

85. Solyom, Z., Schwarten, M., Geist, L., Konrat, R., Willbold, D., and Brutscher, B. (2013) BEST-TROSY experiments for time-efficient sequential resonance assignment of large disordered proteins. *J. Biomol. NMR* **55**, 311–321

86. Kovacs, H., and Gossert, A. (2014) Improved NMR experiments with 13C-isotropic mixing for assignment of aromatic and aliphatic side chains in labeled proteins. *J. Biomol. NMR* **58**, 101–112

87. Findeisen, M., Brand, T., and Berger, S. (2007) A 1H-NMR thermometer suitable for cryoprobes. *Magn. Reson. Chem.* **45**, 175–178

88. Grzesiek, S., and Bax, A. (1993) The importance of not saturating water in protein NMR. Application to sensitivity enhancement and NOE measurements. *J. Am. Chem. Soc.* **115**, 12593–12594

89. Marion, D., Ikura, M., Tschudin, R., and Bax, A. (1989) Rapid recording of 2D NMR spectra without phase cycling. Application to the study of hydrogen exchange in proteins. *J. Magn. Reson. (1969)* **85**, 393–399

90. Kay, L., Keifer, P., and Saarinen, T. (1992) Pure absorption gradient enhanced heteronuclear single quantum correlation spectroscopy with improved sensitivity. *J. Am. Chem. Soc.* **114**, 10663–10665

91. Schleucher, J., Sattler, M., and Griesinger, C. (1993) Coherence selection by gradients without signal attenuation: Application to the three-dimensional HNCO experiment. *Angew. Chem. Int. Ed. Engl.* **32**, 1489–1491

92. Johnson, B. A., and Blevins, R. A. (1994) NMR view: A computer program for the visualization and analysis of NMR data. *J. Biomol. NMR* **4**, 603–614

93. Markley John, L., Bax, A., Arata, Y., Hilbers, C. W., Kaptein, R., Sykes Brian, D., Wright Peter, E., and Wüthrich, K. (1998) Recommendations for the presentation of NMR structures of proteins and nucleic acids (IUPAC recommendations 1998). *Pure Appl. Chem.* **70**, 117–142

94. Shen, Y., and Bax, A. (2013) Protein backbone and sidechain torsion angles predicted from NMR chemical shifts using artificial neural networks. *J. Biomol. NMR* **56**, 227–241

95. Han, B., Liu, Y., Ginzinger, S. W., and Wishart, D. S. (2011) SHIFTX2: Significantly improved protein chemical shift prediction. *J. Biomol. NMR* **50**, 43

96. Schulte, C. F., Tolmie, D. E., Maziuk, D., Nakatani, E., Akutsu, H., Yao, H., Markley, J. L., Lin, J., Doreleijers, J. F., Livny, M., Kent Wenger, R., Mading, S., Ioannidis, Y. E., Harano, Y., Miller, Z., *et al.* (2007) BioMagResBank. *Nucleic Acids Res.* **36**, D402–D408

97. Calzolai, L., and Zahn, R. (2003) Influence of pH on NMR structure and stability of the human prion protein globular domain. *J. Biol. Chem.* **278**, 35592–35596

98. Colvin, M. T., Silvers, R., Frohm, B., Su, Y., Linse, S., and Griffin, R. G. (2015) High resolution structural characterization of Aβ42 amyloid fibrils by magic angle spinning NMR. *J. Am. Chem. Soc.* **137**, 7509–7518

99. Ravotti, F., Wälti, M. A., Güntert, P., Riek, R., Böckmann, A., and Meier, B. H. (2016) Solid-state NMR sequential assignment of an Amyloid-β(1–42) fibril polymorph. *Biomol. NMR Assign.* **10**, 269–276

Supporting Information

Structural details of amyloid beta oligomers in complex with human prion protein as revealed by solid-state MAS NMR spectroscopy

Anna S. König[1,2], Nadine S. Rösener[1,2], Lothar Gremer[1,2,3], Markus Tusche[1], Daniel Flender[2#], Elke Reinartz[2], Wolfgang Hoyer[1,2], Philipp Neudecker[1,2], Dieter Willbold[1,2,3]* and Henrike Heise[1,2]*

[1]Institute of Biological Information Processing (IBI-7: Structural Biochemistry) and JuStruct: Jülich Center for Structural Biology, Forschungszentrum Jülich, Wilhelm-Johnen-Straße, 52428 Jülich, Germany
[2]Physikalische Biologie, Heinrich-Heine-Universität Düsseldorf, Universitätsstraße 1, 40225 Düsseldorf, Germany
[3]Research Center for Molecular Mechanisms of Aging and Age-Related Diseases, Moscow Institute of Physics and Technology (State University), Dolgoprudny, Russia

[#]Present address: Institut für Mikrobiologie, Universität Greifswald, Felix-Hausdorff-Str.8, 17489 Greifswald

*To whom correspondence should be addressed: Prof. Dr. Dieter Willbold: d.willbold@fz-juelich.de; Tel.: +492461612100, and Prof. Dr. Henrike Heise: h.heise@fz-juelich.de; Tel. +492461614658

Running title: Solid-state MAS NMR of the complex of huPrP and $A\beta_{oligo}$

Keywords: Alzheimer disease, amyloid-beta (Aβ), prion protein, oligomer, solid state NMR, solution NMR, nuclear magnetic resonance (NMR), structural biology
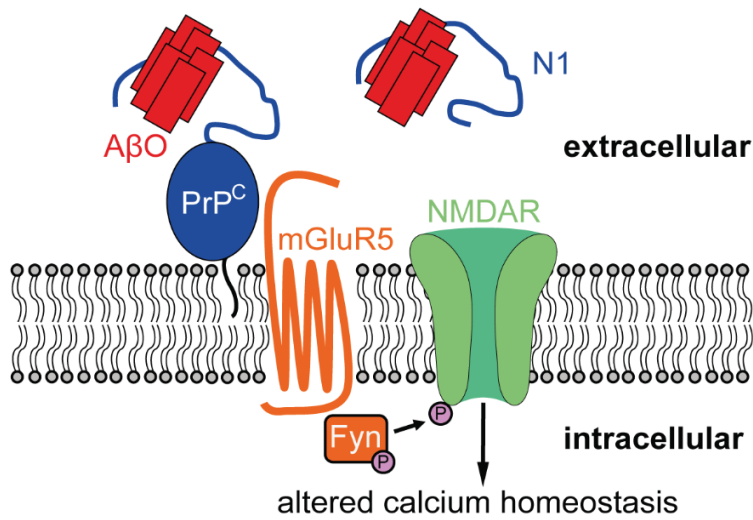
Figure S1: Concept of $A\beta_{oligo}$-binding induced signaling pathways of PrP^C resulting in neurodegeneration for full-length PrP^C or neuroprotection for N1. Specifically, $A\beta_{oligo}$ binding to membrane-anchored PrP^C mediates synapse damage (24) and the blockade of long-term potentiation by $A\beta_{oligo}$ (19,25) via activation of Fyn-kinase pathways (26,27). In contrast, soluble PrP (32) as well as its N-terminal fragment PrP(23-111) (N1) (33,34) inhibit $A\beta$ fibrillation and sequester $A\beta_{oligos}$. Full-length PrP^C and N1 are shown in blue, $A\beta_{oligo}$ in red, the mGluR5 receptor and Fyn-kinase in orange, the NMDAR receptor in green and a phosphorylation in purple. Picture adapted from (41).
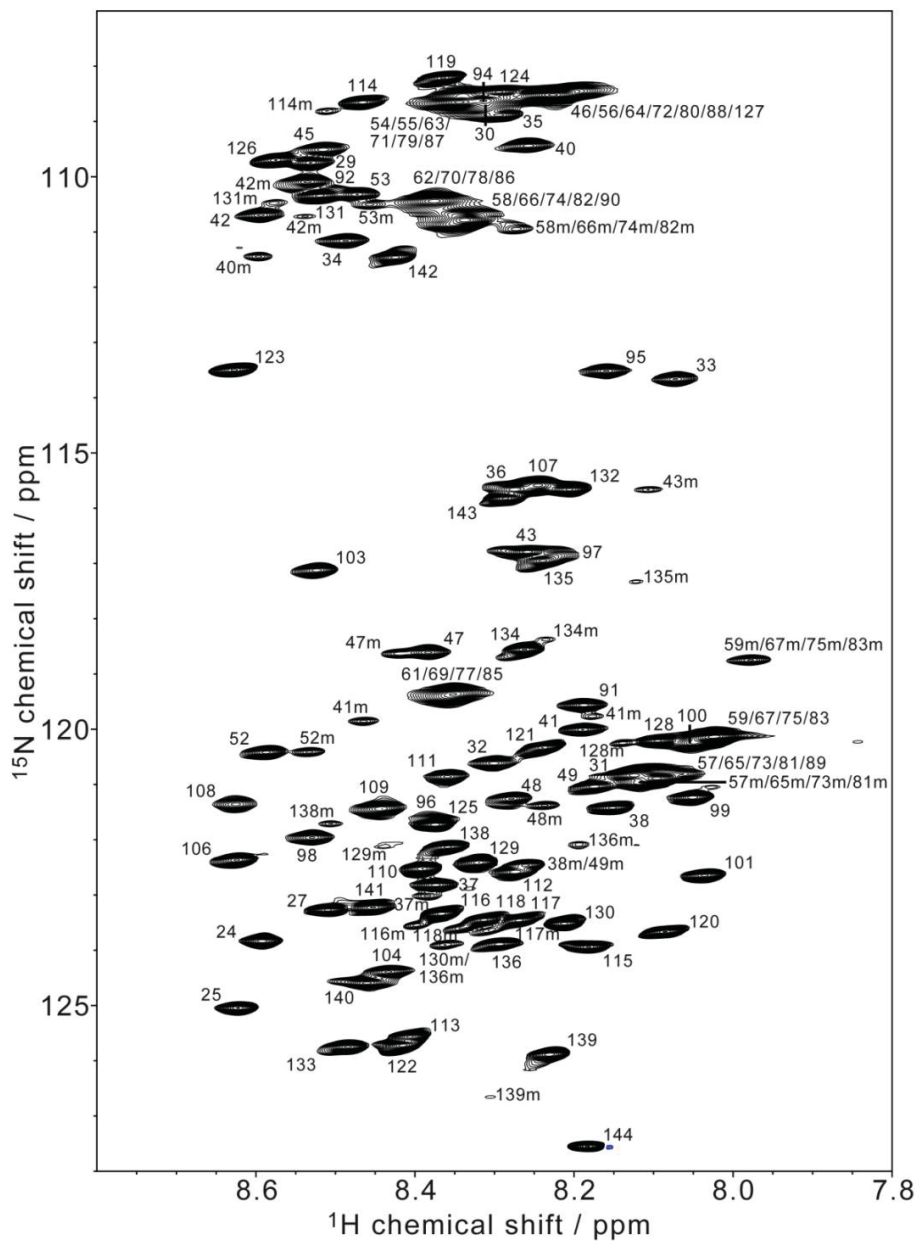
Figure S2. Backbone amide region of the ^{1}H-^{15}N HSQC spectrum of a solution of 0.30 mM [U-^{13}C,^{15}N] huPrP(23-144) in 50 mM HEPES (pH 7.0), 10 % (v/v) D$_2$O recorded at 5.0 °C and 800 MHz (positive contours black, negative contours blue). Backbone resonance assignments are indicated by residue numbers, minor resonances (e. g. due to proline residues in *cis* conformation or methionine oxidation) are indicated by an m. Four octarepeats (P51 to Q91) share the same sequence (**Figure 2A**) and could not be resolved. The backbone amide resonance of G93 could not be identified due to severe resonance overlap.
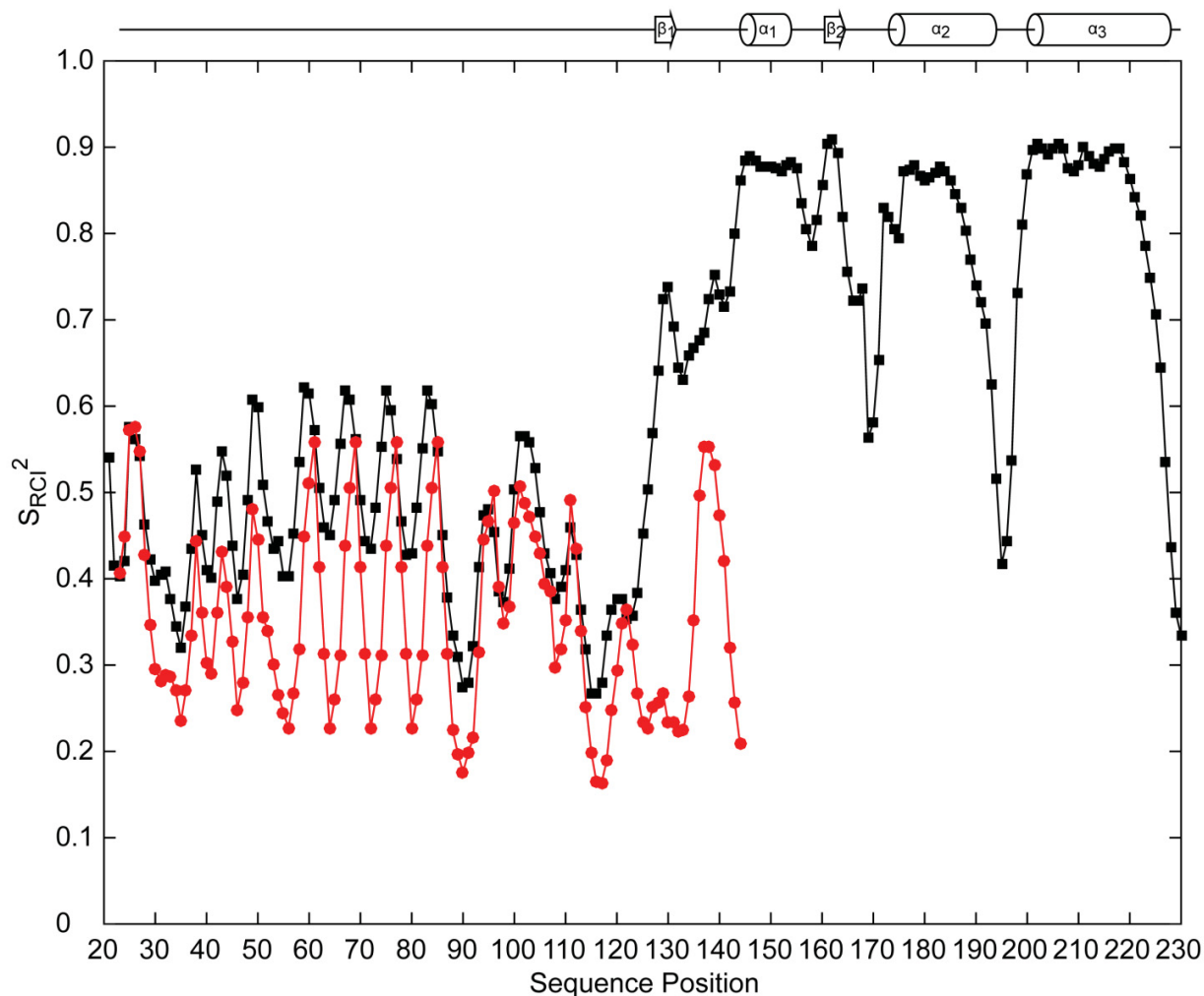
Figure S3. Backbone order parameters predicted from the Random Coil Index (RCI), S_{RCI}^2, for huPrP(23-230) at pH 4.5 (BMRB 4402, ref. (48), black) and huPrP(23-144) at pH 7.0 (BMRB 28116, this work, red), as calculated by TALOS-N (94) with the default parameters. Assigned chemical shifts for the short N-terminal cloning artifact (Gly for huPrP(23-144), Gly-Ser for huPrP(23-230)) were included. Full-length huPrP(23-230) consists of a highly disordered N-terminal region comprising residues 23 to 124 with chemical shifts very close to random coil values and concomitantly low S_{RCI}^2 values below about 0.6 (black), and a globular C-terminal prion domain comprising residues 125 to 228, whose regular secondary structure elements are indicated above the figure. Upon truncation, residues 125 to 144 of huPrP(23-144) also become disordered, with chemical shifts very close to random coil values (**Figure S2**) and concomitantly low S_{RCI}^2 values below ≈ 0.6 for all residues from 23 to 144 (red).
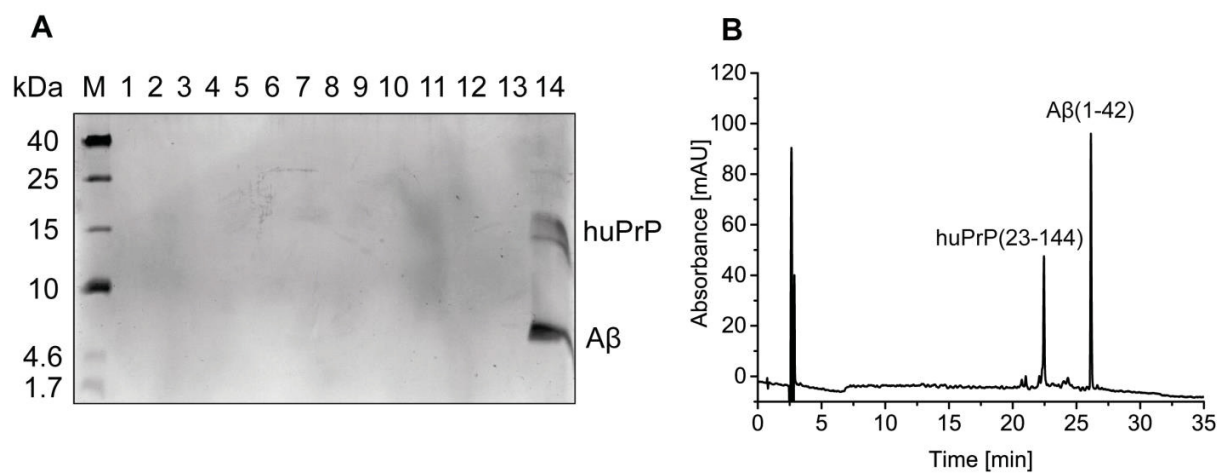
Figure S4. A. Sucrose DGC (40) of a tenfold dilution of huPrP(23-144)-Aβ* (* species is ^{13}C, ^{15}N uniformly labeled) before washing shows huPrP and Aβ only in fraction 14, corresponding to the highest density (40). **B.** Quantitative analysis by RP-HPLC on fraction 14 of the DGC revealed an Aβ(1-42) to huPrP(23-144) stoichiometry of 8.6 to 1 (monomer equivalents, single measurement).
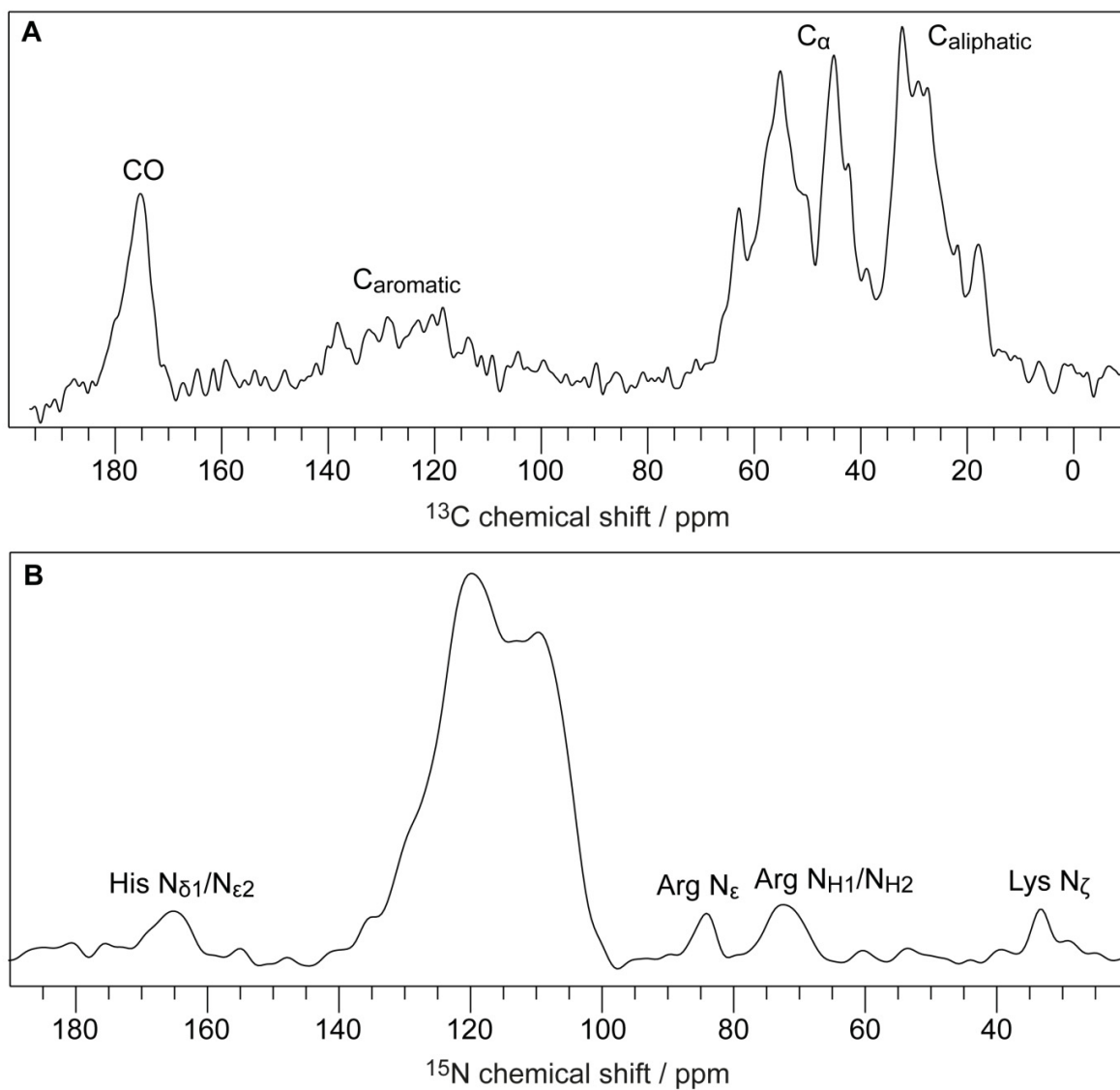
Figure S5. A. ^{1}H-^{13}C CP spectrum of huPrP(23-144)*-Aβ (* species is ^{13}C, ^{15}N uniformly labeled), recorded at a temperature of ≈ 0 °C, at a spinning frequency of 11 kHz and 256 scans. **B.** ^{1}H-^{15}N CP spectrum of huPrP(23-144)*-Aβ, measured at a temperature of ≈ -6 °C, a spinning frequency of 11 kHz and 2000 scans.
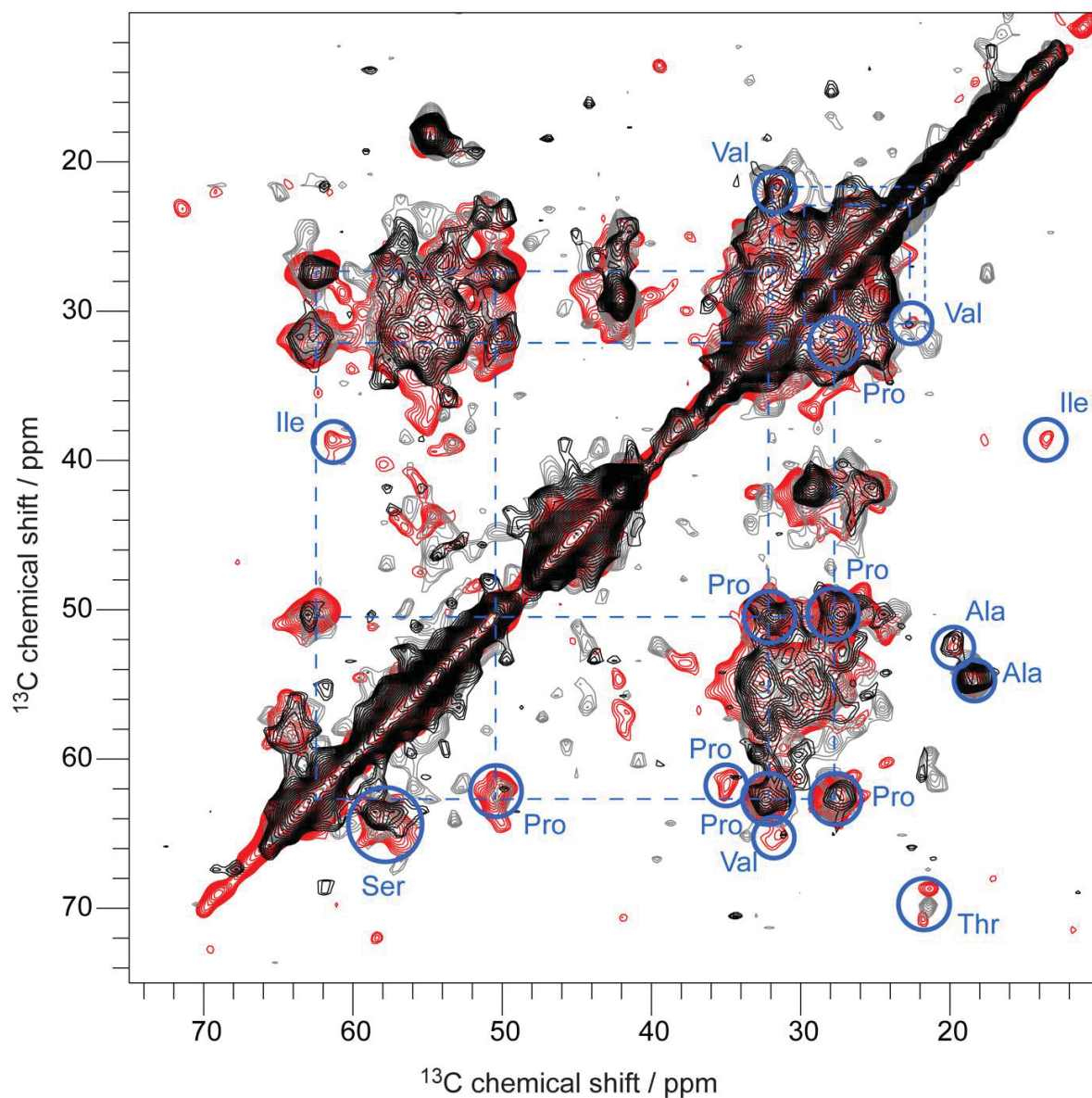
Figure S6. PDSD spectra of huPrP(23-144)*-Aβ (* species is ^{13}C, ^{15}N uniformly labeled), recorded at a spinning frequency of 11 kHz, a temperature of ≈ -6 °C and a mixing time of 30 ms (red) or a temperature of ≈ 0 °C and a mixing time of 50 ms (black) or 100 ms (grey). Blue circles indicate some identified amino acid types, dashed lines Pro and Val connections.
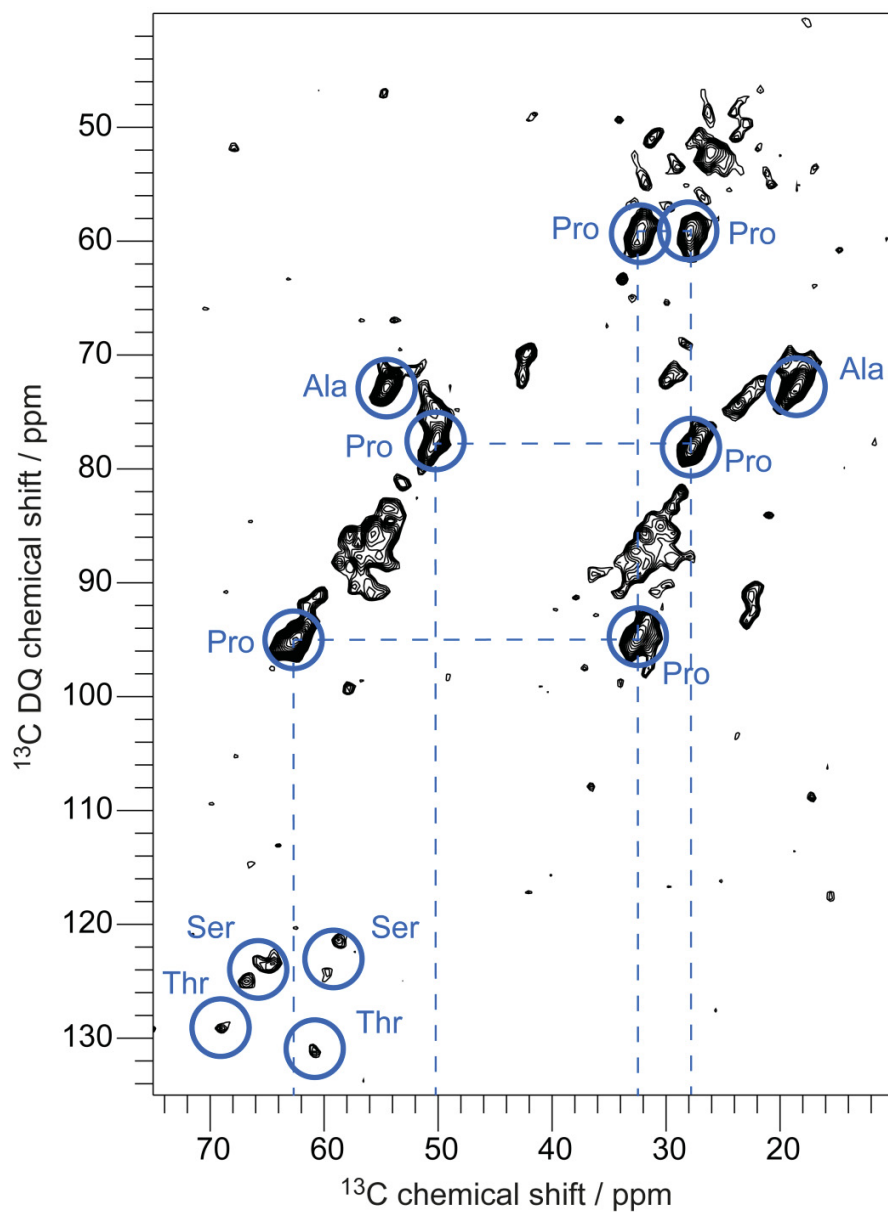
Figure S7. Double-quantum (DQ) correlation spectrum of huPrP(23-144)*-Aβ (* species is ^{13}C, ^{15}N uniformly labeled) with SPC5-recoupling, recorded at a temperature of ≈ -6 °C and a spinning frequency of 8 kHz. Blue circles indicate identified amino acid types, dashed lines Pro connections.
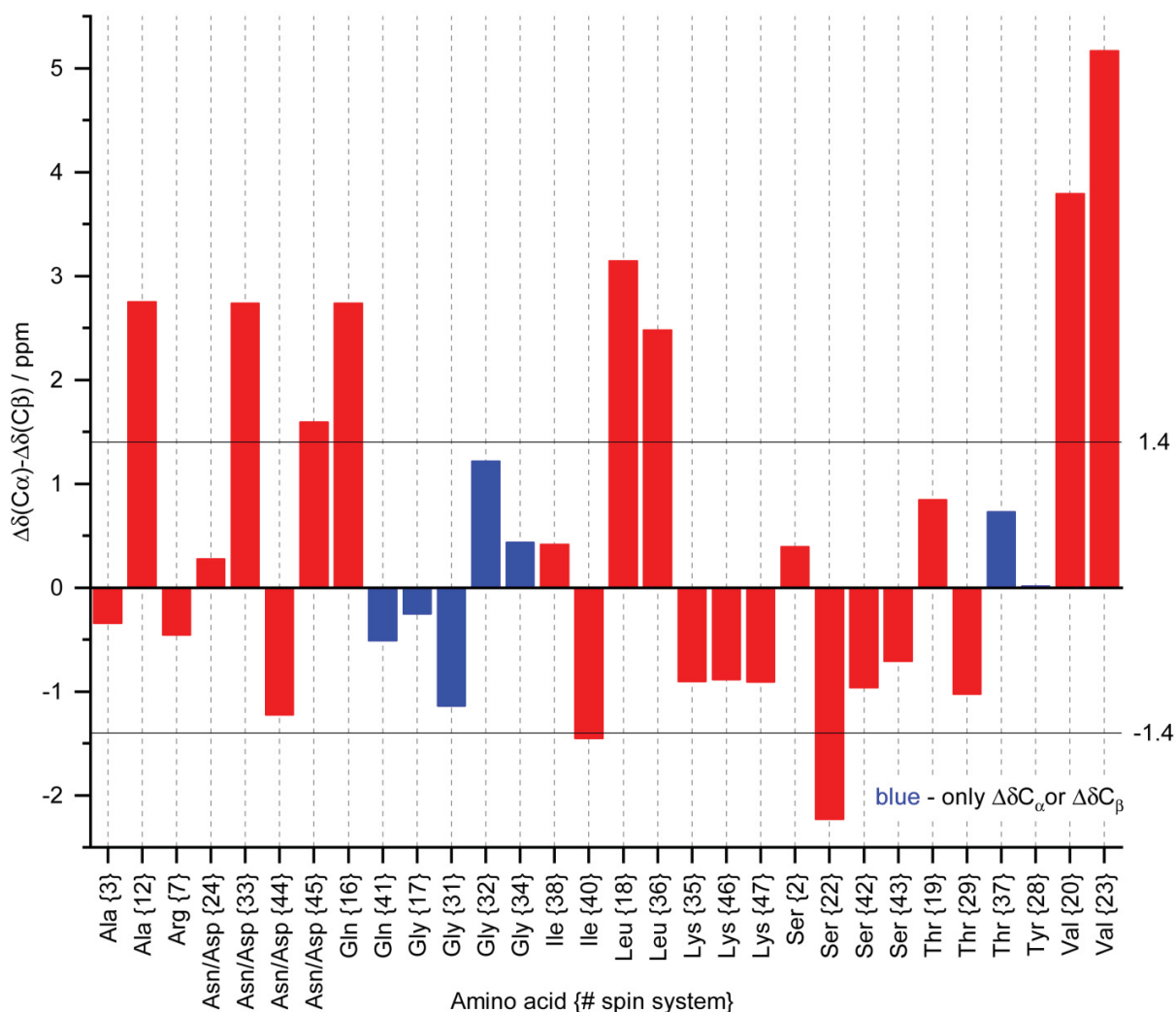
Figure S8. Secondary chemical shifts for huPrP(23-144)*-Aβ (* species is ^{13}C, ^{15}N uniformly labeled). Secondary chemical shifts are calculated as $(C\alpha_{exp}\text{-}C\alpha_{rc})\text{-}(C\beta_{exp}\text{-}C\beta_{rc})$, values above 1.4 ppm are indicative of α-helical-like secondary structure, values below – 1.4 ppm are indicative of β-strand-like secondary structure. In absence of a sequential assignment an arbitrary number for the spin system is given in braces. Note that blue bars indicate spin systems where only either a Cα or Cβ chemical shift was available, therefore $(C\alpha_{exp}\text{-}C\alpha_{rc})$ or $(C\beta_{exp}\text{-}C\beta_{rc})$ was calculated, respectively.
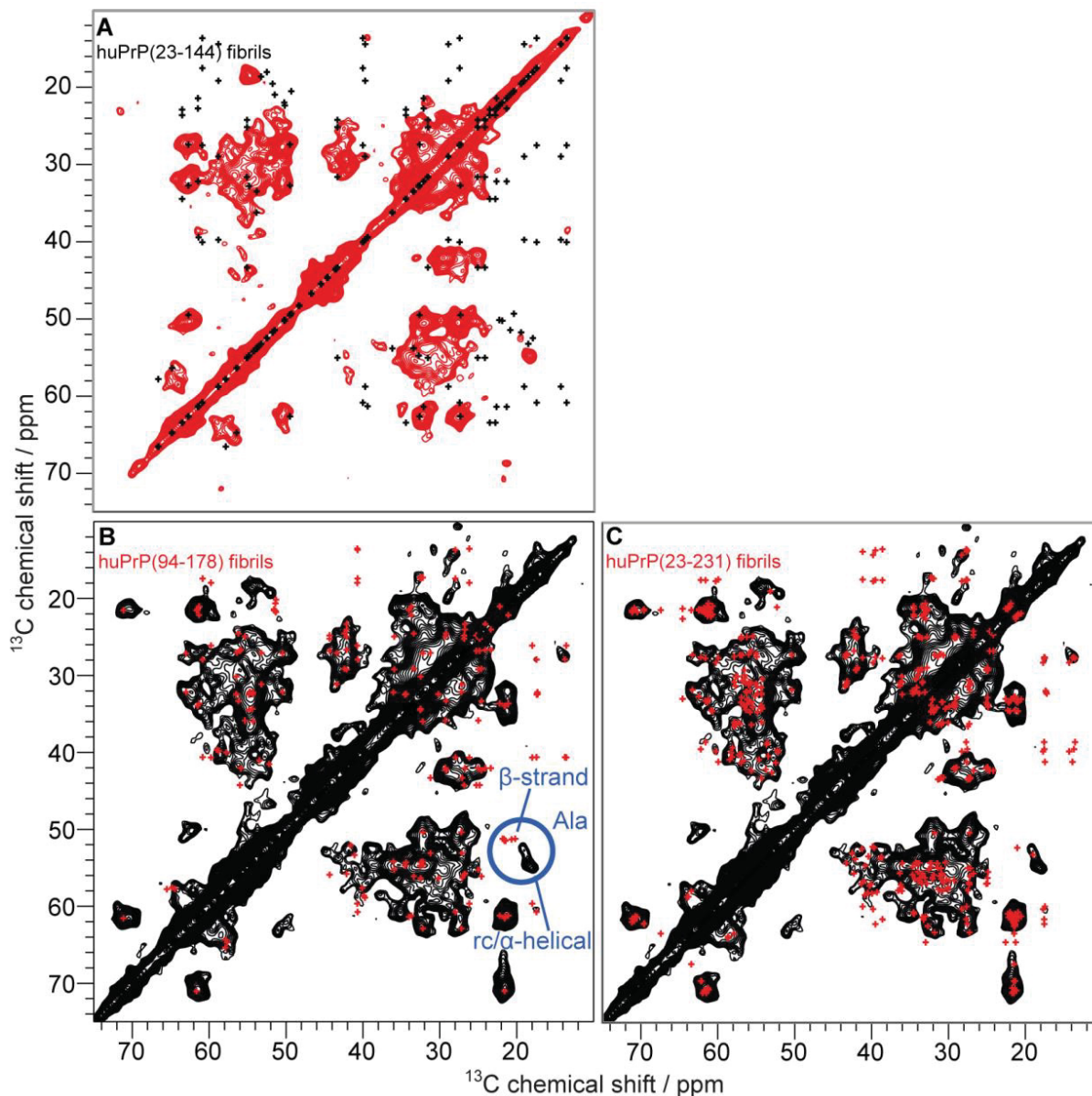
Figure S9. A. Comparison of a PDSD spectrum (recorded at a temperature of $\approx$ -6 °C, a spinning frequency of 11 kHz and a mixing time of 30 ms, same as in **Figure 1C**) of huPrP(23-144)*-Aβ (* species is ^{13}C, ^{15}N uniformly labeled) with the chemical shifts of a huPrP(23-144) fibril recorded by Theint et al. (BMRB entry 26925) (53), shown as black crosses. **B.** Comparison of a PDSD spectrum (black, recorded at a temperature of $\approx$ 0 °C, a spinning frequency of 11 kHz and a mixing time of 30 ms, same as in **Figure 4**) of huPrP(23-230)*-Aβ (* species is ^{13}C, ^{15}N uniformly labeled) with predicted chemical shifts (ShiftX2 (95)) of a huPrP(94-178) fibril structure determined through Cryo-EM by Glynn et al. (PDB 6UUR) (54), shown as red crosses. The difference in Ala chemical shifts (rc or α-helical like in this study vs. β-strand like in (54)) is highlighted in blue. **C.** Comparison of a PDSD spectrum (black, recorded at a temperature of $\approx$ 0 °C, a spinning frequency of 11 kHz and a mixing time of 30 ms, same as in **Figure 4**) of huPrP(23-230)*-Aβ (* species is ^{13}C, ^{15}N uniformly labeled) with predicted chemical shifts (ShiftX2 (95)) of a huPrP(23-231) fibril structure determined through Cryo-EM by Wang et al. (PDB 6LNI) (55), shown as red crosses. Values for unstructured regions are taken from the BMRB (random coil value).
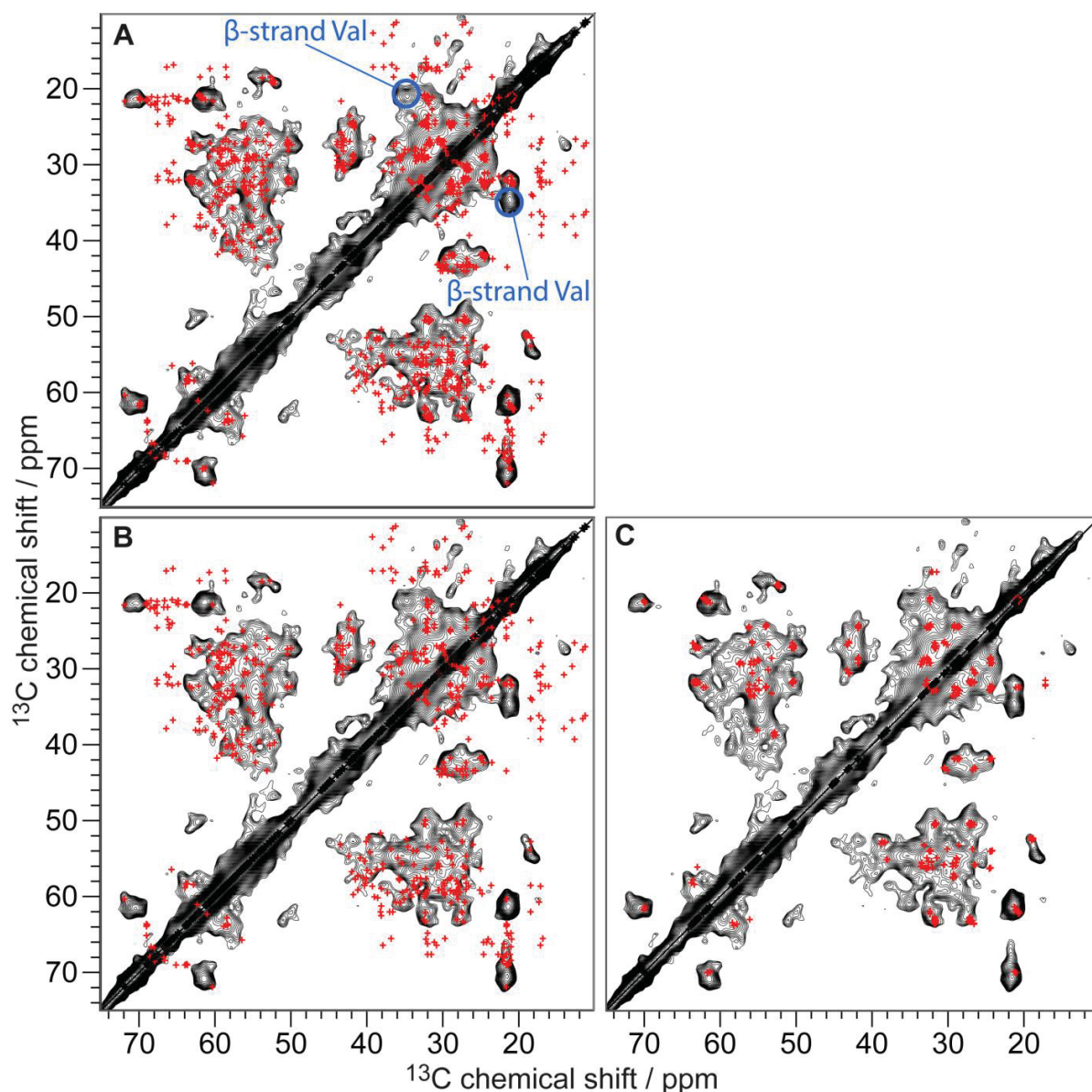
Figure S10. Comparison of a PDSD spectrum of huPrP(23-230)*-Aβ (black) (* species is ^{13}C, ^{15}N uniformly labeled) to predicted peaks, indicated as red crosses. Measured chemical shifts of Zahn et al. (BMRB entry 4402) were used for the prediction. For those carbon atoms in the structured C terminus (starting from residue 125) for which no chemical shift assignments were made by Zahn et al., chemical shifts were predicted from the PDB-structure of monomeric huPrP (PDB-Entry 1QLZ) (48) with SHIFTX2 (95). For residues from the unstructured N-terminal part for which no chemical shift assignments were made by Zahn et al., random coil BMRB values (96) were used. Cross peaks of up to two bonds were included in the prediction. Full spin-systems were simulated, but at 30 ms mixing time not all cross-correlations necessarily show up with sufficient intensity in the experimental spectrum. **A.** Values for residues MK23-S230, **B.** L125-S230 (C terminus only), and **C.** MK23-G124 (N terminus only) were used. The separation between N-terminal and C-terminal regions is made between G124 and L125, where the ordered region of the solution NMR structure starts (**Figure 2A**). The PDSD spectrum was recorded at a temperature of ≈ 0 °C, a spinning frequency of 11 kHz and a mixing time of 30 ms. β-strand-like Val is indicated with blue circles, it is the only peak in the spectrum of huPrP(23-230)*-Aβ which is not superimposed at all. Note that

these structural changes are not due to the different pH of huPrP(23-230)*-Aβ (pH 7.4) and soluble huPrP(23-230) (pH 4.5), as the conformation of the globular domain (residues 125 to 230) of monomeric huPrP(23-230) at pH 4.5 and pH 7.0 is extremely similar (97).
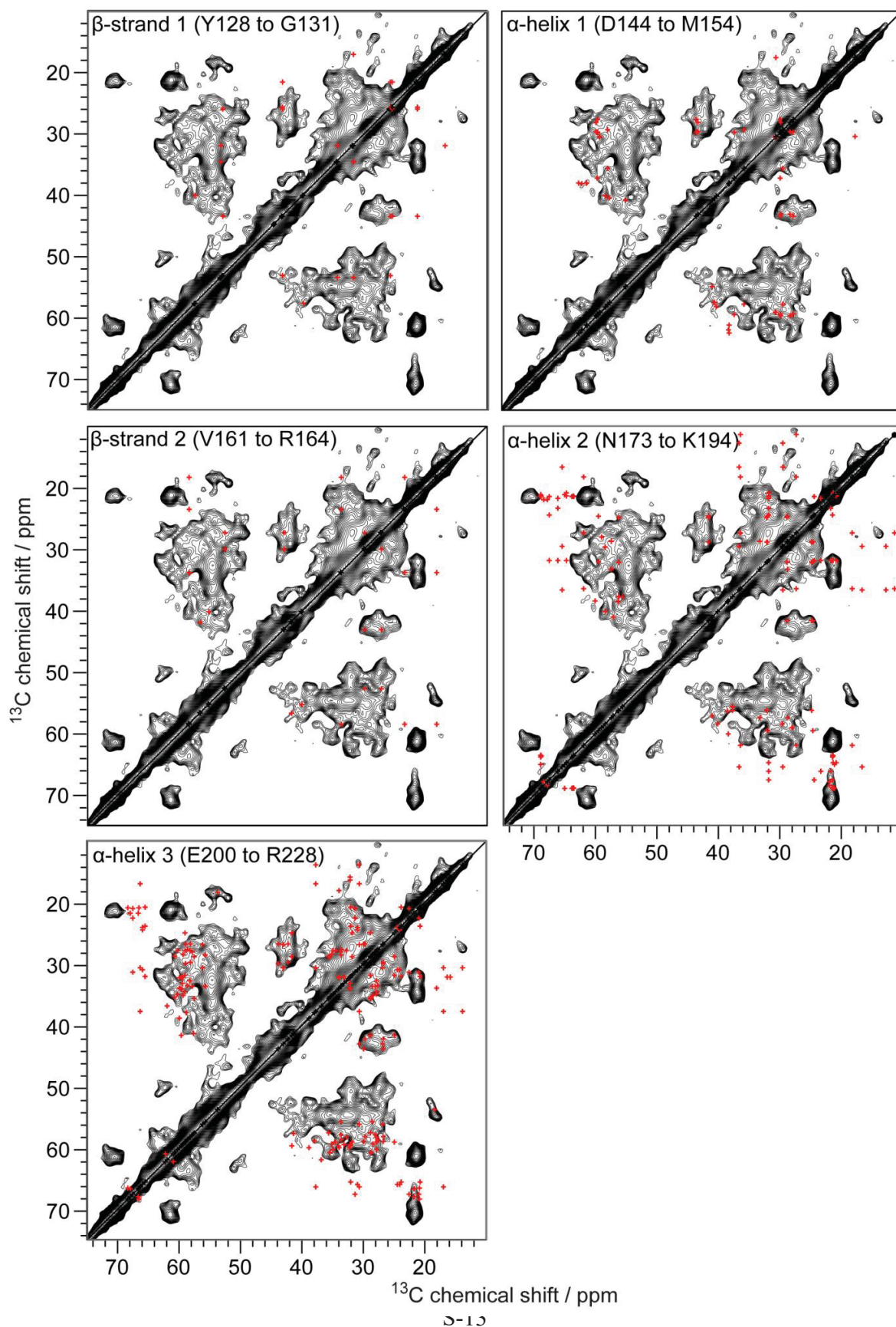
β-strand 1 (Y128 to G131)

α-helix 1 (D144 to M154)

β-strand 2 (V161 to R164)

α-helix 2 (N173 to K194)

α-helix 3 (E200 to R228)

^{13}C chemical shift / ppm

^{13}C chemical shift / ppm

Figure S11. Comparison of a PDSD spectrum of huPrP(23-230)*-Aβ (black) (* species is ^{13}C, ^{15}N uniformly labeled) to predicted peaks, indicated as red crosses. Measured chemical shifts of Zahn et al. (BMRB entry 4402) were used for the prediction. For those carbon atoms in the structured C terminus (starting from residue 125) for which no chemical shift assignments were made by Zahn et al., chemical shifts were predicted from the PDB-structure of monomeric huPrP(23-230) (PDB-Entry 1QLZ) (48) with SHIFTX2 (95). Cross peaks of up to two bonds were included in the prediction. Full spin-systems were simulated, but at 30 ms mixing time not all cross-correlations necessarily show up with sufficient intensity in the experimental spectrum. (β-strand 1) Values for residues Y128 to G131, (α-helix 1) D144 to M154, (β-strand 2) V161 to R164, (α-helix 2) N173 to K194 and (α-helix 3) E200 to R228 were used. The PDSD spectrum was recorded at a temperature of ≈ 0 °C, a spinning frequency of 11 kHz and a mixing time of 30 ms. Except for longer correlations over three or four bonds, some side chains of Leu, Met and V161, the resonances of the two β-strands and the first α-helix determined by Zahn et al. align well with the resonances of huPrP(23-230)*-Aβ. But as these resonances determined by Zahn et al. overlap with other resonances in the spectrum of huPrP(23-230)*-Aβ, it is possible that they are either not visible or shifted. Therefore, no conclusion can be drawn about the conservation of the two β-strands and the first α-helix. For the last two α-helices also longer correlations are missing. But interestingly all α-helical like Ile, Val and, in the second α-helix, Thr resonances are missing, too. This means Ile, Val and Thr are more random coil or β-strand like in huPrP(23-230)*-Aβ or partly undetectable, i.e. flexible on an intermediate time scale (as no signals are observed in an INEPT experiment (data not shown)).
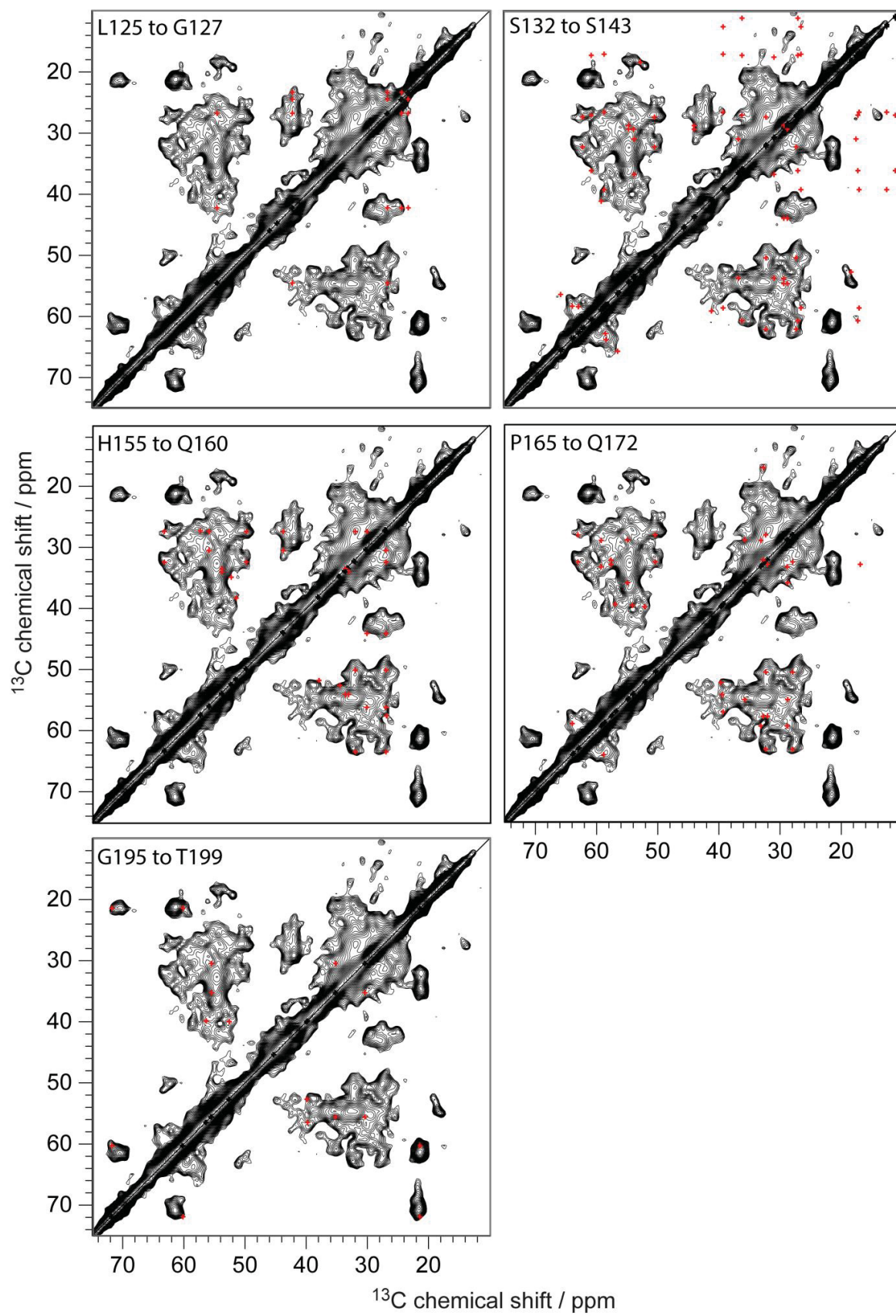
L125 to G127

S132 to S143

H155 to Q160

P165 to Q172

G195 to T199

^{13}C chemical shift / ppm

^{13}C chemical shift / ppm

S-15

Figure S12. Comparison of a PDSD spectrum of huPrP(23-230)*-Aβ (black) (* species is ^{13}C, ^{15}N uniformly labeled) to predicted peaks, indicated as red crosses. Measured chemical shifts of Zahn et al. (BMRB entry 4402) were used for the prediction. For those carbon atoms in the structured C terminus (starting from residue 125) for which no chemical shift assignments were made by Zahn et al., chemical shifts were predicted from the PDB-structure of monomeric huPrP (PDB-Entry 1QLZ) (48) with SHIFTX2 (95). Cross peaks of up to two bonds were included in the prediction. Full spin-systems were simulated, but at 30 ms mixing time not all cross-correlations necessarily show up with sufficient intensity in the experimental spectrum. Here it is shown for all loop regions between the β-strands and α-helices, namely L125 to G127, S132 to S143, H155 to Q160, P165 to Q172 and G195 to T199. The PDSD spectrum was recorded at a temperature of ≈ 0 °C, a spinning frequency of 11 kHz and a mixing time of 30 ms. In the loop regions between the β-strands and α-helices only correlations over two or more bonds plus S143 are missing or shifted.
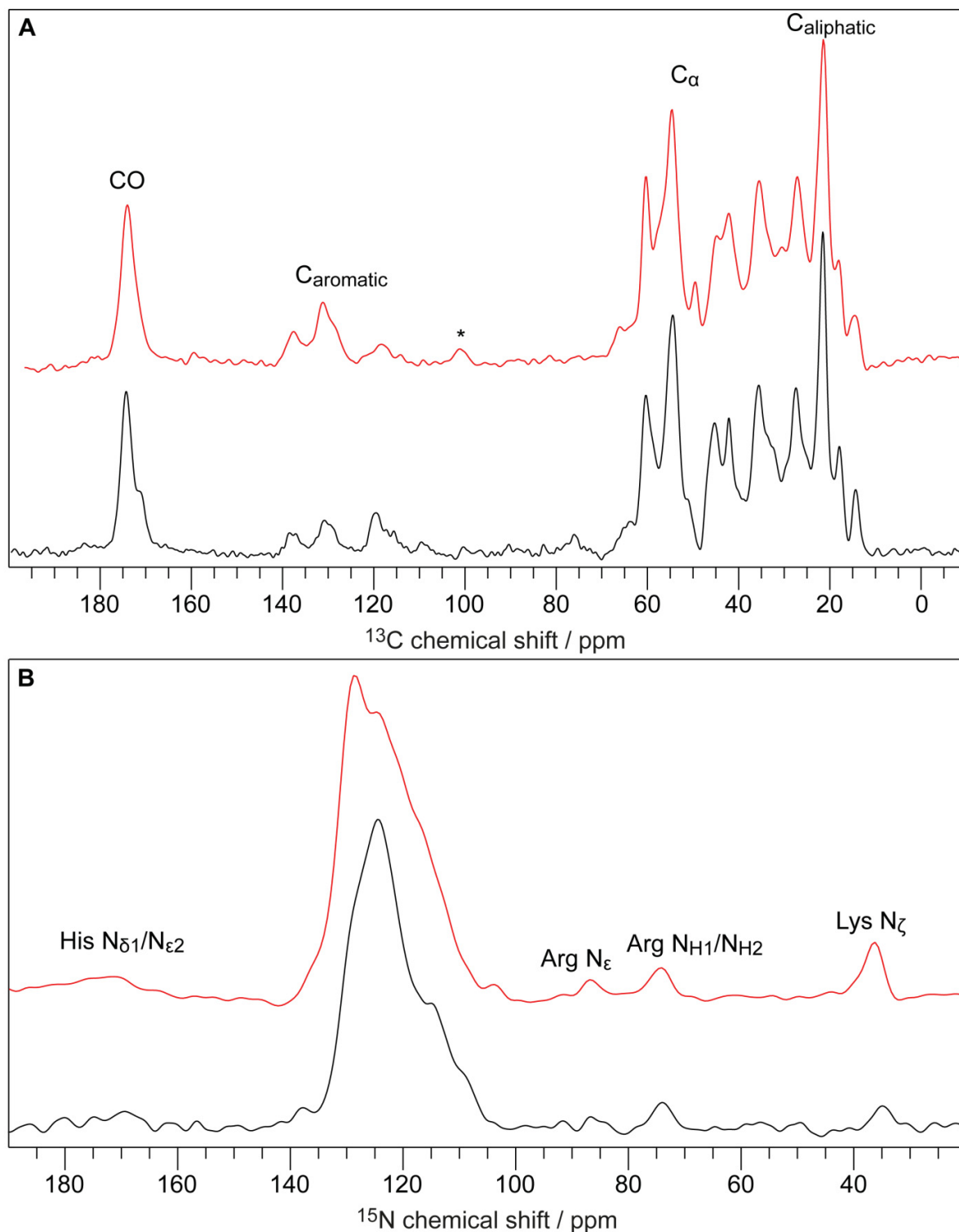
Figure S13. A. (red) ^{1}H-^{13}C CP spectrum of huPrP(23-144)-Aβ* (* species is ^{13}C, ^{15}N uniformly labeled), recorded at a temperature of ≈ 0 °C, at a spinning frequency of 11 kHz and 128 scans. Spinning side bands are marked with an asterisk. **A.** (black) ^{1}H-^{13}C CP spectrum of huPrP(23-144)$_{exc}$-Aβ* ($_{exc}$ huPrP is in excess; * species is ^{13}C, ^{15}N uniformly labeled), recorded at a temperature of ≈ 7 °C, at a spinning frequency of 5

kHz and 256 scans. **B.** (red) ^{1}H-^{15}N CP spectrum of huPrP(23-144)-Aβ*, recorded at a temperature of ≈ 0 °C, a spinning frequency of 11 kHz and 2000 scans. **B.** (black) ^{1}H-^{15}N CP spectrum of huPrP(23-144)$_{exc}$-Aβ*, recorded at a temperature of ≈ 0 °C, a spinning frequency of 11 kHz and 2048 scans.
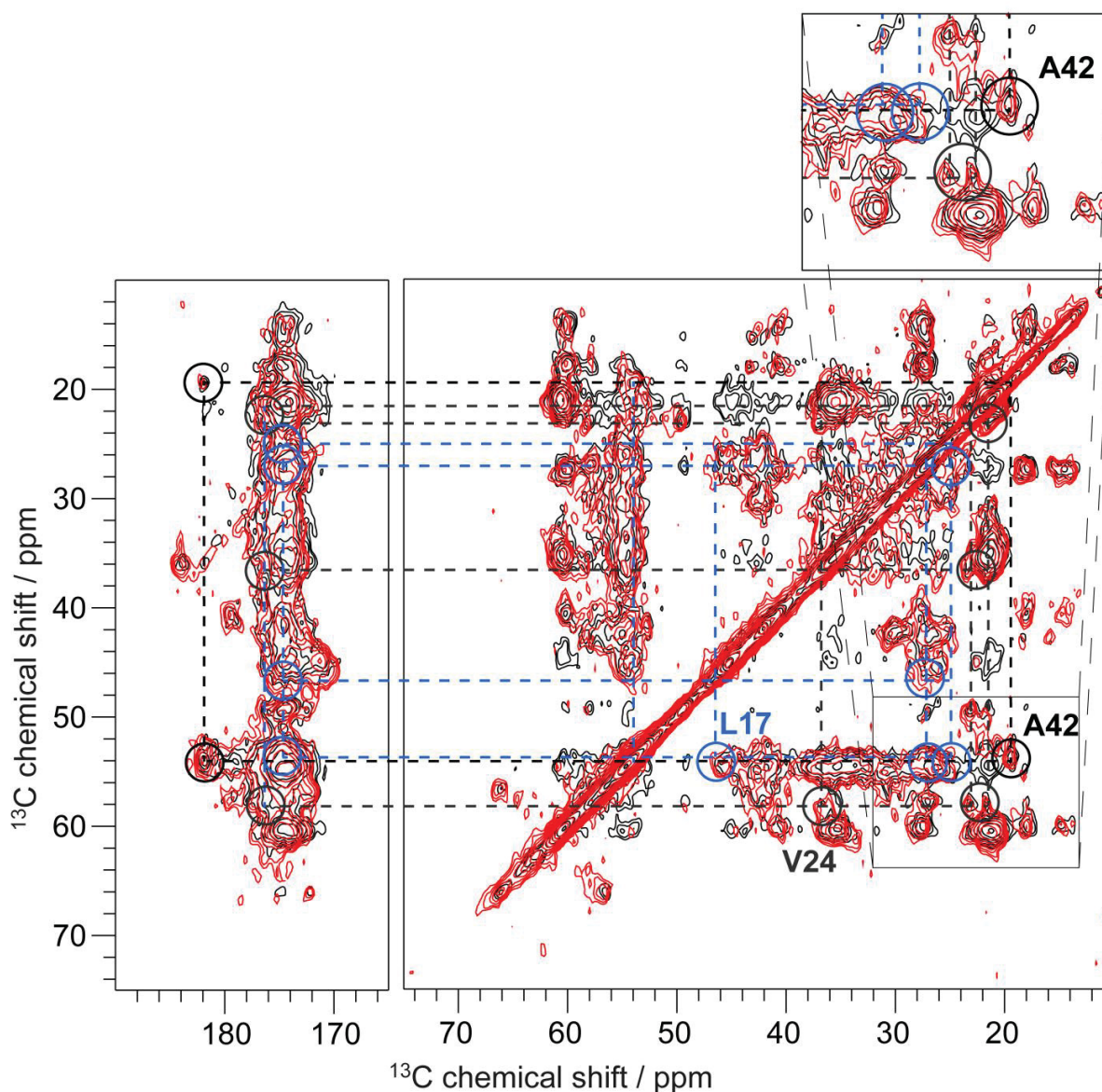
Figure S14. Two PDSD spectra of huPrP(23-144)-Aβ* (* species is ^{13}C, ^{15}N uniformly labeled), recorded at a temperature of ≈ 0 °C, a spinning frequency of 11 kHz and a mixing time of 50 ms (red) and 200 ms (black). Three identified residues are shown exemplarily with colored circles and dashed lines: L17 (blue), V24 (grey) and A42 (black). For L17 $C_{\delta1}$ and $C_{\delta2}$ chemical shifts are not separated due to the low signal dispersion. In contrast, V24 shows two separated $C_{\gamma1}$ and $C_{\gamma2}$ chemical shifts, which has been also observed in the Aβ(1-42) fibril polymorph of Gremer et al. (47). Note the high CO chemical shift of A42 (182 ppm) (left part, black circles). This can be explained by a free and deprotonated state of the C-terminal carboxyl group. At 200 ms mixing time several multi-bond and inter-residual correlations appear, which are not visible at 50 ms mixing time, for example for residues Q15 to F20. As these residues additionally do not show multiple peaks, this is the structurally most conserved part in the oligomer. Altogether, these characteristics made it possible to assign these resonances to the appropriate residue in the amino acid sequence.
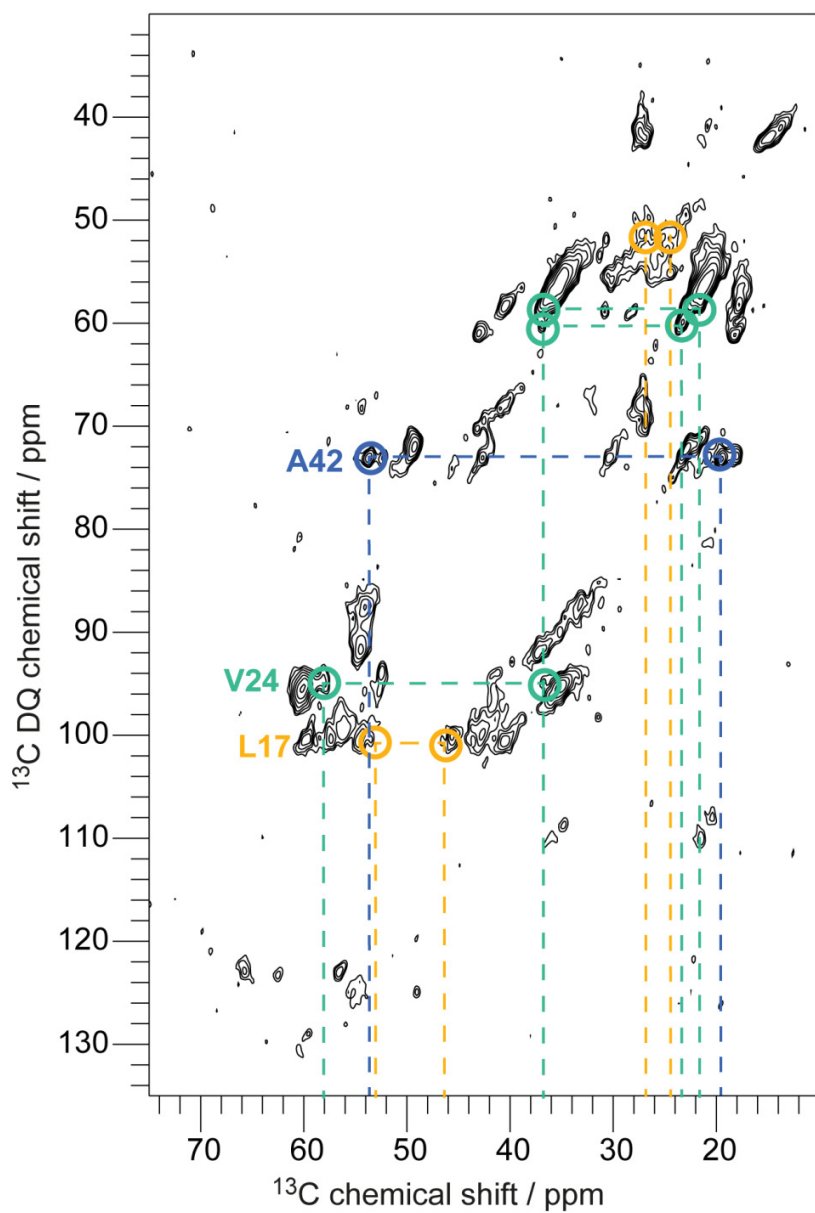
Figure S15. Double-quantum (DQ) correlation spectrum of huPrP(23-144)-Aβ* (* species is ^{13}C, ^{15}N uniformly labeled) with SPC5-recoupling, recorded at a temperature of ≈ 0 °C and a spinning frequency of 8 kHz. Three identified residues are shown exemplarily with colored circles and dashed lines: L17 (orange), V24 (green) and A42 (blue).

Figure S16. NCA spectrum of huPrP(23-144)-Aβ* (* species is ^{13}C, ^{15}N uniformly labeled), recorded at a temperature of ≈ 0 °C and a spinning frequency of 11 kHz. Blue circles indicate some identified amino acids.
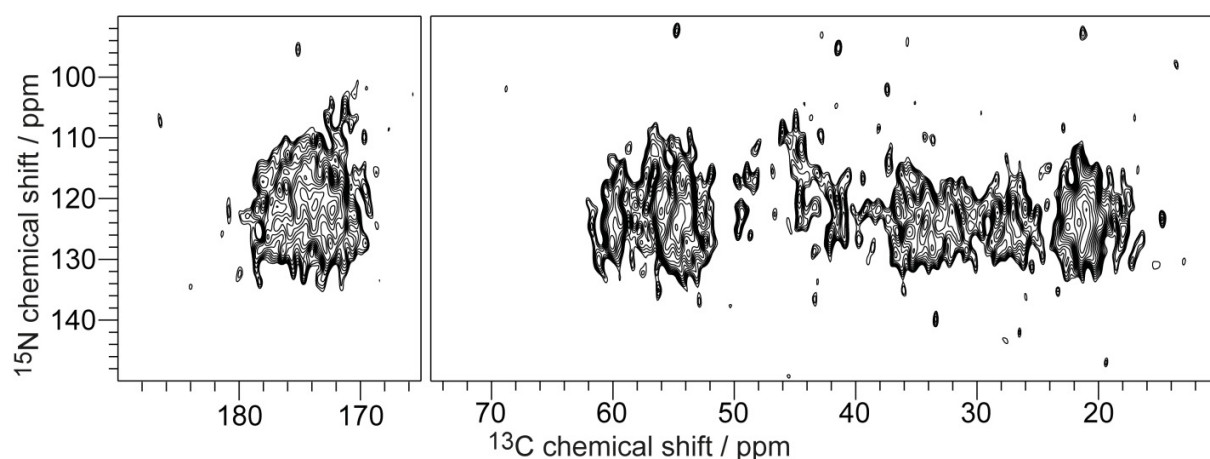
Figure S17. 2D NCACX spectrum of huPrP(23-144)-Aβ* (* species is ^{13}C, ^{15}N uniformly labeled), recorded at a temperature of ≈ 0 °C and a spinning frequency of 11 kHz.

Figure S18. Representative strip plot of huPrP(23-144)-Aβ* (* species is ^{13}C, ^{15}N uniformly labeled), 2D slices of 3D-NCACX (red) and 3D-NCOCX (black) spectra, recorded at a temperature of ≈ 0 °C, a spinning frequency of 11 kHz and subsequent DARR-mixing with 60 (NCACX) or 70 (NCOCX) ms mixing time. The sequential walk for residues Q15 to F20 is shown in blue.
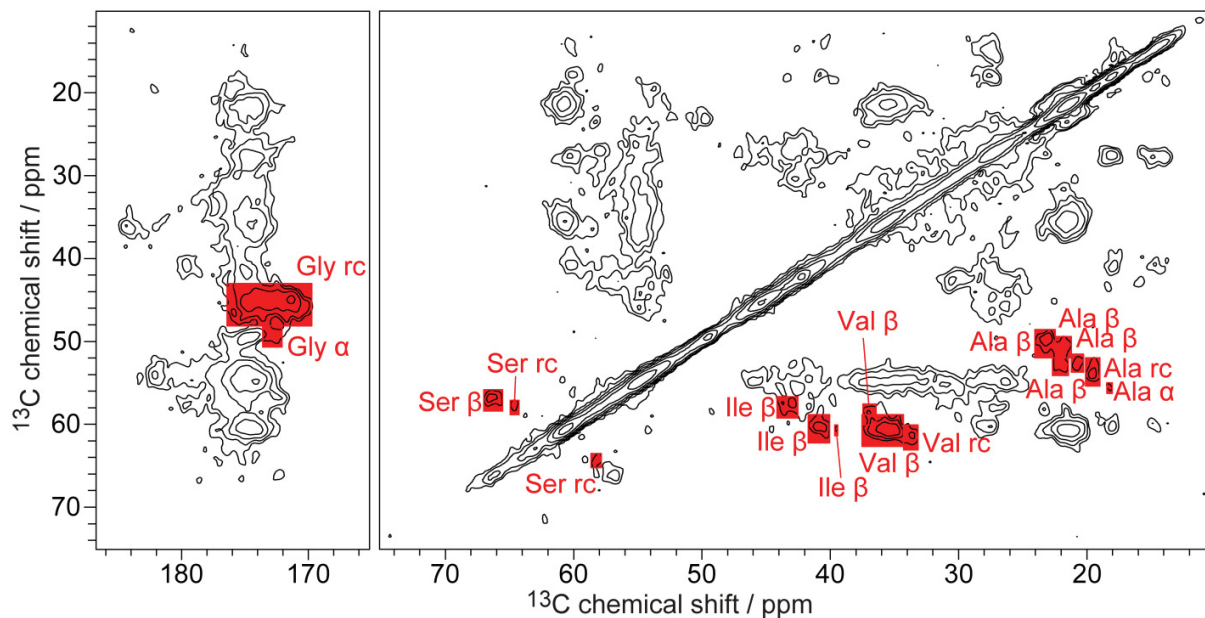
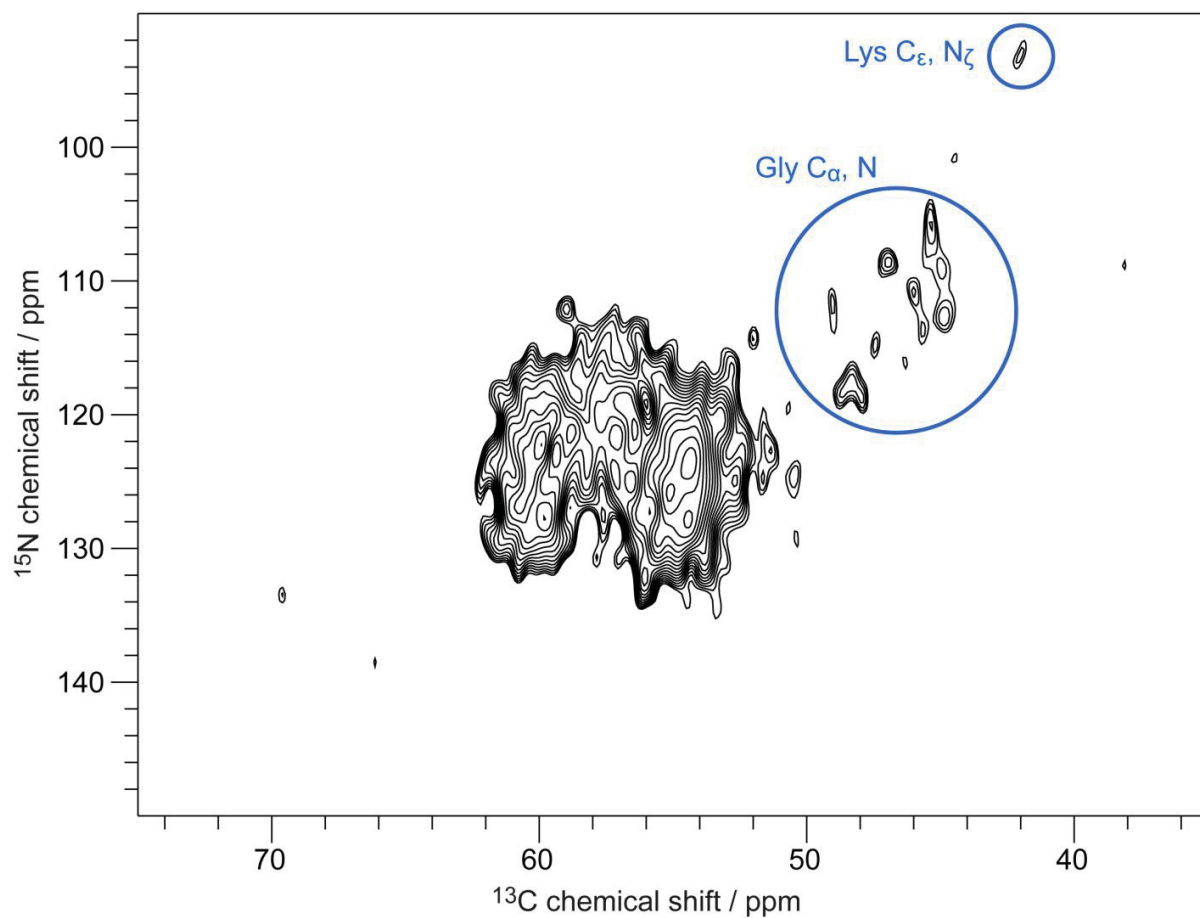**Figure S19.** 2D PDSD spectrum of huPrP(23-144)-Aβ* (* species is ^{13}C, ^{15}N uniformly labeled), recorded at a temperature of ≈ 0 °C, a spinning frequency of 11 kHz and a mixing time of 50 ms. α-helical (labeled with 'α'), unstructured (labeled with 'rc', random coil) and β-strand like (labeled with 'β') conformations were integrated by the box sum method in Topspin (red boxes).
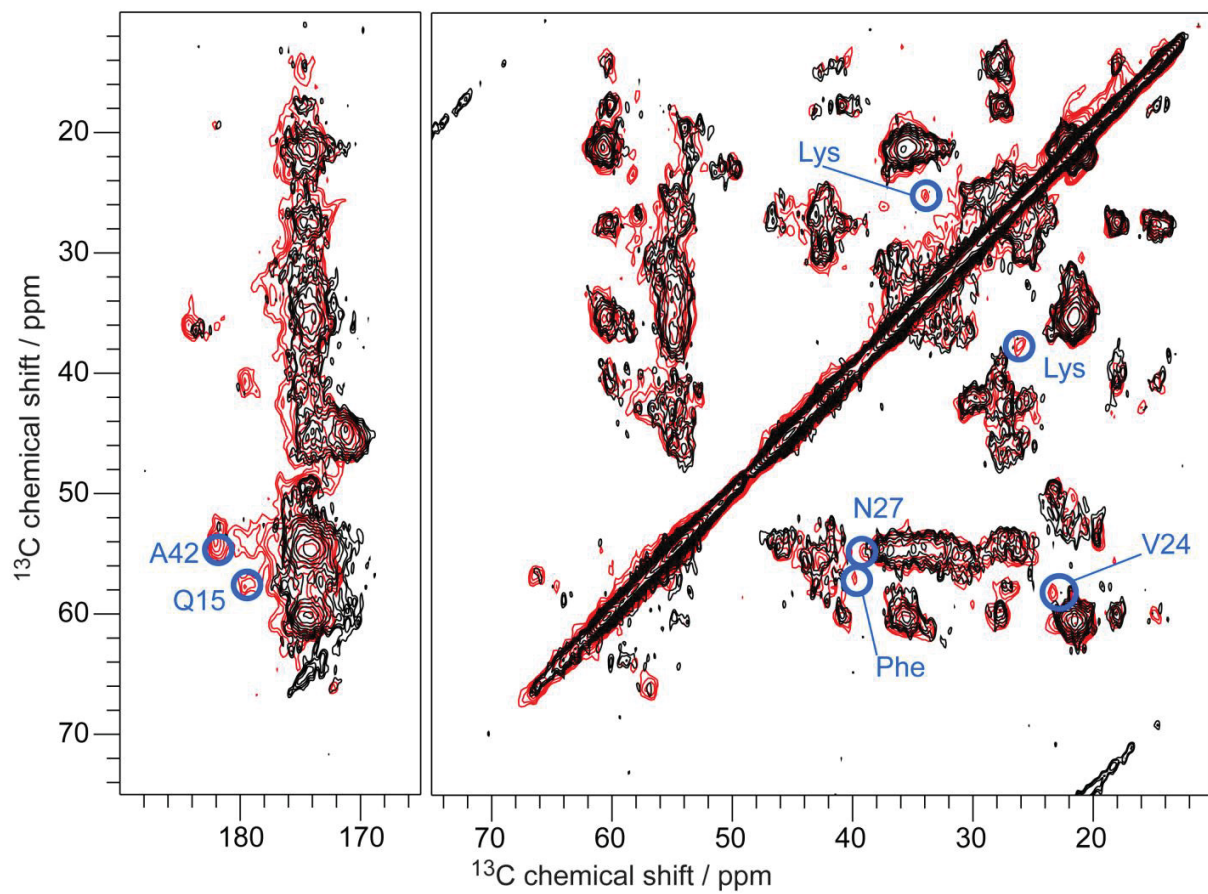
Figure S20. PDSD spectra of huPrP(23-144)-Aβ* (red) (* species is ^{13}C, ^{15}N uniformly labeled) and huPrP(23-144)$_{exc}$-Aβ* (black) ($_{exc}$ huPrP is in excess; * species is ^{13}C, ^{15}N uniformly labeled), recorded at a temperature of ≈ 0 °C, at a spinning frequency of 11 kHz and a mixing time of 50 ms at either a 600 MHz (huPrP(23-144)-Aβ*) or 800 MHz (huPrP(23-144)$_{exc}$-Aβ*) spectrometer. Blue circles highlight differences between the two samples.

Figure S21. Overlay of a PDSD spectrum (blue) of huPrP(23-144)-Aβ* (* species is ^{13}C, ^{15}N uniformly labeled), recorded at a temperature of ≈ 0 °C, a spinning frequency of 11 kHz and a mixing time of 50 ms (same spectrum as in **Figure 5**), and a DARR spectrum (red) of the Aβ(1-42) fibril at pH 7.4 of Colvin et al. (98), recorded at a ω(^{1}H)/2π field strength of 800 MHz, a temperature of 277 K, a spinning frequency of 20 kHz and a mixing time of 80 ms. There is substantial signal overlap, but for the Aβ(1-42) fibril line widths are much smaller. Picture adapted with permission of ref. (98).
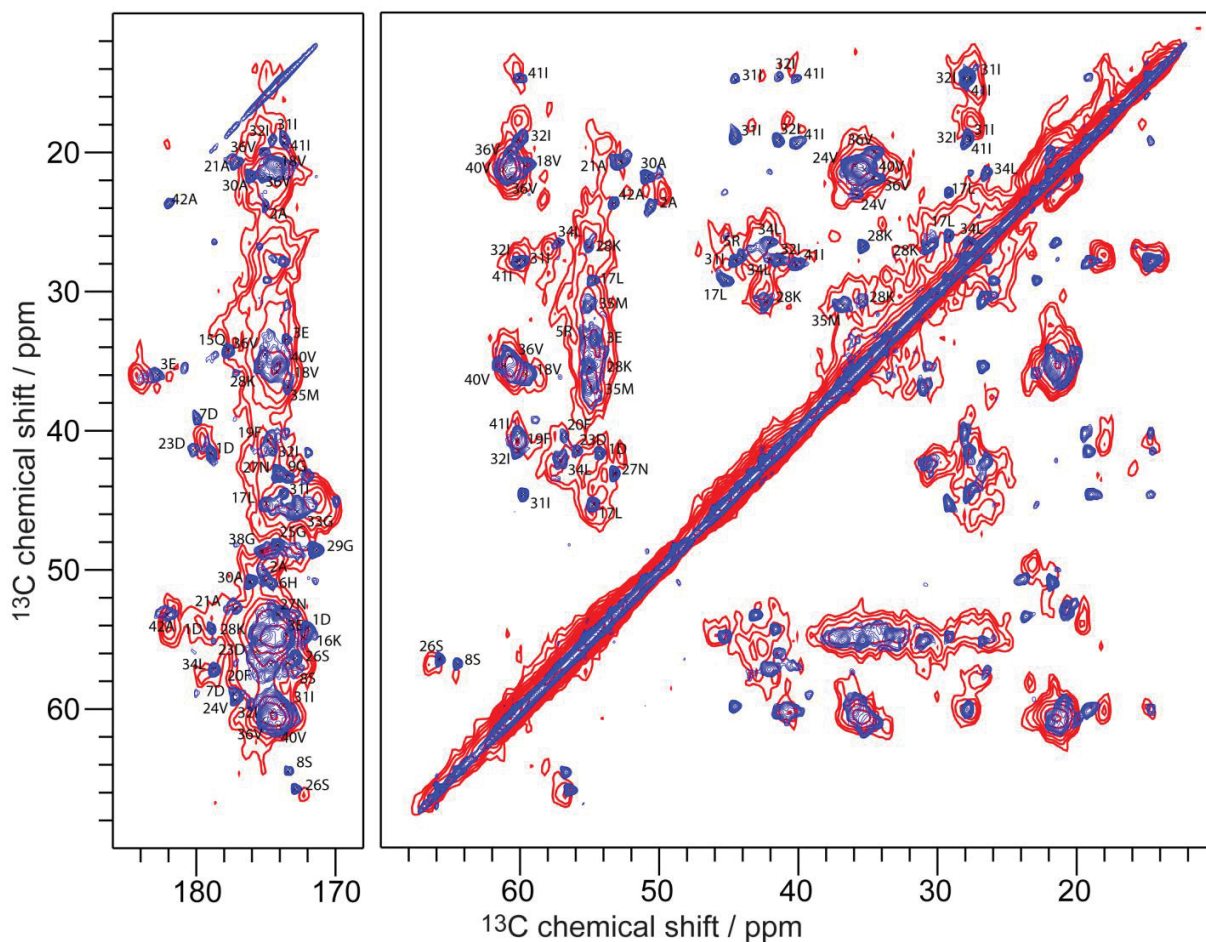
Figure S22. Overlay of a PDSD spectrum (red) of huPrP(23-144)-Aβ* (* species is ^{13}C, ^{15}N uniformly labeled), recorde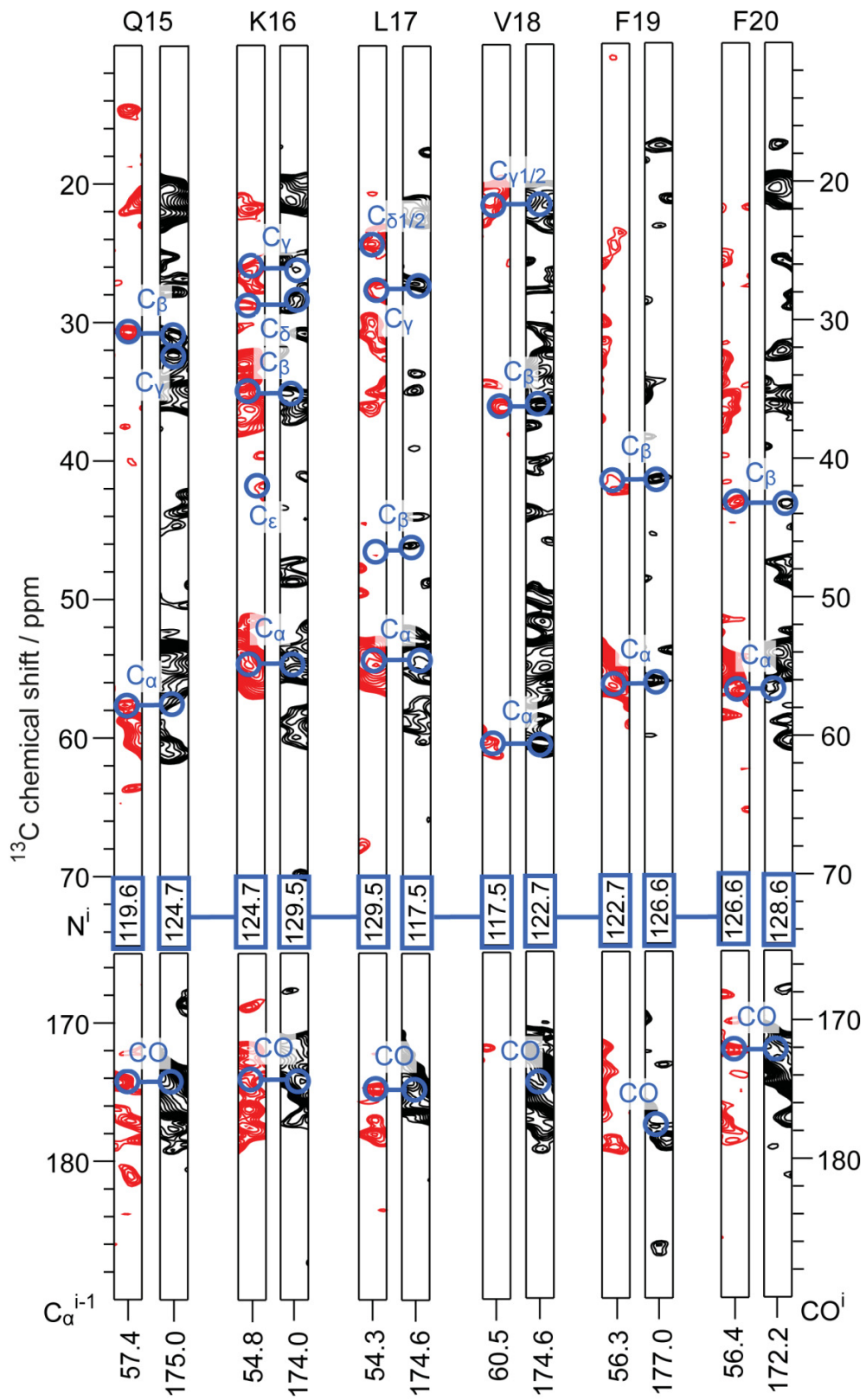d at a temperature of ≈ 0 °C, a spinning frequency of 11 kHz and a mixing time of 50 ms (same spectrum as in **Figure 5**), and a DARR spectrum (blue) of the Aβ(1-42) fibril at pH 7.4 of Ravotti et al. (99), recorded at a magnetic field strength of 20.0 T, a spinning frequency of 17 kHz and a mixing time of 20 ms. There is substantial signal overlap, but for the Aβ(1-42) fibril line widths are much smaller. Picture adapted with permission of ref. (99).

Figure S23. Overlay of two PDSD spectra of huPrP(23-144)-Aβ* (* species is ^{13}C, ^{15}N uniformly labeled), recorded at a temperature of ≈ 0 °C, a spinning frequency of 11 kHz and a mixing time of 50 ms (red, same spectrum as in **Figure 5**), and of the Aβ(1-42) fibril at pH 2 of Gremer et al. (blue) (47), recorded at a magnetic field strength of 18.8 T, a temperature of 0±5 °C, a spinning frequency of 12.5 kHz and a mixing time of 20 ms. There is substantial signal overlap, but for the Aβ(1-42) fibril line widths are much smaller. Picture adapted with permission of ref. (47).
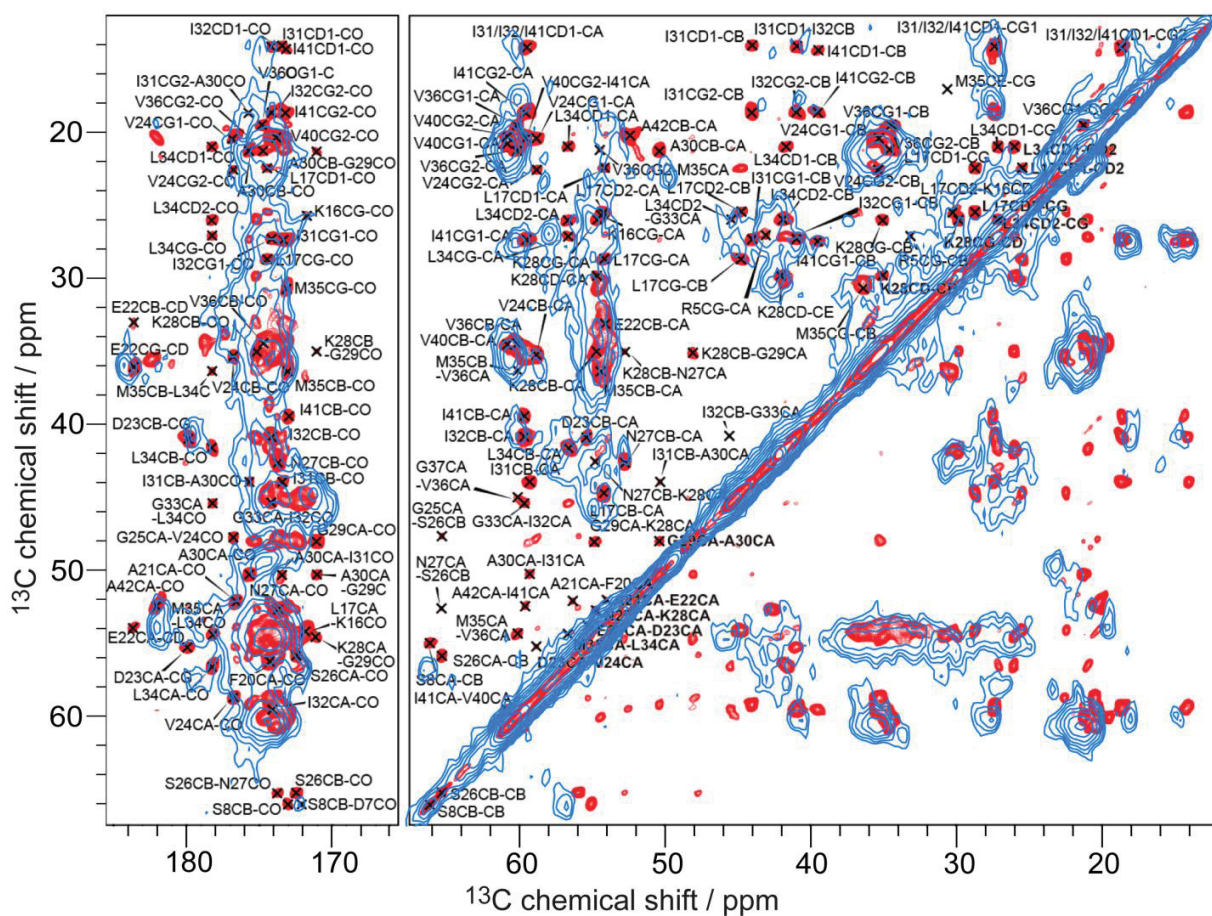
Figure S24. Overlay of a PDSD spectrum (red) of huPrP(23-144)-Aβ* (* species is ^{13}C, ^{15}N uniformly labeled), recorded at a temperature of ≈ 0 °C, a spinning frequency of 11 kHz and a mixing time of 50 ms (same spectrum as in **Figure 5**), and a DARR spectrum (black) of a hexameric Aβ42cc protofibril (mutated at A21C, A30C) of Lendel et al. (13), recorded at a ω(^{1}H)/2π field strength of 700 MHz, a temperature of ≈ 4 °C, a spinning frequency of 12 kHz and a mixing time of 50 ms. There is some signal overlap, although some peaks are not existing in the other Aβ species, but line widths are almost similar. Picture adapted with permission of ref. (13).

Table S1. Chemical shifts of unambiguously assigned resonances in huPrP(23-144)-Aβ* (* species is ^{13}C, ^{15}N uniformly labeled).

#	Amino acid	N (ppm)	CO (ppm)	CA (ppm)	CB (ppm)	CG1 (ppm)	CG2 (ppm)	CD1 (ppm)	CD2 (ppm)	CE1 (ppm)	CE2 (ppm)	CZ (ppm)	ND2 (ppm)	NE1 (ppm)	NE2 (ppm)	NZ (ppm)
1	D															
2	A															
3	E															
4	F															
5	R	122.4	174.4	54.5	30.3	28.1		42.2				-		-		
5	R	126.7	-	53.3	30.9	25.0		43.7				165.0		67.7		
6	H	-	-	-	-	-			-	-					-	
7	D															
8	S															
9	G															
10	Y															
11	E															
12	V															
13	H	-	-	-	-	-			-	-					-	
14	H	-	-	-	-	-			-	-					-	
15	Q	119.6	175.0	57.4	30.5	32.2		179.9							124.3	
16	K	124.7	174.0	54.8	35.3	25.9		28.4		42.1						34.8
17	L	129.5	174.6	54.3	46.5	27.2		24.8	24.8							
18	V	117.5	174.6	60.5	35.5	21.2	21.2									
19	F	122.7	177.0	56.3	41.0	137.1		131.7	131.7	130.8	130.8	129.0				
20	F	126.6	172.2	56.4	43.5	137.3		131.8	131.8	129.9	129.9	127.5				
21	A															
22	E															
23	D	123.3	174.6	54.6	41.6	178.9										
24	V	122.1	176.6	58.2	36.8	23.2	21.6									
25	G	113.6	171.3	45.8												
26	S	119.5	172.2	56.6	66.2											
27	N	116.4	174.9	53.0	43.2	179.1							114.3			
27	N	129.9	174.1	54.8	38.5	177.1							124.8			
28	K	119.1	176.8	54.4	33.7	25.1		28.8		42.2						32.9
29	G	116.7	172.6	49.2												
30	A	124.4	175.1	49.5	22.9											

31	I	124.1	173.9	57.7	43.0	27.0	18.1	15.4
32	I	126.9	174.7	60.2	40.7	27.4	17.9	14.7
33	G	119.1	173.8	48.6				
34	L							
35	M	-	-	-	-	-		
36	V							
37	G							
38	G							
39	V							
40	V	120.6	175.0	60.6	32.0	21.6	21.6	
41	I	122.3	175.3	60.2	39.4	27.5	17.9	13.9
42	A	117.3	182.1	53.9	19.4			

S-30

Table S2. Overview of the performed solid-state NMR measurements.

experiment	description	dimen-sions	transfer	purpose	samples
INEPT (75)	insensitive nuclei enhanced by polarization transfer	1D	^{1}H to ^{13}C	to selectively excite mobile regions	huPrP(23-144)*-Aβ huPrP(23-230)*-Aβ huPrP(23-144)-Aβ* huPrP(23-144)$_{exc}$-Aβ*
CP	cross polarization	1D	^{1}H to ^{13}C	to excite rigid parts	huPrP(23-144)*-Aβ huPrP(23-230)*-Aβ huPrP(23-144)-Aβ* huPrP(23-144)$_{exc}$-Aβ*
			^{1}H to ^{15}N	to excite rigid parts	huPrP(23-144)*-Aβ huPrP(23-144)-Aβ* huPrP(23-144)$_{exc}$-Aβ*
PDSD (76)	proton driven spin diffusion	2D	^{13}C to ^{13}C	to excite all correlations	huPrP(23-144)*-Aβ huPrP(23-230)*-Aβ huPrP(23-144)-Aβ* huPrP(23-144)$_{exc}$-Aβ*
DARR	dipolar assisted rotational resonance	2D	^{13}C to ^{13}C	to excite all correlations	huPrP(23-144)-Aβ*
DQ-SPC5 (77)	double quantum excitation with SPC5-recoupling	2D	^{13}C to ^{13}C	to excite only one-bond correlations	huPrP(23-144)*-Aβ huPrP(23-144)-Aβ*
NCA (78)	with SPECIFIC-CP	2D	^{15}N to ^{13}Cα	frequency selective polarization transfers from ^{15}N to ^{13}Cα	huPrP(23-144)*-Aβ huPrP(23-144)-Aβ*
NCACX (78)	with SPECIFIC-CP	2D and 3D	^{15}N to ^{13}Cα to ^{13}C$_{sidechain}$	frequency selective polarization transfers from ^{15}N to ^{13}Cα, subsequent DARR mixing to distribute magnetization to side chains	huPrP(23-144)-Aβ*
NCOCX (78)	with SPECIFIC-CP	3D	^{15}N to ^{13}CO to ^{13}C$_{sidechain}$	frequency selective polarization transfers from ^{15}N to ^{13}CO, subsequent DARR mixing to distribute magnetization to side chains	huPrP(23-144)-Aβ*

Table S3. Experimental parameters for solid-state NMR measurements of sample huPrP(23-144)*-Aβ (* species is ^{13}C, ^{15}N uniformly labeled).

Sample huPrP(23-144)*-Aβ	HC CP	HN CP	INEPT	PDSD	SPC5_2	NCA
	1D	1D	1D	2D	2D	2D
Mixing time (ms)	-	-	-	1) 20 2) 30 3) 50 4) 100 5) 200 6) 200 R²	-	-
^{1}H frequency (MHz)	600	600	600	600	600	600
MAS (kHz)	11	11	4	1) & 2) & 3) & 4) & 5) 11 6) 9.375	8	11
VT gas temperature (°C)	-10	-16	RT	1) & 3) & 4) -10 2) & 5) & 6) -16	-16	-16
Transfer 1	HC CP	HN CP	INEPT	HC CP	HC CP	HN CP
Carrier (ppm)	70.525	119.979	70.525	1) & 3) & 4) 70.525 2) & 5) & 6) 90.046	70.525	119.973
Duration of 1st transfer (µs)	200	600	-	1) & 3) & 4) 200 2) & 5) & 6) 350	300	600
Transfer 2	-	-	-	-	SPC5	N-CA CP
Carrier (ppm)	-	-	-	-	60.579	57.058
Duration of 2nd transfer (µs)	-	-	-	-	-	1800
^{13}C rf field (kHz)	-	-	-	-	-	8.205
^{15}N rf field (kHz)	-	-	-	-	-	18.803
t_1 increments	454	136	454	1) & 3) & 4) 454 2) & 5) & 6) 379	454	366
t_1 spectral width (kHz)	37.879	13.587	37.879	37.879	37.879	30.488
t_2 increments	-	-	-	1) & 5) 180 2) 260 3) & 4) 128 6) 190	240	22
t_2 spectral width (kHz)	-	-	-	1) & 3) & 4) 29.996 2) & 5) 33.003 6) 37.700	40.000	3.600
Number of scans	256	2000	256	1) 128 2) & 3) & 4) 320	592	1600

				5) 216 6) 568		
Duration (h)	0.15	1.7	0.15	1) 26.25 2) 95 3) 47.25 4) 48.5 5) 43.75 6) 133.5	160.5	40

Table S4. Experimental parameters for solid-state NMR measurements of sample huPrP(23-230)*-Aβ (* species is ^{13}C, ^{15}N uniformly labeled).

Sample huPrP(23-230)*-Aβ

	^{13}C DE	^{13}C DE	^{13}C DE	HC CP	HC CP	HC CP	HC CP	INEPT	PDSD
	1D	1D	1D	1D	1D	1D	1D	1D	2D
Mixing time (ms)	-	-	-	-	-	-	-	-	1) 30 2) 50
^1H frequency (MHz)	600	600	600	600	600	600	600	600	600
MAS (kHz)	11	11	11	11	11	11	11	11	11
VT gas temperature (°C)	20	0	-20	20	0	-20	20	20	1) -10 2) 0
Transfer 1	-	-	-	HC CP	HC CP	HC CP	HC CP	INEPT	HC CP
Carrier (ppm)	79.967	79.967	79.967	79.967	79.967	79.967	79.967	79.967	79.967
Duration of 1st transfer (µs)	-	-	-	200	200	200	200	-	200
t_1 increments	750	750	750	750	750	750	750	750	750
t_1 spectral width (kHz)	62.500	62.500	62.500	62.500	62.500	62.500	62.500	62.500	62.500
t_2 increments	-	-	-	-	-	-	-	-	1) 140 2) 134
t_2 spectral width (kHz)	-	-	-	-	-	-	-	-	36.199
Number of scans	2304	1021	2400	512	512	512	512	5659	1) 1267 2) 272
Duration (h)	13	5.75	13.5	0.29	0.29	0.29	0.29	3.25	1) 201.75 2) 42

Table S5. Experimental parameters for solid-state NMR measurements of sample huPrP(23-144)-Aβ* (* species is ^{13}C, ^{15}N uniformly labeled).

Sample huPrP(23-144)-Aβ*

	HC CP	HN CP	INEPT	PDSD	DARR	SPC5_2	NCA	NCACX DARR	NCACX DARR	NCACX DARR	NCOCX DARR
	1D	1D	1D	2D	2D	2D	2D	2D	3D	3D	3D
Mixing time (ms)	-	-	-	1) 10 2) 30 3) 50 4) 50 5) 50 R² 6) 100 7) 200 8) 200 R² 9) 300	30	-	-	60	60	60	70
^{1}H frequency (MHz)	600	600	600	1) & 2) & 3) & 6) & 7) & 8) & 9) 600 4) & 5) 800	600	600	600	600	600	600	600
MAS (kHz)	11	11	8	1) & 2) & 3) & 4) & 6) & 7) & 9) 11 5) 12.5 8) 9.375	11	8	11	11	11	11	11
VT gas temperature (°C)	-10	-10	10	-10	-10	-10	-10	-10	-10	-10	-10
Transfer 1	HC CP	HN CP	INEPT	HC CP	HC CP	HC CP	HN CP	HN CP	HN CP	HN CP	HN CP
Carrier (ppm)	70.978	120.159	70.978	1) & 2) & 3) & 6) & 7) & 8) & 9) 70.978 4) & 5) 70.307	70.978	1) 70.525 2) 70.153	119.979	119.979	119.979	119.979	119.979
Duration of 1st transfer (µs)	400	500	-	400	400	1) 400 2) 500	900	900	900	900	900
Transfer 2	-	-	-	-	-	SPC5	N-CA CP	N-CA CP	N-CA CP	N-CA CP	N-CO CP
Carrier (ppm)	-	-	-	-	-	1) 67.210 2) 23.735	57.057	57.057	57.057	57.057	174.950

Parameter										
Duration of 2nd transfer (µs)	1800	1600	1600	1600	-	-	-	-	-	-
^{13}C rf field (kHz)	38.156	18.824-19.078	17.806-18.824	17.806	-	-	-	-	-	-
^{15}N rf field (kHz)	27.676	28.490-29.304	28.490-29.304	28.490	-	-	-	-	-	-
t_1 increments	536	402	536	366	1) 454 2) 536	1) & 2) & 3) & 6) & 7) & 8) & 9) 454 4) & 5) 1250	454	454	181	454
t_1 spectral width (kHz)	59.524	44.643	44.643	30.488	1) 37.879 2) 44.643	1) & 2) & 3) & 6) & 7) & 8) & 9) 37.879 4) & 5) 104.167	37.879	37.879	18.116	37.879
t_2 increments	12	18	22	22	1) & 2) 240	1) & 2) & 3) & 6) & 7) & 9) 200 4) & 5) 264 8) 225	200	-	-	-
t_2 spectral width (kHz)	2.400	3.600	3.600	3.600	1) & 2) 40.000	1) & 2) & 3) & 6) & 7) & 9) 33.003 4) & 5) 44.000 8) 37.700	33.003	-	-	-
t_3 increments	13	20	-	-	-	-	-	-	-	-
t_3 spectral width (kHz)	3.300	5.100	-	-	-	-	-	-	-	-
Number of scans	1072	736	1696	864	1) 320 2) 496	1) 304 2) & 3) & 5) & 7) 288 4) 224 6) 368 8) 320 9) 352	288	256	2000	128
Duration (h)	387.75	612	159.25	21.25	1) 86.75 2) 133.25	1) 69 2) 66 3) & 4) 66.5	66	0.15	1.75	0.08

5) & 6) 87
7) 71.25
8) 89
9) 91

Table S6. Experimental parameters for solid-state NMR measurements of sample huPrP(23-144)$_{exc}$-Aβ* (* species is ^{13}C, ^{15}N uniformly labeled).

Sample huPrP(23-144)$_{exc}$-Aβ*

	HC CP	HN CP	INEPT	PDSD
	1D	1D	1D	2D
Mixing time (ms)	-	-	-	1) 50
				2) 50 (after 4 months)
^{1}H frequency (MHz)	800	800	800	800
MAS (kHz)	5	11	8	11
VT gas temperature (°C)	-3	-10	10	-10
Transfer 1	HC CP	HN CP	INEPT	HC CP
Carrier (ppm)	70.183	124.191	70.000	70.183
Duration of 1sttransfer (μs)	600	600	-	600
t$_1$ increments (half of STATES-TPPI)	778	949	778	778
t$_1$ spectral width (kHz)	52.083	59.524	52.083	52.083
t$_2$ increments (half of STATES-TPPI)	-	-	-	256
t$_2$ spectral width (kHz)	-	-	-	50.505
Number of scans	256	2048	1024	432
Duration (h)	0.15	3	0.5	127.75

Table S7. Overview of the performed solution NMR measurements.

experiment	description	dimensions	transfer	purpose	Samples
HSQC	heteronuclear single-quantum coherence	2D	^1H to ^{15}N and back	amide groups	huPrP(23-144) monomers
HNCO	triple resonance	3D	^1H to ^{15}N to ^{13}CO and back	resonance assignment	huPrP(23-144) monomers
HNCACB	triple resonance	3D	^1H to ^{15}N to $^{13}C\alpha$ to $^{13}C\beta$ and back	resonance assignment	huPrP(23-144) monomers
BEST-TROSY-(H)N(COCA)NH	triple resonance	3D	^1H to ^{15}N to ^{13}CO to $^{13}C\alpha$ to ^{15}N to ^1H	resonance assignment	huPrP(23-144) monomers
TOCSY	total correlated spectroscopy	2D	^{13}C to ^{13}C	to excite all correlations	huPrP(23-144) monomers Aβ monomers

A D-enantiomeric peptide interferes with heteroassociation of amyloid-β oligomers and prion protein

Nadine S. Rösener[‡§], Lothar Gremer[‡§], Elke Reinartz[‡], Anna König[§], Oleksandr Brener[‡§], Henrike Heise[‡§], Wolfgang Hoyer[‡§], ◉ Philipp Neudecker[‡§], and ◉ Dieter Willbold[‡§1]

From the ‡Institut für Physikalische Biologie, Heinrich-Heine-Universität Düsseldorf, 40225 Düsseldorf, Germany and §Institute of Complex Systems, Structural Biochemistry (ICS-6), Forschungszentrum Jülich, 52425 Jülich, Germany

Edited by Paul E. Fraser

Alzheimer's disease (AD) is a progressive neurodegenerative disorder that affects millions of people worldwide. One AD hallmark is the aggregation of β-amyloid (Aβ) into soluble oligomers and insoluble fibrils. Several studies have reported that oligomers rather than fibrils are the most toxic species in AD progression. Aβ oligomers bind with high affinity to membrane-associated prion protein (PrP), leading to toxic signaling across the cell membrane, which makes the Aβ–PrP interaction an attractive therapeutic target. Here, probing this interaction in more detail, we found that both full-length, soluble human (hu) PrP(23–230) and huPrP(23–144), lacking the globular C-terminal domain, bind to Aβ oligomers to form large complexes above the megadalton size range. Following purification by sucrose density–gradient ultracentrifugation, the Aβ and huPrP contents in these heteroassemblies were quantified by reversed-phase HPLC. The Aβ:PrP molar ratio in these assemblies exhibited some limited variation depending on the molar ratio of the initial mixture. Specifically, a molar ratio of about four Aβ to one huPrP in the presence of an excess of huPrP(23–230) or huPrP(23–144) suggested that four Aβ units are required to form one huPrP-binding site. Of note, an Aβ-binding all-D-enantiomeric peptide, RD2D3, competed with huPrP for Aβ oligomers and interfered with Aβ–PrP heteroassembly in a concentration-dependent manner. Our results highlight the importance of multivalent epitopes on Aβ oligomers for Aβ–PrP interactions and have yielded an all-D-peptide–based, therapeutically promising agent that competes with PrP for these interactions.

Alzheimer's disease (AD)[2] is the most common cause of dementia in the elderly population. One of its hallmarks is the accumulation of extracellular neuritic plaques consisting mainly of fibrillar β-amyloid (Aβ) peptide (1). Initially, these plaques were thought to be the toxic species in AD, but several lines of evidence now indicate that the levels of soluble oligomeric forms of Aβ (Aβ_oligo) correlate best with the neurotoxic effects observed during AD (2, 3).

Many Aβ receptors have been described to date (4). One of them is the cellular prion protein (PrP^C), which binds Aβ_oligo with nanomolar affinity (5–10). PrP^C is a glycosylphosphatidylinositol (GPI)-anchored glycoprotein highly expressed in the brain. PrP^C itself can misfold into the scrapie isoform PrP^Sc sporadically or after infection, leading to neuronal damage and disease such as the transmissible spongiform encephalopathies (11). The interaction of Aβ_oligo with PrP^C bound to the metabotropic glutamate receptor 5 leads to toxic signaling across the cell membrane by activating intracellular Fyn kinase (12, 13). Fyn kinase phosphorylates N-methyl-D-aspartate (NMDA) receptors (14, 15) and alters NMDA receptor localization, leading to destabilization of dendritic spines (12). Furthermore, Fyn kinase hyperphosphorylates the tau protein, which assembles into neurofibrillary tangles, a further hallmark of AD (16). Hyperphosphorylation of tau depends on the Aβ–PrP interaction (17). Therefore, understanding the Aβ–PrP pathway will open new therapeutic strategies by targeting the Aβ–PrP interaction (18).

The binding regions of Aβ_oligo have been mapped to residues 23–27 and ~95–110 in the N-terminal part of PrP (5, 19–22) (see Fig. 1A). Soluble N-terminal PrP fragments inhibit the assembly of Aβ into amyloid fibrils and block neurotoxic effects of soluble oligomers (20, 23), presumably by competing with membrane-anchored PrP^C for Aβ_oligo. This competition might also explain the suggested neuroprotective function of the naturally produced soluble N1 fragment (amino acids 23–110/111) of PrP (24), which contains both Aβ_oligo-binding regions. The binding regions on Aβ, however, have not been identified so far and might constitute a specific conformational epitope of Aβ_oligo (21). All these data show that the Aβ–PrP interaction is a promising point of intervention to prevent the toxic signaling in AD.

[1] To whom correspondence should be addressed: Institut für Physikalische Biologie, Heinrich-Heine-Universität Düsseldorf, 40204 Düsseldorf, Germany. E-mail: d.willbold@fz-juelich.de.
[2] The abbreviations used are: AD, Alzheimer's disease; Aβ, β-amyloid; PrP, prion protein; Aβ_oligo, soluble oligomeric forms of Aβ; PrP^C, cellular prion protein; GPI, glycosylphosphatidylinositol; PrP^Sc, scrapie isoform of PrP; NMDA, N-methyl-D-aspartate; QIAD, quantitative determination of interference with Aβ aggregate size distribution; DGC, density–gradient ultracentrifugation; RP, reversed-phase; huPrP, human PrP; AFM, atomic force microscopy; IMAC, immobilized metal ion affinity chromatography; Tricine, N-[2-hydroxy-1,1-bis(hydroxymethyl)ethyl]glycine; DLS, dynamic light scattering; MTT, 3-(4,5-dimethylthiazol-2-yl)-2,5-diphenyltetrazolium bromide.

SASBMB

In the past years, we have identified a number of D-enantiomeric peptides as promising drug candidates for direct elimination of Aβ(1–42)$_{oligo}$ (25–30). The advantage of D-peptides over L-peptides is their higher protease resistance, resulting in slower degradation and longer half-life (31, 32). For Aβ(1–42)-directed D-peptides, high stability in media simulating the route of orally administered drugs (33) and enhanced proteolytic stability in murine plasma and organ homogenates were shown (34). The lead compound of these D-peptides, D3, had been selected by mirror-image phage display (26, 35). D3 and its tandem version, D3D3, convert toxic Aβ species into nontoxic species (25, 28). Treatment with D3 reduces the number of amyloid plaques (26) and improves cognition in transgenic AD mice (28). One derivative of D3 called RD2 shows enhanced binding to Aβ (36, 37), and both RD2 and D3 have demonstrated desirable pharmacokinetic properties (29, 38). A further promising derivative is the D-peptide RD2D3, a head-to-tail tandem combination of RD2 and D3 (30, 34, 39). RD2D3 binds Aβ(1–42) with a K_D of 486 ± 69 nM (39). All of these therapeutically promising D-peptides contain a high fraction of basic residues, which is reminiscent of the proposed binding sites for Aβ on PrP (5, 19–21). Therefore, the Aβ-binding D-peptides might be suitable compounds for interference with the Aβ–PrP interaction by competing with PrP for Aβ(1–42)$_{oligo}$.

Recently, we introduced the "quantitative determination of interference with Aβ aggregate size distribution" (QIAD) assay, which allows the determination of a compound's efficacy to eliminate Aβ(1–42)$_{oligo}$ (25). This assay enables the separation of Aβ assemblies by density–gradient ultracentrifugation (DGC) and the quantification of these assemblies by UV-detected reversed-phase (RP)-HPLC. For the present study, we have refined the QIAD assay to achieve simultaneous quantification of Aβ(1–42), recombinant anchorless human PrP (huPrP) constructs, and D-peptides in a single RP-HPLC run to (i) characterize the Aβ-huPrP interaction in detail and (ii) evaluate the influence of the tandem D-peptide RD2D3 on this interaction. We investigated four different huPrP protein constructs, namely huPrP(23–230), huPrP(23–144), huPrP(90–230), and huPrP(121–230) (see Fig. 1A), and added them in different concentrations to preformed Aβ(1–42)$_{oligo}$. In the case of huPrP(23–230) and huPrP(23–144), this resulted in high-molecular-weight Aβ(1–42)$_{oligo}$–huPrP complexes. The separation of these complexes from Aβ(1–42) or huPrP monomers and Aβ(1–42)$_{oligo}$ by sucrose DGC and subsequent RP-HPLC analytics (see Fig. 1B) allowed the determination of molar ratios between Aβ(1–42) and huPrP within the complexes. We show that these ratios are dependent on the concentration of huPrP added. We imaged Aβ(1–42)$_{oligo}$–huPrP(23–144) complexes by atomic force microscopy (AFM) and observed a correlation between the applied huPrP(23–144) concentration and the size and morphology of the heteroassemblies. We analyzed the influence of the D-peptide RD2D3 on the Aβ(1–42)$_{oligo}$–huPrP(23–144) interaction by determining its effect on the Aβ(1–42):huPrP ratio within the assemblies. We show that RD2D3 competes with the Aβ(1–42)$_{oligo}$–huPrP(23–144) interaction and might thus be a potential therapeutic agent.

Results

Aβ(1–42)$_{oligo}$ and all huPrP protein constructs are soluble when analyzed separately

In addition to full-length huPrP (huPrP(23–230)), three huPrP deletion constructs were investigated: the N-terminal fragment huPrP(23–144) and the C-terminal fragments huPrP(90–230) and huPrP(121–230) (Fig. 1A). huPrP(23–230) and huPrP(23–144) contain both regions (residues 23–27 and ~95–110) described to be necessary for high-affinity binding of Aβ(1–42)$_{oligo}$ (5, 19–22). In huPrP(90–230), the N-terminal binding region (residues 23–27) is missing, whereas in huPrP(121–230) the second binding region (residues ~95–110) is missing as well. All huPrP protein constructs were expressed in *Escherichia coli*. Therefore, they did not contain any posttranslational modifications (glycosylation or GPI anchor). They were purified either by immobilized metal ion affinity chromatography (IMAC) or by size exclusion chromatography and subsequent RP-HPLC, yielding highly pure samples as confirmed by SDS-PAGE and analytical RP-HPLC (Fig. S1). The purified huPrP(23–230), huPrP(90–230), and huPrP(121–230) proteins contain the disulfide bond between Cys-179 and Cys-214 as confirmed by comparative RP-HPLC analyses of the purified *versus* their tris(2-carboxyethyl)phosphine hydrochloride–reduced states (Fig. S2).

Before investigating the Aβ(1–42)$_{oligo}$–huPrP interaction, we checked the binding partners separately in their purified states to confirm that they remain soluble at the chosen buffer conditions, which were a compromise between neutral pH and conditions required for stability of Aβ oligomers and detergent-free solubility of huPrP constructs favoring absence of phosphate and low salt. This is of note as all huPrP protein constructs (40–43) as well as Aβ (44, 45) are able to convert into fibrils under certain conditions, and such a conversion may hamper the analysis of Aβ(1–42)$_{oligo}$–huPrP complexes. We performed CD spectroscopy analysis of huPrP(23–144), huPrP(23–230), and huPrP(90–230); solution NMR spectroscopy of huPrP(23–144) and huPrP(23–230); and AFM measurements of huPrP(23–144).

CD spectroscopy of huPrP(23–144) (Fig. 2A) indicated a disordered conformation at neutral pH, consistent with reports in the literature (46). In addition, AFM measurements of huPrP(23–144) confirm the absence of fibrils or large aggregates. Here, huPrP(23–144) forms a thin film on the mica surface with a height of 1–2 nm. Very rarely, single amorphous particles were observed (Fig. 2B). CD spectroscopy of the C-terminal huPrP(90–230) construct and full-length huPrP(23–230) (Fig. 2A) both showed the predominantly α-helical structures typical for the native prion protein fold (47) rather than the predominantly β-sheet conformation of amyloid fibrils.

The solubility and overall conformational properties of huPrP(23–230) and huPrP(23–144) were confirmed in more detail by solution NMR spectroscopy. The solution structure of huPrP had originally been determined in acetate buffer at pH 4.5 and 20 °C (47) and found to comprise a highly disordered N-terminal region (residues 23–124) followed by a globular C-terminal domain (residues 125–228) featuring three long α-helices and a relatively small two-stranded antiparallel β-sheet.

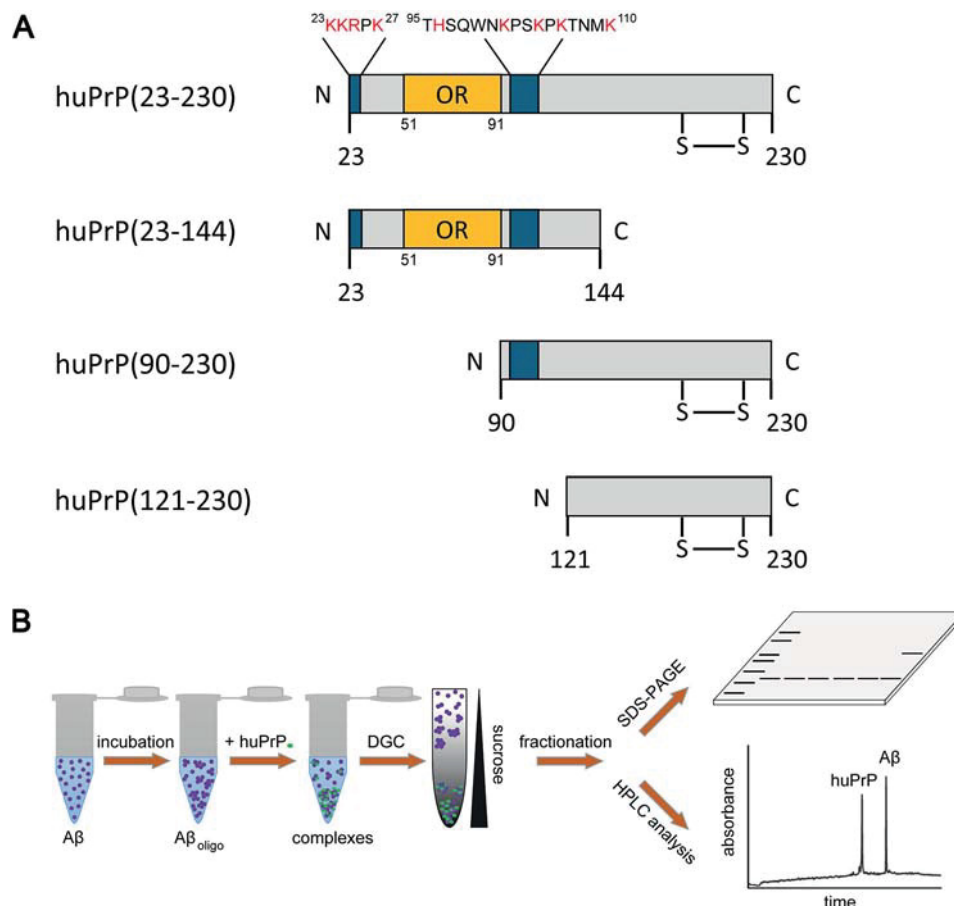## Interference with Aβ–PrP complex formation

Figure 1. Schematics of the investigated huPrP constructs huPrP(23–230), huPrP(23–144), huPrP(90–230), and huPrP(121–230) (A) and of the assay to quantify the composition of heteroassemblies (B). *A*, the binding sites for Aβ(1–42)$_{oligo}$ (5, 19–22) are marked in *blue*, and the corresponding sequence is shown in the huPrP(23–230) construct with basic amino acid residues highlighted in *red*. *OR* marks the octarepeat region from residues 51 to 91. huPrP(23–230), huPrP(90–230), and huPrP(121–230) contain a disulfide bond between Cys[179] and Cys[214] in the structured C-terminal part of the protein. *B*, 80 μM Aβ(1–42) was incubated for 2 h to obtain Aβ(1–42)$_{oligo}$ before different quantities of the respective prion protein were added to the sample. After 30-min coincubation, the sample was separated by sucrose DGC and fractionated. Each fraction was analyzed by SDS-PAGE as well as by quantitative RP-HPLC.
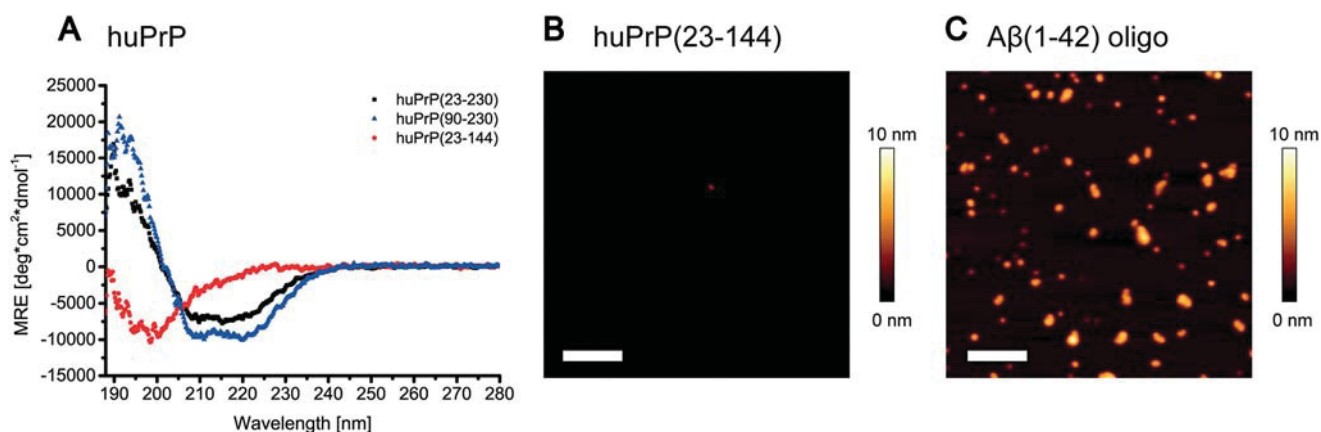

Figure 2. Analysis of purified huPrP by CD spectroscopy (A) and AFM (B) and of Aβ(1–42)$_{oligo}$ by AFM (C). huPrP(23–230) (*A*, *black*) and huPrP(90–230) (*A*, *blue*) show predominantly α-helical CD spectra, whereas the N-terminal huPrP(23–144) (*A*, *red*) is present in random-coil conformation (*MRE*, mean residue ellipticity; *deg*, degrees). Shown are 1-μm² AFM images of 200 nM huPrP(23–144) (*B*) or 800 nM Aβ(1–42)$_{oligo}$ (*C*). *Scale bars*, 200 nm. huPrP(23–144) forms a thin film on the mica surface, not higher than 1–2 nm (*B*). The generated Aβ(1–42)$_{oligo}$ species are seen as spherical particles with heights ranging from 1 to 6 nm (*C*).

Under these buffer conditions, we indeed obtained well dispersed solution NMR spectra of excellent quality for huPrP(23–230) (Fig. S3*A*) with sharp narrow line shapes and chemical shifts similar to those reported in the literature (47), thereby demonstrating that the protein is soluble and natively folded. huPrP(23–144) also exhibits high-quality solution NMR spectra under these buffer conditions (Fig. S3*A*). As expected for huPrP(23–144), only backbone amide resonances in the random-coil region (^{1}H chemical shifts between about 8.0 and 8.6 ppm (48)) were observed (Fig. S3*A*), suggesting that not only
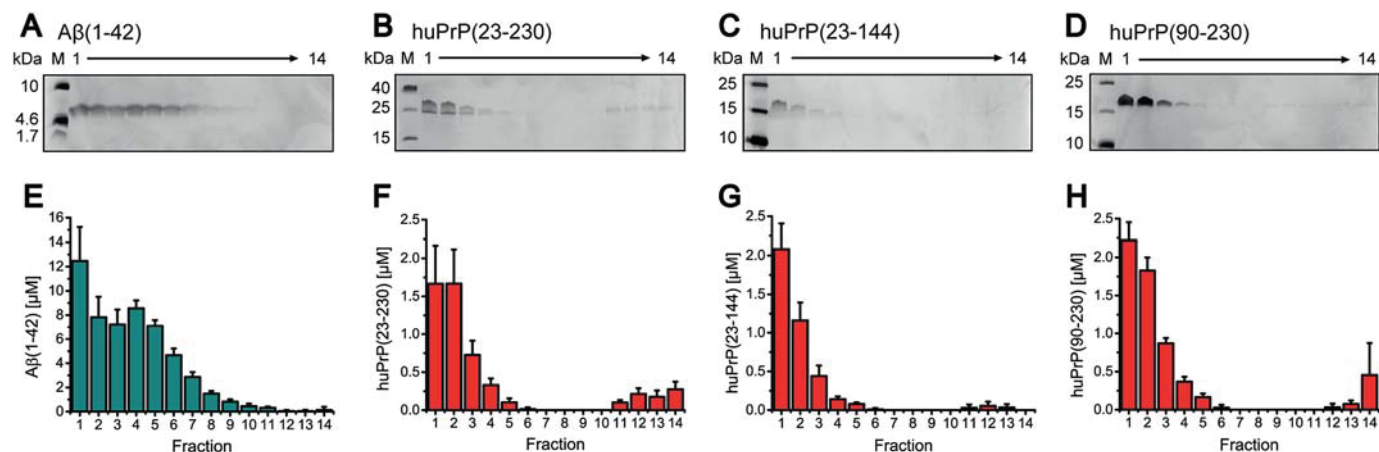
Figure 3. Distribution of incubated Aβ(1–42) (*A* and *E*), huPrP(23–230) (*B* and *F*), huPrP(23–144) (*C* and *G*), and huPrP(90–230) (*D* and *H*) after sucrose DGC. Silver-stained Tris/Tricine SDS-PAGE gels (*A–D*) and corresponding histograms after RP-HPLC analysis (*E–H*) are shown. In every image, fractions are shown from *left* to *right* corresponding to the fractions from top to bottom of the gradient. Aβ(1–42) can be found in fractions 1–10 (*A* and *E*) with fractions 3–7 being the main Aβ(1–42)$_{oligo}$-containing fractions. All huPrP constructs are mainly detected in fractions 1–3, but low concentrations can also be found in fractions 11–14, especially in the case of huPrP(23–230). Experiments are done in replicates of $n = 5$ (*E*), $n = 4$ (*F*), $n = 6$ (*G*), and $n = 4$ (*H*). *Error bars* represent S.D.

the N-terminal region from residues 23 to 124 is highly disordered but that also residues 125–144 are disordered in huPrP(23–144). To build a bridge between the quality control of the huPrP samples done at pH 4.5 and the solution conditions used for the interaction studies done at pH 7, we investigated the pH dependence of the overall conformational properties of huPrP(23–144) by solution NMR spectroscopy in a series of pH steps from 4.5 to 7.0. Although the shift in protonation equilibrium of the seven histidine side chains upon increasing the pH was associated with readily identifiable chemical shift changes for several backbone amide resonances, the quality and overall appearance of the solution NMR spectra of huPrP(23–144), including the limited resonance dispersion indicative of a disordered conformation, remained very similar over this pH range (Fig. S3*B*). Over the course of several days to weeks, the NMR samples did not show obvious signs of any significant formation of visible precipitate, any deterioration, or signal loss of the solution NMR spectra. To test for any sample degradation or aggregation in a more quantitative fashion, we monitored the intensity of 58 sufficiently well resolved amide resonances of a sample of 89 μM [U-^{15}N]huPrP(23–144) in 50 mM Tris-HCl, pH 7.2, in 10% D$_2$O in a series of ^{1}H,^{15}N heteronuclear single quantum coherence spectra recorded at 600 MHz at 5.0 °C, but no change in resonance intensity exceeding even a fraction of a percent was observed over the monitoring period of more than 48 h (Fig. S3*D*). Taken together, these NMR spectroscopic results show that huPrP(23–144) is readily soluble up to concentrations of about 0.3 mM, is highly disordered in solution under mildly acidic to neutral buffer conditions, and remains soluble and disordered for at least several days at the conditions tested.

Aβ(1–42)$_{oligo}$ was prepared by incubating monomeric Aβ(1–42) in buffer at pH 7.4 for 2 h at 22 °C under agitation. AFM of the Aβ(1–42)$_{oligo}$ samples showed small spherical particles with heights of 1–6 nm, rarely up to 10 nm (Figs. 2*C* and S4) and confirmed that the chosen incubation conditions produce high amounts of Aβ(1–42)$_{oligo}$ without formation of Aβ(1–42) fibrils or larger aggregates.

Our assay for studying the Aβ(1–42)$_{oligo}$–huPrP interaction is based on the QIAD protocol (25). In the present work, this assay includes the separation of a sample containing Aβ(1–42) assemblies and/or huPrP by sucrose DGC followed by qualitative and quantitative analyses of the interaction partners by SDS-PAGE and RP-HPLC (Fig. 1*B*). For calibration of the sucrose gradient, standard proteins ranging from 43 to 669 kDa were used (Fig. S5). Thyroglobulin, the reference protein with the highest molecular mass (669 kDa), was found in fractions 7–10, indicating that proteins, complexes, or aggregates that can be found in higher (and thus denser) fractions (fractions 11–14) must have molecular masses in the megadalton range or larger.

Initially, Aβ(1–42)$_{oligo}$ and huPrP were separately analyzed by sucrose DGC. Either 80 μM of preincubated Aβ(1–42) or a 10 or 20 μM concentration of the respective huPrP protein construct was applied on a sucrose gradient and centrifuged for 3 h. Silver-stained Tris/Tricine SDS-PAGE gels as well as RP-HPLC quantification of all gradient fractions revealed the distribution of the proteins among the fractions and hence among different assembly states (Figs. 3 and S6*A*). The preincubated Aβ(1–42) sample showed a broad distribution of Aβ(1–42) within the sucrose gradient (Fig. 3, *A* and *E*), containing mainly Aβ(1–42)$_{oligo}$ (fractions 3–7) as well as residual monomeric Aβ(1–42) (fractions 1 and 2) as we have established previously (25). The highest concentrations of huPrP(23–230), huPrP(23–144), huPrP(90–230), and huPrP(121–230) were found in fractions 1–3, confirming that huPrP occurs predominantly in a soluble monomeric state. In addition, minor amounts of huPrP were present in fractions 4–6 and 11–14, the latter representing high-molecular-weight aggregates. AFM and CD spectroscopy (Fig. 2) suggest that these were nonfibrillar, amorphous aggregates.

Aβ(1–42)$_{oligo}$ forms high-molecular-weight heteroassemblies with huPrP(23–230) as well as with huPrP(23–144)

After confirmation of the soluble, nonfibrillar state of all huPrP constructs as well as the size distribution of preincu-

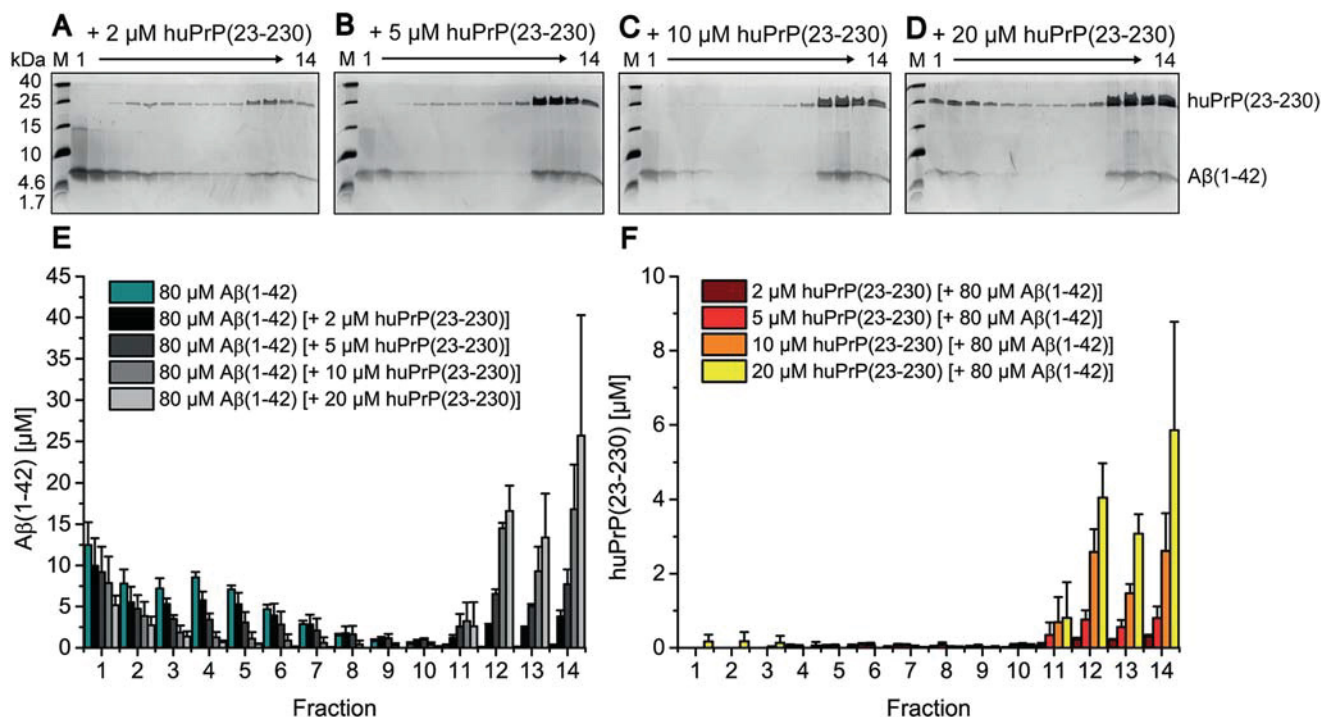## Interference with Aβ–PrP complex formation

Figure 4. Formation of heteroassemblies of Aβ(1–42)$_{oligo}$ and huPrP(23–230). Silver-stained Tris/Tricine SDS-PAGE gels after application of 80 μM preincubated Aβ(1–42) with varying huPrP(23–230) concentrations onto a sucrose gradient (*A–D*) and corresponding histograms after RP-HPLC analysis (*E* and *F*) show the distribution of Aβ(1–42) and huPrP(23–230). With increasing applied huPrP(23–230) concentrations, Aβ(1–42)$_{oligo}$ (fractions 3–7 in *E*) decreases. Moreover, both Aβ(1–42) and huPrP(23–230) appear in fractions 11–14 (bottom of the gradient). Concentrations of Aβ(1–42) in each gradient fraction according to the applied huPrP(23–230) concentration are shown in *E*, and concentrations of huPrP(23–230) are shown in *F*. Experiments are done in replicates of *n* = 3 for all huPrP(23–230) concentrations applied. *Error bars* represent S.D.

bated Aβ(1–42), we analyzed the effect of huPrP binding on the size distribution of Aβ(1–42)$_{oligo}$. Aβ(1–42), preincubated to form Aβ(1–42)$_{oligo}$, was added to full-length huPrP(23–230) to yield samples with final concentrations of 80 μM Aβ(1–42) and 2, 5, 10, or 20 μM huPrP(23–230) (concentrations refer to the samples before separation by sucrose DGC).

After DGC, each fraction was qualitatively analyzed by SDS-PAGE as well as quantitatively analyzed by RP-HPLC with respect to the Aβ(1–42) and huPrP(23–230) contents (Fig. 4). The increase of the applied concentration of huPrP(23–230) correlated with the decrease of the concentration of Aβ(1–42) in fractions 3–7 along with the increase of Aβ(1–42) concentration in fractions 11–14. For example, upon addition of 20 μM huPrP(23–230), the average Aβ(1–42) concentration fell from 6 to 0.3 μM in fractions 4–7 but rose from 0.1 to 15 μM in fractions 11–14 (Fig. 4). huPrP(23–230) was mainly detected in fractions 11–14 (see below). This clearly confirms direct interaction between huPrP(23–230) and Aβ(1–42)$_{oligo}$. huPrP(23–230) interaction was preferential with Aβ(1–42)$_{oligo}$ as the concentration of Aβ(1–42) monomers in fractions 1 and 2 decreased only slightly with increasing huPrP(23–230) concentration. Moreover, instead of simply forming one-to-one complexes, which would be found not far away from fractions 3–7, huPrP(23–230) and Aβ(1–42)$_{oligo}$ form large supramolecular heteroassemblies, which are located in fractions 11–14 and hence have molecular masses in or above the megadalton range (according to the calibration of the density gradient; Fig. S5).

In the absence of Aβ(1–42), huPrP(23–230) appeared in fractions 1–4 (Fig. 3, *B* and *F*). In contrast, in samples contain-

ing 10 or 20 μM huPrP(23–230) and 80 μM preincubated Aβ(1–42), the vast majority of huPrP(23–230) was observed in fractions 11–14 (Fig. 4, *C*, *D*, and *F*), indicative of heteroassociation with Aβ(1–42)$_{oligo}$. Interestingly, at lower huPrP(23–230) concentrations of 2 and 5 μM, faint huPrP(23–230) bands were observed in fractions 4–10. This observation can be explained by an initial formation of smaller Aβ(1–42)$_{oligo}$–huPrP(23–230) complexes, potentially of lower density, which convert to larger complexes when increasing the applied huPrP(23–230) concentration (see also Fig. 8).

The quantitative analysis of the DGC fractions by RP-HPLC enabled the determination of the molar ratios between Aβ(1–42) and huPrP(23–230) within the complexes (Table 1) calculated for every experiment from the total amount of Aβ(1–42) molecules and the total amount of huPrP(23–230) in fractions 11–14. Averaging over fractions 11–14 was necessary as the occurrence of the complexes in the individual fractions can slightly vary between experiments due to the manual fractionation of the gradients. This also explains the larger error bars of Aβ(1–42) and huPrP(23–230) in the complex-containing fractions 11–14 compared with the error bars in fractions 1–10.

Incubation of Aβ(1–42)$_{oligo}$ with 2 μM huPrP(23–230) led to an Aβ:PrP ratio of 12.1 ± 1.7 within the DGC-purified complexes (Table 1). Application of higher huPrP(23–230) concentrations resulted in the decrease of the Aβ:PrP ratio due to higher huPrP(23–230) content within the heteroassemblies. Incubation of Aβ(1–42)$_{oligo}$ with 20 μM huPrP(23–230) led to an Aβ:PrP ratio of 4.2 ± 0.9. At this applied concentration of huPrP(23–230), it can additionally be found in fractions

Table 1

Aβ:huPrP ratios within Aβ(1–42)$_{oligo}$– huPrP heteroassemblies

The ratios were calculated for every experiment as the quotient of the total amount of Aβ(1–42) molecules and the total amount of huPrP in fractions 11–14 after sucrose DGC. For the calculation of Aβ(1–42):huPrP(23–230) ratios the huPrP(23–230) concentrations in fractions 11–14 found with huPrP(23–230) alone (Fig. 3, *B and F*) were not considered as they were negligibly small. For concentrations labeled with "ND," molar ratios were not determined for huPrP(23–230). Comparing the same (huPrP) concentration, similar ratios were obtained for both huPrP(23–144) and huPrP(23–230). Full saturation of the PrP-binding capacity of Aβ(1–42)$_{oligo}$ as evident in the case of 40 μM and 60 μM huPrP(23–144) by the presence of free monomeric huPrP(23–144) (Figs. 5F and S8) resulted in a ratio of about 4 Aβ:1 huPrP(23–144). Experiments were done in replicates of *n* = 3 for all huPrP(23–230) concentrations applied; for 5, 20, 40, and 60 μM huPrP(23–144) in the presence of 80 μM Aβ(1–42); and for 20 and 60 μM Aβ(1–42) in the presence of 40 μM huPrP(23–144); *n* = 4 for 40 μM Aβ(1–42) in the presence of 40 μM huPrP(23–144); and *n* = 5 for 2 and 10 μM huPrP(23–144) in the presence of 80 μM Aβ(1–42). Errors represent S.D.

Aβ	huPrP	Aβ:huPrP(23–144)	Aβ:huPrP(23–230)
μM	μM		
80	2	10.1 ± 1.7	12.1 ± 1.7
80	5	11.3 ± 0.6	9.6 ± 2.3
80	10	8.3 ± 1.1	6.3 ± 1.7
80	20	4.9 ± 0.3	4.2 ± 0.9
80	40	3.93 ± 0.04	ND
80	60	4.04 ± 0.08	ND
60	40	3.6 ± 0.2	ND
40	40	4.1 ± 0.8	ND
20	40	4.2 ± 0.6	ND

1–4 (Fig. 4, *D* and *F*), indicating that the PrP-binding capacity of Aβ(1–42)$_{oligo}$ is fully saturated such that an excess of huPrP(23–230) remains monomeric and unbound to Aβ(1–42)$_{oligo}$. The saturability of the Aβ(1–42)$_{oligo}$–huPrP(23–230) heteroassociation indicates that it occurs by a defined binding mode and is not just an unspecific coprecipitation of both proteins.

The N-terminal PrP construct huPrP(23–144) shows a similar behavior as the full-length huPrP(23–230) upon interaction with Aβ(1–42)$_{oligo}$. With increasing huPrP(23–144) concentrations ranging from 2 to 40 μM, Aβ(1–42)$_{oligo}$ in fractions 3–7 disappeared, and higher Aβ(1–42) concentrations were detected in fractions 11–14 (Fig. 5) due to the formation of high-molecular-weight Aβ(1–42)$_{oligo}$–huPrP(23–144) complexes. Formation of assemblies with molecular masses larger than the megadalton range was confirmed by dynamic light scattering (DLS), showing that the Aβ(1–42)$_{oligo}$–huPrP(23–144) assemblies mainly have sizes from 0.6 to 6 μm (Fig. 6).

When huPrP(23–144) was added in final concentrations of 2, 5, 10, and 20 μM, huPrP(23–144) was identified exclusively in fractions 11–14 after DGC. Upon application of 40 μM huPrP(23–144) to Aβ(1–42)$_{oligo}$, about 10% of the detected huPrP(23–144) was found in fractions 1–4 (Fig. 5, *F* and *H*), indicating an excess of huPrP(23–144) and thus a saturation of Aβ(1–42)$_{oligo}$–huPrP(23–144) complexes with huPrP(23–144). Although huPrP(23–144) was in excess at the applied concentration of 40 μM (Fig. 5, *F* and *H*), there was still some monomeric Aβ(1–42) left in fractions 1 and 2 (Fig. 5, *F* and *G*), again confirming that huPrP(23–144) forms complexes only with oligomeric but not with monomeric Aβ(1–42), an observation in full accordance with previous studies (5, 19, 20).

Incubation of Aβ(1–42)$_{oligo}$ with 2 μM huPrP(23–144) resulted in an Aβ:PrP ratio of 10.1 ± 0.8 in the Aβ(1–42)$_{oligo}$–huPrP(23–144) complexes (Table 1). Increasing the applied huPrP(23–144) concentration to 40 μM progressively lowered

the Aβ:PrP ratio down to a value of 3.93 ± 0.04. Further increase of the applied huPrP(23–144) concentration to 60 μM (Fig. S8) did not further decrease the Aβ:PrP ratio (4.04 ± 0.08; Table 1) in the high-molecular-weight complexes, in agreement with the Aβ:PrP ratio of ~4 observed when an excess of huPrP(23–230) was applied. This indicates that four Aβ units are required to form one PrP-binding site. The similar behavior of huPrP(23–144) and huPrP(23–230) with respect to Aβ(1–42)$_{oligo}$ binding suggests that huPrP(23–144) contains all epitopes required for binding to Aβ(1–42)$_{oligo}$, in line with previous findings of other groups (5, 19–22).

We verified that the Aβ:PrP ratio of ~4 is constant when Aβ(1–42)$_{oligo}$ is saturated with huPrP by adding different final Aβ(1–42)$_{oligo}$ concentrations of 20, 40, 60, and 80 μM to a saturating concentration (40 μM) of huPrP(23–144). At all Aβ(1–42)$_{oligo}$ concentrations, the Aβ:PrP ratio in the heteroassociates was ~4 with deviations within the experimental error (Table 1).

Deletion of the huPrP N terminus impairs Aβ(1–42)$_{oligo}$– huPrP heteroassociation

Besides the N-terminal huPrP(23–144) and full-length huPrP(23–230), we further analyzed the C-terminal PrP constructs huPrP(90–230) and huPrP(121–230), which lack the proposed Aβ-binding site at positions 23–27 and, in the case of huPrP(121–230), the proposed binding site at positions ~95–110 (see Fig. 1A). At all applied concentrations of huPrP(90–230), ranging from 2 to 20 μM, the protein concentrations detected in fractions 11–14 were only slightly elevated (Fig. 7). Even in the presence of 20 μM huPrP(90–230), the majority of Aβ(1–42)$_{oligo}$ was still present in fractions 3–7. The majority of huPrP(90–230) was found in fractions 1–4 at all applied huPrP(90–230) concentrations, similar to the distribution of huPrP(90–230) without Aβ(1–42)$_{oligo}$ (Fig. 3, *D* and *H*). When 20 μM huPrP(90–230) was applied to Aβ(1–42)$_{oligo}$, only about 15% of huPrP(90–230) was found in fractions 11–14. This is in contrast to the observations that, when 20 μM huPrP(23–230) or huPrP(23–144) was applied to Aβ(1–42)$_{oligo}$, about 96% of huPrP(23–230) or 100% of huPrP(23–144), respectively, were found in these fractions. Therefore, compared with huPrP(23–230) (Fig. 4) and huPrP(23–144) (Fig. 5), huPrP(90–230) (Fig. 7) is almost incapable of forming high-molecular-weight Aβ(1–42)$_{oligo}$–huPrP complexes. This is in full agreement with previous studies that demonstrated the importance of both Aβ(1–42)$_{oligo}$-binding sites on PrP (19–22).

When 20 μM huPrP(121–230) was applied to Aβ(1–42)$_{oligo}$, even less Aβ(1–42) and huPrP were found in fractions 11–14 than in the case of huPrP(90–230) (Fig. S6, *B* and *C*). This demonstrates that the proposed binding site at positions ~95–110, although on its own not sufficient for high-affinity interaction, does contribute to Aβ(1–42)$_{oligo}$ binding.

The morphology of Aβ(1–42)$_{oligo}$– huPrP(23–144) heteroassemblies depends on the huPrP concentration

For structural characterization of the Aβ(1–42)$_{oligo}$–huPrP complexes, we focused on the N-terminal huPrP(23–144) construct as the PrP C terminus is not required for complex formation. Heteroassemblies formed in the presence of different huPrP(23–144) concentrations ranging from 1 to 40 μM were
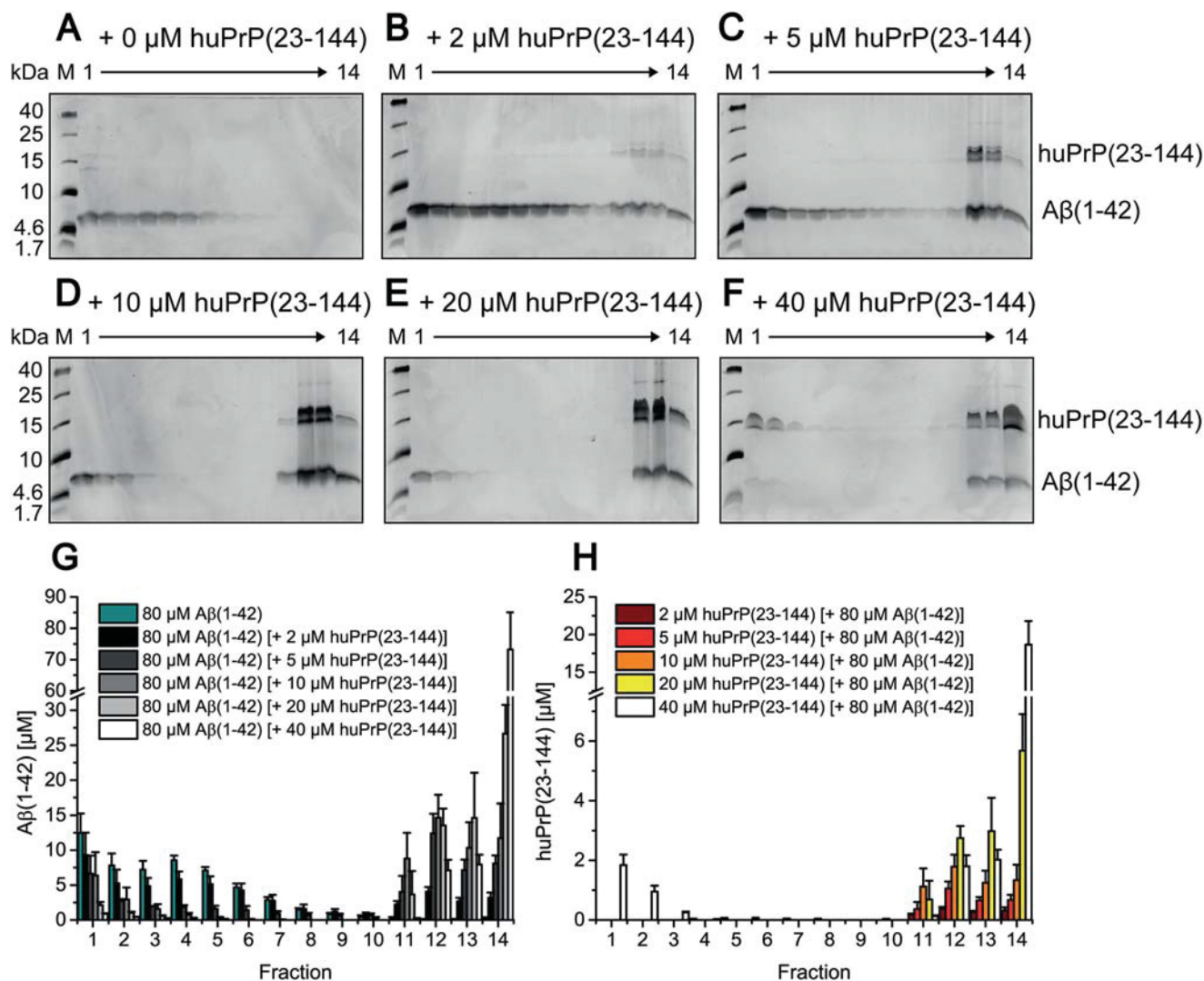
Figure 5. Formation of heteroassemblies of Aβ(1–42)$_{oligo}$ and huPrP(23–144). Silver-stained Tris/Tricine SDS-PAGE gels after application of 80 μM preincubated Aβ(1–42) with varying huPrP(23–144) concentrations on a sucrose gradient (*A–F*) and corresponding histograms after RP-HPLC analysis (*G* and *H*) show the distribution of Aβ(1–42) and huPrP(23–144). With increasing applied huPrP(23–144) concentrations, Aβ(1–42)$_{oligo}$ (fractions 3–7 in *G*) decreases. Moreover, both Aβ(1–42) and huPrP(23–144) appear in fractions 11–14 (bottom of the gradient). When 40 μM huPrP(23–144) is added, the Aβ(1–42)$_{oligo}$–huPrP(23–144) interaction becomes saturated, reflected by the presence of huPrP(23–144) in fractions 1–3 (*F* and *H*). Concentrations of Aβ(1–42) according to the applied huPrP(23–144) concentration are shown in *G*, and concentrations of huPrP(23–144) are shown in *H*. In addition to silver staining of Tris/Tricine SDS-PAGE gels, dot-blot analysis detecting either Aβ or huPrP of the DGC fractions after application of 80 μM Aβ(1–42) and 40 μM huPrP(23–144) was performed (Fig. S7), confirming qualitative analyses by silver staining of Tris/Tricine SDS-PAGE gels as well as quantitative RP-HPLC analyses. Experiments are done in replicates of *n* = 5 (for 2 and 10 μM huPrP(23–144) applied) and *n* = 3 (for 5, 20, and 40 μM huPrP(23–144) applied). *Error bars* represent S.D.

analyzed by AFM. Unbound Aβ(1–42) or huPrP(23–144) was removed by centrifugation and repeated washing steps followed by imaging of the heteroassemblies on mica in air using intermittent contact mode. Imaging was particularly challenging because the assemblies were several micrometers high with deep holes and high stickiness, which led to rapid contamination of cantilever tips. To display the different features of the samples in more detail, images were taken of the outer surfaces of the heteroassemblies (Fig. 8) several hundred nanometers above the mica support.

For complexes prepared from 80 μM Aβ(1–42) and 1 μM huPrP(23–144) (Fig. 8*B*), we observed loose clusters of irregular spheres or globules, which again exhibited globular substructures. The clusters typically measured about 200 nm in height and up to 2.5 μm in width with substructures of 20–70 nm in height. Because of the curvature of the surfaces, only a crude

estimate of the size of these heteroassemblies and their substructures was possible due to their clustering.

Heteroassemblies prepared at an increased huPrP(23–144) concentration of 5 μM (Fig. 8*C*) were up to 500 nm high and had a more compact appearance, suggesting a tighter interaction between the subassemblies. The surface of the globular subassemblies seemed to be smoother in this case. When the huPrP(23–144) concentration for heteroassociation was further raised to 40 μM (Fig. 8*D*), the resulting heteroassemblies were up to 1 μm high, exhibiting globular subassemblies with smooth surface appearance and unresolved substructure. In all cases, Aβ(1–42)$_{oligo}$–huPrP(23–144) heteroassemblies (Figs. 8, *B–D*) were much larger than Aβ(1–42)$_{oligo}$ (Fig. 8*A*), demonstrating that the heteroassemblies contain multiple copies of Aβ(1–42)$_{oligo}$.

We have previously shown that an average Aβ(1–42)$_{oligo}$ consists of about 23 monomeric units (25). Combining this
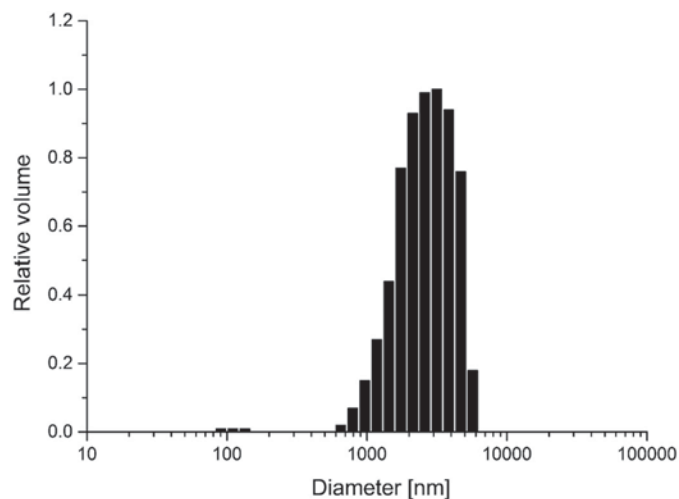
Figure 6. Size distribution of Aβ(1–42)$_{oligo}$–huPrP(23–144) complexes measured by dynamic light scattering. The Aβ(1–42)$_{oligo}$–huPrP(23–144) assemblies mainly have sizes in the range from 0.6 to 6 μm.

finding with the Aβ:PrP ratios determined here, the heteroassemblies contain approximately six huPrP(23–230) or huPrP(23–144) molecules on average per Aβ(1–42)$_{oligo}$ in the presence of an excess of huPrP. Therefore, a simplified model of Aβ(1–42)$_{oligo}$–huPrP assemblies can be drawn (Fig. 8, *E* and *F*). This model also considers the potential of huPrP to cross-link Aβ(1–42)$_{oligo}$ via its two basic N-terminal binding sites (residues 23–27 and ~95–110), which of course cannot be formed by huPrP(90–230) or huPrP(121–230). Such cross-links may play a crucial role in Aβ(1–42)$_{oligo}$–huPrP assembly due to the multivalent presentation of epitopes on Aβ(1–42)$_{oligo}$.

At low concentrations of huPrP(23–144), the huPrP-binding sites on Aβ(1–42)$_{oligo}$ are only partially occupied (Fig. 8*E*), leading to moderate assembly of Aβ(1–42)$_{oligo}$, presumably promoted by charge neutralization and huPrP-induced cross-linking. This is in line with the loose appearance of heteroassemblies in AFM (Fig. 8*B*). At high concentrations of huPrP(23–144), the huPrP-binding sites on Aβ(1–42)$_{oligo}$ are fully occupied (Fig. 8*F*), resulting in saturated Aβ(1–42)$_{oligo}$ assembly, in agreement with the compact appearance of heteroassemblies in AFM (Fig. 8*D*).

The D-enantiomeric peptide RD2D3-FITC competes with huPrP for binding to Aβ(1–42)$_{oligo}$

Soluble N-terminal PrP fragments, including the naturally produced neuroprotective N1 fragment, block neurotoxic effects of soluble oligomers (20, 23, 24), presumably by competing with membrane-anchored PrP^C for Aβ$_{oligo}$. In line with this, we found that huPrP(23–144) rescues the viability of PC-12 cells from Aβ(1–42)$_{oligo}$-induced toxicity in a concentration-dependent manner according to the 3-(4,5-dimethylthiazol-2-yl)-2,5-diphenyltetrazolium bromide (MTT) cell viability test (Fig. S9). Compounds that compete with membrane-anchored PrP^C for Aβ$_{oligo}$ in a similar fashion might therefore be of therapeutic interest. Similarly to huPrP, our well characterized Aβ-binding D-peptides form heteroassemblies with Aβ(1–42)$_{oligo}$ (28). These specific D-peptides contain a high ratio of basic amino acid residues and are in that respect similar to the

Interference with Aβ–PrP complex formation

Aβ(1–42)$_{oligo}$-binding sites within the PrP N terminus (5, 19–22). Similar to the soluble N-terminal PrP fragment huPrP(23–144), the D-peptide RD2D3 shows rescue of PC-12 cell viability from Aβ(1–42)$_{oligo}$-induced toxicity in the MTT test (Fig. S9 and Ref. 30). Therefore, the D-peptides might act by a similar mechanism as N-terminal huPrP fragments, *i.e.* competition with membrane-anchored PrP^C for Aβ$_{oligo}$. To investigate this hypothesis, we analyzed the effect of the D-peptide RD2D3, labeled with a fluorescent dye (FITC), on the Aβ(1–42)$_{oligo}$–huPrP(23–144) interaction.

Determination of Aβ:PrP ratios within the heteroassemblies might be a suitable approach to identify potential drug candidates that interfere with the Aβ–huPrP interaction. If a compound competes with huPrP(23–144) for Aβ(1–42)$_{oligo}$, the Aβ(1–42):huPrP(23–144) ratio within the complexes will change to higher values due to decreased huPrP(23–144) binding to Aβ(1–42)$_{oligo}$.

First, we verified that huPrP(23–144) and RD2D3-FITC do not form high-molecular-weight complexes with each other (Fig. S10). For studying the effect of RD2D3-FITC, constant final concentrations of 80 μM Aβ(1–42) and 40 μM huPrP(23–144) in the samples applied to DGC were chosen. Under these conditions, in the absence of RD2D3-FITC, the PrP-binding capacity of Aβ(1–42)$_{oligo}$ is fully exploited, resulting in an Aβ(1–42):huPrP(23–144) ratio of 4:1 in the heteroassemblies (Table 1) and a slight excess of huPrP(23–144) that remains monomeric (Fig. 5). The Aβ(1–42):huPrP(23–144) ratio of 4:1 was set as reference for the analysis of potential effects of RD2D3-FITC on the Aβ–huPrP interaction. We compared the effect of different orders of application of RD2D3-FITC or huPrP(23–144) to the sample. Either RD2D3-FITC or huPrP(23–144) was preincubated with Aβ(1–42), and the other compound was applied after 2 h for a further 30 min. Alternatively, Aβ(1–42)$_{oligo}$ was preformed, and RD2D3-FITC and huPrP(23–144) were mixed and simultaneously applied to Aβ(1–42)$_{oligo}$ for a further 30 min. When 40 μM RD2D3-FITC was applied after preincubation of huPrP(23–144) with Aβ(1–42)$_{oligo}$ (Fig. 9, *C* and *D*), the majority of RD2D3-FITC was located in fractions 1–3 after DGC. Although low concentrations of RD2D3-FITC were found in the fractions containing heteroassemblies (fractions 11–14), the Aβ(1–42):huPrP(23–144) ratio remained at 4:1 as in the reference (Fig. 10). The preincubation of 40 μM RD2D3-FITC with Aβ(1–42) before huPrP(23–144) application (Fig. 9, *E* and *F*), however, resulted in a drastic decrease of huPrP(23–144) bound in the heteroassemblies and an increase of RD2D3-FITC in fractions 11–14. At the same time, the Aβ(1–42):huPrP(23–144) ratio changed to 14.3 ± 0.5 (Fig. 10). huPrP(23–144) was mainly found in fractions 1–3, in agreement with a monomeric, unbound state. Simultaneous application of huPrP(23–144) and RD2D3-FITC to Aβ(1–42)$_{oligo}$ resulted in an intermediate outcome (Fig. 9, *A* and *B*). Here, the Aβ(1–42):huPrP(23–144) ratio was 10.4 ± 0.4, which is significantly increased compared with the ratio for early huPrP(23–144) application but lower than that for early RD2D3-FITC application. Reduction of the RD2D3-FITC concentration from 40 to 20 μM (Figs. 10 and S11) resulted in the same tendency with respect to the ratios and the protein distributions within the gradient and reduced Aβ(1–42):huPrP(23–144) ratios

ASBMB

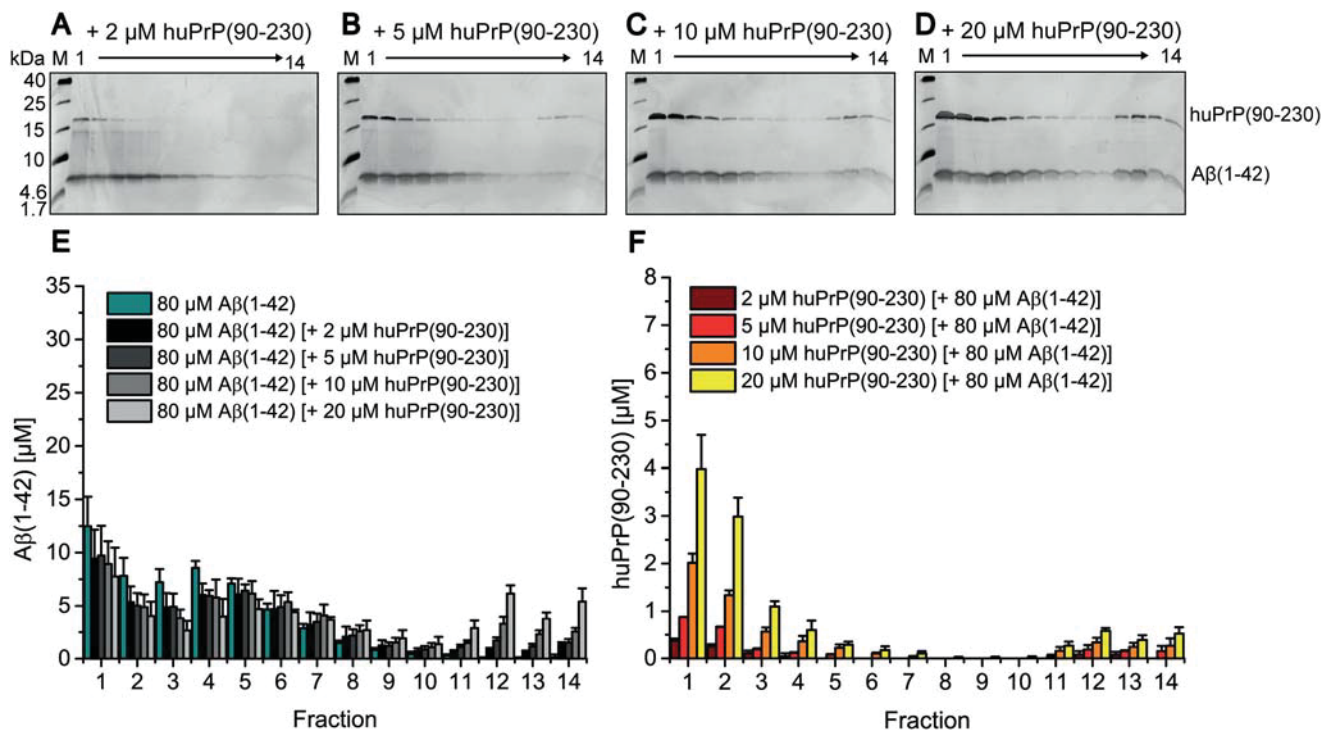*J. Biol. Chem.* (2018) 293(41) 15748–15764 **15755**

Figure 7. Impaired formation of heteroassemblies of Aβ(1–42)$_{oligo}$ and huPrP(90–230). Silver-stained Tris/Tricine SDS-PAGE gels after application of 80 μM preincubated Aβ(1–42) with varying huPrP(90–230) concentrations on a sucrose gradient (*A–D*) and corresponding histograms after RP-HPLC analysis (*E* and *F*) show the distribution of Aβ(1–42) and huPrP(90–230). With increasing applied huPrP(90–230) concentrations, just slightly increased protein concentrations of both Aβ(1–42) and huPrP(90–230) are found in bottom fractions 11–14. Concentrations of Aβ(1–42) according to the applied huPrP(90–230) concentration are shown in *E*, and concentrations of huPrP(90–230) are shown in *F*. Experiments are done in replicates of *n = 3* for all huPrP(90–230) concentrations applied. *Error bars* represent S.D.

due to the decreased D-peptide concentration. These results demonstrate the competition between huPrP(23–144) and RD2D3-FITC for Aβ(1–42)$_{oligo}$. The degree of competition of RD2D3-FITC depended on the concentration as well as on the order of RD2D3-FITC and huPrP(23–144) application.

Discussion

In 2009, Laurén *et al.* (5) reported that oligomeric Aβ binds to membrane-anchored PrP^C, leading to toxic signaling across the cell membrane. Although subsequent studies questioned the role of PrP^C in toxic signaling (7, 49–51), further evidence was gained in support of the original findings (5, 12, 13, 20). According to the current view of PrP^C–Aβ$_{oligo}$-induced signaling, metabotropic glutamate receptor 5 interacts with PrP^C and activates the intracellular Fyn kinase when Aβ oligomers are bound to membrane-anchored PrP^C (12, 13). This activation leads to hyperphosphorylation of tau protein as well as to phosphorylation of NMDA receptors, two mechanisms that finally lead to neuronal damage (12, 14, 15, 17). The elucidation of these mechanisms has opened new strategies to prevent toxic signaling in AD by targeting one of these proteins or mediators.

The Aβ(1–42)$_{oligo}$–PrP interaction is at the core of the PrP-mediated toxic signaling cascade. Here, we have characterized the Aβ(1–42)$_{oligo}$–PrP interaction by applying a set of soluble huPrP constructs and by taking advantage of the QIAD assay (25), which enables determination of the size distribution of Aβ assembly species and their complexes based on separation by DGC. We found that Aβ(1–42)$_{oligo}$ and huPrP readily associate to form heteroassemblies above the megadalton range (Figs. 4–6 and 8). The heteroassemblies were

imaged by AFM as μm-sized clusters of nm-sized globular substructures (Fig. 8).

Heteroassociation is greatly impaired for the huPrP variants devoid of the N terminus, huPrP(90–230) and huPrP(121–230) (Figs. 7 and S6), in agreement with the notion that both Aβ-binding sites in the huPrP N terminus (residues 23–27 and ~95–110 (5, 19–22)) are required for high-affinity interaction. This is in line with recent reports showing that the effect of soluble, anchorless PrP(90–231) with respect to prevention of Aβ-mediated cytotoxicity was substantially weaker compared with full-length huPrP or N-terminal huPrP (52). In addition, Nieznanski *et al.* (23) showed that about 10-fold higher concentrations of huPrP(90–231) than of huPrP(23–231) or huPrP(23–144) were required to achieve comparable inhibitory effects on Aβ(1–42) fibril formation. Similarly, a complete loss of binding capacity to Aβ(1–42)$_{oligo}$ after deletion of the N-terminal region 23–89 was observed (19). The Aβ-binding sites in huPrP constitute positively charged patches, suggesting that an electrostatic component may promote the interaction. In this context, it is worth noting that the presence of negatively charged patches on Aβ(1–42)$_{oligo}$ has been inferred from engineering of Aβ(1–42)$_{oligo}$-binding proteins (53).

Further distinctive features of the Aβ(1–42)$_{oligo}$–huPrP heteroassociation comprise (i) disordered conformation of the binding sites in free PrP, (ii) multivalency (an average Aβ(1–42)$_{oligo}$ can interact with six huPrP molecules), and (iii) a stoichiometry that is not fixed but constrained to a relatively narrow window (the Aβ:PrP ratio is in the range of 4:1–12:1). We
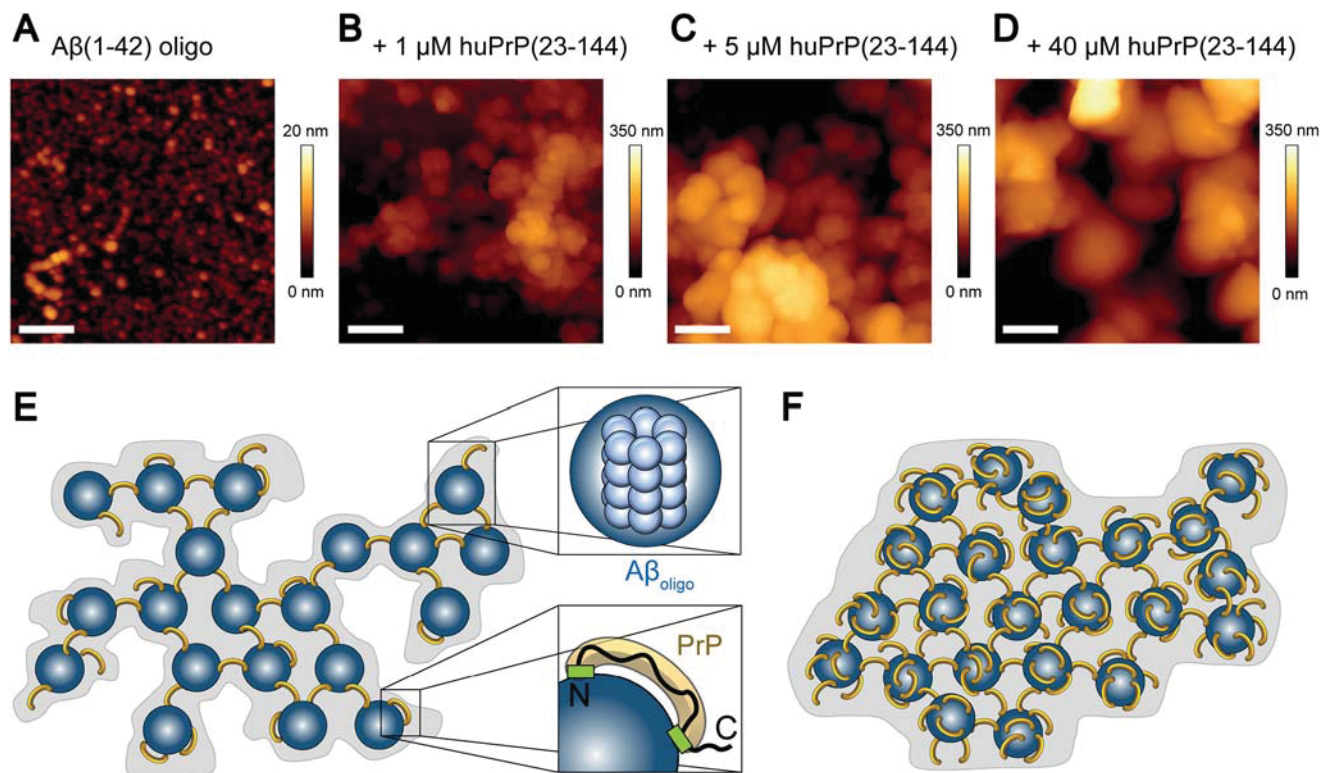
Figure 8. AFM images of Aβ(1–42)$_{oligo}$–huPrP(23–144) complexes (*A–D*) and model of the complexes (*E* and *F*). *A–D*, 1-μm^2 AFM images of Aβ oligomers (*A*) and Aβ(1–42)$_{oligo}$–huPrP(23–144) complexes generated with 80 μM preincubated Aβ(1–42) and either 1 (*B*), 5 (*C*), or 40 μM huPrP(23–144) (*D*). *Scale bars*, 200 nm. *E* and *F*, model of Aβ(1–42)$_{oligo}$–huPrP complexes with low (*E*) and high (*F*) huPrP content. For clarity, complexes are shown two-dimensional. Aβ(1–42)$_{oligo}$ is shown in *blue*, huPrP is in *yellow*, binding sites on huPrP are in *green* (*E, bottom right corner*). One Aβ(1–42)$_{oligo}$ is composed of 23 monomers on average (25) (*E, top right corner*). Based on the ratio of four Aβ (monomer equivalent) to one huPrP in the case of saturation with huPrP, the heteroassemblies contain six huPrP molecules per Aβ(1–42)$_{oligo}$. The heteroassemblies show many detailed substructures at low huPrP concentrations (*E*), symbolized by the *gray background* in the model. After saturation with huPrP, all binding sites on Aβ(1–42)$_{oligo}$ are occupied, leading to compact complexes with smooth surface (*D* and *F*).

searched the literature for protein–protein interactions with similar characteristics and found two notable cases, the interaction of nucleophosmin with nucleophosmin-binding proteins (54) and heteroprotein coacervation of β-lactoglobulin and lactoferrin (55, 56). The interaction of nucleophosmin with binding proteins containing arginine-rich linear motifs is involved in nucleolus formation by liquid-liquid phase separation. The interaction features an electrostatic component, intrinsic disorder in the free binding motifs, as well as multivalency: acidic oligomers of nucleophosmin interact with proteins that contain at least two basic linear motifs (54). Heteroprotein coacervation of β-lactoglobulin and lactoferrin features a constrained stoichiometry with some variation depending on the molar ratio of the initial mixture (55, 56).

The molar ratios in the Aβ(1–42)$_{oligo}$–huPrP heteroassemblies suggest that an average Aβ(1–42)$_{oligo}$ can directly interact with up to six huPrP molecules. This multivalent interaction, established here for soluble huPrP constructs, may also have consequences for GPI-anchored PrP^C. For example, clustering of PrP^C can promote the activation of Fyn kinase (57, 58). Moreover, the multivalency of Aβ(1–42)$_{oligo}$ may contribute to the formation of ternary complexes with other membrane receptors (59). N1, a secreted, soluble N-terminal fragment resulting from α-cleavage of huPrP, comprises both Aβ(1–42)$_{oligo}$-binding sites and is therefore primed for heteroassociation with Aβ(1–42)$_{oligo}$. Intriguingly, N1 is neuroprotective,

inhibits Aβ(1–42)$_{oligo}$-mediated neurotoxicity (20), and forms coaggregates with Aβ that have been detected in post-mortem brain tissue (60).

As the Aβ–PrP interaction might be a possible therapeutic target in treating Alzheimer's disease, there is great effort to identify either Aβ- or PrP-binding compounds that inhibit the Aβ–PrP^C interaction. For example, dextran sulfate sodium (61) and Chicago Sky Blue 6B (62) inhibit binding of Aβ(1–42)$_{oligo}$ to PrP. Similarly, anti-PrP antibodies blocked oligomeric Aβ binding to PrP and prevented Aβ oligomer–induced neurotoxicity (5, 63–65). The QIAD assay in its version introduced here, permitting simultaneous quantification of Aβ(1–42), huPrP, and compound, allows identification and characterization of a compound's interference with the Aβ–PrP interaction. We found that the Aβ:PrP ratio in the heteroassociates (Fig. 10) is a suitable indicator of a compound's competition with PrP for Aβ(1–42)$_{oligo}$.

We have previously identified a number of D-enantiomeric peptides as promising drugs that eliminate Aβ(1–42)$_{oligo}$ and improve cognition in transgenic AD mice (25–27, 66). Here, we have observed that the D-peptide RD2D3 interferes with the binding of huPrP(23–144) to Aβ(1–42)$_{oligo}$. As a rescue of cell viability of Aβ-treated cells (Fig. S9 and Ref. 30) and enhancement of cognition (39) were shown for RD2D3, our studies suggest that interference with the Aβ–PrP interaction might be one potential mechanism of action of this class of D-peptides.
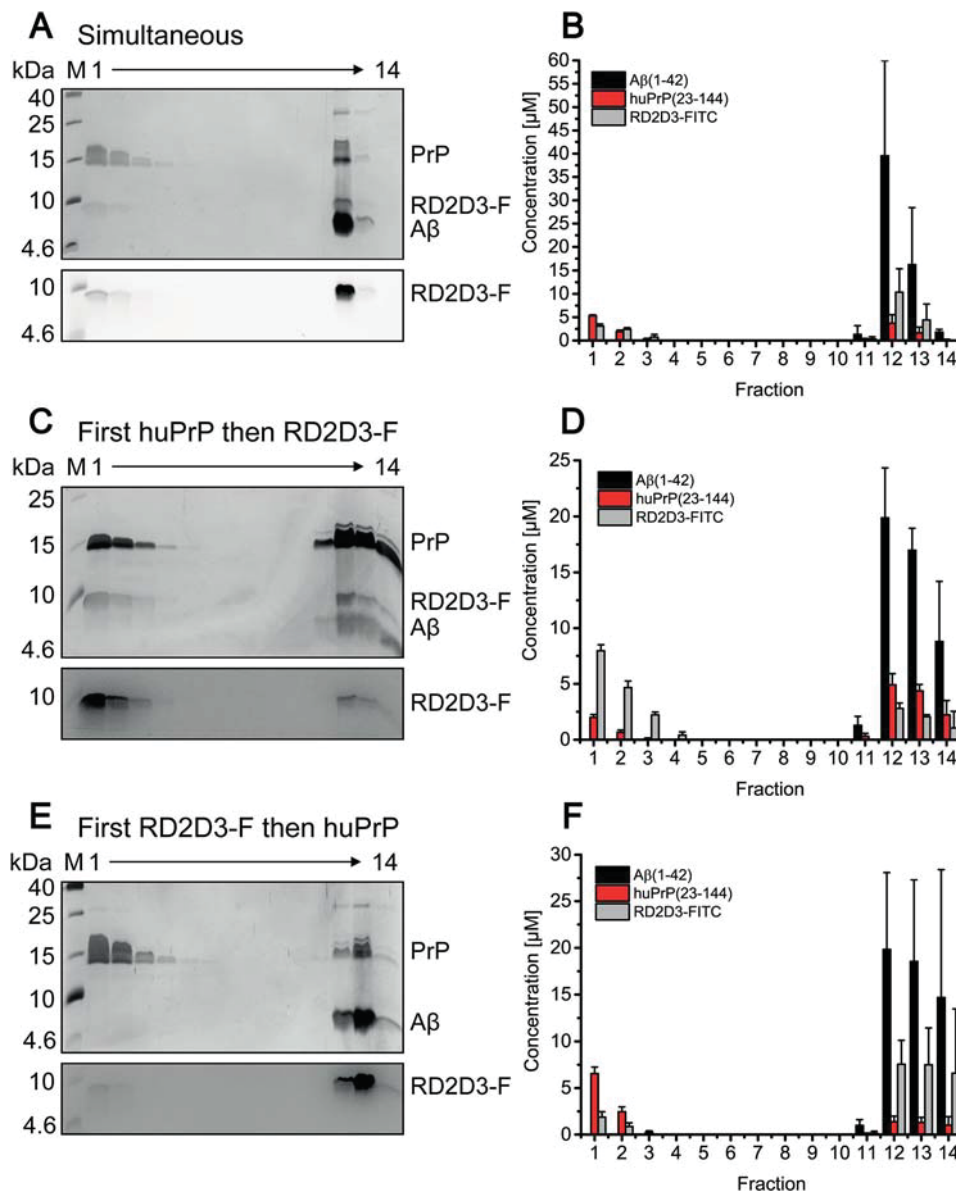
Interference with Aβ–PrP complex formation

Figure 9. Interference of the Aβ(1–42)$_{oligo}$– huPrP(23–144) interaction by RD2D3-FITC. Shown is the distribution of 80 μM Aβ(1–42), 40 μM huPrP(23–144), and 40 μM RD2D3-FITC after sucrose DGC for different orders of RD2D3-FITC and huPrP(23–144) addition. *A*, *C*, and *E*, Aβ(1–42) and huPrP(23–144) distributions in silver-stained Tris/Tricine SDS-PAGE gels and the distribution of RD2D3-FITC after fluorescence detection on the same gels are shown. *B*, *D*, and *F*, quantification by RP-HPLC of each component. Either huPrP(23–144) and RD2D3-FITC were simultaneously added to Aβ(1–42)$_{oligo}$ (*A* and *B*), huPrP(23–144) was preincubated with Aβ before RD2D3-FITC addition (*C* and *D*), or RD2D3-FITC was preincubated with Aβ before huPrP(23–144) addition (*E* and *F*). Dependent on the order of application of RD2D3-FITC or huPrP(23–144) to the sample, the distributions of huPrP(23–144) and RD2D3-FITC change. Experiments were done in replicates of *n* = 3 for all orders of application of RD2D3-FITC or huPrP(23–144) to the sample. *Error bars* represent S.D.

Experimental procedures

Purification of huPrP

All huPrP constructs, huPrP(23–230), huPrP(23–144), huPrP(90–230), and huPrP(121–230), were generated recombinantly in *E. coli*. huPrP(23–230) and huPrP(90–230) were cloned in pET-11a vectors and transformed in Rosetta 2 (DE3) as described by Luers *et al.* (67). Both constructs contain the natural polymorphism Met-129. Before induction, *E. coli* was grown in terrific broth medium at 37 °C and 160 rpm shaking. At an OD$_{600}$ of 0.7, recombinant protein expression was induced by adding 0.5 mM isopropyl 1-thio-β-D-galactopyranoside, and the growth temperature was lowered to 25 °C. Cells were harvested after overnight expression. For the preparation of iso-

tope-labeled [U-^{15}N]huPrP(23–230) or [U-^{13}C,^{15}N]huPrP(23–230), M9 minimal medium containing the desired isotopes was used. The purification is based on the protocol of Mehlhorn *et al.* (68). Harvested cells were washed with 1× PBS buffer for 30 min, harvested again, and resuspended in 3 ml of digestion buffer (1× PBS, 20 mM MgCl$_2$, DNase I containing protease inhibitor mixture (Complete EDTA-free, Roche Applied Science, one tablet/100 ml)) per gram of cells and stored at −20 °C. The cells were disrupted at 1.2 kbar in a cell disruption system (Constant Systems), and the lysate was centrifuged at 28,700 × *g* for 1 h at 4 °C. The insoluble inclusion bodies were dissolved in about 10 ml of 6 M guanidinium HCl, 5 mM DTT, 12.5 mM Tris-HCl, pH 8.0, and centrifuged again (see above). The super-
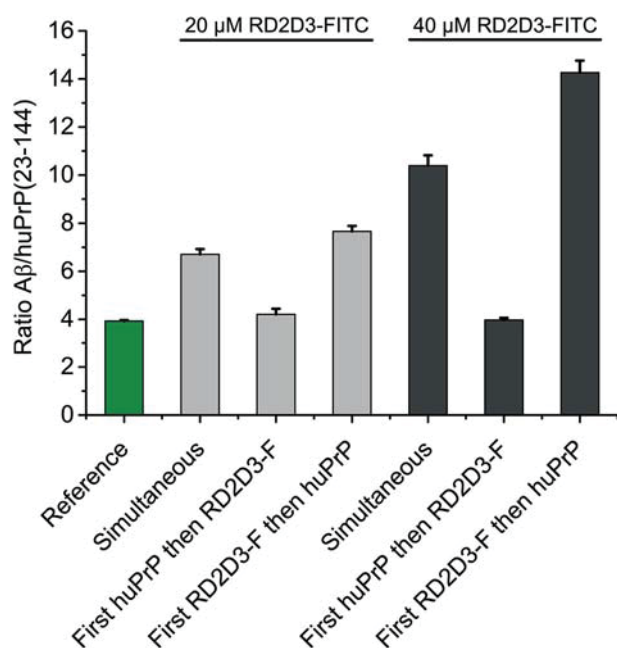
Figure 10. Altered Aβ:huPrP(23–144) ratios within Aβ(1–42)$_{oligo}$–huPrP(23–144) assemblies show the interference by RD2D3-FITC. For all experiments, constant concentrations of 80 μM Aβ(1–42) and 40 μM huPrP(23–144) were used. The reference of 3.93 $\pm$ 0.04 Aβ:huPrP(23–144) results from data obtained in the absence of RD2D3-FITC (Table 1). The strongest interference of RD2D3-FITC with the Aβ(1–42)$_{oligo}$–huPrP(23–144) interaction was observed at the higher RD2D3-FITC concentration (40 μM) when RD2D3-FITC was preincubated with Aβ before addition of huPrP(23–144). Experiments were done in replicates of $n = 3$ for all orders of application of RD2D3-FITC or huPrP(23–144) to the sample. *Error bars* represent S.D.

natant was separated by size exclusion chromatography on a HiLoad 26/60 Superdex 200 preparative grade column. Analytical samples of every second elution fraction were precipitated with 20% (w/v) TCA to remove the guanidinium HCl and investigated by SDS-PAGE. huPrP(23–230)- or huPrP(90–230)-containing fractions were pooled and purified by RP-HPLC. A semipreparative C$_8$ column (Zorbax 300 SB-C8 semiprepara-tive, 9.4 × 250 mm, Agilent) allowed the separation of huPrPs from impurities using a 20–30% (v/v) gradient of acetonitrile + 0.1% (v/v) TFA within 15 min followed by a 10-min step of isocratic 30% (v/v) acetonitrile + 0.1% (v/v) TFA. The purifica-tions were performed at 80 °C at a flow rate of 4 ml/min. The elution fractions containing huPrP were pooled, dried by lyoph-ilization, finally dissolved in Milli-Q water and adjusted to con-centrations ranging from 96 to 140 μM. Stocks of 100–200 μl were frozen in liquid nitrogen and stored at −80 °C. We chose water for the preparation of the huPrP stock solutions as huPrP is highly soluble in water.

huPrP(23–144) was cloned in a pET302/NT-His vector and transformed in *E. coli* BL21(DE3). This huPrP construct also contains the natural polymorphism Met-129. Cells were grown in LB medium at 37 °C and 160 rpm shaking and incubated overnight after induction at these conditions. For the preparation of isotope-labeled [U-^{15}N]huPrP(23–144) or [U-^{13}C,^{15}N]huPrP(23–144), M9 minimal medium containing the desired isotopes was used. Resuspension and disruption of the cells were performed as described above. The insoluble inclusion bodies were dissolved in 10 ml of 6 M guanidinium HCl, 100 mM NaCl, 30 mM Tris-HCl, pH 7.4, and centrifuged

(see above). The supernatant was separated by IMAC with two serially connected 5-ml Protino nickel-nitrilotriacetic acid col-umns (Macherey-Nagel). A washing step with 30 mM Tris-HCl, pH 7.4, allowed the removal of the denaturing agent guani-dinium HCl. The elution occurred with a linear gradient from 0 to 500 mM imidazole, 30 mM Tris-HCl, pH 7.4. The huPrP(23–144)-containing fractions (verified by SDS-PAGE) were pooled, and the hexahistidine tag was cleaved by tobacco etch virus protease. RP-HPLC purification, lyophilization, and storage of the protein were performed as described above.

The expression plasmid for huPrP(121–230) was obtained from Dr. Werner Kremer, University of Regensburg. As described previously (47), it was cloned in pRSET A vector with an N-terminal histidine tail and thrombin cleavage site. The plasmid was transformed in Rosetta 2 (DE3). Before induction, *E. coli* was grown in 2YT medium (3.5% Tryptone, 2% yeast extract, 0.5% NaCl) at 37 °C and 160 rpm shaking. At an OD$_{600}$ of 0.6, recombinant protein expression was induced by adding 1 mM isopropyl 1-thio-β-D-galactopyranoside, and the growth temperature was lowered to 22 °C for overnight expression. After harvesting and washing the cells twice with 5 mM EDTA, 25 mM Tris-HCl, pH 8.0, they were resuspended in 2 mM EDTA, 1% Triton X-100, 0.1 mg/ml lysozyme, 50 mM Tris-HCl, pH 8.0, and incubated for 30 min at 37 °C. After addition of 0.1 mg/ml DNase and 15 mM MgCl$_2$ and incubation for 30 min at 37 °C, they were sonicated on ice five times for 1 min (Bandelin Sono-puls, sonotrode VS 70 T, 60% amplitude).

The insoluble inclusion bodies were harvested by centrifuga-tion (see above); washed with 5 mM EDTA, 12.5 mM Tris-HCl, pH 8.0; and dissolved in 8 M guanidinium HCl, 12.5 mM Tris-HCl, pH 8.0, at 4 °C. After 1-h centrifugation (see above), the supernatant was separated by IMAC with two serially con-nected 5-ml Protino nickel-nitrilotriacetic acid columns. The elution of the hexahistidine-tagged PrP(121–230) occurred with a linear gradient of 500 ml from 0 to 500 mM imidazole in 6 M guanidinium HCl, 12.5 mM Tris-HCl, pH 8.0.

huPrP(121–230)-containing fractions were pooled and puri-fied by RP-HPLC. A semipreparative C$_8$ column (Zorbax 300 SB-C8, 9.4 × 250 mm) allowed the separation of huPrP(121–230) from impurities using a 20–48% (v/v) gradient of acetoni-trile + 0.1% (v/v) TFA within 20 min followed by a 10-min step of isocratic 48% (v/v) acetonitrile + 0.1% (v/v) TFA. The puri-fication was performed at 80 °C at a flow rate of 4 ml/min. The elution fractions containing huPrP(121–230) were pooled and dried by lyophilization. Thrombin cleavage of the fusion pro-tein was performed with 2.5 mg/ml fusion protein in 50 mM MES, pH 6.0, with a final concentration of 8 units of thrombin (Serva 36402.02)/mg of protein for 7 days, when nearly 98% of the protein was digested. RP-HPLC purification, lyophilization and storage of the protein were performed as described above.

Preparation of Aβ(1–42) stocks

1 mg of synthetic Aβ(1–42) (Bachem AG) was incubated with 700 μl of hexafluoro-2-propanol (HFIP) overnight. The solution was divided in 36-μg aliquots in LoBind reaction tubes (Eppendorf AG) and lyophilized in a rotational vacuum concentrator system connected to a cold trap (both Martin Christ Gefriertrocknung-sanlagen GmbH). The lyophilizates were stored at room temperature.

Interference with Aβ–PrP complex formation

Standard proteins for DGC calibration

40 μg of the standard proteins ovalbumin, conalbumin, aldolase, apoferritin, and thyroglobulin in 30 mM Tris-HCl, pH 7.4, from a gel filtration high-molecular-weight calibration kit (GE Healthcare) were analyzed by sucrose DGC (see below) to calibrate the gradient.

Preparation of samples containing Aβ(1–42) and huPrP (any construct)

Preincubation of Aβ(1–42)—For formation of Aβ(1–42)$_{oligo}$, Aβ(1–42) was incubated at concentrations of typically 81-100 μM to achieve an identical final concentration of 80 μM Aβ after huPrP addition in all samples prepared for DGC. The incubation was performed in 30 mM Tris-HCl buffer, pH 7.4, at 22 °C and 600 rpm shaking for 2 h. This particular incubation time ensures the production of high amounts of Aβ(1–42)$_{oligo}$ without formation of larger aggregates or fibrils that would appear in the bottom fractions of the density gradient and might affect analytics of Aβ– huPrP complexes.

Addition of huPrP—huPrP stock solutions in Milli-Q water were centrifuged directly before use in a TL 100 ultracentrifuge with a TLA-55 rotor (Beckman) for 30 min at 4 °C and 100,000 × g to remove potential aggregates. Final concentrations of 2– 60 μM huPrP(23–144), of 20 μM huPrP(121–230), or 2–20 μM of either huPrP(23–230) or huPrP(90–230) were added to the preformed Aβ(1–42)$_{oligo}$ for a further 30 min at 22 °C and 600 rpm shaking. The final volume of each sample was 100 μl. In another set of experiments, the concentration of Aβ(1–42)$_{oligo}$ was varied (20, 40, and 60 μM), and the huPrP(23–144) concentration was set constant to 40 μM.

Preparation of samples containing Aβ(1–42), huPrP(23–144), and RD2D3-FITC

Three different orders of application of RD2D3-FITC and huPrP(23–144) were analyzed.

Mixture of huPrP(23–144) and RD2D3-FITC (simultaneous)—Aβ(1–42)$_{oligo}$ was generated as described under "Preincubation of Aβ(1–42)" above. After 2-h preincubation, huPrP(23–144) and RD2D3-FITC were added simultaneously to yield samples with final concentrations of 40 μM huPrP(23–144), 80 μM Aβ(1–42), and 20 or 40 μM RD2D3-FITC. The samples were incubated for a further 30 min at 22 °C and 600 rpm shaking.

Addition of huPrP(23–144) during Aβ incubation (first huPrP and then RD2D3-FITC)—Aβ preincubation was done as described before but in the presence of 0.5 molar eq of huPrP(23–144). After 2-h preincubation, RD2D3-FITC was added to yield samples with final concentrations of 40 μM huPrP(23–144), 80 μM Aβ(1–42), and 20 or 40 μM RD2D3-FITC. The samples were incubated for a further 30 min at 22 °C and 600 rpm shaking.

Addition of RD2D3-FITC during Aβ incubation (first RD2D3-FITC and then huPrP)—Aβ preincubation was done as described before but in the presence of 0.5 or 0.25 molar eq of RD2D3-FITC. After 2-h preincubation, huPrP(23–144) was added to yield samples with final concentrations of 40 μM huPrP(23–144), 80 μM Aβ(1–42), and 20 or 40 μM RD2D3-FITC. The samples were incubated for a further 30 min at 22 °C and 600 rpm shaking.

DGC and RP-HPLC analysis of the fractions

This method is an adjusted assay based on the QIAD assay described in Brener *et al.* (25). In our case, not only Aβ(1–42) but also the prion protein (either huPrP(23–230), huPrP(23–144), or huPrP(90–230)) and the D-peptide RD2D3-FITC are quantified. This assay contains the following steps.

DGC—Each 100-μl sample (see "Preparation of samples containing Aβ(1–42) and huPrP (any construct)" or "Preparation of samples containing Aβ(1–42), huPrP(23–144), and RD2D3-FITC") was applied on a discontinuous 30 mM Tris-HCl, pH 7.4, buffered sucrose gradient containing the following volumes and sucrose concentrations (from bottom to top): 300 μl of 60% (w/w), 200 μl of 50% (w/w), 200 μl of 25% (w/w), 400 μl of 20% (w/w), 400 μl of 15% (w/w), 150 μl of 10% (w/w), and 150 μl of 5% (w/w). Each gradient was stepwise layered in a 11 × 34-mm polyallomer centrifuge tube. Gradients were centrifuged in a TL 100 ultracentrifuge using a TLS-55 rotor (Beckman) for 3 h at 4 °C and 259,000 × g. The centrifuged gradients were manually fractionated from top to bottom into 13 142-μl fractions. The remaining volume (arithmetically 54 μl) was mixed with 80 μl of 30 mM Tris-HCl, pH 7.4, forming fraction 14. For all calculations, a dilution factor of 2.48 was included for fraction 14.

RP-HPLC analysis—Each fraction was analyzed by Tris/Tricine SDS-PAGE (see below) and RP-HPLC. For the quantification of Aβ(1–42), huPrP (all constructs), and RD2D3-FITC, 20 μl of each fraction was applied on a Zorbax 300 SB-C8 Stable Bond Analytical column, 4.6 × 250 mm (Agilent) and measured with an Agilent 1260 Infinity system. Each compound was separated by a 10 – 40% (v/v) acetonitrile gradient + 0.1% (v/v) TFA within 25 min at 80 °C and a flow rate of 1 ml/min. These harsh conditions are necessary to ensure the dissociation of the formed complexes, especially in density gradient fractions 11–14. For detection of the substances, the UV absorbance at 214 nm was used. Known concentrations of Aβ(1–42), huPrP (all constructs), as well as RD2D3-FITC and their corresponding plot of peak area *versus* protein concentration enabled the calibration and finally the calculation of the protein concentrations present in the fractions. The program package ChemStation by Agilent allowed data recording and peak area integration. All histograms were illustrated with OriginPro 9.0.

Determination of Aβ:huPrP ratios—All generated complexes containing Aβ(1–42) and huPrP (and RD2D3-FITC) were verified in gradient fractions 11–14. For the calculation of Aβ: huPrP ratios, Aβ(1–42) and huPrP amounts in fractions 11–14 were summed. Averaging over fractions 11–14 was necessary as the appearance of the complexes can shift a little within the different fractions due to manual fractionation of the gradients. Then Aβ(1–42) amounts were divided by huPrP amounts to get a ratio for each experiment. The mean ± S.D. of the ratios was calculated over all performed experiments.

Verification of the disulfide bond in huPrPs between Cys-179 and Cys-214 by RP-HPLC

To analyze whether purified huPrP(23–230), huPrP(90–230), and huPrP(121–230) under study contain a disulfide bond between Cys-179 and Cys-214 in the fully oxidized state, purified samples of 5 μM protein were reduced overnight with 25

mM tris(2-carboxyethyl)phosphine hydrochloride in 6 M guanidinium HCl, 100 mM Tris-HCl, pH 7.4, and analyzed by RP-HPLC as described above. Samples treated only with 6 M guanidinium HCl, 50 mM Tris-HCl, pH 7.4, were used as controls. The reductive opening of the disulfide bond results in a characteristic elongation of the retention time for the reduced state when compared with the oxidized states.

SDS-PAGE and silver staining

Qualitative analysis of the DGC fractions was done by Tris/Tricine SDS-PAGE followed by silver staining. To this end, 15 μl of each fraction was diluted 1:1 in sample buffer (12% glycerol, 4% SDS, 50 mM Tris-HCl, pH 7.4, 2% β-mercaptoethanol), applied onto 20% Tris/Tricine gels, and subjected to gel electrophoresis at 40 mA/gel. The preparation of the Tris/Tricine gels is based on the protocol by Schägger and von Jagow (69). Gels containing samples with RD2D3-FITC were analyzed by fluorescence detection (excitation, 470 nm; emission, 530 nm) before silver staining. Silver staining of the gels based on the protocol by Heukeshoven and Dernick (70) allowed visualization of protein bands.

Dot-blot analysis

For further qualitative verification of the Aβ(1–42) and huPrP(23–144) contents within DGC fractions, a dot blot was performed. 2 μl of all 14 denatured sucrose DGC fractions was pipetted onto two pieces of Biotrace NT nitrocellulose membrane (Pall) and allowed to air dry. After blocking with 5% milk powder in 30 mM Tris-HCl, pH 7.6, for 30 min, the membranes were incubated for 15 min with 0.2 μg/ml prion protein mAb Saf32 (Bertin Bioreagent) or 0.6 μg/ml cell culture supernatants of Aβ(1–8)-recognizing IC16 antibody in 5% milk powder, 30 mM Tris-HCl, pH 7.6. After three 5-min washes with 30 mM Tris-HCl, pH 7.6, the membranes were incubated for 15 min with 0.1 μg/ml peroxidase-conjugated AffiniPure goat anti-mouse IgG (heavy + light) (Jackson ImmunoResearch Laboratories) in 5% milk powder, 30 mM Tris-HCl, pH 7.6. After three 5-min washes with 30 mM Tris-HCl, pH 7.6, the immunoreactivity was visualized with SuperSignal West Pico chemiluminescence substrate (Pierce).

Dynamic light scattering

DLS was performed on a submicron particle sizer, Nicomp 380 (Particle Sizing Systems Nicomp, Santa Barbara, CA). Data were analyzed with the Nicomp algorithm using the volume-weighted Nicomp distribution analysis. The DLS sample of Aβ(1–42)$_{oligo}$–huPrP(23–144) complexes derived from 80 μM Aβ(1–42) and 40 μM PrP(23–144) was prepared by pooling fractions 11–14 after sucrose DGC. For data analysis, a measured refractive index in the sample of 1.409 corresponding to 44.8% sucrose and a viscosity of 9.2 centipoise was taken into account (71).

MTT cell viability assay

MTT-based cell viability assays (37) were performed to investigate the cytotoxicity of 1 μM Aβ(1–42)$_{oligo}$ either in the absence or after mixing and further incubation of Aβ(1–42)$_{oligo}$ with 0.02, 0.1, or 0.5 μM huPrP(23–144) or with 0.2 or 1 μM RD2D3, respectively. Rat pheochromocytoma PC12 cells (Leibniz Insti-

tute DSMZ, Braunschweig, Germany) were cultivated in Dulbecco's modified Eagle's medium supplemented with 10% fetal bovine serum and 5% horse serum. 10,000 cells/well were seeded on collagen-coated 96-well plates (Gibco, Life Technologies) and incubated in a 95% humidified atmosphere with 5% CO_2 at 37 °C for 24 h.

Added Aβ(1–42)$_{oligo}$, either alone or after mixing and further incubation with huPrP(23–144) or RD2D3, was prepared as described under "Preparation of samples containing Aβ(1–42) and huPrP (any construct)." The prepared stock solutions contained either 80 μM preincubated Aβ(1–42) alone or 80 μM preincubated Aβ(1–42) mixed and further incubated with 1.6, 8, or 40 μM huPrP(23–144) or 80 μM preincubated Aβ(1–42) mixed and further incubated with 16 or 80 μM RD2D3.

After further incubation for 24 h in a 95% humidified atmosphere with 5% CO_2 at 37 °C, cell viability was measured using Cell Proliferation Kit I (MTT) (Roche Applied Science) according to the manufacturer's instruction. The absorbance of the formazan product was determined by measuring at 570 nm after subtracting the absorption at 660 nm in a Polarstar Optima plate reader (BMG LABTECH, Offenburg, Germany). All results were normalized to cells that were treated with buffer only. The arithmetic mean of all 15 measurements per approach was calculated.

AFM

AFM was done using a Nanowizard 3 system (JPK Instruments AG). All samples were prepared as described under "Preparation of samples containing Aβ(1–42) and huPrP (any construct)". 50 μl of Aβ(1–42)$_{oligo}$ or 25 μl of huPrP(23–144) was incubated on freshly cleaved mica for 3 or 30 min, respectively. Aβ(1–42)$_{oligo}$–huPrP(23–144) heteroassemblies had to be cleared from unbound Aβ(1–42) or huPrP(23–144) and were therefore centrifuged at 16,100 × g at 4 °C for 30 min and washed twice with 100 μl of 30 mM Tris-HCl, pH 7.4, respectively. The complexes were then resuspended in 100 μl of 30 mM Tris-HCl, pH 7.4. Then 50 μl of the complexes was incubated for 30 min on freshly cleaved mica. All samples were washed three times with Milli-Q water and dried in a gentle stream of N_2.

The samples were measured using intermittent contact mode with a resolution of 512 or 1024 pixels and line rates of 0.5–1 Hz in ambient conditions with a silicon cantilever with nominal spring constant of 26 newtons/m and average tip radius of 7 nm (Olympus OMCL-AC160TS). Due to the differing composition of the megadalton-sized aggregates concerning adhesion, stiffness, and perforation, the imaging parameters (amplitude, set point, and gain) had to be adapted slightly, and the cantilever had to be changed often.

The height images of Aβ(1–42)$_{oligo}$ and huPrP(23–144) were flattened with JPK Data Processing software 5.0.69. The statistics of particle dimensions of Aβ(1–42)$_{oligo}$ were done with Gwyddion 2.44 grain analysis. After plane leveling, grains were marked with a threshold of 13%. The maximum height of the individual grain was corrected with subtraction of the grain minimum.

The lateral size is affected by tip convolution effects (Δ) in AFM images. Considering the nominal radius of $r_{tip} = 7$ nm of the AFM tip, we corrected the size of the lateral dimension according to

Interference with Aβ–PrP complex formation

Equation 1 for objects below the tip round end as shown in Canet-Ferrer *et al.* (72). *h* describes the height of the object.

$$\Delta r_{\text{tip}} \times \cos\left[\arcsin\left(\frac{r_{\text{tip}} - h}{r_{\text{tip}}}\right)\right] \qquad \text{(Eq. 1)}$$

CD spectroscopy

6 μM huPrP(23–230), huPrP(23–144), or huPrP(90–230) in 10 mM Tris-HCl, pH 7.4, was analyzed by CD spectroscopy. Each sample was transferred into a cuvette (110-QS, 1 mm, Hellma Analytics), and spectra from 186 to 280 nm were recorded at a scan speed of 50 nm/min in a Jasco J-815 spectropolarimeter. Spectra of 10 mM Tris-HCl, pH 7.4, were used as reference and subtracted from the protein spectra. Ten spectra of each huPrP sample were recorded and accumulated to improve the signal-to-noise ratio.

Solution NMR spectroscopy

NMR samples of 0.2 mM [U-^{15}N]huPrP(23–230) with 10 mM sodium acetate, pH 4.5, in 10% (v/v) D$_2$O and of between 0.11 and 0.36 mM [U-^{15}N]huPrP(23–144) or [U-^{13}C,^{15}N]huPrP(23–144) with different buffers (50 mM, pH ranging from 4.5 to 7.2) in 10% (v/v) D$_2$O were investigated by recording 2D ^{1}H,^{15}N heteronuclear single quantum coherence spectra (73) at different temperatures ranging from 5.0 to 20.0 °C on a Bruker 600-MHz, Varian 800-MHz, or Varian 900-MHz NMR spectrometer equipped with cryogenically cooled triple- or quadruple-resonance probes with *z*-axis pulsed-field gradient capabilities. The sample temperature was calibrated using methanol-d_4 (99.8%) (74). The ^{1}H$_2$O resonance was suppressed by gradient coherence selection with quadrature detection in the indirect ^{15}N dimension achieved by the echo-antiecho method (75, 76). A WALTZ-16 sequence (77) with a field strength of at least 1.1 kHz was used for ^{15}N decoupling during acquisition. At least 927 (128) complex data points were acquired with a spectral width of 16 ppm (26.0 ppm) in the ^{1}H (^{15}N) dimension. All NMR spectra were processed using NMRPipe and NMRDraw (78) and analyzed with NMRViewJ (79). ^{1}H chemical shifts were referenced with respect to external 4,4-dimethyl-4-silapentane-1-sulfonic acid in D$_2$O, and ^{15}N chemical shifts were referenced indirectly (80).

References

1. Selkoe, D. J., and Hardy, J. (2016) The amyloid hypothesis of Alzheimer's disease at 25 years. *EMBO Mol. Med.* **8,** 595–608 CrossRef Medline
2. Walsh, D. M., Klyubin, I., Fadeeva, J. V., Rowan, M. J., and Selkoe, D. J. (2002) Amyloid-β oligomers: their production, toxicity and therapeutic inhibition. *Biochem. Soc. Trans.* **30,** 552–557 CrossRef Medline
3. Walsh, D. M., Klyubin, I., Fadeeva, J. V., Cullen, W. K., Anwyl, R., Wolfe, M. S., Rowan, M. J., and Selkoe, D. J. (2002) Naturally secreted oligomers of amyloid β protein potently inhibit hippocampal long-term potentiation *in vivo. Nature* **416,** 535–539 CrossRef Medline
4. Jarosz-Griffiths, H. H., Noble, E., Rushworth, J. V., and Hooper, N. M. (2016) Amyloid-β receptors: the good, the bad, and the prion protein. *J. Biol. Chem.* **291,** 3174–3183 CrossRef Medline
5. Laurén, J., Gimbel, D. A., Nygaard, H. B., Gilbert, J. W., and Strittmatter, S. M. (2009) Cellular prion protein mediates impairment of synaptic plasticity by amyloid-β oligomers. *Nature* **457,** 1128–1132 CrossRef Medline
6. Nygaard, H. B., and Strittmatter, S. M. (2009) Cellular prion protein mediates the toxicity of β-amyloid oligomers. *Arch. Neurol.* **66,** 1325–1328 CrossRef Medline
7. Balducci, C., Beeg, M., Stravalaci, M., Bastone, A., Sclip, A., Biasini, E., Tapella, L., Colombo, L., Manzoni, C., Borsello, T., Chiesa, R., Gobbi, M., Salmona, M., and Forloni, G. (2010) Synthetic amyloid-β oligomers impair long-term memory independently of cellular prion protein. *Proc. Natl. Acad. Sci. U.S.A.s* **107,** 2295–2300 CrossRef Medline
8. Purro, S. A., Nicoll, A. J., and Collinge, J. (2018) Prion protein as a toxic acceptor of amyloid-β oligomers. *Biol. Psychiatry* **83,** 358–368 CrossRef Medline
9. Salazar, S. V., and Strittmatter, S. M. (2017) Cellular prion protein as a receptor for amyloid-β oligomers in Alzheimer's disease. *Biochem. Biophys. Res. Commun.* **483,** 1143–1147 CrossRef Medline
10. Dohler, F., Sepulveda-Falla, D., Krasemann, S., Altmeppen, H., Schlüter, H., Hildebrand, D., Zerr, I., Matschke, J., and Glatzel, M. (2014) High molecular mass assemblies of amyloid-β oligomers bind prion protein in patients with Alzheimer's disease. *Brain* **137,** 873–886 CrossRef Medline
11. Prusiner, S. B. (1998) Prions. *Proc. Natl. Acad. Sci. U.S.A.* **95,** 13363–13383 CrossRef Medline
12. Um, J. W., Nygaard, H. B., Heiss, J. K., Kostylev, M. A., Stagi, M., Vortmeyer, A., Wisniewski, T., Gunther, E. C., and Strittmatter, S. M. (2012) Alzheimer amyloid-β oligomer bound to postsynaptic prion protein activates Fyn to impair neurons. *Nat. Neurosci.* **15,** 1227–1235 CrossRef Medline
13. Um, J. W., Kaufman, A. C., Kostylev, M., Heiss, J. K., Stagi, M., Takahashi, H., Kerrisk, M. E., Vortmeyer, A., Wisniewski, T., Koleske, A. J., Gunther, E. C., Nygaard, H. B., and Strittmatter, S. M. (2013) Metabotropic glutamate receptor 5 is a coreceptor for Alzheimer Aβ oligomer bound to cellular prion protein. *Neuron* **79,** 887–902 CrossRef Medline
14. Suzuki, T., and Okumura-Noji, K. (1995) NMDA receptor subunits ε1 (NR2A) and ε2 (NR2B) are substrates for Fyn in the postsynaptic density fraction isolated from the rat brain. *Biochem. Biophys. Res. Commun.* **216,** 582–588 CrossRef Medline
15. Nakazawa, T., Komai, S., Tezuka, T., Hisatsune, C., Umemori, H., Semba, K., Mishina, M., Manabe, T., and Yamamoto, T. (2001) Characterization of Fyn-mediated tyrosine phosphorylation sites on GluRε2 (NR2B) subunit of the *N*-methyl-D-aspartate receptor. *J. Biol. Chem.* **276,** 693–699 CrossRef Medline
16. Grundke-Iqbal, I., Iqbal, K., Tung, Y. C., Quinlan, M., Wisniewski, H. M., and Binder, L. I. (1986) Abnormal phosphorylation of the microtubule-associated protein tau (tau) in Alzheimer cytoskeletal pathology. *Proc. Natl. Acad. Sci. U.S.A.* **83,** 4913–4917 CrossRef Medline
17. Larson, M., Sherman, M. A., Amar, F., Nuvolone, M., Schneider, J. A., Bennett, D. A., Aguzzi, A., and Lesné, S. E. (2012) The complex PrPc-Fyn couples human oligomeric Aβ with pathological tau changes in Alzheimer's disease. *J. Neurosci.* **32,** 16857–16871 CrossRef Medline
18. Elezgarai, S. R., and Biasini, E. (2016) Common therapeutic strategies for prion and Alzheimer's diseases. *Biol. Chem.* **397,** 1115–1124 CrossRef Medline

19. Chen, S., Yadav, S. P., and Surewicz, W. K. (2010) Interaction between human prion protein and amyloid-β (Aβ) oligomers: role of N-terminal residues. *J. Biol. Chem.* **285,** 26377–26383 CrossRef Medline

20. Fluharty, B. R., Biasini, E., Stravalaci, M., Sclip, A., Diomede, L., Balducci, C., La Vitola, P., Messa, M., Colombo, L., Forloni, G., Borsello, T., Gobbi, M., and Harris, D. A. (2013) An N-terminal fragment of the prion protein binds to amyloid-β oligomers and inhibits their neurotoxicity *in vivo*. *J. Biol. Chem.* **288,** 7857–7866 CrossRef Medline

21. Kang, M., Kim, S. Y., An, S. S., and Ju, Y. R. (2013) Characterizing affinity epitopes between prion protein and β-amyloid using an epitope mapping immunoassay. *Exp. Mol. Med.* **45,** e34 CrossRef Medline

22. Younan, N. D., Sarell, C. J., Davies, P., Brown, D. R., and Viles, J. H. (2013) The cellular prion protein traps Alzheimer's Aβ in an oligomeric form and disassembles amyloid fibers. *FASEB J.* **27,** 1847–1858 CrossRef Medline

23. Nieznanski, K., Choi, J. K., Chen, S., Surewicz, K., and Surewicz, W. K. (2012) Soluble prion protein inhibits amyloid-β (Aβ) fibrillization and toxicity. *J. Biol. Chem.* **287,** 33104–33108 CrossRef Medline

24. Altmeppen, H. C., Puig, B., Dohler, F., Thurm, D. K., Falker, C., Krasemann, S., and Glatzel, M. (2012) Proteolytic processing of the prion protein in health and disease. *Am. J. Neurodegener. Dis.* **1,** 15–31 Medline

25. Brener, O., Dunkelmann, T., Gremer, L., van Groen, T., Mirecka, E. A., Kadish, I., Willuweit, A., Kutzsche, J., Jürgens, D., Rudolph, S., Tusche, M., Bongen, P., Pietruszka, J., Oesterhelt, F., Langen, K.-J., *et al.* (2015) QIAD assay for quantitating a compound's efficacy in elimination of toxic Aβ oligomers. *Sci. Rep.* **5,** 13222 CrossRef Medline

26. van Groen, T., Wiesehan, K., Funke, S. A., Kadish, I., Nagel-Steger, L., and Willbold, D. (2008) Reduction of Alzheimer's disease amyloid plaque load in transgenic mice by D3, a D-enantiomeric peptide identified by mirror image phage display. *ChemMedChem* **3,** 1848–1852 CrossRef Medline

27. Wiesehan, K., Buder, K., Linke, R. P., Patt, S., Stoldt, M., Unger, E., Schmitt, B., Bucci, E., and Willbold, D. (2003) Selection of D-amino-acid peptides that bind to Alzheimer's disease amyloid peptide Aβ1–42 by mirror image phage display. *ChemBioChem* **4,** 748–753 CrossRef Medline

28. Funke, S. A., van Groen, T., Kadish, I., Bartnik, D., Nagel-Steger, L., Brener, O., Sehl, T., Batra-Safferling, R., Moriscot, C., Schoehn, G., Horn, A. H., Müller-Schiffmann, A., Korth, C., Sticht, H., and Willbold, D. (2010) Oral treatment with the D-enantiomeric peptide D3 improves the pathology and behavior of Alzheimer's disease transgenic mice. *ACS Chem. Neurosci.* **1,** 639–648 CrossRef Medline

29. Leithold, L. H., Jiang, N., Post, J., Ziehm, T., Schartmann, E., Kutzsche, J., Shah, N. J., Breitkreutz, J., Langen, K. J., Willuweit, A., and Willbold, D. (2016) Pharmacokinetic properties of a novel D-peptide developed to be therapeutically active against toxic β-amyloid oligomers. *Pharm. Res.* **33,** 328–336 CrossRef Medline

30. Kutzsche, J., Schemmert, S., Tusche, M., Neddens, J., Rabl, R., Jürgens, D., Brener, O., Willuweit, A., Hutter-Paier, B., and Willbold, D. (2017) Large-scale oral treatment study with the four most promising D3-derivatives for the treatment of Alzheimer's disease. *Molecules* **22,** E1693 CrossRef Medline

31. Van Regenmortel, M. H., and Muller, S. (1998) D-peptides as immunogens and diagnostic reagents. *Curr. Opin. Biotechnol.* **9,** 377–382 CrossRef Medline

32. Dintzis, H. M., Symer, D. E., Dintzis, R. Z., Zawadzke, L. E., and Berg, J. M. (1993) A comparison of the immunogenicity of a pair of enantiomeric proteins. *Proteins* **16,** 306–308 CrossRef Medline

33. Elfgen, A., Santiago-Schübel, B., Gremer, L., Kutzsche, J., and Willbold, D. (2017) Surprisingly high stability of the Aβ oligomer eliminating all-D-enantiomeric peptide D3 in media simulating the route of orally administered drugs. *Eur. J. Pharm. Sci.* **107,** 203–207 CrossRef Medline

34. Leithold, L. H., Jiang, N., Post, J., Niemietz, N., Schartmann, E., Ziehm, T., Kutzsche, J., Shah, N. J., Breitkreutz, J., Langen, K. J., Willuweit, A., and Willbold, D. (2016) Pharmacokinetic properties of tandem D-peptides designed for treatment of Alzheimer's disease. *Eur. J. Pharm. Sci.* **89,** 31–38 CrossRef Medline

35. Schumacher, T. N., Mayr, L. M., Minor, D. L., Jr., Milhollen, M. A., Burgess, M. W., and Kim, P. S. (1996) Identification of D-peptide ligands through mirror-image phage display. *Science* **271,** 1854–1857 CrossRef Medline

36. Olubiyi, O. O., Frenzel, D., Bartnik, D., Glück, J. M., Brener, O., Nagel-Steger, L., Funke, S. A., Willbold, D., and Strodel, B. (2014) Amyloid aggregation inhibitory mechanism of arginine-rich D-peptides. *Curr. Med. Chem.* **21,** 1448–1457 CrossRef Medline

37. van Groen, T., Schemmert, S., Brener, O., Gremer, L., Ziehm, T., Tusche, M., Nagel-Steger, L., Kadish, I., Schartmann, E., Elfgen, A., Jürgens, D., Willuweit, A., Kutzsche, J., and Willbold, D. (2017) The Aβ oligomer eliminating D-enantiomeric peptide RD2 improves cognition without changing plaque pathology. *Sci. Rep.* **7,** 16275 CrossRef Medline

38. Jiang, N., Leithold, L. H., Post, J., Ziehm, T., Mauler, J., Gremer, L., Cremer, M., Schartmann, E., Shah, N. J., Kutzsche, J., Langen, K. J., Breitkreutz, J., Willbold, D., and Willuweit, A. (2015) Preclinical pharmacokinetic studies of the tritium labelled D-enantiomeric peptide D3 developed for the treatment of Alzheimer's disease. *PLoS One* **10,** e0128553 CrossRef Medline

39. Cavini, I. A., Munte, C. E., Erlach, M. B., Van Groen, T., Kadish, I., Zhang, T., Ziehm, T., Nagel-Steger, L., Kutzsche, J., Kremer, W., Willbold, D., and Kalbitzer, H. R. (2018) Inhibition of amyloid Aβ aggregation by high pressures or specific D-enantiomeric peptides. *Chem. Commun.* **54,** 3294–3297 CrossRef Medline

40. Kundu, B., Maiti, N. R., Jones, E. M., Surewicz, K. A., Vanik, D. L., and Surewicz, W. K. (2003) Nucleation-dependent conformational conversion of the Y145Stop variant of human prion protein: structural clues for prion propagation. *Proc. Natl. Acad. Sci. U.S.A.* **100,** 12069–12074 CrossRef Medline

41. Choi, J.-K., Cali, I., Surewicz, K., Kong, Q., Gambetti, P., and Surewicz, W. K. (2016) Amyloid fibrils from the N-terminal prion protein fragment are infectious. *Proc. Natl. Acad. Sci. U.S.A.* **113,** 13851–13856 CrossRef Medline

42. Baskakov, I. V., Legname, G., Baldwin, M. A., Prusiner, S. B., and Cohen, F. E. (2002) Pathway complexity of prion protein assembly into amyloid. *J. Biol. Chem.* **277,** 21140–21148 CrossRef Medline

43. Theint, T., Nadaud, P. S., Aucoin, D., Helmus, J. J., Pondaven, S. P., Surewicz, K., Surewicz, W. K., and Jaroniec, C. P. (2017) Species-dependent structural polymorphism of Y145Stop prion protein amyloid revealed by solid-state NMR spectroscopy. *Nat. Commun.* **8,** 753 CrossRef Medline

44. Selkoe, D. J. (2001) Alzheimer's disease: genes, proteins, and therapy. *Physiol. Rev.* **81,** 741–766 CrossRef Medline

45. Gremer, L., Schölzel, D., Schenk, C., Reinartz, E., Labahn, J., Ravelli, R. B. G., Tusche, M., Lopez-Iglesias, C., Hoyer, W., Heise, H., Willbold, D., and Schröder, G. F. (2017) Fibril structure of amyloid-β(1–42) by cryo-electron microscopy. *Science* **358,** 116–119 CrossRef Medline

46. Morillas, M., Swietnicki, W., Gambetti, P., and Surewicz, W. K. (1999) Membrane environment alters the conformational structure of the recombinant human prion protein. *J. Biol. Chem.* **274,** 36859–36865 CrossRef Medline

47. Zahn, R., Liu, A., Lührs, T., Riek, R., von Schroetter, C., López García, F., Billeter, M., Calzolai, L., Wider, G., and Wüthrich, K. (2000) NMR solution structure of the human prion protein. *Proc. Natl. Acad. Sci. U.S.A.* **97,** 145–150 CrossRef Medline

48. Wishart, D. S., Bigam, C. G., Holm, A., Hodges, R. S., and Sykes, B. D. (1995) 1H, ^{13}C and ^{15}N random coil NMR chemical shifts of the common amino acids. I. Investigations of nearest-neighbor effects. *J. Biomol. NMR* **5,** 67–81 CrossRef Medline

49. Calella, A. M., Farinelli, M., Nuvolone, M., Mirante, O., Moos, R., Falsig, J., Mansuy, I. M., and Aguzzi, A. (2010) Prion protein and Aβ-related synaptic toxicity impairment. *EMBO Mol. Med.* **2,** 306–314 CrossRef Medline

50. Kessels, H. W., Nguyen, L. N., Nabavi, S., and Malinow, R. (2010) The prion protein as a receptor for amyloid-β. *Nature* **466,** E3–E4 CrossRef Medline

51. Cissé, M., Sanchez, P. E., Kim, D. H., Ho, K., Yu, G.-Q., and Mucke, L. (2011) Ablation of cellular prion protein does not ameliorate abnormal neural network activity or cognitive dysfunction in the J20 line of human amyloid precursor protein transgenic mice. *J. Neurosci.* **31,** 10427–10431 CrossRef Medline

52. Scott-McKean, J. J., Surewicz, K., Choi, J. K., Ruffin, V. A., Salameh, A. I., Nieznanski, K., Costa, A. C. S., and Surewicz, W. K. (2016) Soluble prion protein and its N-terminal fragment prevent impairment of synaptic plas-

SASBMB

ticity by Aβ oligomers: implications for novel therapeutic strategy in Alzheimer's disease. *Neurobiol. Dis.* **91,** 124–131 CrossRef Medline

53. Wahlberg, E., Rahman, M. M., Lindberg, H., Gunneriusson, E., Schmuck, B., Lendel, C., Sandgren, M., Löfblom, J., Ståhl, S., and Härd, T. (2017) Identification of proteins that specifically recognize and bind protofibrillar aggregates of amyloid-β. *Sci. Rep.* **7,** 5949 CrossRef Medline

54. Mitrea, D. M., Cika, J. A., Guy, C. S., Ban, D., Banerjee, P. R., Stanley, C. B., Nourse, A., Deniz, A. A., and Kriwacki, R. W. (2016) Nucleophosmin integrates within the nucleolus via multi-modal interactions with proteins displaying R-rich linear motifs and rRNA. *Elife* 5, e13571 CrossRef Medline

55. Tavares, G. M., Croguennec, T., Hamon, P., Carvalho, A. F., and Bouhallab, S. (2015) Selective coacervation between lactoferrin and the two isoforms of β-lactoglobulin. *Food Hydrocoll.* **48,** 238–247 CrossRef

56. Peixoto, P. D., Tavares, G. M., Croguennec, T., Nicolas, A., Hamon, P., Roiland, C., and Bouhallab, S. (2016) Structure and dynamics of heteroprotein coacervates. *Langmuir* **32,** 7821–7828 CrossRef Medline

57. Stuermer, C. A., Langhorst, M. F., Wiechers, M. F., Legler, D. F., Von Hanwehr, S. H., Guse, A. H., and Plattner, H. (2004) PrPc capping in T cells promotes its association with the lipid raft proteins reggie-1 and reggie-2 and leads to signal transduction. *FASEB J.* **18,** 1731–1733 CrossRef Medline

58. Pantera, B., Bini, C., Cirri, P., Paoli, P., Camici, G., Manao, G., and Caselli, A. (2009) PrPc activation induces neurite outgrowth and differentiation in PC12 cells: role for caveolin-1 in the signal transduction pathway. *J. Neurochem.* **110,** 194–207 CrossRef Medline

59. Wulf, M.-A., Senatore, A., and Aguzzi, A. (2017) The biological function of the cellular prion protein: an update. *BMC Biol.* **15,** 34 CrossRef Medline

60. Béland, M., Bédard, M., Tremblay, G., Lavigne, P., and Roucou, X. (2014) Aβ induces its own prion protein N-terminal fragment (PrPN1)-mediated neutralization in amorphous aggregates. *Neurobiol. Aging* **35,** 1537–1548 CrossRef Medline

61. Aimi, T., Suzuki, K., Hoshino, T., and Mizushima, T. (2015) Dextran sulfate sodium inhibits amyloid-β oligomer binding to cellular prion protein. *J. Neurochem.* **134,** 611–617 CrossRef Medline

62. Risse, E., Nicoll, A. J., Taylor, W. A., Wright, D., Badoni, M., Yang, X., Farrow, M. A., and Collinge, J. (2015) Identification of a compound that disrupts binding of amyloid-β to the prion protein using a novel fluorescence-based assay. *J. Biol. Chem.* **290,** 17020–17028 CrossRef Medline

63. Kudo, W., Lee, H.-P., Zou, W.-Q., Wang, X., Perry, G., Zhu, X., Smith, M. A., Petersen, R. B., and Lee, H.-G. (2012) Cellular prion protein is essential for oligomeric amyloid-β-induced neuronal cell death. *Hum. Mol. Genet.* **21,** 1138–1144 CrossRef Medline

64. Freir, D. B., Nicoll, A. J., Klyubin, I., Panico, S., Mc Donald, J. M., Risse, E., Asante, E. A., Farrow, M. A., Sessions, R. B., Saibil, H. R., Clarke, A. R., Rowan, M. J., Walsh, D. M., and Collinge, J. (2011) Interaction between prion protein and toxic amyloid β assemblies can be therapeutically targeted at multiple sites. *Nat. Commun.* **2,** 336 CrossRef Medline

65. Peters, C., Espinoza, M. P., Gallegos, S., Opazo, C., and Aguayo, L. G. (2015) Alzheimer's Aβ interacts with cellular prion protein inducing neuronal membrane damage and synaptotoxicity. *Neurobiol. Aging* **36,** 1369–1377 CrossRef Medline

66. van Groen, T., Kadish, I., Funke, S. A., Bartnik, D., and Willbold, D. (2013) Treatment with D3 removes amyloid deposits, reduces inflammation, and improves cognition in aged AβPP/PS1 double transgenic mice. *J. Alzheimer's Dis.* **34,** 609–620 Medline

67. Luers, L., Panza, G., Henke, F., Agyenim, T., Weiss, J., Willbold, D., and Birkmann, E. (2010) Amyloid formation: age-related mechanism in Creutzfeldt-Jakob disease? *Rejuvenation Res.* **13,** 214–216 CrossRef Medline

68. Mehlhorn, I., Groth, D., Stöckel, J., Moffat, B., Reilly, D., Yansura, D., Willett, W. S., Baldwin, M., Fletterick, R., Cohen, F. E., Vandlen, R., Henner, D., and Prusiner, S. B. (1996) High-level expression and characterization of a purified 142-residue polypeptide of the prion protein. *Biochemistry* **35,** 5528–5537 CrossRef Medline

69. Schägger, H., and von Jagow, G. (1987) Tricine-sodium dodecyl sulfate-polyacrylamide gel electrophoresis for the separation of proteins in the range from 1 to 100 kDa. *Anal. Biochem.* **166,** 368–379 CrossRef Medline

70. Heukeshoven, J., and Dernick, R. (1988) Improved silver staining procedure for fast staining in PhastSystem Development Unit. I. Staining of sodium dodecyl sulfate gels. *Electrophoresis* **9,** 28–32 CrossRef Medline

71. Dawson, R. M. C., Elliott, D. C., Elliott, W. H., and Jones, K. M. (1986) *Data for Biochemical Research*, 3rd Ed., p. 545, Oxford Science Publications, Oxford, UK

72. Canet-Ferrer, J., Coronado, E., Forment-Aliaga, A., and Pinilla-Cienfuegos, E. (2014) Correction of the tip convolution effects in the imaging of nanostructures studied through scanning force microscopy. *Nanotechnology* **25,** 395703 CrossRef Medline

73. Zhang, O., Kay, L. E., Olivier, J. P., and Forman-Kay, J. D. (1994) Backbone ^{1}H and ^{15}N resonance assignments of the N-terminal SH3 domain of drk in folded and unfolded states using enhanced-sensitivity pulsed field gradient NMR techniques. *J. Biomol. NMR* **4,** 845–858 CrossRef Medline

74. Findeisen, M., Brand, T., and Berger, S. (2007) A ^{1}H-NMR thermometer suitable for cryoprobes. *Magn. Reson. Chem.* **45,** 175–178 CrossRef Medline

75. Kay, L. E., Keifer, P., and Saarinen, T. (1992) Pure absorption gradient enhanced heteronuclear single quantum correlation spectroscopy with improved sensitivity. *J. Am. Chem. Soc.* **114,** 10663–10665 CrossRef

76. Schleucher, J., Sattler, M., and Griesinger, C. (1993) Coherence selection by gradients without signal attenuation: application to the three-dimensional HNCO experiment. *Angew. Chem. Int. Ed. Engl.* **32,** 1489–1491 CrossRef

77. Shaka, A. J., Keeler, J., Frenkiel, T., and Freeman, R. (1983) An improved sequence for broadband decoupling: WALTZ-16. *J. Magn. Reson.* **52,** 335–338 CrossRef

78. Delaglio, F., Grzesiek, S., Vuister, G. W., Zhu, G., Pfeifer, J., and Bax, A. (1995) NMRPipe: a multidimensional spectral processing system based on UNIX pipes. *J. Biomol. NMR.* **6,** 277–293 Medline

79. Johnson, B. A., and Blevins, R. A. (1994) NMR View: a computer program for the visualization and analysis of NMR data. *J. Biomol. NMR* **4,** 603–614 CrossRef Medline

80. Markley, J. L., Bax, A., Arata, Y., Hilbers, C. W., Kaptein, R., Sykes, B. D., Wright, P. E., and Wuethrich, K. (1998) Recommendations for the presentation of NMR structures of proteins and nucleic acids (IUPAC Recommendations 1998). *Pure Appl. Chem.* **70,** 117–142 CrossRef

SASBMB

A d-enantiomeric peptide interferes with heteroassociation of amyloid-β oligomers and prion protein

Nadine S. Rösener, Lothar Gremer, Elke Reinartz, Anna König, Oleksandr Brener,
Henrike Heise, Wolfgang Hoyer, Philipp Neudecker and Dieter Willbold

---

Access the most updated version of this article at doi: 10.1074/jbc.RA118.003116

Alerts:
- When this article is cited
- When a correction for this article is posted

Click here to choose from all of JBC's e-mail alerts

This article cites 79 references, 21 of which can be accessed free at
http://www.jbc.org/content/293/41/15748.full.html#ref-list-1

SUPPORTING INFORMATION (11 figures)

A D-enantiomeric peptide interferes with hetero-association of amyloid-β oligomers and prion protein*

Nadine S. Rösener[1,2], Lothar Gremer[1,2], Elke Reinartz[1], Anna König[1,2], Oleksandr Brener[1,2], Henrike Heise[1,2], Wolfgang Hoyer[1,2], Philipp Neudecker[1,2] and Dieter Willbold[1,2]

From the [1]Institut für Physikalische Biologie, Heinrich-Heine-Universität Düsseldorf, 40225 Düsseldorf, Germany, [2]Institute of Complex Systems, Structural Biochemistry (ICS-6), Forschungszentrum Jülich, 52425 Jülich, Germany

*Running title: *Interference with Aβ-PrP complex formation*

Material included:

Figure S1. Sample purity of the used huPrP variants (huPrP(23-144), huPrP(90-230), huPrP(23-230) and huPrP(121-230))

Figure S2: Purified huPrP(23-230), huPrP(90-230) and huPrP(121-230) under study contain a disulfide bond between Cys-179 and Cys-214

Figure S3. [^{1}H,^{15}N] HSQC spectra of huPrP(23-144) and huPrP(23-230) in solution

Figure S4. Heights and radii of the generated Aβ(1-42)$_{oligo}$ species as seen by AFM

Figure S5. Distribution of standard proteins after sucrose DGC

Figure S6: Impaired formation of hetero-assemblies of Aβ(1-42)$_{oligo}$ and huPrP(121-230)

Figure S7. Distribution of Aβ(1-42) and huPrP(23-144) in a sucrose gradient after incubation of 80 µM Aβ(1-42)$_{oligo}$ with 40 µM huPrP(23-144) by immune dot blot

Figure S8. Distribution of Aβ(1-42) and huPrP(23-144) in a sucrose gradient after incubation of Aβ(1-42)$_{oligo}$ with 60 µM huPrP(23-144)

Figure S9: Anchorless huPrP(23-144) or RD2D3 rescues the negative impact of Aβ(1-42)$_{oligo}$ on cell viability in PC-12 cells

Figure S10. Distribution of 40 µM RD2D3-FITC alone (A) and of 20 µM RD2D3-FITC with 10 µM huPrP(23-144) (B) after sucrose DGC

Figure S11. Interference of the Aβ(1-42)$_{oligo}$-huPrP(23-144) interaction by RD2D3-FITC

References:

1.   Orekhov, V. Y., Ibraghimov, I. V., and Billeter, M. (2001) MUNIN: A new approach to multi-dimensional NMR spectra interpretation. *J. Biomol. NMR*. **20**, 49–60
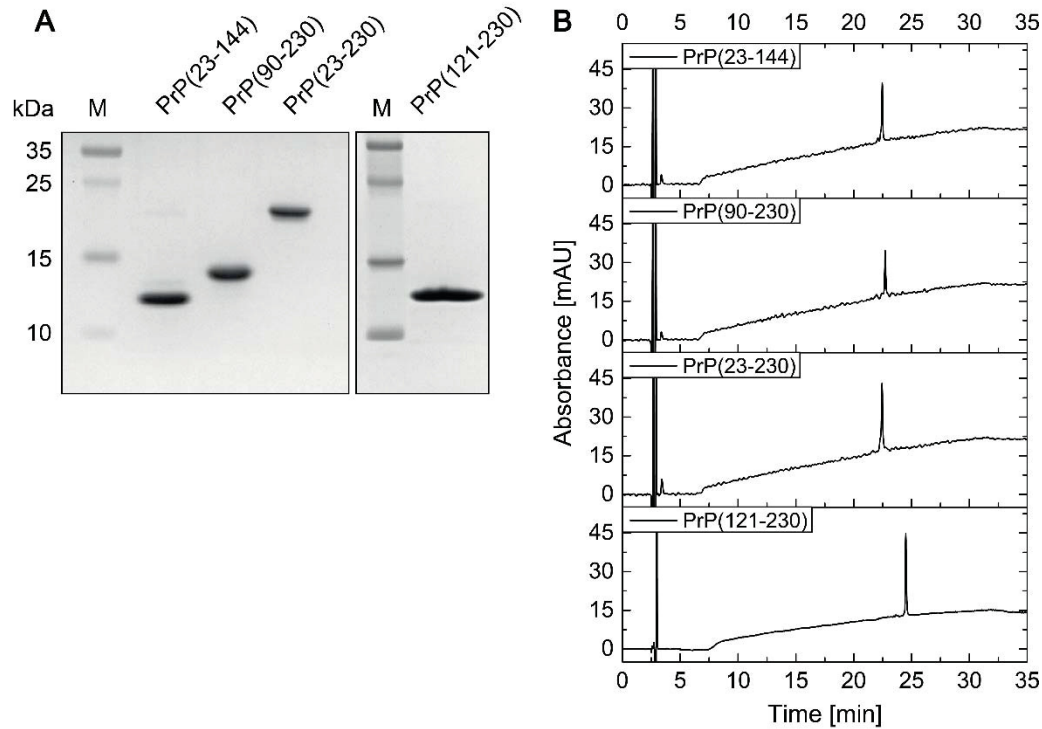
Figure S1: Sample purity of the used huPrP variants (huPrP(23-144), huPrP(90-230), huPrP(23-230) and huPrP(121-230)). 5 µg of each purified huPrP were qualitatively analysed by Tris/Glycine SDS-PAGE (A). RP-HPLC chromatograms show the purity of 1 µM of each huPrP variant (B). The huPrP variants have retention times of about 22 to 24.5 min and were generated in high purity as there are no further peaks visible.
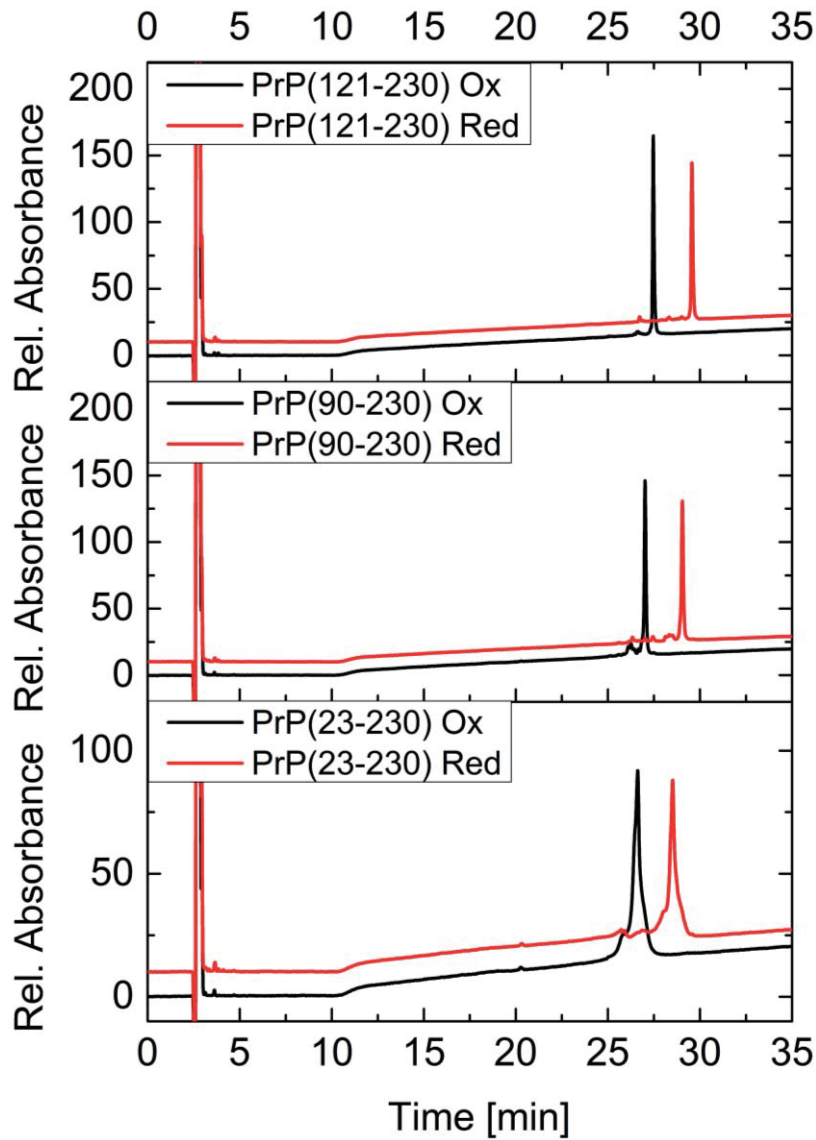
Figure S2: Purified huPrP(23-230), huPrP(90-230) and huPrP(121-230) under study contain a disulfide bond between Cys-179 and Cys-214. The reductive opening of the disulfide bond leads to a characteristic elongation of the retention time in RP-HPLC analyses and verify the exclusive presence of the disulfide bond in purified huPrP(23-230), huPrP(90-230) and huPrP(121-230) and the absence of any reduced fraction in the samples.
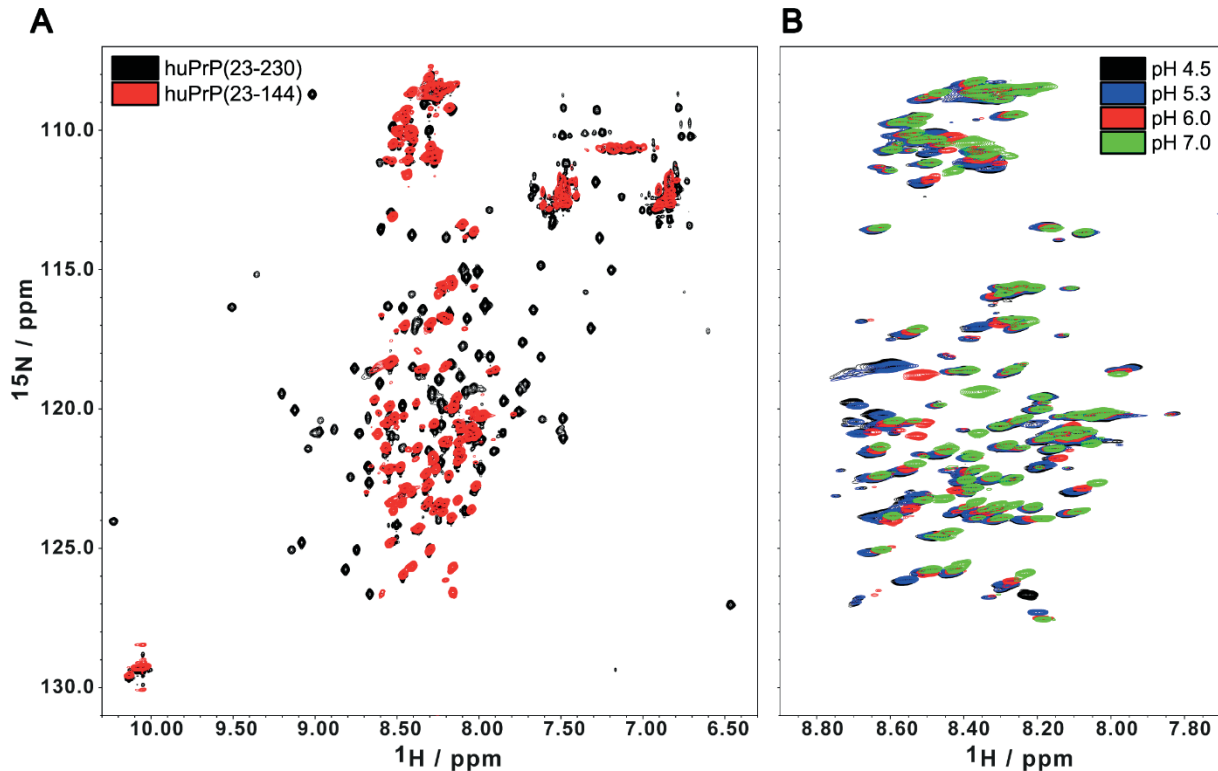
Figure S3: [¹H,¹⁵N] HSQC NMR spectra of huPrP(23-144) and huPrP(23-230) in solution. (A) Overlay of the [¹H,¹⁵N] HSQC spectra of 0.2 mM [U-¹⁵N] huPrP(23-230) in 10 mM sodium acetate (pH 4.5) in 10 % (v/v) D₂O (black) and of 0.36 mM [U-¹³C,¹⁵N] huPrP(23-144) in 50 mM sodium acetate (pH 4.5) in 10 % (v/v) D₂O (red) recorded at 20.0 °C at 900 MHz and 600 MHz, respectively. Arginine ¹⁵Nε side-chain resonances resonating at about 85 ppm are aliased to about 111 ppm in the ¹⁵N dimension and show side bands in the ¹H dimension due to the limited bandwidth of the WALTZ-16 ¹⁵N decoupling during acquisition. Whereas huPrP(23-230) exhibits the well-dispersed backbone amide resonances of the globular C-terminal prion domain, only backbone amide resonances in the random coil region (8.0 ppm < ¹H < 8.6 ppm) are visible in the spectrum of the truncation construct huPrP(23-144). (B) Overlay of the backbone amide region of the [¹H,¹⁵N] HSQC spectra of 0.36 mM [U-¹³C,¹⁵N] huPrP(23-144) in 50 mM sodium acetate (pH 4.5) (black), 0.11 mM [U-¹³C,¹⁵N] huPrP(23-144) in 50 mM sodium acetate (pH 5.3) (blue), 0.28 mM [U-¹³C,¹⁵N] huPrP(23-144) in 50 mM MES (pH 6.0) (red), and 0.30 mM [U-¹³C,¹⁵N] huPrP(23-144) in 50 mM HEPES (pH 7.0) (green) in 10 % (v/v) D₂O recorded at 5.0 °C at 600 MHz, 600 MHz, 800 MHz, and 800 MHz, respectively.

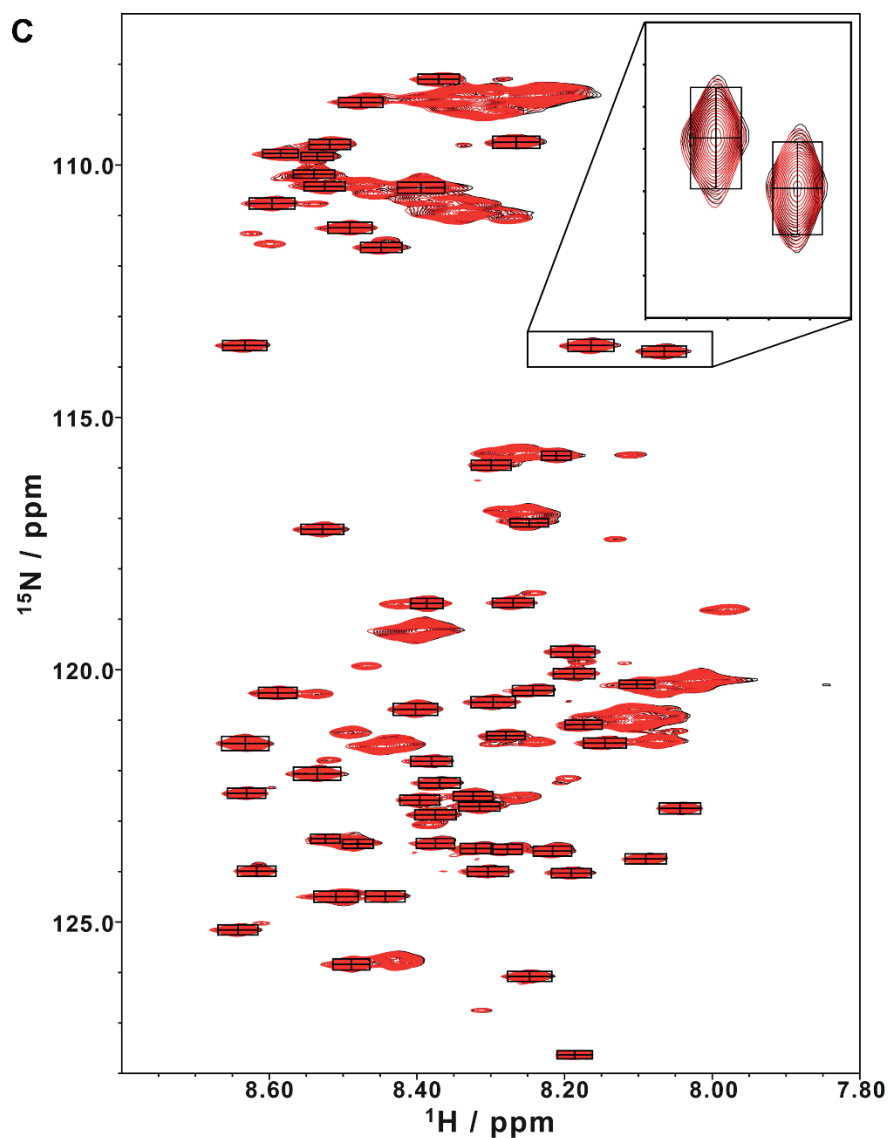**Figure S3 continued:** (C) Overlay of the first (time *t* = 0, black) and the last (*t* = 55.6 h later, red) [^{1}H,^{15}N] HSQC spectra of a sample of 89 µM [U-^{15}N] huPrP(23-144) with 50 mM Tris-HCl (pH 7.2) in 10 % D$_2$O in a series of [^{1}H,^{15}N] HSQC spectra recorded at 600 MHz, 5.0 °C. The spectra are so stable over this time period that the contour levels are virtually superimposable, as highlighted by expanding a small region containing two example resonances in the inset. 57 sufficiently well-resolved backbone amide resonances (black rectangular boxes) plus the side-chain indole resonance of Trp99 (which resonates at 10.16 ppm/129.78 ppm in a different region of the spectrum) were selected for quantitative analysis of the peak intensities.

D
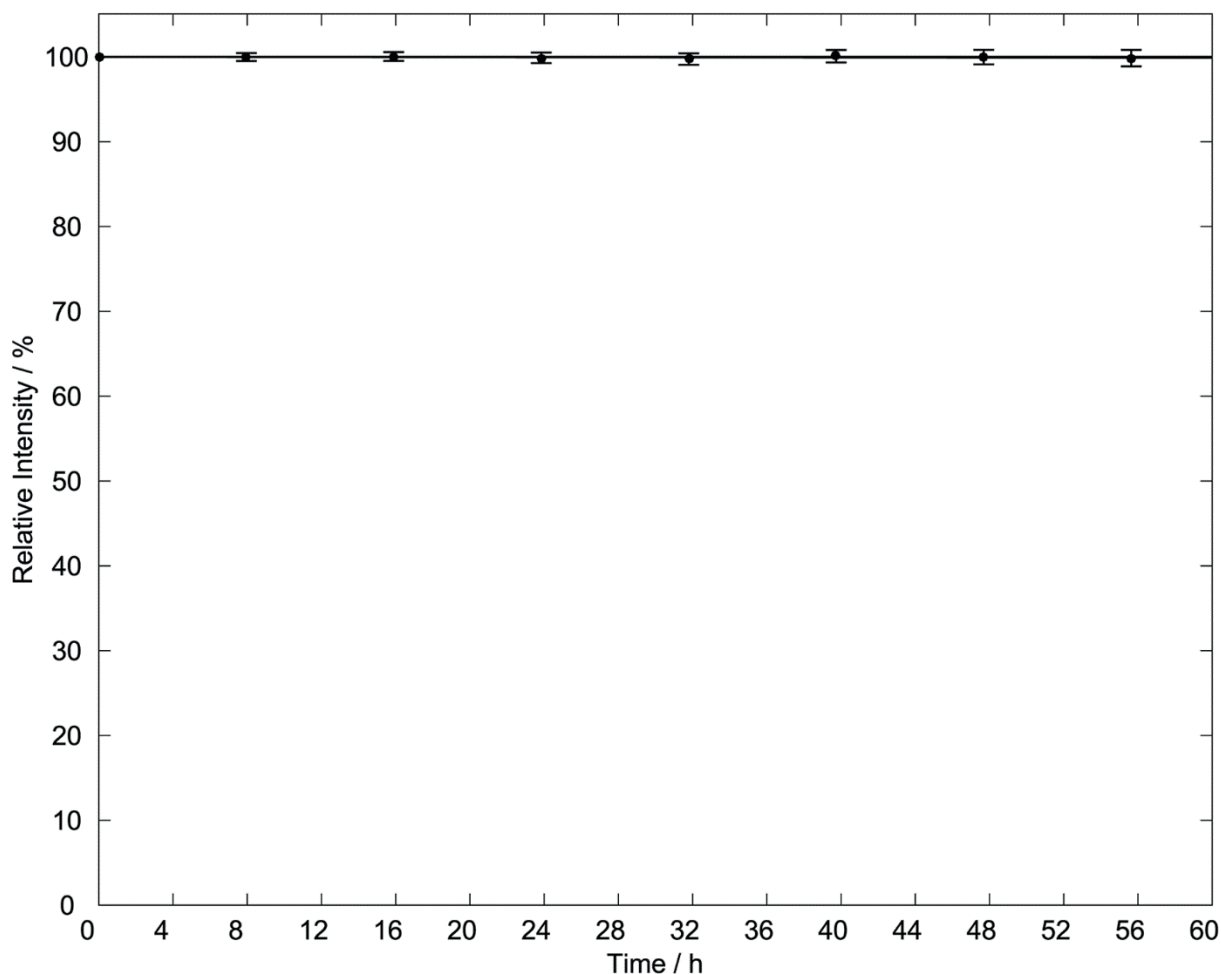
Figure S3 continued: (D) Relative amide resonance intensity of a sample of 89 µM [U-^{15}N] huPrP(23-144) with 50 mM Tris-HCl (pH 7.2) in 10 % D$_2$O in a series of [^{1}H,^{15}N] HSQC spectra recorded at 600 MHz, 5.0 °C. The intensity of the 58 sufficiently well-resolved amide resonances in the rectangular boxes shown in (C) in the spectrum recorded at time *t* relative to the respective intensity in the first spectrum (time *t* = 0, relative intensity 100 % per definition) was quantified by three-way decomposition using MUNIN: A new approach to multi-dimensional NMR spectra interpretation, *J. Biomol. NMR* **20**, 49-60 (1) and is reported in the form average ± standard deviation. Linear regression yields are relative intensity of 99.992 % - 0.0017 %/h×*t* (solid line), corresponding to an intensity loss of about 0.1 % over the entire observation period of 55.6 h. Because this is within the standard error of the average relative intensity at 55.6 h, we conclude that no statistically significant change in resonance intensity was observed over a period of 55.6 h. The sample had been prepared four days before the start of the first experiment (defined as *t* = 0). Even after four days of storage at 4 °C no significant degradation or nucleation of aggregation had occurred, as evidenced by fact that the [^{1}H,^{15}N] HSQC spectra are free of any degradation products (C) and that no signal loss expected for any sample aggregation was detectable (D).
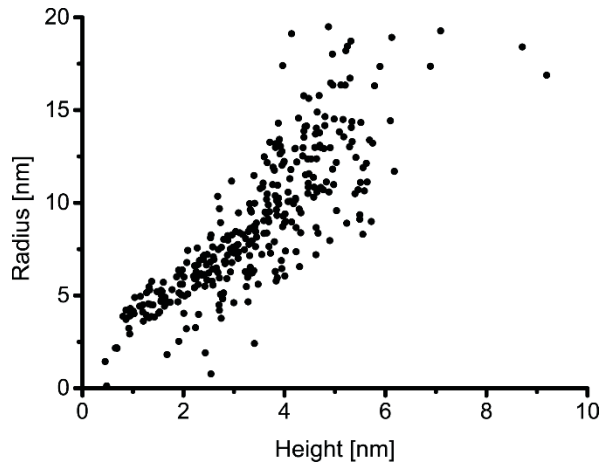
Figure S4: Heights and radii of the generated Aβ(1-42)oligo species as seen by AFM. Aβ(1-42)oligo show a size distribution with heights ranging from 1 nm to 6 nm, very rarely up to 10 nm, and radii up to 20 nm.
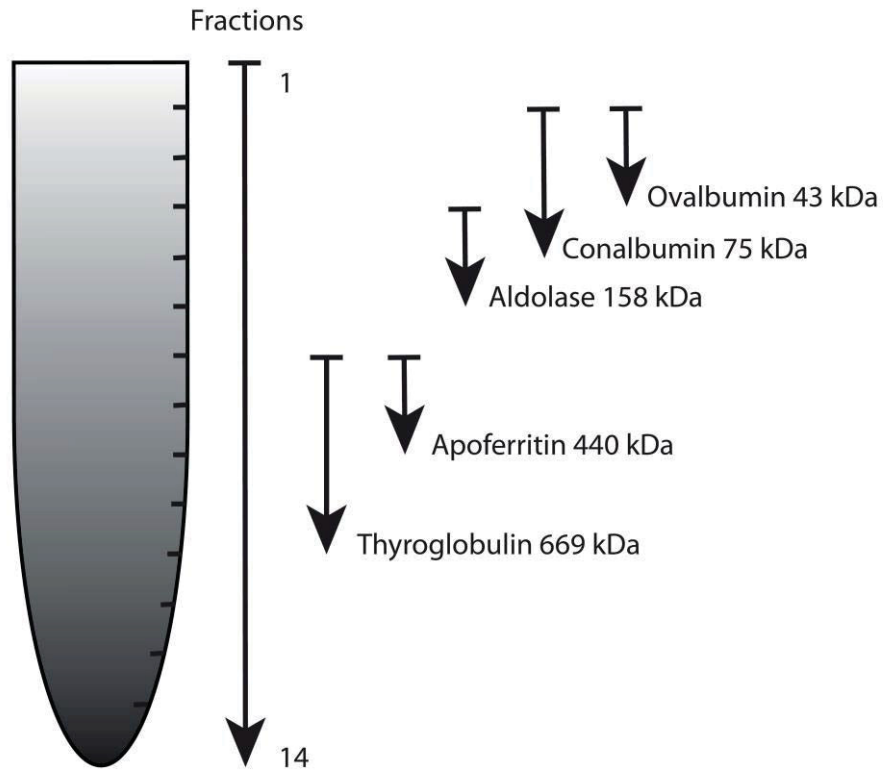
Figure S5: Distribution of standard proteins after sucrose DGC. The protein with the highest molecular mass (thyroglobulin, 669 kDa) was found in fractions 7 to 10.
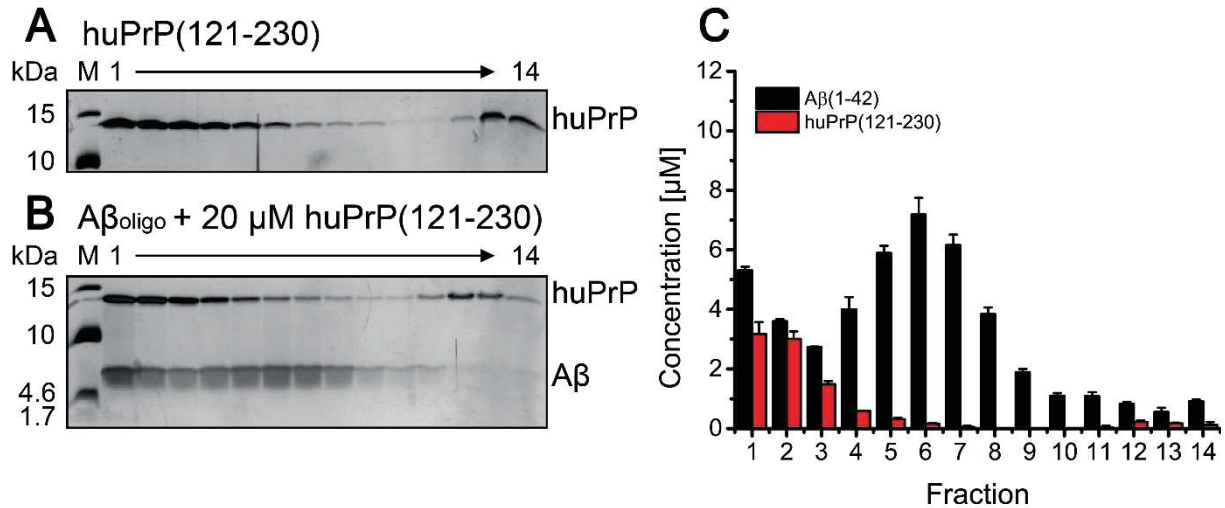
Figure S6: Impaired formation of hetero-assemblies of Aβ(1-42)$_{oligo}$ and huPrP(121-230). (A) Silver-stained Tris/Tricine SDS-PAGE gel after application of 20 µM huPrP(121-230) on a sucrose gradient. (B) Silver-stained Tris/Tricine SDS-PAGE gel after application of 80 µM of pre-incubated Aβ(1-42) with 20 µM huPrP(121-230) on a sucrose gradient and (C) corresponding histogram after RP-HPLC analysis shows the distribution of Aβ(1-42) and huPrP(121-230). huPrP(121-230) was found in fractions 1 to 6 for both the control (A) and in presence of Aβ(1-42)$_{oligo}$ (B). Just very low concentrations below 0.2 µM of huPrP(121-230) were detected in the bottom gradient fractions 11 to 14 as confirmed by RP-HPLC (C). The majority of Aβ(1-42) was observed in fractions 1 to 8 showing a characteristic distribution of Aβ(1-42)$_{oligo}$ in fractions 4 to 8. Just low concentrations of Aβ were found in fractions 11 to 14. Thus, Aβ(1-42)$_{oligo}$ and huPrP(121-230) do not form high molecular weight hetero-assemblies. Experiments are done in replicates of n = 3 (C) ± SD.
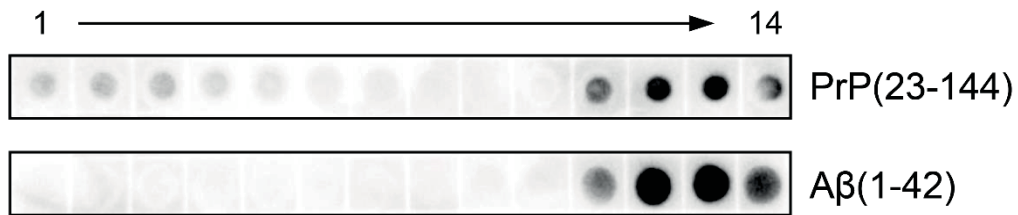
Figure S7: Distribution of Aβ(1-42) and huPrP(23-144) in a sucrose gradient after incubation of 80 μM Aβ(1-42)$_{oligo}$ with 40 μM huPrP(23-144) by immune dot blot. Qualitative analysis was performed by an immune dot blot assay of the DGC fractions with prion antibody Saf32 or Aß42 binding IgG IC16. Aβ(1-42) is entirely bound to huPrP(23-144) and thereby detected in fractions 11 to 14. huPrP(23-144) was used in excess and is found in fractions 11 to 14 (complexes) as well as in fractions 1 to 4 in its soluble non-aggregated state.
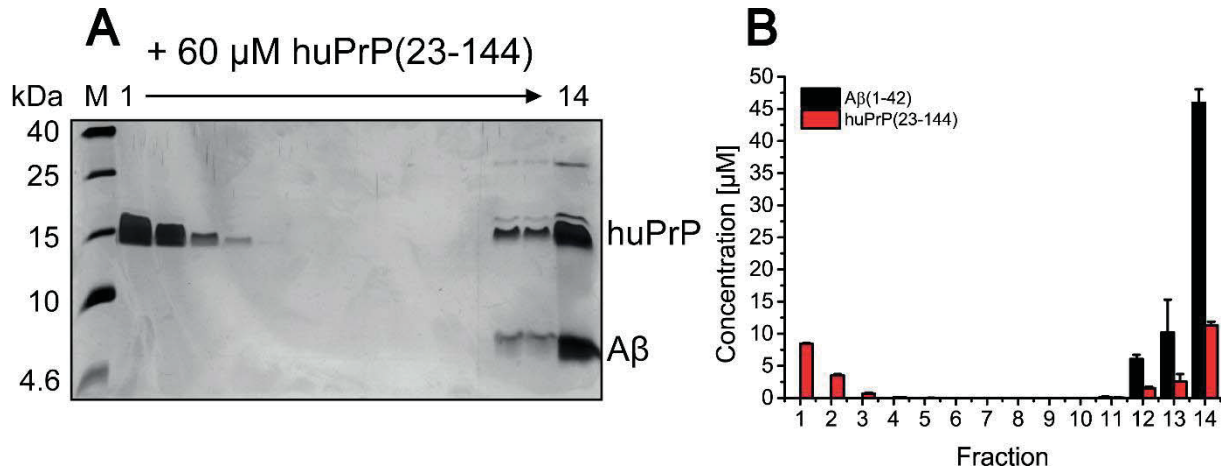
Figure S8: Distribution of Aβ(1-42) and huPrP(23-144) in a sucrose gradient after incubation of Aβ(1-42)$_{oligo}$ with 60 µM huPrP(23-144). (A) Silver-stained Tris/Tricine SDS-PAGE gel after application of 80 µM of pre-incubated Aβ(1-42) with 60 µM huPrP(23-144) on a sucrose gradient and (B) corresponding histogram after RP-HPLC analysis shows the distribution of Aβ(1-42) and huPrP(23-144). Aβ(1-42) is entirely bound to huPrP(23-144) and thereby detected in fractions 12 to 14. huPrP(23-144) was used in excess and is found in fraction 12 to 14 (complexes) as well as in fractions 1 to 4 in its soluble non-aggregated state. Experiments are done in replicates of n = 3 (B) ± SD.
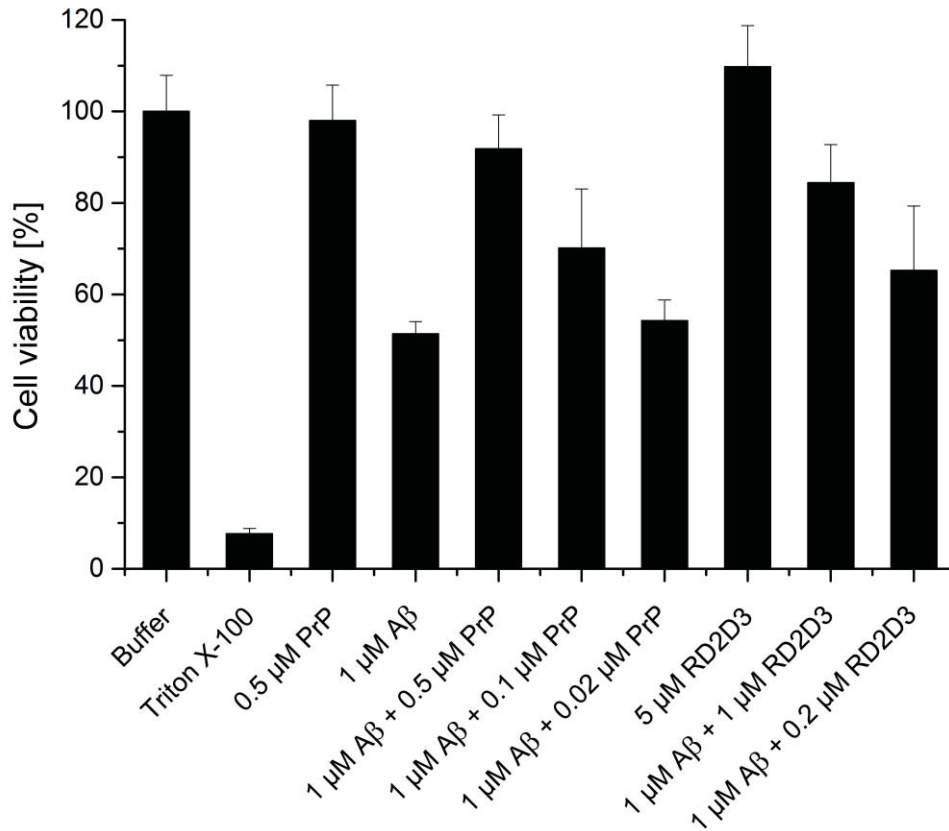
Figure S9: Anchorless huPrP(23-144) or RD2D3 rescue the negative impact of Aβ(1-42)$_{oligo}$ on cell viability in PC-12 cells. Cell viability was assessed by MTT assay after incubation of PC-12 cells with 1 μM Aβ(1-42)$_{oligo}$ alone or either after mixing and further incubation of Aβ(1-42)$_{oligo}$ with 0.02, 0.1 or 0.5 μM huPrP(23-144) or with 0.2, or 1 μM RD2D3, respectively. Data confirms the efficacy of anchorless huPrP(23-144) or RD2D3 to rescue the cell viability in a concentration-dependent manner after incubation with Aβ(1-42)$_{oligo}$ compared to Aβ(1-42)$_{oligo}$ alone. Cells treated with 0.125 % Triton X-100 were used as a positive control. Results were normalised to cells treated with buffer only. Values are means ± SD of 15 replicates.
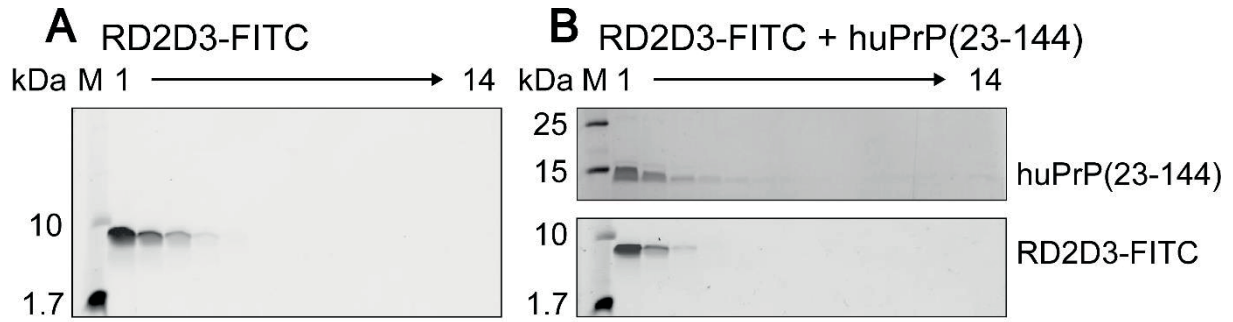
Figure S10: Distribution of 40 µM RD2D3-FITC alone (A) and of 20 µM RD2D3-FITC with 10 µM huPrP(23-144) (B) after sucrose DGC. RD2D3-FITC alone was detected in fractions 1 to 4 after fluorescence detection of a Tris/Tricine SDS-PAGE gel and is therefore present in a soluble and not aggregated state (A). RD2D3-FITC and huPrP(23-144) were incubated for 30 min before analysis by sucrose DGC and were both found in fractions 1 to 4 in a Tris/Tricine SDS-PAGE gel (B). The Tris/Tricine SDS-PAGE gel on the top was stained with silver and the gel on the bottom shows the same gel after fluorescence detection of RD2D3-FITC and before silver staining. As there are no bands visible in fractions 11 to 14, huPrP(23-144) and RD2D3-FITC do not form high molecular weight aggregates.
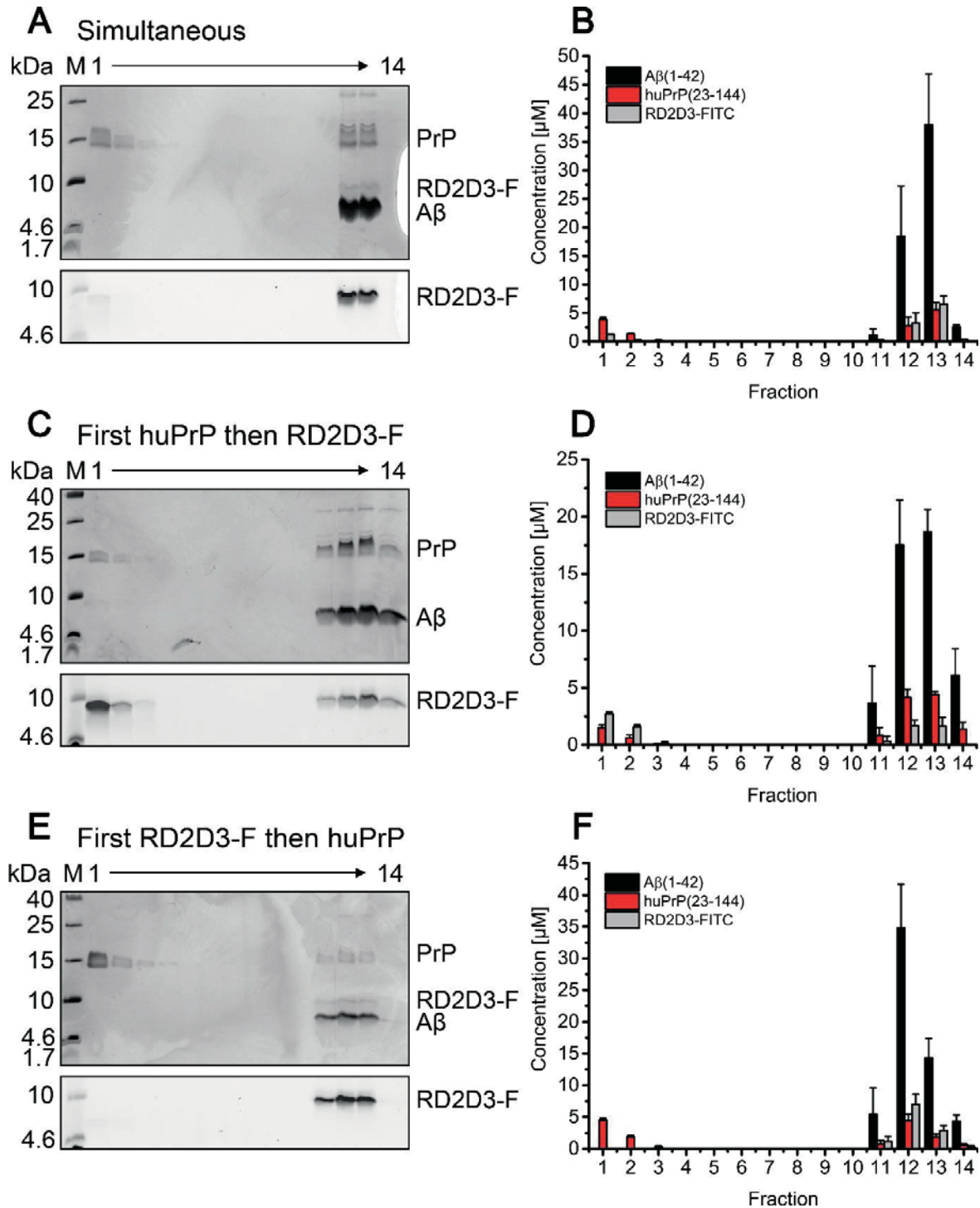
Figure S11: Interference of the Aβ(1-42)$_{oligo}$-huPrP(23-144) interaction by RD2D3-FITC. Distribution of 80 µM Aβ(1-42), 40 µM huPrP(23-144), and 20 µM RD2D3-FITC, after sucrose DGC for different orders of RD2D3-FITC and huPrP(23-144) addition. (A, C and E) Aβ(1-42) and huPrP(23-144) distributions are shown in silver-stained Tris/Tricine SDS-PAGE gels and the distribution of RD2D3-FITC after fluorescence detection on the same gels. (B, D and F) Quantification by RP-HPLC of each component. huPrP(23-144) and RD2D3-FITC were either (A, B) simultaneously added to Aβ(1-42)$_{oligo}$, (C, D) huPrP(23-144) was pre-incubated with Aβ before RD2D3-FITC addition, or (E, F) RD2D3-FITC was pre-incubated with Aβ before huPrP(23-144) addition. Dependent on the order of application of RD2D3-FITC or huPrP(23-144) to the sample, the distributions of huPrP(23-144) and RD2D3-FITC change. Experiments are done in replicates of n = 3 ± SD for all orders of application of RD2D3-FITC or huPrP(23-144) to the sample.

Development of a new largely scalable *in vitro* prion propagation method for the production of infectious recombinant prions for high resolution structural studies

Hasier Eraña[1,2], Jorge M. Charco[1], Michele A. Di Bari[3], Carlos M. Díaz-Domínguez[1], Rafael López-Moreno[1], Enric Vidal[4], Ezequiel González-Miranda[1], Miguel A. Pérez-Castro[1], Sandra García-Martínez[1,2], Susana Bravo[5], Natalia Fernández-Borges[1], Mariví Geijo[6], Claudia D'Agostino[3], Joseba Garrido[6], Jifeng Bian[7], Anna König[8,9], Boran Uluca-Yazgi[8,9], Raimon Sabate[10,11], Vadim Khaychuk[7], Ilaria Vanni[3], Glenn C. Telling[7], Henrike Heise[8,9], Romolo Nonno[3], Jesús R. Requena[12], Joaquín Castilla[1,13]*
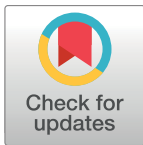
1 CIC bioGUNE, Derio (Bizkaia), Spain, 2 ATLAS Molecular Pharma S. L. Derio (Bizkaia), Spain, 3 Department of Veterinary Public Health and Food Safety, Istituto Superiore di Sanità, Rome, Italy, 4 Centre de Recerca en Sanitat Animal (CReSA), UAB-IRTA, Barcelona, Spain, 5 Proteomics Lab, IDIS, Santiago de Compostela, Spain, 6 Animal Health Department, NEIKER-Instituto Vasco de Investigación y Desarrollo Agrario, Derio (Bizkaia), Spain, 7 Prion Research Center (PRC), Colorado State University, Fort Collins, Colorado, United States of America, 8 Institute of Complex Systems (ICS-6) and Jülich Center for Structural Biology (JuStruct), Forschungszentrum Jülich, Jülich, Germany, 9 Physikalische Biologie, Heinrich-Heine-Universität Düsseldorf, Düsseldorf, Germany, 10 Department of Pharmacy and Pharmaceutical Technology and Physical-Chemistry, Faculty of Pharmacy and Food Sciences, University of Barcelona, Spain, 11 Institute of Nanoscience and Nanotechnology (IN2UB), University of Barcelona, Spain, 12 CIMUS Biomedical Research Institute, University of Santiago de Compostela-IDIS, Spain, 13 IKERBasque, Basque Foundation for Science, Bilbao (Bizkaia), Spain

* castilla@joaquincastilla.com

Abstract

The resolution of the three-dimensional structure of infectious prions at the atomic level is pivotal to understand the pathobiology of Transmissible Spongiform Encephalopathies (TSE), but has been long hindered due to certain particularities of these proteinaceous pathogens. Difficulties related to their purification from brain homogenates of disease-affected animals were resolved almost a decade ago by the development of *in vitro* recombinant prion propagation systems giving rise to highly infectious recombinant prions. However, lack of knowledge about the molecular mechanisms of the misfolding event and the complexity of systems such as the Protein Misfolding Cyclic Amplification (PMCA), have limited generating the large amounts of homogeneous recombinant prion preparations required for high-resolution techniques such as solid state Nuclear Magnetic Resonance (ssNMR) imaging. Herein, we present a novel recombinant prion propagation system based on PMCA that substitutes sonication with shaking thereby allowing the production of unprecedented amounts of multi-labeled, infectious recombinant prions. The use of specific cofactors, such as dextran sulfate, limit the structural heterogeneity of the *in vitro* propagated prions and makes possible, for the first time, the generation of infectious and likely homogeneous samples in sufficient quantities for studies with high-resolution structural techniques as

demonstrated by the preliminary ssNMR spectrum presented here. Overall, we consider that this new method named Protein Misfolding Shaking Amplification (PMSA), opens new avenues to finally elucidate the three-dimensional structure of infectious prions.

Author summary

Prion disorders are a group of devastating neurodegenerative diseases caused by an aberrantly folded isoform of the endogenous prion protein. The molecular mechanisms by which this proteinaceous pathogen is able to propagate in the central nervous system and cause neuronal death are poorly understood, partially due to the difficulties elucidating the three-dimensional structure of the aggregation-prone aberrant isoform or prion. Obtaining sufficient amounts of highly pure and homogeneous prions for high-resolution structural studies has been limited until now due to technical reasons. Here, we present a novel method for the production of large amounts of highly infectious recombinant prions suitable for solid state Nuclear Magnetic Resonance imaging, which could help to unveil the molecular pathogenesis of these particular pathogens.

Introduction

The generation of recombinant prions *in vitro* able to cause Transmissible Spongiform Encephalopathy (TSE) *in vivo* has been one of the greatest advances of the last decades in the field [1–12] and has been successfully achieved by several research groups, although there are still several unsolved issues that make this process of particular interest: 1) The recombinant prions generated by different research groups applying similar techniques yielded highly variable results. From generating prions with infectivity similar to that of some mammalian prions [8, 10], to producing prions with very low infectious ability or even lacking infectivity *in vivo*, requiring in some cases multiple *in vivo* passages to cause clinical prion disease [1–3, 6]. 2) It is unknown whether any other component, besides PrP^Sc, may be the infectious particle. Many different molecules have been tested (RNA, lipids, dextran sulfate, plasmid, etc.) and, in some cases, those are claimed as a requirement for *in vitro* infectious prion formation [4, 8, 13–15], however, credible evidence is lacking. There are several methods capable of generating misfolded self-propagating recombinant PrP but given the disparity of infective abilities, it is impossible to clarify which is the best to generate infectious recombinant prions and which may yield only non-infectious misfolded recombinant PrPs. 3) Finally, these techniques could help to determine the critical difference between infectious and non-infectious self-propagating, protease-resistant misfolded recombinant PrPs.

The vast majority of studies for *in vitro* recombinant prion generation have been performed using PrPs from well-known rodent species, mainly mouse (*Mus musculus*) [1, 8] and hamster (*Mesocricetus auratus*) [5]. Both are some of the best-characterized models of TSE and are the preferred ones for evaluating *in vivo* infectivity due to short incubation period and ease of handling. Recently, another rodent species, bank vole (*Myodes glareolus*) has become increasingly popular due to its particular attributes. A polymorphic variant of the bank vole PrP, bearing isoleucine at position 109, shows the ability to misfold spontaneously *in vitro* [10] and its over-expression in transgenic mice leads to a spontaneous and transmissible prion disease [16]. The bank vole is also considered to be an almost universal acceptor of prions since can be infected with a large diversity of prion strains from different donor species [17] and when infected with

Chronic Wasting Disease (CWD), a TSE from cervids, has the shortest incubation period of any known prion disease [18].

This combination of bank vole-based rodent models and the development of new generation recombinant prion propagation systems may finally decipher the mechanisms of infectivity of prions and may allow elucidation of the different structural features of various prion strains. The generation of the first highly infectious recombinant prion, using recombinant mouse PrP complemented with RNA and lipids, resulted in spontaneous misfolding of the protein using protein misfolding cyclic amplification (PMCA) [8]. This proved that prions able to cause clinical disease *in vivo* could be generated *in vitro* with minimal synthetic components. The presence of lipids and RNA in the mixture and previous research claiming the need of cofactors for the generation of infectious recombinant prions [12, 14, 15, 19–21] suggested that recombinant PrP alone was not sufficient to give rise to infectious prions *in vitro*. However, the actual role of cofactors was never investigated further so the true characteristics of prion infectivity remain unknown.

Recently, infectious recombinant prions have been generated in the absence of cofactors using PMCA and recombinant PrPs as the reaction substrate [10]. Recombinant bank vole I109 prions were generated by two distinct procedures: spontaneously and using a seed based on infectious prions of mammalian origin [18]. Several distinct infectious recombinant prion strains were generated in both ways using a variety of substrates containing different cofactors: from complete brain homogenates of PrP knock-out transgenic mice (*Prnp$^{0/0}$*) to substrates containing cofactors such as RNA, dextran sulfate or plasmid DNA, or in the absence of any cofactor. Among the conclusions derived from this research is that, in a cofactor rich environment (i.e. PrP and *Prnp$^{0/0}$* brain homogenate), the recombinant PrP misfolds in many different conformations, giving rise to a mixture of strains with distinct properties regarding their electrophoretic migration patterns and their abilities to cause disease *in vivo*. This is in agreement with recent studies on prion strain evolution that propose the existence of pools of slightly different prion conformers called prion substrains or quasispecies [22–24]. Our previous work, in which substrates with minimal components (i.e. dextran sulfate, RNA and plasmid DNA) were proven useful to select or specifically propagate certain strains [10], highlighted the possibility of generating more homogeneous samples that could facilitate the application of ssNMR to infectious prions. Although the selection of a single strain could not be definitively demonstrated, our results clearly indicated that using selective substrates, the conformer variety of the original seed could be reduced.

To understand the nature of prion infectivity, which would allow us to understand the nature of different prion strains, knowledge of the three dimensional structure of different prions at the atomic level appears necessary [25]. Techniques such as Hydrogen/Deuterium exchange [26–28], limited proteolysis coupled to mass spectrometry [29–33] and electron microscopy [34, 35] have been used for that purpose and the information obtained from them was highly valuable although insufficient to definitively understand the essence of prion infectivity. The incomplete knowledge about prion structural features is obvious considering the radically distinct structural models currently proposed for prions [34, 36, 37], both based on different techniques. The limited success of the aforementioned techniques and the constraints imposed by infectious prions, which are intrinsically aggregated making them unsuitable for high resolution techniques such as X-ray crystallography or nuclear magnetic resonance (NMR) imaging, reduces the possibilities of determining the atomic structure of infectious prions except by techniques such as solid state NMR (ssNMR) [38]. This technique has already resolved the structures of proteins with similar properties to mammalian prions like HET-S [39], Aβ amyloid [40] and even a synthetic infectious PrP23-144 amyloid that seems to propagate *in vivo* by templating endogenous PrP^C into PrP^{Sc} [41]. Despite its potential, ssNMR has

only been successfully applied to the resolution of a single truncated mammalian prion structure [42] due to two main limitations as it requires: 1) significant homogeneity of the sample under study and, 2) large amounts of isotopically labeled material.

Here, we present a new technique for propagation *in vitro* of infectious recombinant prions that overcomes the limitation of generating large amounts of isotopically labeled sample required for ssNMR studies. The procedure is based on PMCA, from where the misfolded recombinant seed is obtained. This infectious seed has been adapted to a new system in which shaking [43] is used instead of sonication for *in vitro* propagation of recombinant prions and this novel propagation method has been named Protein Misfolding Shaking Amplification (PMSA). This methodology eliminates the need of complex and expensive equipment permitting its implementation in any basic laboratory and allows the generation of 2.5 mg of protease-K digested infectious recombinant prion per day ready to be studied. The optimization applied to PMSA permits greater than 1,000-fold scaling up from minute amounts of seed of isotopically labeled material (and also multiple labeling) suitable for ssNMR studies, as shown by the preliminary spectrum presented here.

Results

Selection of an infectious recombinant prion for ease of indefinite *in vitro* propagation

With ssNMR studies in mind, a recombinant misfolded PrP was selected that fulfilled the following ideal characteristics: 1) minimal additional components required to be propagated *in vitro*, 2) additional components cheap and easily obtainable, 3) highly permissible to *in vitro* propagation allowing rapid generation of large amounts, and 4) infectious *in vivo* (100% attack rate with reasonable incubation times using a wild-type or no overexpression model).

In a previous study, a recombinant bank vole PrP complemented with $Prnp^{0/0}$ mouse brain homogenate (to provide any cofactor from the brain that may be required) was misfolded by PMCA (named H/L-seeded-03). The resultant strain mixture could be selected or adapted to different *in vitro* propagation environments in which the $Prnp^{0/0}$ brain homogenate was replaced by single cofactor complemented substrate such as dextran sulfate or RNA [10]. The latter recombinant seeds, requiring minimal additional components, were infectious *in vivo*, resulted in classical electrophoretic migration patterns and were more homogeneous than those complemented with brain homogenate, in which strain mixtures were detected upon *in vivo* inoculation [10]. Among these, the dextran-complemented recombinant prion (from now on named L-seeded-PMCA) resulted in slightly higher attack rates and much shorter incubation times, as well as a better *in vitro* propagation capacity [10]. Therefore, the recombinant bank vole seed generated in $Prnp^{0/0}$ brain homogenate and adapted to dextran-complemented substrate by serial PMCA rounds was chosen as the most suitable prion to adapt to PMSA.

Adaptation of the chosen recombinant prion to the new PMSA method

PMSA was developed based on PMCA, but seeking increased product output. Its success lies on propagating at least 1,000 times larger volumes of misfolded recombinant PrP, from the hundreds of microliters that can be propagated by PMCA (space limited by plate sonicators) to hundreds of millilitres, avoiding the use of complex or expensive equipment.

Therefore, the first step consisted on designing a method avoiding sonication, but efficient enough propagating the seed of choice. To address this, all the parameters used in PMCA for recombinant prion propagation (i. e. temperature, incubation times, number of propagation rounds) were retained except the quantity limiting sonication, which was substituted with

shaking. Standard shakers with appropriate temperature control would allow development of a highly scalable method by designing specific racks for tubes of any size allowing the production of the volumes required for structural studies. The L-seeded-PMCA recombinant seed, of proven infectivity and showing distinctive strain features [10], was propagated serially for 40 rounds at 1:10 dilution over a substrate containing bank vole recombinant PrP with dextran sulfate in order to adapt it to PMSA (named L-seeded-PMSA). Its stability through the serial rounds was checked and compared to the PMCA-derived prion also. Both the electrophoretic patterns (Fig 1A and 1B), as well as the abilities to propagate by PMCA in whole brain homogenate substrates (indicator of their potential *in vivo* infectivity), were conserved suggesting adaptation to PMSA (Fig 1C).

Once the seed was adapted to serial propagation in the novel system, the propagative abilities of both methods were compared by performing a serial dilution of each seed over a single round of PMCA or PMSA (Fig 2). Both seeds showed a similar propagation capacity after applying both methodologies. Dilutions of 10^4–10^5 could be detected by WB after PK treatment, a reasonable dilution but suggesting the need for optimization.

Optimization

To improve the propagative capacity of the PMSA, all parameters possibly relevant for PrP misfolding were considered and the propagation ability evaluated by serial dilution of the seed in a variety of conditions. Optimisation of the parameters for recombinant prion propagation was performed using three different shakers. Two different shakers with thermoblocks (Thermomixer from Eppendorf and a digital heating shaking drybath from Thermo-Scientific) and a simple plate shaker without temperature control placed in an oven to control temperature. The outcome of each parameter-variation was evaluated by Thioflavin T measurement and by proteinase K digestion and Western blotting as detailed in Materials and methods. The initial parameters set for PMSA were an adaptation of our regular recombinant PMCA settings. Recombinant protein concentration (2 μM) and PMCA substrate preparation were conserved as well as the temperature (38˚C), addition of 1 mm zirconia/silica beads and 24 h propagation rounds. As the energy provided by the system is presumably lower than by sonication, the maximum speed of the shakers (1,200 rpm) was used and to increase shaking cycles with respect to PMCA, cycles of 60 s shaking and 5 min incubation were used. However, all parameters were modified to optimize the propagation capacity evaluated by serial dilution of the recombinant seed in a range of different parameters. Shaking speed, shaking/incubation cycles, type of beads, temperature and rec-PrP concentration were optimized. Optimal conditions were found to be shaking at 1,000 rpm continuously, with 1.0 mm zirconium silicate beads at 39˚C and 2 μM of rec-PrP (Fig 3).

Scalability of PMSA

Once the propagation parameters were optimized, the scalability and repeatability of the novel method needed to be assessed. A serial dilution study was performed using tubes of different size with specific adaptors, designed by 3D printing, for each of them (Supplementary information, S1 Fig). PCR tubes (volume 50 μl), 2 ml tubes (volume 1 ml) and 5 ml tubes (volume 4.5 ml) were tested, as the scalability levels demanded to the system required tubes where large volumes could be propagated. In all the cases, 1 mm zirconium silicate beads were added and the tube orientated to favour bead movement. Propagation capacities were compared by serial dilutions of the seed as described previously.

Propagation was most and equally efficient in the 2 and 5 ml tubes, although all tube sizes resulted in reasonable propagative capacity. Thus, 2 and 5 ml tubes, apart from being the best
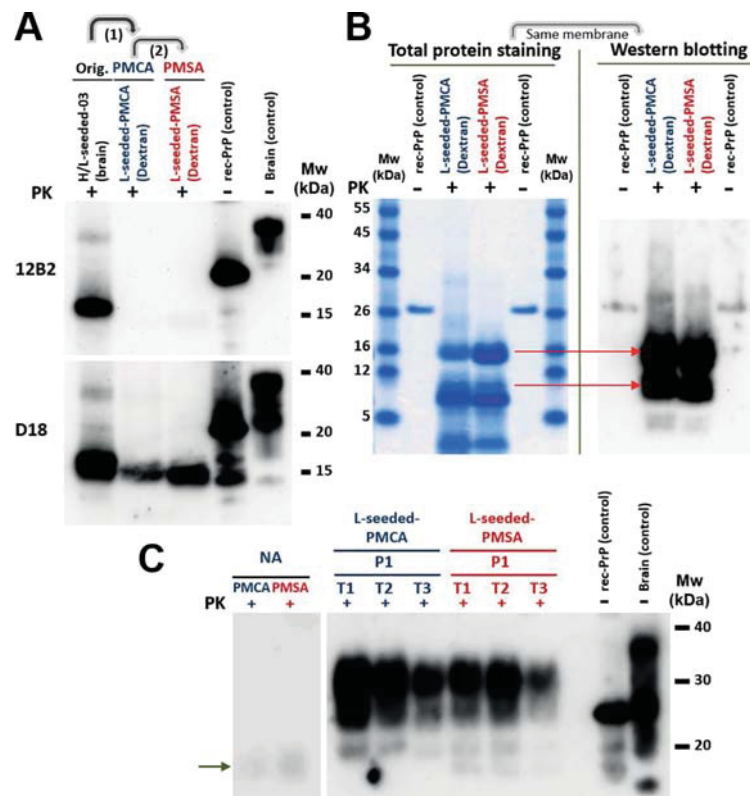
Fig 1. Adaptation of the infectious recombinant prion (L-seeded-PMCA) to the new *in vitro* propagation method (L-seeded-PMSA). A) Immunodetection of the characteristic protease resistant core resulting from cleavage of the amino-terminal tail of the original PMCA-derived recombinant prions (H/L-seeded-03 and L-seeded-PMCA) and the PMSA-adapted one (L-seeded-PMSA) by Western blotting. Samples were digested with 85 µg/ml of proteinase-K (PK) and analyzed by Western blotting using monoclonal antibodies 12B2 (1:2,500) and D18 (1:5,000). Differential digestion of the N-terminal makes the two recombinant prions adapted to propagate in dextran sulfate-complemented substrates (L-seeded-PMCA and L-seeded-PMSA) undetectable by 12B2 mAb (epitope 88–92) whereas the $Prnp^{0/0}$-complemented sample (H/L-seeded-03), which according to previous results (10) is a mixture of strains, detectable by both 12B2 and D18 mAbs (epitope 143–149). **B)** Electrophoretic migration patterns of L-seeded-PMCA and L-seeded-PMSA recombinant prions. The two recombinant prions were digested with PK and analyzed by BlueSafe staining (total protein) to examine all the proteolytic fragments derived from digestion. The same gel was transferred for Western blotting and developed with D18 mAb. Both recombinant misfolded PrPs show a similar banding pattern, suggesting similar if not identical conformations. The differences on electrophoretic patterns detected by D18 antibody between the gel in panel A and the one in panel B are due to the amount of sample loaded in each case. For total protein staining and posterior western blotting from panel B, 50x more sample is loaded than for panel A, making some minor PrP fragments detectable. **C)** Determination of potential infectivity (ability to propagate on brain-derived PrP) of L-seeded-PMCA and L-seeded-PMSA recombinant prions by brain-PMCA. Conservation of the capacity to misfold brain-derived PrP^C, as an indication of potential *in vivo* infectivity, was evaluated using equal amounts of the two recombinant inocula as seeds in TgVole brain homogenate at 1:10 dilution during one round of PMCA. Triplicates (T1, T2 & T3) were performed for both samples and PK-resistant PrP formation was monitored by Western blotting with D18 mAb. Misfolded brain-derived PrP arises from the first round for the dextran sulfate-complemented seeds with no difference between PMCA- or PMSA-adapted seeds (L-seeded-PMCA and L-seeded-PMSA). (→) Signals of PK-digested misfolded rec-PrPs appear lower than those of the non-glycosylated band due to the absence of the GPI anchor. rec-PrP (control): undigested bank vole rec-PrP protein. Brain (control): undigested TgVole whole brain homogenate. NA: Non-amplified samples.

vessels to reach the amounts of misfolded protein required ([Fig 4](#)) are easier to handle than the smaller ones and with just one standard shaker and oven allowed the generation of milligrams of misfolded sample per day (with 10 shakers, up to 400 ml can be produced daily).
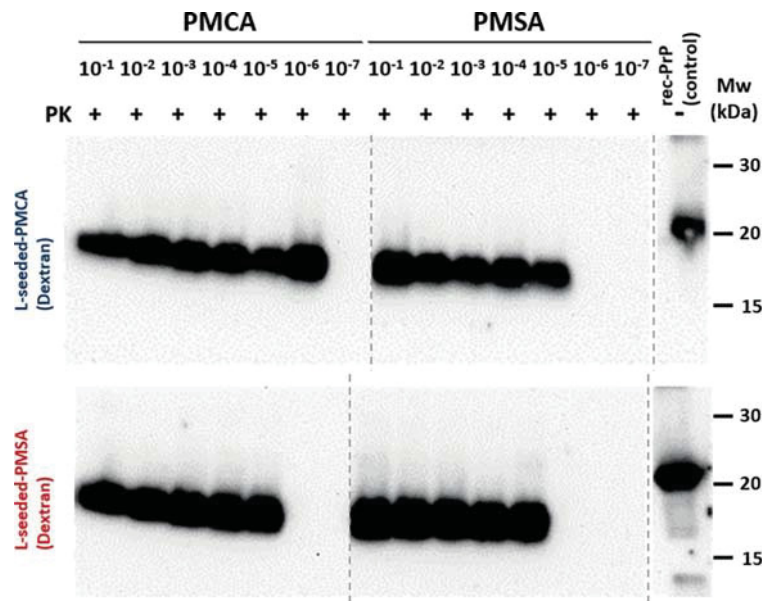
Fig 2. Propagation capacity of L-seeded-PMCA and L-seeded-PMSA recombinant prions in PMCA and PMSA.
The propagation efficiency of both recombinant prions *in vitro* in PMCA in comparison with PMSA was evaluated by serial dilutions of the seeds (from 10^{-1} to 10^{-7}) in the same substrate (bank vole 109I rec-PrP complemented with dextran sulfate) subjected to 24 h rounds of PMCA and PMSA. Protease resistant rec-PrP formation was monitored by PK-digestion and western blot, using D18 mAb (1:5,000). L-seeded-PMSA showed a similar propagation capacity to PMCA. This blot shows a slight difference (1 log) when comparing the propagation capacity of both seeds in PMCA but not in PMSA. However, these small differences were not significant. Despite all the samples being run at the same time, the blot was cropped as indicated by the vertical dotted line to avoid displaying unrelated samples. rec-PrP (control): undigested bank vole rec-PrP protein.

In vitro propagation efficiency

To estimate the efficiency of prion propagation by PMSA, the formation of protein aggregates that could be pelleted by centrifugation was undertaken. Since infectious PK-sensitive aggregates have also been described [31], the quantification of only protease-resistant misfolded PrP was considered inaccurate. However, the formation of amorphous aggregates without infectious capacity, which may also be protease sensitive, needs to be taken into account for the quantification of infectious prion formation *in vitro*. For that, unseeded and seeded (1: 100,000 dilution) substrates were submitted to a 24 h PMSA round taking samples at several time points. The soluble rec-PrP in the supernatant of the seeded sample was not detectable after 2 h (Fig 5A), indicating all PrP from the substrate had been aggregated, thus, only the samples taken at 1h and 2 h were considered for the calculation of the propagation efficiency.

Comparison of the amount of pelleted material (PrP in pellet vs. PrP in supernatant) by total protein staining (Fig 5A) shows that around 50% of the total PrP in the unseeded sample is in the pellet. This is composed entirely by non-infectious amorphous aggregates which are highly PK-sensitive (Fig 5B and 5C), providing an estimation of the maximum percentage of amorphous aggregates that could be formed in seeded reactions and which is subtracted from the total pelleted material found in seeded PMSA reactions for the final calculation of conversion efficiency. The seeded reaction reveals a faster aggregate formation, with all the PrP pelleted after 2 h of reaction. This pelleted material is purportedly composed by PK-sensitive amorphous aggregates, PK-sensitive infectious prions and infectious protease-resistant prions (Fig 5C).
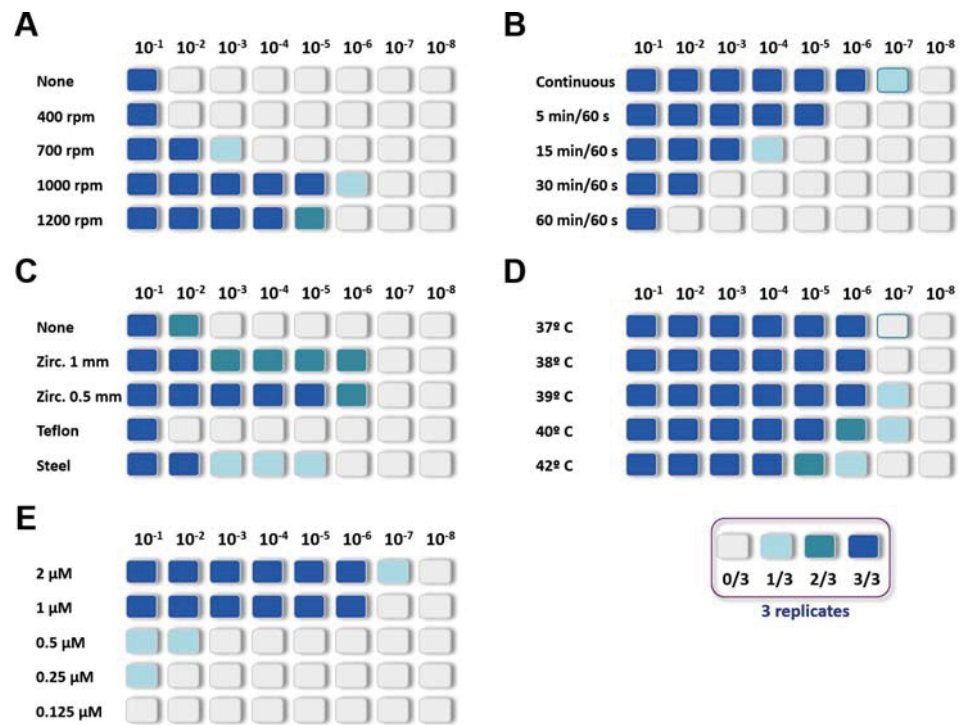
Fig 3. Optimization of PMSA parameters to increase propagation efficiency. Variations of several operational parameters for PMSA were tested using serial dilutions of the L-seeded-PMSA (from 10^{-1} to 10^{-8}) in a substrate composed of bank vole 109I rec-PrP complemented with dextran sulfate. For each parameter variation triplicates of the dilutions were included and the maximum dilution that showed protease-resistant rec-PrP was monitored by PK digestion and Western blot after one 24 h round of PMSA. Dilutions with detectable protease-resistant rec-PrP in each triplicate are represented in different shades of blue. Studied parameters include: **(A) Shaking speed**, ranging from no shaking (none) to 1,200 rpm; optimal propagation was achieved at 1,000 rpm; **(B) Shaking/incubation intervals,** from continuous shaking to cycles of 60 s shaking and 60 min of incubation, the optimal result was with continuous shaking; **(C) Types of beads,** several beads made of different materials or sizes were tested, some previously shown to improve propagation in PMCA [84, 85]. Similar amounts of each bead type were added to the dilutions: zirconium silicate 1.0 mm and 0.5 mm, polytetrafluoroethylene (PTFE) 1.8 mm and steel 1.0 mm. Dilutions without beads were also included. Propagation in the presence of zirconium silicate beads was significantly better, beads of PTFE or steel being similar to the absence of beads. Although 0.5 mm zirconium beads were more consistent than the 1.0 mm ones both reached 10^{-6} maximum dilutions and thus, 1.00 mm ones were chosen due to ease of handling; **(D) Temperature** variations in the range tested from 37 to 42˚C, did not affect the propagation efficiency of seed greatly. However, propagation from the lowest dilutions was achieved at 39 and 40˚C and so 39˚C was chosen as optimum temperature setting; and **(E) PrP concentration was evaluated in substrates varying from** 0.125 μM to 2 μM. This is critical to obtain optimal amounts of material for structural studies with in vitro recombinant prion propagation methods. A balance is required between a high enough concentration to induce good propagation without wasting recombinant PrP and minimizing the amount of non-misfolded PrP remaining at the end of the reaction which will need to be eliminated prior to the structural studies. Below 1 μM PrP concentration was insufficient to efficiently propagate and the substrate with the highest protein concentration was best, so 2 μM was chosen as preferred concentration.

https://doi.org/10.1371/journal.ppat.1008117.g003

To calculate the percentage of PrP that misfolds into the latter two species, infectious but just partially PK-resistant *bona fide* prions, the percentage of pelleted material was estimated according to the PrP signal intensity in contrast to the amount of PrP in the supernatant and the percentage of amorphous aggregates derived from PrP in the pellet of the unseeded reaction. Therefore, considering that 100% of the PrP from the seeded reaction sediments after 2 h of PMSA and that the maximum percentage of amorphous aggregates in the unseeded reaction corresponds to 50% of the total PrP, the conversion efficiency at 10^{-5} seed dilution was estimated to be at least 50%. Although a greater amount of seed might reduce the formation of amorphous aggregates by driving the misfolding towards *bona fide* recombinant prion conversion pathway,
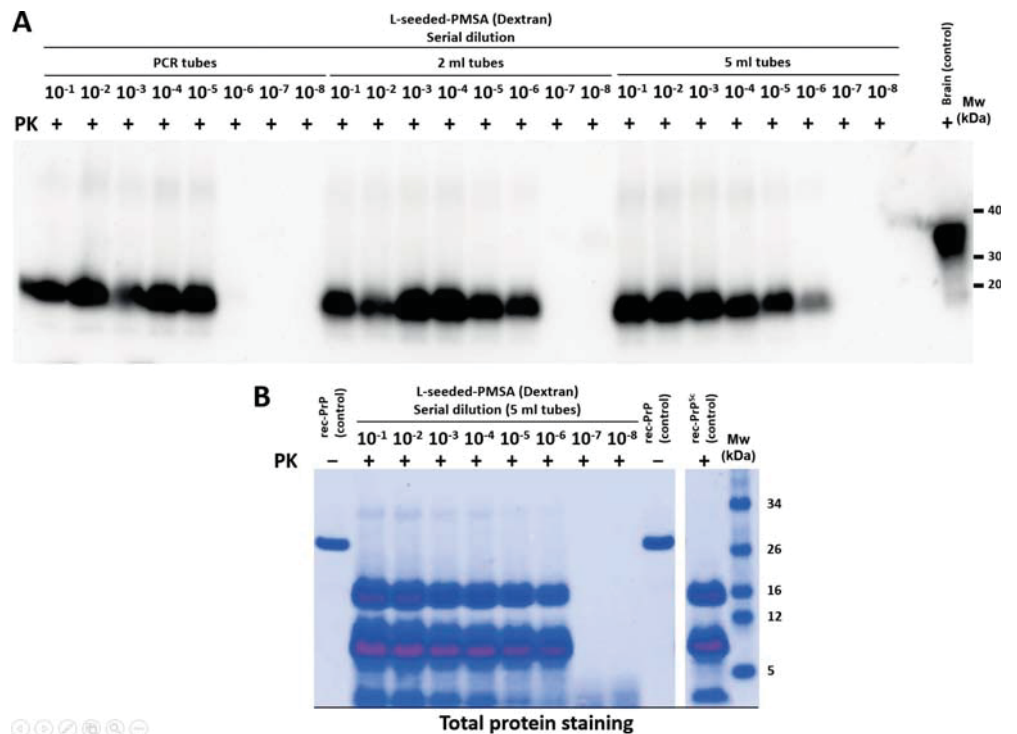
Fig 4. Propagation of serially diluted L-seeded-PMSA using different volumes and tube sizes. A) Western blot showing propagation capacity of L-seeded-PMSA in PCR tubes (0.2 ml) and 2 ml and 5 ml tubes using dilutions 10^{-1} to 10^{-8} after a single 24 h round of PMSA. All samples were digested at 25 μg/ml of PK. The three tube sizes allow propagation of the seed up to dilutions of 10^{-5}–10^{-6} with slightly better results in 2 ml and 5 ml tubes, demonstrating the system can be adapted to the production of large volumes. Brain (control): undigested TgVole whole brain homogenate. mAb D18 (1:5,000). **B)** Total protein staining of the serial dilution performed in the 5 ml tubes. 500 μl of each dilution were digested with PK (25 μg/ml) and concentrated by centrifugation after digestion. The resuspended pellets were subjected to electrophoresis and total protein stained with BlueSafe. Intense signal could be detected even at a dilution of 10^{-6} confirming the suitability of the system for propagation of large volumes. rec-PrP (control): undigested bank vole rec-PrP protein. rec-PrP^{Sc} (control): original seed digested and concentrated as per the other samples.

https://doi.org/10.1371/journal.ppat.1008117.g004

the high dilution used for the seeded reaction allows minimization of the effect of the seed in the formation of amorphous aggregates versus *bona fide* prions. This 50% of amorphous aggregates would be the worst case scenario, in which the effect of the seed on driving the misfolding pathway towards *bona fide* prion propagation is negligible and the amorphous aggregates formed are equal to the maximum amount observed in the unseeded reaction. Nonetheless, it is likely that seeding may reduce amorphous aggregate formation and that this is an underestimation of the real conversion efficiency, which was probably greater than the 50% calculated.

Relative amounts of PK-resistant and PK-sensitive *bona fide* prions were also estimated by evaluating the self-propagation ability of the same PK-digested and undigested PMSA product (Fig 6). This digested or undigested seeds were serially diluted in fresh substrate and submitted to a 24 h PMSA.

The same amount of PK-treated seed showed approximately 10 to 100 folds lower propagation capacity than the undigested seed, suggesting that up to 90–95% of the seed could be composed of PK-sensitive auto-propagative prions.

Biochemical characterization of the scaled-up seed

Prior to its biochemical characterization, the capacity for stable self-propagation of the recombinant dextran-complemented seed was evaluated. For that, 33 serial rounds of PMSA were
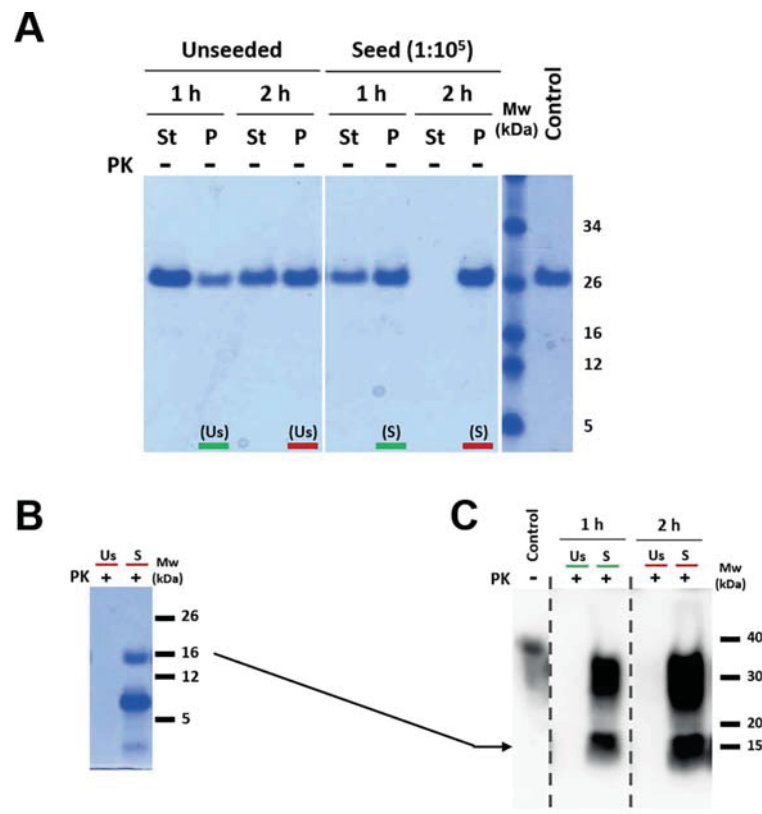
Fig 5. Propagation efficiency in PMSA analyzed by sedimentation and protease digestion. A) Total protein staining of the undigested pellet (P) vs. supernatant (St) fractions to monitor the amounts of aggregated and soluble rec-PrP in the course of PMSA. Fractions corresponding to 1 and 2 h from a 24 h-round of unseeded and seeded (1:100,000 dilution) PMSA reactions were collected at the indicated time points, in which all the PrP from the supernatant of the seeded sample was converted to insoluble material. Samples were centrifuged at 19,000 g for 15 min and supernatant and pellet (resuspended in a volume equal to that of the collected fraction) subjected to electrophoresis and stained for total protein with BlueSafe. The amount of aggregated PrP (pellet) and soluble PrP (supernatant) were compared in order to calculate conversion efficiency without protease digestion due to the possibility of protease-sensitive prions being an important part of the PMSA product. The unseeded reaction indicated the maximum amount of amorphous aggregates that can be formed after 2 h of the process was approximately 50% of the total PrP, which was subtracted from the aggregated fraction of the seeded reaction to estimate *bona fide* misfolding percentage. A highly diluted seed (10^{-5}) was used to minimize its effect on driving the misfolding process towards the *bona fide* prion formation pathway at the expense of the formation of amorphous aggregates. Therefore, it is likely that *bona fide* prion propagation efficiency is higher than the 50% estimated based on the amount of amorphous aggregates formed in an unseeded reaction. Mw: molecular weight marker. Control: total PrP on the substrate at time 0, before PMSA. **B) Total protein staining of protease digested PMSA products at 2 h.** To differentiate samples containing only amorphous aggregates (non-infectious completely protease-sensitive) from samples containing *bona fide* recombinant prions (partially protease-resistant), samples form unseeded (Us) and seeded (S) reactions were collected after 2 h of PMSA and digested with PK (25 μg/ml) for 1h at 42˚C. As expected, the unseeded reaction contained only PK-sensitive aggregates, while the seeded one showed the characteristic PK-resistant core that remains after amino-terminal digestion, indicating that at least part of the misfolded material formed in the seeded reaction were PK-resistant *bona fide* prions. Mw: molecular weight marker. **C) Potential infectivity of unseeded and seeded samples by brain-PMCA.** In order to confirm that the unseeded sample did not contain PK-sensitive *bona fide* prions able to propagate their conformation in brain-derived PrP whereas the seeded sample was, the two samples at 2 h were used as seeds to inoculate TgVole (1x) brain homogenate at 1:10 dilution and submitted to brain-PMCA. The PMCA products were PK-digested and visualized by Western blotting, which showed the presence of PK-resistant PrP for both seeded samples while there was no detectable propagation for the unseeded ones after 1 and 2 h PMSA. The high dilution of the original L-seeded-PMSA inoculum (10^{-5}) protects against the possibility of being the original inoculum and not the propagated material, the result of brain PrP^C misfolding, since the propagation capacity of L-seeded-PMSA in brain-PMCA did not reach 10^{-6} dilution. mAb: D18 (1:5,000). Mw: molecular weight marker. Control: undigested Tgvole (1x) PrP.
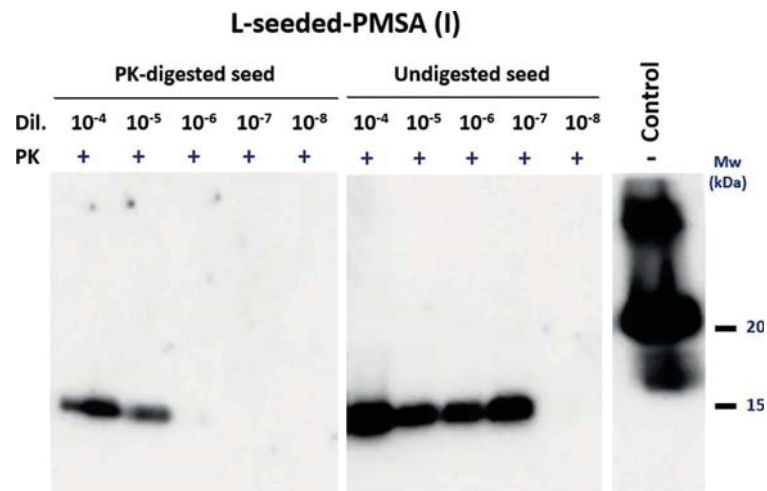
Fig 6. Self-propagation ability of protease-digested and undigested L-seeded-PMSA. To estimate the amount of PK-sensitive *bona fide* recombinant prion fraction in the L-seeded-PMSA sample, the propagation capacity of PK-digested and undigested seeds was compared by serial dilution (from 10^{-4} to 10^{-8}) on PMSA and monitored by PK digestion and Western blot. The PK-digested L-seeded-PMSA seed showed reduced propagation capacity of approximately 1–2 logs compared to the non-digested seed, indicating that approximately 90–95% of the seed could be composed of PK-sensitive prions. mAb D18 (1:5,000). Mw: molecular weight marker. Control: undigested bank vole rec-PrP.

performed at 1:1,000 to a 10^{-100} dilution of the initial seed that was used for subsequent extensive biochemical characterization studies including PK digestion, electrophoresis, total protein staining and epitope mapping with several antibodies. All studies revealed no alteration of its electrophoretic migration pattern after protease digestion (Fig 7).

Total protein staining and epitope mapping of the same sample showed major bands of; ~15 kDa, corresponding to complete protease-resistant rec-PrP with partial N-terminal digestion encompassing residues ~97–231 according to the antibodies used, ~9 kDa formed by proteolytic fragments containing residues ~153–231, and ~2 kDa that includes regions 97 to ~117 of the PrP [see ($\rightarrow$) in Fig 7C]. Another two minor bands reflected other PK cleavage sites yielding two fragments of ~12 and ~6 kDa [see green and red bands in Fig 7C]. To evaluate the PK resistance, equal amounts of the misfolded recombinant PrP were digested with increasing concentrations of proteinase-K (from 50 to 1,000 μg/ml; rec-PrP:PK ratio from 1:2 to 1:40) at 42˚C for 1 h followed by visualization by electrophoresis and total protein staining (Fig 7B). At 1,000 μg/ml of PK digestion was incomplete indicating high resistance to protease characteristic of many prion isolates.

Analysis of PK-treated PMSA product by ESI-TOF allowed the exact identification of several PK-resistant fragments (Supplementary information, S1 Table) and confirmed that PK cleaves between positions H_{96}/N_{97} and N_{97}/Q_{98} generating amino-terminal ragged ends, and also vigorously between positions E_{152}/N_{153} and N_{153}/M_{154} generating PK-resistant N- and C-terminal shorter fragments of ~5–6 and ~9 kDa, respectively. Very minor peaks corresponding to additional minor cleavages at A_{116}/A_{117}, S_{132}/A_{133} and M_{134}/S_{135} were also detected. These data are consistent with results obtained from SDS-PAGE/total protein staining and epitope mapping analyses (Fig 7C). The higher sensitivity of WB and the large amount of loaded sample allowed identification of some additional PK cleavage sites within the misfolded PrP propagated by PMSA that were not observed previously in the WB done with the usual sample amounts.

In order to gain some insight on the ultrastructural characteristics of the L-seeded-PMSA sample, the size distribution of the aggregates was evaluated by zonal sedimentation analysis
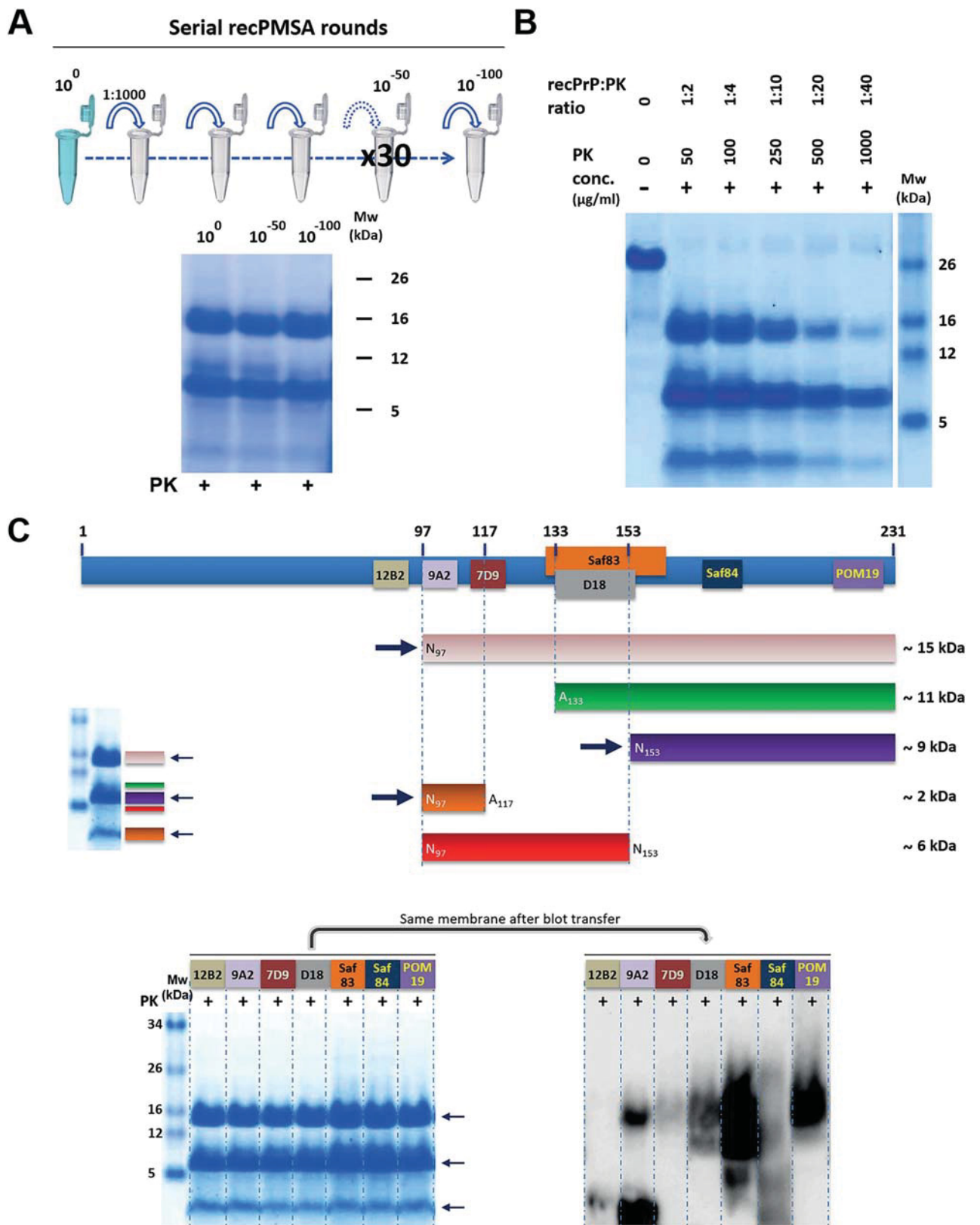
Fig 7. Biochemical characterization of L-seeded-PMSA. A) The ability of L-seeded-PMSA to self-propagate indefinitely shown through 30 serial rounds of PMSA at 1:1,000 dilution. 500 μl of the original seed (10^0 dilution), the product of round 17 of PMSA (10^{-50} dilution) and the product of round 33 (10^{-100} dilution) were PK-digested, concentrated by centrifugation and visualized by total protein staining and showed no detectable pattern differences throughout the propagation process. **B)** Protease-K (PK) resistance of L-seeded PMSA was evaluated by submitting fractions of the same sample to increasing PK concentrations for 1h at 42°C. L-seeded-PMSA showed high resistance to protease, as the main PK-resistant bands are maintained even at the highest PK concentration used. **C)** Identification of the proteolytic fragments of L-seeded-PMSA by epitope mapping was performed with the same PK-digested and concentrated sample divided in seven that were stained for total protein to guarantee equal protein amounts in each lane. The stained gel was then transferred for Western blotting and the following antibodies were used for epitope mapping: 12B2 (1:2,500), 9A2 (1:4,000), 7D9 (1:1,000), D18 (1:5,000), Saf83 (1:400), Sa84 (1:400) and POM19 (1:10,000). The theoretical reconstruction of the PrP fragments recognized by each antibody are represented in the cartoon, the most abundant fragments were (see arrows) ~15 (pink), ~9 (purple) and ~2 (orange) kDa. Another two minor bands reflect other PK cleavages yielding two fragments of ~12 and ~6 kDa (green and red bands, respectively). These fragments are not always detected by all the antibodies used for the epitope mapping due to their low amounts, below the detection limit of some of the antibodies. MW: Molecular weight.

on continuous sucrose density gradient. The sample produced in PMSA, either undigested or digested with PK, was submitted to ultracentrifugation through 10–80% sucrose gradient to determine the degree of quaternary structure heterogeneity by total PrP or PrP^{res} detection in Western blot (Supplementary information, S3 Fig). A continuous distribution of PrP aggregates is observed starting in fractions with around 30–35% sucrose to the end of the gradient with 80% sucrose with no monomeric PrP in upper fractions. This suggest that all PrP is misfolded during the process forming mostly large fibrillary aggregates with quite heterogeneous sizes, densities ranging from 1.1 g/cm^3 to higher than 1.3 g/cm^3 [44]. The analysis of PK-treated sample reveals a similar sedimentation velocity pattern, with a continuous distribution of aggregates from 40–45% sucrose to 80%, indicating that part of the smallest aggregates could be PK-sensitive or composed by amorphous aggregates. In any case, the linearity of the signal and the major signal intensity towards the bottom fractions clearly indicates that the sample is mainly composed by very big PK-resistant aggregates able to reach and even cross the 80% sucrose gradient, although smaller PK-resistant aggregates are also detected as proof of some quaternary structure heterogeneity dominated by large aggregates.

Biological characterization of the scaled-up seed

Infectivity and transmissibility in animal models. The definitive demonstration of the infectivity of the recombinant seed propagated by PMSA, in comparison with the original inoculum generated by PMCA, was done by intracerebral inoculation in TgVole (1x) mouse and bank vole models, both bearing bank vole I109 PrP with similar expression levels (Supplementary information, S2 Fig).

In TgVole (1x) model, which is very similar to bank voles as shown by similar short incubation periods for CWD-vole prion strain [58±1 days post inoculation (dpi) in TgVole and 35–40 dpi in bank voles] in both models [18], the original PMCA-derived seeds caused clinical disease in all inoculated animals with incubation periods of 175±6 (*Prnp*$^{0/0}$ complemented) and 326±9 dpi (dextran sulfate complemented). Two different preparations of the PMSA-adapted seed showed the same attack rate (100%) with incubation times of 250±4 and 266±3 dpi. Negative control groups inoculated with non-misfolded rec-PrP and with the same rec-PrP fibrillated following another protocol [45] showed no signs of disease after > 500 dpi, as expected (Table 1).

A second passage was performed using TgVole (1x) animals, which showed shorter incubation periods of 120±1 dpi for the PMCA-derived seed and of 116±2 dpi for the PMSA-derived one. A biochemical analysis of Proteinase-K (PK)-resistant PrP^{Sc} in brain homogenates from these inoculated TgVole (1x) showed that the CWD-vole and all the *bona fide* misfolded rec-PrPs accumulated in the classical PrP^{Sc} three-banded electrophoretic migration pattern. However, brains from animals inoculated with the non-infectious fibrillary rec-PrP and non-fibrillated rec-PrP were devoid of any PK-resistant bands (Fig 8).

Table 1. First passage of PMCA and PMSA-adapted recombinant samples inoculated into TgVole (1x) mice.

Inoculum	Substrate	Model	Survival time of positive animals (dpi) (mean±SEM)	Attack rate[a]
CWD-vole	Brain	TgVole	58±1	10/10 (100%)
H/L-seeded-03	Brain	TgVole	175±6	8/8 (100%)
L-seeded-PMCA	PMCA	TgVole	326±9	5/5 (100%)
L-seeded-PMSA (1)[b]	PMSA	TgVole	266±3	9/9 (100%)
L-seeded-PMSA (2)[b]	PMSA	TgVole	250±4	10/10 (100%)
Fibrillary vole rec-PrP	Urea	TgVole	>500	0/6 (0%)
Non-fibrillary vole rec-PrP	-	TgVole	>500	0/6 (0%)

[a] Data obtained based on clinical signs and protease-resistant PrP detection.

[b] (1) and (2) indicate two different preparations of L-seeded-PMSA done independently by PMSA propagation of L-seeded-PMCA in a substrate based on recombinant bank vole I109 PrP.

SEM: Standard Error of Mean. dpi: day post inoculation.

https://doi.org/10.1371/journal.ppat.1008117.t001

Regarding bank vole I109, the same PMCA and PMSA-derived seeds caused disease in 239 ±46 dpi [10] and 318±3 dpi, respectively, again with 100% attack rates (Table 2).

The biochemical and immunohistopathological examination of the brain samples from inoculated bank voles shows classical PK-resistant PrP and clear PrP^Sc plaque deposition (Fig 9), confirming the *bona fide* prion disease induced by L-seeded-PMSA inoculum.

Both seeds were able to cause disease in all the inoculated animals, either bank voles or transgenic mouse models with no PrP overexpression, with similar incubation times and complete attack rate. Therefore, the PMSA propagates this recombinant infectious prion faithfully, providing material suitable for structural studies.
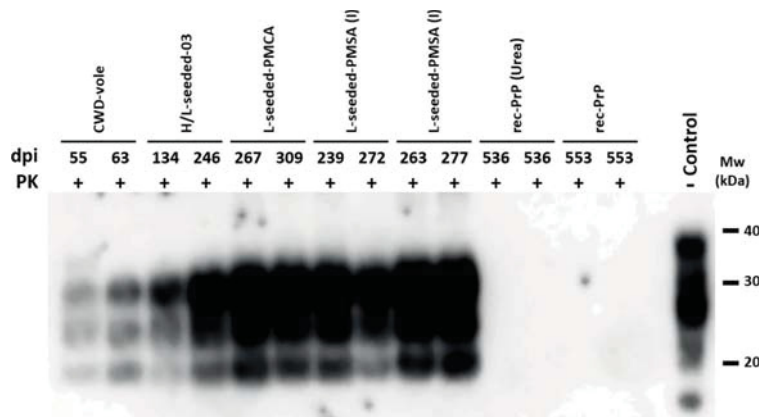
Fig 8. PrP^Sc detection in diseased TgVole (1x) brains inoculated with CWD-vole, H/L-seeded-03, L-seeded-PMCA, L-seeded-PMSA, non-infectious fibrillary rec-PrP and non-fibrillated rec-PrP. Biochemical analysis of Proteinase-K (PK)-resistant PrP^Sc in brain homogenates from TgVole (1x) inoculated with different misfolded PrPs: CWD-vole, H/L-seeded-03, L-seeded-PMCA, L-seeded-PMSA (I & II), non-infectious fibrillary rec-PrP and non-fibrillated rec-PrP. Representative TgVole brain homogenates were digested with 200 μg/ml of PK. The CWD-vole and the PMCA and PMSA-derived misfolded rec-PrPs inoculated TgVole brains accumulated a classical PrP^Sc type characterized by a three bands electrophoretic migration pattern. Brains from animals inoculated with the non-infectious fibrillary rec-PrP and non-fibrillated rec-PrP, used as negative controls, did not show any PK resistant band. D18 monoclonal antibody (1:5,000). Control: undigested TgVole (1x) whole brain homogenate. MW: Molecular weight. dpi: days post-inoculation at which each animal was culled due to neurological clinical signs.

https://doi.org/10.1371/journal.ppat.1008117.g008

Table 2. First passage of PMCA and PMSA-adapted recombinant samples inoculated into bank voles.

Inoculum	Substrate	Model	Survival time of positive animals (dpi) (mean±SEM)	Attack rate[a]
CWD[b]	Brain	Bank vole	37±1	9/9 (100%)
L-seeded-PMCA[c]	PMCA	Bank vole	239±46	8/8 (100%)
L-seeded-PMSA (1)	PMSA	Bank vole	318±3	4/4[d] (100%)

[a] Data obtained based on clinical signs and protease-resistant PrP detection.

[b] Data obtained and published previously using CWD: Chronic Wasting Disease adapted to bank vole I109 (10).

[c] Data obtained and published previously using the dextran-complemented recombinant sample (10).

[d] From a group of eight animals, four had to be killed due to unrelated intercurrent disease and were excluded from these calculations.

SEM: Standard Error of Mean. dpi: day post inoculation.

https://doi.org/10.1371/journal.ppat.1008117.t002
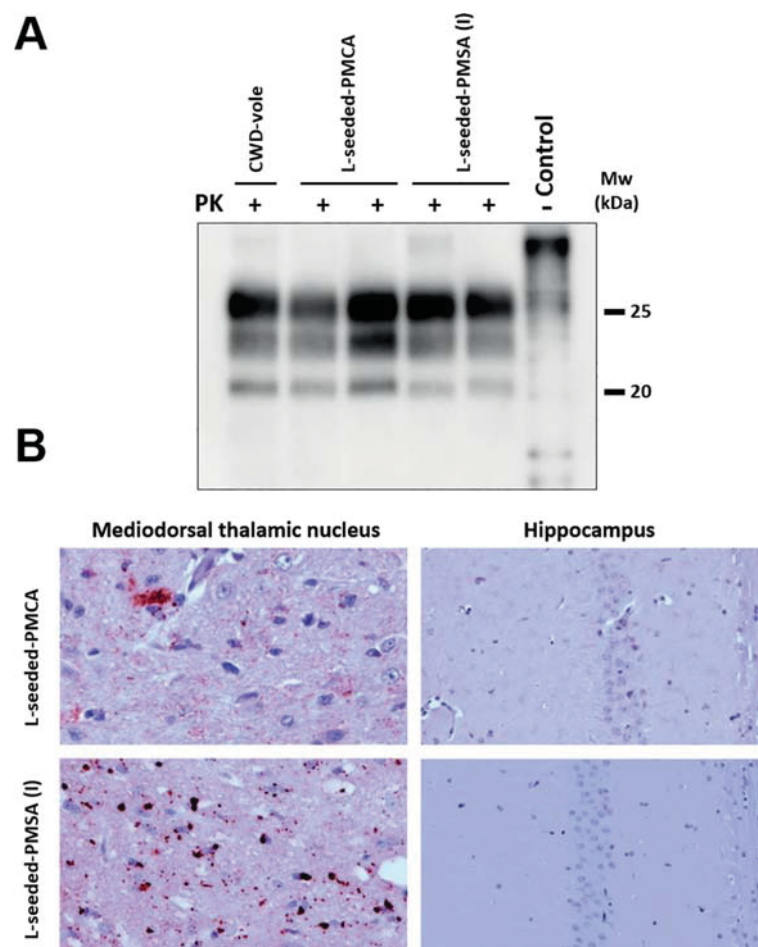
Fig 9. PrP^Sc detection and histopathological analysis of diseased bank vole 109I brains inoculated with CWD-vole, L-seeded-PMCA and L-seeded-PMSA. A) Biochemical analysis of Proteinase-K (PK)-resistant PrP^{Sc} in brain homogenates from bank vole I109 inoculated with the misfolded rec-PrPs: L-seeded-PMCA and L-seeded-PMSA, and CWD-vole as control. Representative bank vole brain homogenates were digested with PK (200 μg/ml). All rec-PrP^{Sc} inoculated bank vole brains accumulated a classical PrP^{Sc} type characterized by a three-banded electrophoretic migration pattern, indistinguishable from the CWD-vole inoculated vole brains. 9A2 monoclonal antibody (1:5,000). Control: undigested bank vole whole brain homogenate. MW: Molecular weight. **B)** Brain deposition of PrP^{Sc} in the mediodorsal thalamic nucleus and the hippocampus of bank voles inoculated with L-seeded-PMCA or L-seeded-PMSA was assessed by immunohistochemistry using the monoclonal antibody 6C2 (1:300). Note, with both seeds, deposition of PrP^{Sc} could be observed in the mediodorsal thalamic nucleus but not in the hippocampus.

https://doi.org/10.1371/journal.ppat.1008117.g009

Specific infectivity of L-seeded-PMSA. The end-point *in vivo* titration and determination of specific infectivity was assessed in TgVole using tenfold dilutions of L-seeded-PMSA being 10^{-4} (Table 3).

From these data, the specific infectivity of L-seeded-PMSA in TgVole (1x) was also calculated using the Spearman-Karber method [46]. Taking into account that the dose causing fatal disease in 50% of the animals (LD_{50}) is between dilutions 10^{-4} and 10^{-5}, of which 10 μl were inoculated with a total PrP content of 0.25 μg, specific infectivity was calculated to be of 6.34 x 10^4 / μg of PrP in TgVole (1x).

Preliminary ssNMR study of the recombinant prion

With this highly scalable method that is able to propagate a *bona fide* recombinant prion, preparing up to 400 ml of misfolded seed per day is easily feasible in any laboratory requiring large amounts of material for structural studies. As proof of concept, a preliminary ssNMR experiment was conducted using 400 ml of a PMSA product containing dual isotopically labeled bank vole I109 rec-PrP (C^{13} and N^{15}), seeded with unlabeled L-seeded-PMSA 1:100 and prepared as follows. To obtain a misfolded sample to act as a seed, with at least 99.99% of the protein labeled, two serial rounds of PMSA were performed using in the first passage, the non-labeled L-seeded-PMSA seed diluted 1:100. Subsequently, 4 ml of the isotopically labeled seed was scaled 100-fold up to reach, in a single round (24 h), 400 ml of misfolded material labeled at 99.9999%. With an estimated efficiency of conversion of at least 50%, approximately 9 mg of converted material were obtained from the 400 ml at 2 μM rec-PrP concentration (containing around 18.4 mg of rec-PrP). However, the final amount of PK-digested material was approximately 0.75–1.0 mg, indicating that around 90–95% of the misfolded material was PK-sensitive, in agreement with the ability of the PK-undigested L-seeded-PMSA seed to propagate by PMSA 10–100 times (1–2 logs) more than when is PK-digested. In order to reduce the 400 ml of seed produced by PMSA to the standard ssNMR working volumes of 10–100 μl, the sample was digested with PK (25 μg/ml for 1 h at 42˚C), based on the previous characterization. After digestion, the sample was concentrated by centrifugation.

An INEPT spectrum recorded at 15˚C nominal temperature did not show any signals, demonstrating that misfolded rec-PrP^{Sc} does not contain any highly flexible parts [47]. Conversely, ^{13}C CP/MAS based NMR spectra which exhibit signals from immobilized parts of the protein, showed the full set of resonances. Additionally, two-dimensional NMR-spectroscopy was possible (Fig 10) in which signal sets for the spin systems of the amino acid types alanine, threonine, isoleucine and valine were clearly identified.

The preliminary results obtained from the ssNMR spectra demonstrate that large amounts of isotopically labeled prions suitable for this and other biophysical methods can be propagated by PMSA, to enable elucidation of the three-dimensional structure of prions or at least of the most relevant structural motifs.

Table 3. Titration of the PMSA-adapted recombinant samples inoculated into TgVole (1x).

Inoculum	Dilution	Model	Survival time of positive animals (dpi) (mean±SEM)	Attack rate[a]
L-seeded-PMSA (1)	10^{-1}	TgVole	266±3	10/10 (100%)
L-seeded-PMSA (1)	10^{-2}	TgVole	281±6	4/4 (100%)
L-seeded-PMSA (1)	10^{-4}	TgVole	321±6	5/5 (100%)
L-seeded-PMSA (1)	10^{-5}	TgVole	434±21	2/5 (40%)

[a] Data obtained based on neurological clinical signs and protease-resistant PrP detection.
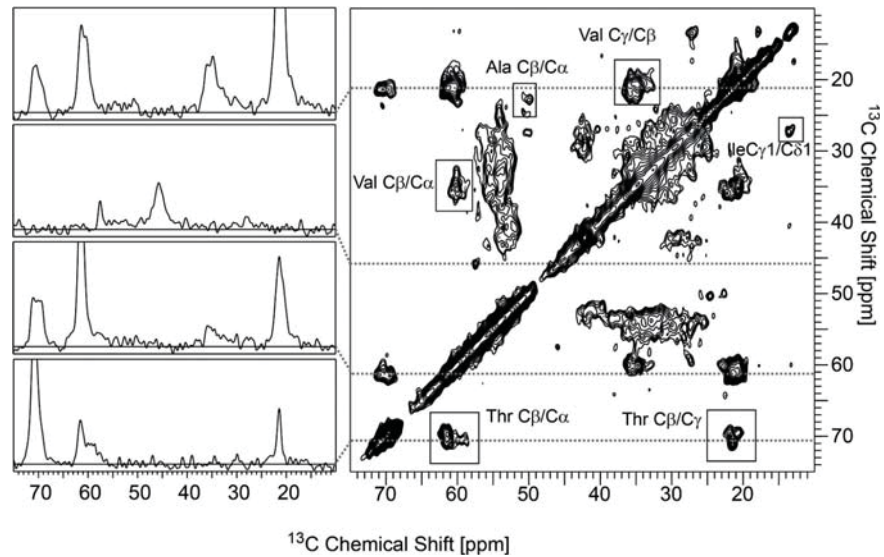
SEM: Standard Error of Mean. dpi: day post inoculation.

https://doi.org/10.1371/journal.ppat.1008117.t003

Fig 10. ssNMR. Right side: 2D ^{13}C/^{13}C correlation spectrum employing proton driven spin diffusion (50 ms) for homonuclear polarization transfer. Cross correlation signals of selected amino acids are highlighted in the spectrum. On the left side, four representative 1D slices through the spectrum are displayed. The spectrum was recorded at a nominal temperature of 0˚C and a field strength of 14.1 T with a spinning frequency of 11 kHz.

https://doi.org/10.1371/journal.ppat.1008117.g010

Discussion

Deciphering the three dimensional structure of prions at high resolution has been long hindered by several characteristics of these proteins. Isolation and purification of PrP^{Sc} from brain homogenates in sufficient quantities required for most of the high-resolution biophysical techniques is extremely difficult, despite advances in GPI-deficient PrP-expressing animal models [34]. Although *in vitro* prion conversion assays and the use of recombinant PrP addressed many of the purification issues [1–10], that PrP^C and, in particular, rec-PrP can misfold into multiple different conformations and aggregated states (amorphous, amyloid fibrils or 2D crystals) with some unrelated to disease or some disease-associated but not transmissible, complicates structural studies [48]. Even among transmissible, diseases-associated aggregates, known as PrP^{Sc}, the co-existence of distinct strains and the variety of quaternary structures ranging from oligomers to fibrils with different sizes make structural characterization of prions extremely challenging [37]. Considering the variety of misfolded forms PrP can adopt and the lack of knowledge on the event itself, it is not unexpected that the propagation of recombinant prions *in vitro* resulted in many different products ranging from biologically inert aggregates to highly transmissible and neurotoxic species or *bona fide* prions [1–10, 12, 15, 21]. We and others have previously reported the generation of recombinant prions using PMCA and *Prnp$^{0/0}$* brain homogenates or specific cofactors [5, 8–10, 14, 15, 49]. Our group also proposed a way to reduce the heterogeneity of these *in vitro* generated prions by propagation in the presence of specific cofactors [10]. However, lack of knowledge of the molecular events underlying prion propagation by PMCA and the difficulty controlling sonication parameters render highly variable results; i. e. non-infectious misfolded rec-PrP was produced with the exact conditions that had previously yielded a highly infectious recombinant prion [12, 50]. Additionally, the complexity of the equipment necessary for PMCA inherently limits scalability and generation of large amounts of misfolded material. Herein we present a new system that overcomes all the issues of complexity, variability and scalability of PMCA, which allows generation of suitable material for high-resolution protein structural studies.

Fundamentally based on the PMCA: with the same substrate preparations complemented with a single cofactor (dextran sulfate) for recombinant prion propagation [10], zirconia/silica beads shown previously to enhance the performance of classical brain-homogenate based PMCA [51] and reaction temperature, the critical difference is the substitution of sonication by shaking, hence the name Protein Misfolding Shaking Amplification (PMSA). Although shaking has been used extensively in several cell-free systems for amyloid formation or prion propagation, none showed the capacity to yield recombinant prions capable of causing classical clinical prion disorder with a 100% attack rate, neurological signs, spongiform change and misfolded PrP accumulation in the CNS upon first passage in wild-type animal models and transgenic models devoid of *PRNP* gene overexpression [1, 5, 52]. Contrary to other methodologies and previous assumptions, PMSA shows that, under appropriately optimized conditions, vigorous shaking provides sufficient energy to achieve *bona fide* prion propagation in the presence of an adequate concentration of the polyanionic cofactor dextran sulfate. Thus, the idea that high energy input, as purportedly provided by sonication in PMCA, could be required to cause fibril breakage and efficiently misfold PrP into its infectious counterpart *in vitro* needs to be reexamined [53].

The adaptation of an infectious recombinant prion generated by PMCA to this new PMSA system was successful and seemed to conserve biochemical features, as indicated by their electrophoretic migration patterns after PK digestion and the ability to propagate on brain-based substrates in a single round of brain-PMCA. In particular, the PK fragmentation pattern of L-seeded-PMSA was consistent with those reported for its precursor obtained by PMCA [33]. MALDI analysis of such samples produced spectra that were dominated by a large peak corresponding to fragment N_{153}-S_{231} and a group of peaks that were believed to correspond to doubly N- and C-terminal-truncated fragments which the lower mass accuracy of MALDI did not allow to identify, some of which would correspond to N_{97}/Q_{98}-E_{152}/N_{153}. Very small peaks, corresponding to additional minor cleavages at A_{116}/A_{117}, S_{132}/A_{133} and M_{134}/S_{135}, were detected also. Conversely, some minor differences might exist between the two products. This pattern of fragmentation, as discussed in our previous publication [33] strongly suggests that both PMCA- and PMSA-generated recombinant PrP^{Sc} share the same architecture. Besides the main cleavage at N_{97}/Q_{98}, which marks the division between the disordered N-terminal tail and the compact 'PrP27-30' domain, a significant secondary cleavage site was seen for both brain-derived and recombinant PrP^{Sc} at N_{153}-M_{154} [32]. In recombinant prion samples, cleavage at this site was much more extensive than in brain-derived PrP^{Sc}, and the resultant N- and C-terminal-truncated fragments were detected readily. We have proposed previously that the secondary cleavage site, which is close to proline P_{158} might correspond to a particularly accessible flexible linker connecting β-strands [54]. Other shared minor cleavage sites also support the notion that brain-derived PrP^{Sc} and the recombinant prion described here are comprised of a set of β-strands connected by flexible linkers, spanning from position 90–98 to the C-terminus, and that the identity of the β-strands and linkers are similar in both molecules. The data from epitope mapping and ESI-TOF of the proteolytic fragments of this recombinant prion could fit with one of the suggested structural models for prions, the 4-rung β-solenoid model [34, 48], according to the scheme proposed (Fig 11). However, it does not unequivocally exclude the possibility of other structures giving rise to the same proteolytic fragments.

Another possibility that we cannot completely exclude, although it contradicts Occam´s principle, is that a mixture of strains is responsible for the multiple-banded pattern, some proteolytic fragments originating from certain conformer, while other fragments would derive from different structural variants. Our attempts to separate this possible strain mixture through clonal selection of limiting dilutions (highest dilution able to propagate in each PMSA round was diluted from 10^{-1} to 10^{-8} in a subsequent round and this process was repeated
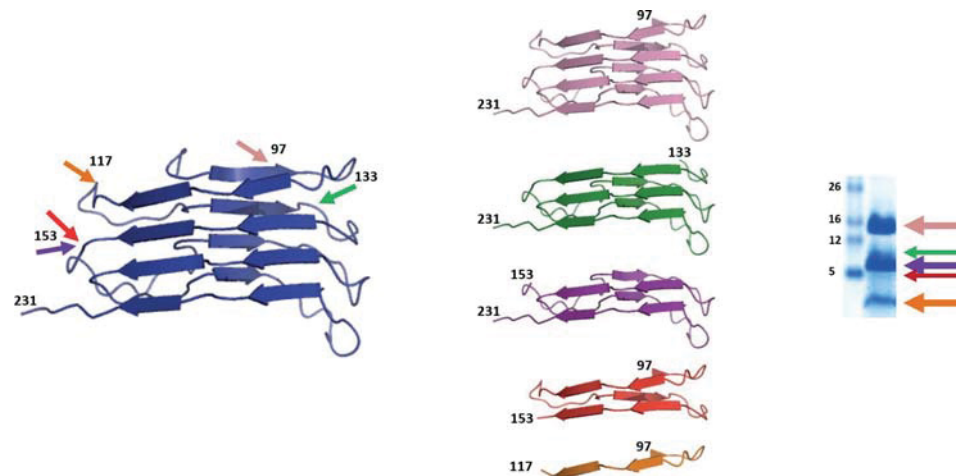
Fig 11. Graphical representation of the PrP fragments identified after PK-digestion of L-seeded-PMSA by epitope mapping and ESI-TOF and their origin based on the 4 rung β-solenoid model for PrP^Sc. The identification of the main proteolytic fragments of L-seeded-PMSA after PK digestion (characteristic whole PK-resistant core after amino terminal digestion represented in blue, encompassing residues 89–231) by epitope mapping and ESI-TOF showed four major cleavage sites at positions ~97, ~117, ~133 and ~153 that give rise to five fragments of ~15 (pink, encompassing residues ~97–231, rungs 1 to 4), ~11 (green, encompassing residues ~133–231, rungs 2/3 to 4), ~9 (purple, encompassing residues ~153–231, rungs 3 and 4), ~6 (red, encompassing residues ~97–153, rungs 1 to 3) and ~2 (orange, encompassing residues ~97–117 rungs 1 and 2) kDa. Based on the assumption that PK cleaves accessible and flexible sites of the protein, most likely loops linking β-strands, the main fragments and cleavage sites may indicate that the overall structure of L-seeded-PMSA could fit with the 4-rung β-solenoid model proposed previously for brain-derived prions [34].

https://doi.org/10.1371/journal.ppat.1008117.g011

along more than 5 serial rounds) always resulted in the same proteolytic fragments, suggesting a single conformer or the existence of multiple conformers with exactly the same propagation abilities and thus, undistinguishable by this method.

The sedimentation velocity analysis could also shed some light on the heterogeneity of the sample produced by PMSA, mainly in terms of quaternary structure heterogeneity. This methodology has been applied previously to establish the relation between infectivity and specific prion aggregates [55], to determine the heterogeneity of PrP assemblies in prions from brains [56] and to characterize prion strains based on the differential properties of the assemblies present in each isolate [57]. The ultrastructural heterogeneity on samples containing PrP assemblies, either recombinant or brain-derived, can indicate the presence of a continuous range of aggregates with the same tertiary structure but different fibril sizes or the existence of structurally distinct conformers that adopt slightly different quaternary structures. The continuous distribution for aggregates observed with L-seeded-PMSA, with predominance of very large aggregates and similar pattern of PK-digested and undigested samples (Supplementary information, S3 Fig), together with the other biochemical characteristics evaluated, suggests a single population with a unique tertiary structure forming assemblies of distinct sizes. Nonetheless, the existence of slightly different tertiary structures giving rise to distinct assemblies cannot be completely discarded with the present evidences. The first scenario should not pose a great limitation for the ssNMR studies aimed to elucidate the tertiary structure of our recombinant PrP^res preparations, since the main problems associated to sample heterogeneity are not related to the size of the assemblies (i. e. number of monomers within a fibril). As long as the tertiary structure is homogeneous the large majority of monomers within the fibrils will have the same surrounding (same distances between residues) and the few molecules at the fibril ends will be too few to be detected. So the average fibril length is not necessarily

correlated with the monomer structure and thus, variations in particle size *per se* (considering the same structure for monomers forming them) would not affect the quality of the NMR spectra. The proof of the relative importance of fibril-length heterogeneity is provided by other amyloid structures solved using preparations with variable length fibrils and oligomers [58]. In the less probable second scenario, the different monomeric structures within the sample would be critical for structural resolution by ssNMR but this would also lead to structural polymorphism (i.e. different fibril morphologies like straight/twisted and it may also be accompanied by different numbers of monomers per layer). Presumably, such morphological differences would be reflected on different majoritarian populations with distinct density in the sedimentation velocity profile. The issue could also be addressed by negative stain EM [59] but only if differences were quite notorious. Moreover, despite fibril polymorphism can be associated with different monomer folds, fibrils with very different fiber morphology but still the identical monomer conformations have also been demonstrated [60]. In any case, any effect of the morphological variability of the PrP fibrils will be continuously monitored during the ssNMR spectra generation, in order to introduce further improvements in sample preparations, if required, to solve issues related to quaternary structure of assemblies.

Regarding the biological properties of L-seeded-PMSA upon inoculation in TgVole (Table 1) and bank voles (Table 2), there is no doubt about its infectivity and the capacity to cause a *bona fide* prion disease. It is noteworthy that differences in incubation times were detected between TgVole and bank voles in the first passage of L-seeded-PMSA, despite the identical PrP sequence and very similar expression levels (S2 Fig). Although unexpected, this difference might be explained by the differences between both models and the existence of a transmission barrier between the recombinant inoculum and the PrP^C from brain. The significant reduction of disease incubation times in a second passage observed in TgVole for L-seeded-PMSA (from 266–250 dpi to 116 dpi) and also for L-seeded-PMCA (from 326 dpi to 120 dpi) strongly suggest the existence of a transmission barrier, most likely due to the absence of glycosylation and GPI anchoring of the recombinant inoculum. Usually, a transmission barrier is associated to prolonged incubation times upon first passage and higher dispersion in disease onset and duration between animals of the same group [61], but may also enhance the effect of small differences in PrP expression levels and the genetic background of the models used to evaluate infectivity. This could be the reason for the differences observed in incubation times, since small differences in expression levels undetectable by western blotting are plausible and genetic background differences obvious being two different species. In any case, L-seeded-PMSA with 100% attack rates in both models, is undoubtedly infectious and gives rise to a classical prion disorder with all its hallmarks.

Despite the possibility of strain mixtures could not be definitively excluded, the stable serial propagation of this prion over 33 rounds of PMSA at a dilution of 1:1,000 demonstrated its stability and therefore suitability for high resolution structural studies, demonstrated further by a good ssNMR spectra being obtained. Although the signal dispersion was limited in the preliminary spectra shown in this manuscript (Fig 10), such that site-specific resonance assignment was not feasible, it can clearly be seen that most of the cross-correlation signals have chemical shifts which are indicative of β-strand-like conformations, in agreement with the β-sheet rich secondary structure of amyloid fibrils. However, single residues may have random-coil or even α-helical conformation. Further structural characterization, such as the determination of the registry and supramolecular arrangement of the β-strands within the fibril will be possible despite a lack of a site-specific resonance assignment and in the presence of some degree of structural heterogeneity if dedicated labeling schemes and pulse sequences for distance measurements are applied [62–64].

The titer of recombinant prions produced *in vitro* has always been a concern regarding the biological significance of the samples analyzed and their resemblance with brain-derived

prions. The possibility of obtaining large amounts of non-infectious self-propagative aggregates that could resist PK treatment together with *bona fide* prions or the existence of heterogeneous strain mixtures are complicated issues to assess. The specific infectivity of our intracerebrally inoculated L-seeded-PMSA preparation according to the Spearman-Karber method is 6.34 x 10^4 LD_{50} / μg of PrP in TgVole (1x). This is similar, in fact slightly higher, than that obtained for the first highly infectious synthetic prion generated with RNA and POPG as cofactors in wild type mice (10^4 LD_{50} / μg of PrP) [65]. More recently, the same authors reported on a recombinant mouse PrP^{Sc} also made with RNA and POPG as cofactors, with higher specific infectivity, namely, 2 x 10^5 LD_{50} / μg of PrP; however this was assessed in a transgenic mouse model (Tga20) that overexpresses mouse PrP at 8x the level of a wild type mouse and has repeatedly shown to exhibit increased susceptibility to prion infection compared to wild type animals [66], therefore, comparison is not straightforward. Other phospholipid-complemented preparations have been reported with specific infectivity of 2.2 x 10^6 LD_{50} / ug of PrP [15], in this case tested in wild type models, and 5.6 x 10^5 LD_{50} / μg of PrP using the same substrate preparation but a different *in vitro* propagation method [67]. All in all, the specific infectivity of our preparation lies within the range of values reported. It should be noted that while differences in infectivity titer of different samples of a given PrP^{Sc} strain are a direct indication of purity and structural integrity, comparing specific infectivity of different PrP^{Sc} strains is problematic, as different strains exhibit not just different incubation times but also different specific infectivity, a classic example being the different properties of Drowsy and Hyper [68]. Furthermore, the propagation dynamics can be decisively altered by the quaternary structure that each strain or even specific preparation of a given strain acquires *in vitro* in comparison with the behavior of PrP^{Sc} formed or transmitted in the encephalon [69]. It should be noted also, that specific activity is usually lower in recombinant prions due to lack of post-translational modifications [49, 70]. All of the above likely explains the range of specific infectivity reported for different strains of infectious recombinant PrP^{Sc} which, on the other hand, differ clearly from the several reported propagative but non-infectious PrP samples, whose specific infectivity is essentially zero [12, 21]. In this respect, it is noteworthy that in contrast to other methods reported [12, 21, 45, 49], we have never observed generation of similar non-infectious propagative PrP species with our method. In fact, we have purposefully tried by introducing an array of different minor changes in the experimental conditions, with the objective of obtaining such material for comparative purposes, and have never been able to propagate such non-infectious conformers. This, together with the sedimentation velocity analysis and our cloning studies (*vide supra*) makes very unlikely the possibility that our material consists of a mixture of a small quantity of a highly infectious material and a bulk of "inert", non–infectious material, a very important consideration for structural studies.

Overall, we demonstrate here that shaking can be used to continuously propagate infectious recombinant prions as long as appropriate conditions and specific cofactors, such as dextran sulfate, are used. Moreover, we present a set of tools to extensively characterize misfolded PrP species generated *in vitro*, including a method to evaluate potential infectivity *in vitro* (brain-PMCA) prior to the more costly and protracted bioassays. The simplicity, scalability and robustness of this novel propagation method makes it easily implementable in any laboratory interested on generating large amounts of recombinant prion samples which is likely to be successful for other recombinant prions previously reported to propagate *in vitro* in presence of single cofactors [8, 10, 14, 15, 21]. This system might be adapted to the propagation of other prion strains apart from the one presented here and may open the way to detailed structural studies on many different prions shedding light on the strain phenomenon. Importantly, PMSA can become an invaluable source of distinct recombinant prions that can be labeled in multiple ways and provide the amounts (in the milligram range) of infectious prions required

for one of the most critical open questions underlying prion biology, the atomic structure of this extraordinary pathogen.

Materials and methods

Preparation of purified recombinant PrP

Bacterial expression and purification of bank vole I109 recombinant PrP (amino acids 23–231) (rec-PrP) was performed as described previously [71]. Briefly, pOPIN E expression vector containing the wild type I109 bank vole *Prnp* gene was prepared by standard molecular biology techniques using the oligonucleotides 5' AGGAGATATACCATGAAGAAGCGGCCAAAG CCTGG3' and 5' GTGATGGTGATGTTTGGAACTTCTCCCTTCGTAGTA3' to derive the PrP of interest from genomic DNA of bank vole I109 and clone in the pOPIN E expression vector. *E. coli* Rosetta (DE3) Competent Cells (EMD Millipore) were transformed with the expression vector using standard molecular biology procedures allowing the expression of the recombinant protein in LB broth (Pronadisa) upon Isopropyl β-D-1-thiogalactopyranoside (IPTG) (Gold biotechnology) induction. Although the protein does not contain a His-tag, purification of the protein was performed with a histidine affinity column (HisTrap FF crude 5 ml, GE Healthcare Amersham) taking advantage of the natural His present in the octapeptide repeat region of PrP. After elution in buffer (20 mM Tris-HCl, 500 mM NaCl, 500 mM imidazole and 2 M guanidine-HCl, pH 8), the quality and purity of protein batches was assessed by BlueSafe (NZYtech) staining after electrophoresis in SDS-PAGE gels (BioRad). Finally, guanidine-HCl was added, to a final concentration of 6 M, for long-term storage of purified protein preparations at -80˚C. For uniformly ^{13}C, ^{15}N labeled recombinant bank vole I109 PrP preparation, the same vector and *E. coli* strain were used growth in minimal medium composed of M9 minimal medium (Thermofisher Scientific), ^{13}C-glucose (3 g/liter) (Eurisotop, Cambridge Isotope Laboratories) and ^{15}NH$_4$Cl (1 g/liter) (Cortecnet, Paris) as the sole carbon and nitrogen sources and 1M MgSO$_4$ (1 ml/liter), 0.1 M CaCl$_2$ (1 ml/liter), 10 mg/ml thiamine (1 ml/liter) and 10mg/ml biotin (1 ml/liter). (Sigma-Aldrich). Induction of protein expression with IPTG and purification using histidine affinity column was performed in the same way as for the unlabeled recombinant PrP.

Generation of transgenic mice expressing bank vole PrP I109

The bank vole PrP (BvPrP) encoding isoleucine at residue 109 was synthesized according to the BvPrP sequences (GeneBank accession numbers: AF367624.1 and EF455012.1) by mutating the residue 109 codon ATG to ATT. Transgenic vector, MoPrP.Xho was modified by replacing the XhoI with BsiWI and FseI. The coding sequence of BvPrP I109 was cloned into BsiWI and FseI sites of the modified transgenic vector and the coding sequence was confirmed by DNA sequencing. The transgene expression cassette was then released with NotI and microinjected into pronuclei of fertilized FVB/N oocytes. One transgenic line, referred to as Tg(BvPrP-I109)C594+/−, was established. The expression level of BvPrP^C in the brains of Tg mice was determined by Western blotting assay using serial dilutions of brain homogenates and was compared to that of wild type FVB mice. Tg(BvPrP-I109)C594+/- mice express the same level of PrP^C as the wild type FVB mice.

In vitro propagation of prions by PMCA and PMSA

Preparation of recombinant PrP-based in vitro propagation substrates was performed as described previously for recombinant PrP-based substrates, either complemented with brain homogenates from *Prnp*$^{0/0}$ transgenic mice [9, 10, 71, 72] or with dextran sulfate sodium salt,

from *Leuconostoc spp*. with molecular weights ranging from 6,500 to 10,000 (Sigma-Aldrich) [10]. Briefly, the purified rec-PrP stored with 6 M of guanidine-HCl was diluted 1:5 in phosphate buffered saline (PBS) and dialyzed against PBS at 1:2,000 ratio for 1 h at room temperature. The dialyzed sample was centrifuged at 19,000 g for 15 min at 4°C and the supernatant used for substrate preparation. Rec-PrP concentration in the supernatant was measured (BCA protein assay kit, Thermo Scientific) and adjusted to the working concentration, which, unless otherwise indicated, was of 20 µM to reach a final concentration of 2 µM when diluted in the substrate. The protein, after dialysis and concentration adjustment was mixed with conversion buffer (CB) [71] 1:9 and dextran sulfate sodium salt, from *Leuconostoc spp*. with molecular weights ranging from 6,500 to 10,000 (Sigma-Aldrich), was added to a final concentration of 0.5% (w/v). The substrate was aliquoted and stored at -80°C until required.

Preparation of brain PrP-based in vitro propagation substrates. Brain PrP-based substrates from transgenic mice expressing 4-fold or 1-fold of bank vole I109 PrP [TgVole (4x) and TgVole (1x), respectively] under the control of the murine PrP promoter in a murine *Prnp⁰/⁰* background which were generated and characterized in a similar way as described previously [73], were prepared also as previously described [10]. Briefly, perfused whole brains, were homogenized at 10% (w/v) in CB with protease inhibitor cocktail (Roche) in a glass potter pestle (Fisher scientific), aliquoted and stored at -80°C until required.

Brain-PMCA was performed based on modified versions of the PMCA described previously [74–76], to estimate the potential *in vivo* infectivity of the recombinant seeds generated prior to bioassays [10]. Using TgVole (4x) or TgVole (1x) brain homogenates as substrates, seeded at 1:10 dilution for the first 24 h round of PMCA, in a S-4000 Misonix sonicator with microplate system (Qsonica) with incubation cycles of 30 min followed by sonication pulses of 20 s at 80% power at 38°C regulated by a circulating water bath. To avoid cross-contamination, all PMCA tubes were sealed with plastic film (Parafilm) prior to introduction in the bath sonicator to prevent accidental opening. For serial rounds of PMCA, the product of the previous round was diluted 1:10 in fresh substrate and another 24 h round of PMCA performed under identical conditions. After each round of PMCA, the external surfaces of all the tubes were cleaned thoroughly with sodium hypochlorite and tubes containing different seeds or from different experiments were treated separately. 1 mm zirconium silicate beads (BioSpec Products) were included in each reaction to favor the reproducibility of the results [77]. Unseeded controls were included together with all the seeded samples subjected to brain-PMCA. Propagation was determined by PK-digestion of the PMCA products followed by Western blotting.

recPMCA was performed as described previously [9, 71, 72, 78] using a Q-700 Misonix sonicator with microplate system (Qsonica) with incubation cycles of 30 min, followed by sonication pulses of 15–20 s at 60–80% power at 37–39°C regulated by a circulating water bath. To determine the propagation capacity of each recombinant seed they were diluted serially 1:10 in recombinant PrP-based substrate containing recombinant bank vole I109 PrP complemented with dextran sulfate. Dilutions from 10^{-1} to 10^{-7} were subjected to a single 24 h round of recPMCA. Again, all the PMCA tubes were sealed with plastic film prior to introduction in the bath sonicator to prevent accidental opening and 1 mm zirconium silicate beads (BioSpec Products) were added to favor the reproducibility of the results [77].

PMSA was performed using rec-PrP derived substrates complemented with dextran sulfate. Initially the temperature was set at 38°C using a Thermomixer (Eppendorf) with internal temperature control or a shaker (Monoshake, Thermo Scientific) placed inside an incubator (Nahita) and shaking at 700 rpm set to 60 s of shaking and 5 min incubation cycles for 24 h propagation rounds unless indicated otherwise. With the same substrates and tubes used for recPMCA and the addition of 1 mm zirconium silicate beads, serial rounds at 1:10 to 1:1,000 dilutions (up to 30 rounds) and serial seed dilutions (from 10^{-1} to 10^{-8}) in single 24 h rounds

were performed. After optimization, all PMSA reactions were performed at 39˚C and 1,000 rpm in a continuous mode.

Preparation of fibrillary bank vole rec-PrP in the presence of urea

The preparation of non-infectious fibrillary bank vole rec-PrP was performed following the protocol reported previously [79]. Briefly, recombinant bank vole PrP (120 µM in 6 M Gnd-HCl) was diluted to a final concentration of 20 µM in 20 mM sodium acetate buffer (pH 5) and dialyzed against 10 mM sodium acetate (pH 5). The dialyzed protein was incubated in 1 M Gnd-HCl, 3 M urea and 150 mM of NaCl in PBS (pH7) at 37˚C and continuous shaking (600 rpm) for 72 h. Fibril formation was monitored using Thioflavin T.

Biochemical characterization of *in vitro*- and *in vivo*-generated prion strains

Protease K digestion: recPMCA products based on *Prnp*$^{0/0}$ complemented substrates were digested by mixing the sample with N-Lauroylsarcosine sodium salt (sarkosyl) (Sigma-Aldrich) 10% in PBS 1:1 (v/v) and adding proteinase K (PK) (Roche) at 85 µg/ml for 1 h at 42˚C and shaking at 450 rpm as described previously [9]. Digestion was stopped by addition of loading buffer 1x (NuPage LDS, Invitrogen). For recPMCA and PMSA products, complemented with dextran sulfate, digestion was exactly the same but with 25 µg/ml of PK. For Blue-Safe staining, 500 µl of dextran complemented PMSA or recPMCA products were digested without any additional buffer at 25 µg/ml of PK for 1 h at 42˚C and shaking at 450 rpm. After digestion samples were immediately centrifuged at 19,000 g at 4˚C for 15 min, the supernatant was discarded and the pellet resuspended and washed with 700 µl PBS. After a further 5 min at 19,000 g at 4˚C, the supernatant was discarded and the washed pellet resuspended in 15 µl of loading buffer 1x (NuPage LDS, Invitrogen). In occasional cases other PK concentrations were used and indicated. For brain-derived samples, both obtained from diseased animals and brain-PMCA, samples were mixed 1:1 (v/v) with a digestion buffer containing 2% Nonidet P40 (Sigma-Aldrich), 2% Tween-20 (Sigma-Aldrich) and 5% sarkosyl in PBS and digested at 85 µg/ml for 1 h at 42˚C and shaking at 450 rpm. Digestion was stopped by addition of loading buffer 1x (NuPage LDS 1X, Invitrogen).

PK-resistant PrP detection: for total protein detection, PK-digested and concentrated samples in loading buffer were boiled for 10 min at 100˚C and loaded onto 4–12% acrylamide gels (NuPAGE Midi gel, Invitrogen Life Technologies) and subjected to electrophoresis for 1 h and 20 min (10 min at 70 V, 10 min at 110 V and 1 h at 150 V) and stained with BlueSafe (NZY-Tech) for 1 h at room temperature. For prion protein immunodetection, Western blotting was performed as described previously [78]. Briefly, PK-digested samples were boiled for 10 min and loaded on 4–12% acrylamide gels (NuPAGE Midi gel Invitrogen Life Technologies), subjected to electrophoresis for approximately 1 h and 20 min and transferred to a PVDF membrane (Trans-Blot Turbo Transfer Pack, Bio-Rad) using the Trans-Blot Turbo transfer system (Bio-Rad). After blocking non-specific antibody binding of the membranes by incubation in 5% non-fat milk powder for 1 h at room temperature, monoclonal antibodies 12B2 (1:2,500), D18 (1:5,000) or Saf83 (1:400) were added at the indicated dilutions and incubated for 1 h at room temperature, prior to washing, incubation with peroxidase-conjugated secondary anti-mouse antibody (m-IgGκ BP-HRP, Santa Cruz Biotechnology) or goat anti-human IgG (H+L, Thermo Scientific) and developed with an enhanced chemiluminescent horseradish peroxidase substrate (West Pico Plus, Thermo Scientific).

Epitope mapping: the characterization of misfolded recombinant PrP fragments resulting from PK digestion by epitope mapping was performed using the same protease digested

sample (25 μg/ml for 1 h at 42°C and shaking at 450 rpm) processed for BlueSafe staining and same amount loaded in multiple lanes of 4–12% acrylamide gels. After checking that each lane contained the same amount of protein by BlueSafe staining, the gel was transferred to a PVDF membrane (Trans-Blot Turbo Transfer Pack, Bio-Rad) using the Trans-Blot Turbo transfer system (Bio-Rad). The membranes were blocked to prevent non-specific antibody binding in 5% non-fat milk powder for 1 h at room temperature, individual lanes were cut and incubated separately with the following antibodies: 12B2 (1:2,500), 9A2 (1:4,000), 7D9 (1:1,000), D18 (1:5,000), Saf83 (1:400), Sa84 (1:400) and POM19 (1:10,000).

ESI-TOF: for mass spectrometry-based analysis of PK-resistant fragments of L-seeded-PMSA, the pellet from 2 ml of PK-treated sample was resuspended in 70 μl of 6M Guanidine-HCl by 3 pulses of tip sonication and incubated at 37°C for 1 h. Trifluoracetic acid was then added to a final concentration of 1%. 4 μl of the sample were injected into a micro liquid chromatography system (Eksigent Technologies nanoLC 400, SCIEX) coupled to high speed Triple TOF 6600 mass spectrometer (SCIEX) with a micro flow source. The sample was injected to a YMC-TRIART C18 trap column (YMC Technologies, Teknokroma) with a 3 mm particle size and 120 Å pore size. The loading pump delivered a wash solution of 0.1% formic acid in water at 10 μl/min. Then the sample eluted and fed into a silica-based 150×0.30 mm, 3 mm particle size and 120 Å pore size Chrom XP C18 reversed phase analytical column (Eksigent, SCIEX) by a micro-pump operating at 5 μl/min and applying a gradient consisting of 0.1% formic acid in water as mobile phase A, and 0.1% formic acid in acetonitrile as mobile phase B. Peptides were separated using a 40 min gradient ranging from 2% to 90% mobile phase B (mobile phase A: 2% acetonitrile, 0.1% formic acid; mobile phase B: 100% acetonitrile, 0.1% formic acid). TOF MS data were acquired in a TripleTOF 6600 System (SCIEX, Foster City, CA) using the following parameters; source and interface conditions were ion spray voltage floating (ISVF) 5500 V, curtain gas (CUR) 25, collision energy (CE) 10 and ion source gas 1 (GS1) 25. Finally, the protein was reconstructed using the Bio tool integrated algorithm. Data were deconvolved using a m/z range of 350–1400.

Evaluation of size distribution of aggregates by sedimentation velocity analysis in continuous sucrose gradient: Based on experiments performed previously [55], adapted to the recombinant samples devoid of any material but 5% (w/v) dextran sulfate, 1% (w/v) Triton-X-100 and 0.15 M NaCl. A wide range continuous sucrose gradient was prepared from 10% (top) to 80% (bottom) (w/v) expecting large aggregates and using a total volume of 12.5 ml in order to achieve a good resolution in case of high heterogeneity of aggregate size. The gradient was prepared by diffusion of a discontinuous gradient that included 2.5 ml layers of 80-60-40-20 and 10% (w/v) sucrose solutions with 0.2% of sarkosyl to favor correct partition of weakly interacting PrP species. The discontinuous gradient, prepared on ultra-clear centrifuge tubes (14x89 mm, Beckman Coulter) sealed with parafilm, were carefully rotated to horizontal position and incubated overnight at 4°C before loading the sample. Immediately before ultracentrifugation, 2.5 ml from the top were replaced by 2.5 ml of either PK-digested (85 μg/ml for 1 h at 42°C) or undigested L-seeded-PMSA and centrifuged at 40,000 rpm (approximately 200,000 *g*) for 18 h in a swinging-bucket SW-41 rotor using an Optima ultracentrifuge (Beckman Coulter). After centrifugation, 500 μl fractions were manually collected from top to bottom and pellet also resuspended in 500 μl and processed as follows for western blotting: 4 μl of each fraction of the undigested sample was diluted in 16 μl of PBS and 10 μl of NuPage 4X loading buffer, loading 15 μl from this mix in the gel. 200 μl of each PK-digested sample fraction were precipitated with methanol, resuspended in 30 μl of 1:3 PBS and NuPage 4X buffer from which 10 μl were loaded. Thus, approximately 30 times more sample was loaded for PK-digested sample with respect to undigested sample. Western blot was performed as described in previous sections and developed with Saf83 mAb (1:400).

Biological characterization of *in vitro* generated prion strains

Preparation of in vivo and in vitro derived inocula: 10% brain homogenates from vole-adapted chronic wasting disease (CWD) were diluted 10^{-1} in sterile PBS prior to intracerebral inoculation into TgVole (1x) and bank voles 109I (Bv109I). Equally, PMCA and PMSA products were diluted 10^{-1} in sterile PBS prior to intracerebral inoculation in the same models. The protease-resistant rec-PrP amount, estimated by Western blotting, was comparable in all samples. The inocula for the second passage were prepared, as 10% (w/v) brain homogenates in PBS form the first passage animals.

Animal inoculations: groups of eight-week-old bank voles (Bv109I) were inoculated intracerebrally with 20 μl of homogenate into the left cerebral hemisphere using a sterile disposable 27-gauge hypodermic needle while under ketamine anesthesia (ketamine 0.1 μg/g). Groups of 5 to 10 TgVole (1x) animals were inoculated in the same way but using tribromoethanol (Avertin) (0.5 mg/g) as anesthetic. The animals were examined twice a week until neurological clinical signs appeared, after which they were examined daily. Clinically affected animals were culled at the terminal stage of the disease, but before neurological impairment compromised their welfare, by exposure to a rising concentration of carbon dioxide. Survival time was calculated as the interval between inoculation and culling or death. *Post-mortem*, the brain was removed and divided sagitally to be stored at -80˚C and fixed in formalin.

Neuropathology: histology and immunohistochemistry were performed on formalin-fixed tissues as described previously [80]. Briefly, brains were trimmed at standard coronal levels, dehydrated through graded alcohols, embedded in paraffin wax, sectioned (6 μm) and stained with hematoxylin and eosin. Immunohistochemistry for PrP was performed using the 6C2 mAb (1:300) as described previously [81].

Preparation of recombinant prions for structural studies

Large volumes of PMSA products for structural studies, such as solid state Nuclear Magnetic Resonance (ssNMR), were generated in 5 ml tubes (Eppendorf) at optimized PMSA conditions and the resulting products were digested using 25 μg/ml of PK for 1 h at 42˚C and centrifuged immediately at 19,000 g for 1 h at 4˚C. The pellets were washed with PBS and centrifuged again at 19,000 g for 15 min at 4˚C. The supernatants were discarded and the pellet resuspended in water.

Solid state Nuclear Magnetic Resonance

For MAS NMR measurements, the sample was sealed hermetically in a custom-built unbreakable polyformaldehyde rotor insert designed to fit into 3.2 mm Varian rotors. The ^{13}C NMR signal of this material at 89.1 ppm does not interfere with the protein spectra [82]. Solid-state NMR spectra were recorded using a 3.2 mm MAS probe head in double resonance mode ($^{1}H,^{13}C$) at a static magnetic field of 14.1 T (Varian) and a MAS frequency of 11 kHz ± 3 Hz, at a nominal temperature of 0˚C (temperature of the cooling gas). The ^{1}H 90˚ pulse length was 3 μs, the ^{13}C 90˚ pulse length 6.5 μs. The Proton-driven spin-diffusion (PDSD) experiment was recorded with a longitudinal mixing time of 50 ms, during indirect evolution and detection SPINAL-64 proton decoupling [83] at an rf field strength of 83 kHz. 196 complex points were recorded in the indirect dimension, corresponding to a maximum t_1 acquisition time of 6 ms. In total five spectra with 128, 176 and 3·320 scans were recorded and summated, such that the total number of scans was 1,264. The 2D spectrum was processed using the squared cosine window functions in both dimensions and referenced to DSS by using adamantane as an external reference. A control INEPT spectrum, which exclusively displays signals of highly mobile protein regions, was recorded with 400 scans at a nominal temperature of 15˚C, but no signals were visible [47].

Ethics statement

TgVole mice were obtained from the breeding colony at CIC bioGUNE (Spain) and were inoculated at the University of Santiago de Compostela. All experiments involving animals in Spain adhered to the guidelines included in the Spanish law "Real Decreto 1201/2005 de 10 de Octubre" on protection of animals used for experimentation and other scientific purposes, which is based on the European Directive 86/609/EEC on Laboratory Animal Protection. The project was approved by the Ethical Committees on Animal Welfare (project codes assigned by the Ethical Committee P-CBG-CBBA-0314 and 15005/16/006) and performed under their supervision. Bank voles were obtained from the breeding colony at the Istituto Superiore di Sanità (ISS), Italy. Experiments involving animals followed the "Principles of laboratory animal care" (NIH publication No. 86–23, revised 1985) as well as the guidelines contained in the Italian Legislative Decree 116/92, which is based on the European Directive 86/609/EEC on Laboratory Animal Protection, and then in the Legislative Decree 26/2014, which transposed the European Directive 2010/63/UE on Laboratory Animal Protection. The research protocol was performed under the supervision of the Service for Biotechnology and Animal Welfare of the ISS and was approved by the Italian Ministry of Health (decree number 84/12.B).

Supporting information

S1 Fig. Shaking system and *ad hoc* designed racks for different tube sizes. Photograph on the left shows the rack designed with 96 wells for 0.2 ml PCR tubes on the shaker used for PMSA reactions. The photograph on the right shows the rack with 6 horizontal cells for 5 ml tubes suitable for the same shaker. Both racks were designed *ad hoc* and 3D-printed (I+3D). Racks for any desired tube can be designed and printed making PMSA a highly versatile method for misfolded protein production.
(PDF)

S2 Fig. PrP expression levels in TgVole (1x) animals compared to PrP expression levels of bank vole I109 by Western blot. 10% brain homogenates from TgVole (1x) (I109I) mouse and bank vole 109I were diluted 1:16, 1:32, 1:64 and 1:128 and analyzed by Western blot using monoclonal antibody D18 (1:5,000). The PrP expression levels of TgVole (1x) were equal to PrP^C levels in bank vole brain based on signal intensity. No significant differences were observed in the electrophoretic migration patterns. Mw: Molecular weight.
(PDF)

S3 Fig. Sedimentation velocity analysis of L-seeded-PMSA by ultracentrifugation through a continuous sucrose gradient. Proteinase K-digested and undigested L-seeded-PMSA were subjected to ultracentrifugation at ~200,000 g through a continuous sucrose gradient ranging from 10 to 80% (w/v) with 0.2% sarkosyl to determine the size distribution of total PrP and PrPres assemblies by Western blot. The equivalent of 2 μl of each fraction of the gradient were loaded for the undigested sample, while for PK-digested sample, fractions were precipitated with methanol loading the equivalent to 60 μl, thus PK-digested gel shows 30-fold higher sample amount than the gel of undigested fractions. Briefly, the sedimentation pattern shows total absence of monomeric PrP in the top fractions and a continuum in the aggregate size from fractions containing around 30% to 80% sucrose for the untreated sample and from around 40% to 80% sucrose for the PK-digested sample, suggesting predominance of large PK-resistant assemblies in the sample. This indicates the presence of a heterogeneous size assemblies but does not reveal clearly different majoritarian populations that could point towards the existence of distinct assembly types regarding tertiary structure. Developed with Saf83 mAb

(1:400). PK: Proteinase K, MW; molecular weight marker.
(PDF)

S1 Table. L-seeded-PMSA protease K-resistant fragments identified by ESI-TOF.
(PDF)

Acknowledgments

Author Contributions

Conceptualization: Hasier Eraña, Natalia Fernández-Borges, Jesús R. Requena, Joaquín Castilla.

Funding acquisition: Jesús R. Requena, Joaquín Castilla.

Investigation: Hasier Eraña, Jorge M. Charco, Michele A. Di Bari, Carlos M. Díaz-Domínguez, Rafael López-Moreno, Enric Vidal, Ezequiel González-Miranda, Miguel A. Pérez-Castro, Sandra García-Martínez, Susana Bravo, Natalia Fernández-Borges, Mariví Geijo, Claudia D'Agostino, Jifeng Bian, Anna König, Boran Uluca-Yazgi, Raimon Sabate, Vadim Khaychuk, Ilaria Vanni, Glenn C. Telling, Henrike Heise, Romolo Nonno, Jesús R. Requena, Joaquín Castilla.

Methodology: Jorge M. Charco, Michele A. Di Bari, Carlos M. Díaz-Domínguez, Rafael López-Moreno, Enric Vidal, Ezequiel González-Miranda, Miguel A. Pérez-Castro, Sandra García-Martínez, Susana Bravo, Mariví Geijo, Claudia D'Agostino, Joseba Garrido, Jifeng Bian, Anna König, Boran Uluca-Yazgi, Raimon Sabate, Vadim Khaychuk, Ilaria Vanni, Glenn C. Telling, Romolo Nonno, Jesús R. Requena.

Project administration: Joaquín Castilla.

Supervision: Mariví Geijo, Joseba Garrido, Glenn C. Telling, Henrike Heise, Jesús R. Requena, Joaquín Castilla.

Writing – original draft: Hasier Eraña, Henrike Heise, Jesús R. Requena, Joaquín Castilla.

Writing – review & editing: Hasier Eraña, Jorge M. Charco, Michele A. Di Bari, Carlos M. Díaz-Domínguez, Rafael López-Moreno, Enric Vidal, Ezequiel González-Miranda, Miguel A. Pérez-Castro, Sandra García-Martínez, Natalia Fernández-Borges, Joseba Garrido, Anna König, Glenn C. Telling, Henrike Heise, Romolo Nonno, Jesús R. Requena, Joaquín Castilla.

References

1. Legname G, Baskakov IV, Nguyen HO, Riesner D, Cohen FE, DeArmond SJ, et al. Synthetic mammalian prions. Science. 2004; 305(5684):673–6. Epub 2004/08/03. https://doi.org/10.1126/science.1100195 305/5684/673 [pii]. PMID: 15286374.

2. Bocharova OV, Breydo L, Salnikov VV, Gill AC, Baskakov IV. Synthetic prions generated in vitro are similar to a newly identified subpopulation of PrPSc from sporadic Creutzfeldt-Jakob Disease. Protein

Sci. 2005; 14(5):1222–32. Epub 2005/04/02. ps.041186605 [pii] https://doi.org/10.1110/ps.041186605 PMID: 15802644; PubMed Central PMCID: PMC2253268.

3. Legname G, Nguyen HO, Baskakov IV, Cohen FE, Dearmond SJ, Prusiner SB. Strain-specified characteristics of mouse synthetic prions. Proc Natl Acad Sci U S A. 2005; 102(6):2168–73. Epub 2005/01/27. 0409079102 [pii] https://doi.org/10.1073/pnas.0409079102 PMID: 15671162; PubMed Central PMCID: PMC548557.

4. Deleault NR, Harris BT, Rees JR, Supattapone S. Formation of native prions from minimal components in vitro. Proc Natl Acad Sci U S A. 2007; 104(23):9741–6. Epub 2007/05/31. 0702662104 [pii] https://doi.org/10.1073/pnas.0702662104 PMID: 17535913; PubMed Central PMCID: PMC1887554.

5. Makarava N, Kovacs GG, Bocharova O, Savtchenko R, Alexeeva I, Budka H, et al. Recombinant prion protein induces a new transmissible prion disease in wild-type animals. Acta Neuropathol. 2010; 119 (2):177–87. Epub 2010/01/07. https://doi.org/10.1007/s00401-009-0633-x PMID: 20052481; PubMed Central PMCID: PMC2808531.

6. Kim JI, Cali I, Surewicz K, Kong Q, Raymond GJ, Atarashi R, et al. Mammalian prions generated from bacterially expressed prion protein in the absence of any mammalian cofactors. J Biol Chem. 2010; 285 (19):14083–7. Epub 2010/03/23. C110.113464 [pii] https://doi.org/10.1074/jbc.C110.113464 PMID: 20304915; PubMed Central PMCID: PMC2863186.

7. Colby DW, Wain R, Baskakov IV, Legname G, Palmer CG, Nguyen HO, et al. Protease-sensitive synthetic prions. PLoS Pathog. 6(1):e1000736. Epub 2010/01/29. https://doi.org/10.1371/journal.ppat.1000736 PMID: 20107515; PubMed Central PMCID: PMC2809756.

8. Wang F, Wang X, Yuan CG, Ma J. Generating a prion with bacterially expressed recombinant prion protein. Science. 2010; 327(5969):1132–5. Epub 2010/01/30. science.1183748 [pii] https://doi.org/10.1126/science.1183748 PMID: 20110469; PubMed Central PMCID: PMC2893558.

9. Elezgarai SR, Fernández-Borges N, Erana H, Sevillano A, Moreno J, Harrathi C, et al. Generation of a new infectious recombinant prion: a model to understand Gerstmann–Sträussler–Scheinker syndrome. Sci Rep. 2017. https://doi.org/10.1038/s41598-017-09489-3 PMID: 28851967

10. Fernández-Borges N, Di Bari MA, Erana H, Sanchez-Martin M, Pirisinu L, Parra B, et al. Cofactors influence the biological properties of infectious recombinant prions. Acta Neuropathol. 2017. https://doi.org/10.1007/s00401-017-1782-y PMID: 29094186.

11. Charco JM, Erana H, Venegas V, Garcia-Martinez S, Lopez-Moreno R, Gonzalez-Miranda E, et al. Recombinant PrP and Its Contribution to Research on Transmissible Spongiform Encephalopathies. Pathogens. 2017; 6(4). https://doi.org/10.3390/pathogens6040067 PMID: 29240682; PubMed Central PMCID: PMC5750591.

12. Wang F, Wang X, Orru CD, Groveman BR, Surewicz K, Abskharon R, et al. Self-propagating, protease-resistant, recombinant prion protein conformers with or without in vivo pathogenicity. PLoS Pathog. 2017; 13(7):e1006491. https://doi.org/10.1371/journal.ppat.1006491 PMID: 28704563; PubMed Central PMCID: PMC5524416.

13. Zhang Y, Wang F, Wang X, Zhang Z, Xu Y, Yu G, et al. Comparison of 2 synthetically generated recombinant prions. Prion. 2014; 8(2):215–20. https://doi.org/10.4161/pri.28669 PMID: 24721728

14. Deleault NR, Piro JR, Walsh DJ, Wang F, Ma J, Geoghegan JC, et al. Isolation of phosphatidylethanolamine as a solitary cofactor for prion formation in the absence of nucleic acids. Proc Natl Acad Sci U S A. 2012; 109(22):8546–51. Epub 2012/05/16. https://doi.org/10.1073/pnas.1204498109 PMID: 22586108; PubMed Central PMCID: PMC3365173.

15. Deleault NR, Walsh DJ, Piro JR, Wang F, Wang X, Ma J, et al. Cofactor molecules maintain infectious conformation and restrict strain properties in purified prions. Proc Natl Acad Sci U S A. 2012; 109(28): E1938–46. Epub 2012/06/20. https://doi.org/10.1073/pnas.1206999109 PMID: 22711839; PubMed Central PMCID: PMC3396481.

16. Watts JC, Giles K, Stohr J, Oehler A, Bhardwaj S, Grillo SK, et al. Spontaneous generation of rapidly transmissible prions in transgenic mice expressing wild-type bank vole prion protein. Proc Natl Acad Sci U S A. 2012; 109(9):3498–503. Epub 2012/02/15. https://doi.org/10.1073/pnas.1121556109 PMID: 22331873; PubMed Central PMCID: PMC3295307.

17. Watts JC, Giles K, Patel S, Oehler A, DeArmond SJ, Prusiner SB. Evidence that bank vole PrP is a universal acceptor for prions. PLoS Pathog. 2014; 10(4):e1003990. https://doi.org/10.1371/journal.ppat.1003990 PMID: 24699458; PubMed Central PMCID: PMC3974871.

18. Di Bari MA, Nonno R, Castilla J, D'Agostino C, Pirisinu L, Riccardi G, et al. Chronic wasting disease in bank voles: characterisation of the shortest incubation time model for prion diseases. PLoS Pathog. 2013; 9(3):e1003219. Epub 2013/03/19. https://doi.org/10.1371/journal.ppat.1003219 PMID: 23505374; PubMed Central PMCID: PMC3591354.

19. Deleault NR, Kascsak R, Geoghegan JC, Supattapone S. Species-dependent differences in cofactor utilization for formation of the protease-resistant prion protein in vitro. Biochemistry. 2010; 49(18):3928–

34. Epub 2010/04/10. https://doi.org/10.1021/bi100370b PMID: 20377181; PubMed Central PMCID: PMC3021175.

20. Lawson VA, Lumicisi B, Welton J, Machalek D, Gouramanis K, Klemm HM, et al. Glycosaminoglycan sulphation affects the seeded misfolding of a mutant prion protein. PLoS One. 2010; 5(8):e12351. Epub 2010/09/03. https://doi.org/10.1371/journal.pone.0012351 PMID: 20808809; PubMed Central PMCID: PMC2925953.

21. Supattapone S. Synthesis of high titer infectious prions with cofactor molecules. J Biol Chem. 2014; 289 (29):19850–4. https://doi.org/10.1074/jbc.R113.511329 PMID: 24860097; PubMed Central PMCID: PMC4106305.

22. Bruce ME. TSE strain variation. Br Med Bull. 2003; 66:99–108. Epub 2003/10/03. https://doi.org/10.1093/bmb/66.1.99 PMID: 14522852.

23. Weissmann C, Li J, Mahal SP, Browning S. Prions on the move. EMBO Rep. 2011; 12(11):1109–17. Epub 2011/10/15. https://doi.org/10.1038/embor.2011.192 PMID: 21997298; PubMed Central PMCID: PMC3207107.

24. Collinge J. Medicine. Prion strain mutation and selection. Science. 2010; 328(5982):1111–2. Epub 2010/05/29. https://doi.org/10.1126/science.1190815 PMID: 20508117.

25. Erana H, Castilla J. The architecture of prions: how understanding would provide new therapeutic insights. Swiss Med Wkly. 2016; 146:w14354. https://doi.org/10.4414/smw.2016.14354 PMID: 27684312.

26. Lu X, Wintrode PL, Surewicz WK. Beta-sheet core of human prion protein amyloid fibrils as determined by hydrogen/deuterium exchange. Proc Natl Acad Sci U S A. 2007; 104(5):1510–5. Epub 2007/01/24. 0608447104 [pii] https://doi.org/10.1073/pnas.0608447104 PMID: 17242357; PubMed Central PMCID: PMC1785245.

27. Nazabal A, Hornemann S, Aguzzi A, Zenobi R. Hydrogen/deuterium exchange mass spectrometry identifies two highly protected regions in recombinant full-length prion protein amyloid fibrils. J Mass Spectrom. 2009; 44(6):965–77. Epub 2009/03/14. https://doi.org/10.1002/jms.1572 PMID: 19283723.

28. Smirnovas V, Kim JI, Lu X, Atarashi R, Caughey B, Surewicz WK. Distinct structures of scrapie prion protein (PrPSc)-seeded versus spontaneous recombinant prion protein fibrils revealed by hydrogen/ deuterium exchange. J Biol Chem. 2009; 284(36):24233–41. Epub 2009/07/15. M109.036558 [pii] https://doi.org/10.1074/jbc.M109.036558 PMID: 19596861; PubMed Central PMCID: PMC2782017.

29. Eberl H, Tittmann P, Glockshuber R. Characterization of recombinant, membrane-attached full-length prion protein. J Biol Chem. 2004; 279(24):25058–65. Epub 2004/03/20. https://doi.org/10.1074/jbc.M400952200 [pii]. PMID: 15031284.

30. Sajnani G, Pastrana MA, Dynin I, Onisko B, Requena JR. Scrapie prion protein structural constraints obtained by limited proteolysis and mass spectrometry. J Mol Biol. 2008; 382(1):88–98. Epub 2008/07/ 16. S0022-2836(08)00797-3 [pii] https://doi.org/10.1016/j.jmb.2008.06.070 PMID: 18621059.

31. Sajnani G, Silva CJ, Ramos A, Pastrana MA, Onisko BC, Erickson ML, et al. PK-sensitive PrP is infectious and shares basic structural features with PK-resistant PrP. PLoS Pathog. 2012; 8(3):e1002547. Epub 2012/03/08. https://doi.org/10.1371/journal.ppat.1002547 PMID: 22396643; PubMed Central PMCID: PMC3291653.

32. Vazquez-Fernandez E, Alonso J, Pastrana MA, Ramos A, Stitz L, Vidal E, et al. Structural organization of mammalian prions as probed by limited proteolysis. PLoS One. 2012; 7(11):e50111. Epub 2012/11/ 28. https://doi.org/10.1371/journal.pone.0050111 PMID: 23185550; PubMed Central PMCID: PMC3502352.

33. Sevillano AM, Fernandez-Borges N, Younas N, Wang F, S RE, Bravo S, et al. Recombinant PrPSc shares structural features with brain-derived PrPSc: Insights from limited proteolysis. PLoS Pathog. 2018; 14(1):e1006797. https://doi.org/10.1371/journal.ppat.1006797 PMID: 29385212; PubMed Central PMCID: PMC5809102.

34. Vazquez-Fernandez E, Vos MR, Afanasyev P, Cebey L, Sevillano AM, Vidal E, et al. The Structural Architecture of an Infectious Mammalian Prion Using Electron Cryomicroscopy. PLoS Pathog. 2016; 12 (9):e1005835. https://doi.org/10.1371/journal.ppat.1005835 PMID: 27606840; PubMed Central PMCID: PMC5015997.

35. Wan W, Wille H, Stohr J, Kendall A, Bian W, McDonald M, et al. Structural studies of truncated forms of the prion protein PrP. Biophys J. 2015; 108(6):1548–54. https://doi.org/10.1016/j.bpj.2015.01.008 PMID: 25809267; PubMed Central PMCID: PMC4375555.

36. Groveman BR, Dolan MA, Taubner LM, Kraus A, Wickner RB, Caughey B. Parallel in-register intermolecular beta-sheet architectures for prion-seeded prion protein (PrP) amyloids. J Biol Chem. 2014; 289 (35):24129–42. https://doi.org/10.1074/jbc.M114.578344 PMID: 25028516; PubMed Central PMCID: PMC4148845.

37. Baskakov IV, Caughey B, Requena JR, Sevillano AM, Surewicz WK, Wille H. The prion 2018 round tables (I): the structure of PrP(Sc). Prion. 2019; 13(1):46–52. https://doi.org/10.1080/19336896.2019.1569450 PMID: 30646817.

38. Laws DD, Bitter HM, Liu K, Ball HL, Kaneko K, Wille H, et al. Solid-state NMR studies of the secondary structure of a mutant prion protein fragment of 55 residues that induces neurodegeneration. Proc Natl Acad Sci U S A. 2001; 98(20):11686–90. Epub 2001/09/20. https://doi.org/10.1073/pnas.201404298 [pii]. PMID: 11562491; PubMed Central PMCID: PMC58790.

39. Siemer AB, Ritter C, Ernst M, Riek R, Meier BH. High-resolution solid-state NMR spectroscopy of the prion protein HET-s in its amyloid conformation. Angew Chem Int Ed Engl. 2005; 44(16):2441–4. Epub 2005/03/17. https://doi.org/10.1002/anie.200462952 PMID: 15770629.

40. Gremer L, Schölzel D, Schenk C, Reinartz E, Labahn J, Ravell RBG, et al. Fibril structure of amyloid-β (1–42) by cryo–electron microscopy. Science. 2017; 358(6359):116–9. https://doi.org/10.1126/science.aao2825 PMID: 28882996

41. Theint T, Nadaud PS, Aucoin D, Helmus JJ, Pondaven SP, Surewicz K, et al. Species-dependent structural polymorphism of Y145Stop prion protein amyloid revealed by solid-state NMR spectroscopy. Nat Commun. 2017; 8(1):753. https://doi.org/10.1038/s41467-017-00794-z PMID: 28963458; PubMed Central PMCID: PMC5622040.

42. Aucoin D, Xia Y, Theint T, Nadaud PS, Surewicz K, Surewicz WK, et al. Protein-solvent interfaces in human Y145Stop prion protein amyloid fibrils probed by paramagnetic solid-state NMR spectroscopy. J Struct Biol. 2018. https://doi.org/10.1016/j.jsb.2018.04.002 PMID: 29679649.

43. Ladner-Keay CL, Griffith BJ, Wishart DS. Shaking alone induces de novo conversion of recombinant prion proteins to beta-sheet rich oligomers and fibrils. PLoS One. 2014; 9(6):e98753. https://doi.org/10.1371/journal.pone.0098753 PMID: 24892647; PubMed Central PMCID: PMC4043794.

44. Darros-Barbosa R, Balaban MO, Teixeira AA. Temperature and Concentration Dependence of Density of Model Liquid Foods. International Journal of Food Properties. 2003; 6(2):195–214. https://doi.org/10.1081/jfp-120017815

45. Makarava N, Kovacs GG, Savtchenko R, Alexeeva I, Budka H, Rohwer RG, et al. Genesis of mammalian prions: from non-infectious amyloid fibrils to a transmissible prion disease. PLoS Pathog. 2011; 7 (12):e1002419. Epub 2011/12/07. https://doi.org/10.1371/journal.ppat.1002419 PMID: 22144901; PubMed Central PMCID: PMC3228811.

46. Ramakrishnan MA. Determination of 50% endpoint titer using a simple formula. World J Virol. 2016; 5 (2):85–6. https://doi.org/10.5501/wjv.v5.i2.85 PMID: 27175354; PubMed Central PMCID: PMC4861875.

47. Andronesi OC, Becker S, Seidel K, Heise H, Young HS, Baldus M. Determination of Membrane Protein Structure and Dynamics by Magic-Angle-Spinning Solid-State NMR Spectroscopy. Journal of the American Chemical Society. 2005; 127(37):12965–74. https://doi.org/10.1021/ja0530164 PMID: 16159291

48. Vazquez-Fernandez E, Young HS, Requena JR, Wille H. The Structure of Mammalian Prions and Their Aggregates. Int Rev Cell Mol Biol. 2017; 329:277–301. https://doi.org/10.1016/bs.ircmb.2016.08.013 PMID: 28109330.

49. Burke C, Walsh D, Steele A, Agrimi U, Di Bari MA, Watts JC, et al. Full restoration of specific infectivity and strain properties from pure mammalian prion protein. PLoS Pathog. 2019; 15(3):e1007662. https://doi.org/10.1371/journal.ppat.1007662 PMID: 30908557.

50. Timmes AG, Moore RA, Fischer ER, Priola SA. Recombinant prion protein refolded with lipid and RNA has the biochemical hallmarks of a prion but lacks in vivo infectivity. PLoS One. 2013; 8(7):e71081. https://doi.org/10.1371/journal.pone.0071081 PMID: 23936256; PubMed Central PMCID: PMC3728029.

51. Fernandez-Borges N, Castilla J. PMCA. A Decade of In Vitro Prion Replication. Current Chemical Biology. 2010; 4(3):200–7. https://doi.org/10.2174/187231310792062693

52. Baskakov IV. Autocatalytic conversion of recombinant prion proteins displays a species barrier. J Biol Chem. 2004; 279(9):7671–7. Epub 2003/12/12. https://doi.org/10.1074/jbc.M310594200 [pii]. PMID: 14668351.

53. Piening N, Weber P, Giese A, Kretzschmar H. Breakage of PrP aggregates is essential for efficient autocatalytic propagation of misfolded prion protein. Biochem Biophys Res Commun. 2005; 326 (2):339–43. Epub 2004/12/08. S0006-291X(04)02608-7 [pii] https://doi.org/10.1016/j.bbrc.2004.11.039 PMID: 15582583.

54. Silva CJ, Vazquez-Fernandez E, Onisko B, Requena JR. Proteinase K and the structure of PrPSc: The good, the bad and the ugly. Virus Res. 2015; 207:120–6. https://doi.org/10.1016/j.virusres.2015.03.008 PMID: 25816779.

55. Tixador P, Herzog L, Reine F, Jaumain E, Chapuis J, Le Dur A, et al. The physical relationship between infectivity and prion protein aggregates is strain-dependent. PLoS Pathog. 2010; 6(4):e1000859. Epub

2010/04/27. https://doi.org/10.1371/journal.ppat.1000859 PMID: 20419156; PubMed Central PMCID: PMC2855332.

56. Igel-Egalon A, Bohl J, Moudjou M, Herzog L, Reine F, Rezaei H, et al. Heterogeneity and Architecture of Pathological Prion Protein Assemblies: Time to Revisit the Molecular Basis of the Prion Replication Process? Viruses. 2019; 11(5). https://doi.org/10.3390/v11050429 PMID: 31083283.

57. Igel-Egalon A, Beringue V, Rezaei H, Sibille P. Prion Strains and Transmission Barrier Phenomena. Pathogens. 2018; 7(1). https://doi.org/10.3390/pathogens7010005 PMID: 29301257; PubMed Central PMCID: PMC5874731.

58. Van Melckebeke H, Wasmer C, Lange A, Ab E, Loquet A, Bockmann A, et al. Atomic-resolution three-dimensional structure of HET-s(218–289) amyloid fibrils by solid-state NMR spectroscopy. J Am Chem Soc. 2010; 132(39):13765–75. Epub 2010/09/11. https://doi.org/10.1021/ja104213j PMID: 20828131.

59. Heise H, Hoyer W, Becker S, Andronesi OC, Riedel D, Baldus M. Molecular-level secondary structure, polymorphism, and dynamics of full-length alpha-synuclein fibrils studied by solid-state NMR. Proc Natl Acad Sci U S A. 2005; 102(44):15871–6. https://doi.org/10.1073/pnas.0506109102 PMID: 16247008; PubMed Central PMCID: PMC1276071.

60. Seuring C, Verasdonck J, Ringler P, Cadalbert R, Stahlberg H, Bockmann A, et al. Amyloid Fibril Polymorphism: Almost Identical on the Atomic Level, Mesoscopically Very Different. J Phys Chem B. 2017; 121(8):1783–92. https://doi.org/10.1021/acs.jpcb.6b10624 PMID: 28075583.

61. Bartz JC, McKenzie DI, Bessen RA, Marsh RF, Aiken JM. Transmissible mink encephalopathy species barrier effect between ferret and mink: PrP gene and protein analysis. J Gen Virol. 1994; 75 (Pt 11):2947–53. Epub 1994/11/01. https://doi.org/10.1099/0022-1317-75-11-2947 PMID: 7964604.

62. Tycko R. Symmetry-based constant-time homonuclear dipolar recoupling in solid state NMR. J Chem Phys. 2007; 126(6):064506. https://doi.org/10.1063/1.2437194 PMID: 17313228.

63. Shewmaker F, Kryndushkin D, Chen B, Tycko R, Wickner RB. Two prion variants of Sup35p have in-register parallel beta-sheet structures, independent of hydration. Biochemistry. 2009; 48(23):5074–82. Epub 2009/05/05. https://doi.org/10.1021/bi900345q PMID: 19408895; PubMed Central PMCID: PMC2744896.

64. Ohhashi Y, Yamaguchi Y, Kurahashi H, Kamatari YO, Sugiyama S, Uluca B, et al. Molecular basis for diversification of yeast prion strain conformation. Proc Natl Acad Sci U S A. 2018; 115(10):2389–94. https://doi.org/10.1073/pnas.1715483115 PMID: 29467288; PubMed Central PMCID: PMC5877990.

65. Wang X, McGovern G, Zhang Y, Wang F, Zha L, Jeffrey M, et al. Intraperitoneal Infection of Wild-Type Mice with Synthetically Generated Mammalian Prion. PLoS Pathog. 2015; 11(7):e1004958. https://doi.org/10.1371/journal.ppat.1004958 PMID: 26136122; PubMed Central PMCID: PMC4489884.

66. Wang F, Wang X, Abskharon R, Ma J. Prion infectivity is encoded exclusively within the structure of proteinase K-resistant fragments of synthetically generated recombinant PrP(Sc). Acta Neuropathol Commun. 2018; 6(1):30. https://doi.org/10.1186/s40478-018-0534-0 PMID: 29699569; PubMed Central PMCID: PMC5921397.

67. Walsh DJ, Tuttle MD, Burke CM, Zilm KW, Supattapone S, editors. Large-scale production of phospholipid cofactor recombinant prions with high specific infectivity. Prion 2019; 2019 May 2019; Edmonton, Canada: Taylor & Francis Online (Prion).

68. Bessen RA, Marsh RF. Identification of two biologically distinct strains of transmissible mink encephalopathy in hamsters. J Gen Virol. 1992; 73 (Pt 2):329–34. Epub 1992/02/01. https://doi.org/10.1099/0022-1317-73-2-329 PMID: 1531675.

69. Laferriere F, Tixador P, Moudjou M, Chapuis J, Sibille P, Herzog L, et al. Quaternary structure of pathological prion protein as a determining factor of strain-specific prion replication dynamics. PLoS Pathog. 2013; 9(10):e1003702. https://doi.org/10.1371/journal.ppat.1003702 PMID: 24130496; PubMed Central PMCID: PMC3795044.

70. Katorcha E, Makarava N, Savtchenko R, D'Azzo A, Baskakov IV. Sialylation of prion protein controls the rate of prion amplification, the cross-species barrier, the ratio of PrPSc glycoform and prion infectivity. PLoS Pathog. 2014; 10(9):e1004366. https://doi.org/10.1371/journal.ppat.1004366 PMID: 25211026; PubMed Central PMCID: PMC4161476.

71. Fernandez-Borges N, Erana H, Elezgarai SR, Harrathi C, Venegas V, Castilla J. A Quick Method to Evaluate the Effect of the Amino Acid Sequence in the Misfolding Proneness of the Prion Protein. Methods Mol Biol. 2017; 1658:205–16. https://doi.org/10.1007/978-1-4939-7244-9_15 PMID: 28861792.

72. Erana H, Fernandez-Borges N, Elezgarai SR, Harrathi C, Charco JM, Chianini F, et al. In Vitro Approach To Identify Key Amino Acids in Low Susceptibility of Rabbit Prion Protein to Misfolding. J Virol. 2017; 91(24). https://doi.org/10.1128/JVI.01543-17 PMID: 28978705; PubMed Central PMCID: PMC5709604.

73. Otero A, Hedman C, Fernandez-Borges N, Erana H, Marin B, Monzon M, et al. A Single Amino Acid Substitution, Found in Mammals with Low Susceptibility to Prion Diseases, Delays Propagation of Two

Prion Strains in Highly Susceptible Transgenic Mouse Models. Mol Neurobiol. 2019. https://doi.org/10.1007/s12035-019-1535-0 PMID: 30847740.

74. Castilla J, Saa P, Hetz C, Soto C. In vitro generation of infectious scrapie prions. Cell. 2005; 121 (2):195–206. Epub 2005/04/27. S0092-8674(05)00156-X [pii] https://doi.org/10.1016/j.cell.2005.02.011 PMID: 15851027.

75. Saa P, Castilla J, Soto C. Ultra-efficient replication of infectious prions by automated protein misfolding cyclic amplification. J Biol Chem. 2006; 281(46):35245–52. Epub 2006/09/20. M603964200 [pii] https://doi.org/10.1074/jbc.M603964200 PMID: 16982620.

76. Saborio GP, Permanne B, Soto C. Sensitive detection of pathological prion protein by cyclic amplification of protein misfolding. Nature. 2001; 411(6839):810–3. Epub 2001/07/19. https://doi.org/10.1038/35081095 PMID: 11459061.

77. Fernandez-Borges N, de Castro J, Castilla J. In vitro studies of the transmission barrier. Prion. 2009; 3 (4):220–3. Epub 2009/12/17. 10500 [pii]. https://doi.org/10.4161/pri.3.4.10500 PMID: 20009509; PubMed Central PMCID: PMC2807695.

78. Harrathi C, Fernandez-Borges N, Erana H, Elezgarai SR, Venegas V, Charco JM, et al. Insights into the Bidirectional Properties of the Sheep-Deer Prion Transmission Barrier. Mol Neurobiol. 2018. https://doi.org/10.1007/s12035-018-1443-8 PMID: 30592012.

79. Bocharova OV, Breydo L, Parfenov AS, Salnikov VV, Baskakov IV. In vitro conversion of full-length mammalian prion protein produces amyloid form with physical properties of PrP(Sc). J Mol Biol. 2005; 346(2):645–59. Epub 2005/01/27. S0022-2836(04)01539-6 [pii] https://doi.org/10.1016/j.jmb.2004.11.068 PMID: 15670611.

80. Nonno R, Di Bari MA, Cardone F, Vaccari G, Fazzi P, Dell'Omo G, et al. Efficient transmission and characterization of Creutzfeldt-Jakob disease strains in bank voles. PLoS Pathog. 2006; 2(2):e12. Epub 2006/03/07. https://doi.org/10.1371/journal.ppat.0020012 PMID: 16518470; PubMed Central PMCID: PMC1383487.

81. Pirisinu L, Marcon S, Di Bari MA, D'Agostino C, Agrimi U, Nonno R. Biochemical characterization of prion strains in bank voles. Pathogens. 2013; 2(3):446–56. https://doi.org/10.3390/pathogens2030446 PMID: 25437201; PubMed Central PMCID: PMC4235696.

82. Muller H, Brener O, Andreoletti O, Piechatzek T, Willbold D, Legname G, et al. Progress towards structural understanding of infectious sheep PrP-amyloid. Prion. 2014; 8(5):344–58. https://doi.org/10.4161/19336896.2014.983754 PMID: 25482596; PubMed Central PMCID: PMC4601355.

83. Fung BM, Kithrin AK, Ermolaev K. An improved broadband decoupling sequence for liquid crystals and solids. Journal of Magnetic Resonance. 2000; 142(1):97–101. https://doi.org/10.1006/jmre.1999.1896 PMID: 10617439

84. Gonzalez-Montalban N, Makarava N, Ostapchenko VG, Savtchenk R, Alexeeva I, Rohwer RG, et al. Highly efficient protein misfolding cyclic amplification. PLoS Pathog. 2011; 7(2):e1001277. Epub 2011/02/25. https://doi.org/10.1371/journal.ppat.1001277 PMID: 21347353; PubMed Central PMCID: PMC3037363.

85. Johnson CJ, Aiken JM, McKenzie D, Samuel MD, Pedersen JA. Highly efficient amplification of chronic wasting disease agent by protein misfolding cyclic amplification with beads (PMCAb). PLoS One. 2012; 7(4):e35383. Epub 2012/04/20. https://doi.org/10.1371/journal.pone.0035383 PMID: 22514738; PubMed Central PMCID: PMC3325955.
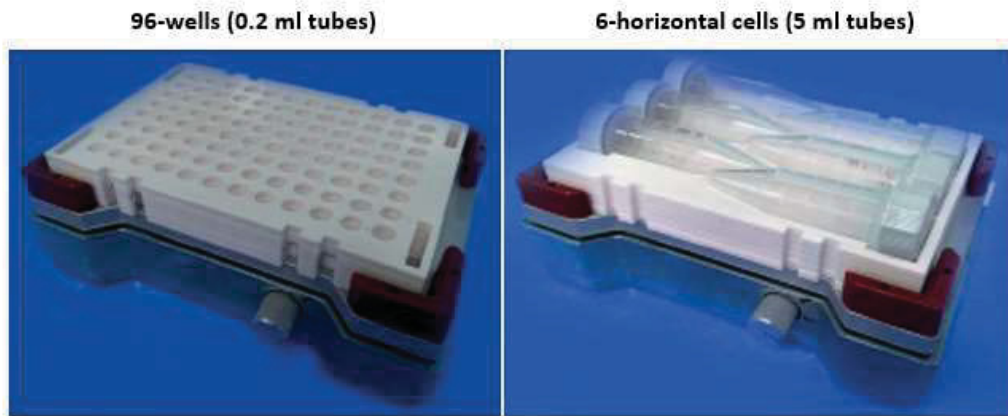
Fig. S1. Shaking system and *ad hoc* designed racks for different tube sizes. Photograph on the left shows the rack designed with 96 wells for 0.2 ml PCR tubes on the shaker used for PMSA reactions. The photograph on the right shows the rack with 6 horizontal cells for 5 ml tubes suitable for the same shaker. Both racks were designed *ad hoc* and 3D-printed (I+3D). Racks for any desired tube can be designed and printed making PMSA a highly versatile method for misfolded protein production.
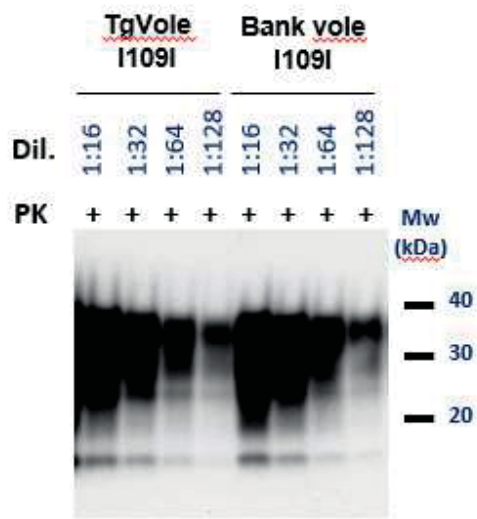
Fig. S2. PrP expression levels in TgVole (1x) animals compared to PrP expression levels of bank vole I109 by Western blot. 10% brain homogenates from TgVole (1x) (I109I) mouse and bank vole 109I were diluted 1:16, 1:32, 1:64 and 1:128 and analyzed by Western blot using monoclonal antibody D18 (1:5,000). The PrP expression levels of TgVole (1x) were equal to PrP^C levels in bank vole brain based on signal intensity. No significant differences were observed in the electrophoretic migration patterns. Mw: Molecular weight.

Fig. S3. Sedimentation velocity analysis of L-seeded-PMSA by ultracentrifugation through a continuous sucrose gradient. Proteinase K-digested and undigested L-seeded-PMSA were subjected to ultracentrifugation at ~200,000 g through a continuous sucrose gradient ranging from 10 to 80 % (w/v) with 0.2 % sarkosyl to determine the size distribution of total PrP and PrP^{res} assemblies by Western blot. The equivalent of 2 μl of each fraction of the gradient were loaded for the undigested sample, while for PK-digested sample, fractions were precipitated with methanol loading the equivalent to 60 μl, thus PK-digested gel shows 30-fold higher sample amount than the gel of undigested fractions. Briefly, the sedimentation pattern shows total absence of monomeric PrP in the top fractions and a continuum in the aggregate size from fractions containing around 30 % to 80 % sucrose for the untreated sample and from around 40 % to 80 % sucrose for the PK-digested sample, suggesting predominance of large PK-resistant assemblies in the sample. This indicates the presence of a heterogeneous size assemblies but does not reveal clearly different majoritarian populations that could point towards the existence of distinct assembly types regarding tertiary structure. Developed with Saf83 mAb (1:400). PK: Proteinase K, MW; molecular weight marker.

S1 Table. L-seeded-PMSA protease K-resistant fragments identified by ESI-TOF.

Experimental mass	Sequence	Theoretical mass
9435.13	N153-S231	9436.44
9321.03	M154-S231	9322.34
9451.43	N153-S231 (MetSO)[1]	(+16)
9337.81	M154-S231 (MetSO)	(+16)
	[1]	
6105.20	N97-E152	6106.93
	Q98-N153	6106.93
6219.46	N97-N153	6221.03
6088.28	N97-E152 (N-terminal aspartic succinimide)[2]	(-17)
	Q98-N153 (N-terminal pyroglutamic acid)[2]	(-17)
5991.26	N97-E153	5995.83
5974.18	N97-N153 (N-terminal pyroaspartate)[1]	(-17)

[1] Oxidation of Met to methionine sulfoxide (MetSO).
[2] https://abrf.org/delta-mass
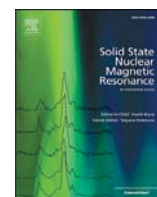
Hyperpolarized MAS NMR of unfolded and misfolded proteins

Anna König [a,b], Daniel Schölzel [a,b], Boran Uluca [a,b], Thibault Viennet [a,b], Ümit Akbey [a,b], Henrike Heise [a,b,*]

[a] *Institute of Complex Systems, Structural Biochemistry (ICS-6), Research Center Jülich, 52425, Jülich, Germany*
[b] *Institute of Physical Biology, Heinrich-Heine-University Düsseldorf, Universitätsstraße 1, 40225, Düsseldorf, Germany*

ARTICLE INFO

ABSTRACT

In this article we give an overview over the use of DNP-enhanced solid-state NMR spectroscopy for the investigation of unfolded, disordered and misfolded proteins. We first provide an overview over studies in which DNP spectroscopy has successfully been applied for the structural investigation of well-folded amyloid fibrils formed by short peptides as well as full-length proteins. Sample cooling to cryogenic temperatures often leads to severe line broadening of resonance signals and thus a loss in resolution. However, inhomogeneous line broadening at low temperatures provides valuable information about residual dynamics and flexibility in proteins, and, in combination with appropriate selective isotope labeling techniques, inhomogeneous linewidths in disordered proteins or protein regions may be exploited for evaluation of conformational ensembles. In the last paragraph we highlight some recent studies where DNP-enhanced MAS-NMR-spectroscopy was applied to the study of disordered proteins/protein regions and inhomogeneous sample preparations.

1. Introduction

The "native fold" of every protein which is invariably determined by its primary sequence has been a central paradigm of structural biology. However, this notion has lost its unrestricted validity by the notion that (i) a large class of proteins, the intrinsically disordered proteins (IDPs) do not possess one stable globular fold but exhibit many local minima and thus are highly flexible [1] and (ii) by the fact that most proteins are able to adopt alternative "misfolded" β-sheet rich conformations which all share a common structural cross-β motif [2].

Intrinsically disordered proteins are characterized by their high degree of conformational freedom which is due to a rather flat free energy landscape, comprising low energy barriers and many local minima. These allow IDPs to fluctuate rapidly over an ensemble of conformations in solution, instead of adopting a well-defined three-dimensional structure. Essential biological processes rely on IDPs, e.g. molecular recognition between kinases and substrates, transcription factors and effectors, etc. IDPs make up to 33% of eukaryotic proteins [3]; furthermore, many well-folded proteins in their native structure contain intrinsically disordered or highly flexible parts or domains in addition to the well-folded domains. The function of an IDP is thus not linked to one globular structure, but rather to a full ensemble of conformations, and a lot of effort has been made in trying to elucidate structural ensembles of IDPs

[1,3,4].

Amyloid fibrils are involved in a large number of (neuro)degenerative diseases, such as Parkinson's disease, Alzheimer's disease and type-II diabetes. The misfolding of intrinsically disordered or globular proteins finally leads to the deposition of insoluble protein plaques which mainly consist of long, unbranched amyloid fibrils. Amyloid fibrils share certain structural features irrespective of their primary sequence. However, details of the amino acid residues involved in the cross-β-core region, the relative arrangement and registry of β-strands as well as the supramolecular and the macroscopic arrangement are not only determined by the amino acid sequence, but also depend critically on the exact fibrillation conditions. Thus, amyloid fibrils often exhibit a high degree of structural polymorphism. The central structural motif of amyloid fibrils is a cross β-pattern with β-strands perpendicular to the fiber axis. Intermolecular hydrogen bonds as well as hydrophobic and polar interactions between the amino acid side chains contribute to the high stability and robustness of amyloid fibrils. Amyloid formation occurs not only in protein misfolding diseases; indeed, amyloid fibers in bacteria, fungi, insects, invertebrates and humans also play functional roles (i.e. functional amyloids) [5]. Prominent examples of functional amyloids are yeast prions like HET-s, Ure2p and Sup35p, which are involved in horizontal gene transfer, as well as curli or TasA proteins, which stabilize the extracellular matrix of bacterial biofilms [6].

---

* Corresponding author. Institute of Complex Systems, Structural Biochemistry (ICS-6), Research Center Jülich, 52425, Jülich, Germany.
E-mail address: h.heise@fz-juelich.de (H. Heise).

The structural characterization of disordered and misfolded proteins is of paramount importance; however, both types of proteins pose a challenge on classical structural biology. The preferred technique for protein structure determination, X-ray crystallography, provides information about well-defined crystalline proteins, and flexible or disordered domains are invisible. Solution NMR spectroscopy on the other hand can only be applied to rather small (<100 kDa) proteins or complexes and is therefore not applicable for larger protein assemblies such as oligomers and protein aggregates. For IDPs, the structural characterization is even more complex, as not only one well-defined conformation, but rather a full conformational ensemble has to be determined. Chemical shifts and residual dipolar couplings in NMR are sensitive to conformational sampling. However, the exact observation of the conformational ensemble is prevented by rapid conformational averaging on the NMR time scale, and conformational distributions in many cases can be detected only indirectly. Nevertheless, it has recently been shown that solution NMR in combination with molecular dynamics simulations can be useful for the study of conformational ensembles of proteins [4].

Solid-state NMR-spectroscopy has lately proven its potential for structural characterization and even high-resolution structure determination of amyloid fibrils and other highly ordered multimeric protein assemblies (for recent reviews see Refs. [7–11], for some selected recent illustrative examples, see Refs. [12–16]). Very recent improvements in resolution obtainable by cryo electron microscopy (cryoEM) have enabled this method for structure determination in non-crystalline ordered protein assemblies, and first amyloid structures have been determined with the help of cryoEM (for selected examples, see Refs. [17–19]), thus improving our understanding of amyloid structures. In disordered or heterogeneous systems, NMR resonance assignment and unambiguous determination of structural constraints may be compromised by inhomogeneous line broadening. Solid-state NMR-spectroscopy at cryogenic temperatures – with or without DNP-enhancement – has been demonstrated to be a viable alternative for the study of intrinsically unfolded proteins or of protein preparations with high degree of conformational heterogeneity: At cryogenic temperatures, residual conformational averaging is prevented and different conformations are frozen out on the NMR timescale [20–22], and as a consequence, resonance lines are broadened [23,24]. However, these inhomogeneously broadened line-shapes contain information about the full conformational ensemble, which can be retrieved if the spectral overlap is reduced by adequate sparse isotope labeling techniques. The protein concentration in frozen solutions is often low, and sensitivity may further be compromised by the line broadening. Low sensitivity due to limited protein concentrations however can nowadays conveniently be overcome by dynamic nuclear polarization (DNP); thus, DNP-enhanced solid-state NMR-spectroscopy is becoming a viable tool to study not only well-ordered systems but also molecular assemblies with a high degree of structural disorder.

In the following article, we will first give a brief historical overview over DNP with a focus on biological applications. For more comprehensive reviews on DNP-enhanced biomolecular solid-state NMR-spectroscopy the reader is referred to the following recent excellent reviews [25–30]. In the second paragraph we will present a selection of examples where DNP-enhanced solid-state NMR-spectroscopy has successfully been applied to investigate well-ordered amyloid fibrils. We limit our overview to amyloid fibrils, but also other multimeric assemblies like intact viruses or capsids [31–33], bacterial secretion systems [34,35] or cell walls [36] have been studied by DNP-enhanced NMR-spectroscopy. For an excellent overview over these studies the reader is referred to a recent review by Jaudzems et al. [30].

In the last paragraph, we give an overview over studies where DNP-enhanced solid-state NMR-spectroscopy has been applied to the study of intrinsically disordered proteins or flexible regions of globular proteins or protein complexes as well as oligomers.

2. Historical overview

The phenomenon of Dynamic Nuclear Polarization (DNP) was first proposed theoretically by Overhauser in 1953 [37,38] and shortly after proved experimentally by Carver and Slichter in metallic Lithium. The general concept of DNP is the transfer of polarization from electrons to nuclei [39]. The originally proposed so-called Overhauser effect is based on T_1 cross-relaxation in a system of dipolar coupled electron-nuclear spins. It was then followed by the conceptual development of other DNP mechanisms: the solid effect by Ferries [40], the cross effect (CE) by Hwang and Hill [41,42], and the thermal mixing effect by Borghini [43]. These different DNP polarization mechanisms mainly depend on paramagnetic resonance properties of the electrons (EPR line-shape) and its magnitude relative to the nuclear Larmor frequency (ω_n) and matching conditions with the nuclei to be polarized (see Table 1).

In an ideal case, the exchange of magnetization between electrons and nuclei is proportional to the ratio of their energy population differences and thus to their gyromagnetic ratios. Therefore, the theoretical maximum enhancement or increase in nuclear magnetization is $|\gamma_e/\gamma_H|$ = 657 for ^1H and $|\gamma_e/\gamma_C|$ = 2615 for ^{13}C. In reality, however, the efficiency of the polarization transfer depends strongly on the T_1 relaxation time of the electron spins. For this reason, DNP is inefficient at high temperatures when fast tumbling rates lead to short electron T_1 relaxation times [44]. Moreover, successful saturation of the electron transition (in the microwave frequency range) is normally required in order to favor the transfer of magnetization from electron to nuclei. All these have three implications: (i) for efficient DNP the samples have to be cooled down to very low temperatures (usually around 100 K), (ii) frozen samples do not tumble and thus use of solid-state NMR is required and (iii) microwave irradiation has to reach the sample requiring special instrumentation [45].

It was more than 40 years later that the concept could be successfully applied to biomolecules after pioneering work of Griffin and coworkers [46–50]. Especially, this was due to the development of stable high frequency microwave sources (gyrotron) delivering resonant microwaves to the high field NMR spectrometers. Notably, this enabled investigation of the photocycle of the protein bacteriorhodopsin [51,52]. The increased sensitivity as well as the fact that the ^{15}N Schiff-base signal of a lysine residue (covalently bound to the retinal cofactor) is well isolated in chemical shift allowed its characterization.

A critical aspect of conducting DNP-enhanced NMR experiments is the choice of adequate polarization sources containing unpaired electrons, like stable organic radicals or transition metal complexes. For most biological applications nitroxide-based (i.e. TEMPO) radicals are used because of their good solubility and stability. For polarization enhancement via the cross effect, biradicals carrying two unpaired electrons of favorable properties have been shown to be very efficient. The TEMPO-based biradical TOTAPOL [53] has long been the compound of choice for cross effect DNP, now succeeded by the better performing AMUPol [54] with an increased longitudinal relaxation time of the electrons. As the EPR linewidth increases linearly with the magnetic field, the enhancement factor obtainable by CE DNP scales inversely with B_0. Therefore, mixed biradicals consisting of a nitroxide moiety with a large g-factor anisotropy and a trityl or BDPA radical with an almost isotropic g-factor are advantageous for CE DNP at high magnetic fields above 14 T [55–57]. Likewise, computationally designed asymmetric bis-nitroxides with large exchange interactions between the electrons where a parallel orientation of the nitroxide units is avoided, have been proven to favor efficient MAS DNP, and also polarizing agents containing two high-spin transition metal complexes are promising candidates for DNP-enhancement [58]. At magnetic fields above 14 T in combination with fast MAS rates, the solid Overhauser effect may become an attractive alternative to CE DNP [59–61]. This solid Overhauser effect is particularly effective at high magnetic fields for narrow line radicals with strong hyperfine interactions, like BDPA.

Another critical point is sample preparation. The radicals used, their

Table 1

Summary of DNP mechanisms' characteristics under MAS conditions (ω_{MW}, frequency of microwave irradiation; ω_e, electron Larmor frequency; ω_n, nuclear Larmor frequency; δ, electron transition homogeneous line broadening; Δ, electron transition inhomogeneous line broadening; d_{ee}, electron-electron distance; θ_{ee}, electron-electron angle, D_{ee}, electron-electron dipolar coupling constant).

Mechanism	Condition	Field dependence	Microwave requirement	Radical properties
Solid Overhauser effect	$\omega_{MW} = \omega_e$	Scales with B_0	Lower power $< 2\,W$	Narrow EPR linewidth, strong hyperfine couplings Short T_{1e}
Solid effect	$\omega_n > \delta, \Delta$ $\omega_{MW} = \omega_e \pm \omega_n$	Scales with B_0^{-2}	Higher power	Narrow EPR line width
Cross effect	$\delta < \omega_n < \Delta$ $\omega_{e1} - \omega_{e2} = \omega_n$	Scales with B_0^{-1}	$\omega_{MW} = \omega_e$ Lower power	Broad EPR linewidth, biradical with fixed d_{ee} and θ_{ee}
Thermal mixing	$\omega_n < \delta$	Scales with B_0^{-1}	$\omega_{MW} = \omega_e$ Lower power	Broad EPR line High radical concentration or large D_{ee}

concentration and their localization throughout the sample are important factors. Optimization of these parameters is a sample dependent procedure and needs to be done individually. While conventional radicals are dissolved in the solvent together with the sample to obtain a statistical distribution and homogeneous hyperpolarization throughout the sample, other approaches using localized [62–65], covalently bound [66–70] or targeted [71,72] radicals are also possible. This presents several advantages such as better handling of paramagnetic relaxation enhancement (PRE) effects resulting from interactions with the unpaired electrons and access to specific information, and it is an interesting approach for the study of proteins in their native environments. Also, as phase separation and clustering of radicals, which may occur during ice crystal formation of water, is avoided, using cryoprotectants like glycerol is not always necessary (e.g. in presence of lipids). Particularly in the case of liposome-reconstituted membrane proteins, matrix-free sample preparation (i.e. a sample preparation in which the use of solvents is not necessary to enable a uniform distributions of polarizing agents) has proven to yield better relaxation properties leading to better signal per unit time [70,73]. Alternatively, sedimentation of proteins in the presence of free radicals leads to the formation of a glassy matrix at low temperatures and is thus an interesting alternative approach for sample preparation without the need for cryoprotectants [74,75]. Note that more or less specific interactions of globular proteins [65,75] and amyloid fibrils [76] with radicals have been shown. Thus, care has to be taken when sensitivity or resolution is compared between samples or regions of a sample.

One main advantage of DNP is its ability to enhance signals which would otherwise lie below the detection limit. The sensitivity enhancement can be attributed to the lowered temperature, causing a favorable Boltzmann distribution, and the microwave mediated polarization transfer from electrons to the nuclei. However, although the sensitivity might be vastly enhanced, the resolution is often drastically diminished under DNP conditions: Caused by the low temperatures, conformational averaging is mostly prevented, and water molecules are not uniformly distributed anymore. Furthermore, homogeneous line broadening due to paramagnetic relaxation enhancement and insufficient proton decoupling adds to the linewidth, a contribution which is particularly pronounced at low magnetic fields and moderate spinning speeds [33]. For uniformly isotope labeled samples the resolution after freezing may therefore not be sufficient. This can be counterbalanced by segmental and/or site-specific, amino-acid specific or sparse isotope labeling to reduce spectral crowding. As an example, in Fig. 1 two homonuclear ^{13}C,^{13}C correlation DNP spectra of globular 117-residue protein at a temperature of 110 K are displayed. While for the uniformly ^{13}C-labeled sample most resonances are overlapped so strongly that even a discrimination of signals from different amino acids is not possible anymore, in a spectrum of a protein uniformly ^{13}C labeled only for Isoleucine, different cross-correlation peaks can clearly be identified.

3. DNP-enhanced MAS NMR of amyloid fibrils

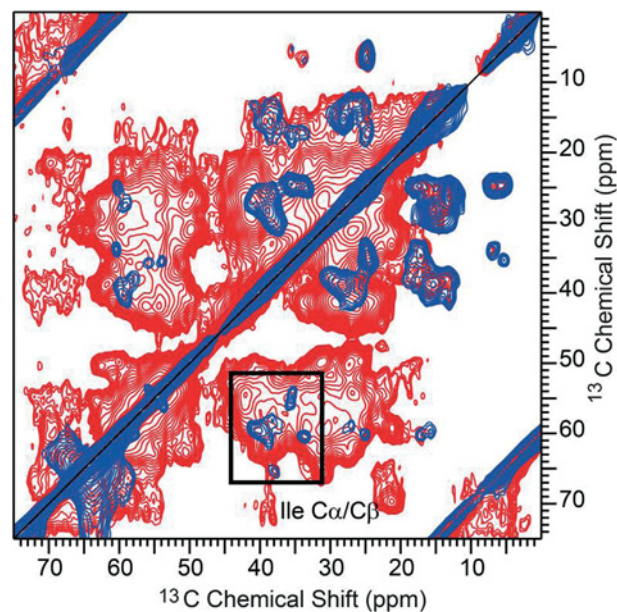Amyloid fibrils, despite being the end product of protein misfolding

Fig. 1. Effect of amino acid-selective isotope labeling: Homonuclear 2D ^{13}C,^{13}C correlation spectra (acquired with proton driven spin diffusion with a mixing time of 10 ms at a field strength of 14.1 T with a spinning frequency of 9 kHz) of the 117-residue protein GABARAP in frozen solution. In the spectrum of the uniformly ^{13}C-labeled protein (red), signal crowding prevents the assignment of individual cross-peaks, whereas in the spectrum of the sample in which only the seven Isoleucine residues are uniformly ^{13}C labeled (blue), individual cross-correlation signals can be identified.

and despite being prone to polymorphism, are often remarkably well-ordered. Valuable information about structural organization of amyloid fibrils has been obtained by conventional solid-state MAS NMR-spectroscopy [7–11]. In favorable cases full 3D structures were determined by solid-state NMR-spectroscopy and – very recently – also by cryo-EM [12–17,19]. In the following section we will focus on studies involving DNP-enhanced NMR-spectroscopy.

Many small peptide fragments of large amyloidogenic proteins are able to form amyloid fibrils. Although secondary structure elements as well as supramolecular structures of such peptide fibrils usually differ substantially from those of fibrils from full-length proteins, peptide fibrils are still valuable model systems enlightening fundamental principles of amyloid formation. One major advantage of chemically synthesized peptides over recombinantly expressed proteins for structure determination is the possibility to introduce isotope labels at any desired position in a site-selective manner.

One of the shortest fibril forming peptides is the seven amino acid residues segment GNNQQNY corresponding to amino acid residues 7 to

13 of the yeast prion Sup35p (vide infra) [77,78]. This peptide can not only form amyloid fibrils, but it can also crystallize into monoclinic and orthorhombic nanocrystals suitable for high-resolution X-ray crystallography. Substantial differences between nanocrystals and fibrils have been identified by solid-state NMR-spectroscopy [78]. Monoclinic crystals of this peptide were used as model systems to study the polarization transfer mechanism between solvent and sample. The tight packing of the peptide molecules within the crystal lattice excludes the bulky TOTAPOL biradicals from the sample. Thus, polarization enhancement of the peptide relies on ^{1}H polarization transfer by ^{1}H-^{1}H spin diffusion across the interface between the glassy solvent matrix and the sample [79]. Despite the rather large crystal dimensions of ~100–200 nm, an enhancement factor corresponding to 75% of the enhancement factor obtained for the solvent matrix was observed, suggesting that nanocrystals with a size of up to 1 μm can be efficiently hyperpolarized by DNP.

The correlation between sample dimensions and DNP-enhancement was further investigated by a comparison of enhancement factors obtained for fibril and crystal samples [80](*). Although the radical concentration in the fibril sample was substantially lower than in the crystal sample, polarization transfer by proton-driven spin diffusion was more efficient for the fibril. Since the rather thin fibrils with a diameter of a few nanometers facilitate closer contacts to the paramagnetic centers, polarization build-up was twice as fast as for the thicker crystals. At low temperatures, longitudinal mixing and build-up rates are enhanced, because dynamics are severely restricted resulting in greater efficiency for dipolar transfers. For fibrils, no significant chemical shift changes between high and low-temperature spectra were observed, while in monoclinic crystals sample freezing resulted in shift changes of up to 1.5 ppm for ^{13}C and 5 ppm for ^{15}N resonances, as well as to severe line broadening. Residues in close contact with water are most affected by shift changes and inhomogeneous line broadening.

A similar study focused on the complete architecture of an amyloid fibril formed by an 11 amino acid residue peptide segment of the transthyretin protein (TTR (105–115)) [81](*) [82]. The 3D structure of the peptides within the fibrils had been determined previously with high resolution by room temperature solid-state NMR-spectroscopy, demonstrating that the full peptide adopts an extended β-strand conformation [83,84]. With the help of DNP-enhanced solid-state NMR spectroscopy, intermolecular as well as intra- and inter-sheet contacts could be obtained on a set of ten different site-selectively isotope labeled samples in a fraction of the conventional measurement time (see Fig. 2 A). In detail, it could be shown that the fibrils are constructed by parallel in-register β-sheets. Furthermore, distance measurements between adjacent β-sheets indicated an anti-parallel arrangement of the sheets within the protofilaments in which odd-numbered side chains from peptides of one β-sheet are packed against even-numbered side chains from the other β-sheet. Thus, peptides in the two β-sheets are not equivalent, a fact which leads to resonance doubling in the NMR spectra. Supporting cryo-EM measurements identified three classes of fibrils consisting of four, six or eight protofilaments (Fig. 2B–D) [82]. Protofilament-to-protofilament contacts were shown to be organized in a head-to-tail fashion by distance measurements between single labels positioned at the N- and the C-terminus of the peptides.

DNP-enhanced solid-state NMR-spectroscopy was also successfully applied to determine the supramolecular arrangement in amyloid fibrils from larger proteins. In contrast to short model peptides which can conveniently be obtained by solid-phase synthesis, proteins with more than 40 to 50 residues usually are expressed recombinantly from *E. coli*, and thus different isotope labeling strategies are necessary to elucidate the supramolecular arrangement (which requires the measurement of long-distance restraints). In uniformly [^{13}C,^{15}N] labeled samples, the acquisition of these restraints is hampered by dipolar truncation effects. To overcome this problem, sparse or differential labeling as achieved e.g. by using 2-^{13}C glucose as sole carbon source in combination with DNP can be an appropriate choice: If fibrils are grown from a 1:1 mixture of sparsely [^{13}C,^{14}N] and [^{12}C,^{15}N] labeled monomers, only intermolecular
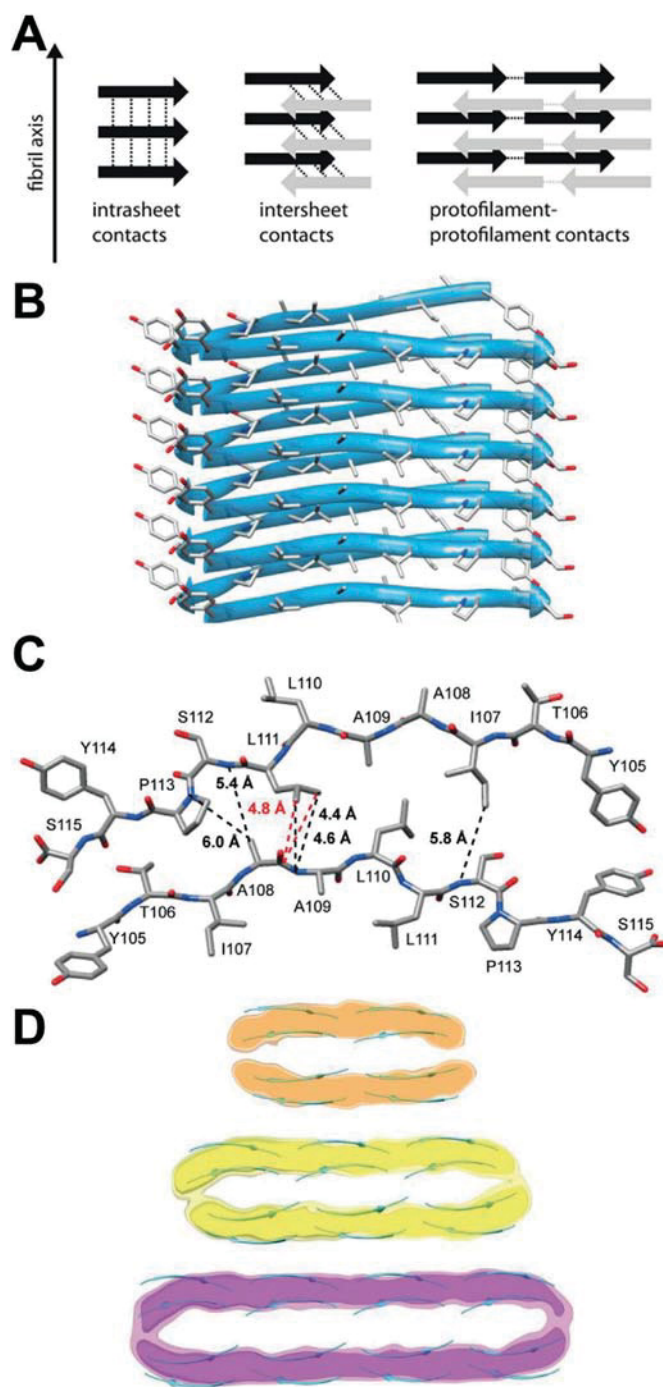
Fig. 2. A) Sketch of interstrand (intrasheet), intersheet and protofilament-to-protofilament contacts within amyloid fibrils. B) Side view and C) top view of one protofilament, composed of two TTR (105–115) peptide molecules. D) Three different fibril types composed of four, six and eight protofilaments, respectively. A-C) adapted with permission from Ref. [81], copyright (2013) American Chemical Society. D) adapted with permission from Ref. [82], copyright (2013) National Academy of Sciences.

contacts are detected in 2D ^{15}N/^{13}C correlation experiments, which in the case of in-register parallel arrangement of β-strands superimpose with intramolecular NCACX spectra of a uniformly labeled sample. For such experiments, signal enhancement by DNP, which boosts the sensitivity on lower gamma nuclei, is extremely helpful. Furthermore, local dynamics which at room temperature might attenuate the desired cross-peak intensities are frozen out at the low temperatures required for DNP, so long-

range polarization transfer efficiency is drastically improved.

This differential [^{13}C,^{15}N] isotope labeling approach has been successfully applied to confirm the parallel in-register alignment of β-strands in amyloid fibrils formed from an 86-residue protein, the PI3-SH3 domain, which is able to form highly ordered fibrils [85](*). Intermolecular N—C contacts in differentially [^{13}C,^{15}N] labeled fibrils were indicative of a parallel in-register alignment of the β-strands. Moreover, the parallel alignment was also corroborated from homonuclear long-range contacts from 2D ^{13}C/^{13}C correlation spectra of a sample sparsely ^{13}C labeled from 2-^{13}C-glucose. At long mixing times pseudo-intraresidual cross correlation signals between neighboring carbon atoms for which ^{13}C labeling occurs statistically, but for which simultaneous ^{13}C labeling within one amino acid residue is not possible, could be observed. This supports a structural alignment in which equivalent amino acid residues are in close proximity to each other.

Another challenging amyloid fibril studied by DNP-enhanced solid-state NMR spectroscopy is the yeast prion protein Sup35p [86], a translation termination factor with an N-terminal prion domain which is able to convert into a self-propagating amyloid form, which leads to sequestration of the protein together with a loss-of-function phenotype. The full-length protein has 684 amino acid residues and is composed of an N-terminal prion domain (called N) rich in uncharged polar residues N and Q, a C-terminal translation termination domain and a highly charged middle domain (M) which connects the latter and provides solubility. The 263 amino acids long fragment SupNM consisting of the N- and M-domain is sufficient to form amyloid fibrils that can transmit the prion phenotype to yeast colonies [87]. Fibrils of Sup35NM have been studied by various groups using solid-state NMR-spectroscopy, however, a converging structural model is still elusive due to the inherent propensity of Sup35p to form different polymorphs associated with different prion strains and also due to high conformational inhomogeneity [88–90]. The exact length and location of the amyloid core has been found to depend on the fibrillation temperature [89] or on the prion strain [90] and may also be influenced by the presence or absence of the C-terminal domain. Furthermore, a second putative amyloid core region has been identified in a single point mutant of Sup35NM [91]. Due to substantial inhomogeneous line broadening as well as considerable spectral overlap resulting from an unfavorable amino acid composition, site-selective resonance assignment was not possible for most of the resonances. Only 22 amino acid residues located N-terminal of position 30 gave rise to extremely well-resolved signals and could be sequentially assigned from 3D triple-resonance spectra [88]. However, signals from less ordered parts of the protein were also visible in the spectrum. Even if a resonance assignment was not possible, these signals could – in combination with site-selective isotope labeling and dedicated recoupling techniques – still be exploited to determine the supramolecular arrangement of these less structured protein regions: A large portion of the amino acids in the N-domain was found to be located in parallel in-register β-sheets [92], albeit less well-structured than the beginning of the N-terminus.

Frederick et al. applied DNP-enhanced solid-state NMR spectroscopy to further study Sup35NM fibrils in a cellular environment by using a cell lysate of yeast cells exhibiting the strong prion phenotype as fibrillation medium for recombinantly expressed [^{13}C,^{15}N], isotope labeled Sup35NM [93](*). In contrast to purified fibrils generated by seeded fibrillation in lysis buffer the fibrils obtained from cell lysates were found to have significantly higher β-sheet content. In particular, signals of residues which are exclusively located in the dynamically disordered M-domain were better defined in the lysate-grown fibrils, a fact which may be explained by specific interactions of this part of the protein with cellular components such as heat shock proteins. In a second study, Frederick et al. investigated the supramolecular arrangement of Sup35NM fibrils by combining sparse differential [^{15}N/^{13}C] labeling with segmental labeling. With the help of the split-intein technology, it was possible to express Sup35NM protein where only the first 14 residues are isotope labeled. Uniform [^{15}N/^{13}C] labeling of these 14 residues

enabled full sequential resonance assignment. Chemical shifts for the ^{7}GNNQQN^{13}Y fragment differ substantially from the corresponding shifts obtained in microcrystals as well as in all fibril types formed by this peptide fragment alone [78]. Thus, the conformation of this amino acid stretch in full-length fibrils clearly differs from that found in fibrils formed by the model peptide. To probe the supramolecular arrangement of the monomers, fibrils were also grown from a mixture of monomers with different isotope labeling: half of the monomers were uniformly [^{15}N] labeled, for the other half of the monomers, only the first 14 amino acid residues were sparsely [^{13}C] labeled [94](*). ^{15}N/^{13}C correlation spectra obtained with long TEDOR transfer did not superimpose with short range TEDOR spectra obtained on fibrils sparsely [^{13}C] and uniformly [^{15}N] labeled for these first 14 residues, a result which would be expected for parallel β-sheets with in-register alignment. This finding indicates that at least not all of the first 14 amino acid residues are part of an antiparallel β-sheet in the fibrils used for this study.

The impact of low temperatures on spectral resolution has been investigated without DNP-enhancement using amyloid fibrils of Aβ(1–40) [95] as well as of HET-s (218–289) [96] as model systems. For well-ordered Aβ(1–40) fibrils, the loss in resolution at low temperatures was moderate at a high static magnetic field of 20 T (corresponding to a proton Larmor frequency of 850 MHz), thus suggesting that conformational heterogeneity in this sample is not limiting the resolution [95]. A similar study, notably in absence of radicals and without the addition of the cryoprotectant glycerol, has been conducted on HET-s (218–289) fibrils at a magnetic field strength of 14.1 T (600 MHz proton Larmor frequency). 2D ^{13}C/^{13}C correlation spectra were acquired at different temperatures ranging from 100 to 280 K. The overall resolution of the ^{13}C NMR-spectra decreases gradually and monotonously with decreasing temperatures, similar as observed for a microcrystalline protein [97]. Resonances from residues in the well-structured hydrophobic core of the fibril are still reasonably resolved at low temperatures, whereas most hydrophilic amino acid residues pointing to the outside of the fibril were broadened beyond detectability upon freezing of the surrounding water shell.

In a similar way, amyloid fibrils formed by human islet amyloid polypeptide IAPP showed inhomogeneous line broadening at low temperatures. While the linewidth of most residues was affected by low temperatures, this effect was particularly pronounced for the seven N-terminal residues which form a loop bridged by a disulfide bond between Cys2 and Cys7 [98]. Signals from these residues were also broadened beyond detectability at low temperatures, an effect which may be attributed to increased intrinsic flexibility of this part of the peptide.

Finally, aggregates involved in bacterial virulence, such as curli (CsgA aggregates), may form amyloid fibrils as well. The biradical TOTAPOL shows a high binding affinity to the amyloid surface of CsgA fibrils, similar to the affinity of the fluorescent dye Thioflavin T (ThT) [76](*). Both molecules share a similar molecular framework and rotational symmetry, which allows them to bind to ridges formed by protruding side chains on the fibrillar surface. As a result, polarization is directly transferred via strong couplings between nitroxide radicals and the nuclear spins at the fibril surface. To achieve a balanced ratio between optimizing the sensitivity while avoiding paramagnetic relaxation enhancement and bleaching effects, the radical concentration has to be decreased (~400 fold), compared to commonly employed concentrations of around 10–20 mM.

In summary, with the help of DNP-enhanced solid-state NMR-spectroscopy valuable structural information on well-ordered protein assemblies may be obtained. Although cryogenic temperatures may cause line broadening and a decrease in resolution, the reduced mobility and increased signal-to noise ratio may enable the observation of several long-range contacts which are otherwise inaccessible by traditional solid-state NMR-spectroscopy. Further, residual line broadening at lower temperatures correlates well with residual flexibility and is thus another important source of information.

4. DNP-enhanced MAS NMR of disordered proteins

Besides the investigation of well-ordered systems with the help of (DNP-enhanced) solid-state NMR, solid-state NMR at cryogenic temperatures (with or without DNP-enhancement) is also a powerful method for obtaining information on disordered or heterogeneous systems, such as unstructured parts of bigger assemblies, intrinsically disordered proteins, or on heterogeneous systems like oligomers. At cryogenic temperatures, the full structural ensemble of an unfolded or partially folded protein is freeze-trapped, and thus the full conformational ensemble may be evaluated by solid-state NMR spectroscopy. The structural ensemble obtained by freeze trapping critically depends on the freezing conditions: if the cooling rate is slower than the time scale for structural rearrangements, the equilibrium conformational ensemble at the temperature of glass formation is obtained. Rapid freezing on time scales much faster than the time scale of conformational averaging on the other hand enables the trapping of transient intermediates and allows in principle to follow protein folding processes [99]. Further, to prevent cold denaturation by ice crystal formation, the addition of cryoprotectants is mandatory. While MAS NMR of frozen solutions at cryogenic temperatures is now possible, freeze-trapped preparation may also be lyophilized in order to stabilize the trapped ensemble state [100].

Chemical shifts in general and secondary chemical shifts of backbone atoms Cα and Cβ in particular are sensitive signatures of the protein conformation and the secondary structure. In principle, secondary structure elements reflect the backbone conformation of the protein, which can be represented as a pair of backbone torsion angles on the Ramachandran plot (Fig. 3A), and different regions of the Ramachandran plot give rise to distinct secondary chemical shifts [101]. In globular proteins with defined backbone fold, accurate predictions on secondary structure elements can be made based on secondary chemical shifts. In disordered proteins or protein regions, on the other hand, typical "random coil chemical shifts" are observed. These random coil shifts do not correspond to a defined "random coil backbone conformation" represented by a distinct area on the Ramachandran plot, but they are the result of rapid averaging over all energetically favored conformations (Fig. 3A and B). If the sample is frozen, all conformations sampled by the protein are present in the sample with their respective probability. As a consequence, every protein conformation gives rise to different chemical shifts, and the resonance lines are thus broadened (Fig. 3C). These inhomogeneously broadened line shapes can in principle be evaluated to obtain information on the relative contents of conformations typical for α-helical or β-sheet-like (extended) conformations [102–104].

Pioneering studies on protein folding of a 35 residue protein domain of the vilin headpiece by cryogenic solid-state NMR-spectroscopy have demonstrated the power of this method (reviewed in Ref. [20]). Equilibrium conformational ensembles of the chemically denatured ([102, 105]) protein domain could be quantified from studies of different site-selectively labeled peptides in frozen solution. Furthermore, rapid freezing from different temperatures above and below the thermal denaturation point allowed for the trapping of a transient folding intermediate [99] with secondary structure elements characteristic of the fully folded protein domain, but with a lower degree of sidechain order, which is an indication of a lack of tertiary structure in this intermediate.

The enhanced sensitivity of DNP makes it possible to study small peptides in large assemblies, which enables the investigation of proteins in environments similar to their natural environments. In this respect Lange et al. were able to study the disulfide oxidoreductase A (DsbA) secretion monitor (SecM) signaling peptide within the exit tunnel of the ribosome. To achieve this, the peptide was uniformly [^{13}C/^{15}N] labeled, whereas the ribosome was unlabeled. Additionally, in order to suppress natural abundance signals of unwanted species, 2D experiments were employed, because the probability of a cross peak of two correlating carbons is reduced by a factor of 100. Upon cooling to 105 K, the conformational states of DsbA-SecM have been studied, and in contrast to earlier studies, it has been shown that only a minor population of DsbA-
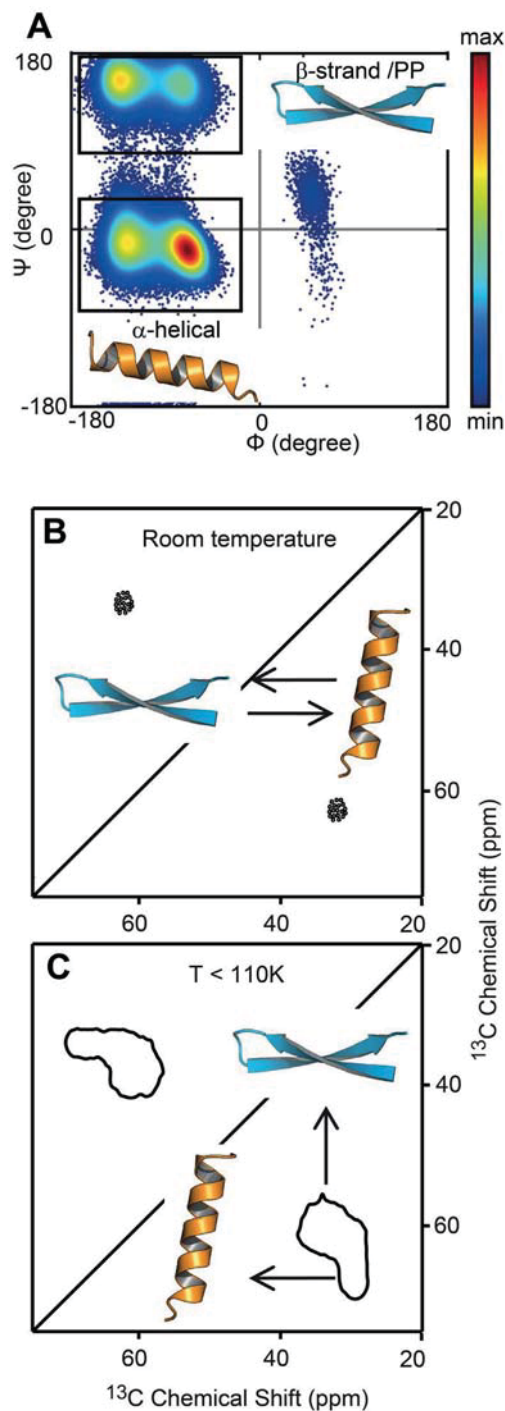

Fig. 3. A) Ramachandran plot displaying the probability distributions for backbone conformations of the residue Valine in an intrinsically disordered peptide. Regions for α-helical and β-strand/Polyproline conformations are indicated with boxes. B) Schematic representation of Cα/Cβ cross correlation peaks (for the amino acid Valine) with random coil chemical shifts in an intrinsically disordered protein. Random coil chemical shifts are averages caused by rapid transitions between α-helical and β-sheet like conformations. C) At low temperatures every molecule is frozen in a different conformation, and different backbone torsion angles in the conformational ensembles give rise to distinct chemical shifts, thus leading to inhomogeneous line broadening (see Ref. [104]). Adapted with permission from Ref. [104], copyright (2018) Elsevier.

SecM adopts an α-helical structure within the ribosome, thus demonstrating that protein folding may already occur during translation [106](*).

Another example for the use of DNP to enhance signals of small peptides in a larger assembly is PL12, a silaffin-derived pentalysine peptide, which catalyzes the silicic acid condensation in vitro. This peptide was embedded in silica to model the cell-wall. An interesting fact of this study is that neither the silica matrix nor the peptide was isotope labeled. Nevertheless, ^{13}C CP-spectra could be obtained at a temperature of 100 K within minutes without major loss of resolution and with an enhancement factor of 30. This shows the unique ability of DNP to study even unlabeled peptides in a larger assembly. With the help of 2D heteronuclear correlation and double-quantum-single-quantum correlation spectra a change in backbone conformation inside the silica in comparison to free PL12 in solution could be detected [107].

The power of DNP to decipher structurally well-ordered and intrinsically disordered parts of proteins was also demonstrated by Gupta et al. The study of tubular capsids of different HIV-1 protein assemblies at different field strengths and temperatures allowed the analysis of line broadening effects in DARR-spectra. With increasing field strength the resolution could be significantly improved, which demonstrates that line broadening in DNP-spectra is not exclusively caused by inhomogeneous line broadening but also contains homogeneous contributions (which can be counterbalanced by high field strengths). The highly dynamic and disordered spacer peptide 1 could be identified and distinguished from the conformational homogeneous capsid proteins at cryogenic temperatures. Decreasing the temperature from 180 K to 109 K did not lead to any further loss in resolution. Moreover, it was possible to assign aromatic side chains in the spectra obtained at cryogenic temperatures, a task which is generally challenging at room temperature [32](*).

The protein α-synuclein is a chimeric protein, because it can adopt different structures in different environments. It is natively unfolded and disordered, but in the progress of Parkinson's disease it forms fibrils with a β-sheet rich core structure, and upon membrane-association it becomes predominantly α-helical. Nevertheless, even in the structured forms some parts remain unstructured and flexible exhibiting random coil chemical shifts. We investigated the conformational ensembles sampled by this protein in different environments with the help of DNP-enhanced solid-state NMR-spectroscopy. In order to reduce spectral crowding, the protein was sparsely isotope labeled by using 2-^{13}C-glucose as main carbon source and supplying ten amino acids in natural abundance to the growth medium [108]. With this labeling scheme, simultaneous ^{13}C labeling for neighboring Cα and Cβ positions occurs only in Valine residues, such that Cα/Cβ cross correlation signal of Valine may be exploited as a reporter for secondary structure at the Valine positions. At cryogenic temperatures (such as needed for DNP) the Cα/Cβ cross peak of all 19 Valine residues present in the protein separates into specific amounts of α-helical and β-strand content (see Fig. 4 A). We could show that it is possible to obtain information on the conformational ensemble by analyzing the line shapes of the corresponding peaks. In fibrillar (Fig. 4B) α-synuclein, the β-sheet content is increased, but residual intensity at chemical shifts indicative of α-helical conformations suggests that not only the highly charged C-terminus but also the first ~38 N-terminal residues are disordered, a finding which is in agreement with current structural models [12,109]. We also investigated the secondary structure of α-synuclein in the presence of lipid bilayers. By using nanodiscs as membrane mimetics we were able to exactly control the ratio between α-synuclein monomers and membrane surface [110]. As expected, a large part of the α-synuclein protein adopted α-helical conformation upon contact with lipid bilayers. The exact amount of helical conformation, however, strongly depended on the protein-to-lipid ratio. We could quantify the extent of the unstructured regions in different membrane-bound forms by comparing intensities of different parts of the cross-peak to those of the monomeric form. Increasing protein-to-lipid ratios resulted in larger disordered fractions of the protein, a finding which was also supported by solution NMR [110]. Furthermore, we demonstrated that consecutive residues have a strong tendency to adopt the same secondary structure (Fig. 4A), a finding which may be indicative of formation of transient secondary structure elements even in the disordered form [104](*).
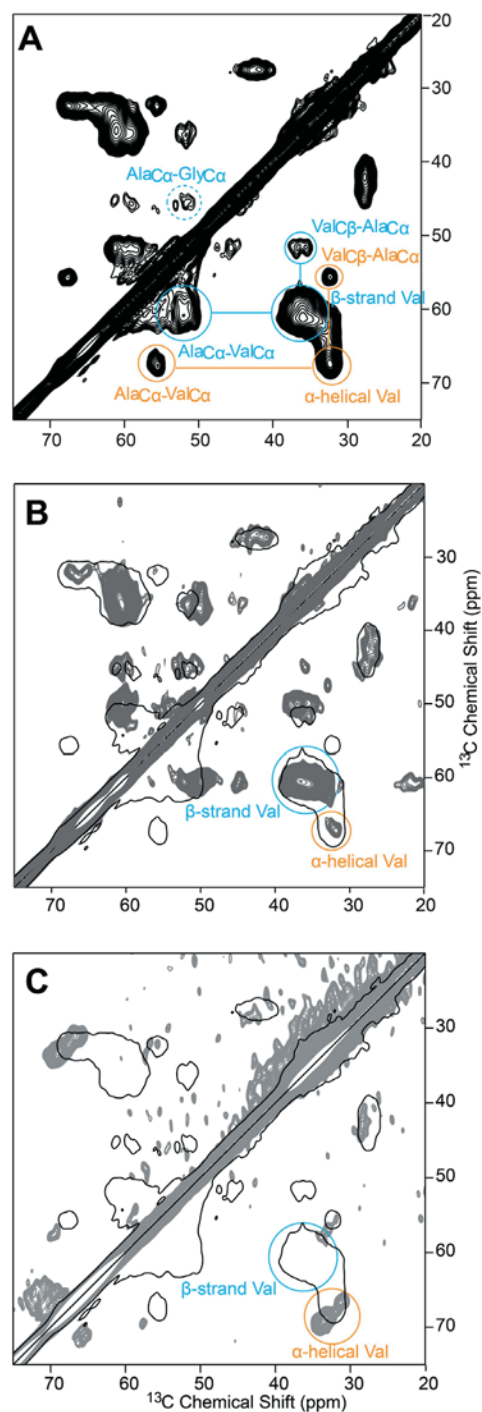
Fig. 4. 2D ^{13}C/^{13}C-correlation spectra (acquired with proton-driven spin-diffusion with a mixing time of 1 s, at a field strength of 14.1 T, with a spinning frequency of 9 kHz) of sparsely ^{13}C labeled α-synuclein in frozen solution in different environment. A) For disordered monomeric α-synuclein in a glycerol-water solution the Valine Cα/Cβ cross-correlation signal is largely inhomogeneously broadened, shift regions typical for α-helical as well as for β-strand like conformations are covered. Further, interresidual cross-correlation signals to neighboring Alanine residues are indicative of a correlation between similar conformations for neighboring residues. B) For a frozen suspension of fibrillar α-synuclein (grey spectrum) the β-sheet content is increased with respect to monomeric α-synuclein (black outline), whereas for α-synuclein in contact with lipid bilayers (C) only α-helical shifts are observed. Adapted with permission from Ref. [104], copyright (2018) Elsevier.

To our knowledge to date there is only one study on metastable, transient species using DNP. Potapov et al. measured DNP on different Aβ(1–40) species at different stages of the fibrillation pathway [111]. Samples were not lyophilized, but were measured in frozen solution. Thus the use of DNP was essential to obtain sufficient sensitivity. In total, four samples with different Aβ(1–40) species were investigated, the first containing primarily monomers, the second monomers and oligomers of different sizes and morphologies, the third metastable protofibrils and the fourth fibrils formed out of the protofibrils. With the help of 2D ^{13}C PDSD or DARR spectra extended β-sheet-like conformations could be identified in all samples, which are even predominant in the monomeric and oligomeric samples despite higher conformational disorder. Secondly, a close contact between F19 and L34 was observed in all four samples, indicating contacts between these two residues even before the development of structurally ordered assemblies. This contact is most pronounced in the protofibrils, which indicates a lower distance between F19 and L34 in protofibrils compared to fibrils. These findings reveal that the predominant molecular conformation is similar at all stages of fibrillation. Additionally, intermolecular ^{13}C spin polarization transfers between labeled carbonyl and aliphatic sites were measured. Aβ(1–40) protofibrils did not adopt an in-register, parallel β-sheet structure as in mature fibrils, i.e. Aβ(1–40) protofibrils are metastable 'off-pathway' intermediates with a more rapid nucleation [111](*).

Finally, the potential of DNP-enhanced solid-state NMR-spectroscopy has not only been applied to study disordered but isolated and purified proteins, but also to investigate proteins in their cellular environments, i.e. cell lysates [72,93,112–114] and whole cells [115–117]. For an extensive overview over the field of in-cell NMR-spectroscopy we refer to an excellent recent review by Luchinat and Banci [118] and limit ourselves here to highlighting one study in which localized DNP was used to site-selectively hyperpolarize the protein of interest [72](*). One of the main challenges of NMR-spectroscopy in cellular environments is the selective detection of NMR signals of the target protein in the presence of a large background of other cellular proteins and macromolecules. Most of the in-cell NMR studies solve this task either by injecting the fully [^{13}C,^{15}N] labeled target protein into cells grown in a growth medium with natural abundance isotope distribution or by overexpressing the target protein directly after adding isotope labeled precursors to the growth medium. Viennet et al. chose a different route to achieve selectivity by covalently attaching the biradical TOTAPOL to a binding partner of the target protein. With this approach it was possible to selectively hyperpolarize Bcl-x$_L$ in non-purified cell lysates, in which the target protein as well as the background were uniformly [^{13}C, ^{15}N] labeled. However, the approach required an almost 100% deuteration level of the background in order to prevent extensive loss of polarization into the solvent. Since no purification and isotope labeling steps are required, the benefits of this approach might be a reduction of workload, sample loss and amount of needed isotopes.

5. Outlook

In this contribution we have demonstrated the broad range of applicability of DNP-enhanced solid-state NMR-spectroscopy to the investigation of unfolded and misfolded proteins, and the large potential of this technique also for structural biology. Recent improvements as well as ongoing research will further increase the application range of this method.

One of the limitations of DNP so far has been the loss of enhancement when increasing external magnetic fields. Nevertheless, recent development of cross effect radicals with more robust relaxation properties (TEKPol series) [119] and design of Overhauser methodologies applicable to MAS-NMR [59–61,120] enabled DNP studies up to 800 MHz, a field strength at which a reasonable resolution may be obtained. One main issue remains, i.e. the inhomogeneous line broadening of samples at very low temperatures with different conformations frozen out. While the homogeneous contribution to line broadening is field independent

and as such can be counterbalanced by high magnetic fields, faster spinning rates and higher proton decoupling [33], the inhomogeneous contribution to the linewidth can mainly be overcome by increasing temperatures (shown as high-temperature DNP, [97]). This is of course possible but usually dramatic for the enhancement because electron longitudinal relaxation times become unfavorable for efficient DNP. Very recently, enhancements up to 15-fold at 200 K have been reported on biomolecules in conventional conditions using either deuterated proteins [121] or AMUPol/CD$_3$-TOTAPOL (note however that it is reported to be very sample-dependent) [122]. Homogeneous line broadening by paramagnetic relaxation enhancement on the other hand may successfully be reduced by decoupling of the electrons [123]. Furthermore, the application of pulsed microwave irradiation instead of continuous wave irradiation [124,125] may have significant advantages. For instance, very short hyperpolarization build-up times using electron spin-lock T$_{1\rho}$ build-up in the order of ns instead of the conventional T$_1$ build-up times of the order of seconds have been successfully carried out at 0.34 T (NOVEL experiment). Implementation of this at high fields would further push the limits of DNP-enhancement.

Acknowledgement

References

[1] P.E. Wright, H.J. Dyson, Intrinsically disordered proteins in cellular signalling and regulation, Nat. Rev. Mol. Cell Biol. 16 (1) (2015) 18–29.

[2] F. Chiti, C.M. Dobson, Protein misfolding, amyloid formation, and human disease: a summary of progress over the last decade, Annu. Rev. Biochem. 86 (1) (2017) 27–68.

[3] J.J. Ward, J.S. Sodhi, L.J. McGuffin, B.F. Buxton, D.T. Jones, Prediction and functional analysis of native disorder in proteins from the three kingdoms of life, J. Mol. Biol. 337 (3) (2004) 635–645.

[4] I.C. Felli, R. Pierattelli, Intrinsically Disordered Proteins Studied by NMR Spectroscopy, Springer, New York, 2015.

[5] D.M. Fowler, A.V. Koulov, W.E. Balch, J.W. Kelly, Functional amyloid - from bacteria to humans, Trends Biochem. Sci. 32 (5) (2007) 217–224.

[6] A. Diehl, Y. Roske, L. Ball, A. Chowdhury, M. Hiller, N. Molière, R. Kramer, D. Stöppler, C.L. Worth, B. Schlegel, M. Leidert, N. Cremer, N. Erdmann, D. Lopez, H. Stephanowitz, E. Krause, B.-J. van Rossum, P. Schmieder, U. Heinemann, K. Turgay, Ü. Akbey, H. Oschkinat, Structural changes of TasA in biofilm formation of *Bacillus subtilis*, Proc. Natl. Acad. Sci. Unit. States Am. 115 (13) (2018) 3237–3242.

[7] W. Hoyer, H. Heise, What does solid-state NMR tell us about amyloid structures? in: D. Otzen (Ed.), Amyloid Fibrils and Prefibrillar Aggregates Wiley-VCH Verlag GmbH & Co. KGaA, 2013, pp. 39–61.

[8] W. Hoyer, H. Shaykhalishahi, S. Ayalur-Karunakaran, H. Heise, Structural characterization of alpha-synuclein amyloids, in: The Prion Phenomena in Neurodegenerative Diseases: New Frontiers in Neuroscience, Nova Science Biomedical, 2015, pp. 111–128.

[9] R. Tycko, Molecular structure of aggregated amyloid-β: insights from solid state nuclear magnetic resonance, Cold Spring Harbor Perspect. Medi. 6 (8) (2016), https://doi.org/10.1101/cshperspect.a024083 a024083.

[10] B.H. Meier, R. Riek, A. Böckmann, Emerging structural understanding of amyloid fibrils by solid-state NMR, Trends Biochem. Sci. 42 (10) (2017) 777–787.

[11] P.C.A. van der Wel, Insights into protein misfolding and aggregation enabled by solid-state NMR spectroscopy, Solid State Nucl. Magn. Reson. 88 (Supplement C) (2017) 1–14.

[12] M.D. Tuttle, G. Comellas, A.J. Nieuwkoop, D.J. Covell, D.A. Berthold, K.D. Kloepper, J.M. Courtney, J.K. Kim, A.M. Barclay, A. Kendall, W. Wan, G. Stubbs, C.D. Schwieters, V.M.Y. Lee, J.M. George, C.M. Rienstra, Solid-state NMR structure of a pathogenic fibril of full-length human [alpha]-synuclein, Nat. Struct. Mol. Biol. 23 (5) (2016) 409–415.

[13] M.A. Wälti, F. Ravotti, H. Arai, C.G. Glabe, J.S. Wall, A. Böckmann, P. Güntert, B.H. Meier, R. Riek, Atomic-resolution structure of a disease-relevant Aβ(1–42) amyloid fibril, Proc. Natl. Acad. Sci. Unit. States Am. 113 (34) (2016) E4976–E4984.

[14] M.T. Colvin, R. Silvers, Q.Z. Ni, T.V. Can, I. Sergeyev, M. Rosay, K.J. Donovan, B. Michael, J. Wall, S. Linse, R.G. Griffin, Atomic resolution structure of

monomorphic Aβ42 amyloid fibrils, J. Am. Chem. Soc. 138 (30) (2016) 9663–9674.

[15] D.T. Murray, M. Kato, Y. Lin, K.R. Thurber, I. Hung, S.L. McKnight, R. Tycko, Structure of FUS protein fibrils and its relevance to self-assembly and phase separation of low-complexity domains, Cell 171 (3) (2017), 615-627.e16.

[16] C. Wasmer, A. Lange, H. Van Melckebeke, A.B. Siemer, R. Riek, B.H. Meier, Amyloid fibrils of the HET-s(218-289) prion form a β−Solenoid with a triangular hydrophobic core, Science 319 (5869) (2008) 1523–1526.

[17] A.W.P. Fitzpatrick, B. Falcon, S. He, A.G. Murzin, G. Murshudov, H.J. Garringer, R.A. Crowther, B. Ghetti, M. Goedert, S.H.W. Scheres, Cryo-EM structures of tau filaments from Alzheimer's disease, Nature 547 (7662) (2017) 185–190.

[18] B. Falcon, W. Zhang, A.G. Murzin, G. Murshudov, H.J. Garringer, R. Vidal, R.A. Crowther, B. Ghetti, S.H.W. Scheres, M. Goedert, Structures of filaments from Pick's disease reveal a novel tau protein fold, Nature 561 (7721) (2018) 137–140.

[19] L. Gremer, D. Schölzel, C. Schenk, E. Reinartz, J. Labahn, R.B.G. Ravelli, M. Tusche, C. Lopez-Iglesias, W. Hoyer, H. Heise, D. Willbold, G.F. Schröder, Fibril structure of amyloid-β(1–42) by cryo−electron microscopy, Science 358 (6359) (2017) 116–119.

[20] K.-N. Hu, R. Tycko, What can solid state NMR contribute to our understanding of protein folding? Biophys. Chem. 151 (1–2) (2010) 10–21.

[21] A.B. Barnes, B. Corzilius, M.L. Mak-Jurkauskas, L.B. Andreas, V.S. Bajaj, Y. Matsuki, M.L. Belenky, J. Lugtenburg, J.R. Sirigiri, R.J. Temkin, J. Herzfeld, R.G. Griffin, Resolution and polarization distribution in cryogenic DNP/MAS experiments, Phys. Chem. Chem. Phys. 12 (22) (2010) 5861–5867.

[22] A.H. Linden, W.T. Franks, U. Akbey, S. Lange, B.J. van Rossum, H. Oschkinat, Cryogenic temperature effects and resolution upon slow cooling of protein preparations in solid state NMR, J. Biomol. NMR 51 (3) (2011) 283–292.

[23] D.L. Jakeman, D.J. Mitchell, W.A. Shuttleworth, J.N. Evans, Effects of sample preparation conditions on biomolecular solid-state NMR lineshapes, J. Biomol. NMR 12 (3) (1998) 417–421.

[24] A.B. Siemer, K.Y. Huang, A.E. McDermott, Protein linewidth and solvent dynamics in frozen solution NMR, PLoS One 7 (10) (2012), e47242.

[25] Y. Su, L. Andreas, R.G. Griffin, Magic angle spinning NMR of proteins: high-frequency dynamic nuclear polarization and 1H detection, Annu. Rev. Biochem. 84 (1) (2015) 465–497.

[26] A.S. Lilly Thankamony, J.J. Wittmann, M. Kaushik, B. Corzilius, Dynamic nuclear polarization for sensitivity enhancement in modern solid-state NMR, Prog. NMR Spectrosc. 102–103 (2017) 120–195.

[27] U. Akbey, H. Oschkinat, Structural biology applications of solid state MAS DNP NMR, J. Magn. Reson. 269 (2016) 213–224.

[28] E.J. Koers, E.A. van der Cruijsen, M. Rosay, M. Weingarth, A. Prokofyev, C. Sauvee, O. Ouari, J. van der Zwan, O. Pongs, P. Tordo, W.E. Maas, M. Baldus, NMR-based structural biology enhanced by dynamic nuclear polarization at high magnetic field, J. Biomol. NMR 60 (2–3) (2014) 157–168.

[29] J.H. Ardenkjaer-Larsen, G.S. Boebinger, A. Comment, S. Duckett, A.S. Edison, F. Engelke, C. Griesinger, R.G. Griffin, C. Hilty, H. Maeda, G. Parigi, T. Prisner, E. Ravera, J. van Bentum, S. Vega, A. Webb, C. Luchinat, H. Schwalbe, L. Frydman, Facing and overcoming sensitivity challenges in biomolecular NMR spectroscopy, Angew. Chem., Int. Ed. Engl. 54 (32) (2015) 9162–9185.

[30] K. Jaudzems, T. Polenova, G. Pintacuda, H. Oschkinat, A. Lesage, DNP NMR of biomolecular assemblies, J. Struct.l Biol. (2019), https://doi.org/10.1016/j.jsb.2018.09.011 in press.

[31] I.V. Sergeyev, B. Itin, R. Rogawski, L.A. Day, A.E. McDermott, Efficient assignment and NMR analysis of an intact virus using sequential side-chain correlations and DNP sensitization, Proc. Natl. Acad. Sci. Unit. States Am. 114 (20) (2017) 5171–5176.

[32] (*) R. Gupta, M. Lu, G. Hou, M.A. Caporini, M. Rosay, W. Maas, J. Struppe, C. Suiter, J. Ahn, I.-J.L. Byeon, W.T. Franks, M. Orwick-Rydmark, A. Bertarello, H. Oschkinat, A. Lesage, G. Pintacuda, A.M. Gronenborn, T. Polenova, Dynamic nuclear polarization enhanced MAS NMR for structural analysis of HIV-1 protein assemblies, J. Chem. Phys. 120 (2) (2016) 329–339.

* This work represents the DNP-enhanced NMR study of a large HIV-1 protein assembly. Additionally shows that the spectral line broadening effects have both homogeneous and inhomogeneous contributions.

[33] K. Jaudzems, A. Bertarello, S.R. Chaudhari, A. Pica, D. Cala-DePaepe, E. Barbet-Massin, A.J. Pell, I. Akopjana, S. Kotelovica, D. Gajan, O. Ouari, K. Tars, G. Pintacuda, A. Lesage, Dynamic nuclear polarization-enhanced biomolecular NMR spectroscopy at high magnetic field with fast magic-angle spinning, Angew. Chem. Int. Ed. 57 (25) (2018) 7458–7462.

[34] P. Fricke, J.P. Demers, S. Becker, A. Lange, Studies on the MxiH protein in T3SS needles using DNP-enhanced ssNMR spectroscopy, ChemPhysChem 15 (1) (2014) 57–60.

[35] P. Fricke, D. Mance, V. Chevelkov, K. Giller, S. Becker, M. Baldus, A. Lange, High resolution observed in 800 MHz DNP spectra of extremely rigid type III secretion needles, J. Biomol. NMR 65 (3) (2016) 121–126.

[36] T. Wang, Y.B. Park, M.A. Caporini, M. Rosay, L. Zhong, D.J. Cosgrove, M. Hong, Sensitivity-enhanced solid-state NMR detection of expansin's target in plant cell walls, Proc. Natl. Acad. Sci. U. S. A 110 (41) (2013) 16444–16449. S16444/1-S16444/12.

[37] A.W. Overhauser, Polarization of nuclei in metals, Phys. Rev. 92 (2) (1953) 411–415.

[38] T.R. Carver, C.P. Slichter, Polarization of nuclear spins in metals, Phys. Rev. 92 (1) (1953) 212–213.

[39] A.W. Overhauser, Paramagnetic relaxation in metals, Phys. Rev. 89 (4) (1953) 689–700.

[40] C.D. Jeffries, Polarization of nuclei by resonance saturation in paramagnetic crystals, Phys. Rev. 106 (1) (1957) 164–165.

[41] C.F. Hwang, D.A. Hill, New effect in dynamic polarization, Phys. Rev. Lett. 18 (4) (1967) 110–112.

[42] C.F. Hwang, D.A. Hill, Phenomenological model for the new effect in dynamic polarization, Phys. Rev. Lett. 19 (18) (1967) 1011–1014.

[43] M. Borghini, Spin-temperature model of nuclear dynamic polarization using free radicals, Phys. Rev. Lett. 20 (9) (1968) 419–421.

[44] K.-N. Hu, G.T. Debelouchina, A.A. Smith, R.G. Griffin, Quantum mechanical theory of dynamic nuclear polarization in solid dielectrics, J. Chem. Phys. 134 (12) (2011) 125105.

[45] M. Rosay, M. Blank, F. Engelke, Instrumentation for solid-state dynamic nuclear polarization with magic angle spinning NMR, J. Magn. Reson. 264 (2016) 88–98.

[46] G.J. Gerfen, L.R. Becerra, D.A. Hall, R.G. Griffin, R.J. Temkin, D.J. Singel, High frequency (140 GHz) dynamic nuclear polarization: polarization transfer to a solute in frozen aqueous solution, J. Chem. Phys. 102 (24) (1995) 9494.

[47] D.A. Hall, D.C. Maus, G.J. Gerfen, S.J. Inati, L.R. Becerra, F.W. Dahlquist, R.G. Griffin, Polarization-enhanced NMR spectroscopy of biomolecules in frozen solution, Science 276 (5314) (1997) 930–932.

[48] M. Rosay, A.C. Zeri, N.S. Astrof, S.J. Opella, J. Herzfeld, R.G. Griffin, Sensitivity-enhanced NMR of biological solids: dynamic nuclear polarization of Y21M fd bacteriophage and purple membrane, J. Am. Chem. Soc. 123 (5) (2001) 1010–1011.

[49] M. Rosay, V. Weis, K.E. Kreischer, R.J. Temkin, R.G. Griffin, Two-dimensional (13) C-(13)C correlation spectroscopy with magic angle spinning and dynamic nuclear polarization, J. Am. Chem. Soc. 124 (13) (2002) 3214–3215.

[50] M. Rosay, J.C. Lansing, K.C. Haddad, W.W. Bachovchin, J. Herzfeld, R.J. Temkin, R.G. Griffin, High-frequency dynamic nuclear polarization in MAS spectra of membrane and soluble proteins, J. Am. Chem. Soc. 125 (45) (2003) 13626–13627.

[51] M.L. Mak-Jurkauskas, V.S. Bajaj, M.K. Hornstein, M. Belenky, R.G. Griffin, J. Herzfeld, Energy transformations early in the bacteriorhodopsin photocycle revealed by DNP-enhanced solid-state NMR, Proc. Natl. Acad. Sci. U.S.A. 105 (3) (2008) 883–888.

[52] V.S. Bajaj, M.L. Mak-Jurkauskas, M. Belenky, J. Herzfeld, R.G. Griffin, Functional and shunt states of bacteriorhodopsin resolved by 250 GHz dynamic nuclear polarization-enhanced solid-state NMR, Proc. Natl. Acad. Sci. U. S. A 106 (23) (2009) 9244–9249. S9244/1-S9244/4.

[53] C. Song, K.N. Hu, C.G. Joo, T.M. Swager, R.G. Griffin, TOTAPOL: a biradical polarizing agent for dynamic nuclear polarization experiments in aqueous media, J. Am. Chem. Soc. 128 (35) (2006) 11385–11390.

[54] C. Sauvee, M. Rosay, G. Casano, F. Aussenac, R.T. Weber, O. Ouari, P. Tordo, Highly efficient, water-soluble polarizing agents for dynamic nuclear polarization at high frequency, Angew. Chem., Int. Ed. Engl. 52 (41) (2013) 10858–10861.

[55] G. Mathies, M.A. Caporini, V.K. Michaelis, Y. Liu, K.N. Hu, D. Mance, J.L. Zweier, M. Rosay, M. Baldus, R.G. Griffin, Efficient dynamic nuclear polarization at 800 MHz/527 GHz with trityl-nitroxide biradicals, Angew. Chem., Int. Ed. Engl. 54 (40) (2015) 11770–11774.

[56] D. Wisser, G. Karthikeyan, A. Lund, G. Casano, H. Karoui, M. Yulikov, G. Menzildjian, A.C. Pinon, A. Purea, F. Engelke, S.R. Chaudhari, D. Kubicki, A.J. Rossini, I.B. Moroz, D. Gajan, C. Copéret, G. Jeschke, M. Lelli, L. Emsley, A. Lesage, O. Ouari, BDPA-nitroxide biradicals tailored for efficient dynamic nuclear polarization enhanced solid-state NMR at magnetic fields up to 21.1 T, J. Am. Chem. Soc. 140 (41) (2018) 13340–13349.

[57] L.F. Pinto, I. Marín-Montesinos, V. Lloveras, J.L. Muñoz-Gómez, M. Pons, J. Veciana, J. Vidal-Gancedo, NMR signal enhancement of >50 000 times in fast dissolution dynamic nuclear polarization, Chem. Commun. 53 (26) (2017) 3757–3760.

[58] M. Kaushik, M. Qi, A. Godt, B. Corzilius, Bis-gadolinium complexes for solid effect and cross effect dynamic nuclear polarization, Angew. Chem., Int. Ed. Engl. 56 (15) (2017) 4295–4299.

[59] T.V. Can, M.A. Caporini, F. Mentink-Vigier, B. Corzilius, J.J. Walish, M. Rosay, W.E. Maas, M. Baldus, S. Vega, T.M. Swager, R.G. Griffin, Overhauser effects in insulating solids, J. Chem. Phys. 141 (6) (2014), 064202.

[60] M. Lelli, S.R. Chaudhari, D. Gajan, G. Casano, A.J. Rossini, O. Ouari, P. Tordo, A. Lesage, L. Emsley, Solid-state dynamic nuclear polarization at 9.4 and 18.8 T from 100 K to room temperature, J. Am. Chem. Soc. 137 (46) (2015) 14558–14561.

[61] S.R. Chaudhari, D. Wisser, A.C. Pinon, P. Berruyer, D. Gajan, P. Tordo, O. Ouari, C. Reiter, F. Engelke, C. Copéret, M. Lelli, A. Lesage, L. Emsley, Dynamic nuclear polarization efficiency increased by very fast magic angle spinning, J. Am. Chem. Soc. 139 (31) (2017) 10609–10612.

[62] C. Fernandez-de-Alba, H. Takahashi, A. Richard, Y. Chenavier, L. Dubois, V. Maurel, D. Lee, S. Hediger, G. De Paepe, Matrix-free DNP-enhanced NMR spectroscopy of liposomes using a lipid-anchored biradical, Chemistry 21 (12) (2015) 4512–4517.

[63] T. Maly, D. Cui, R.G. Griffin, A.F. Miller, 1H dynamic nuclear polarization based on an endogenous radical, J. Phys. Chem. B 116 (24) (2012) 7055–7065.

[64] A.N. Smith, M.A. Caporini, G.E. Fanucci, J.R. Long, A method for dynamic nuclear polarization enhancement of membrane proteins, Angew. Chem., Int. Ed. Engl. 54 (5) (2015) 1542–1546.

[65] H. Takahashi, I. Ayala, M. Bardet, G. De Paepe, J.P. Simorre, S. Hediger, Solid-state NMR on bacterial cells: selective cell wall signal enhancement and resolution improvement using dynamic nuclear polarization, J. Am. Chem. Soc. 135 (13) (2013) 5105–5110.

[66] E.A. van der Cruijsen, E.J. Koers, C. Sauvee, R.E. Hulse, M. Weingarth, O. Ouari, E. Perozo, P. Tordo, M. Baldus, Biomolecular DNP-supported NMR spectroscopy using site-directed spin labeling, Chemistry 21 (37) (2015) 12971–12977.

[67] V. Vitzthum, F. Borcard, S. Jannin, M. Morin, P. Mieville, M.A. Caporini, A. Sienkiewicz, S. Gerber-Lemaire, G. Bodenhausen, Fractional spin-labeling of polymers for enhancing NMR sensitivity by solvent-free dynamic nuclear polarization, ChemPhysChem 12 (16) (2011) 2929–2932.

[68] M.A. Voinov, D.B. Good, M.E. Ward, S. Milikisiyants, A. Marek, M.A. Caporini, M. Rosay, R.A. Munro, M. Ljumovic, L.S. Brown, V. Ladizhansky, A.I. Smirnov, Cysteine-specific labeling of proteins with a nitroxide biradical for dynamic nuclear polarization NMR, J. Phys. Chem. B 119 (32) (2015) 10180–10190.

[69] B.J. Wylie, B.G. Dzikovski, S. Pawsey, M. Caporini, M. Rosay, J.H. Freed, A.E. McDermott, Dynamic nuclear polarization of membrane proteins: covalently bound spin-labels at protein-protein interfaces, J. Biomol. NMR 61 (3–4) (2015) 361–367.

[70] E.S. Salnikov, S. Abel, G. Karthikeyan, H. Karoui, F. Aussenac, P. Tordo, B. Bechinger, O. Ouari, Dynamic nuclear polarization/solid-state NMR spectroscopy of membrane polypeptides: free-radical optimization for matrix-free lipid bilayer samples, ChemPhysChem 18 (15) (2017) 2103–2113.

[71] R. Rogawski, I.V. Sergeyev, Y. Li, M.F. Ottaviani, V. Cornish, A.E. McDermott, Dynamic nuclear polarization signal enhancement with high-affinity biradical tags, J. Phys. Chem. B 121 (6) (2017) 1169–1175.

[72] (*) T. Viennet, A. Viegas, A. Kuepper, S. Arens, V. Gelev, O. Petrov, T.N. Grossmann, H. Heise, M. Etzkorn, Selective protein hyperpolarization in cell lysates using targeted dynamic nuclear polarization, Angew. Chem., Int. Ed. Engl. 55 (36) (2016) 10746–10750.

* Approach for targeted and site-selective in-cell NMR spectroscopy in combination with DNP. By covalently attaching a radical to a ligand peptide, only the receptor for this ligand is selectively hyperpolarized.

[73] H. Takahashi, S. Hediger, G. De Paepe, Matrix-free dynamic nuclear polarization enables solid-state NMR 13C-13C correlation spectroscopy of proteins at natural isotopic abundance, Chem. Commun. (Camb) 49 (82) (2013) 9479–9481.

[74] E. Ravera, B. Corzilius, V.K. Michaelis, C. Rosa, R.G. Griffin, C. Luchinat, I. Bertini, Dynamic nuclear polarization of sedimented solutes, J. Am. Chem. Soc. 135 (5) (2013) 1641–1644.

[75] E. Ravera, B. Corzilius, V.K. Michaelis, C. Luchinat, R.G. Griffin, I. Bertini, DNP-enhanced MAS NMR of bovine serum albumin sediments and solutions, J. Phys. Chem. B 118 (11) (2014) 2957–2965.

[76] (*) M. Nagaraj, T.W. Franks, S. Saeidpour, T. Schubeis, H. Oschkinat, C. Ritter, B.J. van Rossum, Surface binding of TOTAPOL assists structural investigations of amyloid fibrils by dynamic nuclear polarization NMR spectroscopy, Chembiochem 17 (14) (2016) 1308–1311.

* A beautiful representation of the inverse effects of using large radical concentration in resolution. shows also that some radicals bind to fibrils, so there needs to be further optimization protocol for studying every single sample.

[77] R. Nelson, M.R. Sawaya, M. Balbirnie, A.O. Madsen, C. Riekel, R. Grothe, D. Eisenberg, Structure of the cross-[beta] spine of amyloid-like fibrils, Nature 435 (7043) (2005) 773–778.

[78] P.C.A. van der Wel, J.R. Lewandowski, R.G. Griffin, Solid-state NMR study of amyloid nanocrystals and fibrils formed by the peptide GNNQQNY from yeast prion protein Sup35p, J. Am. Chem. Soc. 129 (16) (2007) 5117–5130.

[79] P.C. van der Wel, K.N. Hu, J. Lewandowski, R.G. Griffin, Dynamic nuclear polarization of amyloidogenic peptide nanocrystals: GNNQQNY, a core segment of the yeast prion protein Sup35p, J. Am. Chem. Soc. 128 (33) (2006) 10840–10846.

[80] (*) G.T. Debelouchina, M.J. Bayro, P.C. van der Wel, M.A. Caporini, A.B. Barnes, M. Rosay, W.E. Maas, R.G. Griffin, Dynamic nuclear polarization-enhanced solid-state NMR spectroscopy of GNNQQNY nanocrystals and amyloid fibrils, Phys. Chem. Chem. Phys. 12 (22) (2010) 5911–5919.

* An in-depth investigation and analysis of DNP polarization transfer via spin diffusion into large peptide crystals and amyloid fibrils.

[81] (*) G.T. Debelouchina, M.J. Bayro, A.W. Fitzpatrick, V. Ladizhansky, M.T. Colvin, M.A. Caporini, C.P. Jaroniec, V.S. Bajaj, M. Rosay, C.E. MacPhee, M. Vendruscolo, W.E. Maas, C.M. Dobson, R.G. Griffin, Higher order amyloid fibril structure by MAS NMR and DNP spectroscopy, J. Am. Chem. Soc. 135 (51) (2013) 19237–19247.

* DNP NMR study focusing on the large-scale architecture of fibrils from an 11-residue peptide from transthyretin protein.

[82] A.W.P. Fitzpatrick, G.T. Debelouchina, M.J. Bayro, D.K. Clare, M.A. Caporini, V.S. Bajaj, C.P. Jaroniec, L. Wang, V. Ladizhansky, S.A. Müller, C.E. MacPhee, C.A. Waudby, H.R. Mott, A. De Simone, T.P.J. Knowles, H.R. Saibil, M. Vendruscolo, E.V. Orlova, R.G. Griffin, C.M. Dobson, Atomic structure and hierarchical assembly of a cross-β amyloid fibril, Proc. Natl. Acad. Sci. Unit. States Am. 110 (14) (2013) 5468–5473.

[83] C.P. Jaroniec, C.E. MacPhee, N.S. Astrof, C.M. Dobson, R.G. Griffin, Molecular conformation of a peptide fragment of transthyretin in an amyloid fibril, Proc. Natl. Acad. Sci. U. S. A 99 (26) (2002) 16748–16753.

[84] C.P. Jaroniec, C.E. MacPhee, V.S. Bajaj, M.T. McMahon, C.M. Dobson, R.G. Griffin, High-resolution molecular structure of a peptide in an amyloid fibril determined by magic angle spinning NMR spectroscopy, Proc. Natl. Acad. Sci. U. S. A 101 (3) (2004) 711–716.

[85] (*) M.J. Bayro, G.T. Debelouchina, M.T. Eddy, N.R. Birkett, C.E. MacPhee, M. Rosay, W.E. Maas, C.M. Dobson, R.G. Griffin, Intermolecular structure determination of amyloid fibrils with magic-angle spinning and dynamic nuclear polarization NMR, J. Am. Chem. Soc. 133 (35) (2011) 13967–13974.

* Application of different protein isotope labeling approaches to determine macromolecular arrangements within an amyloid fibril.

[86] J.R. Glover, A.S. Kowal, E.C. Schirmer, M.M. Patino, J.J. Liu, S. Lindquist, Self-seeded fibers formed by Sup35, the protein determinant of [PSI+], a heritable prion-like factor of S-cerevisiae, Cell 89 (5) (1997) 811–819.

[87] L. Li, S. Lindquist, Creating a protein-based element of inheritance, Science 287 (5453) (2000) 661–664.

[88] N. Luckgei, A.K. Schütz, L. Bousset, B. Habenstein, Y. Sourigues, C. Gardiennet, B.H. Meier, R. Melki, A. Böckmann, The conformation of the prion domain of Sup35 p in isolation and in the full-length protein, Angew. Chem. Int. Ed. 52 (48) (2013) 12741–12744.

[89] F. Shewmaker, D. Kryndushkin, B. Chen, R. Tycko, R.B. Wickner, Two prion variants of Sup35p have in-register parallel beta-sheet structures, independent of hydration, Biochemistry 48 (23) (2009) 5074–5082.

[90] Kendra K. Frederick, Galia T. Debelouchina, C. Kayatekin, T. Dorminy, Angela C. Jacavone, Robert G. Griffin, S. Lindquist, Distinct prion strains are defined by amyloid core structure and chaperone binding site dynamics, Chem. Biol. 21 (2) (2014) 295–305.

[91] Y. Ohhashi, Y. Yamaguchi, H. Kurahashi, Y.O. Kamatari, S. Sugiyama, B. Uluca, T. Piechatzek, Y. Komi, T. Shida, H. Müller, S. Hanashima, H. Heise, K. Kuwata, M. Tanaka, Molecular basis for diversification of yeast prion strain conformation, Proc. Natl. Acad. Sci. Unit. States Am. 115 (10) (2018) 2389–2394.

[92] A. Gorkovskiy, K.R. Thurber, R. Tycko, R.B. Wickner, Locating folds of the in-register parallel β-sheet of the Sup35p prion domain infectious amyloid, Proc. Natl. Acad. Sci. Unit. States Am. 111 (43) (2014) E4615–E4622.

[93] (*) K.K. Frederick, V.K. Michaelis, B. Corzilius, T.C. Ong, A.C. Jacavone, R.G. Griffin, S. Lindquist, Sensitivity-enhanced NMR reveals alterations in protein structure by cellular milieus, Cell 163 (3) (2015) 620–628.

* A beautiful representation of the power of structural biology by state-of-the-art DNP NMR, by sensitivity enhancement and proteins prepared in-vitro versus in cell lysate of the yeast prion Sup35NM.

[94] (*) K.K. Frederick, V.K. Michaelis, M.A. Caporini, L.B. Andreas, G.T. Debelouchina, R.G. Griffin, S. Lindquist, Combining DNP NMR with segmental and specific labeling to study a yeast prion protein strain that is not parallel in-register, Proc. Natl. Acad. Sci. U. S. A 114 (14) (2017) 3642–3647.

* Extension of work in ref.89, towards determination of more structural information. The study combines a crucial split-intein labeling technology, that converges structural possibilities from NMR distance restraints.

[95] J.M. Lopez del Amo, D. Schneider, A. Loquet, A. Lange, B. Reif, Cryogenic solid state NMR studies of fibrils of the Alzheimer's disease amyloid-beta peptide: perspectives for DNP, J. Biomol. NMR 56 (4) (2013) 359–363.

[96] T. Bauer, C. Dotta, L. Balacescu, J. Gath, A. Hunkeler, A. Bockmann, B.H. Meier, Line-broadening in low-temperature solid-state NMR spectra of fibrils, J. Biomol. NMR 67 (1) (2017) 51–61.

[97] U. Akbey, A.H. Linden, H. Oschkinat, High-temperature dynamic nuclear polarization enhanced magic-angle-spinning NMR, Appl. Magn. Reson. 43 (1–2) (2012) 81–90.

[98] F. Weirich, L. Gremer, E.A. Mirecka, S. Schiefer, W. Hoyer, H. Heise, Structural characterization of fibrils from recombinant human islet amyloid polypeptide by solid-state NMR: the central FGAILS segment is part of the β-sheet core, PLoS One 11 (9) (2016), e0161243.

[99] K.-N. Hu, W.-M. Yau, R. Tycko, Detection of a transient intermediate in a rapid protein folding process by solid-state nuclear magnetic resonance, J. Am. Chem. Soc. 132 (1) (2010) 24–25.

[100] S. Chimon, M.A. Shaibat, C.R. Jones, D.C. Calero, B. Aizezi, Y. Ishii, Evidence of fibril-like β-sheet structures in a neurotoxic amyloid intermediate of Alzheimer's β-amyloid, Nat. Struct. Mol. Biol. 14 (12) (2007) 1157–1164.

[101] B. Han, Y. Liu, S. Ginzinger, D. Wishart, SHIFTX2: significantly improved protein chemical shift prediction, J. Biomol. NMR 50 (1) (2011) 43–57.

[102] R.H. Havlin, R. Tycko, Probing site-specific conformational distributions in protein folding with solid-state NMR, Proc. Natl. Acad. Sci. U.S.A. 102 (9) (2005) 3284–3289.

[103] H. Heise, S. Luca, B.L. de Groot, H. Grubmüller, M. Baldus, Probing conformational disorder in neurotensin by two-dimensional solid-state NMR and comparison to molecular dynamics simulations, Biophys. J. 89 (3) (2005) 2113–2120.

[104] (*) B. Uluca, T. Viennet, D. Petrović, H. Shaykhalishahi, F. Weirich, A. Gönülalan, B. Strodel, M. Etzkorn, W. Hoyer, H. Heise, DNP-enhanced solid-state NMR at cryogenic temperatures: a tool to snapshot conformational ensembles of α-synuclein in different states, Biophys. J. 114 (7) (2018) 1614–1623, https://doi.org/10.1016/j.bpj.2018.02.011.

* Our study representing different αS conformational ensembles simultaneously. Broad-peaks are not always bad !, but may contain valuable information when tackled correctly.

[105] K.-N. Hu, R.H. Havlin, W.-M. Yau, R. Tycko, Quantitative determination of site-specific conformational distributions in an unfolded protein by solid-state nuclear magnetic resonance, J. Mol. Biol. 392 (4) (2009) 1055–1073.

[106] (*) S. Lange, W.T. Franks, N. Rajagopalan, K. Döring, M.A. Geiger, A. Linden, B.-J. van Rossum, G. Kramer, B. Bukau, H. Oschkinat, Structural analysis of a signal peptide inside the ribosome tunnel by DNP MAS NMR, Sci. Adv. 2 (8) (2016).

* A study of signal-peptide in intact ribosome tunnel, showing the pre-secreted protein conformations. A beautiful model system representing the uniqueness of DNP NMR approach.

[107] Y. Geiger, H.E. Gottlieb, U. Akbey, H. Oschkinat, G. Goobes, Studying the conformation of a silaffin-derived pentalysine peptide embedded in bioinspired silica using solution and dynamic nuclear polarization magic-angle spinning NMR, J. Am. Chem. Soc. 138 (17) (2016) 5561–5567.

[108] M. Hong, K. Jakes, Selective and extensive 13C labeling of a membrane protein for solid-state NMR investigations, J. Biomol. NMR 14 (1) (1999) 71–74.

[109] H. Heise, W. Hoyer, S. Becker, O.C. Andronesi, D. Riedel, M. Baldus, Molecular-level secondary structure, polymorphism, and dynamics of full-length α-synuclein fibrils studied by solid-state NMR, Proc. Natl. Acad. Sci. U.S.A. 102 (44) (2005) 15871–15876.

[110] T. Viennet, M.M. Wördehoff, B. Uluca, C. Poojari, H. Shaykhalishahi, D. Willbold, B. Strodel, H. Heise, A.K. Buell, W. Hoyer, M. Etzkorn, Structural insights from lipid-bilayer nanodiscs link α-Synuclein membrane-binding modes to amyloid fibril formation, Commun. Biol. 1 (1) (2018) 44.

[111] (*) A. Potapov, W.M. Yau, R. Ghirlando, K.R. Thurber, R. Tycko, Successive stages of amyloid-beta self-assembly characterized by solid-state nuclear magnetic resonance with dynamic nuclear polarization, J. Am. Chem. Soc. 137 (25) (2015) 8294–8307.

* A nice example of DNP NMR study on Aβ fibrils. Extends structural information towards different stages of fibrillation process.

[112] M. Kaplan, A. Cukkemane, G.C. van Zundert, S. Narasimhan, M. Daniels, D. Mance, G. Waksman, A.M. Bonvin, R. Fronzes, G.E. Folkers, M. Baldus, Probing a cell-embedded megadalton protein complex by DNP-supported solid-state NMR, Nat. Methods 12 (7) (2015) 649–652.

[113] M. Kaplan, S. Narasimhan, C. de Heus, D. Mance, S. van Doorn, K. Houben, D. Popov-Celeketic, R. Damman, E.A. Katrukha, P. Jain, W.J. Geerts, A.J. Heck, G.E. Folkers, L.C. Kapitein, S. Lemeer, P.M. van Bergen En Henegouwen, M. Baldus, EGFR dynamics change during activation in native membranes as revealed by NMR, Cell 167 (5) (2016), 1241-1251 e11.

[114] T. Jacso, W.T. Franks, H. Rose, U. Fink, J. Broecker, S. Keller, H. Oschkinat, B. Reif, Characterization of membrane proteins in isolated native cellular membranes by dynamic nuclear polarization solid-state NMR spectroscopy without purification and reconstitution, Angew. Chem., Int. Ed. Engl. 51 (2) (2012) 432–435.

[115] M. Renault, S. Pawsey, M.P. Bos, E.J. Koers, D. Nand, R. Tommassen-van Boxtel, M. Rosay, J. Tommassen, W.E. Maas, M. Baldus, Solid-state NMR spectroscopy on cellular preparations enhanced by dynamic nuclear polarization, Angew. Chem., Int. Ed. Engl. 51 (12) (2012) 2998–3001.

[116] K. Yamamoto, M.A. Caporini, S.C. Im, L. Waskell, A. Ramamoorthy, Cellular solid-state NMR investigation of a membrane protein using dynamic nuclear polarization, Biochim. Biophys. Acta 1848 (1 Pt B) (2015) 342–349.

[117] B.J. Albert, C. Gao, E.L. Sesti, E.P. Saliba, N. Alaniva, F.J. Scott, S.T. Sigurdsson, A.B. Barnes, Dynamic nuclear polarization nuclear magnetic resonance in human cells using fluorescent polarizing agents, Biochemistry 57 (31) (2018) 4741–4746.

[118] E. Luchinat, L. Banci, In-cell NMR: a topical review, IUCrJ 4 (2) (2017) 108–118.

[119] D.J. Kubicki, G. Casano, M. Schwarzwälder, S. Abel, C. Sauvée, K. Ganesan, M. Yulikov, A.J. Rossini, G. Jeschke, C. Copéret, A. Lesage, P. Tordo, O. Ouari, L. Emsley, Rational design of dinitroxide biradicals for efficient cross-effect dynamic nuclear polarization, Chem. Sci. 7 (1) (2016) 550–558.

[120] E. Ravera, C. Luchinat, G. Parigi, Basic facts and perspectives of Overhauser DNP NMR, J. Magn. Reson. 264 (2016) 78–87.

[121] U. Akbey, W.T. Franks, A. Linden, S. Lange, R.G. Griffin, B.J. van Rossum, H. Oschkinat, Dynamic nuclear polarization of deuterated proteins, Angew. Chem. Int. Ed. 49 (42) (2010) 7803–7806.

[122] M.A. Geiger, M. Orwick-Rydmark, K. Marker, W.T. Franks, D. Akhmetzyanov, D. Stoppler, M. Zinke, E. Specker, M. Nazare, A. Diehl, B.J. van Rossum, F. Aussenac, T. Prisner, U. Akbey, H. Oschkinat, Temperature dependence of cross-effect dynamic nuclear polarization in rotating solids: advantages of elevated temperatures, Phys. Chem. Chem. Phys. 18 (44) (2016) 30696–30704.

[123] E.P. Saliba, E.L. Sesti, F.J. Scott, B.J. Albert, E.J. Choi, N. Alaniva, C. Gao, A.B. Barnes, Electron decoupling with dynamic nuclear polarization in rotating solids, J. Am. Chem. Soc. 139 (18) (2017) 6310–6313.

[124] T. Maly, G.T. Debelouchina, V.S. Bajaj, K.N. Hu, C.G. Joo, M.L. Mak-Jurkauskas, J.R. Sirigiri, P.C.A. van der Wel, J. Herzfeld, R.J. Temkin, R.G. Griffin, Dynamic nuclear polarization at high magnetic fields, J. Chem. Phys. 128 (5) (2008), 052211.

[125] G. Mathies, S. Jain, M. Reese, R.G. Griffin, Pulsed dynamic nuclear polarization with trityl radicals, J. Phys. Chem. Lett. 7 (1) (2016) 111–116.